
# UNIVERSIDAD DE JAÉN

**ESCUELA POLITÉCNICA SUPERIOR DE JAÉN**
**DEPARTAMENTO DE INGENIERÍA GRÁFICA, DISEÑO Y PROYECTOS**


**TESIS DOCTORAL**

# PROCEDIMIENTO PARA EL ANÁLISIS AUTOMATIZADO DE LA MANUFACTURA DE LA PIEZA DE PLÁSTICO Y DEL MOLDE DE INYECCIÓN


**PRESENTADA POR:**
**JORGE MANUEL MERCADO COLMENERO**

**DIRIGIDA POR:**
**DRA. DÑA. CRISTINA MARTÍN DOÑATE**
**DR. D. MIGUEL ÁNGEL RUBIO PARIMIO**


**JAÉN, 3 DE MAYO DE 2019**


**ISBN 978-84-9159-263-1**

# UNIVERSIDAD DE JAÉN


# TESIS DOCTORAL

PROCEDIMIENTO PARA EL ANÁLISIS AUTOMATIZADO DE LA MANUFACTURA DE LA PIEZA DE PLÁSTICO Y DEL MOLDE DE INYECCIÓN

AUTOR

**Jorge Manuel Mercado Colmenero**

DIRECTORA

**Dra. Dª. Cristina Martín Doñate**

CO-DIRECTOR

**Dr. D. Miguel Ángel Rubio Paramio**

TUTOR

**Dr. D. Julio Terrados Cepeda**

DEPARTAMENTO DE INGENIERÍA GRÁFICA, DISEÑO Y PROYECTOS

JAÉN, DICIEMBRE 2018

# UNIVERSIDAD DE JAÉN

# TESIS DOCTORAL

PROCEDIMIENTO PARA EL ANÁLISIS AUTOMATIZADO DE LA MANUFACTURA DE LA PIEZA DE PLÁSTICO Y DEL MOLDE DE INYECCIÓN

# TRIBUNAL EVALUADOR

**Presidente:**

**Secretario:**

**Vocal:**

**Suplente:**

**Suplente:**

# UNIVERSIDAD DE JAÉN

## DEPARTAMENTE DE INGENIERÍA GRÁFICA, DISEÑO Y PROYECTOS

INGENIERÍA GRÁFICA, DISEÑO Y PROYECTOS

# TESIS DOCTORAL

La memoria titulada: "**Procedimiento para el análisis automatizado de la manufactura de la pieza de plástico y del molde de inyección**" ha sido presentada por el aspirante a doctor por la universidad de Jaén D. Jorge Manuel Mercado Colmenero, bajo la dirección de la Dra. Dª. Cristina Martín Doñate y el Dr. D. Miguel Ángel Rubio Paramio y desarrollada dentro del Departamento de Ingeniería Gráfica, Diseño y Proyectos de la Universidad de Jaén y del grupo de Investigación y Desarrollo en Ingeniería Gráfica, Diseño Industrial y SIG (TIC-159)

JAÉN, DICIEMBRE 2018

El doctorando

Fdo. Jorge Manuel Mercado Colmenero

Directora de Tesis

Fdo. Dra. Dª. Cristina Martín Doñate

Co – Director de Tesis

Fdo. Dr. D. Miguel Ángel Rubio Paramio

# AGRADECIMIENTOS

Quiero reconocer a mi directora y codirector de tesis, Cristina Martín Doñate y Miguel Ángel Rubio Paramio, la atención, dedicación y, especialmente, la confianza depositada en mí. La cual espero que, a lo largo de estos años de trabajo, hayan visto correspondida. Los consejos, pautas y lecciones que han compartido conmigo durante este tiempo han resultado muy enriquecedores en el ámbito científico, académico y también en el personal.

Esta tesis se ha visto respaldada, inestimablemente, por los trabajos de investigación realizados por parte de mis directores de tesis, previos a mi incorporación. Pues la presente tesis doctoral es una continuación de los trabajos de investigación y tesis doctorales de Cristina Martín Doñate y Miguel Ángel Rubio Paramio. Asimismo, quiero mostrar mi agradecimiento a mis compañeros Abelardo Torres Alba, Juan Manuel Montalvo, Francisco Javier Gallego Álvarez, José Valderrama Zafra, Julio Terrados Cepeda y Daniel Díaz Perete, por el acogimiento y ayuda desinteresada. Sin olvidar, y haciendo una especial mención a la visión del director del departamento de Ingeniería Gráfica, Diseño y Proyectos, Miguel Ángel Rubio Paramio y de la directora del grupo de investigación "TIC159: Investigación y desarrollo en Ingeniería Gráfica, Diseño Industrial y SIG" Cristina Martín Doñate, el conocimiento científico generado ha asentado la base sólida de un respetable y riguroso grupo de investigación.

Hago extensibles mis agradecimientos al resto del profesorado, trabajadores y colaboradores del Departamento de Ingeniería Gráfica, Diseño y Proyectos por su amable y generosa acogida. A Julio Terrados Cepeda por la labor de tutor que ha realizado y la ayuda prestada para formar parte del programa de doctorado donde se enmarca la presente tesis. A Antonio Sierra Martín por su disposición, ayuda desinteresada y palabras de ánimo que siempre me ha brindado. A los colaboradores y personal contratado que me han acompañado durante todo este tiempo en el seminario A3-203. A la Universidad de Jaén y la Junta de Andalucía por la concesión del proyecto de investigación "A vertical design software for integrating operations of automated demoldability, tooling design and cost estimation in injection molded plastic parts. (CELERMOLD)" (Project Code TI-12 TIC 1623), a partir del cual comencé mi vinculación con el citado departamento. Y a la Escuela de Doctorado de la Universidad de Jaén por concederme la Ayuda EDUJA para la realización de estancia para la obtención de Mención Internacional, la cual ha permitido complementar mi formación científica con una estancia de investigación en el extranjero.

I would like to mention Annalisa Di Roma and Vincenzo Minenna for the attention, supervision and kind reception they offered me in the DICAR during my period of research stay at the Politecnico di Bari. Thanks to Katia Casavola and Giovanni Pappelettera for assisting me in the Mechanical, Mathematical and Management Department, to share their knowledge and help us in the experimental tests. I would like to extend my acknowledgments to Vitanguelo Ardito for his selfless help. Grazie mille.

Quiero extender mi más profundo agradecimiento a Sara Molina, Ángel Molina, Gabino Jiménez, Manuel Lorite y, en definitiva, a todos mis amigos por toda la ayuda, palabras de ánimo, apoyo y consejos que me han dedicado y que han sido tan necesarios en los momentos difíciles. Por último, y no por ello menos importante, mención especial para toda mi familia, y en concreto mis abuelos, Dolores – Salvador y María Francisco, mis padres, Carmen y Manuel, y mi hermana, Rocío. Todo lo que soy es gracias a ellos.

# RESUMEN

El proceso de manufactura mediante moldes de inyección de plástico es uno de los métodos de producción más versátiles y extendidos para la fabricación de piezas de plástico en cualquier ámbito de la ingeniería. Esencialmente, un molde de inyección de plástico es un conjunto mecánico, compuesto por dos regiones principales (parte fija y parte móvil), diseñado para fabricar piezas de plástico que presenten requerimientos de alta precisión dimensional y calidad superficial en regiones con geometrías complejas y superficies libres. La transformación, cambio de fase y adaptación del material termoplástico fundido a la topología de la pieza final se divide en cuatro fases principales: llenado, compactación, refrigeración y expulsión. De forma que, los sistemas y los elementos mecánicos principales que conforman el molde de inyección se encargan de calibrar y ejecutar cada uno de los procesos que definen a estas fases del ciclo de manufactura. Por ello, el diseño de cada uno de los sistemas principales del molde de inyección es un factor que determina la calidad del producto final, así como la magnitud de las variables económicas que conforman el presupuesto final de todo el conjunto del proceso de fabricación

Actualmente, existe una amplia variedad de sistemas y software de tipo CAD/CAE para el análisis y diseño asistido de la pieza de plástico y los diferentes sistemas del molde de inyección. Sin embargo, las herramientas comerciales desarrolladas hasta la fecha requieren una importante interacción humana por parte del usuario, y por ende amplia experiencia laboral en este proceso de manufactura. Por otro lado, estas metodologías de análisis requieren el acceso a información geométrica y topológica de la pieza vinculada al modelador CAD donde fue realizada, reduciendo la precisión de análisis durante el proceso y, en ocasiones, requiriendo un hardware específico adicional para su resolución.

Para mejorar y optimizar el proceso actual de análisis, diseño y dimensionamiento de la pieza de plástico y del molde de inyección, se propone una metodología basada en algoritmos automatizados de tipo geométrico y experto que no requieran la interacción manual por parte del usuario. En primer lugar, un algoritmo para el análisis de la desmoldeabilidad de la pieza de plástico permite determinar el diseño de los elementos principales que conforman las partes fijas y móviles del molde de inyección. A continuación, un conjunto de algoritmos, que, en base a los resultados del algoritmo de análisis de la desmoldeabilidad, establezcan la distribución, dimensionamiento y diseño óptimo del sistema de expulsión y refrigeración del molde de inyección. Y, por último, un algoritmo que permita determinar con precisión el tiempo de ciclo asociado a las diferentes fases que conforman el ciclo de manufactura de la pieza de plástico analizada. Todo ello, optimiza y reduce el tiempo y coste asociados a las fases iniciales de diseño, modelado CAD, estimación de costes y validación numérica mediante simulaciones de tipo CAE de la pieza de plástico y el molde de inyección.

Asimismo, los algoritmos incluidos en la presente metodología parten de un modelo discreto de la geometría de la pieza de plástico. Es decir, un modelo estructurado formado por elementos notables como son nodos (puntos en el espacio con información acerca de sus coordenadas cartesianas) y facetas poligonales (con información acerca de los nodos que la definen), que determinan la topología de la pieza de plástico objeto de estudio.

Todo ello, hace posible establecer una independencia respecto al modelador CAD donde se genere la geometría de la pieza de plástico. Siendo posible la extensión del conjunto de algoritmos que conforman la presente metodología a cualquier lenguaje de programación.

La metodología desarrollada en los algoritmos incluidos en la presente tesis doctoral plantea soluciones a problemas no resueltos en el entorno del sector industrial del molde de inyección plástico. Y contribuyen a la automatización y optimización de las operaciones principales de análisis, diseño y dimensionamiento de piezas de plásticos y moldes de inyección. Asimismo, y dado que la presente tesis doctoral se enmarca en un programa de doctorado en Energías Renovables, se presenta el diseño de un nuevo producto híbrido, fabricado en material plástico, basado en la adaptación geométrica de una nueva hélice eólica de tipo Savonius para prototipos o productos ya existentes. Este nuevo concepto de eco-diseño sostenible de productos permite la autonomía energética de los mismos o la generación y almacenamiento de energía eléctrica para consumo doméstico o industrial, a partir de la transformación de la energía cinética de las corrientes de viento.

# ABSTRACT

Plastic injection molding is one of the most versatile and widespread manufacturing process for the plastic parts manufacture in any engineering field. Essentially, a plastic injection mold is a mechanical assembly, which is made up of two main regions (fixed part and moving part), designed to manufacture plastic parts with requirements of high dimensional accuracy and surface quality in regions with complex geometric features and freeform surfaces. The transformation, phase change and adaptation of the melt thermoplastic material to the topology of the final part is divided into four main phases: filling, packing, cooling and ejection. Thus, the main mechanical systems and elements, that define the injection mold, carry out the calibration and execution each of the processes that define these phases of the manufacturing cycle. Therefore, the injection mold main systems design is a factor that determines the quality of the final product, as well as the magnitude of the economic variables that establish the final cost of the whole manufacturing process.

Nowadays, there is a wide variety of CAD/CAE type systems and software for the analysis and aided design of the plastic part and the injection molding systems. However, the commercial tools developed so far require an important human interaction on the part of the user, and therefore wide work experience in this manufacturing process. On the other hand, these analysis methodologies require access to geometric and topological information of the plastic part linked to the CAD software where it was defined, reducing the analysis accuracy during the process and, sometimes, requiring additional specific hardware for its resolution.

In order to improve and optimize the current process of the plastic part analysis and design of the injection mold, a new methodology based on automated geometrical and expert algorithms that do not require manual interaction by the user is proposed. Firstly, an algorithm for the analysis of the demoldability of the plastic part allows to determine the design of the main elements that shape the cavity and core plates of the injection mold. Then, a set of algorithms, which, based on the results of the demoldability analysis algorithm, establish the layout, dimensioning and optimal design of the ejection and cooling system of the injection mold. And, finally, an algorithm that allows to define with high accuracy the cycle time associated with the manufacture of the analyzed plastic part. All this optimizes and reduces the time and costs associated with the initial phases of design, CAD modeling, cost estimation and numerical validation using CAE software of the plastic part and the injection mold.

Additionally, the included algorithms in the present methodology start from a discrete model of the plastic part geometry. That is to say, a structured model formed by notable elements such as nodes (3D points with information about their Cartesian coordinates) and polygonal facets (with information about the nodes that define it), which establish the topology of the plastic part case studies. This allows to establish an independence from the CAD software where the geometry of the plastic part is generated. Enabling to extend the set of algorithms that shape the present methodology in any programming language.

The methodology developed in the algorithms approached in this PhD thesis propose solutions to unsolved problems, currently, in the environment of the plastics industry. And they contribute to the automation and optimization of the main operations of analysis and design of plastic parts and injection molds.

Likewise, since the PhD doctoral thesis belongs to a PhD program in Renewable Energies, the design of a new hybrid product is presented, manufactured in plastic material, based on the geometric adaptation of a Savonius type wind rotor for prototypes or existing products. This new concept of sustainable eco-design of product allows the energy autonomy of it or even the generation and storage of electric energy for domestic or industrial consumption, from the transformation of the kinetic energy of the wind flows.

# TABLA DE CONTENIDOS

# ESTRUCTURA DE LA MEMORIA

La memoria de la presente tesis doctoral se estructura en dos partes principales. La primera de ellas, presenta una introducción, descripción de los objetivos de carácter investigador que se proponen para el desarrollo de la tesis, una justificación y alcance de la misma enmarcada en un sector industrial estratégico para la provincia de Jaén como es la manufactura mediante moldes de inyección de plástico, una exposición de la generación y publicación del conocimiento vinculado a cada uno de los trabajos de investigación desarrollados para la consecución de la presente tesis y una breve descripción de los resultados obtenidos. Por último, se exponen los resultados y las principales conclusiones alcanzadas, y se proponen las líneas de investigación futuras que serán abordadas en base al trabajo de investigación realizado.

La segunda parte del presente documento se estructura como un compendio de seis artículos de investigación. De los cuales cinco de ellos se encuentran publicados en revistas científicas de alto impacto y calidad reconocida, indexadas en las bases de datos bibliográficas y bibliométricas ISI JCR (Journal Citation Reports), ISI WOS (Web of Science) e ISIS Scopus. La publicación restante es del tipo Proceeding Paper y se encuentra indexada en las bases de datos bibliográfica y bibliométrica ISI WOS (Web of Science) y Scopus. Dichas aportaciones se han generado en el área del conocimiento donde se enmarca la presente tesis doctoral y conforme a la normativa de la Universidad de Jaén para la defensa de tesis doctorales (Extracto de los artículos del reglamento de estudio de doctorado de la Universidad de Jaén adaptada a las directrices del R.D. 99/2011 y aprobado en Consejo de Gobierno el 6 de febrero de 2012). Asimismo, se citan cuatro aportaciones relevantes en congresos internacionales, cuatro patentes de invención de ámbito nacional y una patente de invención internacional llevadas a cabo durante la etapa de desarrollo de la presente tesis doctoral.

# CAPÍTULO I: MEMORIA

En esta parte de la presente tesis doctoral se realiza una introducción al proceso de manufactura mediante moldes de inyección de plástico. Se describen las fases principales que definen el ciclo de manufactura de la pieza de plástico, los sistemas principales que conforman el molde de inyección y el estado del arte actual en cuanto al diseño y dimensionamiento de éstos. Análogamente, se exponen los principales inconvenientes que se suceden durante dicha etapa de diseño y dimensionamiento de la pieza de plástico y moldes de inyección. Las dificultades y problemas relacionados con la etapa de diseño y dimensionamiento de los elementos principales que conforman el molde de inyección hacen que el avance en la investigación de este sector industrial represente una ventaja competitiva y un valor añadido para el mismo. Por ende, el objetivo del trabajo de investigación desarrollado se centra en la generación de nuevas metodologías y algoritmos de tipo geométrico – experto que se encarguen de automatizar y sistematizar el proceso de diseño y dimensionamiento de los sistemas principales del molde de inyección. Asimismo, se establecen los conceptos básicos en los que se basa la metodología de los algoritmos desarrollados en la presente tesis, junto a la descripción de un caso de estudio, en el cual se aplica todo el conocimiento generado. Dado que la presente tesis doctoral se enmarca en el programa de doctorado de Energías Renovables, en este caso de estudio se adapta la geometría de una nueva hélice de eje vertical de tipo Savonius en el diseño de un nuevo producto fabricado en plástico biodegradable PLA. Este concepto de producto supone un nuevo reto dentro del área del conocimiento de diseño de producto, pues se incluyen requerimientos en términos de eco-diseño, sostenibilidad y ahorro energético que deben ser compatibles con los requerimientos predefinidos de tipo estético, ergonómico y funcional. Finalmente, se especifica el objetivo final y los objetivos intermedios planteados para la realización de la presente tesis doctoral y se presentan los resultados y conclusiones obtenidos en el desarrollo de las metodologías desarrolladas, así como se identifican las futuras líneas de investigación que surgen con la finalización de la presente tesis doctoral.

# 1.1. INTRODUCCIÓN

En la actualidad, el proceso de manufactura mediante moldes de inyección de plástico es uno de los métodos de fabricación más extendidos en el sector industrial del plástico. Un molde de inyección es un sistema de mecánico de alta precisión, diseñado para moldear piezas de plástico con geométrica compleja y superficies libres. El proceso de moldeo por inyección se basa en la transformación y adaptación del plástico fundido a la geometría de la pieza de final. Durante este proceso, se deben cumplir los requerimientos funcionales y de diseño de la pieza (alta precisión dimensional y calidad superficial en el resultado final), los sistemas que conforman el molde de inyección deben tolerar numerosos ciclos de inyección y el tiempo de ciclo obtenido durante el proceso debe ser reducido. Por lo general, dichos requerimientos vienen determinados por el diseño del molde de inyección. Siendo éste un factor determinante a la hora de obtener una calidad alta del producto final y una óptima eficiencia durante el proceso de su fabricación. Además, en la mayoría de los casos, el diseño del molde de inyección determina la magnitud final de las variables económicas que conforman el presupuesto de todo el conjunto del proceso de fabricación.

Sin embargo, el diseño de los sistemas principales del molde de inyección aún se realiza de manera empírica. Es decir, en base a la experiencia de los diseñadores de moldes de inyección profesionales. Asimismo, el proceso de diseño, modelado y dimensionamiento de los componentes que conforman los sistemas principales del molde de inyección requiere ingenieros altamente cualificados en el diseño asistido por ordenador para la representación CAD del molde de inyección, el análisis reológico de los materiales termoplásticos, análisis mecánico de los componentes estructurales del molde de inyección y análisis térmico de los elementos principales del sistema refrigeración del molde de inyección. Implicando, a su vez, que los diseñadores de moldes de inyección adquieran competencias profesionales en softwares específicos de diseño tipo CAD y simulación numérica tipo CAE.

Esencialmente, un molde de inyección está compuesto por dos regiones principales (véase Fig.1), denominadas parte móvil (“Cavity”) y parte fija (“Core”). En el diseño CAD de dichas regiones del molde de inyección los principales parámetros que determinan la estructura y geometría del molde son: la dirección principal de desmoldeo [1-3], las superficies o regiones de la pieza de plástico que desmoldean a partir de la parte fija y móvil del molde [4], la presencia de superficies o regiones desmoldeables mediante mecanismos auxiliarles o correderas [5,6], y la línea de partición que genera la división de la superficie total de la pieza de plástico en superficies que desmoldean mediante la parte fija del molde y superficies que desmoldean mediante la parte móvil del molde [7].

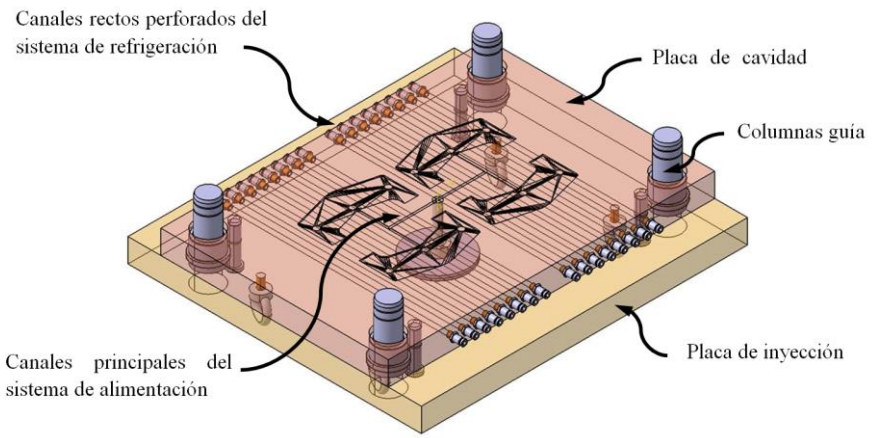

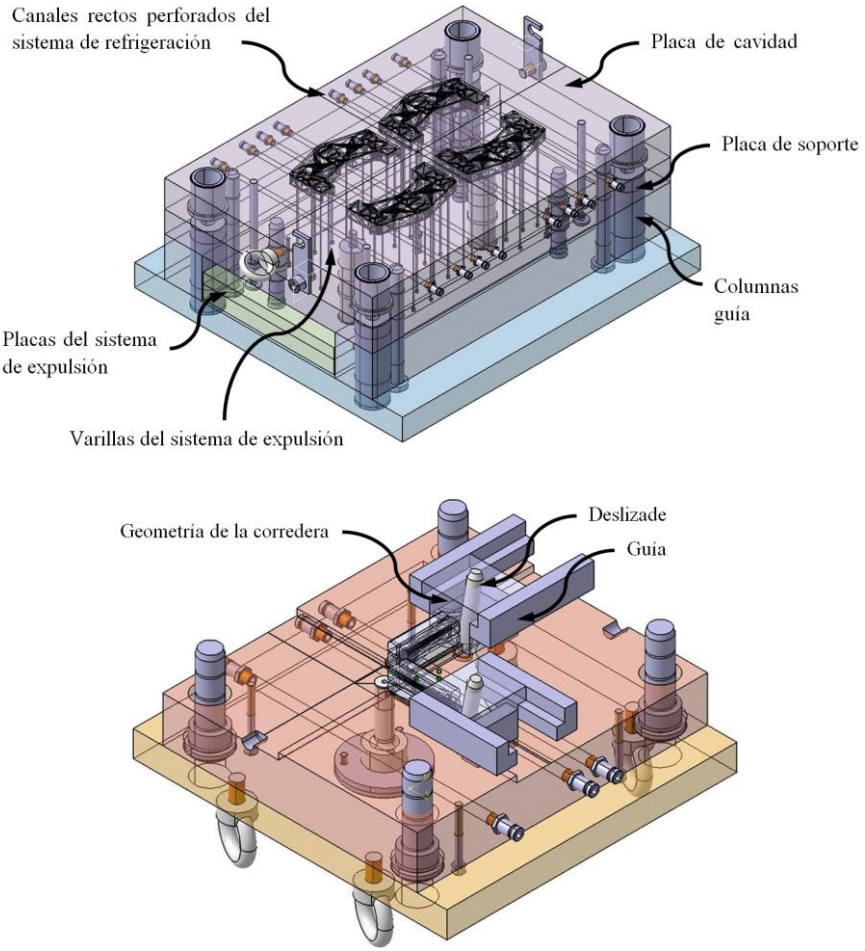


*Fig.1.- A) Parte fija del molde. B) Parte móvil del molde. C) Mecanismo auxiliares de desmoldeo (Correderas).*

Por ende, un análisis de la desmoldeabilidad [8] de la pieza de plástico a modelar (véase Fig.2) que determine dichos parámetros y regiones geométricas a partir de la dirección de desmoldeo y la geometría de la misma, puede resultar de gran ayuda para los diseñadores CAD durante las primeras fases de diseño del molde de inyección. Además, la detección de superficies de la pieza de plástico que requieran mecanismos auxiliares para su desmoldeo (véase Fig.1) es un factor determinante en el diseño del molde de inyección [9,10]. Pues aumenta la complejidad, el coste y tiempo empleado en la manufactura del mismo y de la producción final.

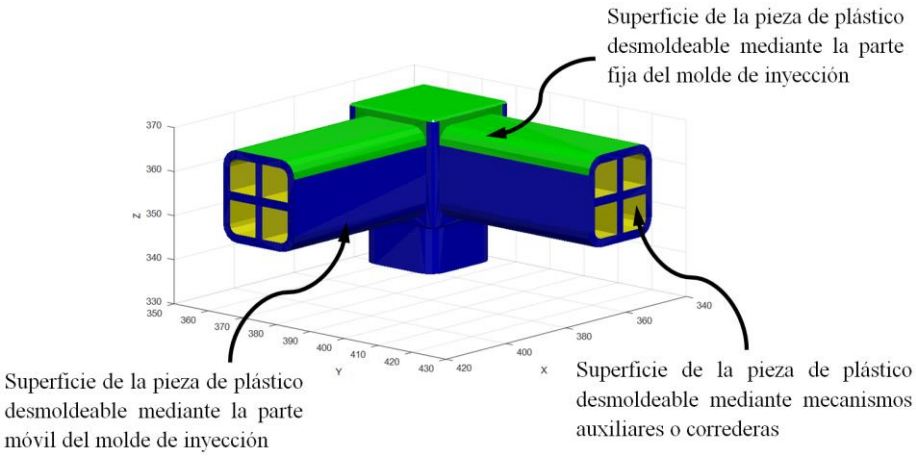


*Fig.2.- Resultado del análisis de la desmoldeabilidad de la pieza de plástico.*

Durante la fase conceptual del proceso de diseño de la pieza de plástico, ésta suele sufrir, en la mayoría de los casos, cambios en sus requerimientos geométricos y estéticos [11,12]. Para cada cambio efectuado sobre la geometría de la pieza, la desmoldeabilidad de la misma debe ser evaluada rápidamente, para detectar si ese cambio ha provocado que superficies de la pieza no puedan ser desmoldeadas de manera directa (Es decir, requieran mecanismos auxiliares para su desmoldeo) o incluso que no puedan ser desmoldeadas. Además, en la elaboración de un presupuesto inicial para determinar el coste de manufactura de una pieza de plástico, una evaluación precisa y rápida de la geometría y desmoldeabilidad de la misma puede ser un factor determinante a la hora de alcanza contratos, convenios y proyectos con proveedores, fabricante o clientes del sector industrial del plástico.

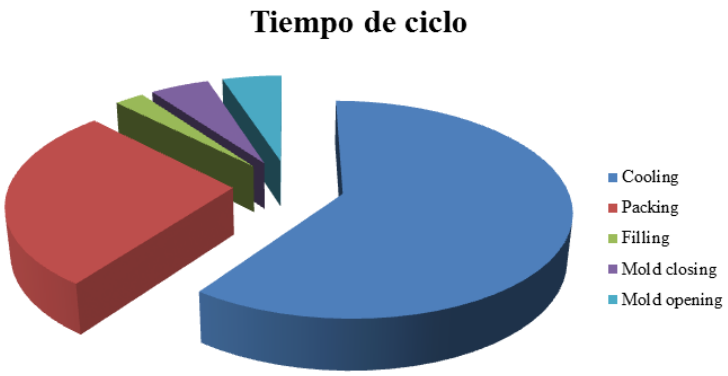


*Fig.3.- Representación porcentual estimada del tiempo empleado en cada una de las fases del ciclo de inyección de plástico.*

Por otro lado, la presente tesis abarca, no solo diseño de las regiones más importantes del molde de inyección (como son la parte fija y parte móvil), sino que también se centra el diseño y dimensionamiento de otros sistemas con una importancia relevante en cuanto a la calidad y precisión dimensional final de la pieza de plástico. Entre los que destacan: el sistema de expulsión de la pieza de plástico y el sistema de refrigeración del molde de inyección. Atendiendo a las diferentes fases que conforman el tiempo de ciclo del proceso de inyección de plásticos (véase Fig.3) [13], cabe destacar que la fase de refrigeración es la aquella que más se prolonga en el tiempo y que por ende que mayor influencia tiene sobre el tiempo final necesario para fabricar una pieza mediante inyección de plástico [14]. Una vez que se completa el llenado de la cavidad del molde y el proceso de compactación del plástico fundido, comienza la fase de refrigeración [15-20]. Por lo general, la duración de un tiempo de ciclo estándar en la industria del plástico no es suficiente para disipar el calor aportado por el frente de plástico fundido a través el material metálico del molde de inyección. Por ello, los moldes de inyección cuentan un conjunto canales con geometría uniforme y homogéneamente repartidos a lo largo de la parte fija y móvil del molde (véase Fig.1) [21-23], en cuales un fluido refrigerante se desarrolla en régimen turbulento, permitiendo mejorar el intercambio térmico con el frente de plástico fundido y por ende mejorar la eficiencia de la fase de refrigeración [24].

Actualmente, existen diferentes soluciones para el diseño de los canales de refrigeración de un molde de inyección [25-27] (véase Fig.4). La selección y definición de este diseño depende de tres factores: las características geométricas de la pieza de plástico, el tamaño y volumen de las partes principales (fija y móvil) del molde de inyección y la tecnología de fabricación empleada para dichas partes. De acuerdo a estos factores, los sistemas de refrigeración pueden clasificarse como sistemas convencionales, definidos por canales rectos perforados fabricados mediante técnicas de manufactura convencionales, y sistemas de tipo conformal, definidos por canales adaptados a la topología de la pieza de plástico y fabricados mediante técnicas de manufactura aditiva e impresión 3D (véase Fig.4) [28].

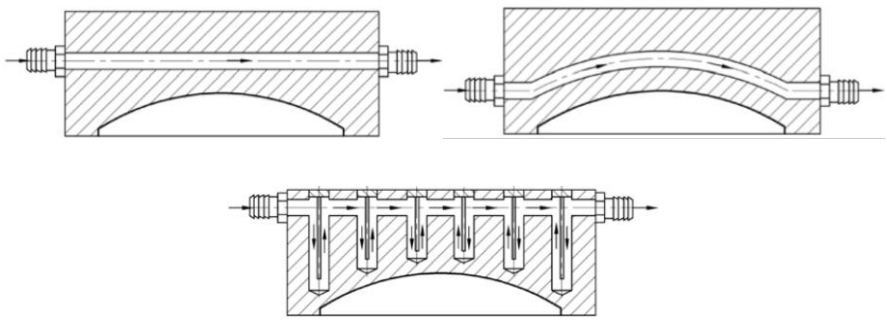

*Fig.4.- A) Canales rectos perforados. B) Canales tipo conformal. C) Elementos auxiliares convencionales tipo conformal (baffles).*

Tal y como se intuye, los sistemas de refrigeración convencionales presentan la ventaja de tener asociado un coste de fabricación más reducido, dado que únicamente requieren técnicas tradicionales de mecanizado. Sin embargo, la aplicación de estos sistemas de refrigeración se limita a regiones de la pieza de plástico esbeltas, con geometrías planas y sin concavidades profundas. Por el contrario, los sistemas de refrigeración de tipo conformal se adaptan mejor a la topología de la pieza de plástico, pues permiten mantener constante la separación de los canales de refrigeración a las superficies del molde que están en contacto con la pieza de plástico. De esta forma, es posible obtener un mapa de temperaturas de refrigeración uniforme y controlado a lo largo de las superficies de las piezas de plástico que presenten geometrías complejas. El sistema de refrigeración tipo conformal requiere "Rapid Tooling Technologies" (Técnicas de manufactura mediante fabricación aditiva e impresión 3D) para la manufactura de las placas "Cavity" (superior) y "Core" (inferior) (véase Fig.1) de las partes fija y móvil del molde de inyección, respectivamente [29]. Sin embargo, presenta, a su vez, una falta de funcionalidad para moldes de gran tamaño para aplicaciones industriales. Para resolver este inconveniente, se presentan sistemas refrigeración híbridos, tales como "Milled Groove" y "Array of Baffles" (véase Fig.4). Los cuales mantienen la premisa de los sistemas de refrigeración tipo conformal, mantener la distancia de separación del canal de refrigeración a la superficie de la pieza de plástico constante, y a su vez pueden ser fabricados mediante de técnicas de mecanizado convencionales. La elección correcta de la tipología o diseño del sistema de refrigeración es fundamental para obtener un intercambio térmico uniforme entre la pieza de plástico y el molde de inyección, sin asumir un costo de fabricación muy elevado. Asimismo, dependiendo de la topología de la pieza de plástico, un sistema de refrigeración puede estar compuesto por elementos de refrigeración convecionales (canales rectos perforados) y elementos de refrigeración de tipo conformal (baffles, bubbles, canales conformal, etc.). De esta forma, se optimiza el tiempo de fabricación y coste total de las placas principales del molde de inyección. Pues para las regiones de la pieza de plástico que presenten extensa planicidad, sean esbeltas y sin concavidades profundas se emplean elementos de refrigeración convencionales y para las regiones de la pieza de plástico con geometrías complejas, con grandes concavidades y poco accesibles se emplean elementos de refrigeración de tipo conformal [30], incluidos en el molde de inyección mediante insertos metálicos alojados en las placas principales del molde de inyección. Por ello, un reconocimiento detallado de la superficie de la pieza de plástico, desde las primeras fases del diseño del molde, permite la detección de sus características geométricas y por ende facilita la elección correcta de la tipología y diseño del sistema de refrigeración.

Una vez completada la fase de refrigeración, es decir cuando la pieza de plástico alcanza una rigidez mecánica suficiente como para ser expulsada del molde de inyección, el sistema de expulsión actúa para extraer la pieza de plástico de la cavidad del molde.

Las contracciones volumétricas originadas por el gradiente de temperaturas negativo que sufre la pieza de plástico durante la fase de refrigeración, ocasionan que la pieza de plástico se adhiera a las superficies de la cavidad del molde [31,32]. Requiriendo, por ende, de un mecanismo auxiliar que permita la expulsión de la pieza de plástico del molde sin comprometer la seguridad estructural de ésta (véase Fig.1) [33,34].

La obtención de tiempos de fabricación de piezas de plástico o tiempos de ciclo reducidos requieren que la fase de expulsión de la pieza de plástico del molde se dé lugar en un instante cercano al instante de cristalización y solidificación del material termoplástico. Ello, puede llegar a ocasionar defectos y deformaciones sobre la pieza de plástico, o incluso comprometer la seguridad estructural de la misma, si el diseño y dimensionamiento del sistema de expulsión no se realiza de acuerdo a los requerimientos establecidos para una correcta expulsión de la pieza de plástico.

Si bien existen varios procedimientos para realizar la expulsión de la pieza de plástico del molde, muchos de ellos pierden funcionalidad y eficacia debido al desgaste de su uso. De esta forma, en las piezas de plástico complejas que incorporan torretas, nervios o áreas de difícil expulsión, se recomienda el empleo de varillas de expulsión (véase Fig.1). Estas varillas o expulsores se caracterizan por su versatilidad a la hora de ser ubicados en la pieza de plástico, así como por la facilidad de implementación en el molde de inyección, a un costo relativamente bajo.

El dimensionamiento y diseño de la distribución de los expulsores sobre la pieza de plástico no es una tarea fácil cuando la topología de la misma es compleja [35]. De acuerdo a los requerimientos de funcionales y de diseño del molde de inyección, el conjunto de fuerzas de expulsión aplicadas por cada expulsor debe ser igual o ligeramente superior a la fuerza con la que la pieza de plástico queda adherida a las superficies molde tras la fase de refrigeración, es decir la fuerza derivada de las tensiones de contracción ocasionadas por el gradiente de temperaturas negativo durante la fase de refrigeración de la pieza [36,37]. Asimismo, para evitar que la pieza de plástico no sufra esfuerzos de flexión durante la fase de expulsión, el conjunto de fuerzas de expulsión, que ejerce cada expulsor, debe ser equilibrado y uniforme. Además, la aplicación de fuerzas de expulsión desequilibradas puede causar interferencias que provoquen que los expulsores penetren a través de la superficie de la pieza de plástico ocasionando roturas, al exceder el límite elástico del material termoplástico, o distorsiones en la geometría final de la misma [38-40]. Por tanto, la tensión aplicada por la varilla de expulsión sobre la pieza de plástico, derivada de la fuerza de expulsión aplicada, no debe exceder el límite elástico del material termoplástico de la pieza a fabricar.

Cada una de las diferentes fases que conforman el ciclo de inyección de una pieza de plástico (llenado, compactación, refrigeración y expulsión) tienen asociado un tiempo de manufactura. La rentabilidad y eficiencia del proceso de manufactura mediante de inyección de plástico depende del tiempo empleado en cada una de las diferentes fases que lo componen [41,42]. Por ello, predecir el tiempo requerido para fabricar una pieza de plástico mediante moldeo por inyección desde las etapas iniciales del diseño es de gran importancia, no solo desde un punto de vista económico sino también desde un punto de visto de la durabilidad mecánica del molde de inyección. No obstante, determinar el tiempo de ciclo con una precisión aceptable es una tarea compleja, dado que éste depende de múltiples factores relacionados con cada una de las diferentes fases que conforman el tiempo de ciclo, como son: las características geométricas de la pieza de plástico, la máquina de inyección empleada, la geometría de los sistemas de alimentación y la tipología del sistema de refrigeración del molde. Por esta razón, la presente tesis doctoral abarca la definición de un modelo analítico-empírico que determine con precisión el tiempo de ciclo de una pieza de plástico.

Actualmente, las grandes empresas enmarcadas en el sector y la industria de inyección de plástico se encuentran bajo una gran presión, en términos de beneficio económico, producción y competitividad. La globalización de los mercados obliga a las empresas productoras y diseñadoras de producto a reducir el tiempo de desarrollo del mismo, aumentando al mismo tiempo la diversidad de productos de alta calidad [43]. De esta forma, ante la licitación o adjudicación de un contrato, convenio o proyecto para el desarrollo del diseño y fabricación de un producto de plástico, una empresa emplazada en el sector industrial de los moldes de inyección requiere acortar y reducir los plazos para la presentación de una oferta competitiva que incluya el prediseño y presupuesto aproximado del molde de inyección.

Por lo general, estas tareas suelen llevarse a cabo por profesionales con gran experiencia en dicho sector. Pues, en base a su experiencia, son capaces de evaluar e identificar los requerimientos y particularidades del producto a desarrollar, determinar la configuración y diseño de los principales sistemas que conforman el molde del producto y establecer un presupuesto aproximado del mismo. La formación de profesionales capaces de diseñar y establecer un presupuesto aproximado de un molde, de manera independiente y en un corto periodo de tiempo, es una tarea que conlleva tiempo. Sin embargo, la rotación de personal puede causar la pérdida de todo conocimiento intangible generado a lo largo de la carrera profesional de un diseñador de moldes de inyección, así como la experiencia acumulada.

Por esta razón, permitir que otros empleados, con poca experiencia profesional en el sector industrial del plástico, aprendan y obtengan conocimientos, en un corto periodo de tiempo, sobre la tecnología del proceso de manufactura mediante moldes de inyección de plástico por medio de una herramienta sistemática y automatizada es una cuestión de verdadera importancia [44]. Actualmente, se extiende la tendencia a integrar el conocimiento y la tecnología en aplicaciones de diseño automatizadas para facilitar las tareas que desempeñan los ingenieros. La automatización sistemática reduce el tiempo y costes asociados a fases de diseño y modelado, así como los posibles errores humanos cometidos durante dichos procesos.

Sin embargo, las aplicaciones desarrolladas hasta la fecha requieren de mucha interacción por parte del usuario [45]. Por ello, en la presente tesis doctoral, se proponen un conjunto de algoritmos y metodologías para sistematizar y automatizar procesos de diseño y dimensionamiento de los sistemas principales del molde de inyección. Permitiendo y facilitando a los usuarios la consecución de dichas tareas de manera autónoma. De esta forma, se obtienen soluciones para el diseño y dimensionamiento de los sistemas principales del molde de inyección válidas y optimizadas, pues el trabajo desarrollado se basa en cálculos analíticos y empíricos de tipo reológico, energético y mecánico, validados de acuerdo a la experiencia de profesionales del sector industrial del plástico y softwares de simulación numérica tipo CAE.

Finalmente, el concepto de diseño industrial es un factor diferenciador del producto y una herramienta estratégica vital para las empresas enmarcadas en el sector industrial del plástico, pues presenta la función de innovar y la capacidad para crear y expandir nuevos mercados futuros. Progresivamente, la sociedad se está concienciando del efecto que produce la actividad humana sobre el medio ambiente. Y en base a ello, los consumidores demandan con mayor asiduidad productos que presenten poco impacto ambiental, tanto en su fabricación como durante su uso a lo largo de su ciclo de vida. Este hecho puede convertirse en una ventaja competitiva para empresas dedicadas al diseño de nuevos productos. Pues establece la oportunidad de diseñar productos que ayuden a reducir los niveles de contaminación, cumpliendo así con los requisitos de las nuevas generaciones de consumidores en términos de sostenibilidad energética, eco-diseño y biodegradabilidad. Una de las principales causas del aumento del impacto ambiental es la energía consumidos por los propios productos [46]. Revisar el diseño desde el punto de vista funcional, buscar nuevas

soluciones para reducir del consumo de energía o incorporar soluciones basadas en energías renovables que otorguen autonomía energética al producto son estrategias a ser seguir que le otorgan grandes ventajas al producto y lo hacen más atractivo para el consumidor [47].

De esta forma, a través del concepto de diseño industrial aplicado al desarrollo de productos sostenibles y energías renovables, nace un nuevo rotor como una variante parametrizada y adaptable de la hélice de eje vertical de tipo Savonius [48-52]. Las aplicaciones de este nuevo rotor se centran en la generación de energía a pequeña escala y en la reducción del consumo de energía o autoabastecimiento de aquellos productos (véase Fig.5) que incluyan este rotor y que presenten requerimientos estéticos y ergonómicos para su uso y venta. El nuevo rotor mantiene las ventajas de la hélice Savonius, al mismo tiempo que se integra perfectamente en la geometría del producto, dándole personalidad y haciéndolo más atractivo para los consumidores.

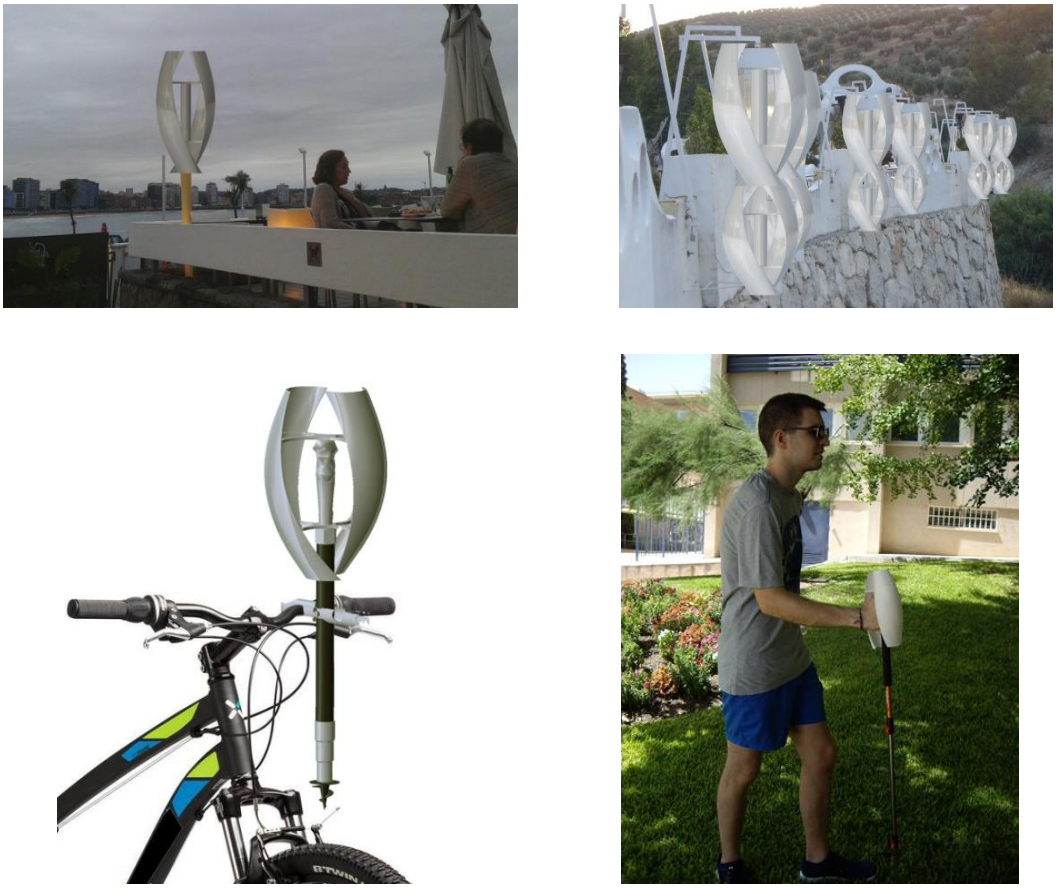

*Fig.5.- Aplicaciones funcionales y estéticas del nuevo rotor de eje vertical tipo Savonius.*

Como se puede apreciar en Fig.5, el rango de aplicación de este nuevo concepto de producto híbrido es amplio y abarca tanto aplicaciones de uso doméstico y deportivo, como aplicaciones de iluminación de entornos urbanos con requerimientos estéticos.

# 1.2. JUSTIFICACIÓN

Actualmente, los softwares comerciales tipo CAD (Computer Aided Design) empleados por las empresas de diseño y manufactura de moldes de inyección de plástico requieren, en gran medida, la interacción manual por parte del ingeniero o usuario. Es decir, no solo se requiere conocer y dominar las herramientas tipo CAD, sino que además se requiere una gran experiencia y cualificación en el área del conocimiento de las tecnologías de fabricación, en especial en moldeo por inyección de plástico.

Reducir el tiempo de diseño y fabricación, alcanzar una buena precisión y calidad en la pieza final y tener la flexibilidad de realizar rápidamente cambios en el diseño de la pieza de plástico son los requerimientos de los diseñadores de nuevos productos en el sector industrial del moldeo por inyección. Resolver estos problemas implica la automatización completa del proceso de análisis de la topología de la pieza de plástico. Es decir, la automatización de un análisis de la desmoldeabilidad ligado a la pieza de plástico a fabricar, que posteriormente determine el diseño geométrico de las regiones principales del molde de inyección. Numerosos investigadores han abordado el análisis de la desmoldeabilidad geométrica de la pieza de plástico. Sin embargo, todo el trabajo de investigación desarrollado hasta el momento presenta la desventaja de estar vinculado al software CAD donde se realiza el modelado 3D de la pieza de plástico. Todo ello, implica la necesidad de realizar un análisis interno de la información almacenada en las operaciones geométricas vinculadas al modelo CAD (denominadas “features”) o disponer de un hardware y dispositivos de computación auxiliares y externos, tales como GPU [55-60] para el análisis de visibilidad o desmoldeabilidad de la pieza de plástico. Es decir, el trabajo de investigación desarrollado hasta la fecha no es universal y válido para cualquier geometría, formato y tipología de piezas de plástico.

Análogamente, el diseño y dimensionamiento de los sistemas principales de expulsión y refrigeración se lleva a cabo de acuerdo a criterios y reglas empíricas basadas en la experiencia de diseñadores profesionales de moldes de inyección [61]. Por ejemplo, atendiendo al sistema de expulsión de un molde de inyección, se extiende la tendencia a usar un exceso de expulsores para evitar daños por penetración y deformación durante la expulsión de la pieza de plástico. Esto provoca un aumento del coste total del molde y disminuye la superficie efectiva de refrigeración, reduciendo, por ende, la eficiencia térmica y productividad del conjunto. Por otro lado, atendiendo al sistema de refrigeración de un molde, el diseño y dimensionamiento del mismo se realiza manualmente validando la eficiencia térmica del sistema a posteriori mediante software de simulación numérica tipo CAE [62-64]. Si el resultado de la simulación numérica indica que el diseño presentado no garantiza los requisitos mínimos de calidad de la pieza de plástico, se modifica el diseño y dimensionamiento nuevamente mediante un proceso iterativo de prueba y error. Esta metodología de trabajo presenta ciertos inconvenientes, entre los que destacan la gran cantidad de tiempo requerido por diseñadores expertos, los cuales no siempre se encuentran disponibles debido a la carga de trabajo de la empresa, el alto nivel de especialización que requieren los mismos y la disponibilidad y coste de las licencias de los softwares tipo CAE empleados.

A pesar de la importancia que adquiere la obtención de un diseño óptimo del sistema de refrigeración y expulsión, existen pocos estudios y trabajos relacionados con la obtención de algoritmos y metodologías para el diseño automatizado de dichos sistemas del molde de inyección. La mayoría de los estudios y trabajos se centran en la confección de algoritmos que solo tienen en cuentan los criterios de diseño geométrico y no abordan este proceso de manera completa.

Siendo, de forma análoga al análisis de desmoldebilidad, no válidos para cualquier geometría de la pieza de plástico, dado que analizan la topología de la pieza de manera interna mediante procedimientos vinculados con el software de modelado CAD empleando para el diseño de la misma [65,66].

Para resolver los problemas descritos previamente, y como justificación de la presente tesis doctoral, se proponen nuevos métodos analíticos-empíricos, automatizados y universales para abordar el análisis de la desmoldeabilidad de la pieza de plástico y el diseño y dimensionamiento de los sistemas principales de expulsión y refrigeración del molde de inyección. Los métodos desarrollados tienen en cuenta parámetros y requerimientos geométricos, técnicos y funcionales que garantizan el correcto funcionamiento de la pieza de plástico y molde de inyección. Por ello, los resultados obtenidos mediante dichos métodos no requieren la ejecución de simulaciones numéricas mediante softwares tipo CAE para su validación funcional. Todo ello, junto a un análisis del llenado de la cavidad del molde, permite establecer una definición completa y exhaustiva de las fases principales de llenado, compactación, refrigeración y expulsión del ciclo de inyección de una pieza de plástico. Haciendo posible, de esta forma, la elaboración automatizada y directa de un presupuesto inicial del molde de inyección que facilite a la empresa la obtención de proyectos y contratos dentro del sector industrial del plástico, es decir aumentando la eficiencia y competitividad de la misma.

Por otro lado, la evolución y desarrollo de las técnicas de manufactura del tipo “Rapid Tooling Technologies” y fabricación aditiva 3D, han permitido mejorar el diseño y funcionamiento de una serie de elementos que componen los sistemas principales del molde de inyección. Especialmente, para el diseño del sistema de refrigeración, la incorporación de estas nuevas tecnologías de manufactura ha permitido mejorar geométricamente la disposición de los canales de refrigeración, permitiendo que éstos se adapten a cualquier geometría de la pieza de plástico. Asimismo, también ha permitido mejorar el diseño de otros elementos de refrigeración existen como son los “baffles” y los “bubbles”. Es por ello, que en la presente tesis doctoral se incluye la propuesta de un nuevo diseño híbrido paramétrizado del sistema de refrigeración. Que combina los canales rectos perforados para regiones de la pieza de plástico fáciles de refrigerar y con poca concavidad, y elementos de refrigeración auxiliares de tipo conformal para regiones de la pieza de plástico difíciles de refrigerar, con detalles esbeltos, torretas, etc. De esta forma, se reduce el coste final del molde de inyección y se optimiza el intercambio térmico entre la pieza de plástico y el mismo, siendo posible la obtención de un tiempo de refrigeración y mapa de temperatura uniforme a lo largo de toda la superficie de la pieza de plástico.

Finalmente, y dado que la presente tesis doctoral se enmarca en un programa de doctorado en Energías Renovables, todo el conocimiento generado en el trabajo presentado se ha aplicado en el diseño, validación y manufactura de un nuevo concepto de producto híbrido aplicado a las energías renovables y fabricado mediante un molde de inyección de plástico. Dicho concepto se basa en la adaptación geométrica de una hélice de eje vertical tipo Savonius para prototipos o productos ya existentes. La energía eólica es una fuente de energía renovable capaz de generar energía limpia, desde un punto de visto económico [67], siendo, a su vez, una alternativa viable para reducir la dependencia de las fuentes de energías convencionales [68]. La energía eólica ha sido empleada por diferentes sectores industriales y adaptada a nivel de usuario doméstico debido a su disponibilidad, facilidad de mantenimiento y operación a bajo coste [69]. De esta forma, a partir de la energía cinética del viento adquirida a través del movimiento de las palas de la hélice, ésta se transforma en energía eléctrica que es almacenada o empleada para reducir el consumo energético y dar autonomía a los productos o prototipos que incorporan dicha hélice.

Asimismo, para cumplir los requerimientos estéticos, ergonómicos y energéticos del prototipo final, la adaptación geométrica de la hélice de eje vertical tipo Savonius se realiza de manera parametrizada y adaptada a la topología del producto donde irá incluido. Permitiendo la simbiosis y mimetización del rotor con el producto y, a su vez, la del prototipo final con su entorno, mejorando la estética del conjunto y haciéndolo más atractivo para los usuarios y consumidores.

# 1.3. OBJETIVOS

El objetivo final de la presente tesis doctoral es **el desarrollo de una metodología para el análisis automatizado de la manufactura de la pieza de plástico que permita el diseño y dimensionamiento de los sistemas principales del molde de inyección de plástico de manera automatizada y con carácter universal**. Es decir, pueda ser aplicable a cualquier geometría de la pieza de plástico, con independencia del formato o el software de modelado CAD donde se haya definido la topología de la misma. Para alcanzar este objetivo se han definido los siguientes objetivos intermedios, que han permitido la consecución del mismo:

- **Desarrollo de un nuevo procedimiento para el análisis automatizado de la desmoldeabilidad geométrica de la pieza de plástico**. Partiendo de la geometría discreta de la pieza de plástico y su dirección de desmoldeo, este análisis automatizado representará sobre la geometría de la misma un mapa de desmoldeabilidad o manufactura que, mediante un código de colores, muestre las superficies que pueden ser desmoldeables a partir de las placas principales del molde de inyección (placas "cavity" y "core"), las superficies que son desmoldeables a partir de elementos o mecanismos auxiliares como son las correderas laterales y las superficies que, ningún caso, puedan ser desmoldables. Asimismo, este análisis debe ser capaz de determinar la línea de partición del molde de inyección en base a requerimientos geométricos, técnicos y funcionales, impuestos por el sector industrial del plástico, que garanticen el correcto desmoldeo de la pieza de plástico.

- **Desarrollo de un nuevo procedimiento automatizado de tipo geométrico – experto para el diseño de la disposición y dimensionamiento de las varillas de expulsión del molde de inyección de plástico.** Partiendo de las propiedades térmicas, mecánicas y elásticas del material termoplástico, la geometría discreta de la pieza y las superficies de la misma que desmoldean por la placa "Core" del molde (placa a partir de la cual el sistema de expulsión actúa para extraer la pieza del molde de inyección), el algoritmo, en una primera fase, debe evaluar la topología de la pieza para establecer la localización de las varillas de expulsión en aquellas regiones que presente resistencia a la expulsión, como son nervios, torretas, etc. Por otro lado, en una segunda fase, el dimensionamiento de los parámetros de fuerza de expulsión y diámetro de las varillas de expulsión se establece mediante algoritmos de optimización genética multi-objetivo que aseguren un balance uniforme y homogeneo de las fuerzas de expulsión, una sumatoria de fuerzas de expulsión aplicadas por las varillas expulsoras que supere la fuerza mínima que mantiene adherida la pieza de plástico al molde de inyección y que la tensión ejercida individualmente por cada varilla expulsión no supere el límite elástico del material termoplástico.

- **Desarrollo de un nuevo procedimiento automatizado de tipo geométrico – experto para el diseño y dimensionamiento de los elementos principales del sistema de refrigeración del molde de inyección de plástico.** Partiendo de la geometría discreta y las propiedades térmicas y reológicas del material termoplástico de la pieza, el algoritmo, en una primera fase, debe evaluar la topología de la pieza de plástico para definir la tipología del diseño del sistema de refrigeración que se empleará para el caso de estudio dado.

De esta forma, para aquellas regiones de la pieza de plástico que presenten mayor concavidad o regiones profundas y complejas (con detalles esbeltos, torretas, nervios, etc.), donde los canales de refrigeración convencionales pierdan eficiencia, el algoritmo empleará elementos auxiliarles de refrigeración tipo conformal denominados "baffles." Y para aquellas regiones de la pieza de plástico con mayor planicidad y menos complejas el algoritmo empleará canales rectos perforados convencionales. A continuación, en una segunda fase, mediante la definición de algoritmos de optimización genética multi-objetivo se establece la localización geométrica de los canales convencionales y elementos auxiliares de refrigeración tipo conformal, para garantizar que el sistema de refrigeración sea uniforme y balanceado para todo el dominio de la pieza de plástico. Análogamente, se emplean algoritmos de optimización genética multi-objetivo, para el dimensionamiento de las variables geométricas que definen el diseño de los elementos principales del sistema de refrigeración (diámetro y separación entre cada elemento del sistema de refrigeración) y las variables tecnológicas que configuran la fase de refrigeración en el molde de inyección (temperatura del molde, temperatura de entrada del fluido refrigerante y tiempo de refrigeración).

- **Procedimiento para la determinación del tiempo empleados en las fases principales del ciclo de inyección de la pieza de plástico, así como el dimensionamiento del sistema de alimentación del molde de inyección.** Con el objetivo de obtener el tiempo total de ciclo de manufactura de una pieza de plástico, se propone la definición de dos nuevos sub-algoritmos que calculen el valor del tiempo transcurrido en cada una de las fases principales del ciclo de inyección de la pieza de plástico y establezcan las variables geométricas que definan los elementos principales del sistema de alimentación del molde de inyección. En una primera fase un nuevo algoritmo geométrico permite el reconocimiento automatizado de la topología de la pieza de plástico en formato discreto, obteniendo el conjunto de parámetros geométricos necesarios para el cálculo del tiempo ciclo. El algoritmo determina el recorrido del frente de plástico fundido y mediante la proyección de una cuadratura nodal sobre la malla discreta de la pieza de plástico determina el mapa de espesores, obteniendo el espesor medio y máximo de la pieza de plástico. En segundo lugar, un algoritmo analítico-empírico realiza un análisis de las simulaciones numéricas de la fase de inyección en una probeta rectangular (cuya geometría se encuentra parametrizada de acuerdo al recorrido del frente de plástico fundido, volumen y espesor), generando un conjunto de funciones polinomiales que determinan el dimensionamiento del sistema de alimentación. Finalmente, a partir de los parámetros geométricos, tecnológicos (obtenidos en ambos sub-algoritmos) y de las propiedades mecánicas, térmicas y reológicas del material termoplástico de la pieza se procede al cálculo del tiempo de ciclo.

- **Diseño parametrizado y análisis numérico – experimental de una nueva hélice vertical de tipo Savonius adaptados a los requerimientos estéticos, ergonómicos, geométricos y energéticos de productos fabricados mediante moldes de inyección de plástico.** Aplicación de todo el trabajo y algoritmos desarrollados en los objetivos intermedios descritos previamente para establecer el diseño parametrizado de un nuevo rotor de eje vertical adaptado a los requerimientos de productos de plástico ya existentes, cuya demanda energética sea de baja escala. Mediante un conjunto de operaciones de translación, simetría, rotación y escalado se transforman las palas de una hélice convencional tipo Savonius en superficies topológicas con formas orgánicas adaptadas a la geometría del producto en el cual se integran.

Asimismo, para determinar el funcionamiento de este nuevo rotor en términos de coeficiente de potencia, coeficiente de par y potencia mecánica generada, se programan simulaciones numéricas tipo CAE mediante software CFD validadas a través de ensayados experimentales en el túnel del viento.

# 1.4. PUBLICACIONES

A continuación, se detallan las publicaciones relevantes, artículos en revista de alto impacto, que surgen a partir del trabajo de investigación realizado para la consecución de los objetivos especificados en la presente tesis doctoral.

El primer objetivo definido (**Desarrollo de un nuevo procedimiento para el análisis automatizado de la desmoldeabilidad geométrica de la pieza de plástico**) ha sido desarrollado en la siguiente publicación:

1. **Mercado-Colmenero, Jorge Manuel,** Paramio, M.A.R, Perez-Garcia, Jesús María y Martín-Doñate, Cristina. *A new hybrid method for demoldability analysis of discrete geometries. Computer-Aided Design 80 (2016) 43-60. DOI: http://dx.doi.org/10.1016/j.cad.2016.06.006.*
2. **Mercado-Colmenero, Jorge Manuel,** Moya-Muriana, José Ángel, Rubio Paramio, Miguel Ángel y Martín-Doñate, Cristina. *Advances on Mechanics, Design Engineering and Manufacturing, Lecture Notes in Mechanical Engineering (2017) 119-128. DOI: http://dx.doi.org/10.1007/978-3-319-45781-9_13.*

En estos artículos, se presenta un nuevo método para el análisis automatizado de la desmoldeabilidad de piezas que se fabricarán mediante moldes de inyección de plástico. Los algoritmos desarrollados en estas publicaciones, se centran en el análisis de la topología y geometría de la pieza de plástico, discretizada a partir de una malla compuesta por nodos y elementos o facetas triangulares. De esta forma, se establece un análisis híbrido de los elementos notables (nodos y facetas) de la malla. Una primera fase de preprocesado clasifica los nodos de la malla según su cota vertical, asignando a cada nodo un plano perpendicular a la dirección de desmoldeo dada. Mediante la proyección selectiva de facetas, se generan contornos cerrados que permiten definir la desmoldeabilidad de los nodos de la malla. A continuación, las facetas de la malla se catalogan de acuerdo a la desmoldeabilidad de los nodos que la definen, obteniendo facetas desmoldeables, no desmoldeables y semi-desmoldeables. Las facetas establecidas como semi-desmoldeables se dividen regiones virtuales poligonales desmoldeables y no desmoldeables. Lo que provoca una redefinición de la malla original, generado una nueva geometría virtual de la pieza de plástico. Finalmente, las regiones de la pieza de plástico no desmoldeables se analizan de nuevo mediante un redireccionamiento de la malla, empleando las direcciones principales perpendiculares a la dirección de desmoldeo. De forma que, aplicando nuevamente los algoritmos de análisis se determina la desmoldeabilidad de dichos nodos y facetas. Asimismo, se determinan las regiones de la pieza de plástico que son desmoldeables mediante mecanismos auxiliares, como correderas. La metodología de análisis híbrida (nodos y facetas) proporciona al diseñador no solo información sobre la geometría de la pieza de plástico, sino también información sobre su manufactura. La geometría discreta de la pieza de plástico, junto con su información sobre su manufactura, se almacena en matrices para su uso posterior en aplicaciones de tipo CAD.

El segundo objetivo definido (**Desarrollo de un nuevo procedimiento automatizado de tipo geométrico – experto para el diseño de la disposición y dimensionamiento de las varillas de expulsión del molde de inyección de plástico**) ha sido desarrollado en la siguiente publicación:

3. **Mercado-Colmenero, Jorge Manuel,** Rubio-Paramio, M.A, Vizan-Idoipe, Antonio y Martín-Doñate, Cristina. *A new procedure for the automated design of ejection systems in injection molds. Robotics and Computer – Integrated Manufacturing 46 (2017) 68-85. DOI: http://dx.doi.org/10.1016/j.rcim.2016.12.006.*

En este artículo, se presenta un nuevo método automatizado para el diseño y dimensionamiento de los elementos principales que conforman el sistema de expulsión de un molde de inyección de plástico, basado en el análisis de la geometría discreta de la pieza de plástico. El algoritmo propuesto consta de una primera fase de análisis geométrico donde se genera una cuadratura nodal sobre las superficies de la pieza de plástico que desmoldean por la parte fija del molde. A continuación, se evalúan los gradientes de espesor de la pieza de plástico entre cada nodo contiguo de la cuadratura generada, localizando y almacenando en matrices aquellos nodos que corresponden con regiones de la pieza de plástico con grandes cambios de espesor. Dos sub-algoritmos de reconocimiento geométrico determinan la ubicación final de los expulsores. Esta ubicación se determina evaluando, para cada nodo de la cuadratura nodal, la concentración de cambios o gradientes de espesor que tengan asociados a su alrededor, y que a su vez corresponde con la ubicación de paredes verticales, nervios, torretas, etc. Es decir, regiones de la pieza de plástico con dificultad para ser expulsadas del molde de inyección. El dimensionamiento de los expulsores se realiza mediante un algoritmo de optimización genética multi-objetivo, lo que garantiza que el sistema de expulsión actúe de forma homogénea, balanceada y uniforme. Esta nueva metodología mejora los métodos desarrollados hasta la fecha, ya que no requiere la implementación de técnicas heurísticas y no utiliza modelos de identificación de características geométricas de la pieza de plástico. Evitando, de esta forma, los problemas de dependencia con el modelador CAD donde se modele la pieza de plástico. Finalmente, el algoritmo proporciona como resultado el diseño de la distribución de los expulsores en el molde de inyección, junto a la magnitud de las variables geométricas y tecnológicas que gobiernan la fase de expulsión, entre las que destacan: la fuerza aplicada por las varillas expulsoras y el diámetro de las mismas. La solución del algoritmo se muestra gráficamente superpuesta sobre la geometría discreta de la pieza de plástico, a modo de mapa de expulsión. Los resultados del algoritmo se pueden almacenar y exportar para su uso en otras aplicaciones y sistemas CAD paramétricos.

El tercer objetivo definido (**Desarrollo de un nuevo procedimiento automatizado de tipo geométrico – experto para el diseño y dimensionamiento de los elementos principales del sistema de refrigeración del molde de inyección de plástico**) ha sido desarrollado en la siguiente publicación:

4. **Mercado-Colmenero, Jorge Manuel,** Rubio-Paramio, Miguel Angel, Marquez-Sevillano, Juan de Juanes y Martín-Doñate, Cristina. *A new method for the automated design of cooling systems in injection molds. Computer-Aided Design 104 (2018) 60-86. DOI: https://doi.org/10.1016/j.cad.2018.06.001*.

En este artículo, se presenta un nuevo método automatizado para el diseño y dimensionamiento de los elementos principales que conforman el sistema de refrigeración de un molde de inyección de plástico, basado en el análisis de la geometría discreta de la pieza de plástico. En una primera fase, el nuevo algoritmo reconoce la topología discreta de la pieza para obtener su mapa de profundidad y detectar las regiones de la misma difíciles de refrigerar. El algoritmo realiza un análisis automatizado del intercambio térmico entre el fluido refrigerante del sistema de refrigeración y la pieza de plástico, teniendo en cuenta parámetros funcionales y tecnológicos que garantizan una refrigeración uniforme de la pieza de plástico. En base a la distancia límite a la pieza en la cual los canales rectos perforados, de un sistema de refrigeración convencional, pierden eficacia de refrigeración y en base al mapa de profundidad, el algoritmo genera el diseño óptimo para el sistema de refrigeración de la pieza de plástico adaptado a su geometría. En una segunda fase, los parámetros geométricos y tecnológicos del sistema de refrigeración se dimensionan mediante algoritmos de optimización genética multi-objetivo que garantizan la uniformidad y el equilibrio en el diseño del sistema refrigeración del molde de inyección de plástico.

Como resultado de esta metodología, se presenta un sistema de refrigeración con un rendimiento análogo al de un sistema de refrigeración tipo conformal, siendo posible la fabricación del mismo mediante técnicas de mecanizado convencionales tipo CNC. Adicionalmente, el algoritmo se encarga de localizar y evitar las posibles interferencias con elementos de otros sistemas del molde de inyección. Esta nueva metodología mejora los métodos desarrollados hasta la fecha, ya que no requiere la validación de los resultados en software de tipo CAE y no utiliza modelos de identificación de características geométricas de la pieza de plástico. Evitando, de esta forma, los problemas de dependencia con el modelador CAD donde se realice el modelado la pieza de plástico. Finalmente, los resultados del algoritmo se pueden almacenar y exportar para su uso en otras aplicaciones y sistemas CAD paramétricos.

El cuarto objetivo definido (**Procedimientos para la determinación del tiempo empleados en las fases principales del ciclo de inyección de la pieza de plástico, así como el dimensionamiento del sistema de alimentación del molde de inyección**) ha sido desarrollado en la siguiente publicación:

5. **Mercado-Colmenero, Jorge Manuel,** Rubio-Paramio, Miguel Angel, Karlinger, Peter, Martín-Doñate, Cristina. *A new procedure for calculating cycle time in injection molding based on plastic part geometry recognition. The International Journal of Advanced Manufacturing Technology 98 (2018) 441-477. DOI: https://doi.org/10.1007/s00170-018-2080-0*.

El artículo presenta un nuevo procedimiento para el cálculo automatizado del tiempo de ciclo requerido en el proceso de manufactura mediante moldes de inyección de plástico. El modelo presentado se basa en el reconocimiento de la topología de la pieza de plástico a fabricar, definiendo como datos de entrada únicamente la geometría de la pieza de plástico en formato discreto (modelo mallado compuesto por nodos y facetas poligonales) y el material termoplástico de la misma. En una primera fase, se establece un nuevo algoritmo geométrico para obtener el conjunto de parámetros geométricos necesarios para el cálculo del tiempo de ciclo, entre los que destacan: el mapa de espesores de la pieza, espesor máximo, espesor máximo y promedio y la distancia máxima recorrida por el frente de plástico fundido en la cavidad del molde durante el proceso de inyección. Posteriormente, un segundo algoritmo analítico – empírico realiza un análisis automatizado de los resultados de las simulaciones numéricas del proceso de inyección en probetas rectangulares, parametrizadas de acuerdo a su espesor, volumen y recorrido máximo del frente de plástico fundido. Generando un conjunto de funciones polinomiales que determinan las variables geométricas del sistema de alimentación del molde de inyección. Finalmente, a partir de los datos geométricos y tecnológicos resultantes de la aplicación de los dos sub – algoritmos, se calcula el tiempo requerido en cada una de las fases del ciclo de inyección para la pieza de plástico objeto de estudio. El nuevo procedimiento presentando no requiere el uso de software de simulación numérica adicional o la evaluación empírica por parte de expertos. No está vinculado al modelador CAD donde se modela la pieza de plástico, ya que analiza su topología externamente a través de su formato discreto o mallado. De esta manera, el presente modelo permite a los diseñadores responder al cliente de forma rápida y precisa, obteniendo el valor del tiempo de ciclo en un tiempo mínimo.

El quinto objetivo definido (**Diseño parametrizado y análisis numérico – experimental de una nueva hélice vertical de tipo Savonius adaptados a los requerimientos estéticos, ergonómicos, geométricos y energéticos de productos fabricados mediante moldes de inyección de plástico**) ha sido desarrollado en la siguiente publicación:

6. **Mercado-Colmenero, Jorge Manuel,** Rubio-Paramio, Miguel Angel, Guerrero – Villar, Francisca, Martín-Doñate, Cristina. *A numerical and experimental study of a new Savonius wind rotor adaptation based on product design requeriments. Energy Conversion and Management 158 (2018) 210-234. DOI: https://doi.org/10.1016/j.enconman.2017.12.058*

El artículo presenta el diseño, adaptación geométrica y estudio análisis – experimental de una nueva hélice de eje vertical de tipo Savonius. Tomando como referente unos requerimientos de tipo estético, ergonómico, funcional y energético, se propone un modelo de rotor paramétrico adaptable a las dimensiones y la geometría de los productos de los que formará parte. Asimismo, para realizar esta adaptación topológica, se han aplicado un conjunto de operaciones geométricas de traslación, simetría, rotación y escala a las secciones curvas de las palas de la hélice de eje vertical Savonius. Bajo las mismas condiciones geométricas del parámetro adimensional Aspect Ratio, se ha ensayado el rotor modificado y el rotor convencional de tipo Savonius en un túnel de viento para evaluar y cuantificar la influencia que han tenido las modificaciones geométricas en el coeficiente de potencia, coeficiente de par y potencia mecánica generada. Los ensayos se han realizado para valores del número adimensional de Reynolds comprendidos en el rango de [$3{,}430 \cdot 10^4$ y $1{,}419 \cdot 10^9$]. Los resultados experimentales se han validado mediante un análisis numérico a través de un software de simulación numérica de tipo CDF, obteniendo error relativo entre los ensayos experimentales y numéricos de un 3,5%. Finalmente, el nuevo rotor se presenta como un elemento auxiliar que complementa y mejora al producto original en términos de sostenibilidad, eco-diseño, biodegradabilidad y autonomía energética. Manteniendo, análogamente, las ventajas de un rotor Savonius convencional (como son su fácil fabricación, montaje, mantenimiento, arranque automático, etc.) y aportando al diseño del producto la capacidad de integrarse en su entorno y de ser personalizable para el consumidor.

# 1.5. CONCLUSIONES Y TRABAJOS FUTUROS

La presente tesis doctoral se define como un conjunto de trabajos de investigación, relativos a la automatización y optimización del proceso de manufactura mediante moldes de inyección de plástico y análisis topológico de superficies complejas de piezas de plástico. Asimismo, con el desarrollo de la presente tesis doctoral se ha generado un conocimiento y aportaciones relevantes en el ámbito de la investigación de esta área del conocimiento, que establecen las bases para ayudar y mejorar las metodologías de trabajo desarrolladas en las empresas del sector industrial del molde de inyección de plástico, y en especial a aquellas empresas de este sector incluidas en el tejido industrial de la provincia de Jaén. En particular, para cada uno de los trabajos de investigación presentados, las principales conclusiones obtenidas han sido las siguientes:

- Para la realización del análisis automatizado de la desmoldeabilidad de la pieza de plástico, se han desarrollado tres subalgoritmos (Inproject, Catalogfaces y Reclassfacet). Estos subalgoritmos se encargan de obtener, mediante técnicas y recursos gráficos, la desmoldeabilidad de los elementos notables (nodos y facetas) de la geometría discreta o malla de la pieza. Todo ello, permite definir las superficies de la pieza desmoldeables a partir de las placas principales "Cavity" y "Core" del molde de inyección, así como la detección de superficies desmoldeables mediante mecanismos auxiliares como correderas y superficies no desmoldeables. Para llevar a cabo la validación del análisis de desmoldeabilidad, se han evaluado 5 piezas reales con diferente geometría. Obteniendo un mapa de desmoldeabilidad correcto y válido de acuerdo a los requerimientos impuestos en la industria y una nueva geometría discreta virtual de cada pieza con información adicional acerca de su manufactura. De esta forma, la nueva información obtenida ayuda y guía al diseñador del molde de inyección en las posibles modificaciones geométricas que surjan al redefinir los requerimientos de la pieza de plástico. Por último, el tiempo computacional requerido en el presente análisis mejora y se reduce notablemente respecto al tiempo computacional de otras metodologías de análisis análogas que buscan el mismo objetivo, pues éste representa un 6% del tiempo computacional total requerido en las metodologías definidas hasta la fecha.

- La metodología presentada, para el diseño y dimensionamiento del sistema de expulsión de un molde de inyección, se ha evaluado y examinado a través de su aplicación en 5 piezas de plástico con diferentes características geométricas (espesor, volumen, dimensiones del bounding box, etc.). Mediante técnicas gráficas, se ha calculado el espesor en cada región del dominio de las piezas objeto de estudio. A continuación, evaluando gráficamente los gradientes de espesor de cada una de ellas, se ha generado el mapa de expulsión con las coordenadas de localización de los expulsores requeridos en cada pieza objeto de estudio. Además, junto a los resultados del diseño de la distribución del sistema de expulsión, se genera, para cada pieza objeto de estudio, un informe técnico que recoge los diferentes parámetros geométricos y tecnológicos que definen la fase de expulsión de la pieza del molde de inyección. Este proceso de dimensionamiento se define a partir de algoritmos de optimización genética que, mediante funciones multi-objetivo, determinan la magnitud óptima de cada variable geométrica y tecnológica que gobiernan la fase de expulsión.

Entre las que destacan: el diámetro de cada expulsor y la fuerza de expulsión mínima aplicada por cada expulsor para extraer la pieza del molde. Asimismo, para no comprometer la seguridad estructural de la pieza, las funciones objetivo del algoritmo de optimización se establecen para que asegurar que el conjunto de fuerzas de expulsión obtenido sea balanceado, homogéneo y uniforme y para evitar que las tensiones generadas por la acción de los expulsores en la pieza no superen el límite elástico del material termoplástico. Por último, este nuevo método mejora respecto a los métodos desarrollados hasta la fecha, dado que éste no requiere de técnicas heurísticas para la obtención de los resultados del diseño y dimensionamiento del sistema de expulsión del molde de inyección.

- La metodología presentada, para el diseño y dimensionamiento del sistema de refrigeración de un molde de inyección, se ha evaluado y examinado a través de su aplicación en 4 piezas de plástico con diferentes características geométricas (espesor, volumen, dimensiones del bounding box, etc.). Mediante técnicas gráficas, se ha calculado la profundidad o concavidad en cada región del dominio de las piezas objeto de estudio. A continuación, evaluando el mapa de profundidades de la pieza, se establece que regiones de ésta pueden refrigerarse mediante elementos convencionales como canales rectos perforados y que regiones requieren elementos auxiliares de refrigeración tipo conformal como son los “baffles”. De esta forma, tanto para las regiones de la pieza esbeltas o planas como para las regiones de la pieza con grandes profundidades o concavidades, donde los canales rectos perforados pierden efectividad de refrigeración, la presente metodología localiza los canales de refrigeración principales y los “baffles” mediante un proceso geométrico de optimización que asegura que el sistema de refrigeración resultante sea uniforme, balanceado y homogéneo. Además, junto a los resultados del diseño de la distribución del sistema de refrigeración, se genera, para cada pieza objeto de estudio, un informe técnico que recoge los diferentes parámetros geométricos y tecnológicos que gobiernan la fase de refrigeración de la misma. Este proceso de dimensionamiento se define a partir de algoritmos de optimización genética que, mediante funciones multi-objetivo, determinan la magnitud óptima de cada variable geométrica y tecnológica que intervienen en la fase de refrigeración. Entre las que destacan: el diámetro de cada canal de refrigeración y baffles, las coordenadas XYZ de localización de los canales de refrigeración y baffles, la temperatura de la superficie en la superficie del molde, la temperatura de entrada del fluido refrigerante al sistema de refrigeración y el tiempo transcurrido en la fase refrigeración. Asimismo, las funciones objetivo del algoritmo de optimización se establecen para asegurar una alta calidad de acabado en las piezas de plástico y la reducción del tiempo transcurrido en la fase refrigeración. Por último, este nuevo método mejora respecto a los métodos desarrollados hasta la fecha, dado que éste no requiere de técnicas heurísticas para la obtención de los resultados del diseño y dimensionamiento del sistema de refrigeración del molde de inyección.

- Se presenta una nueva metodología para obtención del tiempo que transcurre en cada una de las fases que conforman el ciclo de inyección de una pieza de plástico. En una primera fase, un algoritmo geométrico realiza, mediante técnicas gráficas, un análisis de la topología discreta de la pieza para obtener la trayectoria del frente de plástico fundido que mayor distancia recorre durante el llenado de la cavidad del molde, así como el mapa de espesores de la pieza. En una segunda fase, se establece un modelo analítico-empírico para determinar el tiempo de llenado, compactación y refrigeración, así como los parámetros geométricos que definen el sistema de alimentación del molde de inyección.

Dicho modelo se define a partir de la interpolación, mediante funciones polinomiales, de los resultados obtenidos en un conjunto simulaciones numéricas de la fase de llenado de probetas rectangulares parametrizadas. Todo ello, se evaluado y examinado en 6 piezas con diferentes características geométricas y materiales termoplásticos. Además, con los resultados obtenidos se genera un informe técnico que ayuda a generar una rápida estimación del coste total del molde de inyección, mejorando la eficiente y tiempo empleado en las fases iniciales de diseño del producto.

- El diseño de una nueva hélice de eje vertical se ha ensayado experimentalmente en el túnel del viento para evaluar la influencia de los parámetros de geométricos de diseño del producto en términos de coeficiente de potencia, coeficiente de par y potencia mecánica generada. Los experimentos se han llevado a cabo para magnitud del número de Reynolds comprendidos en el rango de [$3{,}436 \cdot 10^4$ y $1{,}419 \cdot 10^5$]. Los resultados experimentales han sido validados a partir de un software de simulación numérica del tipo CFD, obteniendo una variación del 3,5% entre los resultados experimentales y los obtenidos numéricamente. Para el rango de valores de tip speed ratio comprendidos entre 0,223 y 0,335, la hélice cumple los requerimientos funcionales de generación de energía a pequeña escala requerido por los productos donde podrá ir incluida. El nuevo rotor mantiene las ventajas del rotor Savonius al mismo tiempo que se integra perfectamente en la geometría del producto, dándole personalidad y haciéndolo atractivo para los consumidores. A partir de esta metodología de diseño surge una nueva línea de investigación que consiste en incorporar elementos técnicos capaces de contribuir a la autonomía energética del producto, cumpliendo con sus requerimientos de diseño estético y ergonómico con el objetivo de mejorar la sostenibilidad urbana de la sociedad.

El conjunto de trabajos de investigación desarrollados en la presente tesis se caracteriza por ser automatizados, sistemáticos e inteligentes. El coste y tiempo computacional requerido se reduce significativamente, respecto a las metodologías desarrolladas hasta la fecha, ya que el análisis de la geometría discreta de la pieza de plástico (modelo mallado compuesto por nodos y facetas) simplifica las funciones, operaciones y técnicas gráficas empleadas. Asimismo, no se requieren métodos heurísticos y de reconocimiento de información de modelado geométrico de la pieza, evitando problemas de dependencia con el software CAD donde se realizó el modelado de la pieza. Pudiendo aplicar todo el conocimiento desarrollado a cualquier geometría de pieza de plástico, independientemente del software CAD empleado para su modelado geométrico. Todo ello, supone un avance y mejora en el área del conocimiento de la fabricación mediante moldes de inyección, ya que permite optimizar la funcionalidad de los sistemas principales del molde de inyección y reducir errores, coste y tiempo en las fases iniciales de diseño del producto. Así como reducir la dependencia en la experiencia y conocimientos que atesoran los profesionales y expertos del sector.

Finalmente, todo el conocimiento generado en la presente tesis doctoral se ha integrado en una aplicación inteligente para el diseño CAD automatizado de la geometría del molde de inyección de plástico, denominada CELERMOLD [70]. Esta aplicación se encuentra alojada en una plataforma web, de forma que usuario puede cargar la geometría de la pieza de plástico, definir el material termoplástico (a partir de una amplia base de datos que dispone la aplicación), seleccionar la precisión de análisis de la geometría de la pieza, el número de unidades a fabricar de la pieza y el tiempo de entrega del lote de piezas a fabricar. Esta aplicación surge como resultado del proyecto de investigación "A vertical design software for integrating operations of automated demoldability, tooling design and cost estimation in injection molded plastic parts. (CELERMOLD)", desarrollado conjuntamente por el centro tecnológico del plástico Andaltec [71] y el departamento de ingeniería gráfica, diseño y proyectos de la universidad de Jaén.

La aplicación de algoritmo de optimización genética para el diseño dimensionamiento de los sistemas principales del molde de inyección ha marcado un punto de partida en la transferencia e inclusión de técnicas de inteligencia artificial en el sector industrial de fabricación mediante moldes de inyección de plástico. Pues con el creciente desarrollado del concepto de industria 4.0, estas técnicas podrían hacer más eficiente y mejorar procesos tecnológicos que intervienen durante el ciclo de inyección de la pieza de plástico, así como la optimización de los parámetros tecnológicos que gobiernan la máquina inyectora de plástico durante el proceso de manufactura de la pieza de plástico.

Por otro lado, el avance de las tecnologías de manufactura aditiva 3D ("Rapid Tooling Technologies") y la amplia gama de materiales plásticos y metálicos que pueden usarse, hoy en día, en este proceso de manufactura, han permitido su aplicación directa en el sector industrial de los moldes de inyección de plástico. De esta forma, gracias a la flexibilidad que ofrece este proceso de manufactura para la generación geometrías y superficies complejas, se han podido desarrollar nuevos sistemas y elementos de refrigeración de tipo conformal que optimizan el intercambio térmico entre el fluido refrigerante y la pieza de plástico. Siendo posible mejorar la calidad estética y precisión dimensional del producto final y reducir la tensión residual asociada a la pieza de plástico tras el proceso de manufactura.

Asimismo, ante un sector industrial donde los requerimientos estéticos cada vez se hacen más exigente, surge el concepto de ciclo rápido, el cual se base en calentar la superficie del molde de inyección mediante canales de tipo conformal que se adaptan a la geometría y hacen que el mapa de temperaturas del frente de plástico fundido sea uniforme durante la fase de llenado. Esto provoca un aumento en la calidad superficial de la pieza final, disminuye la aparición de defectos estéticos y posibilita la eliminación de los detalles estéticos en las líneas de soldadura [72-74]. Por tanto, en relación a esta nueva tecnológica de manufactura aditiva, hay un gran potencial aún por desarrollar y el reto de aplicar todo el conocimiento generado en la presente tesis en el desarrollo de nuevas metodologías que aborden el proceso de diseño y dimensionamiento de estos novedosos sistemas del molde de inyección.

# 1.6. CONCLUSIONS AND FUTURE RESEARCH LINES

The present PhD thesis is defined as a set of research works, concerning to the manufacturing process automation and optimization via plastic injection molds and topological analysis of complex surfaces of plastic parts. Furthermore, with the development of the present PhD thesis, knowledge and relevant contributions have been generated in the field of manufacturing process research, which establish the bases to help and improve the working methodologies developed in the plastic injection molding companies. Especially, those companies included in the industrial network of the Jaén province. In particular, for each of the research papers presented, the main conclusions obtained were the following:

- For the implementation of the automated demoldability analysis of the plastic part, three sub-algorithms have been developed (Inproject, Catalogfaces and Reclassfacet). These subalgorithms are responsible for obtaining, through graphic techniques, the demoldeability of the notable elements (nodes and facets) of the discrete geometry or mesh of the plastic part. All of this allows to define the plastic part surfaces which are able to be demoldable via the main plates "Cavity" and "Core" of the injection mold, as well as the dectection of demoldable surfaces via auxiliary mechanisms such as side cores and non-demoldable surfaces. To carry out the validation of the demoldeability analysis, 5 real plastic parts with different geometry have been evaluated. Obtaining a correct and valid demoldeability map according to the requirements imposed in the injection molding industry and a new virtual discrete geometry of each part with additional information about its manufacture. In this manner, the new information obtained helps and guides the injection mold designer in the possible geometric modifications that arise during the redefinition of the plastic part requirements. Finally, the computational time required in the present analysis improves and is significantly reduced compared to the computational time of other analogous analysis methodologies with the same objective, since this represents 6% of the total computational time required in the methodologies defined so far.

- The presented methodology, design and dimensioning of the ejection system of an injection mold, has been evaluated and examined through its application in 5 plastic parts with different geometric characteristics (thickness, volume, bounding box dimensions, etc.). By means of graphic techniques, the thickness in each region of the domain of the pieces under study has been calculated. By means of graphic techniques, the thickness in each region of the domain of the case studies parts has been calculated. Then, evaluating graphically the thickness gradients of each of them, the ejection map with the coordinates of the ejectors location required in each case studies parts has been generated. In addition, together with the design results of the ejection system distribution, a technical report is generated for each case studies parts, which includes the different geometric and technological parameters that define the ejection phase of the plastic part from the injection mold. This dimensioning process is defined via genetic optimization algorithms that, through multi-objective fitness functions, determine the optimal magnitudes of each geometric and technological variable that govern the ejection phase.

Among which the following stand out: the diameter of each ejector and the minimum ejection force applied by each ejector to eject the plastic part from the injection mold. Furthermore, in order to not compromise the structural safety of the plastic part, the fitness functions of the optimization algorithm are established to ensure that the set of ejection forces obtained is balanced, homogeneous and uniform, and to avoid exceed the thermoplastic material yield stress during the ejection system operation. Finally, this new method improves the methods developed so far, since it does not require heuristic techniques to obtain the results of the design, layouts and dimensioning of the ejection system of the injection mold.

- The presented methodology, design and dimensioning of the cooling system of an injection mold, has been evaluated and examined through its application in 4 plastic parts with different geometric characteristics (thickness, volume, bounding box dimensions, etc.). By means of graphic techniques, the depth or concavity map in each region of the domain of the pieces under study has been calculated. Then, evaluating the depth map of the piece, it is established the regions that can be cooled by conventional cooling elements such as straight drilled channels and the regions that require conformal cooling elements such as "baffles". In this manner, both for the slender or flat plastic part regions and for the plastic part regions with significant depths or concavities (where the straight drilled channels lose cooling effectiveness), the present methodology locates the main cooling channels and the "baffles" through a geometric optimization process that ensures that the resulting cooling system is uniform, balanced and homogeneous. In addition, together with the results of the cooling system layouts, a technical report is generated, for each case study, that includes the geometric and technological parameters magnitude that govern the cooling phase. This dimensioning process is defined by genetic optimization algorithms that, through multi-objective fitness functions, determine the optimal magnitude of each geometric and technological variable involved in the cooling phase. Among which the following stand out: the diameter of each cooling channel and baffles, the XYZ coordinates of the cooling channels and baffles location, the average of the injection mold surface temperature, the inlet temperature of the coolant to the cooling system and the time to reach the ejection temperature or cooling time. Additionally, the fitness functions of the optimization algorithm are established to ensure a high finish quality and dimensional accuracy in the plastic parts and the reduction of the cooling time. Finally, this new method improves the methods developed so far, since it does not require heuristic techniques to obtain the results of the design, layouts and dimensioning of the cooling system of the injection mold.

- A new methodology to obtain the elapsed time of each one of the phases that conform the injection cycle of a plastic part is presented. In a first phase, a geometric algorithm performs, via graphic techniques, an analysis of the plastic part discrete topology to obtain the path of the melt plastic flow that covers the longest distance during the mold cavity filling phase, as well as the map of thickness of the plastic part. In a second phase, an analytical-empirical model is established to define the filling time, packing and cooling, as well as the geometric parameters that establish the feeding system of the injection mold. This model is defined from the interpolation, by means of polynomial functions, of the results obtained in a set of numerical simulations of the parameterized rectangular specimens filling phase. All of this was evaluated and examined in 6 plastic parts with different geometrical characteristics and thermoplastic materials. In addition, with the results obtained, a technical report is generated that helps to generate a rapid estimate of the injection mold total cost, improving the efficiency and time required in the initial phases of product design.

- The design of a new vertical axis rotor has been experimentally tested in the wind tunnel to evaluate the influence of geometric parameters of product design in terms of power coefficient, torque coefficient and mechanical power generated. The experiments have been carried out for a Reynolds number magnitude in the range of [$3{,}436 \cdot 10^4$ y $1{,}419 \cdot 10^5$]. The experimental results have been validated from a CFD type numerical simulation software, obtaining a standard deviation of 3,5% between the experimental and numerical results. For the range of tip speed ratio values between 0,223 and 0,335, the presented rotor fulfills the functional requirements of small-scale power generation required by the products where the rotor can be included. The new rotor maintains the advantages of the Savonius rotor as well as integrating perfectly in the geometry of the product, giving it personality and making it attractive to consumers. Based on this design methodology, a new line of research emerges that consists of incorporating technical elements capable of contributing to the product energy autonomy, fulfilling its aesthetic and ergonomic design requirements with the main objective of improving the urban sustainability of society.

The set of research works developed in this PhD thesis is characterized by being automated, systematic and smart. The cost and computational time required is significantly reduced, compared to the methodologies developed so far, since the analysis of the plastic part discrete geometry (meshed model composed of nodes and facets) simplifies the functions, operations and graphic techniques used. Additionally, heuristic methods and geometric features recognition of the plastic part are not required, avoiding dependence problems with the CAD software where the plastic part 3D modeling was performed. In this manner, the developed knowledge can be applied to any plastic part geometry, independently of the CAD software used for its geometric 3D modeling. All this, represents an advance and improvement in the knowledge area of manufacturing by means of injection molds, since it allows to optimize the functionality of the injection mold main systems and reduce errors, cost and time in the initial phases of product design. As well as reducing dependence on the experience and knowledge of professionals and experts in this industrial sector.

Finally, all the generated knowledge in this PhD thesis has been integrated into an intelligent application for the automated CAD design of the plastic injection mold geometry, called CELERMOLD [70]. This application is hosted on a web platform, so that users can upload the geometry of the plastic part, define the thermoplastic material (from a wide database that the application has), select the accuracy of the plastic part geometry analysis, the unit number of the plastic part to be manufactured and the delivery time of the batch. This application is the result of the research project "A vertical design software for integrating operations of automated demoldability, tooling design and cost estimation in injection molded plastic parts. (CELERMOLD)", jointly developed by the Plastic Technology Center Andaltec [71] and the Engineering Graphic, Design and Projects department of University of Jaén.

The application of genetic optimization algorithm for the layout design and dimensioning of the injection mold main systems has set a starting point in the transfer and inclusion of artificial intelligence techniques in the manufacturing process by means of plastic injection molds. With the growing development of the industry 4.0 concept, these techniques could provide more efficiency and improve technological processes that intervene during the injection cycle of the plastic part, as well as the optimization of the technological parameters that govern the injection unit during the manufacturing process of the plastic part.

On the other hand, the advance of 3D additive manufacturing technologies ("Rapid Tooling Technologies") and the wide range of plastic and metallic materials that can be used nowadays have allowed their direct application in the plastic injection molding industrial sector. In this manner, due to the flexibility offered by this manufacturing process for the generation of complex geometries and surfaces, it has been possible to develop new conformal cooling systems that optimize the thermal exchange between the refrigerant fluid and the plastic part. While simultaneously improving the aesthetic quality and dimensional accuracy of the final product and reducing the plastic part residual stress after the manufacturing process

Furthermore, awareness an industrial sector where the aesthetic requirements are becoming increasingly demanding, the concept of rapid heating cycle arises. This is based on heating the injection mold surface via conformal channels that adapt to the plastic part geometry and establish a uniform melt plastic flow temperature map during the filling phase. This improves the final quality surface of the plastic part, decreases the appearance of aesthetic defects and enables to eliminate the aesthetic details in the welding lines [72-74]. Therefore, in relation to this new additive manufacturing technology, there is a high potential still to be developed and the challenge of applying all the knowledge generated in this PhD thesis in the development of new methodologies that address the design and dimensioning process of these innovative injection mold systems.

# 1.7. REFERENCIAS

[1] Fu MW, Fuh J,YH, Nee AYC. Generation of optimal parting direction based on undercut features in injection molded parts. IIE Trans 1999;31:947–55.

[2] Ganter MA, Tuss LL. Computer-assisted parting line development for cast pattern production. AFS Trans 1990;795–800.

[3] Wong T, Tan ST, Sze WS. Parting line formation by slicing a trimmed surface model. In: Proceedings of the 1996 ASME design engineering technical conference and computers in engineering conference 1996. August 18–22, Irvine, California.

[4] Fu MW, Nee AYC, Fuh JYH. A core and cavity generation method in injection mold design. Int J Prod Res 2001;39:121–38.

[5] Fu MW, Fuh JYH, Nee AYC. Undercut feature recognition in an injection mould design system. Comput Aided Des 1999;31(12):777–90.

[6] Fu MW. The application of surface demoldability and moldability to side core design in die and mold CAD. Comput Aided Des 2008;40 (5):567–75.

[7] Fu MW, Nee AYC, Fuh JYH. The application of surface visibility and moldability to parting line generation. Comput Aided Des 2002;34(6):469–80.

[8] Fu MW, Fuh J,YH, Nee AYC. Generation of optimal parting direction based on undercut features in injection molded parts. IIE Trans 1999;31:947–55.

[9] Nee AYC, Fu MW, Fuh JYH, Lee KS, Zhang YF. Determination of optimal parting direction in plastic injection mould design. Ann CIRP 1997;46(1):429–32.

[10] Nee AYC, Fu MW, Fuh JYH, Lee KS, Zhang YF. Automatic determination of 3D parting Lines and Surfaces in Plastic Injection Mould Design. Ann CIRP 1998; 47(1):95–9.

[11] Rubio MA, Pérez JM, Rios J. A Procedure for plastic parts demoldability analysis. Robot Comput Integr Manuf 2006;22(1):81–92.

[12] Martin Doñate C, Rubio Paramio MA. New methodology for demoldability analysis based on volume discretization algorithms. Comput Aided Des 2013; 45(2):229–40.

[13] Menges G., Walter M. How to make injection molds, 2001, Hanser, Cincinnati

[14] Ramos, C, et al. (2012) Optimalmould-part II: global optimization of the injection moulding cycle time. AIP Conference Proceedings. Vol. 1479. No. 1. AIP. https://doi.org/10.1063/1.4756465

[15] Xu RX, Sachs E (2009) Rapid thermal cycling with low thermal inertia tools. Polym Eng Sci 49(2):305–316. https://doi.org/10.1002/pen.21261

[16] Dimla DE, Camilotto M, Miani F (2005) Design and optimization of conformal cooling channels in injection moulding tools. J Mater Process Technol 164:1294–1300. https://doi.org/10.1016/j.jmatprotec.2005.02.162

[17] Park HS, Pham NH (2009) Design of conformal cooling channels for an automotive part. Int J Automot Technol 10(1):87–93. https://doi.org/10.1007/s12239-009-0011-7

[18] Park HS, Dang XP (2017) Development of a smart plastic injection mold with conformal cooling channels. Procedia Manuf 10:48–59. https://doi.org/10.1016/j.promfg.2017.07.020

[19] Au KM, Yu KM (2011) Modeling of multi-connected porous passageway for mould cooling. Comput Aided Des 43(8):989–1000. https://doi.org/10.1016/j.cad.2011.02.007

[20] Au KM, Yu KM, Chiu WK (2011) Visibility-based conformal cooling channel generation for rapid tooling. Comput Aided Des 43(4):356–373. https://doi.org/10.1016/j.cad.2011.01.001

[21] Turng LS, Wang KK. A computer-aided cooling-line design system for injection molds. J Eng Ind-Trans ASME 1990;112(2):161–7.

[22] Opolski SW, Kwon TW. Injection molding cooling system design. In: ANTEC'86. 1987. p. 264–8.

[23] Tang LQ, Pochiraju K, Chassapis C, Manoochehri S. A computer- aided optimization approach for the design of injection mold cooling systems. Trans ASME J Mech Des 1998;120:165–74.

[24] Xu XR, Sachs E, Allen S. The design of conformal cooling channels in injection molding tooling. Polym Eng Sci 2001;41(7):1265–79.

[25] Sachs E, Wylonis E, Allen S, Cima M, Guo HL. Production of injection molding tooling with conformal cooling channels using the three dimensional printing process. Polym Eng Sci 2000;40(5):1232–47.

[26] Dalgarno KW, Stewart TD. Manufacture of production injection mould tooling incorporating conformal cooling channels via indirect selective laser sintering. Proc Inst Mech Eng B 2001;215(10):1323–32.

[27] Ilyas I, Taylor C, Dalgarno K, et al. Design and manufacture of injection mould tool inserts produced using indirect SLS and machining processes. Rapid Prototyp J 2010;16(6):429–40.

[28] Au KM, Yu KM. Variable distance adjustment for conformal cooling channel design in rapid tool. J Manuf Sci Eng-Trans ASME 2014;136(4).

[29] Wang Yu, Yu Kai-Min, Wang Charlie CL, et al. Automatic design of conformal cooling circuits for rapid tooling. Comput Aided Des 2011;43(8):1001–10.

[30] Wang Yu, Yu Kai-Min, Wang Charlie CL. Spiral and conformal cooling in plastic injection molding. Comput Aided Des 2015;63:1–11.

[31] A. Griffiths, G. Tosello, S.S. Dimov, S. Scholz, A. Rees, B. Whiteside, Characterisation of demoulding parameters in micro-injection moulding, Microsyst. Technol. 21 (2015) 1677–1690.

[32] A.C. Griffiths, S.S. Dimov, S. Scholz, G. Tosello, A. Rees, Influence of injection and cavity pressure on the demoulding force in micro-injection moulding, J. Manuf. Sci. Eng. 136 (2014) 3.

[33] I. Chan, M. Pinfold, C. Kwong, W. Szeto, A review of research, commercial software packages and patents on family mould layout design automation and optimization, Int J. Adv. Manuf. Technol. 57 (2011) 23–47.

[34] S. Kwak, T. Kim, S. Park, K. Lee, Layout and sizing of ejector pins for injection mould design using the wavelet transform, Proc. Inst. Mech. Eng. 217 (B) (2003) 463–473.

[35] K.D. Delaney, G. Bissacco, D. Kennedy, A structured review and classification of Demolding issues and proven solutions, Int. Polym. Process. 27 (1) (2012) 77–90.

[36] R. Malloy, P. Majeski, Design of pin ejector systems for injection molds, in: Proceedings of the ANTEC 89: 47th Annual Technical Conference-Society of Plastics Engineers, New York, 1989, pp. 1231–1235.

[37] C. Burke, R. Malloy, An experimental study of the ejection forces encountered during injection molding, in: Proceedings of the ANTEC 91: 49th Annual Technical Conference-Society of Plastics Engineers, New York, 1991, pp. 1781–1787.

[38] A.J. Pontes, A.S. Pouzada, R. Pantani, G. Titomanlio, Ejection force of tubular injection moldings. Part I: effect of processing conditions, Polym. Eng. Sci. 44 (5) (2004) 325–332.

[39] N. Bhagabatula, D. Michalski, B. Lilly, G. Glozer, Modelling and verification of ejection forces in thermoplastic injection moulding, Model. Simul. Mater. Sci. Eng. 12 (2004) 234–254.

[40] T. Sasaki, N. koga, K. Shirai, Y. Kobayashi, A. Toyoshima, An experimental study on ejection forces of injection molding, Precis. Eng. 24 (2000) 270–273.

[41] C.K. Mok, K.S. Chin, K.L. Ho, An interactive knowledge-based CAD system for mould design in injection moulding processes, Int. J. Adv. Manuf. Technol. 17 (2001) 27–38.

[42] M.L.H. Low, K.S. Lee, A parametric-controlled cavity layout design system for a plastic injection mould, Int. J. Adv. Manuf. Technol. 21 (2003) 807–819.

[43] Boothroyd G., Dewhurst P., Knight W. Product Design for Manufacture and Assembly, 2011, CRC Press, London and New York.

[44] Galantucci L.M., Spina R., "Evaluation of filling conditions of injection molding by integrating numerical simulations and experimental test", Journal of Materials Processing Technology 141, 266-275 (2002).

[45] Ferreira I., De Weck O., Saraiva P., Cabral J. "Multidisciplinary Optimization of Injection molding Systems" Structural and Multidisciplinary Optimization, 41: 621-635 (2010).

[46] Marinić-Kragić I, Vučina D, Milas Z. Numerical workflow for 3D shape optimization and synthesis of vertical-axis wind turbines for specified operating regimes. Renewable Energy 2018;115:113–27.

[47] Roy S, Saha UK. An adapted blockage factor correlation approach in wind tunnel experiments of a Savonius-style wind turbine. Energy Convers Manage 2014;86:418–27.

[48] Saha UK, Rajkumar MJ. On the performance analysis of Savonius rotor with twisted buckets. Renewable Energy 2006;31(11):1776–88.

[49] Roy S, Saha UK. Wind tunnel experiments of a newly developed two-bucketd Savonius-style wind turbine. Appl Energy 2015;137:117–25.

[50] Kamoji MA, Kedare SB, Prabhu SV. Experimental investigations on single stage modified Savonius rotor. Appl Energy 2009;86(7):1064–73.

[51] Roy S, Ducoin A. Unsteady analysis on the instantaneous forces and moment arms acting on a novel Savonius-style wind turbine. Energy Convers Manage 2016;121:281–96.

[52] Tian W, Mao Z, Zhang B, Li Y. Shape optimization of a Savonius Wind Rotor with Different Convex and Concave Sides. Renewable Energy 2017.

[53] Mcmains S, Chen X. Determining moldability and parting directions for polygons with curved edges. In: International mechanical engineering congress and exposition. ASME Anaheim, CA; 2004.

[54] Mcmains S, Chen X. Finding undercut free directions for polygons with curved edges. ASME J Comput Inf Sci Eng 2006;6(1):60–8.

[55] Priyadarshi AKL, Gupta SK. Geometric Algorithms for automated design of multipiece permanent molds. Comput Aided Des 2004;36(3):241–60.

[56] Dhaliwal S, Gupta SK, Huang J. Computing exact global accessibility cones for polyhedral objects. In: ASME design for manufacturing conference Baltimore MD, September 2000.

[57] Dhaliwal S, Gupta SK, Huang J, Priyadarshi A. Algorithms for computing global accessibility cones. J Comput Inf Sci Eng 2003;3(3):200–9.

[58] Khardekar R, McMains S. Finding mold removal directions using graphics hardware. In: ACM workshop on general purpose computing on graphics processors; 2004, pp. C-19, (abstract).

[59] Khardekar Burton, McMains . Finding feasible mold parting directions using graphics hardware. Comput Aided Des 2006;38(4):327–41.

[60] Chakraborty P, Reddy NV. Automatic determination of parting directions, parting lines and parting surfaces for two

[61] David Kazmer. Injection Mold Design Engineering. 1st ed. Munich: Hanser; 2007.

[62] Sun YF, Lee KS, Nee AYC. The application of U-shape milled grooves for cooling of injection moulds. Proc Inst Mech Eng B 2002;216(12):1561–73.

[63] Dang Xuan-Phuong, Park Hong-Seok. Design of U-shape milled groove conformal cooling channels for plastic injection mold. Int J Precision Eng Manuf 2011;12(1):73–84.

[64] Park HS, Dang XP. Optimization of conformal cooling channels with array of baffles for plastic injection mold. Int J Precision Eng Manuf 2010;11(6):879– 90.

[65] Y.S. Ma, S.B. Tor, G.A. Britton, The development of a standard component library for plastic injection for plastic injection mould design using an object-oriented approach, Int. J. Adv. Manuf. Technol. 22 (2003) 611–618.

[66] V. Kumar, J. Madan, P. Gupta, A system for design of multicavity die casting dies from part product model, Int. J. Adv. Manuf. Technol. 67 (2013) 2083–2107.

[67] Al-Hadhrami LM. Performance evaluation of small wind turbines for off grid applications in Saudi Arabia. Energy Convers Manage 2014;81:19–29.

[68] Roy S, Das R, Saha UK. An inverse method for optimization of geometric parameters of a Savonius-style wind turbine. Energy Convers Manage 2018;155:116–27.

[69] Ducoin A, Shadloo MS, Roy S. Direct Numerical Simulation of flow instabilities over Savonius style wind turbine blades. Renewable Energy 2017;105:374–85.

[70] http://celermold.ujaen.es:8080

[71] http://www.andaltec.org/

[72] Li, X., Zhao, G., Guan, Y. et al. Int J Adv Manuf Technol (2009) 45: 261. https://doi.org/10.1007/s00170-009-1969-z

[73] Yao, D. , Chen, S. and Kim, B. H. (2008), Rapid thermal cycling of injection molds: An overview on technical approaches and applications. Adv. Polym. Technol., 27: 233-255. doi:10.1002/adv.20136

[74] Yao, D. and Kim, B. (2002), Development of rapid heating and cooling systems for injection molding applications. Polym Eng Sci, 42: 2471-2481. doi:10.1002/pen.11133

# CAPÍTULO II: COMPENDIO DE TRABAJOS PUBLICADOS

La presente tesis doctoral se conforma como un compendio de **seis artículos de investigación** que cumplen los criterios establecidos por la Comisión Nacional Evaluadora de la Actividad Investigadora (CNEAI). De los cuales cinco de ellos se encuentran **publicados en revistas científicas de alto impacto y calidad reconocida**, **indexadas** en las bases de datos bibliográficas y bibliométricas **ISI JCR (Journal Citation Reports), ISI WOS (Web of Science) e ISIS Scopus**. Siendo **uno de ellos galardonado con un premio de investigación internacional** en el área del conocimiento Compurter Science: "*21st Annual Best of Computing Notable Article 2016 Area: Computing Methodologies. International Badge otorged by the Prestigious Association of Computing Machinery(ACM)*". La publicación restante es del tipo **Proceeding Paper** y se encuentra **indexada** en las bases de datos bibliográficas y bibliométricas **ISI WOS (Web of Science) y Scopus**. El doctorando aparece como primer autor en cada una de ellas y las fechas de publicación de las mismas están comprendidas entre el inicio y final de los estudios de doctorado del autor. Asimismo, conforme a la normativa de la Universidad de Jáen para la defensa de tesis doctorales (Extracto de los artículos del reglamento de estudio de doctorado de la Universidad de Jaén adaptada a las directrices del R.D. 99/2011 y aprobado en Consejo de Gobierno el 6 de febrero de 2012), estos artículos se enmarcan en el área del conocimiento de la presente tesis y se adjuntan obligatoriamente en esta segunda parte de la memoria. Además, para completar el compendio de trabajos de investigación, se citan **cuatro aportaciones relevantes efectuadas en congresos internacionales, cuatro patentes de invención nacionales y una patente de invención internacional** surgidas, en paralelo, durante la etapa investigadora de la presente tesis doctoral.

# 2.1. ARTICULOS PUBLICADOS EN REVISTAS JCR

1. **Mercado-Colmenero, Jorge Manuel,** Paramio, M.A.R, Perez-Garcia, Jesús María y Martín-Doñate, Cristina. *A new hybrid method for demoldability analysis of discrete geometries. Computer-Aided Design 80 (2016) 43-60. DOI: http://dx.doi.org/10.1016/j.cad.2016.06.006.*

2. **Mercado-Colmenero, Jorge Manuel,** Moya-Muriana, José Ángel, Rubio Paramio, Miguel Ángel y Martín-Doñate, Cristina. *Advances on Mechanics, Design Engineering and Manufacturing, Lecture Notes in Mechanical Engineering (2017) 119-128. DOI: http://dx.doi.org/10.1007/978-3-319-45781-9_13.*

3. **Mercado-Colmenero, Jorge Manuel,** Rubio-Paramio, M.A, Vizan-Idoipe, Antonio y Martín-Doñate, Cristina. *A new procedure for the automated design of ejection systems in injection molds. Robotics and Computer – Integrated Manufacturing 46 (2017) 68-85. DOI: http://dx.doi.org/10.1016/j.rcim.2016.12.006.*

4. **Mercado-Colmenero, Jorge Manuel,** Rubio-Paramio, Miguel Angel, Marquez-Sevillano, Juan de Juanes y Martín-Doñate, Cristina. *A new method for the automated design of cooling systems in injection molds. Computer-Aided Design 104 (2018) 60-86. DOI: https://doi.org/10.1016/j.cad.2018.06.001.*

5. **Mercado-Colmenero, Jorge Manuel,** Rubio-Paramio, Miguel Angel, Karlinger, Peter, Martín-Doñate, Cristina. *A new procedure for calculating cycle time in injection molding based on plastic part geometry recognition. The International Journal of Advanced Manufacturing Technology 98 (2018) 441-477. DOI: https://doi.org/10.1007/s00170-018-2080-0.*

6. **Mercado-Colmenero, Jorge Manuel,** Rubio-Paramio, Miguel Angel, Guerrero – Villar, Francisca, Martín-Doñate, Cristina. *A numerical and experimental study of a new Savonius wind rotor adaptation based on product design requeriments. Energy Conversion and Management 158 (2018) 210-234. DOI: https://doi.org/10.1016/j.enconman.2017.12.058.*

Referencia / Reference: **Mercado-Colmenero, Jorge Manuel,** Paramio, M.A.R, Perez-Garcia, Jesús María y Martín-Doñate, Cristina. *A new hybrid method for demoldability analysis of discrete geometries. Computer-Aided Design 80 (2016) 43-60. DOI: http://dx.doi.org/10.1016/j.cad.2016.06.006.*

Estado / Status: Publicado / Published

Índice de impacto / Impact Factor: 2,444 (JCR Year 2016)

Categoría / Catogory: Computer Science, Software Engineering

Ranking: 22/104 (JCR Year 2016)

Quartile: Q1 (JCR Year 2016)

JIF Percentile: 79.717 (JCR Year 2016)

Este artículo de investigación ha sido seleccionado entre los 273 "notables papers" del año 2016 del mundo en el área del conocimiento "Computer Graphics" por la prestigiosa asociación ACM. (Association of Computing Machinery. Siendo el único artículo de investigación realizado por investigadores de una universidad española. 21st Annual Best of Computing Notable Article 2016 Area: Computing Methodologies. International Badge otorged by the Prestigious Association of Computing Machinery(ACM).

Computer-Aided Design 80 (2016) 43–60

Contents lists available at ScienceDirect

Computer-Aided Design

journal homepage: www.elsevier.com/locate/cad

# A new hybrid method for demoldability analysis of discrete geometries☆

Jorge Manuel Mercado-Colmenero [a], M.A.R. Paramio [a], Jesus Maria Perez-Garcia [b], Cristina Martin-Doñate [a,*]

[a] Department of Engineering Graphics Design and Projects, University of Jaen, Spain

[b] Department of Mechanical Engineering, Polytechnical University of Madrid, Spain

ARTICLE INFO

*Article history:*
Received 1 October 2015
Accepted 27 June 2016

*Keywords:*
Demoldability analysis
Geometric analysis
Injection molding
Computer aided manufacturing

ABSTRACT

In this paper, a new method for demoldability automatic analysis of parts to be manufactured in plastic injection is presented. The algorithm analysis is based on the geometry of the plastic part, which is discretized by a triangular mesh, posing a hybrid discrete demoldability analysis of both the mesh nodes and facets. A first preprocessing phase classifies mesh nodes according to their vertical dimension, assigning each node a plane perpendicular to the given parting direction. By selective projection of facets, closed contours which serve as the basis for calculating the demoldability of the nodes are created. The facets are then cataloged according to demoldability nodes that comprise demoldable, non-demoldable and semi-demoldable facets. Those facets listed as semi-demoldable are fragmented into demoldable and non-demoldable polygonal regions, causing a redefinition of the original mesh as a new virtual geometry. Finally, non-demoldable areas are studied by redirecting the mesh in the direction of the sliding side, and again applying the processing algorithm and cataloging nodes and facets. Resoluble areas of the piece through mobile devices in the mold are obtained. The hybrid analysis model (nodes and facets) takes advantage of working with a discrete model of the plastic part (nodes), supplemented by creating a new virtual geometry (new nodes and facets) that complements the original mesh, providing the designer not only with information about the geometry of the plastic piece but also information on their manufacture, exactly like a CAE tool. The geometry of the part is stored in arrays with information about their manufacture for use in downstream applications.



## 1. Introduction

Injection molding is a manufacturing process of plastic parts which can make parts with complex geometries and freeform surfaces. It is suitable for high production volumes because of its reduced cycle time. Essentially, an injection mold consists of two parts called the upper and lower cavity, within which the plastic is injected, leading to the desired body. The main parameters that largely determine the structure of a mold are: the presence of undercuts, the chosen parting direction, and the parting line generated between the various mold components. Demoldability geometric analysis aims to determine these parameters automatically based on the definition of the geometry of the part to be molded. Selecting the parting direction and the parting surface is of great significance so that the number of side cores is reduced to a strict minimum. The number and volume of the side cores increases the mold complexity and the costs of manufacture and the time spent in the manufacturing cycle of the pieces to be processed and, ultimately, its production cost.

During the conceptual phase of the design process, customers often impose a large number of changes in the geometry of the part. It is necessary to validate demoldability quickly, detecting and differentiating automated small undercuts and areas that cannot be manufactured. Moreover, in the preparation of price studies for the manufacturing of plastic parts, a quick and accurate review of part geometry in their manufacture can be a determining factor in achieving a deal. The commercial CAD systems used today by companies for the resolution of analysis demoldability still involve a great deal of manual interaction on the part of the designer. The

☆ This paper has been recommended for acceptance by Kin-Chuen Hui.

* Correspondence to: Department of Engineering Graphics Design and Projects, University of Jaen, Campus Las Lagunillas, s/n. Building A3-210, 23071 Jaen, Spain. Fax: +34 953212334.

*E-mail addresses:* jmercado@ujaen.es (J.M. Mercado-Colmenero), marubio@ujaen.es (M.A.R. Paramio), jesusmaria.perez@upm.es (J.M. Perez-Garcia), cdonate@ujaen.es (C. Martin-Doñate).

http://dx.doi.org/10.1016/j.cad.2016.06.006
0010-4485/

knowledge of the CAD tool is not sufficient and great experience is required in the manufacture of plastic parts.

Reducing design and manufacturing time, establishing good precision and quality in the finished piece and being able to make design changes quickly are the main concerns of the designers of new products in the industry of injection molding. Solving these problems requires a complete automation of the analysis process of the plastic part for its manufacture. Numerous methods at the research level have addressed the analysis of geometric demoldability, but they have many disadvantages in that they are either linked to the modeler to analyzing the piece internally, or need additional computing devices such as GPU's, or are not valid for analyzing all kinds of plastic parts.

In order to solve the problems described above, a new method for analyzing the geometric demoldability and calculation of the parting line is presented. This method is based on the discrete model of the plastic part consisting of a triangular mesh. This methodology develops a hybrid analysis of the part mesh, analyzing the demoldability of both mesh nodes and their facets. A first preprocessing phase classifies discrete mesh nodes according to their manufacturability. Based on this information, a second algorithm processes the mesh facets and color them based on their demoldability. The geometry of the plastic part is stored in separate arrays of nodes and facets with information on their manufacture for use in downstream applications. The new analysis algorithm developed results in a new virtual mesh of the plastic part that complements the initial nodes and adds new semi-facets to provide information not only on the part geometry but also on part manufacture. The resulting mesh represents the demoldability map of the plastic part. Nodes and facets are colored just as with a CAE tool. This algorithm improves the methods developed so far, since is valid for all kinds of plastic parts, for any modeler, and requires no additional hardware, allowing changes to be implemented quickly during the early stages of design and studies of price.

## 2. Background and related work

Demoldability analysis and calculation of the parting line are considered extremely important tasks in the design of the plastic part due to their influence on the quality and the costs of the manufacturing process. Both academic and industrial researchers have been seeking new methodologies to address the recognition of the surface of the plastic part in its application to the analysis of demoldability in order to achieve high levels of quality while reducing design time and production.

Many methodologies for determining the demoldability of the part along the parting direction are based on visibility analysis. The visibility map of a surface is the set of all directions from which the surface is completely visible. In terms of geometrical analysis of the surface of the plastic part, a parallelism between the concepts of visibility and demoldability can be established. The complexity of calculating the visibility of a surface obviously depends on the complexity of the surface itself which, in the extreme case of freeform surfaces, would be determined by calculating the visibility of each of its points. One of the first methods used for analyzing parts demoldability applying visibility maps was proposed by Chen et al. [1], who introduced the concept of the pocket for the calculation of non-demoldable areas. Chen et al. [2] created an algorithm for obtaining the optimal parting direction, by dividing objects into pockets. In these pockets visibility and moldability play the same role. Chen et al. [3] set both global and local visibility levels in order to extend their work to internal undercuts features and to decompose them into separable portions (based on complete visibility) and undercuts (on partial visibility). Weinstein and Manoochehri [4] obtained optimal parting directions by means of the location of common visibility areas of concave surfaces, the partition line being obtained by analyzing the surfaces belonging to the convex area.

Much research is based on features recognition in casting and plastic parts. A feature is a geometric region of the piece which has additional information about its manufacture. Currently, the solid modeling of the piece does not store this information explicitly. The methods of extracting features allow the development of methodologies that enable us to extract the required information and enter it as an input in a structured algorithm. On the plastic parts, undercut features encompass geometric regions of the piece, which are not accessible along the parting direction. Identifying undercut features directly affects the determination of the partition line and the design of upper and lower cavity, as well as the design of the mobile devices of the mold. Researchers have used different techniques for determining undercut features. Fu et al. developed a complete solution for the computer-aided design of plastic injection molds including the definition, classification and recognition of undercut features [5], determining the parting direction [6], parting line and surfaces [7], upper and lower cavities [8], and design of side cores [9]. Ran and Fu [10] proposed a methodology for obtaining the automatic design of internal pins in injection mold CAD via the automatic recognition of undercut features. Wuerger and Gadh [11,12] used the concavity features to locate the parting direction, using the convex hull of the part and then the Boolean difference with the piece. Kurt and Gadh [13] extended this research to the concavity features created by extrusion or rotation of a flat section. Lu and Lee [14] performed an analysis of the undercut features method by means of the elements of interference. Yin et al. [15] provided an algorithm to recognize undercut features for near net shapes. Ye et al. [16] proposed an undercut features recognition hybrid method that takes advantage of graph recognition methods. With this method the plastic part is configured by 'extended attributed face edge graphs', while undercut features recognition is based on searching for the 'cut sets' of undercut sub-graphs. In [17] Ye extended their work to side core design. Based on the curvature properties of entities in the B-Rep model Zhang et al. [18] describe an approach to recognizing DP features. Bassi et al. [19] proposed an automatic mold feature recognition system to recognize protrusion and depression as well as intersecting depression features. Other methods combine features recognition algorithms with visibility and accessibility analysis. Surti et al. [20] proposed a projection based methodology to analyze the visibility of a part from a given parting direction without discretizing the part. Singh et al. [21] describe an automated identification, classification, division and determination of the parting direction of complex undercut features of die-cast parts. Then the undercut features are classified using a rule-based algorithm. The 3D solid object in the format B-Rep, boundary representation, means the geometric and topological representation of the object may not be unique, since it depends on the procedures used for the CAD model generation, or the internal kernels used by the CAD program. Furthermore, the recognition of features for a piece created in a CAD system is linked to the modeler with which it was created. Another important issue in the automated recognition of features is the treatment of the interacting features. An interacting feature is the result of the intersection of multiple features. The difficulty in recognizing the interacting features is given mainly because, in the interaction between features, a destruction of the adjacency relationships between features that were in contact occurs. Furthermore, the decomposition from a complex feature to several individual features creates problems of multiple interpretations, generated mainly by the sequences in which the features are recognized.

Nee et al. [22,23] addressed the problem of demoldability by classifying plastic part surfaces according to their orientation with

respect to the parting direction and their connection to each other. This method uses the dot product between the normal surface vector and parting direction in order to calculate the parting line. Hui and Tan [24] presented a method for obtaining the optimal parting direction using several parameters such as blocking factor and preference value. This set of values is calculated for all proposed parting directions. Ravi and Srinivasan [25] proposed a set of nine criteria for obtaining partition lines of plastic injection parts and casting parts, and applied an automatic process in order to achieve the optimal solution according to this set of criteria. All of the above-mentioned methods face difficulties in recognizing undercut features from solid objects with free form surfaces. Rappaport and Rosenbloom [26] introduced the concept of moldability in simple polygons, linking it to that of monotonicity. Ahn et al. [27] established the conditions that must be accomplished for a polyhedral part to be moldable in two directions and in [28] they extended this work to arbitrary objects. Nevertheless, the complex implementation of their method lengthens considerably the running time of the complete algorithm. Chen and McMains [29] introduced an algorithm for calculating all the Undercut free parting directions for extrusions. This algorithm is based on a previous study on 2D profile analysis addressed in [30,31].

Mold design methods based on fuzzy logic algorithms are involved with the fact that several influence parameters such as parting direction, parting line, undercut features etc. interact among themselves. It is necessary to develop a methodology that studies these parameters in an integrated way. Yin et al. [32] presented a hybrid approach to obtaining an optimal combination of these parameters. Chen et al. [33] developed a method for finding and locating the minimum bounding box volume of tridimensional CAD parts and proposed a weighting scheme based on fuzzy logic for the automatic selection of parting directions in plastic parts injection.

Other authors have conducted their research into the geometric resolution of multipiece molds based on the study of accessibility. The technology of multipiece molds largely overcomes the restrictions imposed by traditional molds. The multipart mold has several parting directions, with each of its parts incorporating a different parting line. The algorithms encompassed by this group, mainly developed by Huang et al. [34] and Priyadarshi et al. [35], are based on accessibility studies conducted by Dhaliwal. Dhaliwal et al. [36,37] presented an algorithm for calculating global accessibility cones for each side of a polyhedral object. A point belonging to a geometric entity is accessible from a given direction if a semi-infinite ray can be drawn from it towards the given direction without intersecting inside the geometric entity. Based on this concept a parallel between accessibility and demoldability is established. The inaccessible region in every facet due to the presence of another facet is calculated. Priyadarshi et al. [35] developed an algorithm for automating the design of multi-part permanent molds. First, a set of parting directions $d$ are located based on the geometry of the part. Then an analysis of accessibility is performed at each facet along the chosen parting direction, checking occlusion of each facet with the remaining facets. However these molds are of limited application, and are used more in the field of prototype tooling. Multipiece mold design problems are computationally very challenging. Existing techniques work well if the number of mold pieces in the final solution is relatively small (Bourne et al. [38]). Chen and Rosen [39] presented a region-based approach to automated mold design for simple two-piece molds as well as molds with many additional moving sections. With this approach part faces are partitioned into regions, each of which can be formed by a single mold piece. Later they presented an approach [40] based on a reverse glue operation for generating parting faces. A problem definition of parting face generation for a region is provided. Correspondingly, three face generating criteria are identified.

Other researchers perform a demoldability analysis of the plastic part by means of techniques based on making cuts to the model. The result is a variable set of sections, which are then traversed by a bundle of lines to obtain a set of border points. The demoldability and the parting line analysis are deduced by studying the points obtained [41–44]. Ganter et al. [41] analyzed sections made to the plastic part and established a set of nine rules based on the experience as well as a vast bibliography. Wong et al. [42] improves the algorithm extending the scope to pieces with partition lines with various contours and increasing the accuracy of the algorithm. Rubio et al. [43] use a technique of discretization of 3D solids to solve the problem of demoldability, performing a process of analysis by planes. More recently Martin et al. [44,45] propose a method of discretization of the solid, which transforms the solid body into a grid of points, reallocating points in the mesh based on their demoldability. While the main advantage of these methods is that they analyze the part geometry externally, they do not achieve the accuracy of methods based on recognition of features.

Some authors use tessellated models as input to their algorithms. Tessellations of the plastic part provide a great advantage when the piece incorporates complicated and freeform surfaces. Some recognition methods locate non-demoldable areas in the plastic part based on the use of GPU'S. The first applications of programmable GPUs were described by Khardekar et al. [46]. Khardekar et al. [46,47] use the GPU as a means of recognizing parting directions which have no undercuts. They propose a method to detect undercuts and thus enlighten as well as to locate minimal and insufficient demolding angles. Other authors also use tessellated models to obtain the parting direction and the parting line. Chakraborty et al. [48] identifies non-convex regions, determining the set of possible parting directions as well as the accessibility along each parting direction. Finally the best parting direction is selected, and a parting surface corresponding to the best parting direction is generated. The best parting direction is the one that achieves the best value for a factor which is the sum of several individual factors, including visibility, flatness of the parting line, and demolding depth. Singh et al. [49] use a tessellated model and discuss the classification of the die cast part surfaces, identifying undercuts and protrusions, and determining the parting line. By employing Euler operations, Shin and Lee [50] presented a procedure for locating side cores and upper and lower cavities by means of identifying interference surfaces (primary and secondary) of the mold. Banerjee and Gupta [51] described algorithms for generating shapes of side actions. Given a set of undercut facets on a polyhedral part and the main mold opening directions, candidate retraction space for every undercut facet is computed. This space represents the set of candidate translation vectors that can be used by the side action. Li et al. [52] develop a method which computes a smooth parting line which runs through a band of triangles whose normals are approximately perpendicular to the parting direction. The methods presented here use a faceted model as a basis for the implementation of undercut recognition algorithms. However, many of these assume that the part to be produced is moldable, without internal side cores or undercut features that interact. Moreover these methods work with the normal vector of the facets, making the calculations complex and usually requiring additional hardware.

This paper proposes a new method for performing the analysis of demoldability and the calculation parting line for a given parting direction. The algorithm works with an initial file representing discrete surface geometry, and obtains as a result a new virtual discrete geometry which incorporates information of the molding manufacture of the piece. It works with the coordinates of the points and is valid for all kinds of parts and CAD systems independently of the modeler used. The algorithm detects not only lateral undercuts resolvable through side cores, but non-demoldable

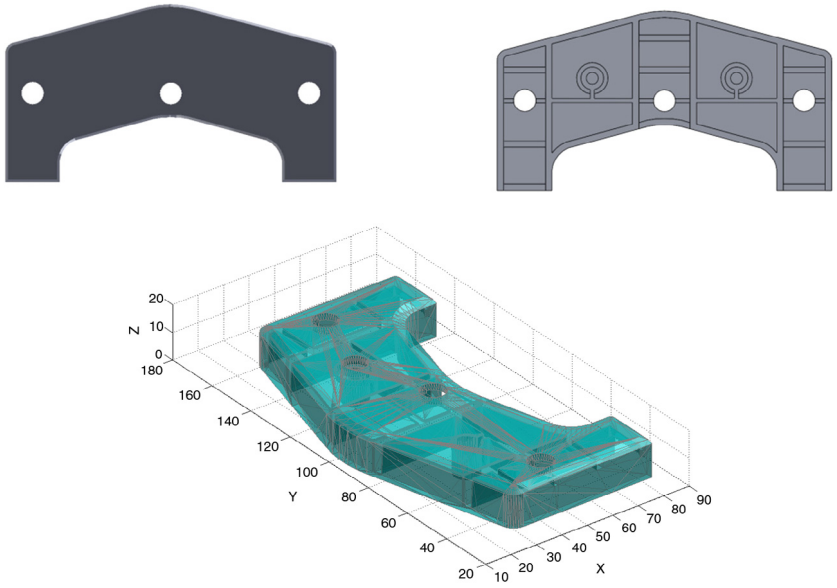


**Fig. 1a.** Converting a CAD model to a virtual faceted model.

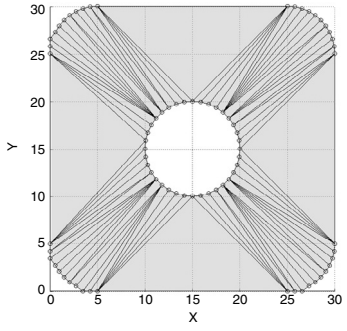


$$\text{Nodes}: \mathcal{B}'_n = \begin{Bmatrix} P_{11} \\ P_{12} \\ P_{13} \\ \vdots \\ P_{n\cdot m1} \\ P_{n\cdot m2} \\ P_{n\cdot m3} \end{Bmatrix} = \begin{bmatrix} x_{11} & y_{11} & z_{11} \\ x_{12} & y_{12} & z_{12} \\ x_{13} & y_{13} & z_{13} \\ \vdots & \ddots & \vdots \\ x_{n\cdot m1} & y_{n\cdot m1} & z_{n\cdot m1} \\ x_{n\cdot m2} & y_{n\cdot m2} & z_{n\cdot m2} \\ x_{n\cdot m3} & y_{n\cdot m3} & z_{n\cdot m3} \end{bmatrix}$$

$$\text{Facets}: \mathcal{B}'_f = \begin{Bmatrix} F_1 \\ \vdots \\ F_n \end{Bmatrix} = \begin{bmatrix} P_{11} & P_{12} & z_1 \\ \vdots & \ddots & \vdots \\ P_{n1} & P_{n2} & P_{n3} \end{bmatrix}$$

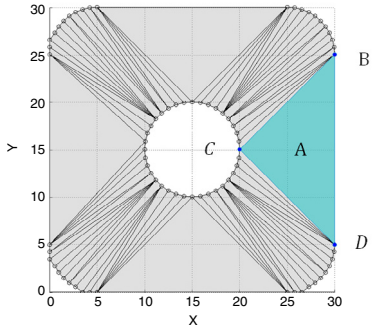


| Elements | Definition |
|---|---|
| A | $F_i = \{P_{i1}, P_{i2}, P_{i3}\}$ |
| B | $P_{i1} = \{x_{i1}, y_{i1}, z_{i1}\}$ |
| C | $P_{i2} = \{x_{i2}, y_{i2}, z_{i2}\}$ |
| D | $P_{i3} = \{x_{i3}, y_{i3}, z_{i3}\}$ |

**Fig. 1b.** Definition of facets and nodes, triangular shell elements.

areas as well, allowing the designer to make changes in the early phases of design.

## 3. Methodology

Let B be the 3D part to be manufactured. The algorithm proposed in this article must be valid for use in any part to be produced with the injection molding technique.

$\forall\, \mathcal{B} \in \mathbb{R}^3$.

First the solid $\mathcal{B}$ is transformed into a discrete mesh $\mathcal{B}'$ consisting of a set of triangular facets and nodes. Thus the discrete mesh $\mathcal{B}'$ is defined as a vector of dimensions $1 \times 2$, formed firstly by a rank $n \times 3$ array $\mathcal{B}'_f$ grouping the entire set of triangular facets ($n$ being the total number of mesh facets), and secondly by the rank $3n \times 3$ array $\mathcal{B}'_n$ grouping the whole set of nodes of the mesh. This allows us to define the geometry of the part externally Figs. 1a and 1b and thus avoid the problems of dependence of the CAD model.

$$\forall\, \mathcal{B} \to \mathcal{B}' \in \mathcal{M}_{1\times 2}\ (\mathbb{R}) \to \mathcal{B}' = \{\mathcal{B}'_f\ \mathcal{B}'_n\}$$

where first term $\mathcal{B}'_{11}$ of array $\mathcal{B}'$, represents the set of facets of the mesh.

$$\mathcal{B}'_{11} = \mathcal{B}'_f \to \mathcal{B}'_f \in \mathcal{M}_{n\times m}\ (\mathbb{R})$$

$$\mathcal{B}'_f := b'_f\ (ij)_{n\times m}\,.$$

Furthermore array $\mathcal{B}'_f$ could be expressed by nodes that compose it. For instance given a facet $F_i$, it can be defined by its

position in array $\mathscr{B}'_f$.

$$\mathscr{b}'^{i}_{f} = F_i.$$

Or it can be defined by nodes $\{P_{i1} \ldots P_{ij} \ldots P_{im}\}$ that compose it.

$$F_i = \left\{P_{i1}, \ldots, P_{ij}, \ldots, P_{im}\right\} \rightarrow \mathscr{b}'_f\,(ij) = P_{ij}$$
$$1 \leq i \leq n;\ 1 \leq j \leq m$$

where $n$ represents the total number of mesh facets and m represents the number of nodes per facet. By working only with triangular facets, then $m = 3$.

$$\mathscr{B}'_{12} = \mathscr{B}'_n \rightarrow \mathscr{B}'_n \in \mathscr{M}_{n\cdot 3\times 3}\ (\mathbb{R})$$

where first term $\mathscr{B}'_{12}$ of array $\mathscr{B}'$, represents the set of nodes of the mesh.

$$\mathscr{B}'_n := \mathscr{b}'_n\,(ij)_{n\cdot 3\times 3}\,.$$

Given a node $P_{ij}$, it can be defined by its position in array $\mathscr{B}'_n$.

$$\mathscr{b}'^{i}_{n} = P_{ij}.$$

Or it can be defined by its coordinates $x, y, z$.

$$P_{ij} = \{x_{ij}, y_{ij}, z_{ij}\}$$
$$1 \leq i \leq n \cdot 3;\ 1 \leq j \leq 3.$$

Each node $P_{ij}(x_{ij}, y_{ij}, z_{ij})$ belonging both to a facet $F_i$ and to the mesh $\mathscr{B}'_n$, must be unique for that facet $F_i$.

$$\left.\begin{array}{c}\forall\, F_i = \{P_{i1}, P_{i2}, P_{i3}\} \in \mathscr{B}'_f \\ 1 \leq i \leq n \\ \forall\, P_{ij} = \{x_{ij}, y_{ij}, z_{ij}\} \in \mathscr{B}'_n \\ 1 \leq i \leq n \cdot 3;\ 1 \leq j \leq 3\end{array}\right\} \rightarrow \{x_{i1}, y_{i1}, z_{i1}\} \neq \{x_{i2}, y_{i2}, z_{i2}\} \neq x_{i3}, y_{i3}, z_{i3}.$$

### 3.1. Classification and recognition of the mesh elements. Preprocessing

During the preprocessing phase the $P_{ij}$ elements of the geometric mesh $\mathscr{B}'_n$ will be classified according to their $z_{ij}$ coordinate, along the direction vector $\left(\overrightarrow{V_z}\right)$ parallel to the parting direction and in the positive direction, Fig. 2. The main parting direction is determined by the user as a starting data so that the choice can be changed if convenient, once the analysis is finished.

Let $V_l \in \mathbb{R}^2$ be a one-dimensional vector, which contains the set of $z_{ij}$ coordinates of the points $P_{ij} = \{x_{ij}, y_{ij}, z_{ij}\}$ belonging to $\mathscr{B}'_n$, sorted in descending order of $\left(\overrightarrow{V_z}\right)$. A set of planes of analysis $Pl_k$ parallel to the plane XOY and perpendicular to $\left(\overrightarrow{V_z}\right)$ will be assigned for each value of the vector $V_l$.

Then the facets $F_i \in \mathscr{B}'_f$, will be classified in levels (sub-arrays $Pl_k$) in a multidimensional array $\Pi_k \in \mathbb{R}^n$. Each dimension $k$ of it will correspond to a plane of analysis $Pl_k$, containing all facets $F_i \in \mathscr{B}'_f$, so that at least one of its vertices $\{P_{i1}, P_{i2}, P_{i3}\}$ belongs to the plane $Pl_k$, Fig. 2.

$$V_l \in \mathscr{M}_{1\times q}\ (\mathbb{R}) \rightarrow V_l = \{z_1, z_2, \ldots z_k, \ldots, z_q\}$$

$$\text{If} \left\{\begin{array}{c} Pl_k : z = Cons; z = z_k = Cons \\ (z_{i1} = z_k) \wedge (z_{i2} = z_k) \wedge (z_{i3} = z_k) \\ 1 \leq i \leq n \cdot 3 \\ 1 \leq k \leq q \\ \Pi_k \in \mathbb{R}^n \end{array}\right\} \rightarrow F_i = \{P_{i1}, P_{i2}, P_{i3}\} \in \Pi_k$$

where $n$ represents the total number of mesh facets and $q$ the number of $z$ coordinates nodes unequal.

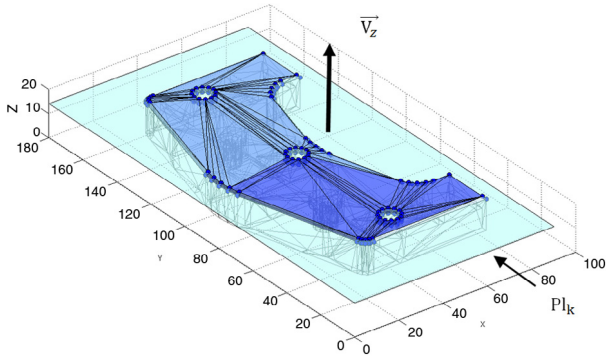


**Fig. 2.** Defining the set of nodes/facets belonging to $Pl_k$.

### 3.2. Algorithm of analysis and classification of mesh nodes, processing

After the grouping of the different facets $F_i \in \mathscr{B}'_f$, according to the value $z_{ij}$ of their respective nodes $\{P_{i1}, P_{i2}, P_{i3}\}$, along the parting direction $\left(\overrightarrow{V_z}\right)$, mesh $\mathscr{B}'$ is processed in order to study its demoldability, analyzing geometrically the facets $F_i \in \mathscr{B}'_f$ and the nodes $P_{ij} \in \mathscr{B}'_n$ according to demoldability criteria. First, the $\mathscr{B}'$ geometry is evaluated, according to the parting direction $\left(\overrightarrow{V_z}\right)$ in the positive direction, in order to estimate the geometric regions of the part to be manufactured by the upper cavity. Subsequently, a reorientation of the part in the opposite direction to the one analyzed previously allows the regions that belong to the lower cavity to be located.

Initially the different facets $F_i$ and points $P_{ij}$ contained in each of the levels ($Pl_k$ sub-arrays) of the multidimensional array $\Pi_k \in \mathbb{R}^n$ are selected. Thus for a sequential $Pl_k$ plane, a closed polygonal analysis contour $C_k \in \mathbb{R}^2$ will be defined from the projection $Proj[\sum_1^{k-1} F_{i,k}]$ of all facets $\sum_1^{k-1} F_{i,k}$ contained in superior levels $[1, k-1]$ of the array $\Pi_k \in \mathbb{R}^n$, Fig. 3.

$$\forall\, F_i = \{P_{i1}, P_{i2}, P_{i3}\} \in \Pi_k : z_k = Cons \rightarrow C_k = \left[Proj[F_{i,k}]\right] \in \mathbb{R}^2.$$

The $F_i$ facets that are in the first level of the multidimensional array $\Pi_k \in \mathbb{R}^n(Pl_1)$, (those that meet the geometrical condition that at least one point $P_{ij} \in Pl_1$) are classified as demoldable facets.

$$\forall F_i = \{P_{i1}, P_{i2}, P_{i3}\} \in \Pi_1 : (P_{i1} \in Pl_1) \wedge (P_{i2} \in Pl_1) \wedge (P_{i3} \in Pl_1) \rightarrow F_i \in \Omega_{f_1}$$

where $\Omega_{f_1} \in \mathscr{B}'_f \in \mathbb{R}^3$ is defined as the locus corresponding to all demoldable facets of the upper mold cavity. For some facets $F_i \in \Pi_1$ which form a coplanar region $\dot{C}_1$, those facets $F_i \in Pl_1$ which are coplanar with each other will be included in $\Omega_{f_1}$.

$$\text{If } \exists\, \dot{C}_1 \subset C_1 : C_1 = Proj\left[F_{i,1}\right] : z = z_1 \rightarrow \dot{C}_1 \in \Omega_{f_1}.$$

Then, for the following levels $k[2, q]$ a series of checkpoints or Gauss points $P_{Gauss} \in F_i$ in all facets $F_i \in C_k$ will be generated. The algorithm will project the set of points $\{(P_{ij} \in \mathscr{B}'_n) - (P_{ij} \in Pl_k)\} \rightarrow z_{ij} < z_k$ and the corresponding control points $P_{Gauss}$ on $C_{k-1}$ [Appendix]; checking whether the points $P_{ij}$ and $P_{Gauss}$, can be demolded along the parting direction $\left(\overrightarrow{V_z}\right)$. Thus if a point $P_{ij}$ is strictly outside the region of study $C_{k-1}$, it is cataloged as an upper demoldable element $\in \Omega_{n_1}$, being $\Omega_{n_1}$ the array for storing the set of points $P_{ij}$ in the demoldable positive direction of parting direction $\left(+\overrightarrow{V_z}\right)$. On the contrary, if an element is placed inside the region $C_{k-1}$ or at the border $Fr(C_{k-1})$, that point $P_{ij}$ is cataloged

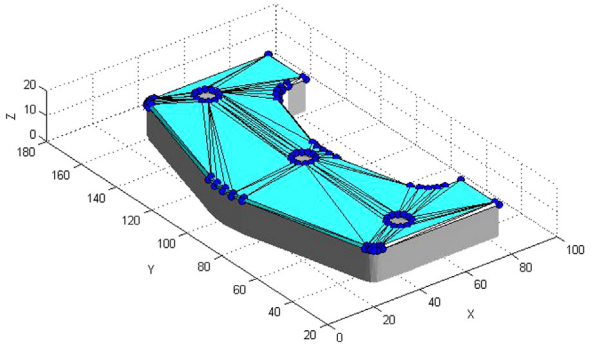

**Fig. 3.** Representation of facets $F_i$ for the level $k$ of $\Pi_k$, definition of $C_k$.

as not demoldable $\in \beta_{n_2} \in$, being $\beta_{n_2}$ the array for storing the set of non-demoldable points $P_{ij}$ in the parting direction $\left(+\overrightarrow{V_z}\right)$.

$\mathscr{B}'_n = \{\Omega_{n_1} \cup \beta_{n_2}\}$

$n_1 + n_2 = n$.

A point $P_{ij} = \{x_{ij}, y_{ij}, z_{ij}\} \in \mathbb{R}^3$ is a border point of $C_k$ if all the surrounding zone of $P_{ij} = \{x_{ij}, y_{ij}, z_{ij}\}$ contains at least some points $\in C_k$ and some points $\notin C_k$. The set of border points of $C_k$ is called the border of $C_k$ and it is denoted by $Fr(C_k)$, where $C(C_k)$ is the complementary set of $C_k$.

$Fr(C_k) = \overline{C_k} \cap \overline{C(C_k)}$

$$\text{If} \begin{Bmatrix} \exists P_{ij} = \{x_{ij}, y_{ij}, z_{ij}\} \in Pl_k \\ 1 \le k \le q \\ 1 \le i \le n \cdot 3;\ 1 \le j \le 3 \end{Bmatrix} : ([x_{ij}, y_{ij}] \notin \overline{C}_k) \wedge ([x_{ij}, y_{ij}] \notin [Fr(\overline{C_k})]) \rightarrow P_{ij} \in \Omega_{n_1}$$

$$\text{If} \begin{Bmatrix} \exists P_{ij} = \{x_{ij}, y_{ij}, z_{ij}\} \in Pl_k \\ 1 \le k \le q \\ 1 \le i \le n \cdot 3;\ 1 \le j \le 3 \end{Bmatrix} : ([x_{ij}, y_{ij}] \in [Fr(\overline{C_k})]) \wedge ([x_{ij}, y_{ij}] \in [\overline{C_k}]) \rightarrow P_{ij} \in \beta_{n_2}.$$

In Fig. 4 the contour border $Fr(C_k)$, bounded by the points $P_{ij} \in Pl_k$ is shown. In Fig. 5 an example is shown of the partial analysis of demoldability for an intermediate plane $Pl_k$. The sub-algorithm whose function is the analysis and classification of nodes $P_{ij}$ of the mesh $\mathscr{B}'_n$ with respect to the parting direction is called InProject (Appendix). For the successive $k$ loops for the execution of InProject, those facets $F_i$ that have been included in the contour $C_{k-1}$ will not be taken into account in the boundary region $C_k$ as a facet can be on two levels and therefore only be considered in one of them.

After the execution of the $k$ analysis, a procedure for comparing the points stored in arrays $\Omega_{n_1}$ and $\beta_{n_2}$ is carried out. It may occur

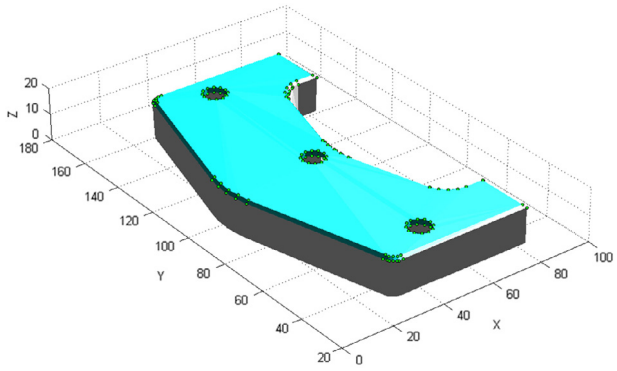

**Fig. 5.** Partial demoldability analysis for a plane ($Pl_k$).

that a point has been identified as demoldable $P_{ij} \in \Omega_{n_1}$ and not demoldable $P_{ij} \in \beta_{n_2}$ at different planes. The points which have this duplication are categorized as non-demoldable. In Fig. 6 the result of the algorithm InProject for solid $\mathscr{B}$ is shown.

$$\text{If} \begin{Bmatrix} P_{ij} = \{x_{ij}, y_{ij}, z_{ij}\} \in \Omega_{n_1} \\ P_{qj} = \{x_{qj}, y_{qj}, z_{qj}\} \in \beta_{n_2} \end{Bmatrix} : \begin{Bmatrix} x_{ij} = x_{qj} \\ y_{ij} = y_{qj} \\ z_{ij} = z_{qj} \end{Bmatrix} \rightarrow P_{ij} = \{x_{ij}, y_{ij}, z_{ij}\} \in \beta_{n_2}.$$

### 3.3. Algorithm for cataloging the mesh facets, processing

After analyzing the demoldability of mesh nodes $P_{ij} \in \mathscr{B}'_n$ (preprocessing and classification of nodes), the objective of this phase is to catalog the facets $F_i \in \mathscr{B}'_f$, according to their demoldability, into demoldable facets, non-demoldable facets, and partially demoldable or semi-demoldable facets, and to store them in arrays with geometric information about the manufacture of the piece.

$\mathscr{B}'_f = \{\Omega_{f_1} \cup \xi_{f_2} \cup \Gamma_{f_3} \cup \Delta_{f_4}\}$

$f_1 + f_2 + f_3 + f_4 = f$.

$\Omega_{f_1}, \xi_{f_2}$: Locus corresponding to all demoldable facets, upper cavity and lower cavity respectively along $\left(\overrightarrow{V_z}\right)$, being $f_1$ and $f_2$ the number of facets stored in arrays $\Omega_{f_1} y \xi_{f_2}$.

$\Gamma_{f_3}$: Locus of the facets set partially demoldable along $\left(\overrightarrow{V_z}\right)$ being $f_3$ the number of facets stored in the array $\Gamma_{f_3}$.

$\Delta_{f_4}$: Locus of the set of facets non-demoldable along $\left(\overrightarrow{V_z}\right)$, being $f_4$ the number of facets stored in the array $\Delta_{f_4}$.

Firstly, the demoldability of the facets $F_i \in \mathscr{B}'_f$ along the positive parting direction $\left(+\overrightarrow{V_z}\right)$, is cataloged. The previously classified

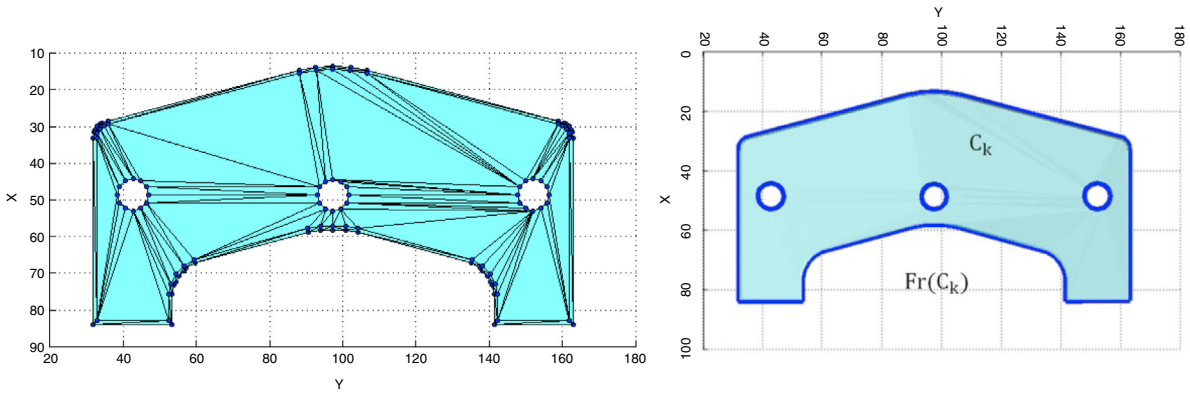


**Fig. 4.** Projection of facets $F_i$ and contour border $Fr(C_k)$ for the level $k$ of $\Pi_k$.

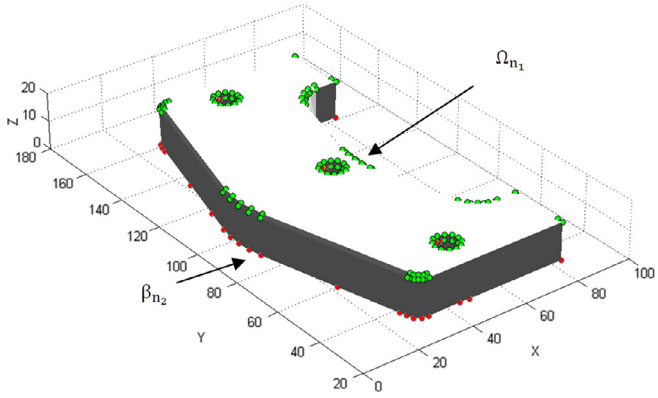


**Fig. 6.** Result of the algorithm InProject in the analysis $\left(+\vec{V_z}\right)$.

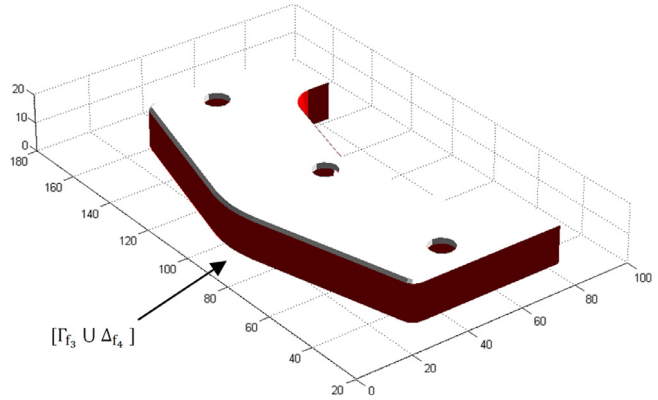


**Fig. 8.** Example of location of the region $[\Gamma_{f_3} \cup \Delta_{f_4}]$.

points $P_{ij}$ in the array $\Omega_{n_1}$, are the basis for cataloging the facets $F_i \in \mathscr{B}'_f$. All the facets $F_i \in \mathscr{B}'_f$ matching the condition that all their vertex $\{P_{i1}, P_{i2}, P_{i3}\}$, belongs to the demoldable region $\Omega_{n_1}$, will be classified as demoldable along $\left(+\vec{V_z}\right)$, being assigned to the array of direct demoldable facets $\Omega_{f_1}$, and they will be removed from the array $\mathscr{B}'_f$. In Fig. 7 the location of the area $\Omega_{f_1}$ is shown on the piece example.

$\forall\, F_i = \{P_{i1}, P_{i2}, P_{i3}\} \in \mathscr{B}'_f$
If $(P_{i1} \in \Omega_{n_1}) \vee (P_{i2} \in \Omega_{n_1}) \vee (P_{i3} \in \Omega_{n_1}) \rightarrow F_i \in \Omega_{f_1}$
$F_i = F_{i_1}$.

The remaining facets $F_i$ belonging to the array $\mathscr{B}'_f$ will be cataloged as non-demoldable or semi-demoldable facets along the direction $\left(+\vec{V_z}\right)$, being assigned to the array formed by the union of the arrays $\Gamma_{f_3}$ and $\Delta_{f_4}$, Fig. 8.

$\forall\, F_i = \{P_{i1}, P_{i2}, P_{i3}\} \in \left[\mathscr{B}'_f - \left(\Omega_{f_1}\right)\right] \rightarrow F_i \in [\Gamma_{f_3} \cup \Delta_{f_4}]$
$\forall\, F_i \in [\Delta_{f_4} \cup \Gamma_{f_3}] \rightarrow F_i = F_{i_{3,4}}$.

The algorithm for analyzing the demoldability of the facets $F_i$ in the mesh $\mathscr{B}'_f$, from the array $\Omega_{f_1}$ is defined as Catalogfaces. For vertical sweep it is taken into account that $\mathscr{B}'_f = \{\Omega_{f_1} \cup \xi_{f_2} \cup \Gamma_{f_3} \cup \Delta_{f_4}\}$ considering facets $F_{i_2} \in \xi_{f_2}$ included in the array of non-demoldable facets $\Delta_{f_4}$.

### 3.3.1. Algorithm for obtaining the demoldability in the case of vertical facets

As a result of applying the Catalogfaces algorithm presented in 3.3, the horizontal facets $F_i$ and inclined facets $\in \mathscr{B}'_f$, demoldable in the upper cavity, have been classified and stored in the array $\Omega_{f_1}$. However there is still a set of facets $\forall\, F_{i_{3,4}} = \left\{P_{i_{3,4}}1, P_{i_{3,4}}2, P_{i_{3,4}}3\right\} \in [\Gamma_{f_3} \cup \Delta_{f_4}]$, which by their geometric configuration may be reclassified as demoldable facets. These facets fulfill the geometrical condition of being perpendicular to the parting direction $\left(\vec{V_z}\right)$.

As a preliminary to the demoldability analysis the algorithm locates in an automated way a set of facets (near-vertical) which should be vertical but nevertheless have a certain deflection angle $\alpha$ with respect to the parting direction because of the discretization process. To do this the algorithm computes the value of $\Delta\alpha$ inclination with respect to the parting direction for each facet $F_{i_{3,4}}$ by means of the arcsine of the ratio between the area of the orthogonally projected facet on XOY *Proj* $[F_{i_{3,4}}]$, and the area of the actual facet $F_{i_{3,4}}$. Thus once calculated the inclination of each side $\alpha_i$ of each $F_{i_{3,4}}$, if the value of $\alpha_i$ is in the range $90° < \alpha_i < 90° + \Delta\alpha$, with $\Delta\alpha = 1.5°$, then the facet $F_{i_{3,4}}$ will be considered a facet $F_{i_{3,4}\ near\text{-}vertical}$ and will be transformed into a virtual facet.

$$\forall\, F_{i_{3,4}} = \left\{P_{i_{3,4}}1, P_{i_{3,4}}2, P_{i_{3,4}}3\right\} \in \mathbb{R}^3 | 90° < \alpha_i < 90° + \Delta\alpha \rightarrow F_{i_{3,4}} \in F_{i_{3,4}\ near\text{-}vertical}.$$

Affinity and geometrical proportionality methods are used on the vertices of the projected facet *Proj* $[F_{i_{3,4}}]$, for obtaining the virtually displaced $P_{i_{3,4}}$ nodes, and the new virtual vertical facets $F_{i_{3,4}\ near\text{-}vertical} \in [\Gamma_{f_3} \cup \Delta_{f_4}]$. Near-vertical facets are classified into back-facing facets and front-facing facets [35]. For the back-facing facets, a virtual movement of $P_{i_{3,4}}$ nodes with $z$ lowest level is achieved, and on the contrary, for front-facing facets, a virtual movement of nodes with $z$ highest level is achieved.

The facets $F_{i_{3,4}} = \left\{P_{i_{3,4}}1, P_{i_{3,4}}2, P_{i_{3,4}}3\right\} \in [\Gamma_{f_3} \cup \Delta_{f_4}]$ located under the border of a facet $F_{i_1} \in \Omega_{f_1}$, so that the projection of

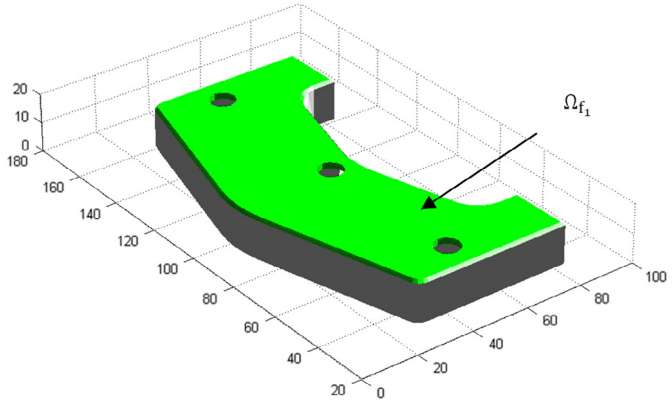


**Fig. 7.** Example of location of the region $\Omega_{f_1}$.

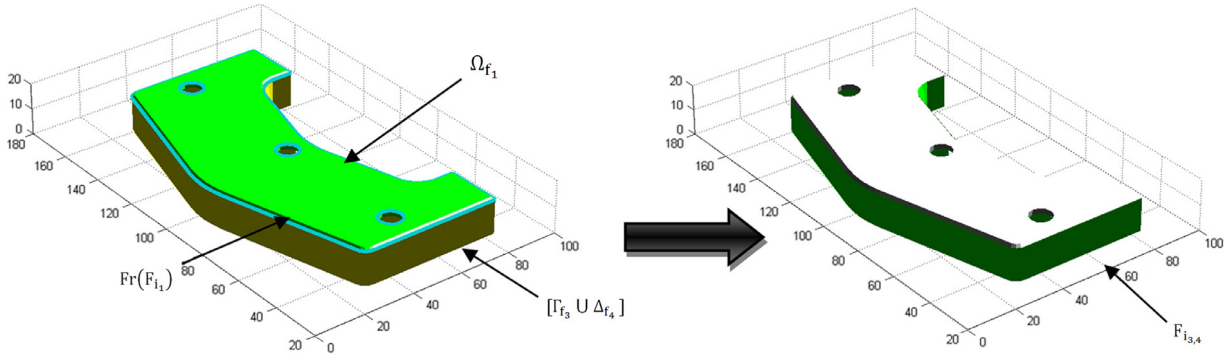


**Fig. 9.** Example location of demoldable facets, perpendicular to $\overrightarrow{V_z}$.

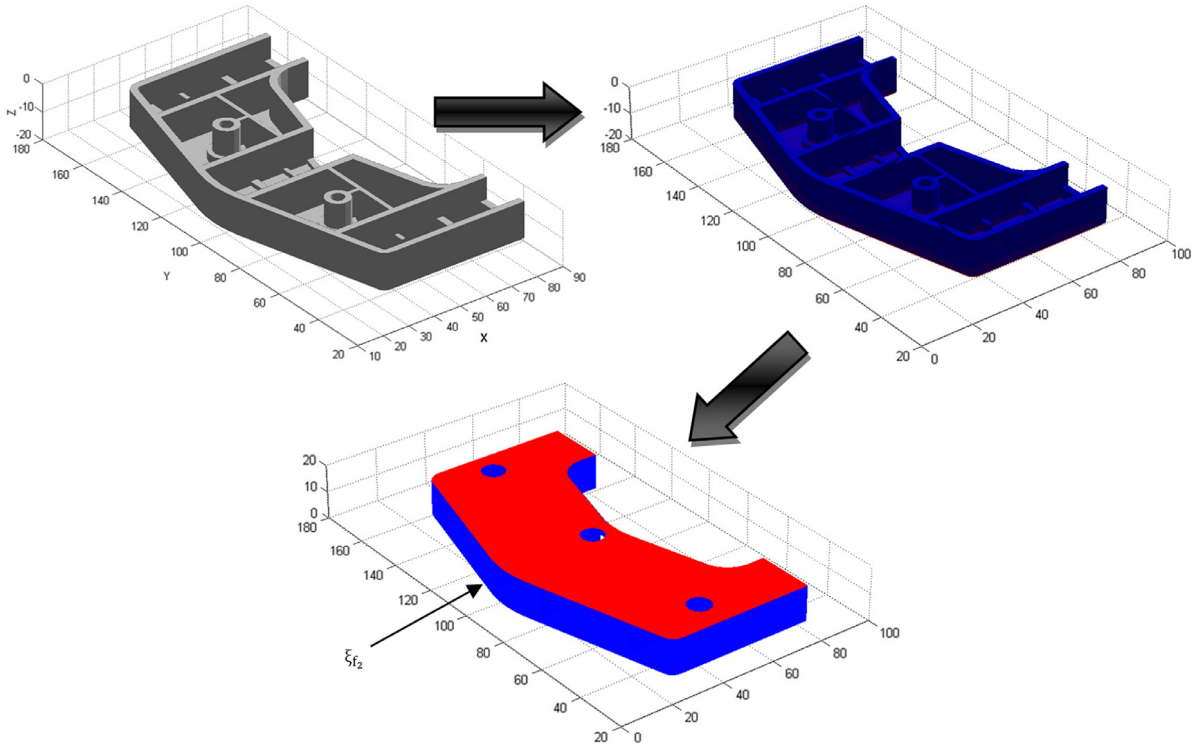


**Fig. 10.** Reorientation of the geometry as the new direction of analysis, and comparison of results of different analyses performed.

the points $\{P_{i_{3,4}1}, P_{i_{3,4}2}, P_{i_{3,4}3}\}$ that make the facet $F_{i_{3,4}}$, belong to $Fr\ (F_{i_1})$, will be demoldable. They will be repositioned in the array $\Omega_{f_1}$, and removed from the array $[\Gamma_{f_3} \cup \Delta_{f_4}]$, Fig. 9.

$$\forall\, F_{i_1} \in \Omega_{f_1} \rightarrow Fr\left(F_{i_1}\right) = \overline{F_{i_1}} \cap \overline{CF_{i_1}}$$

$$\begin{aligned} \forall F_{i_{3,4}} &= \left\{P_{i_{3,4}1}, P_{i_{3,4}2}, P_{i_{3,4}3}\right\} \\ &\in \left[\Gamma_{f_3} \cup \Delta_{f4}\right] : \left\{P_{i_{3,4}1}, P_{i_{3,4}2}, P_{i_{3,4}3}\right\} \\ &\rightarrow \begin{bmatrix} x_{i_{3,4}}1, y_{i_{3,4}}1 \\ x_{i_{3,4}}2, y_{i_{3,4}}2 \\ x_{i_{3,4}}3, y_{i_{3,4}}3 \end{bmatrix} \in Fr\left(F_{i_1}\right) \rightarrow F_{i_{3,4}} \in \Omega_{f_1}. \end{aligned}$$

The other facets $F_i \in \mathscr{B}'_f$ that have not been cataloged after applying the reassignment algorithm as demoldable vertical facets will be stored in the array of non-demoldable and semi-demoldable facets $[\Gamma_{f_3} \cup \Delta_{f_4}]$.

$$\forall\, F_i = \{P_{i1}, P_{i2}, P_{i3}\} \in \left[B'_f - \left(\Omega_{f_1}\right)\right] \rightarrow F_{i_{3,4}} \in [\Gamma_{f_3} \cup \Delta_{f_4}].$$

*3.3.2. Reorientation of geometry, obtaining demoldability on facets belonging to the lower cavity*

In this section, the algorithms stated in paragraphs 3.1–3.3 will be applied again, reorienting the part in the opposite direction to the parting direction $\left(\overrightarrow{-V_z}\right)$, resulting in the set of demoldable facets corresponding to the lower cavity region $\xi_{f_2}$, Fig. 11.

As it is noticed in Fig. 10, it should be established unification criteria for those facets with duplication of results. Such criteria or boundary conditions are as follows:

- All those facets that belong to the demoldable region of the upper and lower cavity will only be stored in the array $\xi_{f_2}$ (lower cavity) and removed from the array $\Omega_{f_1}$ (upper cavity).

  If $\left(F_i = \{P_{i1}, P_{i2}, P_{i3}\} \in \Omega_{f_1}\right)$
  $\vee \left(F_i = \{P_{i1}, P_{i2}, P_{i3}\} \in \xi_{f_2}\right) \rightarrow F_i \in \xi_{f_2}$.

- All those facets that belong to the demoldable region corresponding to the lower cavity $\xi_{f_2}$ and have been cataloged as

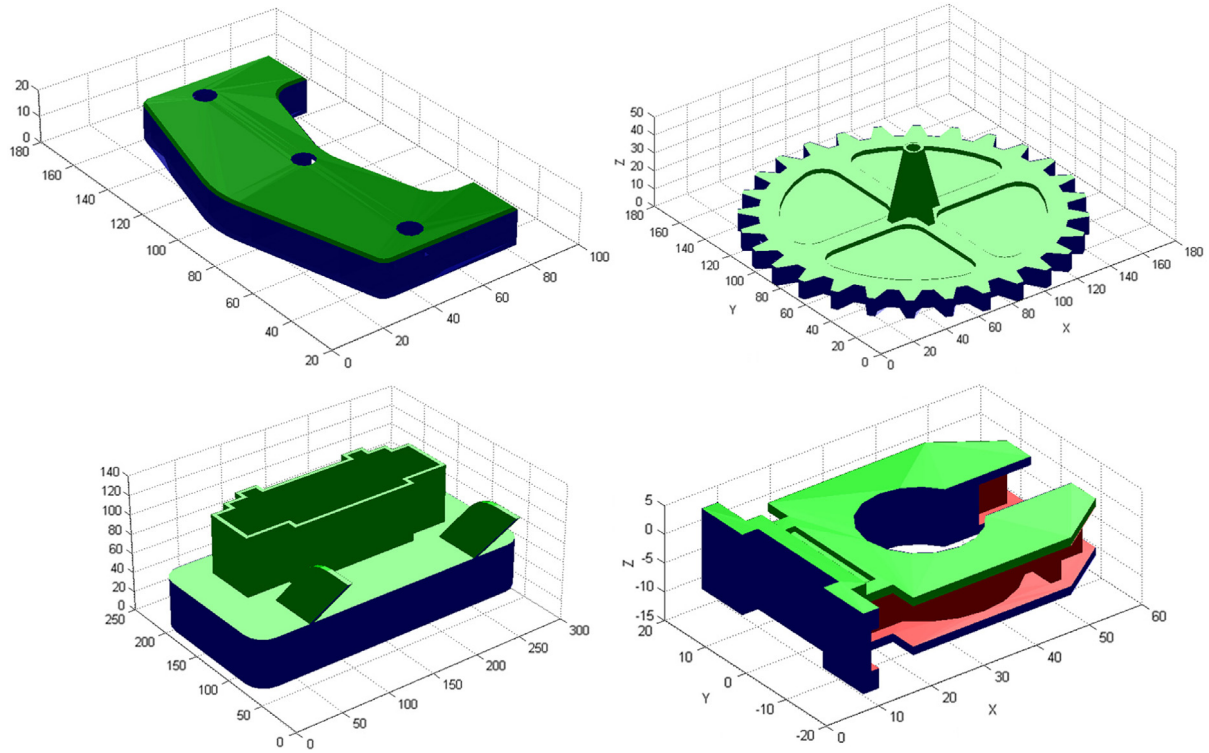

**Fig. 11.** Results of the analysis of demoldability in $+V_z$, $-V_z$ after the implementation of the boundary conditions 3.3.2.

non-demoldable $\in [\Gamma_{f_3} \cup \Delta_{f_4}]$ in the first analysis $\left(\overrightarrow{V_z}\right)$, will be stored in the array $\xi_{f_2}$ (lower cavity), and removed from the array $[\Gamma_{f_3} \cup \Delta_{f_4}]$.

$$\text{If } \left(F_{i_{3,4}} = \left\{P_{i_{3,4}1}, P_{i_{3,4}2}, P_{i_{3,4}3}\right\} \in \left\{\Gamma_{f_3} \cup \Delta_{f_4}\right\}\right) \vee \left(F_{i_{3,4}} = \left\{P_{i_{3,4}1}, P_{i_{3,4}2}, P_{i_{3,4}3}\right\} \in \xi_{f_2}\right) \rightarrow F_i \in \xi_{f_2}.$$

- Similarly, all those facets that belong to the demoldable region corresponding to the upper cavity $\Omega_{f_1}$ and in turn have been cataloged as non-demoldable $\in [\Gamma_{f_3} \cup \Delta_{f_4}]$ in the second analysis $\left(\overrightarrow{-V_z}\right)$, will only be stored in the array $\Omega_{f_1}$ (upper cavity), and removed from the array $[\Gamma_{f_3} \cup \Delta_{f_4}]$.

$$\text{If } \left(F_{i_{3,4}} = \left\{P_{i_{3,4}1}, P_{i_{3,4}2}, P_{i_{3,4}3}\right\} \in \left\{\Gamma_{f_3} \cup \Delta_{f_4}\right\}\right) \vee \left(F_{i_{3,4}} = \left\{P_{i_{3,4}1}, P_{i_{3,4}2}, P_{i_{3,4}3}\right\} \in \Omega_{f_1}\right) \rightarrow F_i \in \Omega_{f_1}.$$

### 3.3.3. Algorithm of reclassification of semi-demoldable and non-demoldable facets

At this point of the demoldability analysis of the mesh, the facets $F_{i_{3,4}} \in [\Gamma_{f_3} \cup \Delta_{f_4}]$ should be reclassified, into non-demoldable facets $F_{i_4} \in \Delta_{f_4}$ and semi-demoldable ones $F_{i_3} \in \Gamma_{f_3}$. To solve this problem the algorithm uses an analysis methodology based on the overlap between the different non-demoldable and semi-demoldable facets.

The algorithm of reclassification of semi-demoldable and non-demoldable facets is called reclassfacet. The application of the reclassfacet algorithm will result in a reclassification of the facets in arrays, in addition to dividing the semi-demoldable facets in regions according to their demoldability. After the application of the reclassfacet algorithm a new set of facets and nodes that complement the mesh $\mathscr{B}'_f y \mathscr{B}'_n$ is created.

For this purpose, the reclassfacet algorithm performs a comparative facet–facet analysis $(F_{i_s} - F_{i_r}) \in [\Gamma_{f_3} \cup \Delta_{f_4}]$ in order to classify the overlapping facets. Given a pair of facets $(F_{i_s} - F_{i_r}) \in [\Gamma_{f_3} \cup \Delta_{f_4}]$, the vertical measurements $\{z_{i_s1}, z_{i_s2}, z_{i_s3}\}$, $\{z_{i_r1}, z_{i_r2}, z_{i_r3}\}$ of their nodes $\{P_{i_s1}, P_{i_s2}, P_{i_s3}\}$, $\{P_{i_r1}, P_{i_r2}, P_{i_r3}\}$ are compared, and the facets which produces overlapping are checked (located on a higher plane).

In order to verify whether there is overlap between a pair of facets belonging to $[\Gamma_{f_3} \cup \Delta_{f_4}]$, both facets are projected onto a plane perpendicular to the parting direction $\left(\overrightarrow{V_z}\right)$ and it is checked by means of a logical Boolean operation if there is contact between these facets. That facet $F_{i_s} \in [\Gamma_{f_3} \cup \Delta_{f_4}]$ that satisfies the condition that $\{z_{i_s1}, z_{i_s2}, z_{i_s3}\} > \{z_{i_r1}, z_{i_r2}, z_{i_r3}\}$ and the intersection is not null will be assigned to the array of non-demoldable facets $\Delta_{f_4}$. The other facet $F_{i_r}$ is assigned to the array of semi-demoldable facets $\Gamma_{f_3}$.

$$\forall \left\{ \begin{array}{l} F_{i_s} = \{P_{i_s1}, P_{i_s2}, P_{i_s3}\} \rightarrow \begin{bmatrix} x_{i_s1}, y_{i_s1}, z_{i_s1} \\ x_{i_s2}, y_{i_s2}, z_{i_s2} \\ x_{i_s3}, y_{i_s3}, z_{i_s3} \end{bmatrix} \\ F_{i_r} = \{P_{i_r1}, P_{i_r2}, P_{i_r3}\} \rightarrow \begin{bmatrix} x_{i_r1}, y_{i_r1}, z_{i_r1} \\ x_{i_r2}, y_{i_r2}, z_{i_r2} \\ x_{i_r3}, y_{i_r3}, z_{i_r3} \end{bmatrix} \end{array} \right\}$$

$$\text{If } \left\{ \begin{array}{c} \{z_{i_s1}, z_{i_s2}, z_{i_s3}\} > \{z_{i_r1}, z_{i_r2}, z_{i_r3}\} \\ F_{i_s} \cap F_{i_r} \neq \emptyset \end{array} \right\} \rightarrow \left\{ \begin{array}{l} F_{i_s} \in \Delta_{f_4} \\ F_{i_r} \in \Gamma_{f_3} \end{array} \right\}.$$

Thus, it can be determined which facets belong to the set of semi-demoldable facets $\Gamma_{f_3}$ and which belong to the set of non-demoldable facets $\Delta_{f_4}$.

After the semi-demoldable facets $F_{i_3} \in \Gamma_{f_3}$ are defined, a fragmentation process is implemented, finding the demoldable upper or lower cavity regions and the non-demoldable region for each facet. The division of semi-demoldable facets is performed by applying a methodology of subtraction and intersection between each of the semi-demoldable facets $\in \Gamma_{f_3}$ and the closed set of non-demoldable facets $\Delta_{f_4}$. The closed set $\{F_{i_4} \in \Delta_{f_4}\}$ and the semi-demoldable facets $\{F_{i_3} \in \Gamma_{f_3}\}$ will be projected onto a horizontal plane perpendicular to the parting direction $\left(\overrightarrow{V_z}\right)$, and

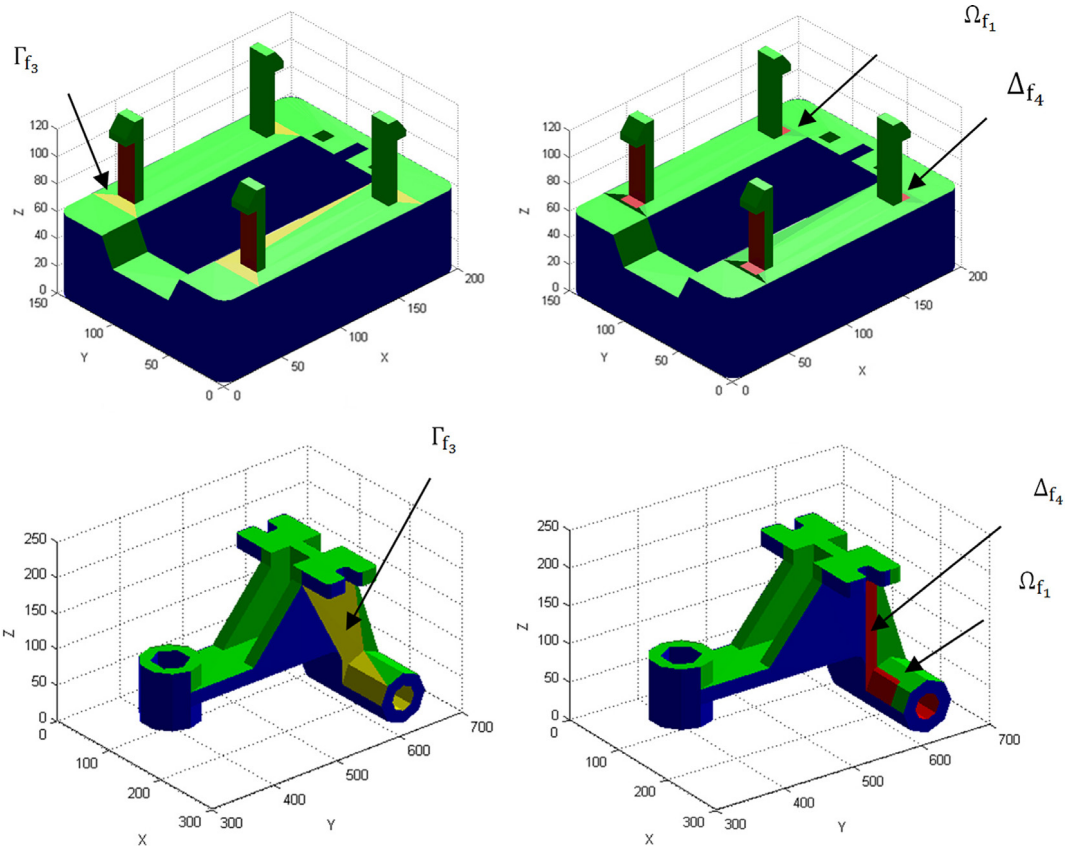


**Fig. 12.** Example of resolution of semi-demoldable facets, Boolean operation (intersection and subtraction).

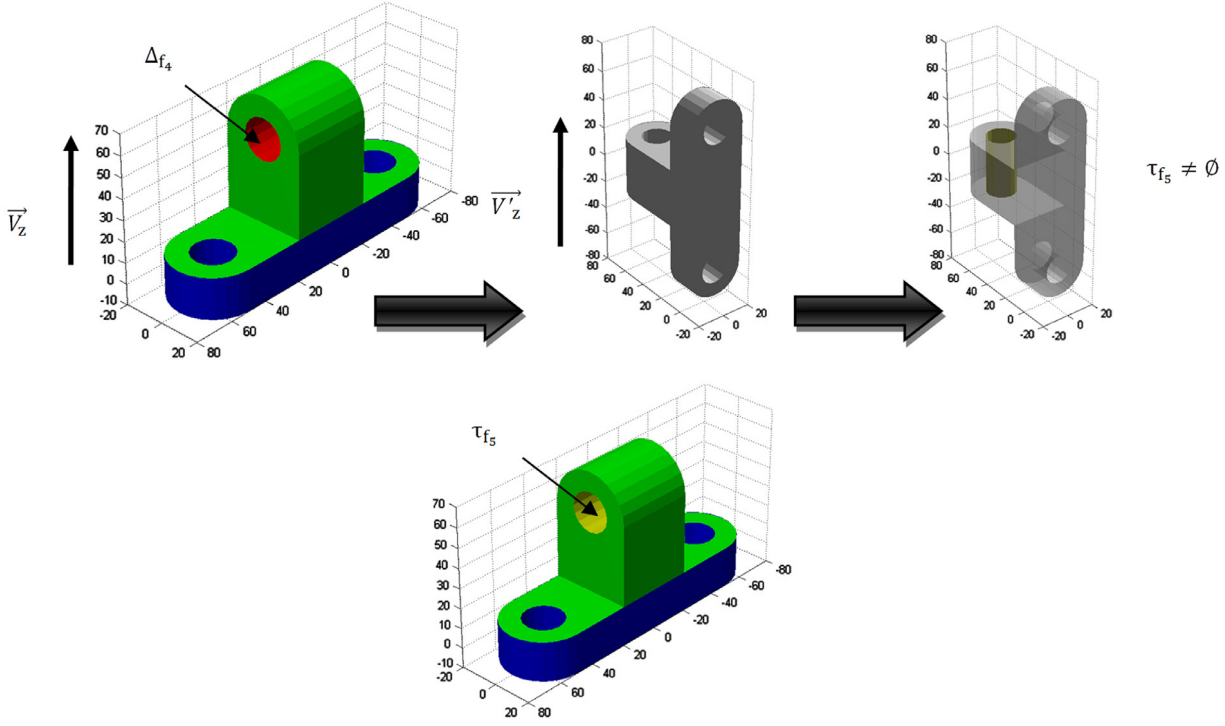


**Fig. 13a.** Allocation of non-demoldable facets to side core facets, Example I.

the intersection and subtraction resulting from these elements is calculated; This geometric information is transferred to the plane of the semi-demoldable facets under consideration.

$$\forall F_{i_3} = \{P_{i_3 1}, P_{i_3 2}, P_{i_3 3}\} \in \Gamma_{f_3} \rightarrow F_{i_3} = F''_{i_1} + F''_{i_4} \rightarrow \begin{Bmatrix} F''_{i_1} \in \Omega_{f_1} \\ F''_{i_4} \in \Delta_{f_4} \end{Bmatrix}.$$

As seen in Fig. 12, the result of the Boolean intersection between the semi-demoldable facets $F_{i_3}$ and non-demoldable facets $F_{i_4}$, for

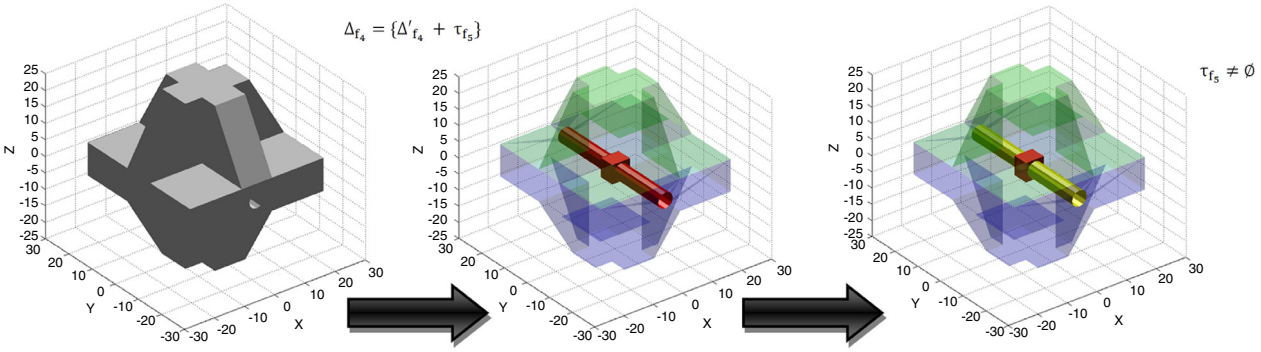


**Fig. 13b.** Allocation of non-demoldable facets to side core facets, Example II.

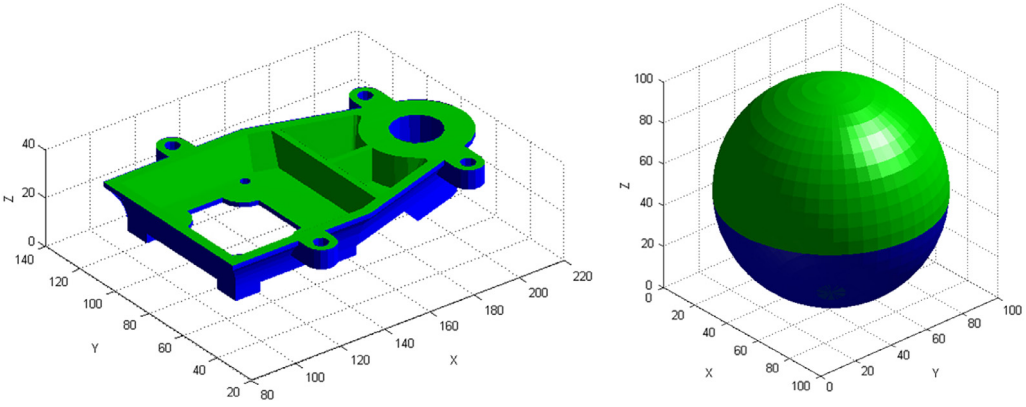

**Fig. 14.** Geometric definition of the parting line.

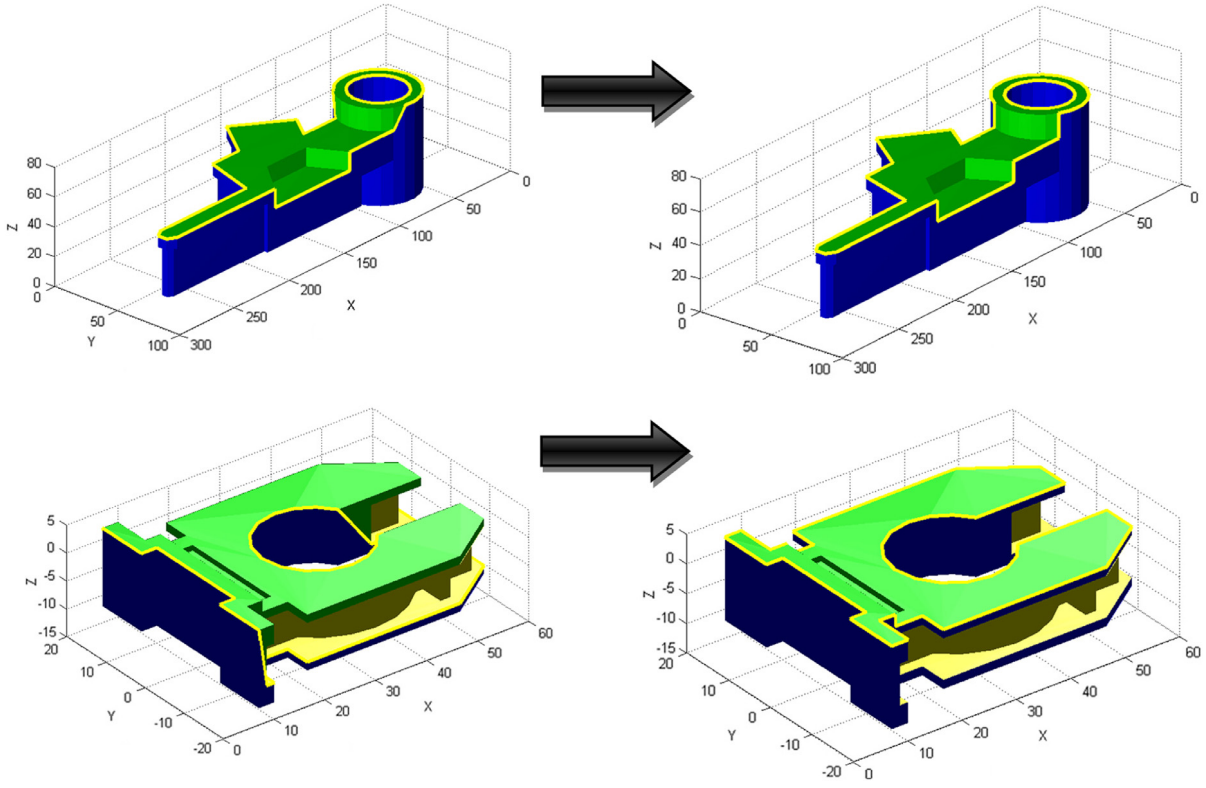

**Fig. 15.** Optimizing the geometrical definition of the parting line.

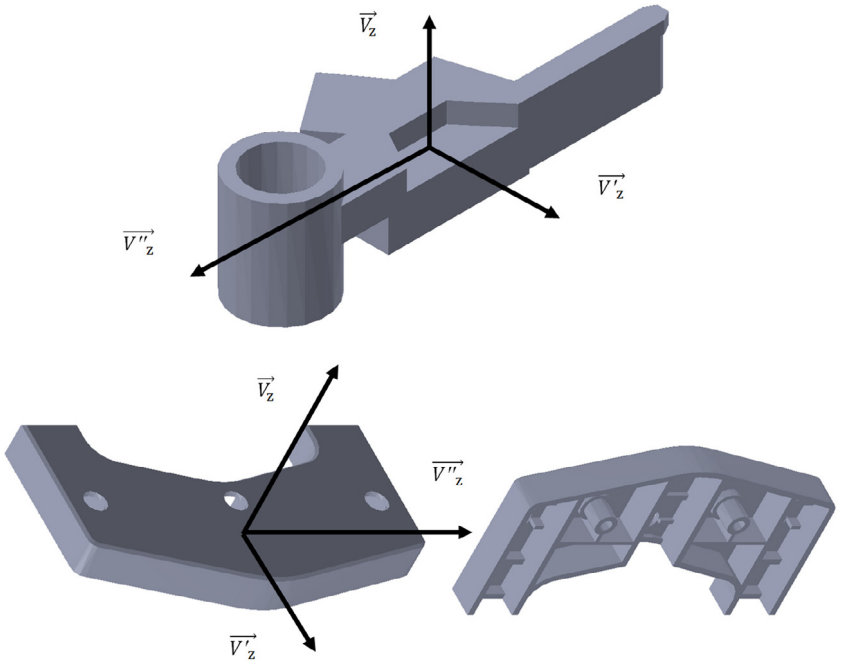


**Fig. 16.** Case A and B, demoldable parts by means of upper and lower cavities.

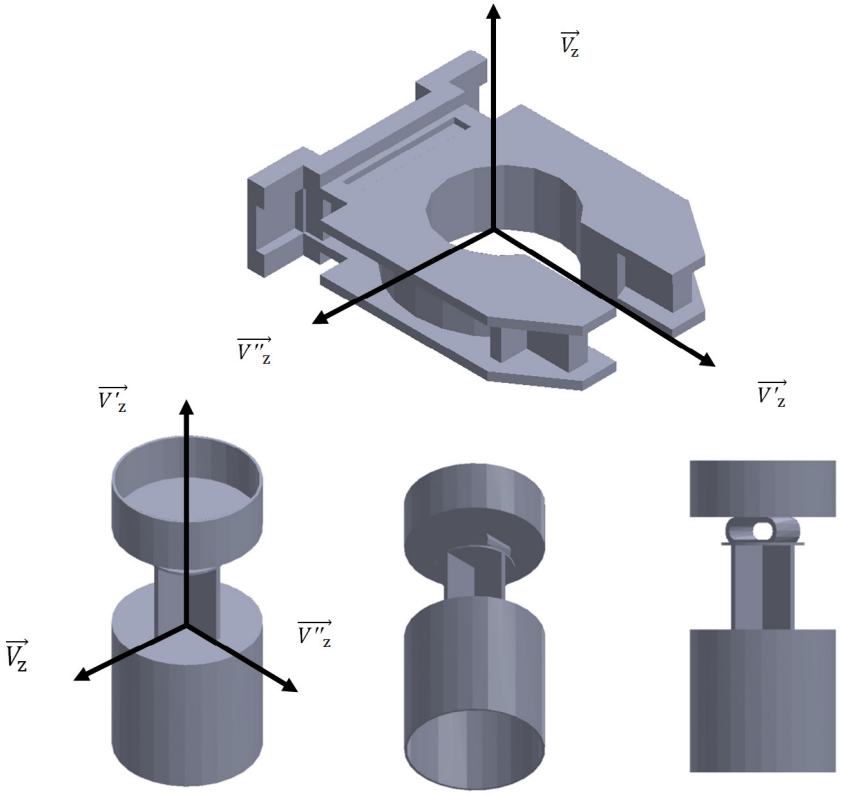


**Fig. 17.** Parts C, D with resoluble demolding regions by means of side cores.

every facet causes the division thereof into two regions, the demoldable region $F''_{i_1} \in \Omega_{f_1}$ and non demoldable region $F''_{i_4} \in \Delta_{f_4}$.

$$\forall F_{i_3} = \{P_{i_3 1}, P_{i_3 2}, P_{i_3 3}\} \in \Gamma_{f_3} \rightarrow \begin{Bmatrix} F_{i_3} \cap \Delta_{f_4} = F''_{i_4} \in \Delta_{f_4} \\ F_{i_3} - \Delta_{f_4} = F''_{i_1} \in \Omega_{f_1} \\ F''_{i_4} \cup F''_{i_1} = F_{i_3} \end{Bmatrix}$$

$\forall \{F''_{i_4}, F''_{i_1}\} \in \mathscr{B}''_f$.

The set of facets $\{F''_{i_4}, F''_{i_1}\}$ which following the reclassification algorithm have been divided according to their demoldability form a new mesh $\mathscr{B}''_f$ containing the new set of virtual polygonal regions $(F''_{i_4}, F''_{i_1})$ to be overlapped on mesh $\mathscr{B}'_f$. The new mesh $\mathscr{B}'''_{Ff} = \{\mathscr{B}''_f \cup \mathscr{B}'_f\}$ will incorporate information about the demoldability of the plastic part B. The new mesh includes geometric information as well as manufacturing information which will be included in the

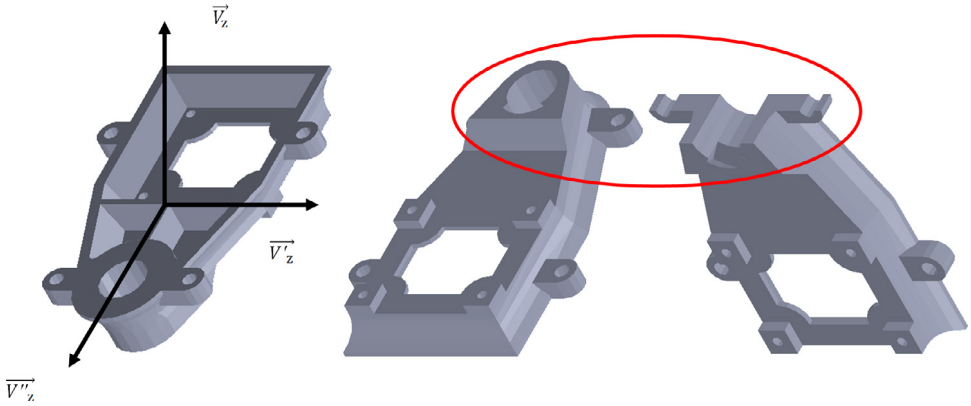


**Fig. 18.** Part E, parts with non-demoldable regions.

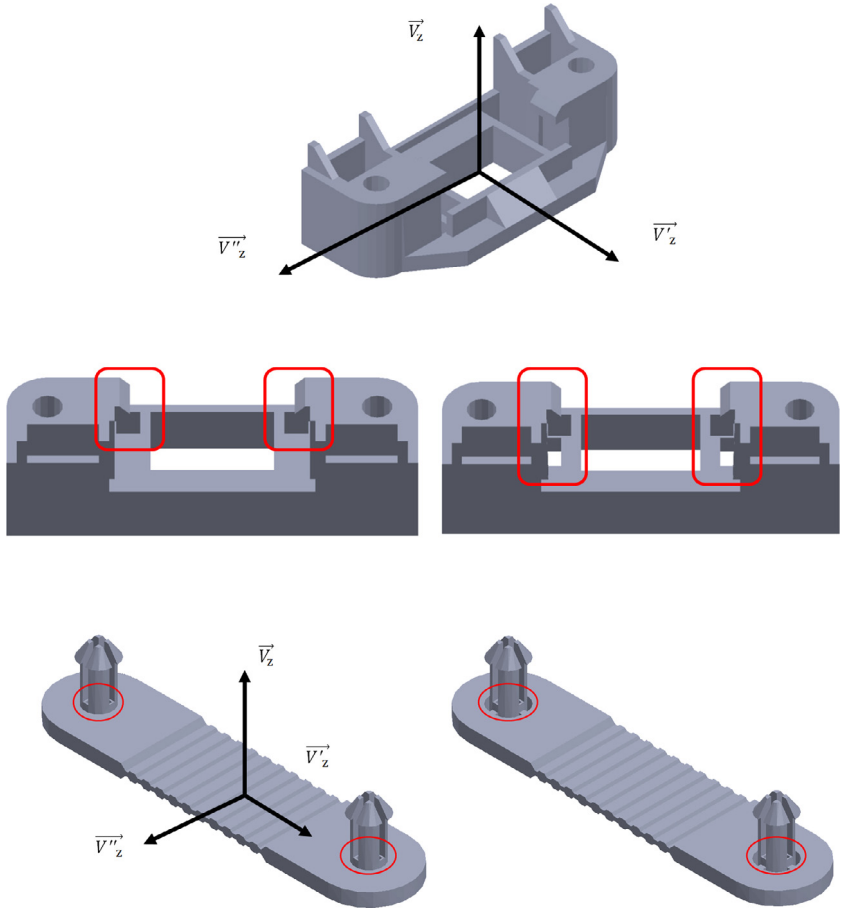


**Fig. 19.** Cases F and G. Parts with non demoldable regions, geometrically modified to improve their demoldability.

files and resulting models

Let be $\mathscr{B}'_f \in \mathbb{R}^n; \exists \mathscr{B}''_f \in \mathbb{R}^n \rightarrow \left\{ \begin{matrix} \mathcal{B}'''_{F_f} = \left\{ \mathcal{B}'_f + \mathcal{B}''_F \right\} \\ F_f \geq n \end{matrix} \right\}$.

Similarly, fragmented facets create new virtual nodes that will be part of the virtual mesh $\mathscr{B}''_n$. $\mathscr{B}''_n$ is overlapped on mesh $\mathscr{B}'_n$ adding information about demoldability of the part and forming the mesh $\mathscr{B}'''_{Nn}$.

Let be $\mathscr{B}'_n \in \mathbb{R}^n; \exists \mathscr{B}''_n \in \mathbb{R}^n \rightarrow \left\{ \begin{matrix} \mathcal{B}'''_{N_n} = \left\{ \mathcal{B}'_n + \mathcal{B}''_N \right\} \\ N_n \geq 3n \end{matrix} \right\}$.

After application of the algorithm reclassfacet in the positive direction of the parting direction, it will be applied analogously in the reverse direction to the parting direction in order to obtain semi-demoldable facets $\in \Gamma_{f_3}$ and $\in \Delta_{f_4}$ in this direction.

The set of facets classified as demoldable $F''_{i_4} \in \Delta_{f_4}$ incorporates a group of facets $F'''_{i_5}$ which may be resolvable by side core along direction $\left(\overrightarrow{V'_z}\right)$ perpendicular to the parting direction. At this moment the piece will be reoriented by turning 90° to axis $X$ and then to axis $Y$. In this position, the preprocessing phase will be applied again by running the algorithm Inproject nodes, the facets processing algorithm by running the algorithm Catalogfaces, and the reclassification of semi-demoldable non-demoldable facets by running the reclassfacet algorithm. The regions previously classified as demoldable $\in [\Omega_{f_1} \cup \xi_{f_2}]$ will be excluded. The facets

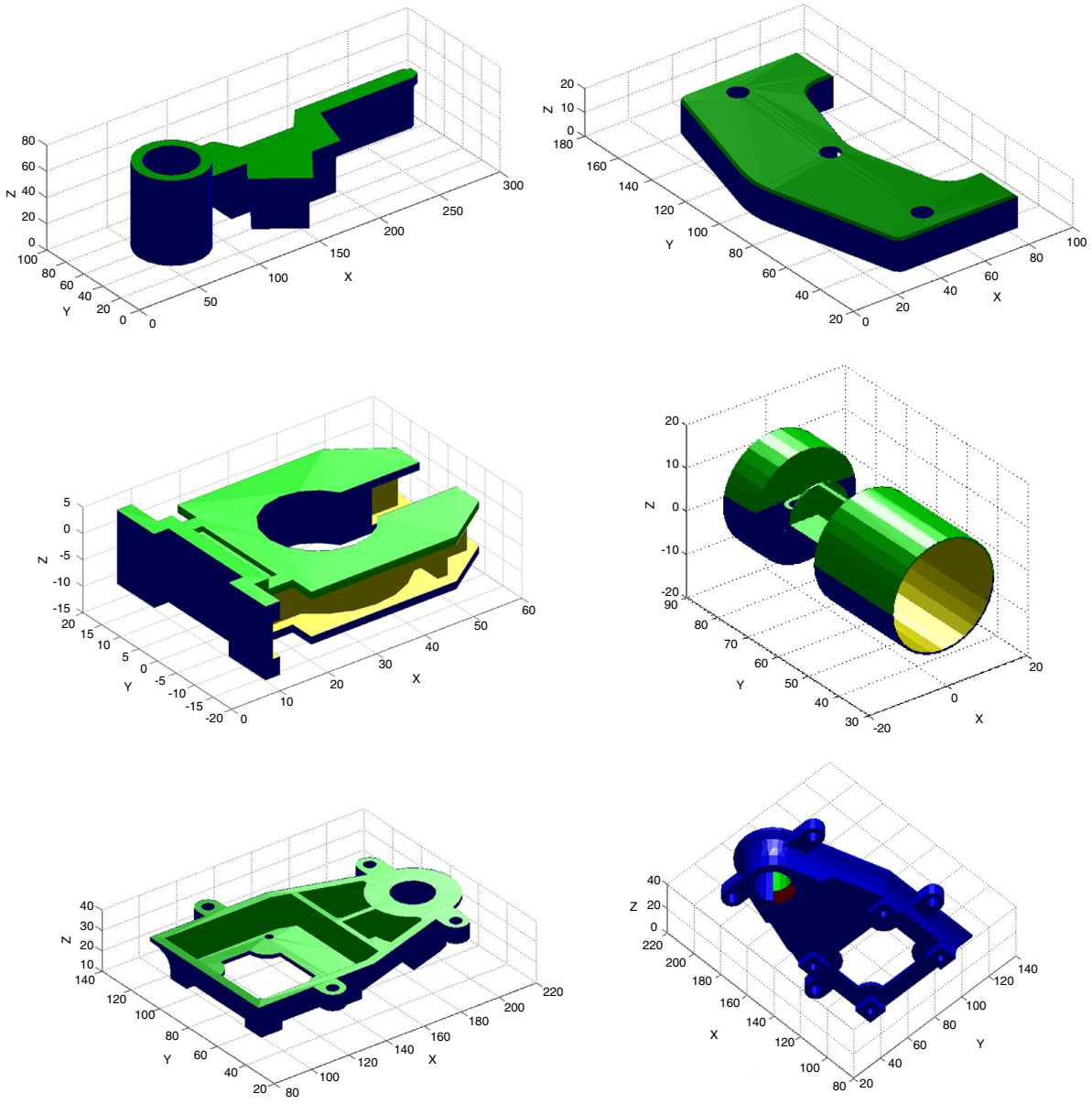


**Fig. 20.** Results of demoldability, Cases A, B, C, D, E.

$F'''_{i_5}$ demoldable along the direction $\left(\overrightarrow{V'_z}\right)$ will be stored in the array $\tau_{f_5}$. Assignment examples of non-demoldable facets to side core facets are shown in Figs. 13a and 13b

$$\Delta_{f_4} = \{\Delta'_{f_4} \cup \tau_{f_5}\}$$
$$\left(\overrightarrow{V'_z}\right) \perp \left(\overrightarrow{V_z}\right)$$
$$\tau_{f_5} = \left\{\Delta_{f_4} - \Delta'_{f_4}\right\}$$
$$\forall F'''_{i_5} \in \tau_{f_5}.$$

### 3.4. Algorithm for defining the parting line, postprocessing

The parting line (PL), by definition, is located in the border region between the upper cavity ($\Omega_{f_1}$) and the lower cavity ($\xi_{f_2}$). The estimation of this geometric feature of the piece is made from the previous definition of the corresponding arrays upper cavity ($\Omega_{f_1}$) and lower cavity ($\xi_{f_2}$). The parting line is determined as the boundary between these regions Fig. 14.

However, for other geometries Fig. 15 whose facet model does not allow us to obtain the line of partition using this algorithm, a sub-algorithm based on the decomposition of demoldable facets is proposed. Thus a Boolean subtraction operation will be performed between the orthogonal projection of facets whose normal vector is perpendicular to the parting direction $\in [\Omega_{f_1} \cup \xi_{f_2}]$ and the facets $\in \xi_{f_2}$. As a result of this operation, virtual polygon slices $F''_{i_1} \in \Omega_{f_1}$, $F''_{i_2} \in \xi_{f_2}$ that define the optimal line are generated [28].

$$\begin{matrix}\forall F_{i_1} \in \Omega_{f_1} : F_{i_1}, F_{i_2} \perp \overrightarrow{V_z} \\ \forall F_{i_2} \in \xi_{f_2}\end{matrix} \rightarrow \begin{Bmatrix} Proj(F_{i_1}) - \xi_{f_2} = F''_{i_1} \\ Proj(F_{i_2}) - \xi_{f_2} = F''_{i_2} \end{Bmatrix}$$
$$F''_{i_1} \in \Omega_{f_1}$$
$$F''_{i_2} \in \xi_{f_2}.$$

Finally, the parting line is defined as

$$\forall P_{ij} = \{x_{ij}, y_{ij}, z_{ij}\} : \left(P_{ij} \in Fr\left(\Omega_{f_1}\right)\right) \vee \left(P_{ij} \in Fr\left(\xi_{f_2}\right)\right) \rightarrow P_{ij} \in [PL].$$

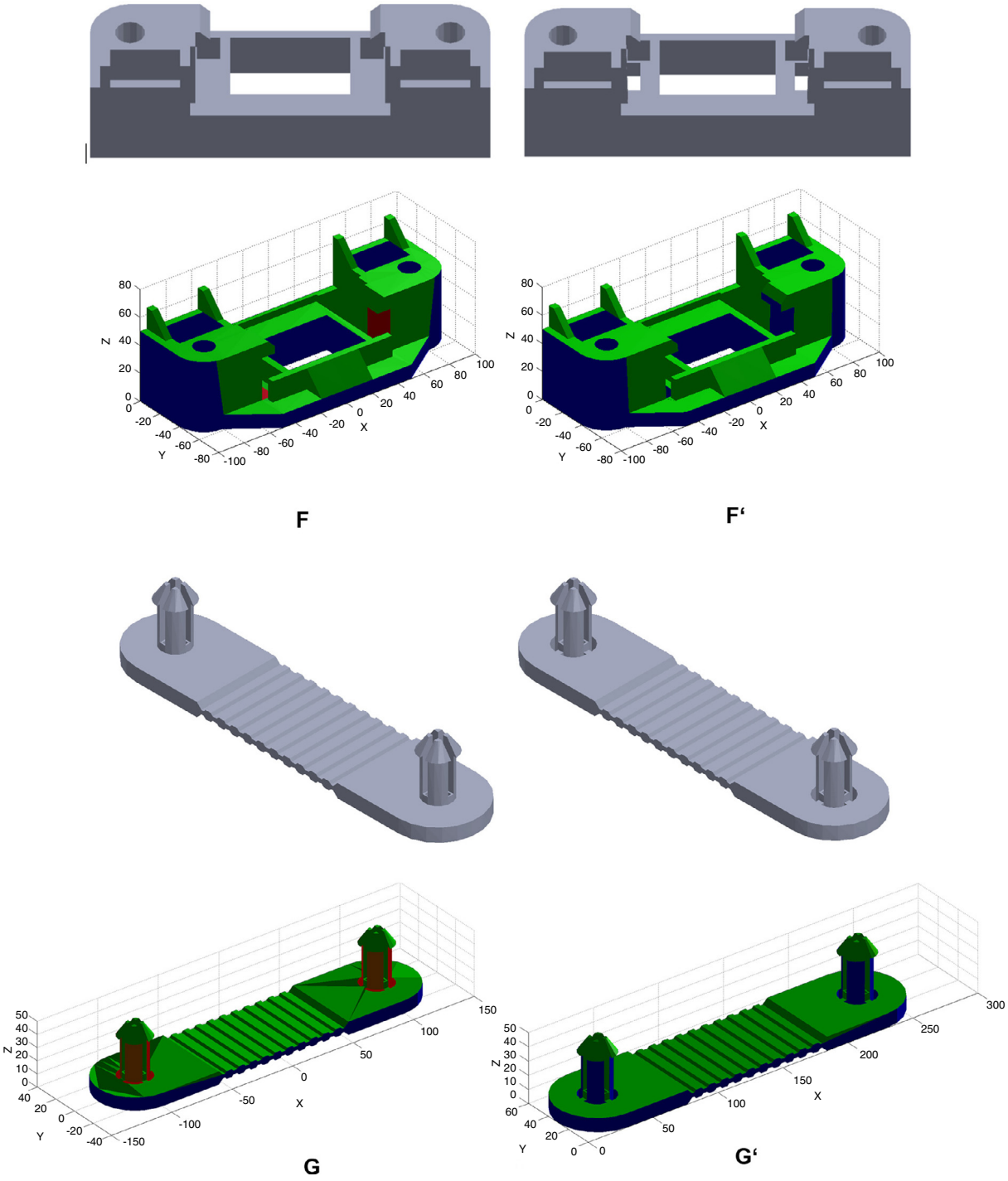


**Fig. 21.** Results of demoldability, Cases F, G original part and Cases F′, G′ optimized part.

## 4. Implementation & results

In order to validate the algorithm proposed, five industrial parts manufactured by injection molding have been tested. The precision of the mesh (angle and deviation) for each stage of the analysis is analogous for different geometries. A comparison of results of the algorithm, and the total computation has been performed Fig. 23. The algorithms have been run with a Toshiba notebook with a Pentium (R) Dual-Core CPU T4200 @ 2.20 GHz processor and a RAM memory of 3.00 GB. It is possible to adapt to any programming language and computer.

### 4.1. Case studies

The results of the application of the algorithm are shown below. They have been classified according to the degree of demoldability. The first, A and B (Fig. 16), are direct demoldability parts, all the surfaces are demoldable towards top and bottom cavities, along the parting direction $\left(\overrightarrow{V_z}\right)$. Part A is composed of 306 facets and part B is composed of 1211 facets.

In Fig. 17 the test pieces C, D are shown. These pieces, unlike parts A and B, have undercuts along the given parting direction $\left(\overrightarrow{V_z}\right)$. Their manufacture is possible by means of side cores that

**Table 1**
Cases A, B, C, D, E.

| Case studies | N° Facets | N° Upper cavity facets | N° Lower cavity facets | N° Side core facets | N° Undercut core facets | Simulation time (s) |
|---|---|---|---|---|---|---|
| A | 306 | 123 | 183 | – | – | 30,282 |
| B | 1211 | 153 | 1058 | – | – | 583,199 |
| C | 400 | 81 | 151 | 168 | – | 85,233 |
| D | 696 | 244 | 316 | 136 | – | 254,073 |
| E | 1110 | 318 | 758 | – | 34 | 653,927 |

**Table 2**
Cases F, G, F′, G′.

| Case studies | N° Facets | N° Upper cavity facets | N° Lower cavity facets | N° Side core facets | N° Undercut core facets | Simulation time (s) |
|---|---|---|---|---|---|---|
| F | 474 | 245 | 205 | – | 24 | 65,433 |
| F′ | 506 | 250 | 256 | – | – | 69,850 |
| G | 1334 | 484 | 772 | – | 78 | 835,267 |
| G′ | 1556 | 433 | 1123 | – | – | 1107,703 |

move perpendicular to the proposed main axis. This allows the demolding of these regions according to the directions $\left(\overrightarrow{V'_z}, \overrightarrow{V''_z}\right)$. Part C has 400 facets in its definition, and part D consists of 696 facets, Table 1.

Fig. 18 shows part E. This part has an inner conical revolution drain region which prevents the part being demoldable. Part E consists of 1110 facets, Table 1.

Fig. 19 shows parts F and G. These parts, as with parts C and D, have undercuts resolvable by side cores. However, once problematic manufacturing areas have been detected the part design has changed, eliminating undercuts and enabling all surfaces to be demoldable as upper and lower cavity. Part F consists of 474 facets and part F′ of 506. Moreover, parts G and G′ consist of 1334 and 1556 facets respectively, Table 2.

In Table 1 and in Fig. 20 the data and graphic results of the demoldability analysis performed over parts A, B, C, D, E are collected. In Table 1 the reallocating of facets after applying the demoldability analysis presented in this paper is shown, as well as the time spent on demoldability analysis.

Parts F and G have been used as an example of optimizing the geometry of the part as a methodology in order to enhance its demoldability, Table 2 shows the results of applying the demoldability analysis algorithm over both parts. The graphic demoldability analysis results are indicated in Fig. 21.

In order to evaluate the computational cost of the algorithm, Fig. 22 shows a graph relating the number of facets for each application of the algorithm to the total time of execution. In the pieces studied a linear relationship between the number of facets of the piece and the time of completion of the analysis is observed, the ratio time/number of facets being 0.85.

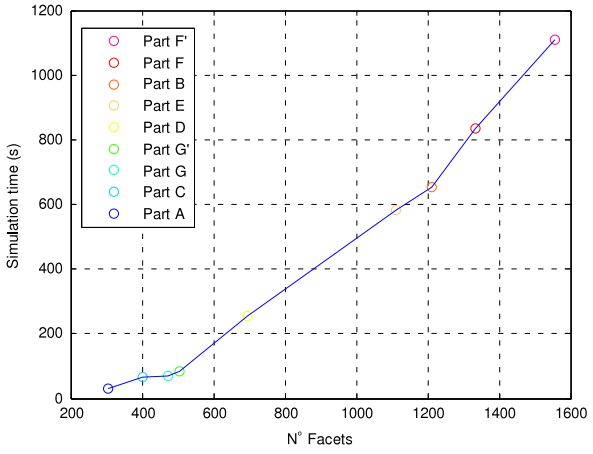


**Fig. 22.** CPU computational cost of demoldability algorithm.

## 5. Conclusions

This paper proposes a new method for performing the analysis of demoldability and the calculation of parting line for a given parting direction; this methodology poses a hybrid analysis of the discrete mesh of the plastic part, analyzing the demoldability of both the mesh nodes and the facets. The developed algorithm works with an initial file with discrete surface geometry, and obtains, after analyzing, a new virtual discrete geometry which incorporates information regarding the manufacture of the piece. It is valid for all kinds of parts and CAD systems, regardless of the modeler used. The algorithm detects not only undercuts resolvable by side cores, but also non-demoldable areas, allowing the designer to modify the design in the early stages.

Three subalgorithms for analyzing demoldability of the plastic part (Inproject, Catalogfaces and Reclasssfacet) have been developed. The first sub-algorithm Inproject executes a mesh preprocessing, resulting in a classification of the nodes by means of arrays according to their demoldability. The Inproject preprocessing phase uses a series of checkpoints or Gauss points on the analyzed facets as a means of discrete checking of the demoldability. Inproject Algorithm ($P_{Gauss}$) was compared with the Isoobstructing algorithm (Boolean operations) [35] resulting in the conclusion that the Inproject algorithm takes only 6% of the time taken by the Isoobstructing algorithm.

The second sub-algorithm Catalogfaces catalogs facets belonging to the mesh according to their demoldability into demoldable facets, non demoldable facets, and semi-demoldable facets, based on the analysis of mesh nodes (Inproject). Finally, the third sub-algorithm Reclassfacet reclassifies and fragments the semi-demoldable facets, obtaining demoldable and non demoldable facets. Applying the sub-algorithm Reclassfacet has resulted in the creation of a new virtual mesh made up of nodes and facets that complement the initial mesh of the plastic part, providing information not only on the geometry but also on manufacture. The side core demoldable areas were calculated by reorienting the part in the direction perpendicular to the parting direction and reapplying the developed subalgorithms.

The algorithm has been validated through its application to five variable demoldability parts and two real parts, eliminating after analysis the areas classified as non-demoldable in order to improve their manufacture. All analyses were carried out using the same precision of the mesh (deviation and angle). We evaluated the relationship between the number of facets and the total execution time of the algorithm, resulting in a linear relationship between the number of facets of the part and the running time of the analysis.

The proposed method improves the methods developed to date in that it allows the realization of demoldability analysis

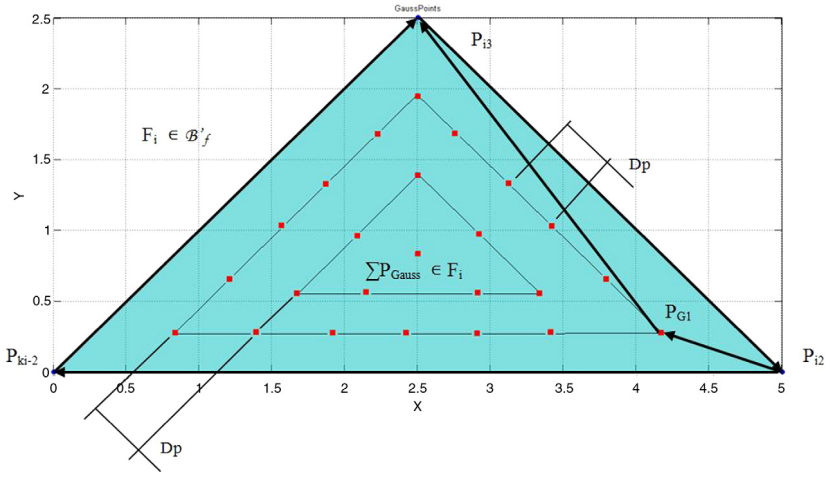


**Fig. 23.** Formal definition of Gauss points of a facet.

independently of the CAD modeler, it does not use the normal vector for the recognition and classification of the areas of the plastic part surface, it is valid for any geometry of the plastic part, and it does not need access to internal information of the part. The geometry of the solid remains stored in arrays for later use in other applications.

## Acknowledgments

This work has been supported by the Consejeria de Economia, Ciencia y Empleo (Junta de Andalucia—Spain) through the project titled "A vertical design software for integrating operations of automated demoldability, tooling design and cost estimation in injection molded plastic parts. (CELERMOLD)" (Project Code TI-12 TIC-1623). The authors would like to thank the reviewers for comments that improved the exposition.

## Appendix

### A.1. InProject algorithm

The goal of the Inproject algorithm is the discrete checking of demoldability in every facet under study. First, given a facet $F_i \in \mathcal{B}'_f$ a series of checkpoints or Gauss points $P_{\text{Gauss}} \in F_i$ are generated on the surface. Gauss points are control points that run and belong to the surface of the facet under study. During the gauss points generation, a set of equidistant lines to edges of facets separated a distance Dp are defined. Distance Dp is equal to the length of the minimum edge that belongs to a set of facets which define the upper boundary. The contour is varying in each plane, adapting the value of $D_p$ to each new level of study. Next, these equidistant lines are segmented in order to get nodes separated a distance Dp. Thus, it is ensuring that the algorithm will be able to identify the minimum detail of a plastic part in successive scans along the parting direction.

Thus, and according to paragraph 3.2, given a facet under study $F_i \in \mathcal{B}'_f$ and a closed control contour $C_k \in Pl_k$, the algorithm is executed sequentially to check whether a point is inside the triangular facets of the closed contour $C_k$.

The orientation of a triangular region is defined by the orientation of the 3 vertices, considering the facet $F_i = \{P_{i1}, P_{i2}, P_{i3}\}$ Fig. 23 and the checkpoint $P_{G1}$.

$$D = [(P_{i1})_x - (P_{i3})_x] \cdot \left[(P_{i2})_y - (P_{i3})_y\right] - \left[(P_{i1})_y - (P_{i3})_y\right] \cdot [(P_{i2})_x - (P_{i3})_x]$$

**Table 3**
Comparison of algorithms for solving overlapping of facets.

| Methodology (Overlap resolution) | Unioperational computational cost (s) |
|---|---|
| IsObstructing [35] | 0.006137 |
| InProject (8 Gauss points) | 0.000432 |

$$D' = \left[(P_{i2})_x - \left(P_{G_1}\right)_x\right] \cdot \left[(P_{i3})_y - \left(P_{G_1}\right)_y\right] - \left[(P_{i2})_y - \left(P_{G_1}\right)_y\right] \cdot [(P_{i3})_x - (P_G)_x]$$

$$\text{If} \quad \left[(D \geq 0) \wedge \left(D' \geq 0\right)\right] \vee \left[(D < 0) \wedge \left(D' < 0\right)\right] \rightarrow P_{G_1} \in F_i = \{P_{i1}, P_{i2}, P_{i3}\}.$$

Applying this methodology, which is computationally faster, the overlap between different facets can be checked, and also whether the set of nodes and control points of a facet are demoldable against a contour $C_k$ type such as that set forth in Section 3.2. In Table 3 the comparison between Iso-obstructing facets overlap algorithms and the Inproject algorithm is indicated.

## References

[1] Chen LL, Woo TC. Computational geometry on the sphere with application to automated machining. ASME Trans J Mech Des 1992;114:288–95.
[2] Chen LL, Chou SY, Woo TC. Parting directions for mould and die design. Comput Aided Des 1993;25(12):762–8.
[3] Chen LL, Chou SY, Woo TC. Partial visibility for selecting a parting direction in mold and die design. J Manuf Syst 1995;14(5).
[4] Weinstein M, Manoochehri S. Optimal parting direction of molded and cast parts for manufacturability. J Manuf Syst 1997;16(1):1–12.
[5] Fu MW, Fuh JYH, Nee AYC. Undercut feature recognition in an injection mould design system. Comput Aided Des 1999;31(12):777–90.
[6] Fu MW, Fuh J,YH, Nee AYC. Generation of optimal parting direction based on undercut features in injection molded parts. IIE Trans 1999;31:947–55.
[7] Fu MW, Nee AYC, Fuh JYH. The application of surface visibility and moldability to parting line generation. Comput Aided Des 2002;34(6):469–80.
[8] Fu MW, Nee AYC, Fuh JYH. A core and cavity generation method in injection mold design. Int J Prod Res 2001;39:121–38.
[9] Fu MW. The application of surface demoldability and moldability to side core design in die and mold CAD. Comput Aided Des 2008;40(5):567–75.
[10] Ran JQ, Fu MW. Design of internal pins in injection mold CAD via the automatic recognition of undercut features. Comput Aided Des 2010;42(7):582–97.
[11] Wuerger D, Gadh R. Virtual prototyping of die design part one: theory and formulation. J Concurr Eng: Res Appl 1997;5(4):307–15.
[12] Wuerger D, Gadh R. Virtual prototyping of die design part two: algorithmic, computational, and practical considerations. J Concurr Eng: Res Appl 1997;5(4):317–26.
[13] Kurth GR, Gath R. Virtual prototyping of die-design: determination of die-open directions for neat-net shape manufactured parts with extruded or rotational features. Comput Integr Manuf Syst 1997;10(1):69–81.
[14] Lu HY, Lee WB. Detection of interference elements and release directions in die-cast and injection-moulded components. Proc Inst Mech Eng B 2000;214(6):431–41.

[15] Yin ZP, Ding Han, Xiong You-Lun. Virtual prototyping of mold design: geometric mouldability analysis for near-net-shape manufactured parts by feature recognition and geometric reasoning. Comput-Aided Des 2001;33(2):137–54.
[16] Ye XG, Fuh JYH, Lee KS. A hybrid method for recognition of undercut features from molded part. Comput-Aided Des 2001;33(14):1023–34.
[17] Ye XG, Fuh JYH, Lee KS. Automotive undercut feature recognition for side core design of injection molds. J Mech Des 2004;126:519–26.
[18] Chunjie Zhang, Xionghui Zhou, Congxin Li. Feature extraction from freeform molded parts for moldability analysis. Int J Adv Manuf Technol 2010;48(1–4):273–82.
[19] Bassi R, Reddy NV, Bedi S. Automatic recognition of intersecting features of side core design in two piece permanent molds. Int J Adv Manuf Technol 2010;50(5–8):421–39.
[20] Surti A, Reddy NV. Non discretized approach to visibility analysis for automatic mold feature recognition using step part model. J Adv Manuf Syst 2012;11(1):1–16.
[21] Singh R, Madan J, Kumar R. Automated identification of complex undercut features for side core design for die casting parts. J Eng Manuf 2014;228(9):1138–52.
[22] Nee AYC, Fu MW, Fuh JYH, Lee KS, Zhang YF. Determination of optimal parting direction in plastic injection mould design. Ann CIRP 1997;46(1):429–32.
[23] Nee AYC, Fu MW, Fuh JYH, Lee KS, Zhang YF. Automatic determination of 3D parting Lines and Surfaces in Plastic Injection Mould Design. Ann CIRP 1998;47(1):95–9.
[24] Hui KC, Tan ST. Mould design with sweep operations, a heuristic search approach. Comput Aided Des 1992;24(2):81–92.
[25] Ravi B, Srinivasan MN. Decision criteria for computer aided parting surface design. Comput Aided Des 1990;22(1):11–8.
[26] Rappaport D, Rosenbloom A. Moldable and castable polygons. Comput Geom: Theory Appl 1994;4:219–33.
[27] Ahn HK, Berg MTde, Bose J, Cheng SW, Halperin D, Matouvsek J. Separating an object from its cast. In: Proceedings 13th annual ACM symposium on computational geometry. New York, (USA): ACM Press; 1997. p. 61–83.
[28] Ahn , De Berg , Bose , Cheng , Halperin , Matousek , Swartzkopf . Separating an object from its cast. Comput Aided Des 2002;34:547–59.
[29] Chen X, McMains S. Finding all undercut-free parting directions for extrusions. In: Geometric modeling and processing. Lecture notes in computer science, vol. 4077. 2006. p. 514–27.
[30] Mcmains S, Chen X. Determining moldability and parting directions for polygons with curved edges. In: International mechanical engineering congress and exposition. ASME Anaheim, CA; 2004.
[31] Mcmains S, Chen X. finding undercut free directions for polygons with curved edges. ASME J Comput Inf Sci Eng 2006;6(1):60–8.
[32] Yin ZP, Ding Han, Li Han-Xiong, Xiong You-Lun. Geometric mouldability analysis by geometric reasoning and fuzzy decision making. Comput Aided Des 2004;36(1):37–50.
[33] Chen YH, Wang YZ, Leung TM. An investigation of parting direction based on dexel and fuzzy decision making. Int J Prod Res 2000;38:1357–75.
[34] Huang J, Gupta SK, Stoppel K. Generating sacrificial multi-piece molds using accessibility driven spatial partitioning. Comput Aided Des 2003;35(3):1147–60.
[35] Priyadarshi AKL, Gupta SK. Geometric Algorithms for automated design of multipiece permanent molds. Comput Aided Des 2004;36(3):241–60.
[36] Dhaliwal S, Gupta SK, Huang J. Computing exact global accessibility cones for polyhedral objects. In: ASME design for manufacturing conference Baltimore MD, September 2000.
[37] Dhaliwal S, Gupta SK, Huang J, Priyadarshi A. Algorithms for computing global accessibility cones. J Comput Inf Sci Eng 2003;3(3):200–9.
[38] Bourne D, Corney J, Gupta SK. Recent advances and future challenges in automated manufacturing planning. J Comput Inf Sci Eng 2011;11(2).
[39] Chen Y, Rosen D. A region based approach to automated design of multipiece molds with application to rapid tooling. In: ASME design engineering technical conference, Pittsburgh PA, 2001, p. 613–23.
[40] Chen Y, Rosen DW. A reverse glue approach to automated construction of multi-piece molds. J Comput Inf Sci Eng 2003;3(3):219–30.
[41] Ganter MA, Tuss LL. Computer-assisted parting line development for cast pattern production. AFS Trans 1990;795–800.
[42] Wong T, Tan ST, Sze WS. Parting line formation by slicing a trimmed surface model. In: Proceedings of the 1996 ASME design engineering technical conference and computers in engineering conference 1996. August 18–22, Irvine, California.
[43] Rubio MA, Pérez JM, Rios J. A Procedure for plastic parts demoldability analysis. Robot Comput Integr Manuf 2006;22(1):81–92.
[44] Martin Doñate C, Rubio Paramio MA. New methodology for demoldability analysis based on volume discretization algorithms. Comput Aided Des 2013;45(2):229–40.
[45] Donate Cristina Martin, Paramio Miguel Angel Rubio, Villar Aurelio Mesa. Método de validación automatizada de la fabricabilidad de diseños de objetos tridimensionales en base a su geometría. Patent number: ES2512940.
[46] Khardekar R, McMains S. Finding mold removal directions using graphics hardware. In: ACM workshop on general purpose computing on graphics processors; 2004, pp. C-19, (abstract).
[47] Khardekar Burton, McMains . Finding feasible mold parting directions using graphics hardware. Comput Aided Des 2006;38(4):327–41.
[48] Chakraborty P, Reddy NV. Automatic determination of parting directions, parting lines and parting surfaces for two piece permanent moulds. J Mater Process Technol 2000;209(5):2464–76.
[49] Singh R, Madan J. Systematic approach for automated determination of parting line for die-cast parts. Robot Comput-Integr Manuf 2013;29(5):346–66.
[50] Shin KH, Lee KW. Design of side cores of injection molds from automatic detection of interference faces. J Des Manuf 1993;3:225–36.
[51] Banerjee AG, Gupta SK. Geometrical algorithms for automated design of side actions in injection moulding of complex parts. Comput Aided Des 2007;39(10):882–97.
[52] Li W, Martin RR, Langbein FC. Molds for meshes: Computing smooth parting lines and undercut removal. IEEE Trans Autom Sci Eng 2009;6(3):423–32.

**Jorge Manuel Mercado-Colmenero** received his B.Eng. and M.Eng. in Mechanical Engineering in 2012 and 2014 respectively from the University of Jaén in Spain. In 2014 he joined the Design, Engineering Graphics and Project department at Jaen university as a Ph.D. student. He is currently developing his thesis about automatic analyses and design of injection plastic mold, including demoldability, ejection system, cooling system design and CAD–CAE design and manufacturing.

**M.A.R. Paramio** received his M.Eng. and Ph.D. in Mechanical Engineering in 1992 and 2000 respectively from Polytechnic University of Madrid in Spain. In 1994 he joined the University of Jaen and currently he teaches courses of Computer-aided Design, Manufacturing and Engineering in the Engineering Graphics, Design and Projects Department. His thesis was focused on automatic analysis of injection plastic part. His research interests include CAD–CAM–CAE, Design for Manufacturing, computational geometry, constraint-based parametric modeling, and their applications on plastic injection mold design and manufacturing.

**Jesus Maria Perez-Garcia** is a professor in the Department of Mechanical and Manufacturing Engineering at Polytechnic University of Madrid. He has led research projects and publication studies in topics related to forming processes, dimensional metrology, process improvement and control, quality, and instrumentation. He held a position of Vice Director for Research in the Industrial Engineering School. His areas of interest include improvement of manufacturing processes, quality control and instrumentation.

**Cristina Martin-Doñate** received her B.Eng. and M.Eng. in Electrical–Electronics Engineering and Industrial Engineering (Polytechnic University of Valencia—Spain) and Ph.D. in Industrial Engineering (University of Jaen—Spain). She performed her master final project at the Technical University of Graz in Austria, in the field of manufacturing systems. She worked for several years as project manager on developing new products in automotive manufacturing industries. She is currently university teacher at Jaen University where she develops research and conduct research projects in manufacturing systems, plastic injection mold design and technology, CAD systems and new products development.

Referencia / Reference: **Mercado-Colmenero, Jorge Manuel,** Moya-Muriana, José Ángel, Rubio Paramio, Miguel Ángel y Martín-Doñate, Cristina. *Advances on Mechanics, Design Engineering and Manufacturing, Lecture Notes in Mechanical Engineering (2017) 119-128. DOI: http://dx.doi.org/10.1007/978-3-319-45781-9_13*

Estado / Status: Publicado / Published

Tipo de publicación / Publication type: Proceedings Paper

Categoría / Catogory: Advances On Mechanics, Design Engineering And Manufacturing

Conferencia / Conference: International Joint Conference on Mechanics, Design Engineering and Advanced Manufacturing (JCM)

Ubicación / Ubication: Catania, ITALY

Fecha / Date: SEP 14-16, 2016

# An automated manufacturing analysis of plastic parts using faceted surfaces

Jorge Manuel Mercado-Colmenero[a], José Angel Moya Muriana[b], Miguel Angel Rubio- Paramio[a], Cristina Martín-Doñate[a]*

[a] *Department of Engineering Graphics Design and Projects. University of Jaen. Spain. Campus Las Lagunillas, s/n. 23071. Jaen (Spain)*

[3]*ANDALTEC Plastic Technological Center, C/Vilches s/n, 23600 Martos -Jaen, Spain*

* Corresponding author. Tel.: +34 953212821; fax: +34 953212334. *E-mail address:* cdonate@ujaen.es

**Abstract**

In this paper a new methodology of automated demoldability analysis for parts manufactured via plastic injection molding is presented. The proposed algorithm uses as geometric input the faceted surface mesh of the plastic part and the parting direction. Demoldability analysis is based on a sequential model to catalog nodes and facets of the given mesh. First, the demoldability of nodes is analyzed, subsequently, from results of previous nodes analysis, facets of the mesh are cataloged in: demoldable (facets belong cavity and core plate), semi-demoldable (plastic part manufactured by mobile mechanisms, side cores) and non-demoldable (plastic part not manufacturable). This methodology uses a discrete model of plastic part, which provides an additional advantage since the algorithm works independent of the modelling software and creates a new virtual geometry providing information on its manufacture, exactly like CAE software. All elements of the mesh (nodes and facets) are stored in arrays, according with their demoldability category, with information about their manufacture for possible uses in other CAD/CAE applications related to design, machining and costs analysis of injection molds.

**Keywords:** Manufacturing analysis; mesh analysis; injection molding; CAD.

## 1 Introduction and Background

The manufacturing process of injection molding is the industrial method most commonly used for producing plastic parts that require: finishing details with tight tolerances, and dimensional control. Currently the plastic industry demands searching for graphics and computational tools to reduce the design time of the plastic parts and the manufacturing of the plastic injection molds that perform



B. Eynard et al. (eds.), *Advances on Mechanics, Design Engineering and Manufacturing*, Lecture Notes in Mechanical Engineering,
DOI 10.1007/978-3-319-45781-9_13

them. Currently, CAD and CAE systems enable design engineers to reduce design time tasks, simulation, analysis of product manufacturability, and cost estimation.

The demoldability analyses of the plastic part, and detection of slides and internal undercuts, have established an important area of research within the field of injection mold design because they affect directly the design and its final cost. Different methodologies have addressed the demoldability analysis of the plastic part by means of visibility techniques along the parting direction. Authors such as Chen et al. [1], which proposed to address the concept of visibility and estimation of optimal parting direction through the concept of pockets, or Manoochehri [2], have been pioneers in this technique.

Other authors have focused their research on the recognition of the features of the plastic part in CAD format. A feature is defined as a discrete region of the part that has information about its modeling and manufacturing. Features extraction methodology makes available the part information and enters it as an input of a structured algorithm. Fu et al. developed a set of algorithms for solving the demoldability analysis by means of the features recognition, including the recognition of undercut features [3], the definition of the parting direction [4], the parting line and parting surface [5] and the recognition of the upper cavity and lower cavity [6], and design of sides cores [7]. Yin et al. [8] proposed a methodology to recognize undercut features for near net shapes. Ye et al. [9] provided an undercut features recognition hybrid method and [10] extended their work to side core design. Other methods combine features recognition with visibility algorithm given a parting direction with discretizing the plastic part. Singh et al. [11] describes an automated identification, classification, division and determination of complex undercut features of die-cast part.

Nee et al. [12, 13] proposed to solve demoldability analysis by means of classifying the plastic part surfaces according to its relative orientation to the parting direction and the connection between them. This method uses the dot product between the parting line and the normal vectors surface in order to define the demoldability of surfaces.

Huang et al. [14] and Priyadarshi et al. [15] have focused their research on the application of demoldability and visibility analysis of multipart molds. Thus, a facet of the discretized geometry of the plastic part is demoldable if accessible along the parting direction and not obstructed by any other facet of the rest of the part. The applicability of this type of mold is very limited to the scope of prototyping.

Rubio et al. [16] and Martin et al. [17,18] based their research of demoldability analysis on algorithms based on model discretization by means of sections by cutting planes, which are crossed by straight lines. A set of intersection points on the workpiece is generated and analyzed according to their demoldability. Nevertheless the obtained precision is far from that obtained by other methods (i.e. recognition features). Finally, other authors used the GPUs as a tool for detecting the undercuts in the plastic part. Khardekar et al. [19] limited the use of the GPU'S to recognize the possible parting directions that do not generate any undercut. This

paper proposes a new method of automated demoldability analysis based on the geometry of the discretized plastic part (set of mesh nodes-facets). It allows the independence from the CAD modeler and is valid for any type of surface mesh in any plastic part. After analysis, a new virtual geometry which incorporates manufacturing information of the plastic part is generated.

## 2 Methodology

### *2.1 XOY Planes Beam Generation, Preprocessing*

Starting from a 3D plastic part to be manufactured, a three-dimensional mesh formed by a set of nodes (N) and facets (F) is generated. The facets that make up the mesh are triangular; hence a facet, $F_i \in \mathbb{R}^3$, has 3 unique nodes, $N_{ij} \in \mathbb{R}^3$, associated to it.

The presented methodology is based, first, on an arrangement of nodes $N_{ij} \in \mathbb{R}^3$ according to their Z coordinate (parting direction, Fig. 1). Then, a sheet set of XOY analysis planes $\pi_p$, such that each node $N_{ij} \in \mathbb{R}^3$ of the mesh belongs to a plane $\pi_{pk} \in \mathbb{R}^3$ (equation 1). Each plane XOY is associated with a node of the mesh and therefore also the facet to which the node belongs.

$$\forall \left(N_{ij} = \{x_{ij}, y_{ij}, z_{ij}\}\right) \exists\, \pi_{pk} \in \mathbb{R}^3 \mid \begin{Bmatrix} \pi_{pk}: z_{pk} = \text{Cons} \\ z_{pk} = z_{ij} \end{Bmatrix} \tag{1}$$

This arrangement of the mesh elements is performed downwardly along the parting direction. Note that a facet $F_i \in \mathbb{R}^3$ belongs to only a plane $\pi_{pk} \in \mathbb{R}^3$ defined by the node of the facet with the greatest z dimension along the parting direction.

### *2.2 Recognition algorithm of demoldable facets along the parting direction, Processing*

Before describing the set of logical operations that make the algorithm, a set of initial premises that complement it should be established:

- Demoldability analysis is performed along the parting direction, $D_z$ (Fig. 1), that is established as an input of the present algorithm.
- For reclassification of facets in cavity and core plate, a double sweep is performed, along the parting direction, with positive and negative sense.
- Vertical and non-vertical facets are analyzed independently.

#### 2.2.1 Not-vertical facets

The algorithm begins with the facets belonging to the first plane $\pi_{p1} \in \mathbb{R}^3$, which are classified as demoldable and therefore both facets and nodes that compose it are classified as demoldable by means of the cavity plate and belonging to $\beta_1 \in \mathbb{R}^3$.

$$\forall F_i \{N_{i1}, N_{i2}, N_{i3}\} \mid \begin{pmatrix} F_i \in \pi_{p1} \\ \neg(F_i \perp \vec{D}_z) \end{pmatrix} \rightarrow F_i \in \beta_f \tag{2}$$

Where $\beta_f \in \mathbb{R}^3$ (Fig. 1) represents the array of facets that are demoldable by means of cavity plate. For the following levels of analysis [2,m], this algorithm proposes to assess the facet demoldability by projecting its nodes and control points $P_{Gauss}$ according the parting direction. Given the analysis plane $\pi_{pk} \in \mathbb{R}^3$, the demoldability of a facet $F_i \in \mathbb{R}^3$ associated with it is analyzed using as a reference the whole information of all facets analyzed in previous planes. Based on the above premise, the facets belonging to the first level are classified as demoldable.

Thus, given a facet $F_i$, it is considered demoldable if the projection of its associated nodes $N_{ij}$ and $P_{Gauss,i}$ do not intersects with the facets assigned as demoldable (belonging to $\beta_f \in \mathbb{R}^3$) or not-demoldable (belonging to $\eta_{fcav} \in \mathbb{R}^3$) in immediately preceding planes.

$$\forall F_i \begin{Bmatrix} N_{i1}, N_{i2}, N_{i3} \\ P_{Gauss,i} \end{Bmatrix} \mid \begin{pmatrix} \text{Proj}\left(\begin{Bmatrix} N_{i1}, N_{i2}, N_{i3} \\ P_{Gauss,i} \end{Bmatrix}\right) \cap \{\beta_f \cup \eta_{fcav}\} = \emptyset \\ \neg(F_i \perp \vec{D}_z) \end{pmatrix} \rightarrow F_i \in \beta_f \tag{3}$$

$$\forall F_i \begin{Bmatrix} N_{i1}, N_{i2}, N_{i3} \\ P_{Gauss,i} \end{Bmatrix} \mid \begin{pmatrix} \text{Proj}\left(\begin{Bmatrix} N_{i1}, N_{i2}, N_{i3} \\ P_{Gauss,i} \end{Bmatrix}\right) \cap \{\beta_f \cup \eta_{fcav}\} \neq \emptyset \\ \neg(F_i \perp \vec{D}_z) \end{pmatrix} \rightarrow F_i \in \eta_{fcav} \tag{4}$$

Where $\eta_{fcav} \in \mathbb{R}^3$ (Fig. 1) represents the array of facets of the mesh that are not demoldable by means of cavity plate or, as provided in subsequent sections, semi-demoldable facets.

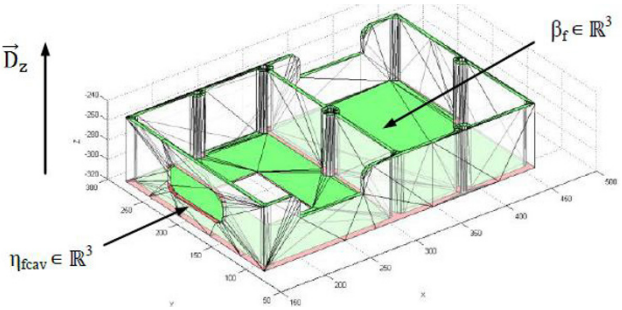


**Fig. 1.** Location of the facets belonging to $\beta_f$ (green, demoldable facets) and to $\eta_{fcav}$ (red, not-demoldable).

### 2.2.2 Vertical facets.

Vertical facets (facets that meet the geometrical condition of perpendicularity to the parting direction $D_z$) are cataloged from the set of facets assigned as non-

vertical and demoldable by means of cavity plate previously analyzed. To do a border contour (equation 5) is established by facets belonging to $\beta_f \in \mathbb{R}^3$.

$$Fr(\beta_f) = \overline{\beta_f} \cap \overline{C\beta_f} \tag{5}$$

So that a vertical facet $F_i \in \mathbb{R}^3$ is demoldable if the projection of its nodes $N_{ij}$ and Gauss points $P_{Gauss,i}$ belong to the border contour Fr($\beta_f$). If so, these facets are stored in the array of facets demoldable by means of cavity plate $\beta_f \in \mathbb{R}^3$ and in the opposite case are stored in the array of facets not-demoldable by means of cavity plate or semi-demoldable $\eta_{cav} \in \mathbb{R}^3$ (Both arrays previously established).

$$\forall F_i \begin{Bmatrix} N_{i1}, N_{i2}, N_{i3} \\ P_{Gauss,i} \end{Bmatrix} \mid \left( \begin{matrix} \begin{Bmatrix} N_{i1}, N_{i2}, N_{i3} \\ P_{Gauss,i} \end{Bmatrix} \in Fr(\beta_f) \\ F_i \perp \vec{D}_z \end{matrix} \right) \rightarrow F_i \in \beta_{cav} \tag{6}$$

$$\forall F_i \begin{Bmatrix} N_{i1}, N_{i2}, N_{i3} \\ P_{Gauss,i} \end{Bmatrix} \mid \left( \begin{matrix} \begin{Bmatrix} N_{i1}, N_{i2}, N_{i3} \\ P_{Gauss,i} \end{Bmatrix} \notin Fr(\beta_f) \\ F_i \perp \vec{D}_z \end{matrix} \right) \rightarrow F_i \in \eta_{fcav} \tag{7}$$

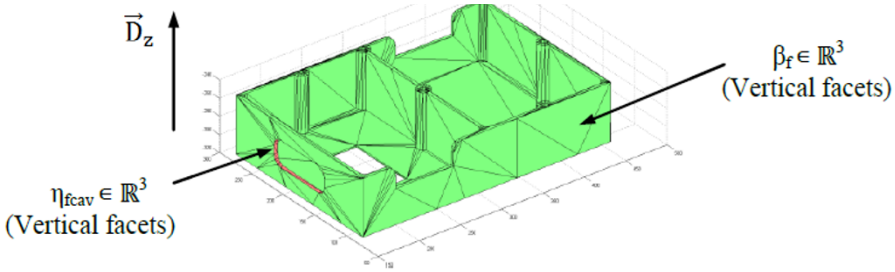


**Fig. 2.** Location of vertical facets belonging to $\beta_f$ and to $\eta_{fcav}$.

### *2.2.3. Reallocating demoldable facets to Core Plate.*

Once the scan is performed along the parting direction and in the positive direction (+$D_z$), the new algorithms defined in paragraphs 2.2.1 and 2.2.2 are implemented, reorienting the part in the negative direction of the parting direction (-$D_z$). Thus it is obtained as a result the set of facets demoldable by means of core plate, which will be stored in the array $\gamma_f \in \mathbb{R}^3$. And the set of facets not-demoldable by means of core plate, which will be stored in the array $\gamma_f \in \mathbb{R}^3$.

To do this, a set of unification requirements for those facets with duplicated results must be established. These being the following:

- Demoldable facets by means of both cavity and core plate (duplication of results) will be stored in the array $\gamma_f \in \mathbb{R}^3$ (core plate), and removed from $\beta_f \in \mathbb{R}^3$ (cavity plate).

$$\text{If } (F_i \{N_{i1}, N_{i2}, N_{i3}\} \in \beta_f) \vee (F_i \{N_{i1}, N_{i2}, N_{i3}\} \in \gamma_f) \rightarrow F_i \in \gamma_f \quad (8)$$

- Facets classified as demoldable by means of core plate (second analysis, $-D_z$), but which have been classified as not-demoldable by means of cavity plate (first analysis, $+D_z$) will be stored in the array $\gamma_f \in \mathbb{R}^3$ (core plate), and removed from $\eta_{cav} \in \mathbb{R}^3$ (Facets not-demoldable by means of cavity plate or semi-demoldable).

$$\text{If } (F_i \{N_{i1}, N_{i2}, N_{i3}\} \in \eta_{fcav}) \vee (F_i \{N_{i1}, N_{i2}, N_{i3}\} \in \gamma_f) \rightarrow F_i \in \gamma_f \quad (9)$$

- Similarly, facets classified as demoldable by means of core plate (second analysis, $-D_z$), but which have been classified as demoldable by means of cavity plate (first analysis, $+D_z$) will be stored in the array $\beta_f \in \mathbb{R}^3$ (cavity plate), and removed from $\eta_{cor} \in \mathbb{R}^3$ (Facets not demoldable by means of core plate or semi-demoldable).

$$\text{If } (F_i \{N_{i1}, N_{i2}, N_{i3}\} \in \eta_{fcor}) \vee (F_i \{N_{i1}, N_{i2}, N_{i3}\} \in \beta_f) \rightarrow F_i \in \beta_f \quad (10)$$

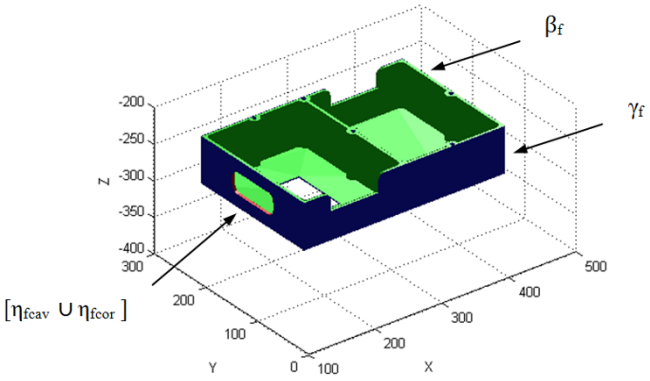


**Fig. 3.** Demoldability analysis along $+D_z$ y $-D_z$. Unification of results, Boundary Conditions.

## *2.3 Reallocation algorithm for facets not-demoldable by means of lateral slides or not-demoldable undercuts.*

This section describes the algorithm for the reclassification of the facets $F_i \in [\eta_{cav} \cup \eta_{cor}]$. As shown in Fig. 4, this set of facets can divide their domain, creating new virtual polygonal facets. Automatic division of these facets allows evaluating inner regions thereof which can be demoldable or not, depending on the presence of overlap between these facets and the facets defined above as demoldable. By means of a comparative facet-to-facet process can be determined that not-demoldable or semidemoldable facets ($[\eta_{cav} \cup \eta_{cor}]$) are entirely or partially overlapped by demoldable facets ($[\beta_f \cup \gamma_f]$). To check for overlapping between a pair of facets, both facets are projected on a plane perpendicular to the parting direction

and is checked by a Boolean logic operation if there is contact between both facets. One facet $F_i \in [\eta_{fcav} \cup \eta_{fcor}]$ is semidemoldable if it meets the condition that its nodes have a z coordinate along the parting direction below the z coordinates of the nodes of the reference facet (belonging to $[\beta_f \cup \gamma_f]$) and if the intersection between these facets it is not zero. Otherwise, it is reclassified as demoldable (belonging to $[\eta_{fcav} \cup \eta_{fcor}]$).

$$\forall F_i \in [\eta_{fcav} \cup \eta_{fcor}] \exists F_{ref} \in [\beta_f \cup \gamma_f] \mid \text{If} \begin{Bmatrix} \{z_{ref\,1}, z_{ref\,2}, z_{ref\,3}\} > \{z_{i\,1}, z_{i\,2}, z_{i\,3}\} \\ F_i \cap F_{ref} \neq \emptyset \end{Bmatrix} \rightarrow F_i \in \delta_f \tag{11}$$

Where $\delta_f \in \mathbb{R}^3$ represents the set of all semi-demoldable facets and $F_{ref} \in \mathbb{R}^3$ represents a reference facet to check for overlap. Once the semi-demoldable facets are defined, they are fragmented, finding for each the demoldable region by means of upper or lower cavity and the not-demoldable region. The division of semi-demoldable facets is performed by applying a methodology of subtraction and intersection between each of the semidemoldable facets and the closed set of reference facets.

$$\forall F_i \in \delta_f \rightarrow F_i = F'_i + F''_i \rightarrow \begin{Bmatrix} F'_i \in [\beta_f \cup \gamma_f] \\ F''_i \in [\eta_{fcav} \cup \eta_{fcor}] \end{Bmatrix} \tag{12}$$

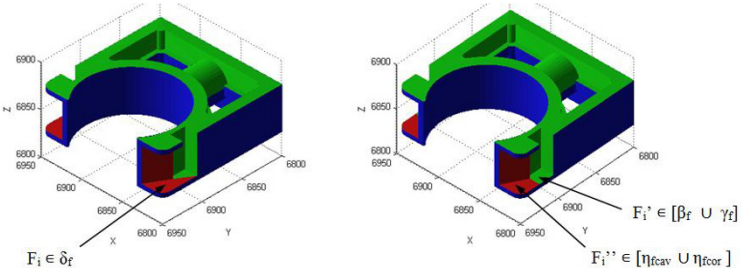


**Fig. 4.** Example of resolution of semi-demoldable facets. Boolean operation.

Finally, the set of facets classified as not-demoldable are again analyzed to check its demoldability by means of applying side cores. Thus, the part is reoriented by turning 90° around the X axis and then around the Y axis (Checking the demoldeability in new parting directiona, $D'_z$, perpendicular to main parting direction), Fig. 5. For each turn, the algorithms presented in previous sections are run, excluding those facets classified as demoldable in this phase.

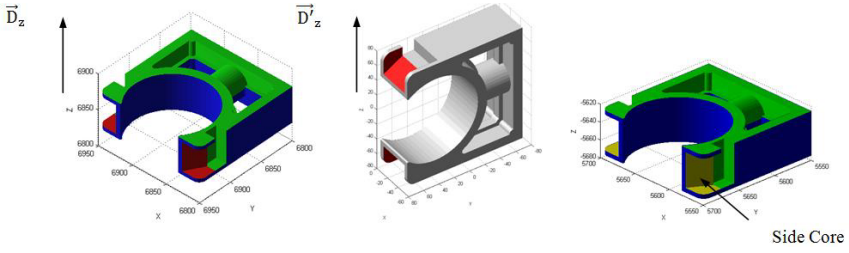


**Fig. 5.** Side Core.

## 3 Implementation and Results

In order to validate this new methodology of automated demoldability analysis, we analyzed three cases of plastic injection parts. All analyzes were performed with the same precision of the mesh (angle and deviation). The implementation of the algorithm has been made from the numerical calculation software Matlab R2013a®. In contradiction to other methods, this algorithm has the advantage of being adaptable to other programming language and its application extends to any type of mesh surface. Results of the algorithm are presented below, as it is shown the proposed cases are grouped according to the degree of demoldability in: demoldable, demoldeable via side core and non-demoldable.

First, Case A (Fig 6) is completely demoldable. Thus, all facets, which are part of the mesh of the plastic part, are demoldable in the parting direction $D_z$:=Z. As it is shown (Fig. 6), Case A is composed (Table 1) of 406 facets demoldables through cavity plate and 554 facets demoldables through core plate. Therefore, its manufacture is trivial and it does not require no slide mechanism.

Then, Case B (Fig. 6) is demoldeable by using side cores. In contradiction to previous case, this plastic parte requires a side core for manufacturing, which as it is shown (Fig. 6) is defined in the direction $D_{Side}$:=Y, perpendicular to the parting direction. Case B is composed (Table 1) of 120 facets demoldables through cavity plate, 358 facets demoldables through core plate and 20 facets demoldables through a slide mechanism or side core.

Finally, Case C is non-demoldable. Case C is composed (Table 1) of 2428 facets demoldables through the main parting direction $D_z$:=Z. As Case B, it has 358 facets demoldables through core plate and 20 facets demoldables through a slide mechanism or side core. As Case B, it possess 80 facets which require a sliding mechanism in order to be demoldable in the side direction $D_{Side}$:=X (perpendicular to the parting direction). Nevertheless, as it is shown in Fig. 6 the core of the plastic parte is not demoldable in any direction. So, 518 facets are categorized as non-demoldable facets. This implies: the need to modify the geometry of the plastic part in order to be demoldeable or non-manufacture of it, by the technique of plastic injection molds.

| Case Studies | Parting Direction | Cavity Facets | Core Facets | Side Core Facets | Side Core Direction | Non-Demold. Facets | Manufacturable |
|---|---|---|---|---|---|---|---|
| A | Z | 406 | 554 | - | - | - | Yes |
| B | Z | 120 | 358 | 50 | Y | - | Yes, through side core |
| C | Z | 1214 | 1214 | 80 | X | 518 | No |

**Table 1.** Demoldability result for the plastic part A, B and C.

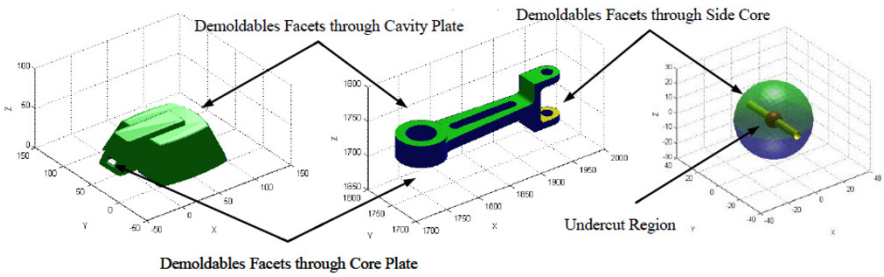


**Fig. 6.** Demoldability result for the plastic part A, B and C.

## 4 Conclusions

In this paper a new methodology for evaluating the demoldability analysis for a given parting direction is proposed. This method proposes a discrete analysis of the geometry of the plastic part to examine the demoldability in facets and nodes belonging to the mesh. The developed algorithm uses as input the discretized surface of the plastic part and generates, after analyzing it, a new virtual geometry that incorporates information about the manufacture of the plastic part.

The algorithm detects facets that are demoldable through cavity and core plate and facets that are non-demoldable. In this second case, demoldability of said facets is evaluated in a perpendicular direction to the parting direction, allowing to define the geometry and direction of side cores. Finally, the designer of the plastic part can adapt and modify the geometry of the part though regions of it that are cataloged as non-demoldable. This reduces time and costs associated with the initial phases of design and manufacturing of injection mold.

The proposed method improves other developed methods so far since it allows the realization of demoldability analysis independently of CAD modeler, is valid for application to any plastic part geometry, and it does not need access to internal information of the part. The geometry of the solid remains stored in arrays for later use in other CAD/CAE applications related to injection mold design, machining of cavity and core plates, etc.

Additionally, a future work is the implementation of the proposed algorithm in an automated mold design system.

**Acknowledgments** This work has been supported by Consejeria de Economía, Ciencia y Empleo (Junta de Andalucia, Spain) through the project titled " A vertical design software for integrating operations of automated demoldability, tooling design and cost estimation in injection molded plastic parts. (CELERMOLD)" (Project Code TI-12 TIC-1623)

## References

1. Chen L.L., Woo T.C. Computational geometry on the sphere with application to automated machining. ASME Transactions. Journal of Mechanical Design 114, 288-295.
2. Weinstein M, Manoochehri S. Optimal parting direction of molded and cast parts for manufacturability. Journal of Manufacturing Systems 1997; 16(1):1-12.
3. Fu M.W, Fuh J.Y.H., Nee A.Y.C. Undercut feature recognition in an injection mould design system. Computer Aided Design 1999; 31(12):777-790.
4. Fu M.W., Fuh J,Y.H., Nee A.Y.C. Generation of optimal parting direction based on undercut features in injection molded parts. IIE Transactions 1999; 31: 947-55.
5. Fu M.W, Nee A.Y.C., Fuh J.Y.H. The application of surface visibility and moldability to parting line generation. Computer Aided Design 2002; 34(6): 469-480.
6. Fu M.W., Nee A.Y.C., Fuh J.Y.H. A core and cavity generation method in injection mold design. International Journal of Production Research 2001; 39:121-38.
7. Fu M.W., The application of surface demoldability and moldability to side core design in die and mold CAD. Computer Aided Design 2008; 40(5): 567-575.
8. Yin ZP, Han Ding, You-Lun Xiong: Virtual prototyping of mold design: geometric mouldability analysis for near-net-shape manufactured parts by feature recognition and geometric reasoning. Computer-Aided Design 2001: 33(2): 137-154
9. Ye X.G. Fuh JYH, Lee K.S.: A hybrid method for recognition of undercut features from molded part. Computer-Aided Design 2001; 33(14):1023-34.
10. Ye X.G. Fuh JYH, Lee K.S.: Automotive undercut feature recognition for side core design of injection molds. Journal of Mechanical Design 2004; 126:519-26.
11. Singh R, Madan J, Kumar R. Automated identification of complex undercut features for side core design for die casting parts. Journal of Engineering Manufacture. 2014;228(9):1138-1152.
12. Nee A.Y.C., Fu, M.W., Fuh J.Y.H., Lee K.S., Zhang Y.F. Determination of optimal parting direction in plastic injection mould design. Annals of the CIRP.1997:,46(1): 429-432.
13. Nee A.Y.C., Fu M.W., Fuh J.Y.H, Lee K.S., Zhang Y.F. Automatic determination of 3D parting Lines and Surfaces in Plastic Injection Mould Design. Annals of the CIRP. 1998: 47(1): 95-99.
14. Huang J, Gupta SK, Stoppel K. Generating sacrificial multi-piece molds using accessibility driven spatial partitioning. Computer Aided Design 2003;35(3):1147–60.
15. Priyadarshi A.K.L., Gupta S.K. Geometric Algorithms for automated design of multipiece permanent molds. Computer Aided Design 2004; 36(3): 241-260.
16. Rubio M.A.,Pérez J.M., Rios J. A Procedure for plastic parts demoldability analysis Robotics and Computer Integrated Manufacturing 2006; 22(1):81-92.
17. Martin Doñate C, Rubio Paramio, M. A. New methodology for demoldability analysis based on volume discretization algorithms. Computer Aided Design.2013; 45(2): 229-240.
18. Martin Doñate C, Rubio Paramio, Mesa Villar A. Método de validación automatizada de la fabricabilidad de diseños de objetos tridimensionales en base a su geometría. Patent number: ES 2512940.
19. Khardekar R, McMains S. Finding mold removal directions using graphics hardware. In: ACM workshop on general purpose computing on graphics processors; 2004, pp. C-19, (abstract).

Referencia / Reference: **Mercado-Colmenero, Jorge Manuel,** Rubio-Paramio, M.A, Vizan-Idoipe, Antonio y Martín-Doñate, Cristina. *A new procedure for the automated design of ejection systems in injection molds. Robotics and Computer – Integrated Manufacturing 46 (2017) 68-85. DOI: http://dx.doi.org/10.1016/j.rcim.2016.12.006*.

Estado / Status: Publicado / Published

Índice de impacto / Impact Factor: 3,464 (JCR Year 2017)

Categoría / Catogory: Engineering, Manufacturing

Ranking: 9/46 (JCR Year 2017)

Quartile: Q1 (JCR Year 2017)

JIF Percentile: 81.522 (JCR Year 2017)

Robotics and Computer--Integrated Manufacturing 46 (2017) 68–85

Contents lists available at ScienceDirect

Robotics and Computer–Integrated Manufacturing

journal homepage: www.elsevier.com/locate/rcim

# A new procedure for the automated design of ejection systems in injection molds

Jorge Manuel Mercado-Colmenero[a], M.A. Rubio-Paramio[a], Antonio Vizan-Idoipe[b], Cristina Martin-Doñate[a,*]

[a] Department of Engineering Graphics Design and Projects, University of Jaen, Spain
[b] Department of Mechanical Engineering, Polytechnical University of Madrid, Spain

ARTICLE INFO

*Keywords:*
Ejection system
Injection molding
Discretization
Geometric analysis
Computer aided manufacturing

ABSTRACT

In this paper a new method of automatic design for the layout and sizing of the ejector pins of the plastic injection mold, based on the discrete geometry of the plastic part, is presented. The proposed algorithm consists of a first phase of geometric analysis in which a node mesh corresponding to the surfaces to be molded by the lower mold cavity is generated. Then the variations of the difference in thickness of the part for each pair of mesh nodes are evaluated, locating areas with varying thicknesses and resembling this geometric value at discrete nodes that are stored in arrays. Two sub-algorithms of discrete geometric recognition enable the location of the nodes which can be points of expulsion. Ejection points will correspond to those nodes which have a maximum in the parameter regarding concentration of nodes near walls, ribs, protrusions, etc. The dimensioning of the ejector pins is performed by an optimization algorithm with three objective functions, ensuring that the system of forces in the ejection of the part will be balanced. This new method improves on the methods used so far as it does not require heuristic methods to achieve the result and does not use the method of identifying features for the geometric recognition of the surface of the plastic part, avoiding the problems of dependency from the modeler and analysis of complex features. It takes the part in discrete format as input data, analyzing in this way the geometry externally, obtaining the advantage of the possibility of implementing the algorithm in any CAD modeler. The proposed algorithm is applicable to any geometry because it works regardless of the CAD system in which the piece has been designed. Finally, the system provides as a result the layout with the location and the diameter of the ejectors on the part while ensuring a suitable distribution of balance of ejection forces. The solution of the algorithm is shown superimposed on the part as a map of ejection. The results of the algorithm can be exported and stored for use in other applications and parametric injection mold CAD systems.

## 1. Introduction

Injection molding is one of the most widely used technological processes in the transformation of thermoplastic polymers. The process begins with the injection of a precise amount of molten thermoplastic material within the mold cavities. Then the plastic begins to solidify, decreasing its volume and shrinking onto the cores of the cavities; this volume loss is compensated by injecting an extra small amount of melt inside the cavities and applying a holding pressure which prevents backflow of the thermoplastic material. The high level of performance that is required today of the mold means that the value of the cycle time must be reduced to the minimum. This is achieved by cooling the piece by means of the cooling channels through which a fluid cooler circulates, thereby accelerating solidification. When the part comes to have sufficient rigidity to be ejected from the mold, the ejection system extracts the part from the cavity to which it has been adhered, through a mechanical system that frees it. After finishing the ejection phase, the mold is closed again and starts the next cycle.

Short cycle times require the extraction of the part from the mold almost to the limit of its solidification. This can cause damage or deformation of the part if the design of the ejection system is not performed properly. While there are several procedures for ejecting the plastic part from the mold, many of them could lose functionality eventually due to wear and clearance with use. Therefore in complex plastic parts that incorporate ribs, protrusions or areas of difficult withdrawal, the use of ejector pins is recommended. These pins are

* Correspondence to: Department of Engineering Graphics Design and Projects, University of Jaen, Campus Las Lagunillas, s/n. Building A3-210, 23071 Jaen, Spain.
*E-mail addresses:* jmercado@ujaen.es (J.M. Mercado-Colmenero), marubio@ujaen.es (M.A. Rubio-Paramio), antonio.vizan@upm.es (A. Vizan-Idoipe), cdonate@ujaen.es (C. Martin-Doñate).

http://dx.doi.org/10.1016/j.rcim.2016.12.006
Received 21 December 2015; Received in revised form 9 December 2016; Accepted 22 December 2016

characterized by their versatility in their location on the part, as well as ease of installation at a relatively low cost.

The calculation and design of ejector pins distribution on the plastic part is not an easy task when the geometry of the part is complex. The application of unbalanced stresses on the pins could cause severe penetrations through the piece surface that lead to breakage by exceeding the elastic limit of the material or distorting the part surface. Therefore it requires a proper balance of the forces applied on the piece in its ejection from the mold. Currently the layout of the ejector pins is projected based on the experience of the mold designer. In the literature some basic empirical rules regarding the design and selection of the ejectors are suggested. To prevent damage by penetration and deformation, the designer tends to use an excessive number of ejector pins. This increases the cost of the mold and decreases the effective area for cooling, reducing its thermal efficiency and causing a negative effect on productivity. In light of these problems, an analysis tool that automates the design process of the mold ejection system is deemed necessary. This must be carried out in parallel with the design of the part, preventing possible manufacturing failures in the early stages of the design. While CAD/CAM systems have been widely used in the design of injection molds, these do not incorporate geometric algorithms to automate the design of the ejection system. Specialized commercial software systems in mold design require a great deal of interaction and experience on the part of the designer as well as specific knowledge of the manufacture of the plastic part. In the field of research few studies dedicated to automating the design of the ejection system have been developed. They are mainly based on the recognition of features of the plastic part or on heuristic optimization methods of the results. On the basis of the problems described, a new methodology for automated obtaining of the layout and size of the ejector pins for ejecting the plastic part is presented. The goal is to minimize the deformation and deterioration of the plastic part. The proposed method will help designers of injection molds to obtain systematically the design of ejectors, substantially reducing the time of interaction between product designers and mold designers needed to validate the design for their manufacture.

## 2. Background and related work

In the plastic parts injection process, a mold basically consists of two parts called the upper cavity and lower cavity within which the plastic is injected leading to the desired body. In order to determine which parts of the piece will be manufactured by the upper cavity and the lower cavity of the mold it is necessary to carry out a preliminary analysis of demoldability. This analysis will detect non-manufacturable areas and areas difficult to manufacture (undercuts, called side cores). The geometric recognition of the plastic part determines this data set automatically and verifies the design of the most favorable part. The design procedure of the ejection system of the plastic part uses as a basis the results obtained by the demoldability analysis applied to the lower cavity. This lower cavity, also called the mobile cavity, is moving in the mold opening and actuates the automatic ejection device of the mold. Therefore, the lower cavity obtained by analyzing demoldability is set as the starting data necessary to perform design and is critical to the realization of a correct automated analysis of ejection. Obtaining demoldability analysis is a research area undergoing rapid development in the field of injection mold design.

Numerous demoldability analysis methodologies are based on the study of the maps of visibility. These include those developed by Chen et al. [1,2] who also created an algorithm for optimal parting direction by means of dividing the object into pockets, where visibility and demoldability play the same role. Other researchers have based their research on the recognition features of the plastic parts. Fu et al. developed a complete solution for analyzing demoldability using recognition features. By means of these studies they achieved the detection of undercuts [3], the parting direction [4], the parting line [5] and the areas of upper and lower cavities [6]. Lu and Lee [7] discuss interference elements in the demolding process. Yin et al. [8] provide an algorithm for recognizing the undercut features for near net shapes. Ye et al. [9] created a graphic method of feature recognition. In feature recognition systems a piece created by means of a CAD system is linked to the modeler in which it was created, thus establishing a relationship of dependency between the recognition method and the part modeler. On the other hand, both pockets-based methods and those based on features provide local results focused on the geometrical singularities of the part. They do not allow a global analysis of the lower cavity in order to obtain an ejection system.

Other methods of demoldability analysis use part discretization procedures by means of tessellated models as input to the analysis algorithm. The models of tessellation of the plastic part provide a great advantage when the part includes complex and freeform surfaces. Khardekar et al. [10,11] use the GPU as a mean of recognizing the directions for demolding undercuts. Chakraborty et al. [12] identify non-convex regions, determining the optimal parting direction and generating the parting surface according to the parting direction. Singh et al. [13] use a tessellated model and discuss the classification of part surfaces of the casting mold, identifying undercuts and protrusions and determining the parting line. These methods offer appropriate discretization results for later ejection analysis because of their global character, but have drawbacks as they either require additional computing devices such as GPU's, or are unable to perform the analysis of all types of plastic parts.

Suitable results for use in subsequent ejection design were also provided by discretization procedures performing flat sections. Ganter et al. [14] analyzed sections performed on the plastic part and established a set of nine rules based on their experience and a vast bibliography. Wong et al. [15] improved the algorithm proposed by Ganter et al. [14] and extended the scope to parts with partition lines consisting of several contours, and increased the accuracy of the algorithm. Rubio [16] developed a discretization technique of 3D solids using a set of sections for demoldability analysis. More recently Martin et al. [17,18] and Mercado [19] proposed an algorithm based on a method of discretization of the solid by means of a grid of points, which were reassigned according to their demoldability. These demoldability analysis methods come to be established as the most appropriate for the achievement of the subsequent ejection system.

Once the process of part demolding is determined, we must establish the design of the mechanical devices for carrying out the injection process. The mold consists of several functional subsystems and one of them is the ejection system. Most of the CAD systems available today provide integrated design for mold component modules. These modules are used in assisting the designer to reduce product development time. Nevertheless, they have several limitations since they focus on the design of only some mold elements, and require knowledge and interaction by the designer for the low level of automation of the geometric algorithms used. In order to solve these problems, several researchers have conducted their work in this area. Ye et al. [20] proposed a representation based on object-oriented features to represent the assembly of the plastic injection mold hierarchically. Though the method incorporates the CAD design of the ejection system, it is not fully automated because the user must place the coordinates where the ejector pins are located, requiring personnel experienced in mold design in order to handle the tool. Mok [21] developed the IKMould system consisting of an interactive CAD system based on knowledge for the design of the injection mold. The goal is to take advantage of the capabilities and experience of the designers in order to improve the functionality of the program. But in order to design the ejection system the software requires the introduction of the information related to the diameters, and the location and orientation of all the ejector pins. Low [22] presented a methodology for designing the cavity layout for plastic injection molds, controlling the geometrical parameters using a standardized template. But they did

not study the mold ejection system. Neo [23] examined various issues and methodologies related to the development of plug-ins on 3D modeling platforms. He first presented a methodology for developing applications based on the plastic part 3D model and then created an application for the mold design using Parasolid. However only the first three stages of the mold design were developed and the ejection system was not studied. Ma [24] presented the definition, design and implementation of a standard library of components within the Quickmold software. Just as in previous systems ejection design was not resolved. Kumar [25] created the Auto-Die-Caster application which has been developed as a vertical application for the Solidworks modeler. While the system covers some parts of the design of the mold it does not address the design of an ejection system. Research into the process of automated mold construction shows a great potential for helping designers to support decisions related to mold design. However, these methods are limited to simple parts and are often too theoretical to be applied to a practical mold design. A review of these studies shows that the automatic ejection system design has received relatively little attention, mainly because the methods developed so far lack a geometric algorithm as a basis for the design of the ejection system.

But the process of expulsion of the plastic is influenced not only by geometrical parameters, but also by parameters of functional and technological type such as the ejection force, the shrinkage of the part when it solidifies, the cooling temperature and other mechanical properties of the plastic material. Since the expulsion process takes place on the parts at high temperature, an excessive value of the ejection forces or the wrong balance of them can deform the part surface, decreasing its quality. A review and classification of demolding issues and proven solutions is found in Delaney [26]. Some researchers have developed models based on equations for calculating the force needed to eject a part from the mobile cavity. For this purpose they used thermodynamic or mechanical models, and CAE simulations. Malloy et al. [27] researched the variables related to the ejection process of an injection molded part. They observed that the ejection forces are difficult to quantify because they are largely influenced by a number of factors. Although this work was a good compilation of the problems that occur in the estimation of the ejection force, they did not finally present any experimental data. Menges et al. [28] performed the first estimate of the ejection forces on the plastic part. In their approach, they obtained the value of the ejection forces based on the geometry and mass of the plastic part in order to manually design in detail the ejection system (number, location, and type of ejecting elements). Burke et al. [29] performed an experimental study of ejection forces during the injection molding process for the particular case of a laterally opened casing, with closed edges. The casing was molded with ABS and HDPE materials in order to validate the results of the research in the case of amorphous low shrinkage materials and crystalline high shrinkage materials. Pontes et al. [30] studied the effect of the influence conditions on the ejection forces required for parts with deep gun turrets, verifying the results for three thermoplastic polymers. Bhagabatula et al. [31] studied the ejection of industrial injection molded parts by comparing the developed simulation model to the experimental results. Sasaki [32] performed a study of the ejection forces in parts manufactured by injection. Through his experiments he concluded that there is an optimum surface roughness of the core necessary for obtaining a minimum ejection force for each material.

In the field of microinjection, Griffiths [33,34] carried out experimental studies with the aim of investigating the behavior of plastic parts in terms of demolding, focusing his research on the effects of pressure and temperature on the demolding forces. The studies show the existence of a direct correlation between the pressure and the demolding force, as well as between the manufacturing factors and the demolding force, identifying those factors that have a significant effect on the demolding behavior of the plastic part.

Regarding the automation of detailed geometric design and the layout of the ejector pins to eject the plastic part from the mold, the research studies were rather limited, and were listed by Chan et al. [35]. Kwak et al. [36] proposed a method for determining the distribution and size of the ejector pins required to eject thermoplastic molded parts, minimizing the deformation of the workpiece and the damage to its surface. Their method computes the distribution of the ejection forces required to overcome the friction between the part and the mold. However, the algorithm uses heuristic methods in order to achieve fine adjustment of the result. Wang [37] presented an algorithm and its implementation in order to optimize the design of the ejector system in the plastic injection mold, ensuring the design that causes less deformation and distortion on the molding part. However, the analytical procedure has the disadvantage that it is restricted to a model based on features. As discussed above, in features recognition systems a part created in a CAD system is linked to the modeler with which it was created. In addition, in the features recognition process there may be some features that interact with each other so that the adjacency relationships between those which were in contact are destroyed, thus preventing their recognition.

The research presented in this paper proposes a new algorithm for automated layout design and dimensioning of the ejector pins for extracting the mold part, based on the geometry of the plastic part. The proposed algorithm consists mainly of two phases: The first stage performs a geometric recognition of the surface of the plastic part in order to locate the ejection points close to very rigid areas of the workpiece in order to avoid deformation zones. The second stage performs the ejector dimensioning implementing optimization algorithms, thereby ensuring that the system of forces in the ejectors is balanced. The method developed here improves on existing ones since it does not use heuristic methods to obtain results, avoiding design evaluation once the physical product has been made. The features recognizing procedure is not used, avoiding the problems of this methodology because the geometry is recognized externally.

## 3. Methodology

Given a 3D part to be manufactured L, the proposed algorithm must be valid for parts to be produced using the injection molding technique.

$$\forall \quad \mathcal{L} \in \mathbb{R}^3$$

First the solid L is transformed into a discrete mesh L′ formed by a set of triangular elements and nodes. Thus the discrete mesh L′ is defined as a vector of dimension 1×2, first formed by the array $L'_f$ nx3 range which groups the entire set of triangular facets (the total number of facets of the mesh being n), and secondly by the array $L'_n$ 3nx3 range which groups entire set of mesh nodes. This allows us to define the geometry of the part externally Fig. 1(a) and (b) and thus avoid the problems of dependence of the CAD modeling.

$$\forall\, \mathcal{L} \quad \rightarrow \quad \mathcal{L}' \in \quad \mathcal{M}_{1x2}(\mathbb{R}) \rightarrow \mathcal{L}' = \{\mathcal{L}'_f \mathcal{L}'_n\} \mathcal{L}'_{11} = \mathcal{L}'_f \rightarrow \mathcal{L}'_f \in \quad \mathcal{M}_{nxm}$$
$$(\mathbb{R})\, \mathcal{L}'_f := \ell'_f\, (ij)_{nxm}\, \ell'^{i}_f = F_i = \{P_{i1}, \ldots, P_{ij}, \ldots, P_{im}\} \rightarrow \ell'_f$$
$$(ij) = P_{ij} \; 1 \le i \le n \; ; 1 \le j \le m$$

Working only with triangular facets then m=3

$$\mathcal{L}'_{12} = \mathcal{L}'_n \rightarrow \mathcal{L}'_n \in \quad \mathcal{M}_{n\cdot 3x3}(\mathbb{R})\, \mathcal{L}'_n := \ell'_n\, (ij)_{n\cdot 3x3}\, \ell'^{i}_n = P_{ij} = \{x_{ij}, y_{ij}, z_{ij}\}$$
$$1 \le i \le n\cdot 3; \; 1 \le j \le 3$$

Each $P_{ij}(x_{ij}, y_{ij}, z_{ij})$ node belonging to $F_i$ facet and also belonging to the mesh $L'_n$, must be unique for that facet $F_i$.

$$\left.\begin{array}{l} \forall \quad F_i = \{P_{i1}, P_{i2}, P_{i3}\} \in \mathcal{L}'_f \\ \qquad 1 \le i \le n \\ \forall \quad P_{ij} = \{x_{ij}, y_{ij}, z_{ij}\} \in \mathcal{L}'_n \\ 1 \le i \le n\cdot 3; \; 1 \le j \le 3 \end{array}\right\} \rightarrow \{x_{i1}, y_{i1}, z_{i1}\} \neq \{x_{i2}, y_{i2}, z_{i2}\} \neq \{x_{i3}, y_{i3}, z_{i3}\}$$

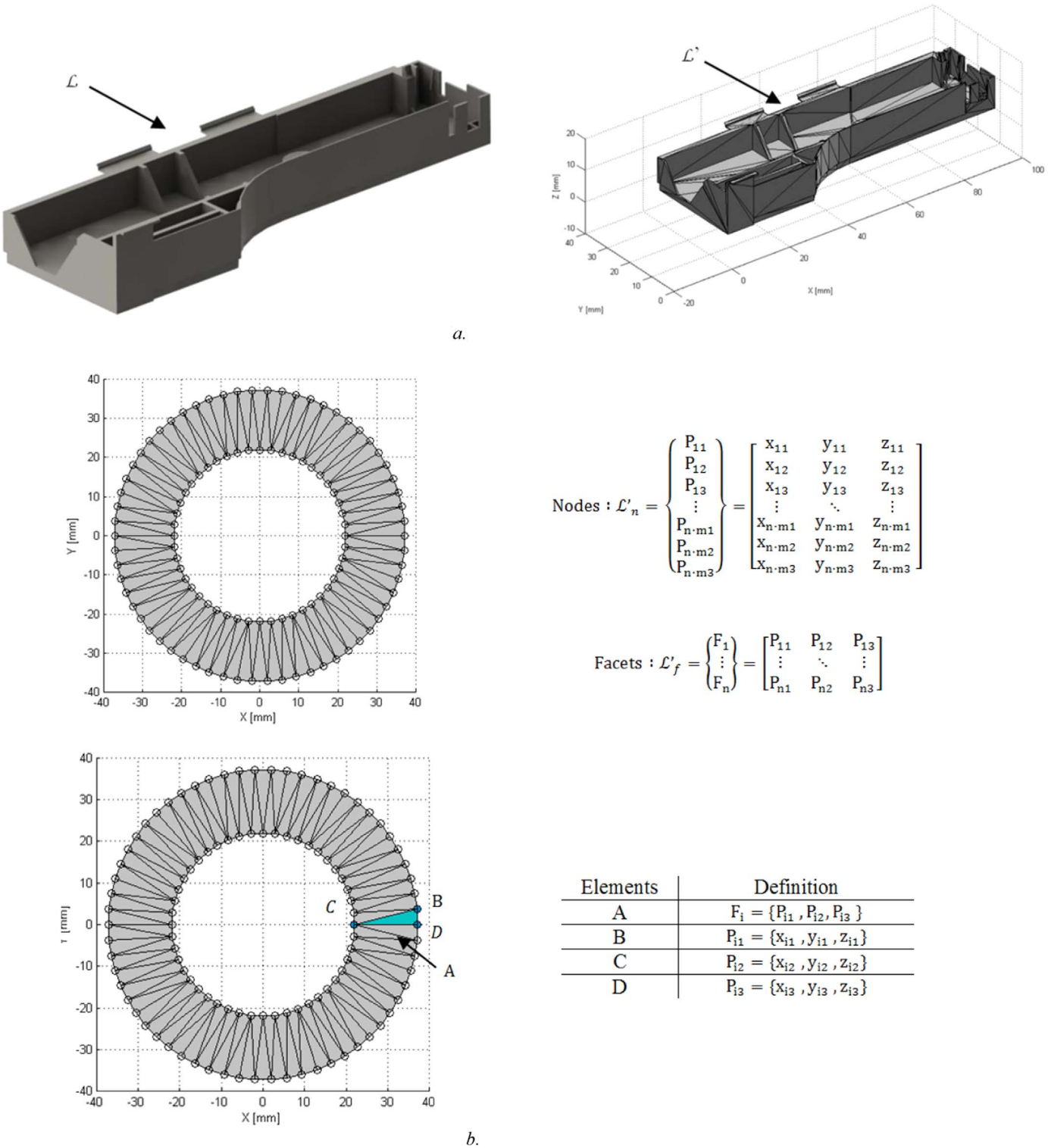


$$\text{Nodes}: \mathcal{L}'_n = \begin{Bmatrix} P_{11} \\ P_{12} \\ P_{13} \\ \vdots \\ P_{n\cdot m1} \\ P_{n\cdot m2} \\ P_{n\cdot m3} \end{Bmatrix} = \begin{bmatrix} x_{11} & y_{11} & z_{11} \\ x_{12} & y_{12} & z_{12} \\ x_{13} & y_{13} & z_{13} \\ \vdots & \ddots & \vdots \\ x_{n\cdot m1} & y_{n\cdot m1} & z_{n\cdot m1} \\ x_{n\cdot m2} & y_{n\cdot m2} & z_{n\cdot m2} \\ x_{n\cdot m3} & y_{n\cdot m3} & z_{n\cdot m3} \end{bmatrix}$$

$$\text{Facets}: \mathcal{L}'_f = \begin{Bmatrix} F_1 \\ \vdots \\ F_n \end{Bmatrix} = \begin{bmatrix} P_{11} & P_{12} & P_{13} \\ \vdots & \ddots & \vdots \\ P_{n1} & P_{n2} & P_{n3} \end{bmatrix}$$

| Elements | Definition |
|---|---|
| A | $F_i = \{P_{i1}, P_{i2}, P_{i3}\}$ |
| B | $P_{i1} = \{x_{i1}, y_{i1}, z_{i1}\}$ |
| C | $P_{i2} = \{x_{i2}, y_{i2}, z_{i2}\}$ |
| D | $P_{i3} = \{x_{i3}, y_{i3}, z_{i3}\}$ |

**Fig. 1.** a) Converting a CAD model to a virtual faceted model. b) Definition of a facet and nodes, triangular shell elements.

### *3.1. Classification of the mesh elements and discretization of the geometry*

First a preliminary demoldability analysis of the geometric mesh $L'_f$ is performed (Martin et al. [19]), obtaining a facet model from the discrete model. Those facets Fi, $\in\xi_{f1}$ that will be molded by the lower mold cavity are located. The array $\xi_{f1}$ stores those facets $F_{core,\ i}$ demoldable by the lower cavity, see Fig. 2.

$\forall\ F_i=\{P_{i1}, P_{i2}, P_{i3}\ \}\rightarrow F_i\in\ \ \xi_{f1}\ \ F_i=F_{core,i}\in\ \ \xi_{f1}\ \ \xi_{f1}\ \ \in\mathbb{R}^3$

After locating the surfaces corresponding to the lower mold cavity the algorithm performs a new discretization process using a technique based on a 2D mesh of nodes. A bounding box is defined to fully frame the plastic part and generate the nodal mesh (s×u). This grid, called $\Delta_t$, consists of a set of points $\delta_t(ij) \in \mathbb{R}^3$ with coordinates $[\delta_t(ij)_x\ \ \delta_t(ij)_y\ \ \delta_t(ij)_z]$ along the axes X, Y, Z, being $\delta_t(ij)_z$ a constant value for all points $\delta_t(ij)$ Fig. 3.

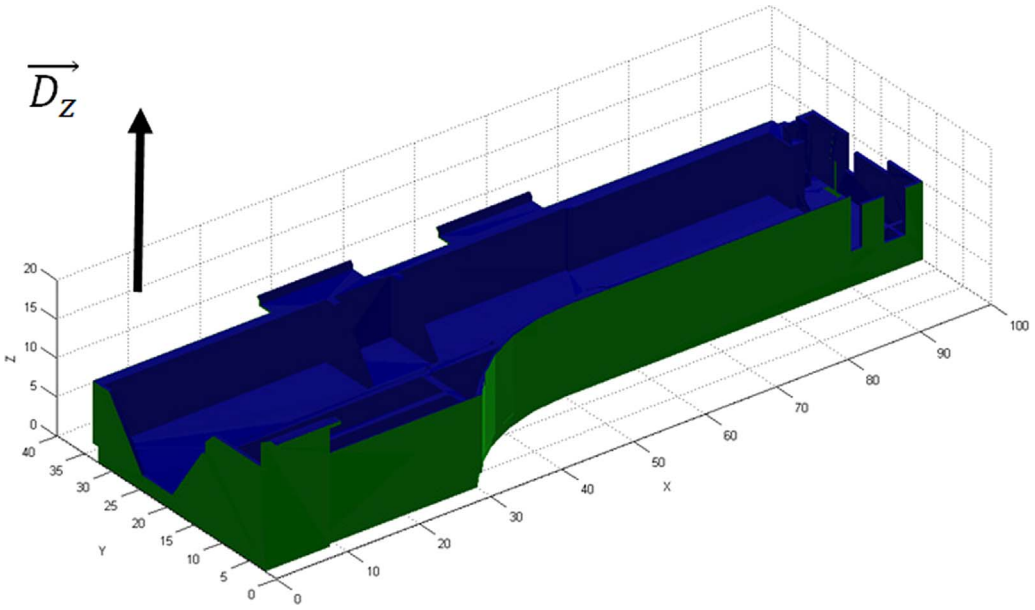


**Fig. 2.** Set of facets molded by lower cavity highlighted in blue. (For interpretation of the references to color in this figure legend, the reader is referred to the web version of this article).

$$\Delta_t := \{\delta_t(ij)_{\frac{s}{\varepsilon}x\frac{u}{\varepsilon}} \Delta_t \in \mathcal{M}_{\frac{s}{\varepsilon}x\frac{u}{\varepsilon}}(\mathbb{R}) \rightarrow \delta_t(ij) = [\delta_t(ij)_x \;\; \delta_t(ij)_y \;\; \delta_t(ij)_z] \in \mathbb{R}^3 \delta_t$$

$$(ij)_z = cte1 \leq i \leq \frac{s}{\varepsilon}; 1 \leq j \leq \frac{u}{\varepsilon}$$

The points $\delta_t(ij) \in \mathbb{R}^3$are spaced at distance $\varepsilon$ from each other, corresponding to the distance between nodes. The $\varepsilon$ value corresponds to the precision of analysis and will be entered by the user, it being always wise to use the half of the geometric dimension of the smallest detail of the L′ part analyzed.

Then the algorithm performs a segmentation $\Delta_{tin}$ of the nodal grid $\Delta_t$; in order to include the set of nodes $\delta_t(ij)_{in}$ that intersect with the discrete mesh $\mathcal{L}'_f$ in $\Delta_{tin}$. The intersection points $\delta_t(ij)_{in}$ are obtained by drawing a straight beam $\mathcal{R}_t$ starting in each node $\delta_t(ij) \in \mathbb{R}^3$ and the direction $\overrightarrow{D_z}$ and calculating the intersections of each line $r_t$ with the mesh $\xi_{f1}$ (see Fig. 4).

$$\Delta_t = \{\Delta_{tin}\Delta_{tout}\}\mathcal{R}_t \in \mathcal{M}_{\frac{s}{\varepsilon}x\frac{u}{\varepsilon}}(\mathbb{R}) \rightarrow \mathcal{R}_t := r_t(ij)_{\frac{s}{\varepsilon}x\frac{u}{\varepsilon}} \forall\, \delta_t(ij) \;\exists$$

$$r_t(ij) = \left\{ \begin{matrix} \text{Origin:} [\delta_t(ij)_x \;\; \delta_t(ij)_y \;\; \delta_t(ij)_z] \\ \text{Direction:} [001] \end{matrix} \right\} \in \mathbb{R}^3 \forall\, r_t(ij) \mid \{ r_t$$

$$(ij) \cap \xi_{f1} \;\; (ij) \} \neq \varnothing \rightarrow \delta_t(ij)_{in} \in \mathbb{R}^3$$

This methodology provides a great advantage, since it allows us to obtain the thickness $\mathcal{T}(ij)$ of the part $\mathcal{L}$ along the direction $\overrightarrow{D_z}$ for each node $\delta_{t\,ij\,in}$ belonging to the mesh $\Delta_{tin} \in \mathbb{R}^3$ directly, evaluating the intersection points between each line $r_t(ij)$ and the 3D mesh $\mathcal{E}'_f(ij)$.

$$\forall\, r_t(ij) \exists\, \mathcal{T}(ij) = \text{Thickness}(ij) = \max(r_t(ij) \cap \mathcal{E}'_f(ij))_Z - \min(r_t(ij) \cap \mathcal{E}'_f(ij))_Z$$

In Fig. 5a the assembly nodes $\delta_t(ij)_{in}$ are represented in blue on the mesh $\mathcal{L}'$. A projection, parallel to the XY coordinate plane, of the thickness map $\mathcal{T}(ij)$ and the iso-contour representative of the variations of thickness of the part is shown. Each iso-contour (closed curve) represents a set of points $\delta_t(ij)_{in}$ with equal thickness. Colors are used to indicate the thickness of the part at each point along the iso-contours. The set of iso-contours in different colors indicates the different thickness variations in mm for the part $\mathcal{L}'$. The lateral colorbar in Fig. 5a indicates the colors for each thickness value in mm. The inner zone of the nerves takes on a yellow color indicative of a greater thickness compared to the blue color of the flat areas of the part, with lesser thicknesses.

One of the geometric requirements for the location of the ejection points is its positioning near the geometric location of the points which offer high resistance to ejection, because thermoplastic materials tend

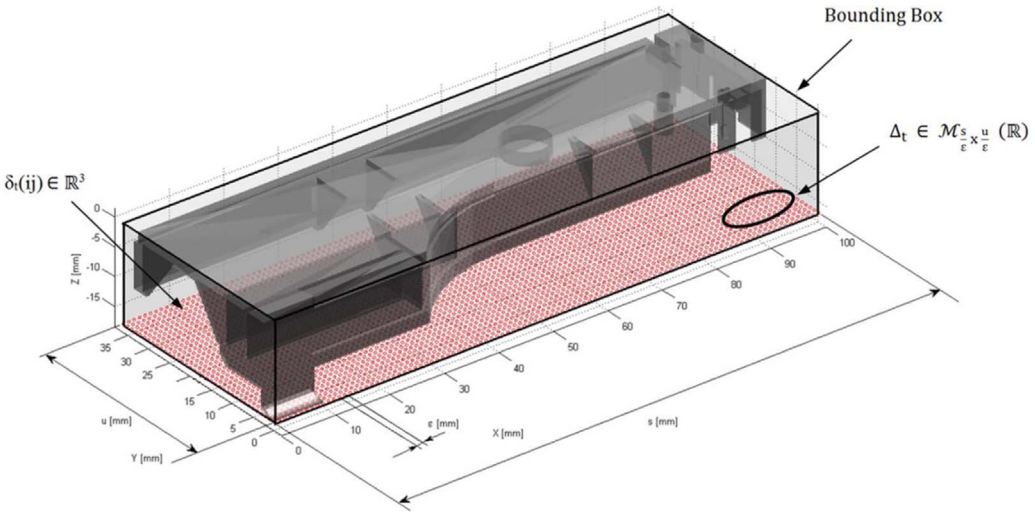


**Fig. 3.** Location of the Bounding Box and the measures s and u on the XY plane.

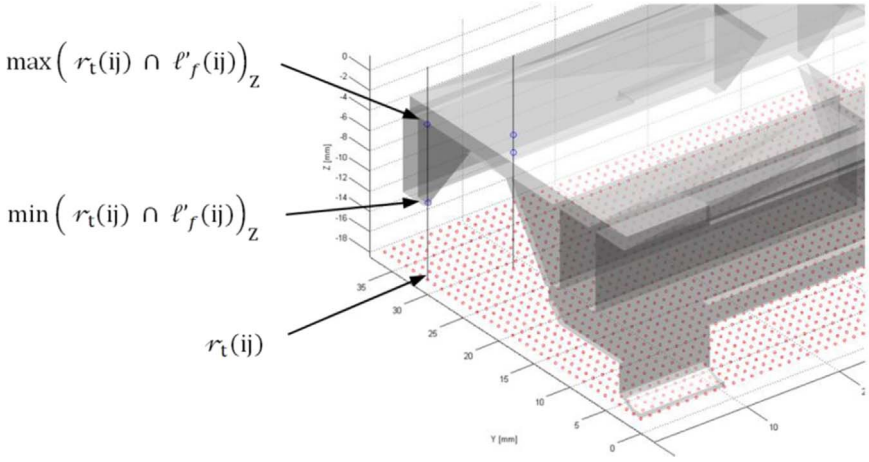


**Fig. 4.** Obtaining points of intersection for an individual line $r_t(ij)$ with the part L′.

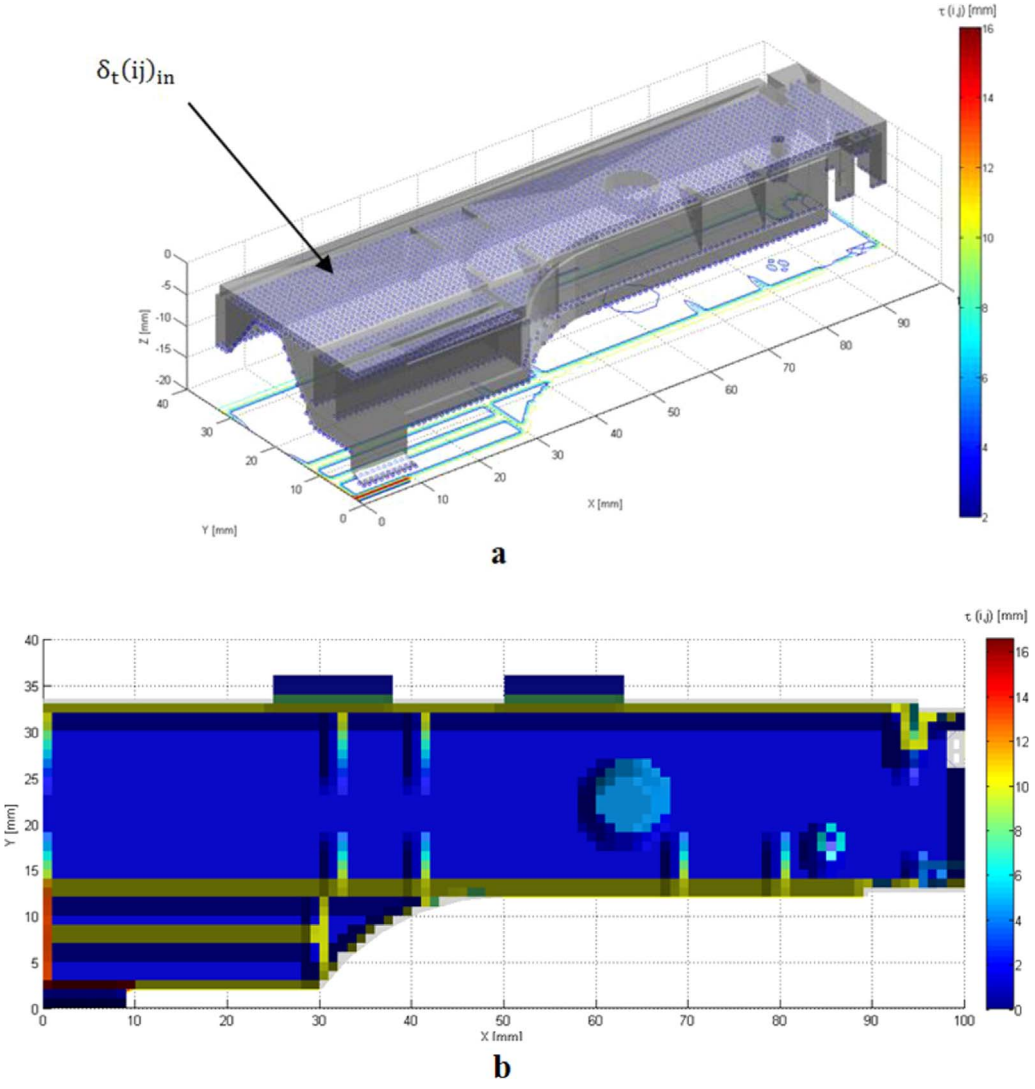


**Fig. 5.** a) Points $\delta_t(ij)_{in}$ and the projected thickness map $\mathcal{T}(ij)$ with the iso-contours representing the thickness variations of the part. b) Thickness map representation $\mathcal{T}(ij)$ for each node $\delta_{tijin} \in \delta_t(ij)_{in}$ , on the part $\mathcal{L}$. (For interpretation of the references to color in this figure, the reader is referred to the web version of this article).

to deform due to their limited mechanical strength. As illustrated in Fig. 6, the location of these ejection points is in the contour of geometrical details such as ribs, sharp corners, etc., in short surfaces of the lower cavity of the plastic part with large curvature changes.

In order to identify in an automated way geometric areas of the part that incorporate ribs, protrusions and corners, the algorithm analyzes the variation in the difference in thickness between each pair of contiguous nodes of the mesh, $\delta_{tin}(ij)$ y $\delta_{tin}(i \pm 1, j \pm 1)$ separated by a

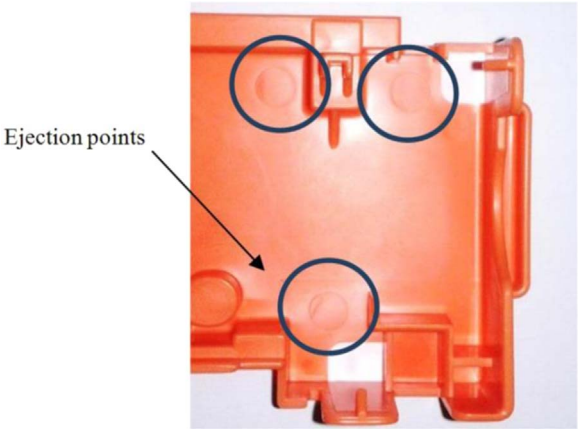


**Fig. 6.** Curvature changes associated with ejection points and geometric features such as corners, ribs, etc. in a study of a real case.

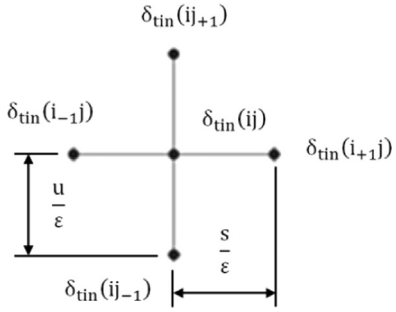


**Fig. 7.** Nodal structure of the analysis of $\delta_{tin}(ij)$.

ε distance equal to the analysis accuracy (see Fig. 7). This analysis takes place bi-directionally in the direction of the coordinate axes X and Y. Thus, if the variation in the difference in node-node thickness remains constant in one of the directions of the coordinate axes X or Y, those nodes will be grouped into a new nodal array $\delta_g(ij)\in \mathbb{R}^3$. On the contrary, if during scanning along the direction of axes X and Y the algorithm detects a change of thickness between two adjacent nodes, the node with the higher magnitude of thickness is stored in a new array $\delta_r(ij)\in \mathbb{R}^3$.

$$\forall\ \delta_t(ij)_{in}\ \mid \begin{pmatrix} \text{Thickness}(ij)_{in}-\text{Thickness}(ij_{+1})_{in}=\Lambda \\ \text{Thickness}(ij)_{in}-\text{Thickness}(i_{+1}j)_{in}=\beta \\ \text{Thickness}(ij)_{in}-\text{Thickness}(ij_{-1})_{in}=\Sigma \\ \text{Thickness}(ij)_{in}-\text{Thickness}(i_{-1}j)_{in}=\Theta \end{pmatrix} \rightarrow \Lambda=\Sigma \quad \bigvee \beta=\Theta \rightarrow \delta_t$$

$$(ij)_{in}=\delta_g(ij)\rightarrow\delta_g(ij)\in\mathbb{R}^3$$

$$\forall\ \delta_t(ij)_{in}\ \mid \begin{pmatrix} \text{Thickness}(ij)_{in}-\text{Thickness}(ij_{+1})_{in}=\Lambda \\ \text{Thickness}(ij)_{in}-\text{Thickness}(i_{+1}j)_{in}=\beta \\ \text{Thickness}(ij)_{in}-\text{Thickness}(ij_{-1})_{in}=\Sigma \\ \text{Thickness}(ij)_{in}-\text{Thickness}(i_{-1}j)_{in}=\Theta \end{pmatrix} \rightarrow \begin{matrix} \Lambda\neq\beta \\ \bigvee \\ \beta\neq\Sigma \\ \bigvee \\ \Sigma\neq\Theta \\ \bigvee \\ \Lambda\neq\Sigma \\ \bigvee \\ \beta\neq\Theta \end{matrix} \rightarrow \delta_t(ij)_{in}=\delta_r(ij)\rightarrow\delta_r(ij)\in\mathbb{R}^3$$

### 3.2. Location of optimal regions for the ejection and determination of the ejectors location

Given the $[\delta_g(ij)\delta_r(ij)]\in\mathbb{R}^3$arrays, a point $\delta_{g\,ij}\in\mathbb{R}^3$ is defined as a possible ejection point, belonging to the array $\delta_{ejec}(ij)\in\mathbb{R}^3$ if there is an r > 0 such as $\delta_{g\,ij}\in D_r(\delta_{g\,ij})\cap\delta_{r\,ij}=\varnothing$; being $D_r(\delta_{g\,ij})$ the inner area of a circle at the XY plane, centered at the point $\delta_{g\,ij}$ and radius r (defined by the dimensions of the minimal detail of the part $\mathcal{L}$). That is, for each node $\delta_{g\,ij}$ a circular area $D_r(\delta_{g\,ij})$ is generated and we check whether any node $\delta_{g\,ij}\in\delta_g(ij)$ is included in this area. In Fig. 8, as an example, a node $\delta_{g\,ij}\in\delta_{ejec}(ij)\in\mathbb{R}^3$ which meets the condition $\in\delta_{ejec}(ij)\in\mathbb{R}^3$ is shown

$$\forall\ \delta_{g\,ij}\in\delta_g(ij)\quad \exists\quad D_r(\delta_{g\,ij})\mid If\ (D_r(\delta_{g\,ij})\cap\delta_{r\,ij}=\varnothing)\rightarrow\delta_{g\,ij}=\delta_{ejec}(ij)\in\mathbb{R}^3\delta_t$$

$$(ij)_{in}=[\delta_g(ij)\delta_r(ij)]\in\mathbb{R}^3 If$$

$$\left\{\begin{matrix} P_{ejec\ ij\ x}=\delta_{g\,ij}+r\cdot\text{Cos}(v) & \forall\ v\in[0,\ 2\pi] \\ \bigvee \\ P_{ejec\ ij\ y}=\delta_{g\,ij}+r\cdot\text{Sin}(v) & \forall\ v\in[0,\ 2\pi] \end{matrix}\right\}\cap\delta_{r\,ij}$$

$$=\varnothing\rightarrow\delta_{g\,ij}\in\delta_{ejec}(ij)\in\mathbb{R}^3$$

In Fig. 9 the result of the grid nodal analysis is indicated. Each of the nodes of the array $\delta_{ejec}(ij)\in\delta_g(ij)$ in blue are possible ejecting points of the part, as they fulfill the boundary conditions established.

Then a new analysis to define the final location of the ejectors is performed. For this purpose, the concentration of nodes $\delta_r(ij)\in\mathbb{R}^3$near each of the nodes of the array $\delta_{ejec}(ij)$ is evaluated. All those nodes $\delta_{ejec}(ij)$ satisfying the condition of containing a large number of nodes $\delta_r(ij)$ inside the circular area located in the XY plane $D_r(\delta_{ejec}(ij))$, with center $\delta_{ejec\ ij}$ and diameter R=2·r, meet the geometrical condition of proximity to regions with thickness variation and therefore proximity to geometric features such as corners, ribs, etc. These nodes require an ejection point near them.

$$R=2\cdot r\ \forall\ \delta_{ejec}(ij)\ \exists\ D_r(\delta_{ejec}(ij))\mid If\left\{\begin{matrix} \delta_{ejec}(ij)+R\cdot\text{Cos}(v) & \forall\ v\in[0,\ 2\pi] \\ \bigvee \\ \delta_{ejec}(ij)+R\cdot\text{Sin}(v) & \forall\ v\in[0,\ 2\pi] \end{matrix}\right\}\cap\delta_r$$

$$(ij)\neq\varnothing\rightarrow n_r(ij)=\sum\left(D_r(\delta_{ejec}(ij))\cap\delta_r(ij)\right)\quad\in\mathbb{R}$$

Where $n_r(ij)$ is a factor associated with each node $\delta_{ejecij}\in\delta_{ejec}(ij)$ which indicates the number of nodes $\delta_{r\,ij}\in\delta_r(ij)\in\mathbb{R}^3$ included in the circular area $D_r(\delta_{ejecij})$. In Fig. 10, two examples of $n_r(ij)$ for two nodes

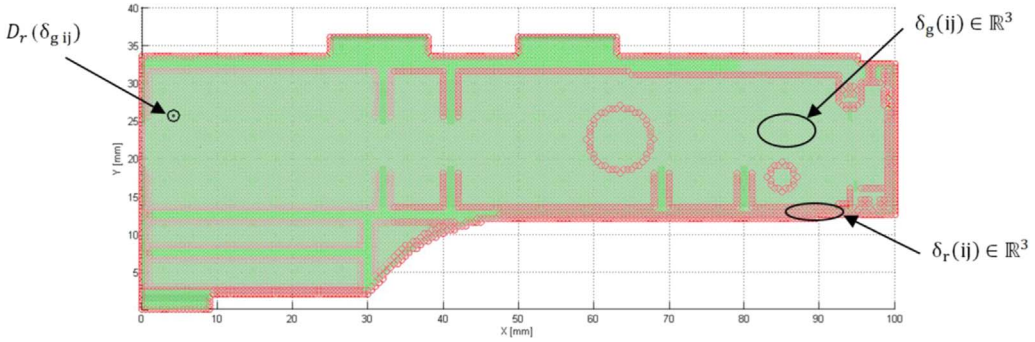


**Fig. 8.** Validation analysis for node $\delta_{gij}$ with respect to array $\delta_r(ij)$.

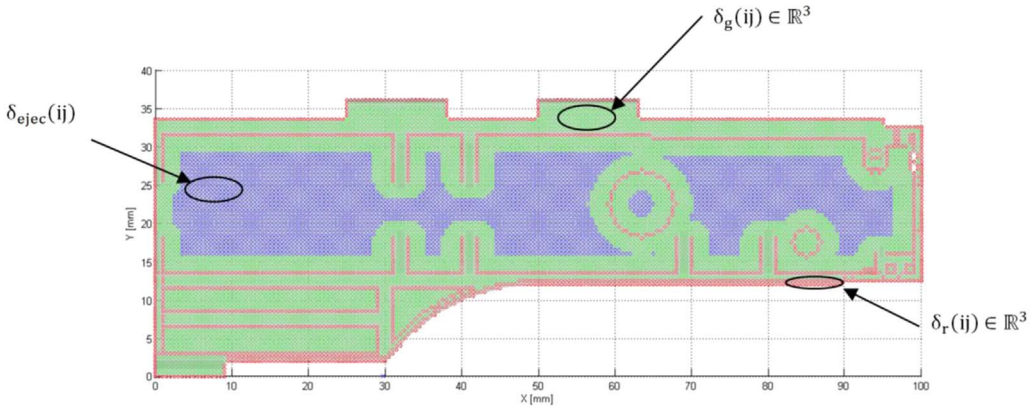


**Fig. 9.** Representation of the nodal grid $\delta_{eject}(ij)$ indicated by the color blue. (For interpretation of the references to color in this figure legend, the reader is referred to the web version of this article).

$\delta_{ejec\ ij} \in \delta_{ejec}(ij) \in \mathbb{R}^3$ are shown. In Fig. 11 the concentration of nodes δr (ij) per node $\delta_{ejec}(ij)$ is shown, by means of a color map on the mesh $\mathcal{L}'$ expressed by unit.

Finally, based on the representative mesh of the concentration of nodes δr (ij) per node $\delta_{ejec}(ij)$ expressed by unit, shown in Fig. 10, the evaluation of its maximum local values is achieved. These will be the optimal ejection points of the injection plastic part. The location of these maximal points can meet the geometrical requirement of the optimal location of the ejectors based on the close location to very rigid areas of the part with the aim of preventing warping. This is the reason that the ejectors are usually placed near the walls of greater thickness or zones with ribs on the plastic part. In Fig. 12 the final location of the ejection points for the mesh $\mathcal{L}'$ is shown.

### 3.3. Dimensioning of the ejection system, ejector pin diameter and ejection force

The method developed here uses optimization algorithms of a genetic type to perform the dimensioning of the ejection system. The application of these algorithms emerges as a response to the need to design a standard mold ejection system suitable for a number of defined features and requirements, and allows the operation of the system to be optimal for the ejection process.

Mechanical design requirements for an optimal ejection system

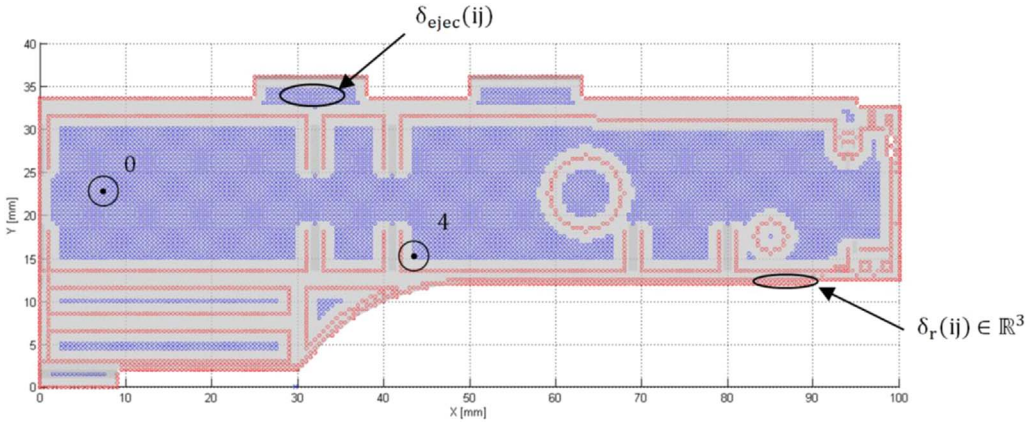


**Fig. 10.** Example of estimate of the number of nodes $\delta_r$ (ij) per node $\delta_{ejec}$ (ij).

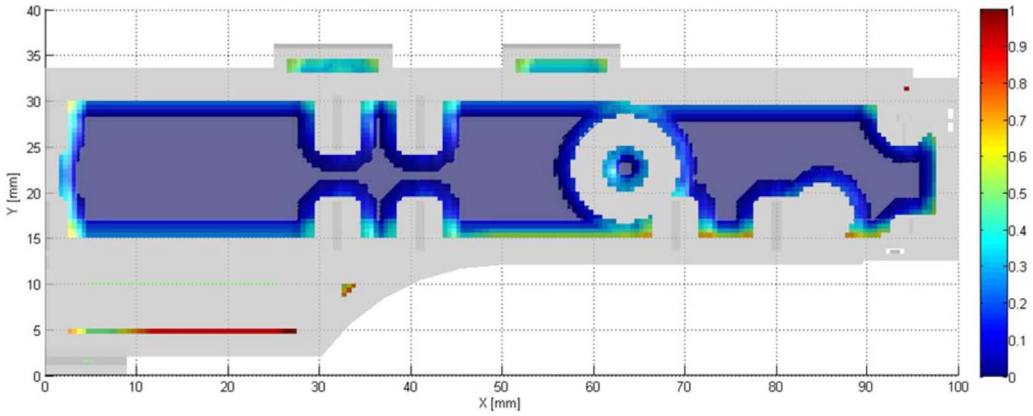


**Fig. 11.** Concentration of nodes $\delta_r$ (ij) per node $\delta_{ejec}$ (ij) expressed by unit. (For interpretation of the references to color in this figure, the reader is referred to the web version of this article).

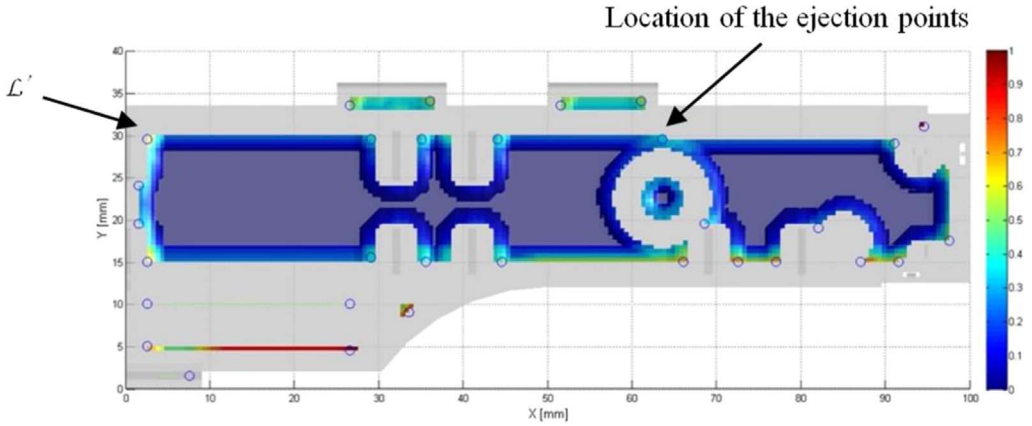


**Fig. 12.** Final location of the ejection points for the given geometry and configuration.

focus on achieving a balanced system of forces that allows a complete ejection of the part, without suffering any kind of failure. Note that the optimization produced by the proposed genetic algorithm will be multi-objective, because an ejection system balanced in terms of force distribution is required, but also that these forces do not generate a map of effort on the part that produces the collapse of material and geometry. However, a safe and complete ejection of the plastic part must be obtained.

Therefore, it can be said that the problem for design optimization consists of three objective functions:

- For generating a balanced system of forces, the sum of momentums (generated by each individual ejector) with respect to the center of mass of the part (CM) should be zero.

$$\sum_{i=1}^{n_{ejec}} M_{CM}(i)=0 \rightarrow \sum_{i=1}^{n_{ejec}} F_{ejec}(i)\cdot d_{CM}(i)=0$$

Where $M_{CM}$ (i) [N mm] represents the momentum generated by an

**Table 1**
Upper and lower boundaries of the studied variables.

| Variables | Bound Lower | Bound Upper |
|---|---|---|
| Ejection force, $F_{ejec}$ (i) (N) | $f_{min}$ | – |
| Ejector diameter, $r_{ejec}$(i) (mm) | $\varnothing_{min}$=0,5 | $\varnothing_{eject}$ |

**Table 2**
Migration variables.

| Direction | Migration interval | Migrated population factor |
|---|---|---|
| Forward | 10 | 0,3 |

**Table 3**
Maximum number of generations.

| Maximum number of generations |
|---|
| 150 |

**Table 4**
Physical and mechanical properties of the ABS material.

| **Plastic material** | **ABS** |
|---|---|
| **Shear Modulus [MPa]** | 2280 |
| **Shear Modulus [MPa] at ejection temperature** | 1260 |
| **Yield Strengh [MPa]** | 44 |
| **Yield Strengh [MPa] at ejection temperature** | 27,9 |
| **Solidification Temperature [°C]** | 132 |
| **Ejection Temperature [°C]** | 97 |
| **Thermal Expansion [1/°C]** | 8,82E−05 |

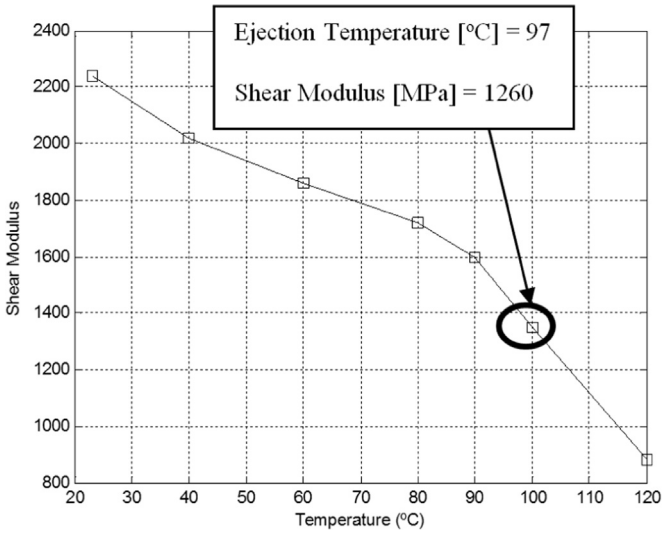


**Fig. 13.** Shear Modulus ($E_s$) vs temperature of the thermoplastic material ABS.

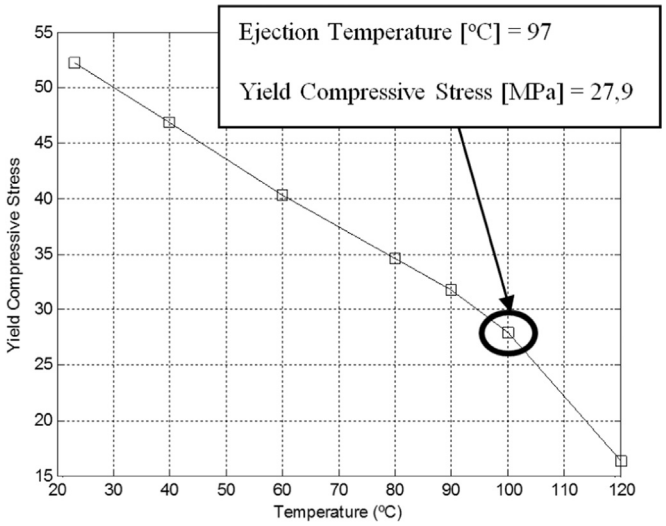


**Fig. 14.** Yield Compressive Stress ($\sigma_y$) vs temperature of the thermoplastic material ABS.

individual ejector with respect to the mass center, $F_{ejec}$ (i) [N] represents the ejection force of an individual ejector and $d_{CM}$ (i) [mm] represents the distance between an individual ejector and the mass center of the plastic part.

- To ensure complete ejection of the part, the sum of the ejection force generated by each ejector on the part must be greater than the minimum ejection force which ensures the ejection of the plastic part. That minimum ejection force depends mainly on: the shrinkage stress of the thermoplastic material which fixes the plastic part to the mold plates, the friction coefficient between the surface of the mold and the thermoplastic material and the draft angle of the plastics part's walls parallel to the ejection direction, Menges et al. [26].

$$\sum_{i=1}^{n_{ejec}} F_{ejec}(i)=F_R \rightarrow \sum_{i=1}^{n_{ejec}} F_{ejec}(i)= \quad \mu_s \cdot \mathrm{Cos}(Ø) \cdot \sigma_C \cdot A_c$$

However, high setting of the injection and packing pressures can increase this pressure field $\sigma_C$ [MPa], Griffiths et al. [34]. The proposed formulation is performed using standard settings without additional high injection and packing pressures.

$$\sigma_C = CTE \cdot E_s(T_{ejec}) \cdot \Delta T \; ; \Delta T = T_{Solid} - T_{ejec}$$

Where $F_{ejec}$(i) [N] represents the ejection force of an individual ejector, $F_R$ [N] represents the minimum ejection force needed to ensure the ejection of the plastic part, $A_c$ [mm$^2$] represents the effective area of the part subjected to the ejection force, $\mu_s$ represents the statics coefficient of friction, Ø [°] the draft angle of plastics part's walls parallel to the ejection direction, CTE [m/m °C] represents the heat transfer coefficient of the material, $E_s$ [MPa] represents the shear modulus of the material at the ejection temperature, $T_{Solid}$ [°C] represents the glass transition temperature of plastic and $T_{ejec}$ [°C] the optimum temperature of ejection of the material.

- To prevent the collapse of plastic material, the pressure generated by each individual ejector must not exceed the yield compressive stress of the material at the ejection temperature.

$$\forall \; F_{ejec}(i) \rightarrow \sigma_y(T_{ejec}) \geq \gamma_s \cdot \frac{F_{ejec}(i)}{A_{ejec}(i)} = \gamma_s \cdot \frac{F_{ejec}(i)}{\pi \cdot r^2_{ejec}(i)}$$

Where $F_{ejec}$ (i) [N] represents the ejection force of an individual ejector, $A_{ejec}$ (i) [mm$^2$] represents the effective area of the part subjected to the ejection force, $\sigma_y$ [MPa] represents the yield compressive stress of material at the ejection temperature, $r_{ejec}$ [mm] the ejector radius and $\gamma_s$

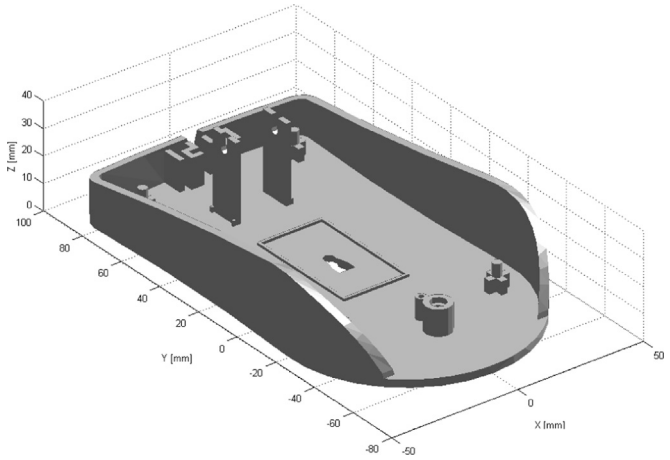


**Fig. 15.** Plastic part. Case A.

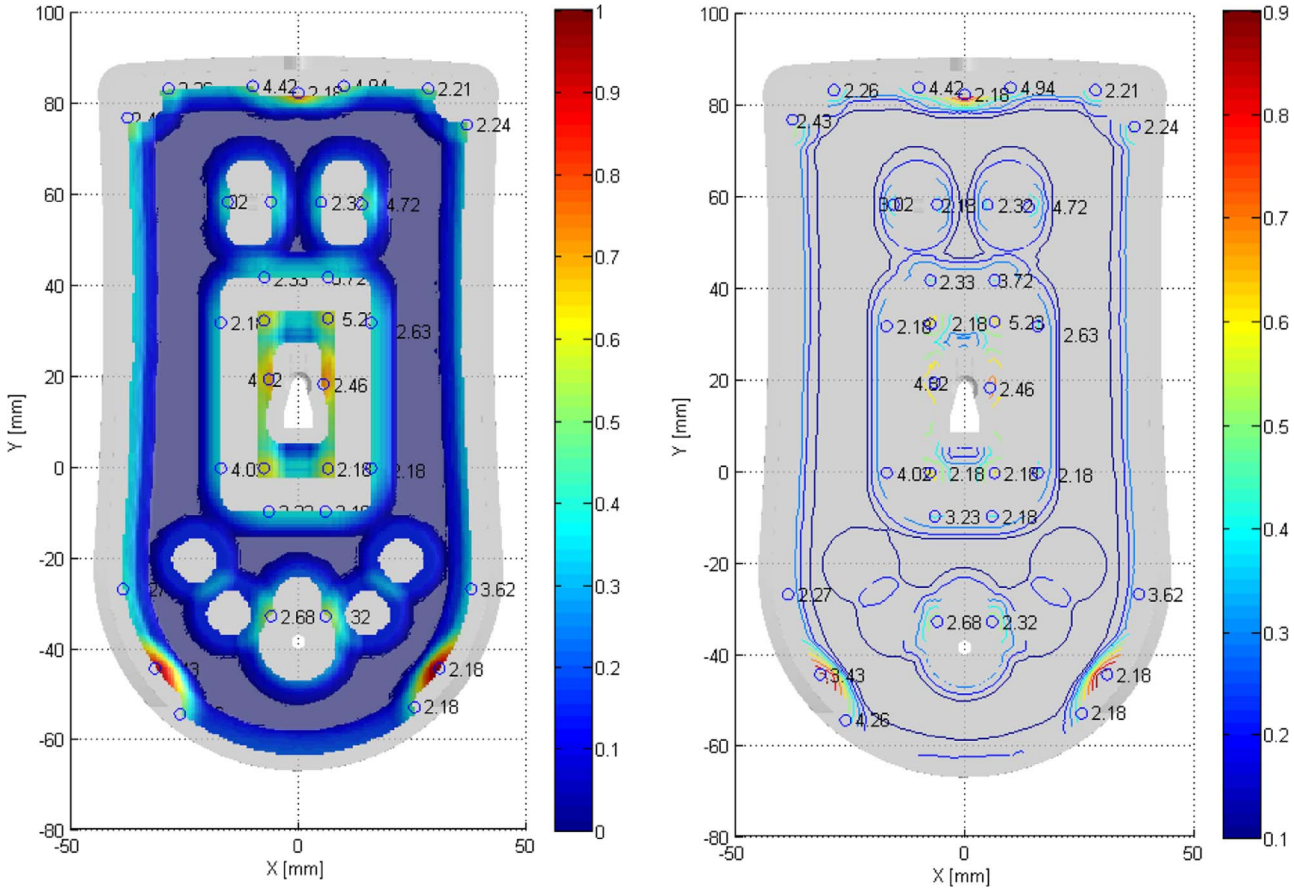


**Fig. 16.** Ejection map for the plastic part, with the ejector pins location and the corresponding diameters. Case A.

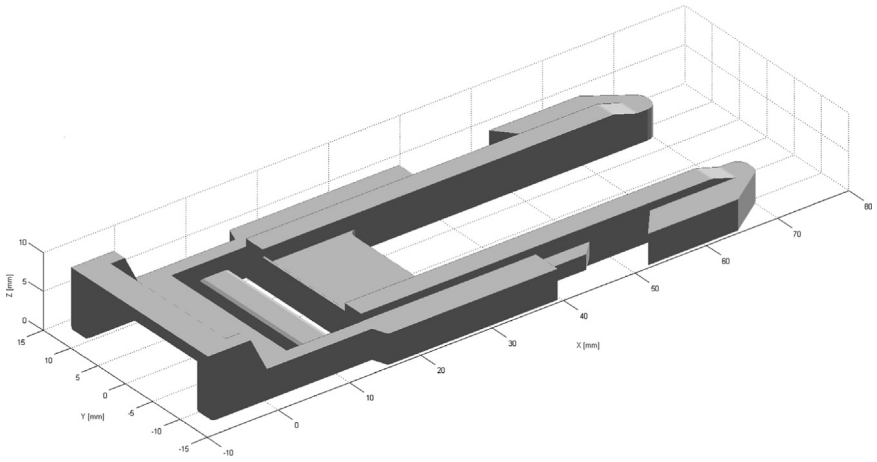


**Fig. 17.** Plastic part. Case B.

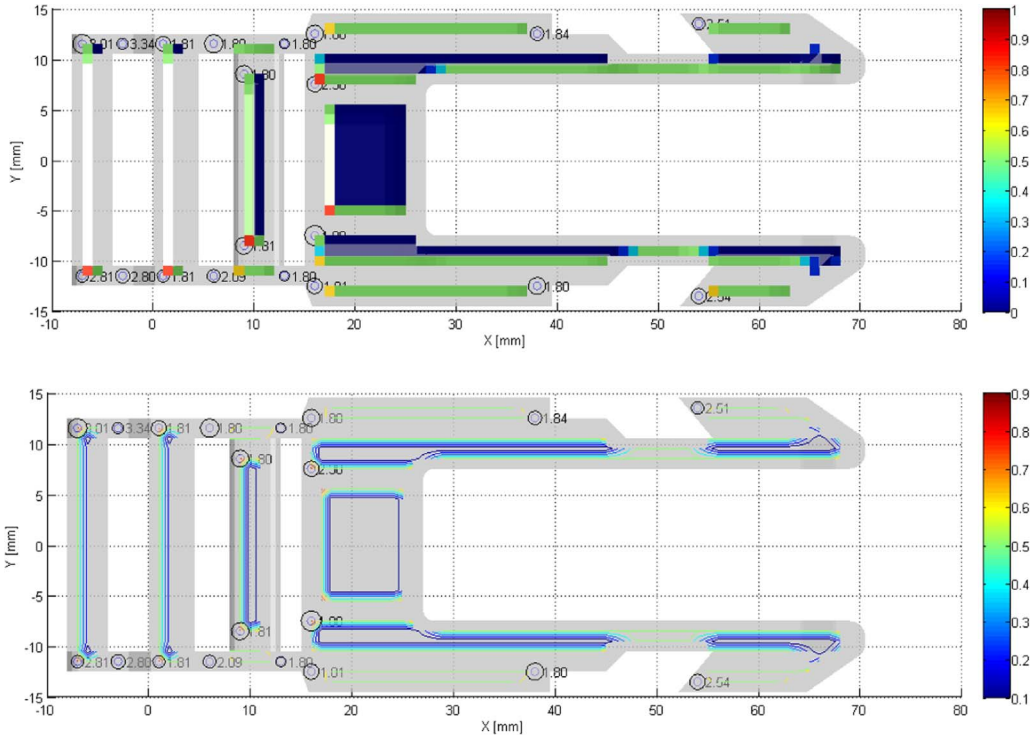


**Fig. 18.** Ejection map for the plastic part, with the ejector pins location and the corresponding diameters. Case B.

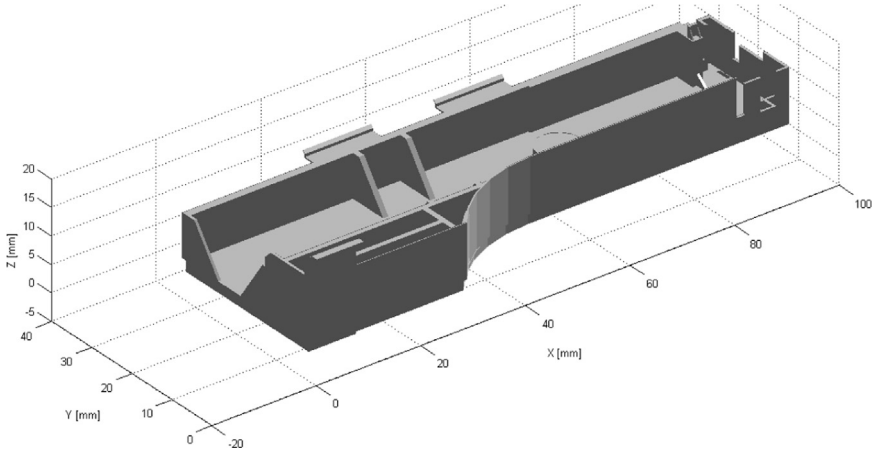


**Fig. 19.** Plastic part. Case C.

represents a safety factor (1.5 in our formulation).

As regards the design variables, they correspond to the total force exerted by each ejector and the diameter thereof ($F_{ejec}$ and $r_{ejec}$). Therefore, the total number of variables of the optimization problem is always double the total number of ejectors.

$$n_{var}=2\cdot n_{ejec}$$

### 3.3.1. Generation of the population

In order to solve the optimization problem, numerical calculation software must start from a solution or initial population from which the genetic cycle starts. Generally, the creation of this initial population is performed randomly. Depending on the nature of the variables, the software allows us to configure the algorithm in order to establish a different method of creation. In our case, the initial population generation has been generated according to the "Double Vector" method since the variables will be of double and decimal type.

The modeling of the genetic algorithm allows us to establish a series of constraints that limit and condition the individuals from each generation in order to delimit their value and prevent the optimum solution from converging outside preset domains. That is, starting from the premise that the order of the variables of the problem is known, boundary values can be defined for each variable. From these values any individual outside this range will be invalid. To do this, a simple vector of upper and lower limit values is established, where each position of the vector is identified with each variable. Additionally, we have established the following boundary vectors:

Where $f_{min}$ represents the set of minimum ejection forces required

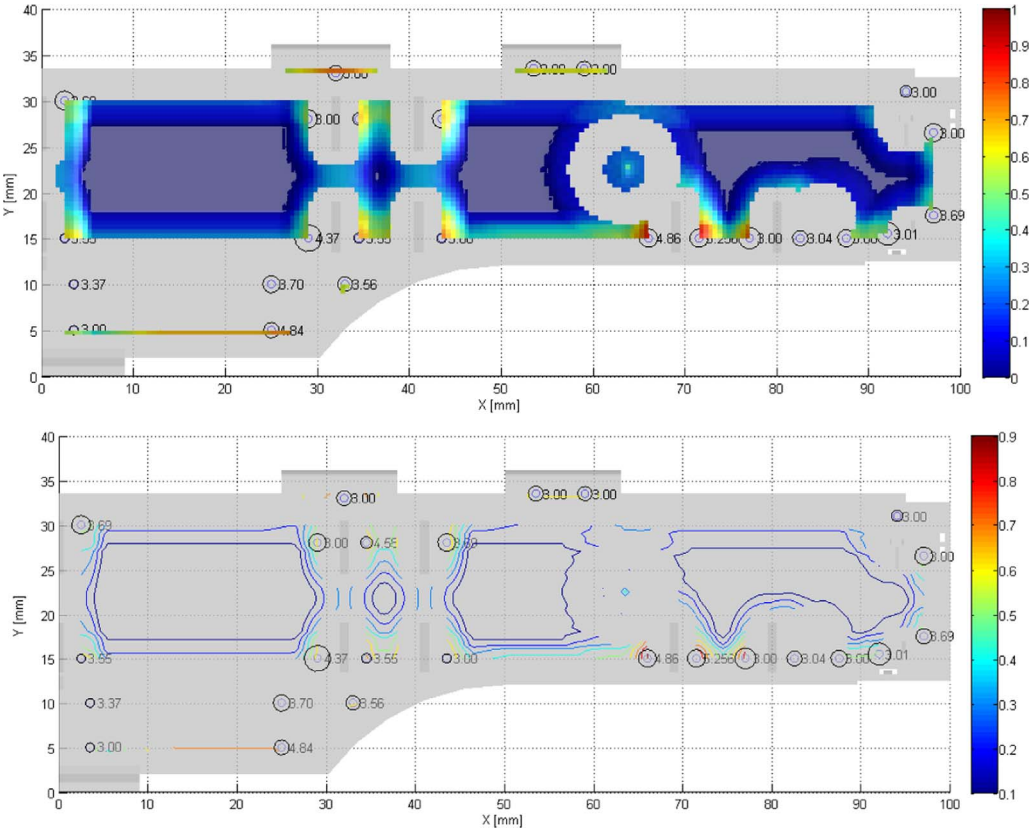


**Fig. 20.** Ejection map for the plastic part, with the ejector pins location and the corresponding diameters. Case C.

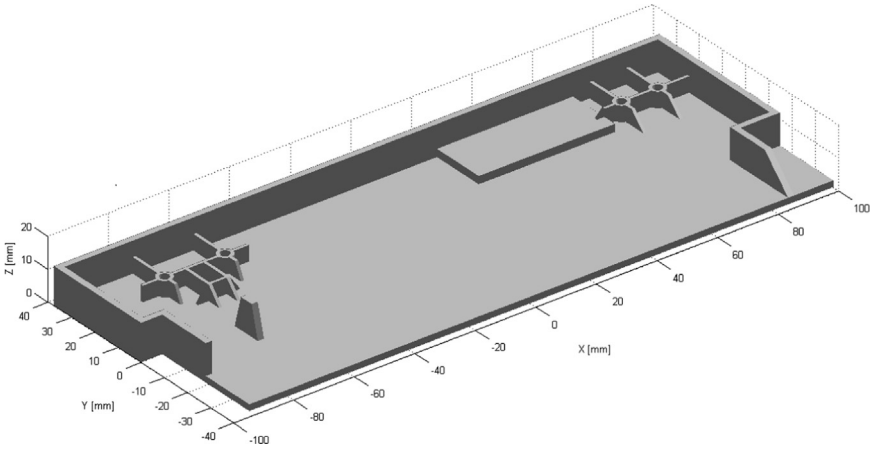


**Fig. 21.** Plastic part. Case D.

to exceed the shrinkage stress of the plastic part in the case where the diameters of the ejectors are in the lower limit.

$$f_{min}=\frac{\sigma_C\cdot\pi\cdot\varnothing_{min}^2}{4}=\frac{CTE\cdot E_s(T_{ejec})\cdot\Delta T\cdot\pi\cdot 0,\ 5^2}{4}\Delta T = T_{Solid}-T_{ejec}$$

Where CTE [m/m °C] represents the heat transfer coefficient of the material, $E_s$ [MPa] represents the shear modulus of the material at the ejection temperature, $T_{Solid}$ [°C] represents the glass transition temperature of plastic and $T_{ejec}$ [°C] the optimum temperature of ejection of the material.

In this way, we ensure that the final optimal solution is positive and is within the boundary values. Thus the computational cost and the resolution time are also shortened, since the domain of study has been reduced.

### 3.3.2. *Scaling function*

Implementing a scaling function improves the efficiency of genetic algorithms. A scaling function increases the differentiation between the optimum individuals and at the same time reduces the probability of obtaining individuals less suitable in next generations, ie that are situated far from the optimal solution. This behavior therefore enables individuals to concentrate around the optimum, rather than remain scattered nearby.

The technique used to define this scaling function has been to create

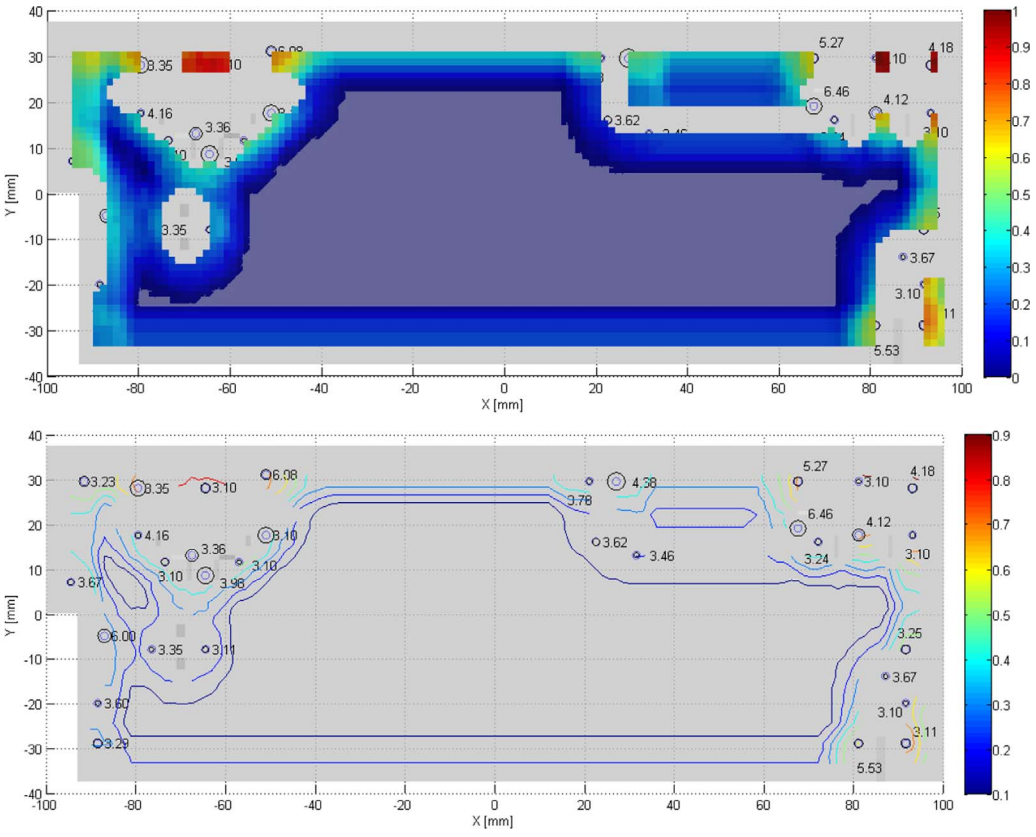


**Fig. 22.** Ejection map for the plastic part, with the ejector pins location and the corresponding diameters. Case D.

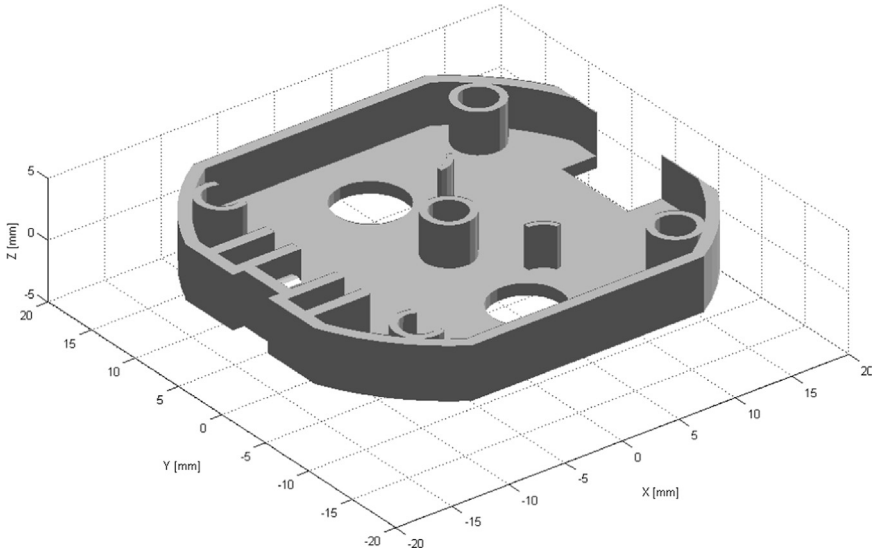


**Fig. 23.** Plastic part. Case E.

a setting value (fitness rank) based on scaling individuals based on their position, considering a classification of the population based on this setting value.

### 3.3.3. Selection

Selection is defined as the operation by which parents for the future generation are chosen. Selection is performed based on the setting values set by the previously-defined scaling function.

Based on the given problem, a uniform stochastic selection function has been chosen which allows local searches to be performed around promising solutions. Additionally, it has the component of randomness, needed to explore other solutions in the search domain.

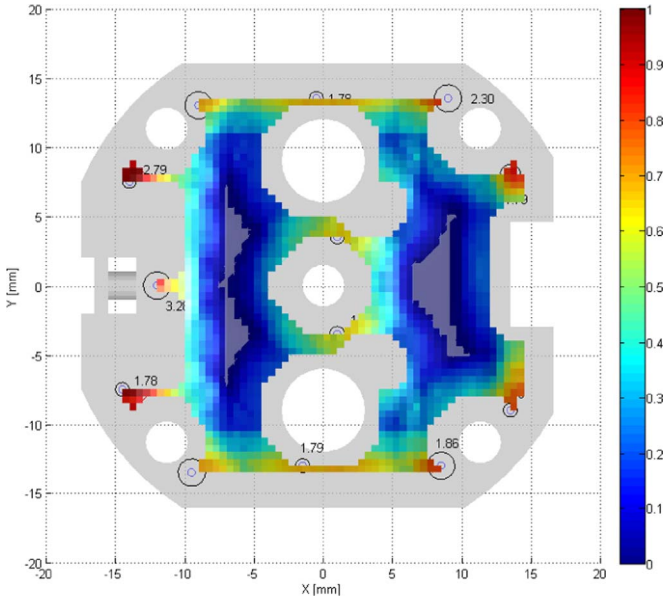


**Fig. 24.** Ejection map for the plastic part, with the ejector pins location and the corresponding diameters. Case E.

### 3.3.4. Reproduction

Reproduction options determine how the genetic algorithm generates the children corresponding to each new generation. To do this, the minimum number of individuals who must survive to the next generation must be specified. This parameter is called recount and must be a positive integer equal to or smaller than the size of the population. For the development of this algorithm a count value of 2 has been used to increase the speed of convergence and reduce the computational cost, ensuring the survival of the population.

Another characteristic parameter in the reproduction phase is the crossing factor. This specifies the fraction of individuals in the next generation which is susceptible to being crossed. This factor varies between values of 0 (one individual crosses) and 1 (all individuals cross). It is recommended to choose a crossing factor of 0.8. This parameter is kept as default.

### 3.3.5. Mutation

The mutation function allows small random changes to be made in individuals of the population and mutate them before loading in the new population. Mutation is usually performed in conjunction with the crossing factor.

There are various mutation functions; however a uniform function has been used in this case. This type of mutation runs in two steps: First, the algorithm selects a fraction of individuals of the population to perform the mutation, where each entry has a probability of changing (Rate). In this case we have chosen a value of 0.02 for this parameter. In the second step, the algorithm replaces each selected entry with a random number chosen uniformly from the range of the population for that entry.

### 3.3.6. Crossing

The crossing phase allows two individuals or any parent to be combined, in order to create a new individual or child who will be part of the new generation. In our case, a method based on the double-point of two individuals of the population has been selected (Two Points). Here, the children are uniformly generated from the arithmetic mean of two parents randomly selected from the population.

**Table 5**
Precision values of the nodal mesh, results of the algorithm: Ejectors Diameter ($\varnothing_{ejec}$) [mm], Total Ejection Force [N], Ejection Force $F_R$ [N], Maximum Ejector Stress [MPa] and Yield Stress [MPa] for Case A.

| Coord. X [mm] | Coord. Y [mm] | Diameter [mm] | Force [N] | Coord. X [mm] | Coord. Y [mm] | Diameter [mm] | Force [N] |
|---|---|---|---|---|---|---|---|
| 31,005 | −44,650 | 1,000 | 2,183 | 28,505 | 82,849 | 1,000 | 3,214 |
| −31,494 | −44,650 | 1,000 | 3,433 | −25,994 | −54,650 | 1,000 | 4,260 |
| 0,005 | 81,849 | 3,000 | 2,183 | −15,494 | 57,849 | 1,000 | 3,018 |
| 5,505 | 17,849 | 1,000 | 2,462 | 14,005 | 57,349 | 1,000 | 4,723 |
| −6,494 | 18,849 | 1,100 | 4,818 | −5,994 | 57,849 | 1,000 | 2,184 |
| −7,494 | −0,650 | 1,400 | 2,183 | 5,005 | 57,849 | 1,530 | 2,317 |
| −7,494 | 31,849 | 1,000 | 2,183 | −6,494 | −10,150 | 1,100 | 3,230 |
| 6,505 | −0,650 | 1,000 | 2,183 | 16,005 | −0,650 | 1,000 | 2,184 |
| 6,505 | 32,341 | 1,000 | 5,233 | 16,005 | 31,349 | 1,000 | 2,634 |
| −9,994 | 83,349 | 1,000 | 4,424 | −7,494 | 41,349 | 1,200 | 2,327 |
| −5,994 | −33,150 | 1,000 | 2,683 | 6,005 | −10,150 | 1,000 | 2,184 |
| 10,00525 | 83,349 | 1,000 | 4,940 | 6,505 | 41,349 | 1,000 | 3,718 |
| 6,005 | −33,150 | 1,000 | 2,325 | −38,494 | −27,150 | 1,000 | 2,273 |
| −37,494 | 76,349 | 1,000 | 2,433 | −16,994 | −0,650 | 1,100 | 4,022 |
| −28,494 | 82,849 | 1,000 | 2,259 | −16,99475 | 31,349 | 1,500 | 2,184 |
| 37,005 | 74,849 | 1,200 | 2,239 | 38,005 | −27,150 | 2,000 | 3,628 |
| 25,505 | −53,150 | 3,750 | 2,183 | – | – | – | – |

| Precision X [mm] | Precision Y [mm] | Total Ejection Force [N] | Minimum Ejection Force [N] | Maximum Ejector Stress [MPa] | Yield Stress [MPa] |
|---|---|---|---|---|---|
| | | $\sum_{i=1}^{n_{ejec}} F_{ejec(i)}$ | $F_R$ | $\max\left(\frac{F_{ejec(i)}}{\pi \cdot r_{ejec(i)}}\right)$ | $\sigma_y(T_{ejec})$ |
| 0,50 | 0,50 | 98,46 | 97,41 | 6,66 | 27,90 |

### 3.3.7. Migration

Migration represents the translation of individuals in the population between different regions of the domain or search space. Thus, in every certain iteration the best individuals of the region are responsible for replacing the worst individuals in another region. The parameters selected to configure this stage of the algorithm are the following (Tables 1–3).

### 3.3.8. Stop criteria

The stop criteria indicate when the running iterations end. Completion of the genetic algorithm is usually achieved either when a maximum number of generations has been performed or when the difference between a possible optimal solution and the previous one falls below a certain value.

A stop criterion based on the maximum number of generations has been employed, since after running the algorithm for approximately 150 generations the genetic algorithm converges on a set of valid solutions.

### 3.3.9. Fitness functions

In order to complete the genetic algorithm, the fitness functions to optimize must be entered. Taking into account the calculation methodology used by the software, note that the fitness functions are optimized in order to find a set of solutions that minimize these functions.

First, this paper proposes using a fitness function oriented toward the uniform distribution of ejection forces. For this purpose, the sum of momentums generated by ejection forces with respect to the center of mass of the part (CM) is minimized.

$$\text{FitnessFunction}_1\text{:Min}\left\{\sum_{i=1}^{n_{ejec}} M_{CM}(i)=\sum_{i=1}^{n_{ejec}} F_{ejec}(i)\cdot d_{CM}(i)\right\}$$

To ensure complete ejection of the part, the sum of the ejection forces generated by all the ejectors on the part minus the minimum ejection force, which ensures the ejection of the plastic part, must be minimal.

**Table 6**
Precision values of the nodal mesh, results of the algorithm: Ejectors Diameter ($\varnothing_{ejec}$) [mm], Total Ejection Force [N], Ejection Force $F_R$ [N], Maximum Ejector Stress [MPa] and Yield Stress [MPa] for Case B.

| Coord. X [mm] | Coord. Y [mm] | Diameter [mm] | Force [N] | Coord. X [mm] | Coord. Y [mm] | Diameter [mm] | Force [N] |
|---|---|---|---|---|---|---|---|
| −3 | −11,5 | 1,5 | 2,803 | 16 | −12,5 | 1,5 | 1,807 |
| −3 | 11,5 | 1,1 | 3,342 | 16 | −7,5 | 2 | 1,803 |
| 6 | −11,5 | 1,3 | 2,094 | 13 | 11,5 | 1 | 1,803 |
| 6 | 11,5 | 1,8 | 1,803 | 13 | −11,5 | 1 | 1,803 |
| −7 | −11,5 | 1,2 | 2,808 | 16 | 7,5 | 1,5 | 2,385 |
| −7 | 11,5 | 1,9 | 3,012 | 16 | 12,5 | 1,7 | 1,803 |
| 1 | −11,5 | 1,2 | 1,806 | 38 | −12,5 | 1,7 | 1,804 |
| 1 | 11,5 | 1,5 | 1,811 | 38 | 12,5 | 1,4 | 1,842 |
| 9 | −8,5 | 1,7 | 1,807 | 54 | −13,5 | 1,5 | 2,542 |
| 9 | 8,5 | 1,7 | 1,803 | 54 | 13,5 | 1,3 | 2,510 |

| Precision X [mm] | Precision Y [mm] | Total Ejection Force [N] $\sum_{i=1}^{n_{ejec}} F_{ejec}(i)$ | Minimum Ejection Force [N] $F_R$ | Maximum Ejector Stress [MPa] $\max\left(\frac{F_{ejec}(i)}{\pi\cdot r_{ejec}(i)}\right)$ | Yield Stress [MPa] $\sigma_y(T_{ejec})$ |
|---|---|---|---|---|---|
| 1,00 | 1,00 | 43,19 | 42,57 | 3,37 | 27,90 |

**Table 7**
Precision values of the nodal mesh, results of the algorithm: Ejectors Diameter ($\varnothing_{ejec}$) [mm], Total Ejection Force [N], Ejection Force $F_R$ [N], Maximum Ejector Stress [MPa] and Yield Stress [MPa] for Case C.

| Coord. X [mm] | Coord. Y [mm] | Diameter [mm] | Force [N] | Coord. X [mm] | Coord. Y [mm] | Diameter [mm] | Force [N] |
|---|---|---|---|---|---|---|---|
| 26,5 | 4,5 | 2 | 1,567 | 61 | 34 | 2,5 | 1,443 |
| 94,5 | 31 | 1,3 | 0,637 | 26,5 | 33,5 | 2 | 4,172 |
| 2,5 | 10 | 1,3 | 1,253 | 51,5 | 33,5 | 2,3 | 1,298 |
| 33,5 | 9 | 2,2 | 0,762 | 91 | 29 | 2,5 | 0,817 |
| 2,5 | 5 | 2,5 | 0,946 | 44,5 | 15 | 1,3 | 0,676 |
| 87 | 15 | 1,8 | 0,622 | 29 | 29,5 | 1,9 | 1,491 |
| 72,5 | 15 | 1,5 | 0,622 | 35 | 29,5 | 2,4 | 1,544 |
| 66 | 15 | 1,7 | 3,578 | 35,5 | 15 | 1,8 | 0,862 |
| 77 | 15 | 1,7 | 2,769 | 44 | 29,5 | 1,2 | 1,035 |
| 91,5 | 15 | 1,2 | 0,637 | 29 | 15,5 | 2 | 0,812 |
| 97,5 | 17,5 | 2,1 | 3,16 | 63,5 | 29,5 | 2 | 0,622 |
| 2,5 | 15 | 2,2 | 3,188 | 68,5 | 19,5 | 1,4 | 0,623 |
| 7,5 | 1,5 | 2,3 | 2,908 | 1,5 | 19,5 | 1,3 | 1,702 |
| 26,5 | 10 | 1,9 | 1,84 | 1,5 | 24 | 2,4 | 2,179 |
| 2,5 | 29,5 | 1,2 | 1,114 | 82 | 19 | 2,3 | 0,633 |
| 36 | 34 | 1,5 | 0,665 | – | – | – | – |

| Precision X [mm] | Precision Y [mm] | Total Ejection Force [N] $\sum_{i=1}^{n_{ejec}} F_{ejec}(i)$ | Minimum Ejection Force [N] $F_R$ | Maximum Ejector Stress [MPa] $\max\left(\frac{F_{ejec}(i)}{\pi\cdot r_{ejec}(i)}\right)$ | Yield Stress [MPa] $\sigma_y(T_{ejec})$ |
|---|---|---|---|---|---|
| 0,50 | 0,50 | 46,18 | 45,11 | 1,576 | 27,90 |

$$\text{FitnessFunction}_2\text{:Min}\left\{F_R - \sum_{i=1}^{n_{ejec}} F_{ejec}(i)\right\}$$

Finally, in order to prevent the collapse of the plastic material the pressure generated by each individual ejector must not exceed the yield compressive stress of the material at the ejection temperature.

$$\text{FitnessFunction}_3\text{:Max}\left\{\sigma_y \quad (T_{ejec}) - \gamma_s \cdot \frac{F_{ejec}(i)}{\pi \cdot r_{ejec}^2(i)}\right\}$$

## 4. Implementation and results

In order to test the algorithm proposed in this paper it has been applied to five industrial parts, manufactured by means of the plastic injection process. The accuracy of the nodal mesh (Δ) for each geometry is set according to the dimension of the smallest detail of the part. The algorithms have been developed with a Toshiba notebook with a Pentium (R) Dual-Core CPU T4200@2.20 GHz processor and a RAM memory of 3.00 GB. It is possible to adapt them to any programming language and computer.

### 4.1. Case studies

The results of applying the algorithm for the five parts (cases A, B, C, D, E) Figs. 15,17,19,21 and 23 are shown in Figs. 16, 18, 20, 22 and 24. Ejection maps with a layout of the thicknesses location on the part and the diameter of each ejector were obtained. Additionally, isocontours regarding the data of thickness variations in the part are indicated on the ejection map. The results of the algorithm for each part include value tables such as nodal mesh accuracy, ejectors diameter $\varnothing_{ejec}$ [mm], the sum of ejection forces [N] of each ejector, $F_R$ [N] minimum ejection force to ensure the ejection of the plastic part, maximum ejection stress [MPa] of an individual ejector and the Yield

**Table 8**
Precision values of the nodal mesh, results of the algorithm: Ejectors Diameter ($\varnothing_{ejec}$) [mm], Total Ejection Force [N], Ejection Force $F_R$ [N], Maximum Ejector Stress [MPa] and Yield Stress [MPa] for Case D.

| Coord. X [mm] | Coord. Y [mm] | Diameter [mm] | Force [N] | Coord. X [mm] | Coord. Y [mm] | Diameter [mm] | Force [N] |
|---|---|---|---|---|---|---|---|
| 81 | 29,5 | 1 | 3,103 | −79,5 | 17,5 | 1,3 | 4,159 |
| 93 | 28 | 2 | 4,177 | −64,5 | 8,5 | 4 | 3,980 |
| −64,5 | 28 | 2,2 | 3,102 | −94,5 | 7 | 1,3 | 3,672 |
| −67,5 | 13 | 2,8 | 3,362 | −51 | 17,5 | 3,5 | 3,102 |
| 93 | 17,5 | 1,3 | 3,102 | 21 | 29,5 | 1,3 | 3,780 |
| 91,5 | −29 | 2,1 | 3,111 | 27 | 29,5 | 4 | 4,380 |
| 81 | 17,5 | 2,7 | 4,118 | 87 | −14 | 1 | 3,667 |
| −79,5 | 28 | 3,5 | 3,352 | −87 | −5 | 3 | 6,002 |
| −51 | 31 | 2,3 | 6,078 | −88,5 | −29 | 2 | 3,289 |
| 67,5 | 29,5 | 2 | 5,269 | −88,5 | −20 | 1,1 | 3,602 |
| 91,5 | −20 | 1,1 | 3,102 | −76,5 | −8 | 1 | 3,353 |
| 81 | −29 | 2 | 5,534 | −64,5 | −8 | 1,3 | 3,109 |
| −91,5 | 29,5 | 2,3 | 3,225 | 31,5 | 13 | 1,1 | 3,459 |
| 72 | 16 | 1,3 | 3,240 | 22,5 | 16 | 1,6 | 3,622 |
| 91,5 | −8 | 2 | 3,246 | −87 | −9,5 | 1 | 3,051 |
| −57 | 11,5 | 1 | 3,102 | −64,5 | −8 | 1 | 3,051 |
| −73,5 | 11,5 | 1,6 | 3,102 | 46,5 | 13 | 1 | 3,051 |
| 67,5 | 19 | 3,5 | 6,457 | −46,5 | 25 | 2,6 | 3,035 |

| Precision X [mm] | Precision Y [mm] | Total Ejection Force [N] $\sum_{i=1}^{n_{ejec}} F_{ejec}(i)$ | Minimum Ejection Force [N] $F_R$ | Maximum Ejector Stress [MPa] $\max\left(\frac{F_{ejec}(i)}{\pi \cdot r_{ejec}(i)}\right)$ | Yield Stress [MPa] $\sigma_y(T_{ejec})$ |
|---|---|---|---|---|---|
| 1,50 | 1,50 | 139,15 | 135,16 | 4,67 | 27,90 |

**Table 9**
Precision values of the nodal mesh, results of the algorithm: Ejectors Diameter ($\varnothing_{ejec}$) [mm], Total Ejection Force [N], Ejection Force $F_R$ [N], Maximum Ejector Stress [MPa] and Yield Stress [MPa] for Case E.

| Coord. X [mm] | Coord. Y [mm] | Diameter [mm] | Force [N] | Coord. X [mm] | Coord. Y [mm] | Diameter [mm] | Force [N] |
|---|---|---|---|---|---|---|---|
| −14 | 7,5 | 1 | 2,784 | −9,5 | −13,5 | 2 | 2,782 |
| −14,5 | −7,5 | 1 | 1,782 | −9 | 13 | 2 | 2,786 |
| −12 | 0 | 2 | 3,282 | −1,5 | −13 | 1 | 1,786 |
| 13,5 | 8 | 1,5 | 1,793 | −0,5 | 13,5 | 1 | 1,784 |
| 9 | 13,5 | 2 | 2,305 | 1 | −3,5 | 1 | 1,785 |
| 8,5 | −13 | 2 | 1,860 | 1 | 3,5 | 1 | 1,845 |
| 13,5 | −9 | 1 | 1,788 | – | – | – | – |

| Precision X [mm] | Precision Y [mm] | Total Ejection Force [N] $\sum_{i=1}^{n_{ejec}} F_{ejec}(i)$ | Minimum Ejection Force [N] $F_R$ | Maximum Ejector Stress [MPa] $\max\left(\frac{F_{ejec}(i)}{\pi \cdot r_{ejec}(i)}\right)$ | Yield Stress [MPa] $\sigma_y(T_{ejec})$ |
|---|---|---|---|---|---|
| 0,50 | 0,50 | 28,36 | 27,73 | 3,11 | 27,9 |

Stress [MPa] of the material at the ejection temperature. All these results are presented as a design report.

It is noteworthy that the material used to obtain the size of the injection plastic part is the thermoplastic ABS. The physical and mechanical properties of the material are indicated in Table 4:

According to [33] (see Figs. 13 and 14), the mechanical properties of the thermoplastic material depend on its temperature, as the temperature increases the mechanical properties of the thermoplastic decrease. Therefore, the definition of Shear modulus [MPa] and Yield stress [MPa] for the ejection analysis should be performed according to the ejection temperature of the plastic part [38]

The ejection maps for the five case studies analyzed (Figs. 16, 18, 20, 22 and 24) and the numerical values given in the tables (Tables 5–9) allow us to state that the results obtained by the algorithm described in this paper are adapted to the basic design criteria of ejection systems of the plastic parts by means of ejector pins. Isocontours represented on the maps indicate the location of the ejectors in zones of maximum thickness variation. The solutions obtained by the system are dimensioned under three conditions: an appropriate balance of forces, a total ejection force exerted by the ejector pins that exceeds the minimum ejection force $F_R$, needed to ensure the ejection, and a maximum ejector stress that does not exceed the yield compression limit of the material at the ejection temperature. The shrinkage stress suffered by the part does not exceed the yield limit of the material in any of the plastic parts analyzed. Finally, the location of the set of pins is adapted to the geometric requirements for a proper ejection as is shown in the ejection maps.

## 5. Conclusions

The work presented in this paper shows a new geometric algorithm for automated design of the layout and dimensioning of the ejector pins of the mold, based on the discrete geometry of the plastic part. The methodology has been tested through its application on five plastic parts with different geometries and dimensions, solving and dimensioning the demolding parameters related to the ejection forces and ejectors diameters. Ejection maps for the five case studies were obtained in an automatic way. Results showed the layout with the location of the ejectors on the part, the circular area and the ejection force for each ejector. Additionally, a detailed data report is obtained as a result of the application. This report includes the ejection force in each ejector, the sum of ejection forces generated by each ejector, minimum ejection force, $F_R$, needed to ensure the ejection, the maximum ejection stress for an individual ejector, the yield compressive stress [MPa] of the material at the ejection temperature, and the diameter of the ejector pins. The algorithm of geometric design performs the correct dimensioning of the ejectors system since the optimization procedure ensures a proper balance of forces, a value of all ejection force exerted by the set of ejectors that exceeds the minimum ejection force, $F_R$, needed for ejecting the part, and that the ejections stress does not exceed the yield limit of the thermoplastic material. These are the criteria imposed on the fitness functions that the system must meet.

This new method improves the methods used so far as it does not require heuristic methods to achieve the result and does not use the feature recognition method as a tool for recognizing the geometric surface of the plastic, avoiding the problems of dependence on the modeler and the recognition of complex features. The proposed algorithm is applicable to any geometry because it works regardless of the CAD system in which the part has been designed.

## Acknowledgement

This work has been supported by the Consejeria de Economia, Innovación, Ciencia y Empleo (Junta de Andalucia-Spain) through the project titled " A vertical design software for integrating operations of automated demoldability, tooling design and cost estimation in injection molded plastic parts. (CELERMOLD)" (Project Code TI-12 TIC 1623). The authors would like to thank the reviewers for their comments, which greatly improved the exposition.

## References

[1] L.L. Chen, S.Y. Chou, T.C. Woo, Parting directions for mould and die design, Comput. Aided Des. 25 (12) (1993) 762–768.
[2] L.L. Chen, S.Y. Chou, T.C. Woo, Partial visibility for selecting a parting direction in mold and die design, J. Manuf. Syst. 14 (1995) 5.
[3] M.W. Fu, J.Y.H. Fuh, A.Y.C. Nee, Undercut feature recognition in an injection mould design system, Comput. Aided Des. 31 (12) (1999) 777–790.
[4] M.W. Fu, J.,Y.H. Fuh, A.Y.C. Nee, Generation of optimal parting direction based on undercut features in injection molded parts, IIE Trans. 31 (1999) 947–955.
[5] M.W. Fu, A.Y.C. Nee, J.Y.H. Fuh, The application of surface visibility and moldability to parting line generation, Comput. Aided Des. 34 (6) (2002) 469–480.
[6] M.W. Fu, A.Y.C. Nee, J.Y.H. Fuh, A core and cavity generation method in injection mold design, Int. J. Prod. Res. 39 (2001) 121–138.
[7] H.Y. Lu, W.B. Lee, Detection of interference elements and release directions in die-cast and injection-moulded components, Proc. Inst. Mech. Eng. Part B J. Eng. Manuf. 214 (6) (2000) 431–441.
[8] Z.P. Yin, Han Ding, You-Lun Xiong, Virtual prototyping of mold design: geometric mouldability analysis for near-net-shape manufactured parts by feature recognition and geometric reasoning, Comput.-Aided Des. 33 (2) (2001) 137–154.
[9] X.G. Ye, J.Y.H. Fuh, K.S. Lee, A hybrid method for recognition of undercut features from molded part, Comput. Aided Des. 33 (14) (2001) 1023–1034.
[10] R. Khardekar, S. McMains, Finding mold removal directions using graphics hardware, in: Proceedings of the ACM Workshop on General Purpose Computing on Graphics Processors, 2004, pp. C-19, (abstract).
[11] Burton Khardekar, McMains, Finding feasible mold parting directions using graphics hardware, Comput. Aided Des. 38 (4) (2006) 327–341.
[12] P. Chakraborty, N.V. Reddy, Automatic determination of parting directions, parting lines and parting surfaces for two piece permanent moulds, J. Mater. Process. Technol. 209 (5) (2000) 2464–2476.
[13] R. Singh, J. Madan, Systematic approach for automated determination of parting line for die-cast parts, Robot. Comput. Integr. Manuf. 29 (5) (2013) 346–366.
[14] M.A. Ganter, L.L. Tuss, Computer-assisted parting line development for cast pattern production, AFS Trans. (1990) 795–800.
[15] T. Wong, S.T. Tan, W.S. Sze, Parting line formation by slicing a trimmed surface model, in: Proceedings of the 1996 ASME Design Engineering Technical Conference and Computers in Engineering Conference, Irvine, California, August 18–22 1996.
[16] M.A. Rubio, J.M. Pérez, J. Rios, A Procedure for Plastic Parts Demoldability Analysis Robotics and Computer Integrated Manufacturing, 22(1), 2006, pp. 81–92.
[17] C. Martin Doñate, M.A. Rubio Paramio, New methodology for demoldability analysis based on volume discretization algorithms, Comput. Aided Des. 45 (2) (2013) 229–240.
[18] Cristina Martin-Doñate, Angel Rubio-Paramio, Aurelio Mesa-Villar. Método de validación automatizada de la fabricabilidad de diseños de objetos tridimensionales en base a su geometría, Patent number: ES2512940B2.
[19] Jorge Manuel Mercado-Colmenero, M.A.R. Paramio, Jesus Maria Perez-Garcia, Cristina Martin-Doñate, A new hybrid method for demoldability analysis of discrete geometries, Comput. Aided Des. 80 (2016) 43–60.
[20] X.G. Ye, Y.H. Fu, X.S. Lee, Automated assembly modeling for plastic injection moulds, Int. J. Adv. Manuf. Technol. 16 (2000) 739–747.
[21] C.K. Mok, K.S. Chin, K.L. Ho, An interactive knowledge-based CAD system for mould design in injection moulding processes, Int. J. Adv. Manuf. Technol. 17 (2001) 27–38.
[22] M.L.H. Low, K.S. Lee, A parametric-controlled cavity layout design system for a plastic injection mould, Int. J. Adv. Manuf. Technol. 21 (2003) 807–819.
[23] T.L. Neo, K.S. Lee, Three-dimensional kernel development for injection mould design, Int. J. Adv. Manuf. Technol. 17 (2001) 453–461.
[24] Y.S. Ma, S.B. Tor, G.A. Britton, The development of a standard component library for plastic injection for plastic injection mould design using an object-oriented approach, Int. J. Adv. Manuf. Technol. 22 (2003) 611–618.
[25] V. Kumar, J. Madan, P. Gupta, A system for design of multicavity die casting dies from part product model, Int. J. Adv. Manuf. Technol. 67 (2013) 2083–2107.
[26] K.D. Delaney, G. Bissacco, D. Kennedy, A structured review and classification of Demolding issues and proven solutions, Int. Polym. Process. 27 (1) (2012) 77–90.
[27] R. Malloy, P. Majeski, Design of pin ejector systems for injection molds, in: Proceedings of the ANTEC 89: 47th Annual Technical Conference-Society of Plastics Engineers, New York, 1989, pp. 1231–1235.
[28] G. Menges, P. Mohren, How to Make Injection Moulds, 3rd ed., Hanser, Munich, Vienna and New York, 2001.
[29] C. Burke, R. Malloy, An experimental study of the ejection forces encountered during injection molding, in: Proceedings of the ANTEC 91: 49th Annual Technical Conference-Society of Plastics Engineers, New York, 1991, pp. 1781–1787.
[30] A.J. Pontes, A.S. Pouzada, R. Pantani, G. Titomanlio, Ejection force of tubular injection moldings. Part I: effect of processing conditions, Polym. Eng. Sci. 44 (5) (2004) 325–332.
[31] N. Bhagabatula, D. Michalski, B. Lilly, G. Glozer, Modelling and verification of ejection forces in thermoplastic injection moulding, Model. Simul. Mater. Sci. Eng.

12 (2004) 234–254.
[32] T. Sasaki, N. koga, K. Shirai, Y. Kobayashi, A. Toyoshima, An experimental study on ejection forces of injection molding, Precis. Eng. 24 (2000) 270–273.
[33] A. Griffiths, G. Tosello, S.S. Dimov, S. Scholz, A. Rees, B. Whiteside, Characterisation of demoulding parameters in micro-injection moulding, Microsyst. Technol. 21 (2015) 1677–1690.
[34] A.C. Griffiths, S.S. Dimov, S. Scholz, G. Tosello, A. Rees, Influence of injection and cavity pressure on the demoulding force in micro-injection moulding, J. Manuf. Sci. Eng. 136 (2014) 3.
[35] I. Chan, M. Pinfold, C. Kwong, W. Szeto, A review of research, commercial software packages and patents on family mould layout design automation and optimization, Int J. Adv. Manuf. Technol. 57 (2011) 23–47.
[36] S. Kwak, T. Kim, S. Park, K. Lee, Layout and sizing of ejector pins for injection mould design using the wavelet transform, Proc. Inst. Mech. Eng. 217 (B) (2003) 463–473.
[37] Z. Wang, K.S. Lee, J.Y.H. Fuh, Z. Li, Y.F. Zhang, A.Y.C. Nee, D.C.H. Yang, Optimum ejector system design for plastic injection mould, Int J. Mater. Prod. Technol. 11 (5/6) (1996) 371–385.
[38] CAMPUS @5.2 Covestro Deutschland AG (Aachen, Germany), Covestro Acrylonitrile butadiene styrene (ABS) – product brochure, 2010. ⟨http://www.campusplastics.com/⟩ (accessed Nov 2015).

Jorge Manuel Mercado Colmenero received his B.Eng. and M.Eng. in Mechanical Engineering in 2012 and 2014 respectively from the University of Jaén in Spain. In 2014 he joined the Design, Engineering Graphics and Project department at Jaen university as a Ph.D. student. He is currently developing his thesis on automatic analyses and design of injection plastic molds, including demoldability, ejection systems, cooling system design and CAD-CAE design and manufacturing.

Dr. Miguel Angel Rubio Paramio received his M.Eng. and Ph.D. in Mechanical Engineering in 1992 and 2000 respectively from the Polytechnic University of Madrid in Spain. In 1994 he joined the University of Jaen and currently he teaches courses of Computer-aided Design, Manufacturing and Engineering in the Engineering Graphics, Design and Projects Department. His thesis was focused on the automatic analysis of plastic parts injection. His research interests include CAD-CAM-CAE, Design for Manufacturing, computational geometry, constraint-based parametric modeling, and their applications in plastic injection mold design and manufacturing.

Prof.Dr. Antonio Vizan Idoipe is a professor in the Department of Mechanical and Manufacturing Engineering at the Polytechnic University of Madrid. He leads research and collaboration with companies and national research centers in the areas of design and production. He held the position of Head of the Department of Mechanical and Manufacturing Engineering and Vice Director of the Spanish Association for Robotics and Production Automation. His research interest relates to machining process optimization, micromachining, injection molding, and concurrent engineering.

Dr. Cristina Martín Doñate received her B.Eng. and M.Eng. in Electrical – Electronics Engineering and Industrial Engineering (Polytechnic University of Valencia – Spain) and Ph.D. in Industrial Engineering (University of Jaen – Spain). She performed her final Masters project at the Technical University of Graz in Austria, in the field of manufacturing systems. She worked for several years as a project manager developing new products in the automotive manufacturing industries. She is currently a university teacher at Jaen University where she develops research and conducts research projects into manufacturing systems, plastic injection mold design and technology, CAD systems and new products development.

Referencia / Reference: **Mercado-Colmenero, Jorge Manuel,** Rubio-Paramio, Miguel Angel, Marquez-Sevillano, Juan de Juanes y Martín-Doñate, Cristina. *A new method for the automated design of cooling systems in injection molds. Computer-Aided Design 104 (2018) 60-86. DOI: https://doi.org/10.1016/j.cad.2018.06.001*.

Estado / Status: Publicado / Published

Índice de impacto / Impact Factor: 2,947 (JCR Year 2017)

Categoría / Catogory: Computer Science, Software Engineering

Ranking: 10/104 (JCR Year 2017)

Quartile: Q1 (JCR Year 2017)

JIF Percentile: 90.865 (JCR Year 2017)

Computer-Aided Design 104 (2018) 60–86

Contents lists available at ScienceDirect

Computer-Aided Design

journal homepage: www.elsevier.com/locate/cad

# A new method for the automated design of cooling systems in injection molds☆

Jorge Manuel Mercado-Colmenero [a], Miguel Angel Rubio-Paramio [a], Juan de Juanes Marquez-Sevillano [b], Cristina Martin-Doñate [a,*]

[a] Department of Engineering Graphics Design and Projects, University of Jaen, Spain
[b] Department of Mechanical Engineering, Polytechnical University of Madrid, Spain

ARTICLE INFO

*Article history:*
Received 22 June 2017
Accepted 23 May 2018

*Keywords:*
Cooling system
Injection molding
Discrete geometry
Surfaces geometric recognition
Genetic optimization

ABSTRACT

This paper presents a new method for the automatic design of the cooling system in injection molds, based on the discrete geometry of the plastic part. In a first phase the new algorithm recognizes the discrete topology of the part, obtaining its depth map and detecting flat, concave regions and slender details which are difficult to cool. The algorithm performs an automatic analysis of the heat transfer, taking into account functional parameters, in order to guarantee a uniform cooling of the part. Based firstly on the limit range distance from which the horizontal straight channels lose cooling effectiveness and secondly on the depth map data, the algorithm provides an optimal layout for the cooling system of the part by adapting it to its geometry. By means of adapting the precision of the algorithm to the molded geometry, both horizontal straight channels for low concavity areas and baffle matrices for concave regions are used. In a second phase, the parameters of the cooling system such as channel diameter, channel separation, etc., are dimensioned by means of genetic optimization algorithms. A second genetic optimization algorithm ensures uniformity and balance in the layout of the cooling system for the plastic part. The result is the design of the cooling system for the plastic part with the same performance as the conformal system. A constant distance between the cooling channels and the part surface is maintained, and at the same time the manufacturing of the mold using CNC techniques and traditional metal materials could be achieved. Complementarily, the algorithm performs an interference analysis with other parts of the mold such as the ejection system. The method does not need a subsequent CAE analysis since it takes into account functional and technical parameters related to heat transfer in its design, thus ensuring its functionality. The algorithm is independent of the CAD modeler used to create the part since it performs a recognition analysis of the part surfaces, being able to be implemented in any CAD system. The data obtained in the design can be used additionally in later applications including the automated design of the injection mold.


## 1. Introduction

The plastic injection molding process begins with the injection of the thermoplastic material at a high temperature into the cavity formed by both mold cavities. Once inside the mold the plastic is compacted, cooling until it acquires the solidification temperature that allows the geometry of the piece to be maintained without deformation. The duration of the molding cycle as such is not enough to dissipate the heat of the injected plastic by means of heat conduction through the metal material of the mold. Thus, in order to improve the efficiency of the process, the mold is cooled using a set of hollow channels made in both cavities through which a cooling fluid performs a better heat exchange. At present there are several possibilities in relation to the design of the cooling channels of the plastic injection mold. The choice of design depends mainly on three factors: the geometric characteristics of the plastic part, the size of the mold and the manufacturing technology required by each cooling system. Taking these factors into account, cooling systems can be designed by means of conventional cooling models or conformal systems, adapted to the part geometry. The conventional systems have the advantage of their low cost of manufacture since they use traditional machining techniques. Nevertheless, they have a limited application only to slender parts with flat geometries, and without deep concavities. Unlike traditional cooling channels, the conformal cooling channels maintain a constant distance between the surface of the mold cavities in contact with the part and the cooling circuit, thus obtaining

☆ This paper has been recommended for acceptance by Horea Ilies.

* Correspondence to: Campus Las Lagunillas, s/n. Building A3-210, 23071 Jaen, Spain.
*E-mail addresses:* jmercado@ujaen.es (J.M. Mercado-Colmenero), marubio@ujaen.es (M.A. Rubio-Paramio), juandejuanes.marquez@upm.es (J.d.J. Marquez-Sevillano), cdonate@ujaen.es (C. Martin-Do nate).

https://doi.org/10.1016/j.cad.2018.06.001
0010-4485/

precise temperature control in parts with complex surfaces. The conformal method requires Rapid Tooling Technologies for the manufacture of mold cavities, with the inconvenience of its lack of functionality in medium size molds for industrial applications. To resolve these problems, the "Milled Groove" and "Array of Baffles" hybrid refrigeration systems take advantage of conformal designs, maintaining a constant distance between the channels and the part, but manufactured with traditional machining processes. The proper choice of the cooling system is fundamental for the uniform transfer of heat in the part, assuming an adequate manufacturing cost. A detailed recognition of the part surface from the first phases of mold design allows detection of its geometric characteristics, which can be decisive for the proper choice of cooling system. While in the automatic analysis of other parts of the mold [1–4] only geometric type parameters have influence, in the design of the cooling system a series of requirements related to the heat transfer in the mold must be fulfilled in parallel. Knowing these parameters and including them as design requirements ensures their good operation regardless of the use of CAE or CFD tools.

The design of the cooling channels layout is currently carried out by experienced designers who usually take as reference a set of geometric criteria based on their experience and related to dimensional values of depth and separation between channels. The design is performed manually by validating the result a posteriori by means of numerical simulation programs. If the result indicates that the design presented does not assure the quality requirements of the part, it is modified again by an iterative trial and error process. This methodology poses several drawbacks, including the large amount of time required by experts who are sometimes not available due to the company's workload, its high level of specialization and the availability of CAE or CFD simulation software. In spite of the importance of rigorously designing the mold cooling system, there are few studies related to obtaining geometric algorithms for the automatic design of the cooling system for injection molds. Most studies focus on conformal design algorithms for later manufacture using rapid-tooling techniques, and these are not valid for use in medium and large industrial molds. Other studies propose algorithms that only take into account geometric design criteria, do not automate the whole design process, or are not valid for any geometry of the plastic part. Finally there are some which analyze the part geometry in an internal way, through procedures closely linked to the CAD Modeler used for the part design.

In order to solve the problems presented above, a new method for the automatic design of the mold cooling system is presented. The method developed takes into account geometric, technical and functional parameters. The first stage of the algorithm recognizes in an automated way the discrete topology of the plastic part, and obtains the depth map of the part with the aim of detecting difficult cooling zones. Using this information, the algorithm automatically proposes the optimum design for cooling the part to suit its geometry. The algorithm recognizes large concavity areas of the part, slender details or internal turrets, which require baffle channels. Flat areas with no deep concavities are recognized and easily cooled by means of conventional horizontal straight channels. In this way a constant distance between the cooling channels and the surface of the part can be maintained, obtaining uniform conformal refrigeration but with reliable manufacturing methods, thus avoiding the high costs of additive manufacture. The algorithm verifies the possible interference of the cooling elements with other parts of the mold, ensuring its functionality. The dimensioning of the channels is performed by applying genetic optimization algorithms, thus guaranteeing the quality of the part. The method implemented presents as an additional advantage its independence from the modeler since it does not need internal information of the part, as the part is analyzed externally. Nor are CAE programs for later design validation required. As a final advantage, the algorithm is valid for any size of mold since it does not require Rapid Tooling techniques for its manufacture, allowing the use of traditional metallic materials by means of CNC procedures. To date there is no algorithm for the automatic design of the mold cooling system that resolves all the problems raised and assures the design efficiency for the industrial mold.

## 2. Background and related work

A large number of researchers and mold designers have focused their work on the cooling phase in injection molding, mainly improving the layout of the cooling channels as well as on the analysis and simulation of their new designs.

The first studies related to the design of cooling systems were carried out in the field of conventional systems [5–7]. Unfortunately all the designs presented had the disadvantage of a totally manual execution. In order to resolve this problem, several authors investigated the possible automation of the system design of conventional cooling channels in the injection mold. Many of the studies were based on the feature recognition method as an automated analysis of the topology of the plastic part. For the specific case of cooling systems, a cooling feature is defined as the surface fragment of the plastic part with information on its cooling. The cooling requirements for each feature are met using several cooling elements (cooling channels, bafflers, bubblers or helical baffles). Currently, the solid modeling of the part does not explicitly provide information about the features. For this reason we need recognition methods capable of extracting this implicit geometric information in the model in order to be used as input to later structured algorithms [8]. Li et al. [9] applied the Design Synthesis methodology together with the development of a new algorithm for the recognition of cooling features in the plastic part. In his study he decomposed the complex geometry of the plastic part into simpler parts. After its decomposition it recognizes the features, assigning to each of them the cooling subsystem best adapted to its geometry. Finally the set of cooling subsystems is synthesized in a single system for the whole part. The feature-based recognition method developed by Li allows the free geometry of the plastic part to be recognized as long as the surfaces forming it are similar to superquadric surfaces. Unfortunately, not all freeform surfaces can be represented as superquadric surfaces and therefore it is not a valid method for any plastic part. In a later study [10] it extends the automation of the conventional cooling system from the preliminary design phase to the layout phase of the channels. In this study preliminary design based on the recognition of features is considered as the basis, and then functional and manufacturing aspects are added. However, this study presents the same drawbacks as [9], based fundamentally on the process of recognition of features in the plastic part. The recognition of features from a part created in a CAD environment must be performed inside the modeler used to design it. It is also necessary to take into account the fact that the features interact. An interacting feature is the result of the intersection of multiple features. The difficulty in the recognition of these interacting features is mainly due to the destruction of the adjacency relations between features in contact. Li et al. [10] use fuzzy logic as an evaluation system for the different designs generated. The weighting ratios used by the evaluation system are selected by the mold maker based on their experience, which fails to meet the automation criteria of the design system, depending on the user. As a solution to the problems described above, Li et al. [11] developed a specific method for the conventional design of the cooling system based on the C-Space methodology, which allows the representation of a set of cooling designs without interfering with the rest of the components of the mold. This new method is an improvement on the heuristic method developed in [8], implementing a genetic algorithm integrated in the representation

of the C-space in order to automatically generate the set of designs for the layouts. In a later paper Li et al. [12] improve on the C-Space method by allowing variations in geometry and topology of the design and incorporating user-defined constraints. However, the goal of their research is solely focused on the geometrical aspect of the cooling system, and technical parameters, related to the heat transfer between the plastic part and the mold, are not considered.

Most of the research work related to the design of cooling systems focuses on the design and analysis of conformal cooling channels. The design of conformal cooling channels in plastic injection has the advantage of greater uniformity in the cooling of the part since the cooling channels surround closely the cavity surface of the mold. The manufacture of molds cooled by conformal cooling channels, and more specifically of the core and cavity inserts, requires the use of rapid tooling techniques. In a pioneering study Sachs et al. [13] used 3D printing with stainless steel powder and a polymer binder to manufacture the mold cavity inserts incorporating a conformal channel design into an open ring-shaped part. However, the thermal properties of the mold material vary using conventional steel, this being a factor of influence not quantified in the behavior of the cooling system. Further research concerning new manufacturing methods for implementing conformal designs is found in [14,15]. In the field of the implementation of conformal designs in prototype molds (rapid soft tools) Ferreira [16] made molds using a material composed of aluminum filled with epoxy resin. Unfortunately soft tooling molds are not useful for the manufacture of parts with a high level of surface quality for industrial use. In addition, the geometries of the channel layout are not fully adapted to the surface of the mold cavity in contact with the part. To solve these problems Saifullah [17] also uses bent copper tubes for the realization of the conformal cooling channels, but in mold manufactured by means of CNC, thus fulfilling the surface finishing requirement. However, the use of cooling channels by means of copper tubes can reduce the mold strength and its useful lifetime. The rapid tooling processes are capable of manufacturing the complex surfaces required by the cooling system, although most of these technologies are still at the laboratory development level and are not suitable for industrial use requirements. Recently Eiamsa [18] has used a new MIG/MAG melding torch manufacturing technique attached to a CNC machine as a hybrid system. In his study he built a layered mold designing the cooling by means of bubbler channels and then machining the surface. In the manufacture of cavities by means of conformal designs different research studies have been carried out aiming to improve the geometric design of conformal cooling channels with the help of CAD systems. Xu et al. [19] presented an analytical model for the dimensioning of the main technical parameters of the cooling system based on the decomposition of the mold surface into small sections called cooling zones, for which it creates an individual channel system. This configuration is again decomposed into smaller elements called cooling cells. A "design window", on which six design rules are applied, is created for each cell. Finally the individual results are grouped in order to construct the complete cooling system. Dimla et al. [20] proposes a method for the design and optimization of conformal cooling channels in cooling and heating processes using virtual prototypes. Quiao et al. [21] implemented a methodology for the optimization of the CAD design of the conformal channels, studying cooling by means of a sensitivity analysis based on the Boundary Elements Method and a hybrid type optimizer. The sensitivity analysis together with Boundary Element Coding showed good results, however they are not yet applicable to real cases of the industrial scope. Au et al. [22] used a uniform accuracy scaffolding architecture for the design of cooling channels. The results in the simulation analysis showed that this type of structure provided a more uniform cooling surface compared to conventional refrigeration designs and increased the mechanical strength of the mold cavities. Park et al. [23] used different types of layout (zigzag, parallel and spiral) for the conformal channels, applying analytical formulas and using CAE flow simulation to verify the results of the optimization process. Unfortunately [19–23] they required the interaction of the designer in some of the phases. In the field of automated design of the conformal cooling channels Au [24] proposed a methodology based on the use of geometric visibility algorithms to generate the automated design of the cooling channels and their application to complex surfaces in injection molds. In Au et al. [25] he continued his research by presenting an alternative design method consisting of a conformal cooling passageway with porous multi-connected characteristics, based on the principle of duality. In order to compensate the gradual increase in the temperature of the coolant from the input to the output pipes Au et al. [26] proposed a method of adjusting the distance between the conformal cooling channels and the surface of the cavities. With this new variable distance design, the heat is extracted more efficiently than by means of the existing conformal cooling channel designs. Wang et al. [27] proposed a new algorithm for the automated design of the conformal cooling circuit. The circuit proposed by the algorithm generates a surface adaptable to the surface of the part. Although the method was fully automated and only required a set of user parameters such as type of coolant, diameter of the cooling channels and cycle time, it also required an interactive optimization process performed by the designer, in order to adjust with enough precision the cooling channels using the cycle time value. Wang et al. [28] proposed a new algorithm for generating conformal cooling channels by means of a spiral layout. This configuration optimized the cooling system and reduced manufacturing costs. The conformal cooling channels provide uniform cooling of the part which reduces cooling time and increases the quality of the molded part, especially for long-sized products and free-form surfaces. The use of rapid prototyping techniques allows the production of cooling channels with very complex geometries in both mold cavities. Unfortunately the powdered metal materials used in 3D prototyping techniques are limited, and the functionality of the manufacturing process is not currently reliable for medium and large size molds as they are not able to meet industry requirements.

In addition to conventional and conformal systems, there are hybrid type systems for the design and manufacture of cooling channels. These methods take advantage of the manufacturing by means of CNC technologies allowing the use of traditional materials while maintaining a constant distance between the channel and the workpiece surface. There are two main hybrid cooling methods, the mechanized groove channel method, and the distribution of array of baffles structure. In the field of research of the design of the channel cooling systems by means of mechanized grooves Sun et al. [29] used a mechanized groove design with a U-shaped cooling channel surface. In their study the method is applied to large and complex free surface parts and compared to the design of conventional straight channels. Subsequently, Dang et al. [30] presented a systematic method for optimizing the design of grooved cooling channels, which reduces cooling time. In order to increase the computational efficiency of the algorithm it combines the analytical method with simulations, assessing the relationship between the thermal behavior of the mold and the parameters of the layout of the cooling channels. The cooling channel systems using a mechanized groove improve product quality by means of a higher uniformity in the cooling stage, and a lower cycle time, while a greater flexibility in the design of cooling channel layout is provided. However, high manufacturing costs prevent their use in large molds. Another hybrid method for the design of the cooling system is the design with structure of an array of baffles. It presents great advantages in its performance and low cost of manufacture. The array of baffles is characterized by being

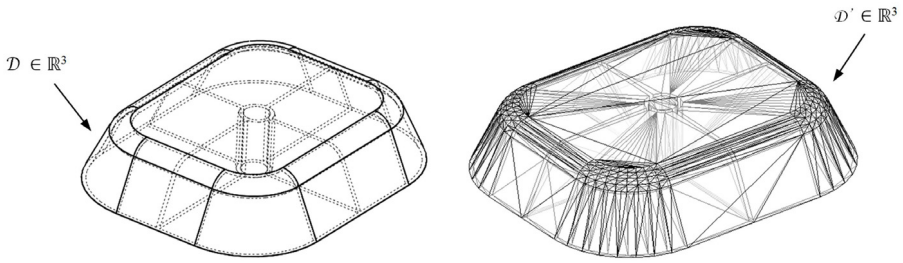


**Fig. 1.** CAD model $\mathcal{D}$ and discrete geometry $\mathcal{D}'$ of the plastic part.

able to cool small regions of the core which are difficult to cool in medium and large size molds in parts with free form surfaces. Despite its many advantages, there are still few studies on how to optimize its distribution. In this regard, Park et al. [31] introduced the design of cooling channels by means of the array of baffles using a systematic method for the optimization of these channels. In his work he expressed, by means of explicit RMS equations, the relationship between the configuration of the cooling channels, the thickness of the part, the temperature distribution and the process parameters. The method proposed by Park improves the behavior of the cooling channels, facilitating the process of design optimization. However, this method still poses limitations since many of the requirements used to obtain the mathematical model are not real, which causes the final model to differ from the real model. In addition, the array of baffles in this study is considered as unique and covers the whole part. Usually the plastic parts have flat parts and concave parts, and it is not necessary to use baffles in reduced concavity areas.

To resolve these problems the paper presents a methodology for the automated design of the cooling system. In a first phase the algorithm recognizes the topology of the part in discrete format and obtains the depth map, detecting flat zones and changes in the geometry which make it difficult to cool. Using this information as a basis the algorithm proposes an optimal layout for the cooling system adapted to the part geometry. The algorithm employs horizontal straight channels in flat or low concave areas and uses the advantages of the design in the form of a baffle matrix for the concave areas, adapting the accuracy of the algorithm to the geometry to be manufactured. The method takes into account functional parameters by performing an automated analysis of the heat transfer in the mold, obtaining the limit distance from which the horizontal straight channels lose effectiveness, and guaranteeing a uniform cooling stage. In a second phase, the parameters of the cooling system such as channel diameter, channel gap, etc., are measured using genetic optimization algorithms. The result is the layout of the cooling system with the conformal system performance, maintaining a constant distance between the cooling channels and the surface of the part. At the same time the manufacture of the mold by means of CNC machines and traditional metallic materials is also possible, without the high costs of additive manufacturing. In addition, the algorithm performs an analysis of the interferences with other parts of the mold such as the ejection system. The method does not need a subsequent CAE analysis since it takes into account functional and technical parameters related to heat transfer in its design, thus ensuring its functionality. The algorithm is independent of the modeler used to design the part since it performs a procedure of surface recognition. Moreover, the design is achieved by means of an external process which can be implemented in any CAD system. The data obtained can be used additionally in later applications including the automated design of the injection mold.

## 3. Methodology

### 3.1. Discrete model of the plastic part

The proposed algorithm performs a previous processing of the part $\mathcal{D} \in \mathbb{R}^3$ in order to obtain the discrete three-dimensional mesh $\mathcal{D}' \in \mathbb{R}^3$, consisting of a set of triangular facets $F_i \in \mathcal{D}'_f$, being n × 3 the range of the array $\mathcal{D}'_f$ and a set of nodes $P_{ij} = \{X_{ij}, Y_{ij}, Z_{ij}\} \in \mathcal{D}'_n$, being the array $\mathcal{D}'_n$ of range 3 · n × 3 Eq. (1). The value of n coincides with the total number of triangular facets $F_i$ that makes up the mesh $\mathcal{D}'$.

$$\forall\, \mathcal{D} \in \mathbb{R}^3 \rightarrow \mathcal{D}' \in \mathcal{M}_{1\times 2}(\mathbb{R}) \rightarrow \mathcal{D}' = \{\mathcal{D}'_f \;\; \mathcal{D}'_n\}$$

$$\mathcal{D}'_f \in \mathcal{M}_{n\times m}\left(\mathbb{R}^3\right) \quad ; \quad \mathcal{D}'_n \in \mathcal{M}_{3\cdot n\times m}\left(\mathbb{R}^3\right) \tag{1}$$

where m is the number of nodes per facet $F_i \in \mathcal{D}'_f$. The proposed method uses triangulate facets with the value of the parameter m being equal to 3, being able to extend the scope of the method to facets with any other flat polygonal geometry. Fig. 1 shows the continuous CAD model $\mathcal{D}$ of the plastic part to be analyzed together with the discrete mesh $\mathcal{D}'$ obtained after the pre-processing phase. Fig. 2 shows a detail of a triangular facet $F_{ij} = \{P_{i1}, P_{i2}, P_{i3}\} \in \mathcal{D}'_f$, and the nodes $P_{ij} \in \mathcal{D}'_n$ that compose it.

### 3.2. Obtaining the depth map of the mesh $\mathcal{D}'$

The objective of this phase of the algorithm is to determine the depth map $[\tau_{cavity}, \tau_{core}] \in \mathbb{R}^3$ of the surfaces belonging to $\mathcal{D}'$ to be molded by the cavity and core plates respectively. The depth map provides information about the surface topology of the $\mathcal{D}'$ mesh. This information is of great help in the automated design of the cooling system since it allows identification of those regions belonging to $\mathcal{D}'$ which, due to their depth, require the use of additional cooling elements such as baffles.

The first step to obtaining the depth map is to locate the set of surfaces belonging to $\mathcal{D} \in \mathbb{R}^3$ to be molded by means of the core and cavity plates. For this, the algorithm developed is based on the results obtained in the demoldability analysis [2] applied to the mesh $\mathcal{D}' \in \mathbb{R}^3$. Thus the mesh $D_f{}' \in \mathbb{R}^3$ is segmented into two regions $\{\Omega_{f1} \cup \xi_{f2}\}$ Eq. (2) sorted by their demoldability with respect to the main parting direction $\overrightarrow{D_z}$.

In Fig. 3 the result of the demoldability analysis [2] applied to the mesh $\mathcal{D}' \in \mathbb{R}^3$ is shown. The zones to be molded by means of the cavity plate have been represented in green and the zones to be molded by means of the core plate in blue, where $\overrightarrow{D_z}$ is the parting direction for $\mathcal{D}$.

$$\forall\, \mathcal{D}'_f \exists\, \{\Omega_{f1} \cup \xi_{f2}\}$$
$$f_1 + f_2 = f \tag{2}$$

Similarly, the nodes $\mathcal{D}'_n \in \mathbb{R}^3$ belonging to the set of facets $\Omega_{f1} \in \mathbb{R}^3$ are grouped in the array $\Omega_{n1} \in \mathbb{R}^3$ Eq. (3), and the nodes

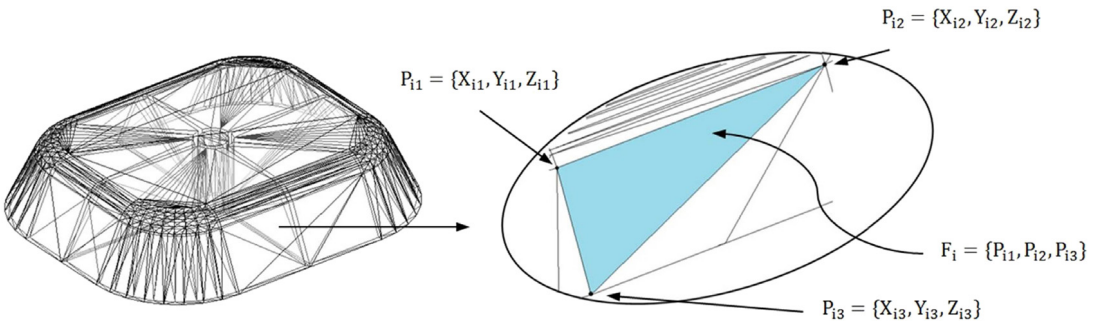


**Fig. 2.** Detail of a triangular facet $F_i$ of the mesh $\mathcal{D}'$ and the nodes $P_{i1}$, $P_{i2}$, $P_{i3}$.

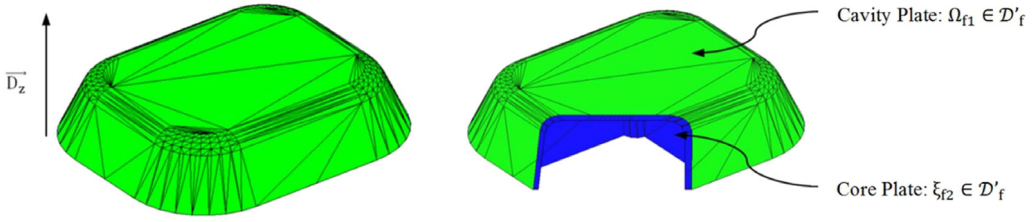


**Fig. 3.** Demolding analysis of part $\mathcal{D}'$.

belonging to the set of facets $\xi_{f2} \in \mathbb{R}^3$ to be molded by means of the core plate, in the array $\xi_{n2} \in \mathbb{R}^3$ (Fig. 4).

$$\forall\, \mathcal{D}'_n \exists\, \{\Omega_{n1} \cup \xi_{n2}\}$$
$$n_1 + n_2 = n \tag{3}$$

After segmenting the set of facets $\mathcal{D}'_f \in \mathbb{R}^3$ according to its demoldability by means of the meshes $\Omega_{f1}$ y $\xi_{f2}$, the depth map is obtained. First, the Bounding Box of the mesh $\mathcal{D}' \in \mathbb{R}^3$ is generated from its principal dimensions *l*, *w* and *h* in the coordinate axes X, Y, Z respectively (see Figs. 5a and 5b). Using the dimensions *w* (width) and *l* (length) of the Bounding Box, two two-dimensional nodal meshes of precision $\varepsilon$ equal to the dimensional value of the minimum thickness of the plastic part $\mathcal{D} \in \mathbb{R}^3$ are created. The nodal mesh corresponding to the region $\Omega_{f1}$, which can be molded by means of the cavity plate, is stored in the array $\Theta_{t_{cavity}}$ and the nodal mesh corresponding to the region $\xi_{f2}$, which can be molded by means of the core plate, is stored in the array $\Theta_{t_{core}}$ (Figs. 5a and 5b) Eq. (4).

$$[\Theta_{t_{cavity}} \quad \Theta_{t_{core}}] \in \mathcal{M}_{\frac{l}{\varepsilon} \times \frac{w}{\varepsilon}}(\mathbb{R}) \tag{4}$$

Both nodal meshes $\Theta_{t_{cavity}}$, $\Theta_{t_{core}}$ are composed of a set of nodes $\theta_{t_{cavity}}(i,j) \in \mathbb{R}^3$ and $\theta_{t_{core}}(i,j) \in \mathbb{R}^3$ with coordinates $\left[\theta_{t_{cavity}}(i,j)_x \quad \theta_{t_{cavity}}(i,j)_y \quad \theta_{t_{cavity}}(i,j)_z\right]$ and $\left[\theta_{t_{core}}(i,j)_x \quad \theta_{t_{core}}(i,j)_y \quad \theta_{t_{core}}(i,j)_z\right]$ Eq. (5). The nodes $\theta_{t_{cavity}}(i,j) \in \mathbb{R}^3$ and $\theta_{t_{core}}(i,j) \in \mathbb{R}^3$ share coordinates in the X, Y axes, differing in the value of the coordinate in the Z axis $\theta_{t_{cavity}}(i,j)_z$ y $\theta_{t_{core}}(i,j)_z$ (see Figs. 5a and 5b).

$$\forall \begin{bmatrix} i \\ j \end{bmatrix} \in \left\{ \begin{matrix} 1, \ldots, i, \ldots, \frac{l}{\varepsilon} \\ 1, \ldots, j, \ldots, \frac{w}{\varepsilon} \end{matrix} \right\}$$
$$\exists \begin{bmatrix} \theta_{t_{cavity}}(i,j) = \left[\theta_{t_{cavity}}(i,j)_x \quad \theta_{t_{cavity}}(i,j)_y \quad \theta_{t_{cavity}}(i,j)_z\right] \in \mathbb{R}^3 \\ \theta_{t_{core}}(i,j) = \left[\theta_{t_{core}}(i,j)_x \quad \theta_{t_{core}}(i,j)_y \quad \theta_{t_{core}}(i,j)_z\right] \in \mathbb{R}^3 \end{bmatrix}$$
$$| \begin{bmatrix} \theta_{t_{cavity}}(i,j)_x = \theta_{t_{core}}(i,j)_x \\ \theta_{t_{cavity}}(i,j)_y = \theta_{t_{core}}(i,j)_y \\ \theta_{t_{cavity}}(i,j)_z \neq \theta_{t_{core}}(i,j)_z \end{bmatrix} \tag{5}$$

For the set of nodes $\Theta_{t_{cavity}} \in \mathbb{R}^3$ the value of $\theta_{t_{cavity}}(i,j)_z$ is constant for each node $\theta_{t_{cavity}}(i,j) \in \mathbb{R}^3$ and equal to the coordinate in the direction $\overrightarrow{D_z}$ of the node with the highest dimension $\Omega_{n1}(i,j)_{zmax}$ belonging to the mesh $\Omega_{n1} \in \mathcal{D}'_n$ (see Fig. 5a) Eq. (6). In the same way, for the set of nodes $\Theta_{t_{core}} \in \mathbb{R}^3$, the value of $\theta_{t_{core}}(i,j)_z$ is constant for each node $\theta_{t_{core}}(i,j)$ and equal to the coordinate in the direction $\overrightarrow{D_z}$ of the node with the lowest dimension $\xi_{n2}(i,j)_{zmin}$, belonging to the mesh $\xi_{n2} \in \mathcal{D}'_n$ (see Fig. 5b).

$$\begin{bmatrix} \theta_{t_{cavity}}(i,j)_z = \Omega_n(i,j)_{zmax} = Cons \\ \theta_{t_{core}}(i,j)_z = \xi_n(i,j)_{zmin} = Cons \end{bmatrix} \tag{6}$$

Next, for each node $\theta_{t_{cavity}}(i,j) \in \Theta_{t_{cavity}} \in \mathbb{R}^3$ and for each node $\theta_{t_{core}}(i,j) \in \Theta_{t_{core}} \in \mathbb{R}^3$ two sets of lines $\mathcal{R}_{t_{cavity}}$ and $\mathcal{R}_{t_{core}}$ are generated Eq. (7). The lines have as starting point each node $\theta_{t_{cavity}}(i,j) \in \mathbb{R}^3$ and $\theta_{t_{core}}(i,j) \in \mathbb{R}^3$, their directing vector being coincident with the parting direction $\overrightarrow{D_z}$. The intersection of the lines $\mathcal{R}_{t_{cavity}}$ and $\mathcal{R}_{t_{core}}$ with the sets of facets $\Omega_{f1} \in \mathbb{R}^3$ and $\xi_{f2} \in \mathbb{R}^3$ generates new nodes $\lambda_{t_{cavity}}(i,j) \in \mathbb{R}^3$ and $\lambda_{t_{core}}(i,j) \in \mathbb{R}^3$ that are contained in $\Omega_{f1} \in \mathbb{R}^3$ and $\xi_{f2} \in \mathbb{R}^3$ respectively Eqs. (8)–(9). The nodes $\lambda_{t_{cavity}}(i,j)$ are shown in Fig. 6a and the nodes $\lambda_{t_{core}}(i,j) \in \mathbb{R}^3$ are shown in Fig. 6b.

$$\begin{aligned} &\left[\mathcal{R}_{t_{cavity}} \quad \mathcal{R}_{t_{core}}\right] \in \mathcal{M}_{\frac{l}{\varepsilon} \times \frac{w}{\varepsilon}}(\mathbb{R}) \rightarrow \left[\mathcal{R}_{t_{cavity}} \quad \mathcal{R}_{t_{core}}\right] \\ &:= \left[\nearrow_{t_{cavity}}(i,j)_{\frac{l}{\varepsilon} \times \frac{w}{\varepsilon}} \quad \nearrow_{t_{core}}(i,j)_{\frac{l}{\varepsilon} \times \frac{w}{\varepsilon}}\right] \end{aligned} \tag{7}$$

$$\forall\, \lambda_{t_{cavity}}(i,j)\, \exists\, \nearrow_{t_{cavity}}(i,j)$$
$$= \left\{ \begin{matrix} Origin : \left[\theta_{t_{cavity}}(i,j)_X \quad \theta_{t_{cavity}}(i,j)_Y \quad \theta_{t_{cavity}}(i,j)_Z\right] \\ Direction : [001] \end{matrix} \right\}$$
$$\in \mathbb{R}^2$$

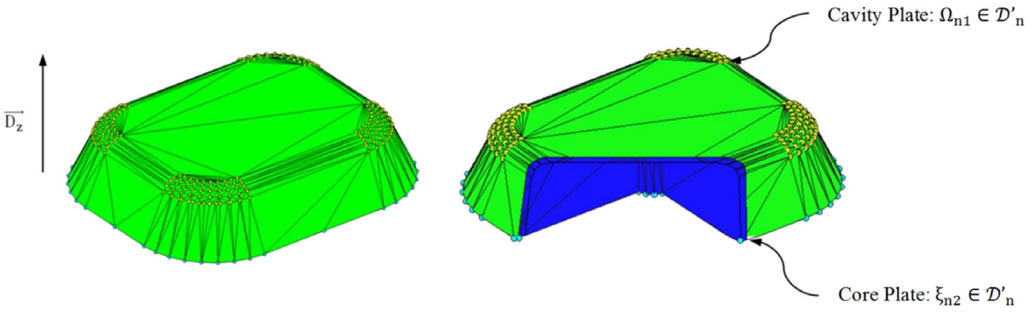


**Fig. 4.** Demoldability analysis of part $\mathcal{D}'$. The nodes belonging to the arrays $\Omega_{n1}$, $\xi_{n2}$ are highlighted.

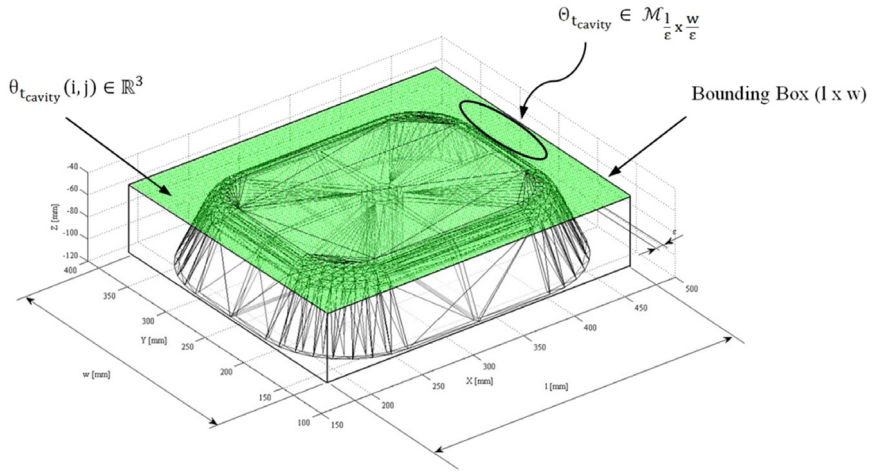


**Fig. 5a.** Location of the Bounding Box and measures w and l on the XY plane in cavity plate analysis.

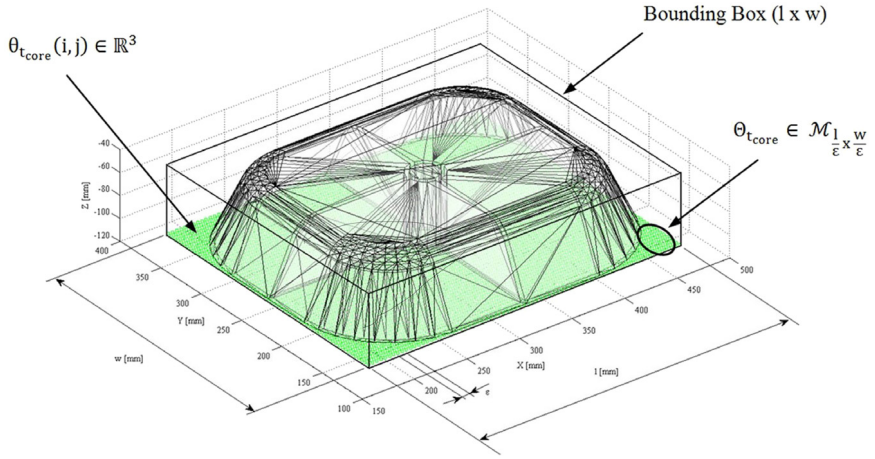


**Fig. 5b.** Location of the Bounding Box and measures w and l on the XY plane in core plate analysis.

$$\forall \lambda_{t_{core}}(i,j)\ \exists \nu_{t_{core}}(i,j) = \left\{ \begin{array}{c} \text{Origin} : \left[\theta_{t_{core}}(i,j)_X \quad \theta_{t_{core}}(i,j)_Y \quad \theta_{t_{core}}(i,j)_Z\right] \\ \text{Direction} : [001] \end{array} \right\} \in \mathbb{R}^2 \tag{8}$$

$$\forall \nu_{t_{cavity}}(i,j) \,|\{\nu_{t_{cavity}}(i,j) \cap \Omega_f\} \neq \emptyset \rightarrow \lambda_{t_{cavity}}(i,j) \in \mathbb{R}^3$$

$$\forall \nu_{t_{core}}(i,j) \,|\{\nu_{t_{core}}(i,j) \cap \xi_f\} \neq \emptyset \rightarrow \lambda_{t_{core}}(i,j) \in \mathbb{R}^3 \tag{9}$$

The map of depths $[\tau_{cavity}, \tau_{core}] \in \mathbb{R}^3$ for the regions $\Omega_{f1} \in \mathbb{R}^3$ y $\xi_{f2} \in \mathbb{R}^3$ is obtained from the distances $\tau_{cavity}(i,j)$ and $\tau_{core}(i,j)$ between each node $\theta_{t_{cavity}}(i,j) \in \mathbb{R}^3$, $\theta_{t_{core}}(i,j) \in \mathbb{R}^3$ and its analogue node $\lambda_{t_{cavity}}(i,j) \in \mathbb{R}^3$ and $\lambda_{t_{core}}(i,j) \in \mathbb{R}^3$ Eq. (10). The depth map $\tau_{cavity} \in \mathbb{R}^3$ for the $\mathcal{D}'$ mesh is shown in Fig. 7a and the depth map $\tau_{core} \in \mathbb{R}^3$ for the $\mathcal{D}'$ mesh is shown in Fig. 7b. The depth parameters $\tau_{cavity}(i,j) \in \mathbb{R}^3$ and $\tau_{core}(i,j) \in \mathbb{R}^3$ are indicated by means of a color coding. The graduated bars on the right in Figs. 7a and 7b indicate the dimensional value in millimeters of the depth parameters $\tau_{cavity}(i,j)$ and $\tau_{core}(i,j)$, respectively.

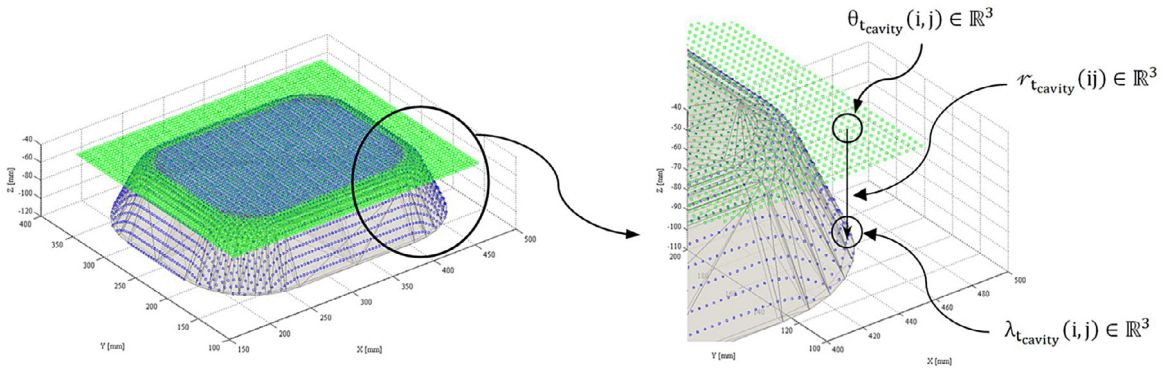


**Fig. 6a.** Obtaining intersection points between an individual line $r_{t_{cavity}}(ij)$ and the part $\mathcal{D}' \in \mathbb{R}^3$.

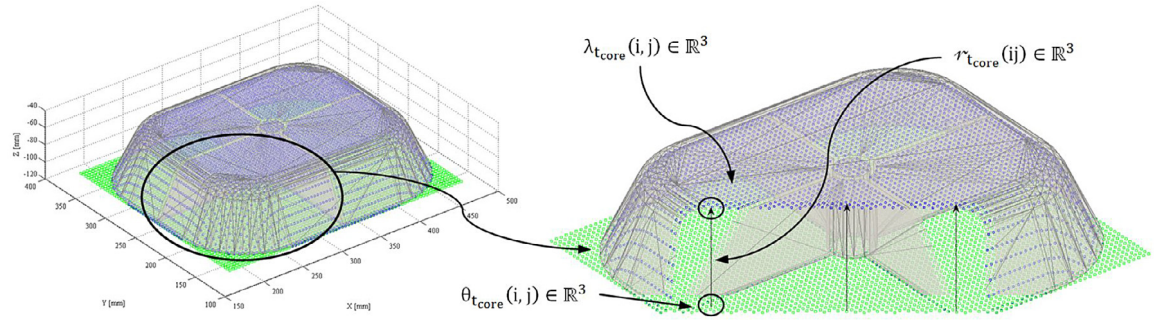


**Fig. 6b.** Obtaining intersection points between an individual line $\nabla_{t_{core}}(ij)$ and the part $\mathcal{D}' \in \mathbb{R}^3$.

$$\forall \lambda_{t_{cavity}}(i,j)\, \exists\, \tau_{cavity}(i,j) \in \mathbb{R} | \tau_{cavity}(i,j) = \left| \theta_{t_{cavity}}(i,j) \quad \lambda_{t_{cavity}}(i,j) \right|$$
$$\forall \lambda_{t_{core}}(i,j)\, \exists\, \tau_{core}(i,j) \in \mathbb{R} | \tau_{core}(i,j) = \left| \theta_{t_{core}}(i,j) \quad \lambda_{t_{core}}(i,j) \right| \tag{10}$$

### 3.3. Dimensioning of the geometric and technical parameters of the cooling system

This section describes the dimensioning process of the geometric and technical parameters that define the cooling system for the plastic part. The dimensioning of the cooling system for the plastic part is performed by genetic optimization algorithms. The use of genetic algorithms allows the cooling system to adapt to a series of requirements or boundary conditions that the design must meet, obtaining the optimum result.

First, the technical and geometric variables of the refrigeration system that the genetic algorithm has to optimize are determined (Table 1).

The value of the variable $L_p$ [mm], corresponding to the distance between the baffle and the plastic part, is assumed constant and equal to 10 mm based on criteria of industrial experience. The magnitude of the other characteristic parameters of the polymer and the mold material are: $\rho_p$, $c_p$, $\delta_s$, $h$, $T_{melt}$, $T_{eject}$ and $\alpha_s$. They are established according the manufacturers' recommendations.

The optimization process using genetic algorithms requires the definition of fitness functions, to be minimized or maximized according to the requirements of an optimum design of the cooling system, and constraint parameters, to be satisfied in terms of optimization variables. For the proposed physical model, the optimization problem can be defined as shown in Table 2.

The constraints have been set according to the limit values that the variables of the optimization problem can take. It is assumed that the coolant temperature will not exceed or fall below the limit values of the vacutherm coolant temperature controller [32]. Mold cavity surface temperature will not exceed the part ejection temperature or be lower than the ambient temperature (assumed for the standard operation of an injection mold). The spacing $L_b$ between baffles or cooling channels will not be less than 10 mm to avoid compromising the structural safety of the mold. And finally, the dimension of the diameters of the cooling channels $D_{baffles}$ will be limited according to the experience and the standardization criteria of the industry.

In order to complete the multi-objective optimization problem, it is necessary to introduce the set of objective functions to be optimized. The first objective function is intended to minimize the difference between mold cavity surface temperature x(1) (variable of the optimization problem) and its resulting value according to the proposed physical model Eqs. (11)–(12).

$$\text{Fitness Function}_1 : \text{Min}\left\{\sigma\left(x(1), \overline{T_m}\right)\right\} \tag{11}$$

where $\sigma\left(x(1), \overline{T_m}\right)$ represents the standard deviation between the variable x(1) and mold cavity surface of the proposed physical model.

$$\text{Fitness Function}_1 : \text{Min}\left\{\sigma\left(x(1), \left[x(2) + \frac{\rho_p \cdot c_p \cdot T_h \cdot \left(2 \cdot \delta_s \cdot x(3) + h \cdot \pi \cdot x(4) \cdot L_p\right) \cdot \left(T_{melt} - T_{eject}\right)}{h \cdot \pi \cdot x(4) \cdot \delta_s \cdot t_{cycle}}\right]\right)\right\} \tag{12}$$

Secondly, in order to ensure the structural integrity of the injection mold and reduce the costs derived from the machining of the mold, it is proposed to maximize the distance between baffles Eq. (13).

$$\text{Fitness Function}_2 : \text{Max}\{x(3)\} \tag{13}$$

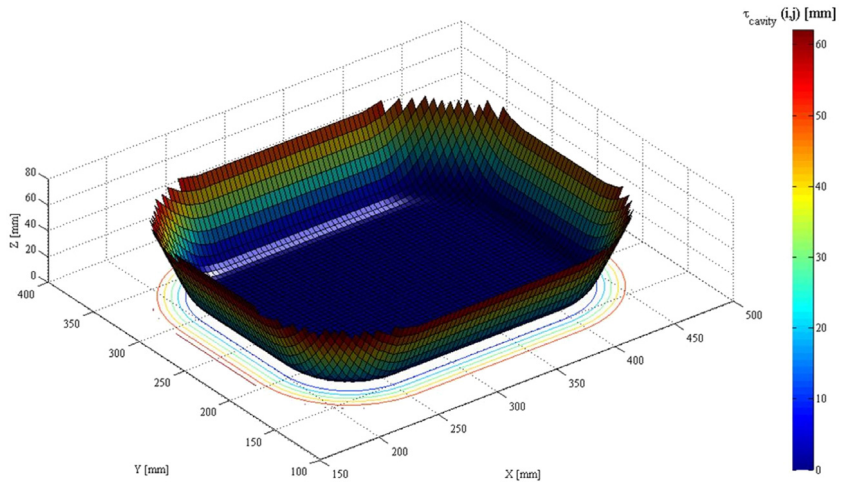


**Fig. 7a.** Depth map $\tau_{cavity}$ for the mesh $\mathcal{D}'$.

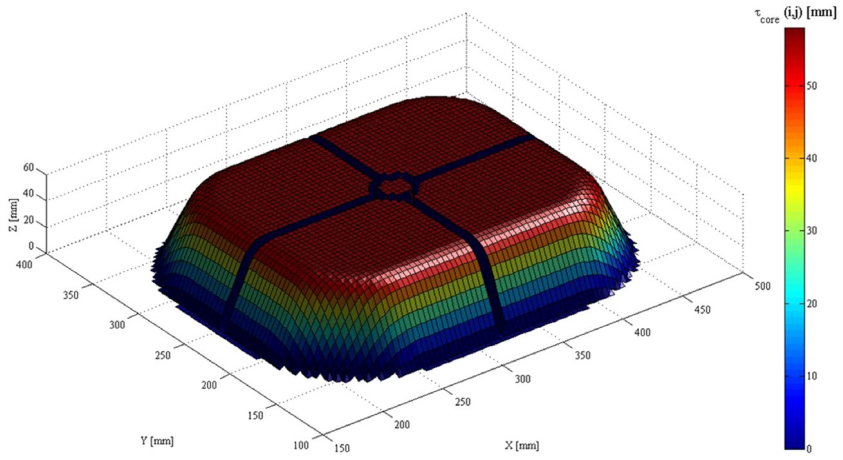


**Fig. 7b.** Depth map $\tau_{core}$ for the mesh $\mathcal{D}'$.

**Table 1**
Variables of the technical optimization problem.

| Nomenclature | Units | Description | Notation on the optimization problem | Constraints |
|---|---|---|---|---|
| $\overline{T_m}$ | °C | Mold cavity surface temperature | x (1) | $23 \leq$ x (1) $\leq T_{ejec}$ |
| $T_c$ | °C | Coolant temperature | x (2) | $10 \leq$ x (2) $\leq 99$ |
| $L_b$ | mm | Distance between cooling channels | x (3) | $10 + 14 \leq$ x (3) |
| $D_{baffles}$ | mm | Diameter of cooling channels | x (4) | $8 \leq$ x (4) $\leq 14$ |

Thirdly, in order to ensure the structural integrity of the injection mold it is proposed to minimize the diameters of the cooling channels Eq. (14).

$$\text{Fitness Function}_3 : \text{Min}\{\text{x}(4)\} \tag{14}$$

Finally, minimizing the cycle time is proposed in order to improve the efficiency and lower the costs of the manufacturing process Eq. (15). It is important to note that minimizing the cycle time involves reducing the mold cavity surface temperature. Occasionally this causes increases in the residual stress of the part, so some constraints of the variables of the optimization problem are established to avoid this unfavorable situation. Finally, the results obtained will be tested using numerical software to check the validity of the physical model.

$$\text{Fitness Function}_4 : \text{Min}\left\{\text{t}_{\text{cycle}}\right\} = \text{Min}\left\{\frac{\text{T}_{\text{h}}^2}{\pi^2 \cdot \alpha_{\text{s}}} \cdot \text{Ln}\left(\frac{4}{\pi} \cdot \frac{\text{T}_{\text{melt}} - \text{x}(1)}{\text{T}_{\text{eject}} - \text{x}(1)}\right)\right\} \tag{15}$$

### *3.4. Locating regions of mesh $\mathcal{D}'$ to be cooled by means of baffles or horizontal straight channels*

Based on the geometric data of the depth map $[\tau_{cavity}, \tau_{core}] \in \mathbb{R}^3$, the proposed algorithm determines the regions belonging to $\mathcal{D}'$ that can be cooled using horizontal straight channels and the regions belonging to $\mathcal{D}'$ which, due to their depth and geometry, require more specific cooling systems such as the use of baffles.

**Table 2**
Definition of the technical optimization problem.

| Genetic algorithm options structure | Defined set-up | Description |
|---|---|---|
| Population | Double vector | Initial population from which the evolutionary cycle begins. "Double Vector" method since the variables are of double and decimal type. |
| Scaling function | Fitness Rank | A scaling function increases the differentiation between the optimal ones, reducing the probabilities of generating individuals with less aptitude in subsequent generations. |
| Selection | Uniform Stochastic | Local search around promising solutions without losing the randomness component needed to explore other solutions in the search domain. |
| Reproduction | Two Points | Generation of the children corresponding to each new generation, based on the arithmetic mean of two randomly selected parents of the population. |
| Mutation | 2% | Fraction of the individuals of the mutated population, whose value is replaced by another random value chosen from the population range. |
| Crossover factor | 80% | Crossover factor specifying the fraction of individuals of the next generation that is susceptible to cross-over. |
| Migration | Direction: Forward<br>Migration interval: 20<br>Migration factor: 0.3 | Forward translation of individuals of the population between regions of the domain. At each migration interval the best individuals of one generation (selected via the migration factor) replace the worst of another region. |

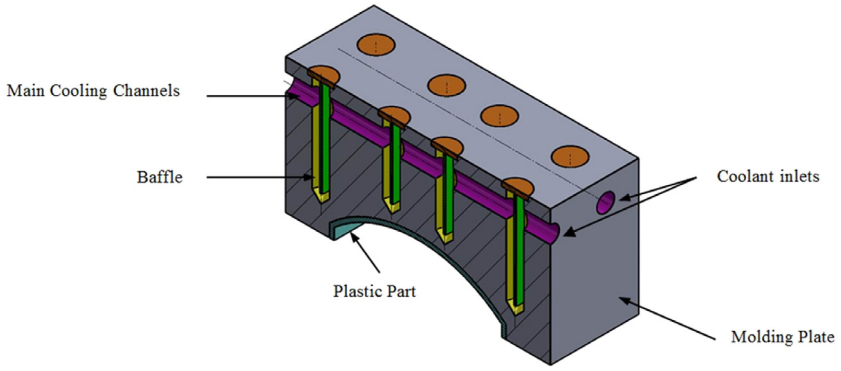


**Fig. 8.** Cooling system by means of baffles.

*3.4.1. Location of regions of the $\mathcal{D}'$ mesh cooled by means of baffles*

This section determines the plastic part regions that require the use of auxiliary cooling elements such as baffles. The location of the main cooling channels, and especially the baffles, depends basically on the geometrical characteristics of the plastic part. Flat, slim and shallow parts can be cooled using a conventional channels system without the need for baffles. However, pieces with large concavities, internal turrets, housings, etc. require the application of baffles to improve the cooling process and to bring the coolant to concave regions where the perforated rectilinear channels lose their functionality. The operating structure of a baffle system is shown in Fig. 8.

The purpose of this section is to determine the magnitude of the limit range distance from which perforated straight channels lose effectiveness and are not capable of cooling deep regions of the plastic part. To do this, the heat flow provided by the melt plastic flow is estimated according to the Fourier Law as Eq. (16).

$$\dot{Q}_{inj} = \frac{\left(c_p \cdot (T_{melt} - T_{eject}) + i_m\right) \cdot \rho_p \cdot \upsilon_p}{t_{cycle}} \tag{16}$$

where $\dot{Q}_{inj}$ [W] represents the heat flow per unit time given by the melt plastic to the mold, $i_m$ [J/kg] the latent heat of fusion of the polymer, and $\upsilon_p$ [mm$^3$] the volume of injected polymer. Since the present model studies the cavity and core plate independently, the heat transferred by the melt plastic flow is evenly distributed according to the region of the part demolded by means of cavity and core plate, respectively Eqs. (17)–(18).

$$\dot{Q}_{inj} = \dot{Q}_{inj_{cavity}} + \dot{Q}_{inj_{core}} \tag{17}$$

where.

$$\dot{Q}_{inj_{cavity}} = \dot{Q}_{inj} \cdot \frac{A_{cavity}}{A_{cavity} + A_{core}} \; ; \quad \dot{Q}_{inj_{core}} = \dot{Q}_{inj} \cdot \frac{A_{core}}{A_{cavity} + A_{core}} \tag{18}$$

$A_{cavity}$ [mm$^2$] is the area of the region of the part that is molded by means of a cavity plate and $A_{core}$ [mm$^2$] the area of the region of the part that is molded by means of core plate. After evaluating the heat flow transferred by the melt plastic to the cavity plate and the core plate respectively, and according to the Fourier law, the safety distances $L_{S_{cavity}}$ and $L_{S_{core}}$ from which the perforated rectilinear channels lose effectiveness are set as Eq. (19).

$$L_{S_{cavity}} = \frac{A_{cavity} \cdot \delta_s}{\dot{Q}_{inj_{cav}}} \cdot \left(\overline{T_m} - T_{C_{min}}\right) \; ; \quad L_{S_{core}} = \frac{A_{core} \cdot \delta_s}{\dot{Q}_{inj_{cor}}} \cdot \left(\overline{T_m} - T_{C_{min}}\right) \tag{19}$$

where $T_{C_{min}}$ [°C] represents the minimum operating temperature of the coolant, i.e. the minimum temperature from which the

fluid loses its cooling properties. The magnitude of this parameter is 10 °C according to the limit values of the vacutherm coolant temperature controller (see Tables 1, 2) [32].

Finally, based on the depth map of the mesh $\mathcal{D}$' ($\tau_{cavity} \in \mathbb{R}^3$ y $\tau_{core} \in \mathbb{R}^3$) (Figs. 7a and 7b) the nodes $\lambda_{t_{cavity}}(i,j) \in \mathbb{R}^3$, $\lambda_{t_{core}}(i,j) \in \mathbb{R}^3$ whose depth $\tau_{cavity}$ (i, j) , $\tau_{core}(i,j)$ is greater than the safety distances $L_{S_{cavity}}$ y $L_{S_{core}}$ are located Eq. (20). Thus, if a node $\lambda_{t_{cavity}}(i,j) \in \mathbb{R}^3$ meets the condition of having a depth $\tau_{cavity}(i,j) \in \mathbb{R}^3$ greater than $L_{S_{cavity}}$ it is stored in the array $\beta_{cavity}(i,j) \in \mathbb{R}^3$. Similarly, if a node $\lambda_{t_{core}}(i,j) \in \mathbb{R}^3$ meets the condition of having a depth $\tau_{\text{core}}$ (i, j) $\in \mathbb{R}^3$ greater than $L_{S_{\text{core}}}$ it is stored in array $\beta_{\text{core}}$(i, j) $\in \mathbb{R}^3$.

$$\begin{aligned}
&\forall\, \lambda_{t_{\text{cavity}}}(\text{i, j}) \in \mathbb{R}^3 \mid \tau_{\text{cavity}}(\text{i, j}) \\
&\quad \geq L_{S_{\text{cavity}}} \rightarrow \lambda_{t_{\text{cavity}}}(\text{i, j}) \in \beta_{\text{cavity}}(\text{i, j}) \in \mathbb{R}^3 \\
&\forall\, \lambda_{t_{\text{core}}}(\text{i, j}) \in \mathbb{R}^3 \mid \tau_{\text{core}}(\text{i, j}) \\
&\quad \geq L_{S_{\text{core}}} \rightarrow \lambda_{t_{\text{core}}}(\text{i, j}) \in \beta_{\text{core}}(\text{i, j}) \in \mathbb{R}^3
\end{aligned} \tag{20}$$

Fig. 9a shows the depth map $\tau_{cavity}(i,j) \in \mathbb{R}^3$ for the surfaces $\Omega_{f1} \in \mathbb{R}^3$. The map $\tau_{cavity}$ represents the depth of each node $\lambda_{t_{cavity}}(i,j)$ of the mesh $\Omega_{f1} \in \mathbb{R}^3$ by means of a color coding. The graduated bar on the right indicates the values $\tau_{cavity}(i,j)$ in millimeters for each node $\lambda_{t_{cavity}}(i,j)$. The locus of the parameter $L_{S_{cavity}}$ is represented by the plane $\pi_p : z = L_{S_{cavity}}$. For the mesh $\Omega_{f1} \in \mathbb{R}^3$ of Fig. 9a the value $L_{S_{cavity}}$ is 20 mm. The regions of $\Omega_{f1}$ whose depth $\tau_{cavity}(i,j)$ is greater than 20 mm are stored in the array $\beta_{cavity}(i,j) \in \mathbb{R}^3$, requiring the use of baffles for the design of their cooling system. Fig. 9b indicates the depth map $\tau_{core}(i,j) \in \mathbb{R}^3$ for the mesh $\xi_{f2} \in \mathbb{R}^3$. The locus of the parameter $L_{S_{core}}$ is represented by the plane $\pi_p : z = L_{S_{core}}$. In Fig. 10b the location of nodes $\beta_{core}(i,j) \in \mathbb{R}^3$ whose depth is greater than $L_{S_{core}}$, and therefore require the use of baffles for the design of their cooling system, has been indicated.

#### 3.4.2. Location of regions of $\mathcal{D}'$ mesh cooled by a straight horizontal channel system

On the other hand, this section determines the plastic part regions that do not require the use of auxiliary cooling elements such as baffles. For those regions of the plastic part whose depth $\tau_{cavity}(i,j) \in \mathbb{R}^3$ and $\tau_{core}(i,j) \in \mathbb{R}^3$ do not exceed the safety distance $L_{S_{cavity}}$ y $L_{S_{core}}$ respectively, the proposed methodology is adapted using a traditional solution of perforated straight channels. Thus, if a node $\theta_{t_{cavity}}(i,j)$ meets the condition of having a depth $\tau_{cavity}(i,j) \in \mathbb{R}^3$ less than $L_{S_{cavity}}$, then it is stored in the array $\omega_{cavity}(i,j) \in \mathbb{R}^3$. Similarly, if a node $\theta_{t_{core}}(i,j)$ satisfies the condition of having a depth $\tau_{core}(i,j) \in \mathbb{R}^3$ greater than $L_{S_{core}}$, then is stored in array $\omega_{core}(i,j) \in \mathbb{R}^3$. Fig. 10a shows the nodes $\omega_{cavity}(i,j) \in \mathbb{R}^3$ by means of the depth map $\tau_{cavity}(i,j) \in \mathbb{R}^3$.

Fig. 10b shows the nodes $\omega_{core}(i,j) \in \mathbb{R}^3$ by means of the depth map $\tau_{core}(i,j) \in \mathbb{R}^3$.

The geometric layout of the straight-drilled channels from the nodes $\omega_{cavity}(i,j) \in \mathbb{R}^3$ and $\omega_{core}(i,j) \in \mathbb{R}^3$ of the $\mathcal{D}$' mesh is performed uniformly according to the technical and geometric parameters obtained in the optimization process of the physical model. To do this, the available domain from the nodes $\omega_{cavity}(i,j) \in \mathbb{R}^3$ and $\omega_{core}(i,j) \in \mathbb{R}^3$ and the required distance between each cooling channel $L_b$ are evaluated as described in Appendix A.1. The number and the uniform geometric layout of the perforated straight channels are also determined. The remaining parameters $D_{baffles}$ and $L_p$ follow the physical model are described in Appendix A.1. The functionality of perforated straight channels is therefore guaranteed since the application region $\omega_{cavity}(i,j) \in \mathbb{R}^3$ and $\omega_{core}(i,j) \in \mathbb{R}^3$ have depths $\tau_{cavity}(i,j) \in \mathbb{R}^3$ and $\tau_{core}(i,j) \in \mathbb{R}^3$, lower than the established limit values $L_{S_{cavity}}$ y $L_{S_{core}}$.

### 3.5. Boundary conditions

In the cavity and core plates of an injection mold several mechanical systems optimize the manufacturing process of the plastic part. The most important systems are the cooling and the ejection system of the plastic part. Therefore, for a properly geometrical design of the injection mold both systems (cooling and ejection) must be compatible and not create interferences between them. In this section, the defined a set of boundary conditions are established so that the design of the cooling system is compatible with the design of the ejection system.

#### 3.5.1. Interference between the cooling system and the ejection system

The algorithm evaluates the interference between the cooling system and the ejection system of the plastic part for the core plate of the mold. To obtain the location of each ejector $\Phi_{ejector}(i,j)$ and its diameter $\emptyset_{\text{ejector}}$ the algorithm takes as input data the result of applying the procedure developed by the authors [33] to the $\mathcal{D}'$ mesh (see Fig. 11) Eq. (21). Using this information, the algorithm detects and eliminates the nodes $\beta_{core}(i,j) \in \mathbb{R}^3$ that lie within the domain $\Delta_{ejec} \in \mathbb{R}^3$ defined as Eq. (22).

$$\forall\, \Phi_{\text{ejector}}(\text{i, j}) \,\exists\, \Delta_{\text{ejec}} \in \mathbb{R}^2 \mid \text{A}\left(\Delta_{\text{ejec}}\right) = \left(\emptyset_{\text{ejector}} + 2 \cdot \text{L}_{\text{p}}\right) \cdot \text{w} \tag{21}$$

$$\forall\, \beta_{\text{core}}(\text{i, j}) \in \mathbb{R}^3 \mid \beta_{\text{core}}(\text{i, j}) \in \Delta_{\text{ejec}} \rightarrow \beta_{\text{core}}(\text{i, j}) = \emptyset \tag{22}$$

where $A\left(\Delta_{ejec}\right)$ is the safety area around the ejectors, $L_p$ is the safety distance on both sides of $\emptyset_{ejector}$ and $w$ is the length of the Bounding Box of the part along the Y axis. The flat geometric region $\Delta_{ejec} \in \mathbb{R}^2$ is defined by the sum of the largest of the ejector diameters and the structural safety distance $L_p$ (see Fig. 11). In this way the design of the cooling system is linked to the ejection system, avoiding any type of interference between both that would compromise the structural safety of the mold.

### 3.6. Baffles location via the genetic algorithm

After applying the boundary conditions on the set of nodes $\beta_{cavity} \in \mathbb{R}^3$ y $\beta_{core} \in \mathbb{R}^3$, this section establishes the location and final coordinates of the baffles of the cooling system. For this purpose the algorithm employs a genetic optimization algorithm that guarantees a balanced and uniform cooling system.

#### 3.6.1. Initial population

First, the population or the set of nodes from which the optimal solution will be obtained are determined. The set of nodes $\beta_{cavity} \in \mathbb{R}^3$ and $\beta_{core} \in \mathbb{R}^3$ is considered as the initial population. However, the algorithm performs a prior segmentation of the node population with the objective of reducing and optimizing both the execution time and the computational cost of the geometric optimization problem, guaranteeing the optimal solution of the problem. For this, the algorithm defines a sequence of 3D isocontours along the surface formed by $\beta_{cavity} \in \mathbb{R}^3$ and $\beta_{core} \in \mathbb{R}^3$, separated at equidistance $D_p$ (see Fig. 12(a) and (b). The value of the parameter $D_p$ is equal to the separation distance between baffles $L_b$ plus their diameter $D_{baffles}$. The parameters $L_b$ and $D_{baffles}$ related to the dimensioning of the cooling system have been defined in the paper in Appendix A.1. The nodes that make up the initial population of study and that belong to the 3D isocontours are defined as $B_{cavity}(i,j) \in \mathbb{R}^3$ and $B_{core}(i,j) \in \mathbb{R}^3$, respectively. In Fig. 14(a) and (b) the 3D isocontours that make up the study population $B_{core} \in \mathbb{R}^3$ are indicated.

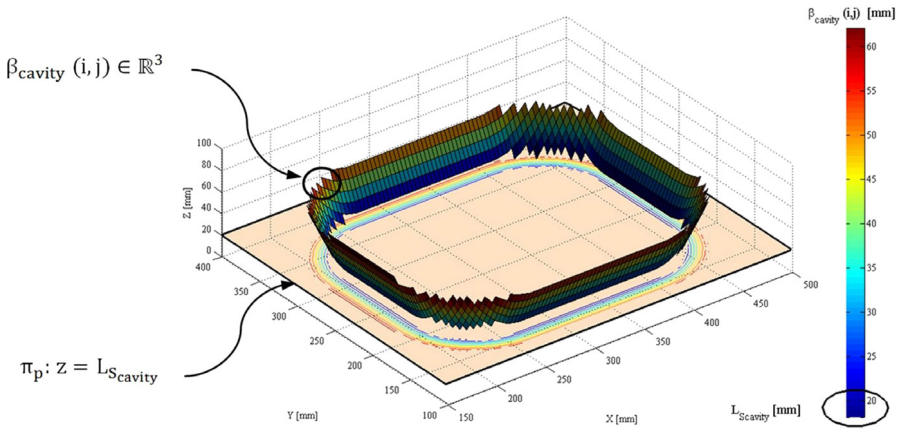


**Fig. 9a.** Obtaining nodes $\beta_{cavity}(i, j)$ from the depth map $\tau_{cavity}$ of the plastic part.

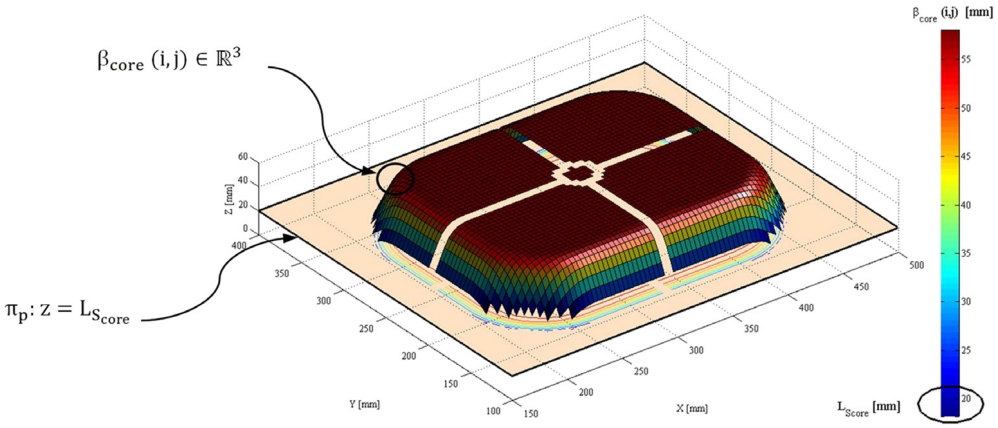


**Fig. 9b.** Obtaining nodes $\beta_{core}(i, j)$ from the depth map $\tau_{core}$ of the plastic part.

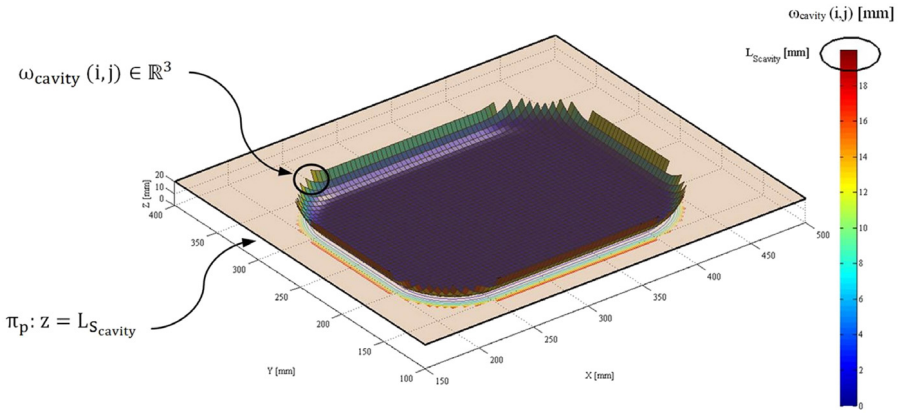


**Fig. 10a.** Obtaining nodes $\omega_{cavity}(i, j)$ from the depth map $\tau_{cavity}$ of the plastic part.

*3.6.2. Number of variables*

The next step of the geometric problem posed is to determine the number of variables. The number of variables is directly proportional to the number of baffles that form the cooling system of the mold. In order to obtain a uniform temperature map on the surface of the cavities that will mold part $\mathcal{D}$, the number of baffles of the cooling system must be maximum. Thus, on each node belonging to $B_{cavity}(i, j) \in \mathbb{R}^3$ and $B_{core}(i, j) \in \mathbb{R}^3$, the center of a circle $r_p\,(i, j) \in \mathbb{R}^2$, with radius equal to $D_p/2$, where $D_p$ is the distance between each 3D isocontour, $B_{cavity}(i, j) \in \mathbb{R}^3$ and $B_{core}(i, j) \in \mathbb{R}^3$. Next, the number of nodes of the 3D isocontours, $B_{cavity} \in \mathbb{R}^3$ or $B_{core} \in \mathbb{R}^3$ contained within each circular contour $r_p\,(i, j) \in \mathbb{R}^2$, except for the node of analysis $B_{cavity}(i, j) \in \mathbb{R}^3$ or $B_{core}(i, j) \in \mathbb{R}^3$ is determined. All nodes $B_{core}(i, j) \in \mathbb{R}^3$ y $B_{cavity}(i, j) \in \mathbb{R}^3$ that meet the geometric condition of being located within the circular contour $r_p\,(i, j) \in \mathbb{R}^2$ will be removed from the count. On the contrary, $B_{cavity}(i, j) \in \mathbb{R}^3$ or $B_{core}(i, j) \in \mathbb{R}^3$ nodes that do not meet the location condition within the locus $r_p\,(i, j) \in \mathbb{R}^2$ will continue to form part of the analysis.

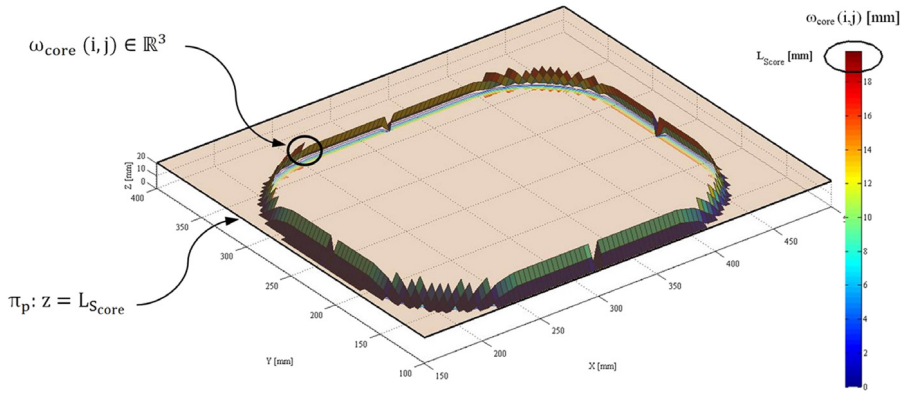


**Fig. 10b.** Obtaining nodes $\omega_{core}(i, j)$ from the depth map $\tau_{core}$ of the plastic part.

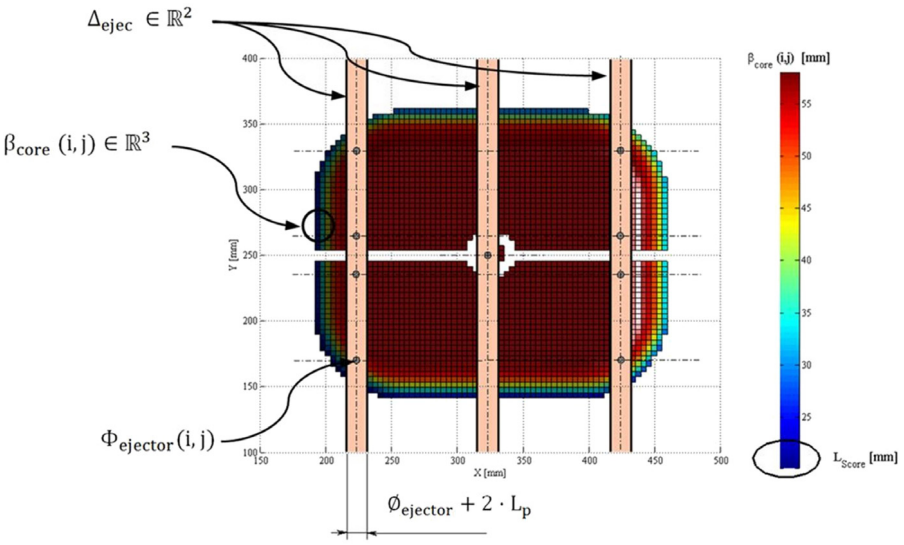


**Fig. 11.** Resolution of the interference between the ejection system , $\Phi_{ejector}$ , and the cooling system in core plate, $\beta_{core}$.

In Fig. 13, an example of locating a circle $r_p\ (i, j)$ from a node $B_{core}(i, j)$ of the geometric region $\beta_{core}$ is indicated.

After applying this condition to each node $B_{cavity} \in \mathbb{R}^3$ and $B_{core} \in \mathbb{R}^3$, the total number of baffles is obtained for the layout for both the cavity plate and the core plate cooling system. The resulting total number of baffles is equal to the number of nodes $B_{cavity}(i, j) \in \mathbb{R}^3$ and $B_{core}(i, j) \in \mathbb{R}^3$ that have met the imposed geometric condition of being located within the contour of one of the circumferences $r_p\ (i, j) \in \mathbb{R}^2$ Eq. (23).

$$\begin{aligned} n_{blaffes_{cavity}} &= \text{size}\left(B_{cavity(in)}\right) \\ n_{blaffes_{core}} &= \text{size}\left(B_{core(in)}\right) \end{aligned} \tag{23}$$

Fig. 14 shows the set of nodes $B_{core}(i, j) \in \mathbb{R}^3$ that have not met the proposed condition. As can be seen, the location of these points is not balanced or uniform, but the total number of these points allows the number of variables of the optimization problem to be determined. Since the variables of the geometric optimization problem represent the coordinates of the geometric center of the different baffles in the coordinate axes X, Y, the final number of variables to be optimized will be equal to twice the maximum number of baffles with which the cooling system is designed for the cavity and core plate, respectively. Thus, the problem variables correspond to the X and Y (xcore, ycore), ($x_{cavity}$, $y_{cavity}$) coordinates of the center of each of the baffles (see Table 3).

### 3.6.3. Options structure and fitness functions

To complete the definition of the optimization problem posed in this section, the rest of the configuration parameters are detailed in Table 4.

The constraints have been set according to the maximum and minimum values of the coordinates of the set of nodes $B_{cavity} \in \mathbb{R}^3$ or $B_{core} \in \mathbb{R}^3$ in the coordinate axes X, Y in order to prevent the solution from converging outside the domain of analysis. To complete the multiobjective optimization problem, the fitness functions to optimize must be entered. First, the optimization algorithm developed in the paper employs a fitness function to ensure that the geometric centers of the baffles are separated from each other at a distance greater than the minimum estimated separation $D_p$ Eq. (27).

The sets of solution nodes are called $P_{baffle_{cavity}} \in \mathbb{R}^3$ and $P_{baffle_{core}} \in \mathbb{R}^3$ Eq. (25). Each solution node $P_{baffle_{cavity}}(i, j) \in \mathbb{R}^3$ and $P_{baffle_{core}}(i, j) \in \mathbb{R}^3$ (see Fig. 15) has associated a distance $d_{baffles_{cavity}}\ (i, j)$ and $d_{baffles_{core}}\ (i, j)$ representing the separation between that node and the nearest solution node Eq. (24). Thus, if all the distances are equal or greater than $D_p$ the fitness function takes a minimum value equal to 0 and otherwise takes maximum

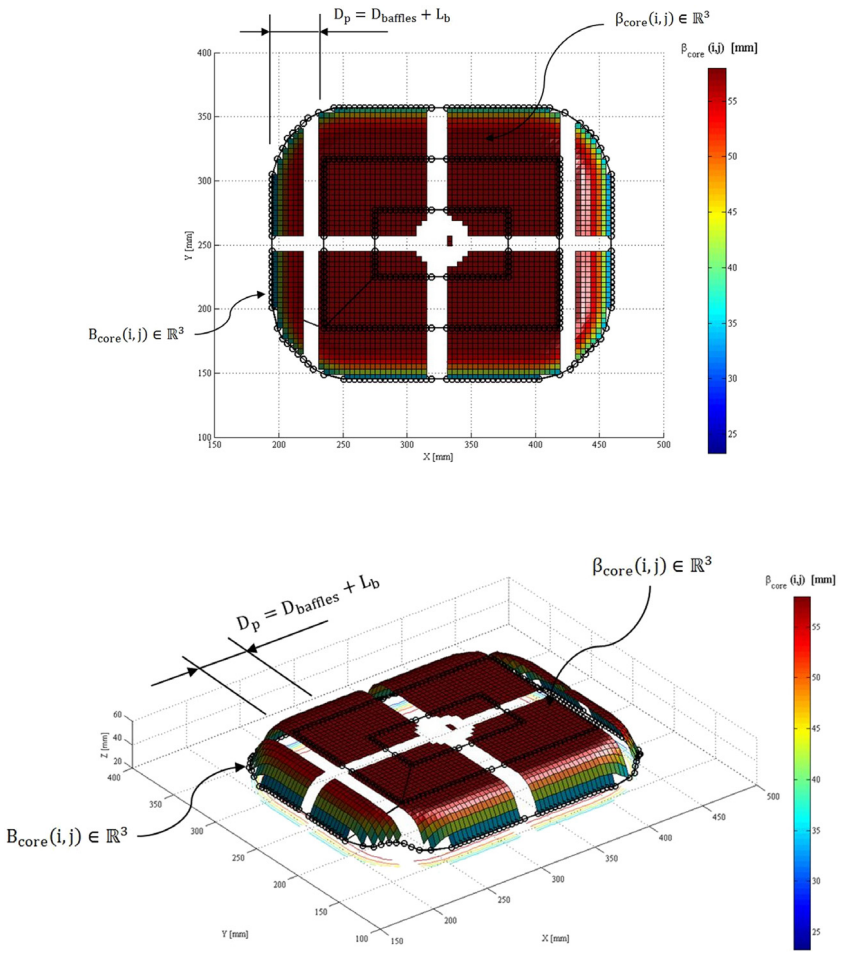


**Fig. 12.** (a) and (b) Representation by isocontours 3D of $\beta_{core}$ nodes of the initial population, $B_{core}$.

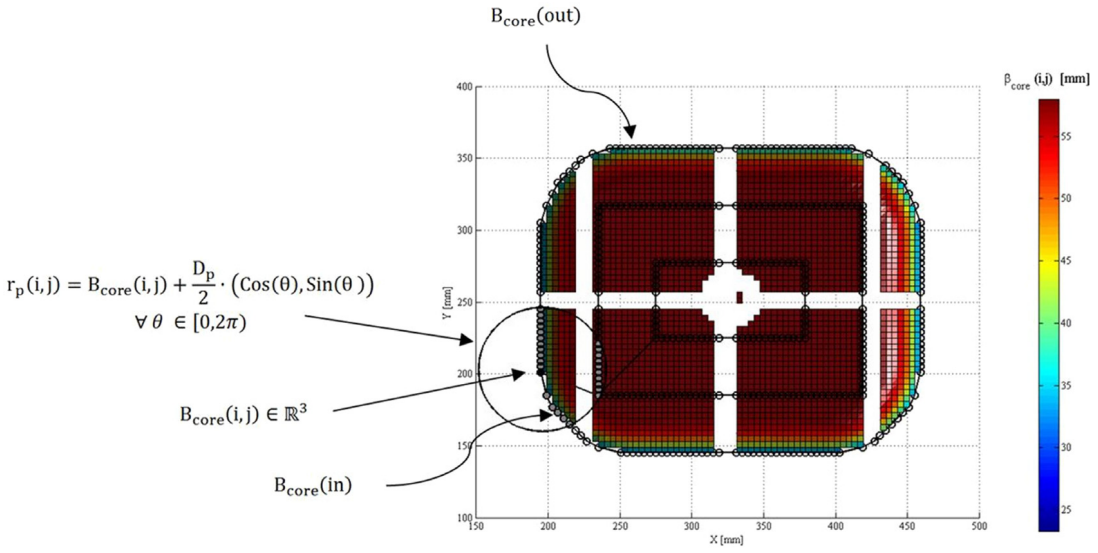


**Fig. 13.** Representation of a circle $r_p$ $(i, j)$ from a node $B_{core}$ $(i, j)$ of the geometric region $\beta_{core}$.

**Table 3**
Variables of the geometric optimization problem.

| Nomenclature | Units | Description | Notation on the optimization problem | Constrains |
|---|---|---|---|---|
| $x_{cavity}$ | mm | X coordinates vector of cavity plate baffles | $x(1) = \{x_{cavity}(1) \quad \ldots \quad x_{cavity}(n_{blaffes_{cavity}})\}$ | $\min(B_{cavity})_x \leq x(1) \leq \max(B_{cavity})_x$ |
| $y_{cavity}$ | mm | Y coordinates vector of cavity plate baffles | $x(2) = \{y_{cavity}(1) \quad \ldots \quad y_{cavity}(n_{blaffes_{cavity}})\}$ | $\min(B_{cavity})_y \leq x(2) \leq \max(B_{cavity})_y$ |
| $x_{core}$ | mm | X coordinates vector of core plate baffles | $x(3) = \{x_{core}(1) \quad \ldots \quad x_{core}(n_{blaffes_{core}})\}$ | $\min(B_{core})_x \leq x(3) \leq \max(B_{core})_x$ |
| $y_{core}$ | mm | Y coordinates vector of core plate baffles | $x(4) = \{y_{core}(1) \quad \ldots \quad y_{core}(n_{blaffes_{core}})\}$ | $\min(B_{core})_y \leq x(4) \leq \max(B_{core})_y$ |

**Table 4**
Definition of the geometric optimization problem.

| Genetic algorithm options structure | Defined set-up |
|---|---|
| Population | Double vector. The set of nodes that are part of the initial population are $B_{cavity,core} \in \mathbb{R}^3$, respectively. See Fig. 13(a), (b). |
| Scaling function | Fitness rank |
| Selection | Uniform stochastic |
| Reproduction | Two points |
| Mutation | 20% |
| Crossover factor | 80% |
| Migration | Direction: Both; Migration interval: 1; Migration factor: 0.8 |

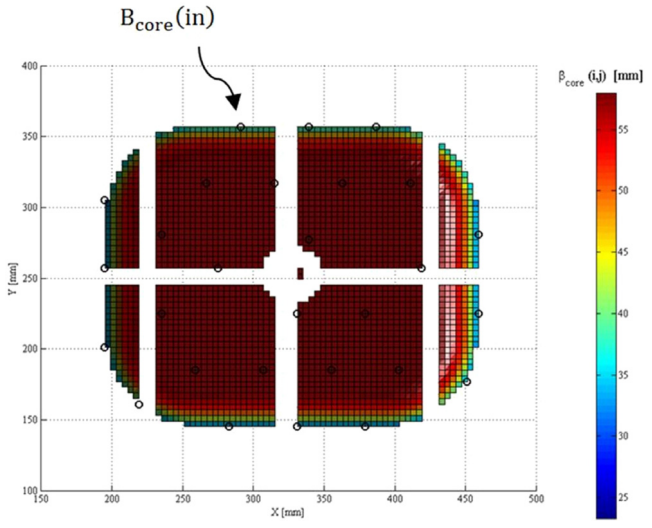


**Fig. 14.** Nodes $B_{core}(i, j)$ that do not meet the condition of being contained in the circular regions $r_p(i, j)$.

values equal to infinity Eq. (26).

$$P_{baffle_{cavity}}(i, j) = \{x_{cavity}(i, j)_x \quad y_{cavity}(i, j)_y \quad z_{cavity}(i, j)_z - L_p\}$$
$$P_{baffle_{core}}(i, j) = \{x_{core}(i, j)_x \quad y_{core}(i, j)_y \quad z_{core}(i, j)_z - L_p\} \tag{24}$$

The Z coordinate of the solution points $P_{baffle_{cavity}}(i, j) \in \mathbb{R}^3$ and $P_{baffle_{core}}(i, j) \in \mathbb{R}^3$ is obtained by projecting solution $P_{baffle_{cavity}}(i, j) \in \mathbb{R}^3$ and $P_{baffle_{core}}(i, j) \in \mathbb{R}^3$ on the surface formed by the set of nodes $\beta_{cavity} \in \mathbb{R}^3$ and $\beta_{core} \in \mathbb{R}^3$. According to the structural safety requirements established in this paper, the magnitude of the coordinates in the Z axis of the solution points are subtracted by the structural safety distance $L_p$.

$$\forall P_{baffle_{cavity}}(i, j) \in \mathbb{R}^3 \exists\, d_{baffles_{cavity}}(i, j)$$
$$\forall P_{baffle_{core}}(i, j) \in \mathbb{R}^3 \exists\, d_{baffles_{core}}(i, j) \tag{25}$$
$$\text{If all } (d_{baffles_{cavity}}) \geq D_p \rightarrow f_{1_{cavity}} = 0;\ \text{else} \rightarrow f_{1_{cavity}} = \text{Inf}$$
$$\text{If all } (d_{baffles_{core}}) \geq D_p \rightarrow f_{1_{core}} = 0;\ \text{else} \rightarrow f_{1_{core}} = \text{Inf} \tag{26}$$
$$\text{Fitness Function}_1 : \text{Min}\{f_{1_{cavity}} \quad f_{1_{core}}\} \tag{27}$$

Secondly, in order to favor heat exchange in regions with greater concavity, the sum of the Z coordinates of the solution nodes $P_{baffle_{cavity}} \in \mathbb{R}^3$ and $P_{baffle_{core}} \in \mathbb{R}^3$ must be maximum Eq. (28).

$$\text{Fitness Function}_2 : \text{Max}\{z_{cavity}(i, j)_z \quad z_{core}(i, j)_z\} \tag{28}$$

Thirdly, in order to obtain a balanced cooling system design the distance between the projection in the XY plane of the mass center of the solution nodes (baffles geometric center) and the projection in the XY plane of the mass center of the plastic part should be minimal.

$$CM_{baffle_{cavity}} = \left[\frac{\sum x_{cavity}(i, j)}{size(x_{cavity})} \quad \frac{\sum y_{cavity}(i, j)}{size(y_{cavity})}\right]$$
$$CM_{baffle_{core}} = \left[\frac{\sum x_{core}(i, j)}{size(x_{core})} \quad \frac{\sum y_{core}(i, j)}{size(y_{core})}\right] \tag{29}$$

$$\text{Fitness Function}_3 : \text{Min}\{|CM_{baffle_{cavity}} \quad CM_{xy}| \quad |CM_{baffle_{core}} \quad CM_{xy}|\} \tag{30}$$

Finally, in order to obtain a uniform cooling system design the variance Eqs. (33)–(36) of the distances between baffles in the coordinate axes X, Y must be minimal Eq. (32). Each solution point $P_{baffle_{cavity}}(i, j) \in \mathbb{R}^3$ and $P_{baffle_{core}}(i, j) \in \mathbb{R}^3$ has associated a vector of distance $d_{baffles_{cavity}}(i, j)_{x,y}$ and $d_{baffles_{core}}(i, j)_{x,y}$ representing the separation distance between that node and the solution node closest to it in the coordinate axes X, Y Eq. (31). In the case where a pair of nodes are aligned with each other on a coordinate axis, the distance between them is assigned as 0. Fig. 15 shows the definition of the distance vectors $d_{baffles_{cavity}}(i, j)_{x,y}$ and $d_{baffles_{core}}(i, j)_{x,y}$ on the final solution of the geometric optimization problem.

$$\forall P_{baffle_{cavity}}(i, j) \in \mathbb{R}^3 \exists\, d_{baffles_{cavity}}(i, j)_{x,y}$$
$$\forall P_{baffle_{core}}(i, j) \in \mathbb{R}^3 \exists\, d_{baffles_{core}}(i, j)_{x,y} \tag{31}$$
$$\text{Fitness Function}_4 : \text{Min}\{\text{Var}(d_{baffles_{cavity_{x,y}}}) \quad \text{Var}(d_{baffles_{core_{x,y}}})\} \tag{32}$$

$$\text{Var}(d_{baffles_{cavity_{x,y}}}) = \frac{1}{size(d_{baffles_{cavity_{x,y}}})} \cdot \sum_{i=1}^{size(d_{baffles_{cavity_{x,y}}})} \times \left|d_{baffles_{cavity_{x,y}}}(i) - \mu_{baffles_{cavity_{x,y}}}\right|^2 \tag{33}$$

where

$$\mu_{\text{baffles}_{\text{cavity}_{x,y}}} = \frac{1}{\text{size}(\text{d}_{\text{baffles}_{\text{cavity}_{x,y}}})} \cdot \sum_{i=1}^{\text{size}(\text{d}_{\text{baffles}_{\text{cavity}_{x,y}}})} \text{d}_{\text{baffles}_{\text{cavity}_{x,y}}}(i) \tag{34}$$

Similarly for the solution corresponding to the core plate Eqs. (35)–(36).

$$\text{Var}\left(\text{d}_{\text{baffles}_{\text{core}_{x,y}}}\right) = \frac{1}{\text{size}(\text{d}_{\text{baffles}_{\text{core}_{x,y}}})} \cdot \sum_{i=1}^{\text{size}(\text{d}_{\text{baffles}_{\text{core}_{x,y}}})} \times \left|\text{d}_{\text{baffles}_{\text{core}_{x,y}}}(i) - \mu_{\text{baffles}_{\text{core}_{x,y}}}\right|^2 \tag{35}$$

where

$$\mu_{\text{baffles}_{\text{core}_{x,y}}} = \frac{1}{\text{size}(\text{d}_{\text{baffles}_{\text{core}_{x,y}}})} \cdot \sum_{i=1}^{\text{size}(\text{d}_{\text{baffles}_{\text{core}_{x,y}}})} \text{d}_{\text{baffles}_{\text{core}_{x,y}}}(i) \tag{36}$$

In addition, in order for the solution to encompass the maximum domain $\beta_{cavity} \in \mathbb{R}^3$ and $\beta_{core} \in \mathbb{R}^3$, the difference between the sum of the distance vectors $d_{baffles_{cavity}}(i,j)_{x,y}$ and $d_{baffles_{core}}(i,j)_{x,y}$ and the lengths of the Bounding Box of the plastic part l and w must be minimal (the definition of the Bounding Box of the plastic part has been detailed in Section 3.2) Eq. (37).

$$\text{Fitness Function}_5 : \text{Min} \left\{ \begin{array}{ll} \sum \text{d}_{\text{baffles}_{\text{cavity}_x}}(\text{i},\text{j}) - \text{l} & \sum \text{d}_{\text{baffles}_{\text{cavity}_y}}(\text{i},\text{j}) - \text{w} \\ \sum \text{d}_{\text{baffles}_{\text{core}_x}}(\text{i},\text{j}) - \text{l} & \sum \text{d}_{\text{baffles}_{\text{core}_y}}(\text{i},\text{j}) - \text{w} \end{array} \right\} \tag{37}$$

After the application of the optimization algorithm in Fig. 16, the result of the geometric centers of the baffles $P_{baffle_{core}}(i,j) \in \mathbb{R}^3$ is presented. As shown in Fig. 16, the cavity plate does not require the use of baffles for the design of the cooling system. The entire domain of $\beta_{cavity} \in \mathbb{R}^3$ meets the boundary conditions detailed in Section 3.4.2 and therefore $\beta_{cavity} \in \mathbb{R}^3$ results in an empty set with respect to the number of baffles. The modeling of the cooling system for the cavity plate is carried out through evenly distributed horizontal channels, according to the technical and geometric parameters obtained in Section 3.3.

Fig. 16 shows the design of the resulting cooling system after applying the algorithm to the plastic part $\mathcal{D}$. The coordinates of the geometric centers of the baffles, and the calculated technical and geometric parameters $\overline{T_m}$ [°C], $T_c$ [°C], $L_b$ [mm] and $D_{baffles}$ [°C] are exported to a calculation software with the objective of performing a simulation in order to validate and verify the efficiency and performance of the proposed model.

## 4. Implementation and results

In order to demonstrate the benefit of the algorithm proposed in this paper it has been applied to four industrial parts with complex shapes, manufactured by means of the plastic injection process. The accuracy of the nodal mesh ($\varepsilon$) for each geometry is set according to the dimension of the smallest detail of the part. The algorithms have been developed in the software Matlab R2013a [34] with a Toshiba notebook with a Pentium (R) Dual-Core CPU T4200@2.20 GHz processor and a RAM memory of 3.00 GB.

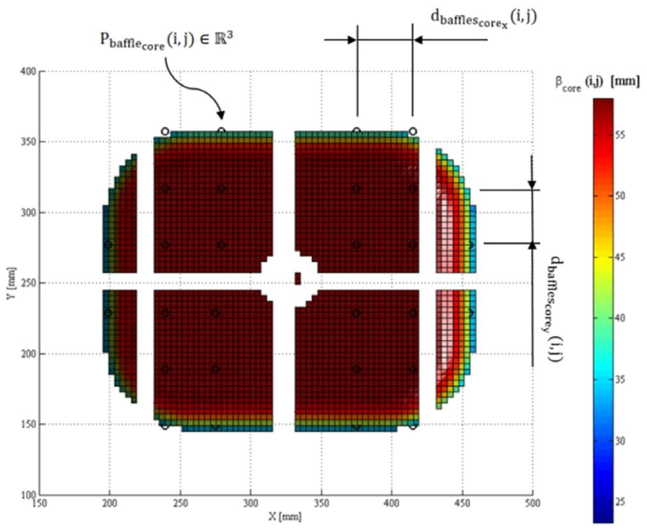


**Fig. 15.** Location of solution nodes $P_{baffle_{core}}(i,j)$ and representation of separating distances $d_{baffles_{core}}(i,j)_{x,y}$.

**Table 5a**
Material properties of the plastic part.

| Material: ABS | Nomenclature | Value | Units |
|---|---|---|---|
| Melt density | $\rho_c$ | 0.979 | kg/mm$^3$ |
| Melt specific heat | $c_p$ | 2012 | J/kg °C |
| Latent heat of fusion of the polymer | $i_m$ | 130 000 | J/kg |
| Melt temperature | $T_{melt}$ | 270 | °C |
| Ejection temperature | $T_{eject}$ | 135 | °C |

The proposed method generates an automatic cooling system design without the need for post-processing operations. In addition, the arrangement of the elements of the cooling system and its technical parameters are automatically defined. The simulations carried out to validate the proposed algorithm have been performed using the injection molding simulation software MoldFlow Advisor [35]. The proposed methodology generates a resulting array that includes: the coordinates X, Y, Z of the points defining the baffles, the diameter of the cooling system elements, the mold surface temperature and the coolant temperature. This information is imported into Moldflow to generate and size the main cooling channels and baffles of the mold cooling system. Acrylonitrile butadiene styrene (ABS) is used as the thermoplastic part material and structural steel (P20) is employed as the material for the plates and components of the injection mold. The materials used for the validation of the proposed algorithm are given in Tables 5a, 5b and 6. The coolant used is water and the value of the nominal flow used is that which maintains the additional Reynolds number equal to $1.5 \cdot 10^4$ (turbulent flow), and the inlet temperature of the coolant is obtained as a result of the proposed algorithm.

Both the injection temperature and the ejection temperature are assumed to be uniform throughout the analytical study presented in this paper. The value of each of these parameters is determined by the manufacturer as standard quantities for correct injection and subsequent ejection of the thermoplastic material.

### 4.1. Case studies

The results of applying the proposed algorithm for the four plastic parts (Case A, B, C, D) Figs. 17, 23, 29 and 35 are shown in Figs. 18, 24, 30 and 36. The geometric distribution and location of the baffles and the main cooling channels and the value of their diameters are calculated automatically. Furthermore, the temperature and pressure distribution of the coolant (Figs. 19, 25,

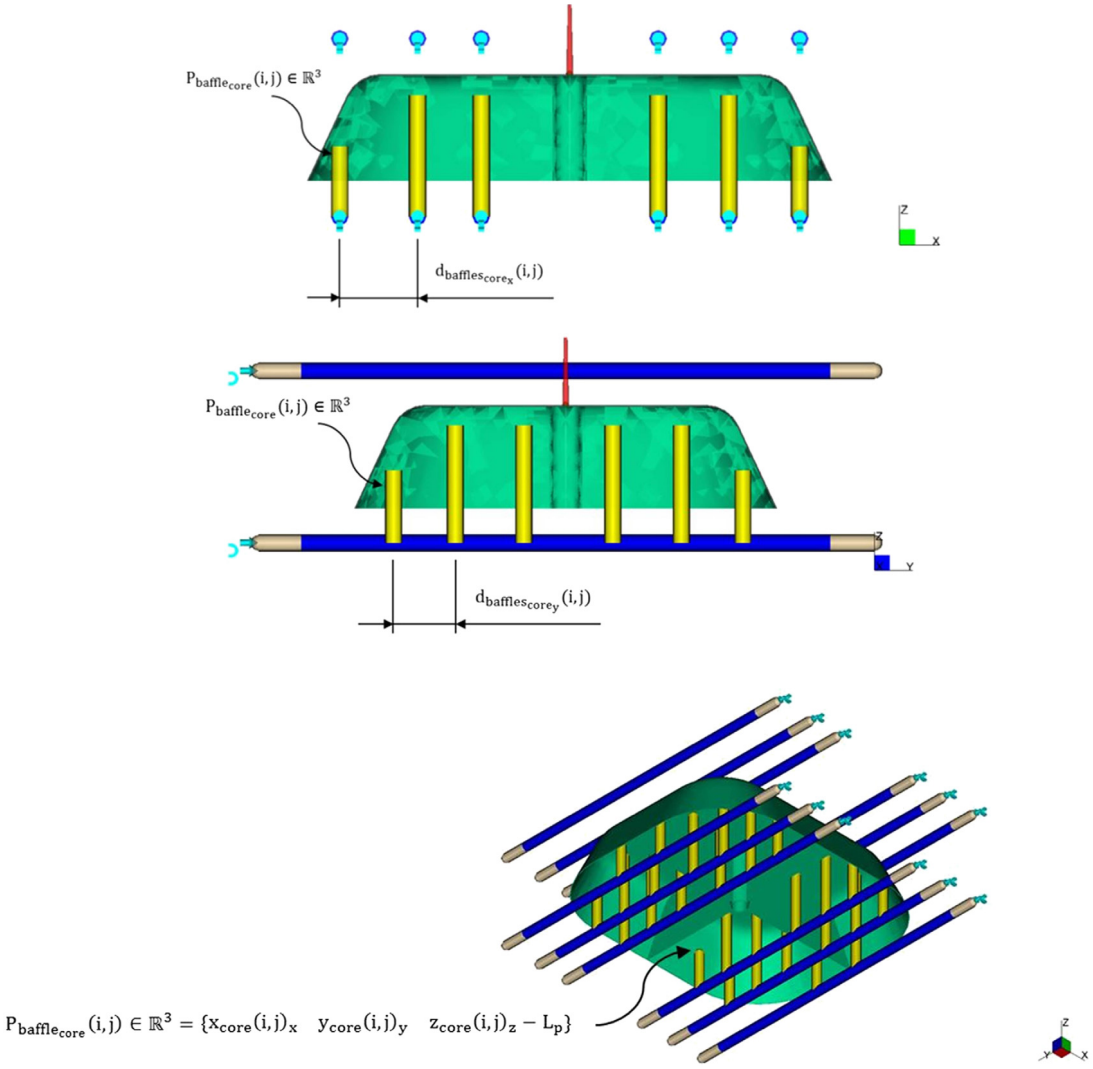


**Fig. 16.** Solution for the design of the cooling system for part $\mathcal{D}$.

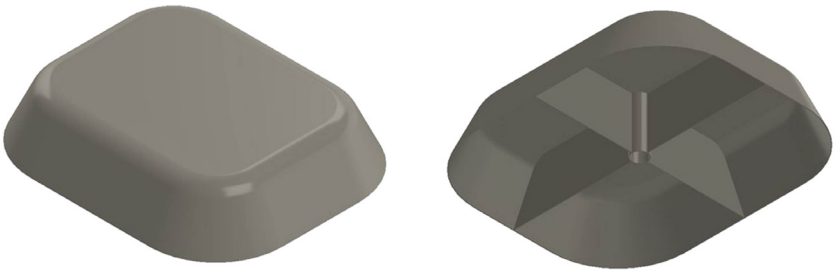

**Fig. 17.** Plastic part, Case A.

**Table 5b**
Material properties of the injection mold.

| Material: Structural steel P-20 | Nomenclature | Value | Units |
|---|---|---|---|
| Thermal conductivity | $\delta_s$ | 45 | W/m °C |
| Heat transfer coefficient between mold and coolant | $h$ | 4500 | W/m$^2$ °C |
| Thermal diffusivity | $\alpha_s$ | $8.73 \cdot 10^{-8}$ | m$^2$/s |

31, 37), the temperature map for each plastic part (Figs. 20, 26, 32, 38) and the cycle time map or time to reach ejection temperature (Figs. 22, 28, 34, 40) were added for the validation of each case study. The results of the algorithm for each plastic part are shown in Tables 7–10 that contain the diameter of the cooling channels and baffles $D_{baffles}$ [mm], the separation distance between baffles $L_b$ [mm], the cooling quality of the system as a percentage, the temperature of the cooling fluid $T_c$ [°C], the average time needed

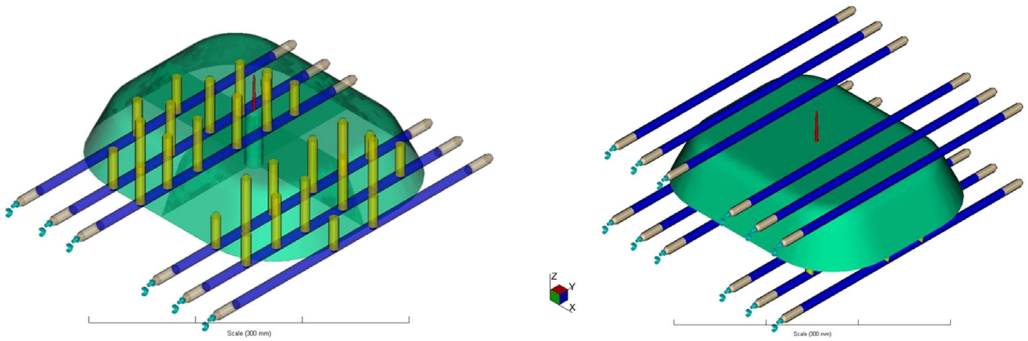

**Fig. 18.** Geometric solution of the hybrid cooling system design, Case A.

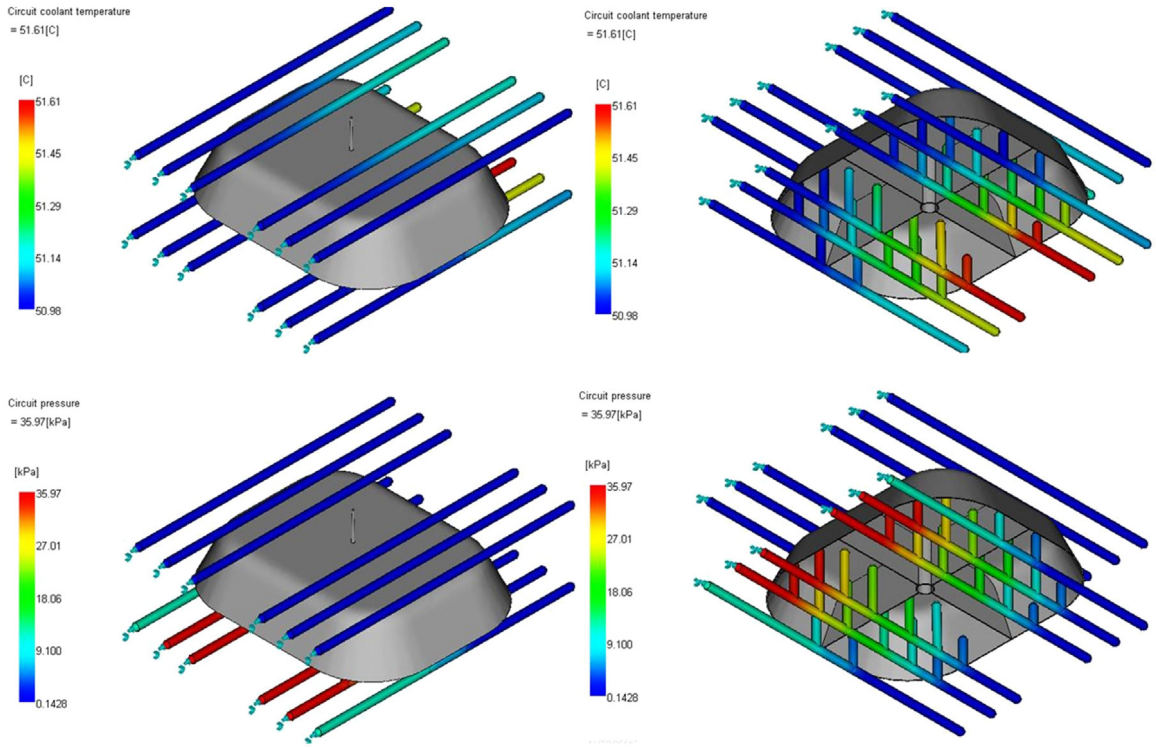


**Fig. 19.** Distribution of the pressure field [kPa] and temperatures [°C] of the coolant along the cooling system, Case A.

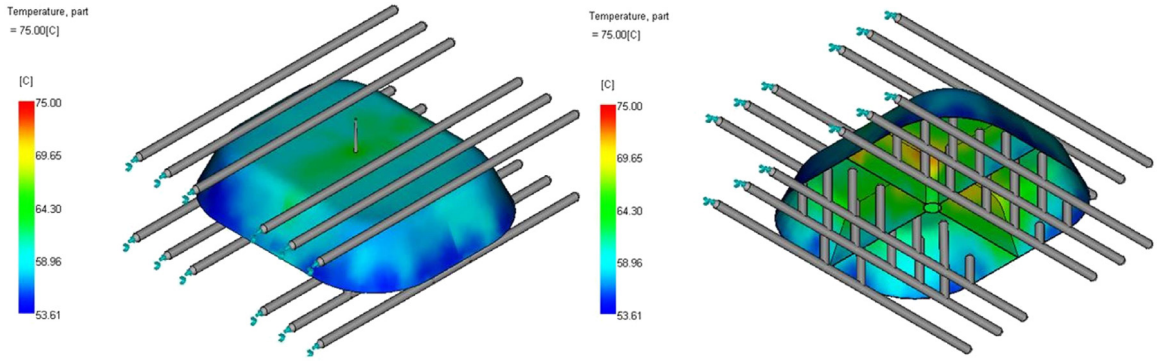


**Fig. 20.** Distribution of the average temperature field at the surface of the plastic part during the cooling phase, Case A.

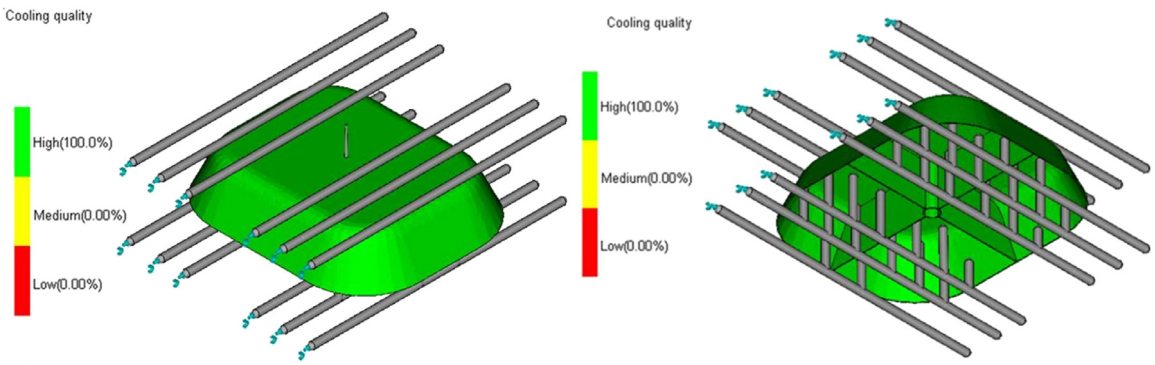


**Fig. 21.** Final quality of cooling along the geometry of the plastic part, Case A.

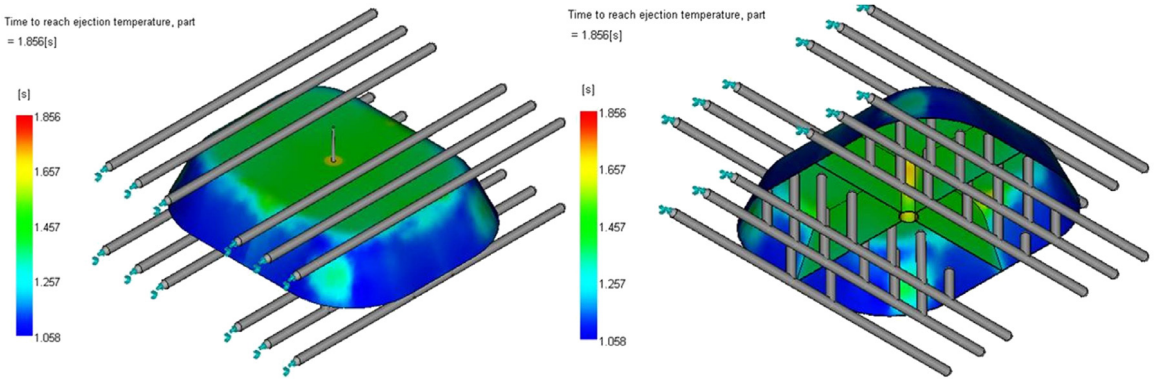


**Fig. 22.** Distribution of the cycle time [s] or time until reaching the ejection temperature on the surface of the plastic part, Case A.

**Table 6**
Geometry properties of plastic parts.

| | Units | Case study A | Case study B | Case study C | Case study D |
|---|---|---|---|---|---|
| Bounding box | $mm^3$ | [300-250-60.5] | [350-600-50] | [670-240-114] | [300-250-60] |
| Thickness | mm | 1 | 3 | 2 | 3 |
| Volume | $mm^3$ | 122 721.9 | 984 119.1 | 6 498 773.9 | 374 188.6 |
| Cavity plate area | $mm^2$ | 99 013.8 | 375 520.8 | 364 571.8 | 81 802.8 |
| Core plate area | $mm^2$ | 156 835.0 | 247 481.7 | 327 056.7 | 166 755.2 |

to reach ejection temperature $t_{cycle}$ [s] and the average mold cavity surface temperature $\overline{T_m}$ [°C]. The values of these last two parameters are shown for both the analytical solution of the proposed algorithm and the solution obtained by means of the injection molding simulation software. In order to evaluate the quality of the final product and the cooling system, Figs. 21, 27, 33 and 39 show the quality obtained by each plastic part after the cooling phase. All this, together with the comparison of results obtained through the proposed algorithm and through the injection molding simulation software, allow us to determine that the results obtained by the methodology described in this paper are adapted to the design criteria of cooling systems of the plastic parts. The efficiency of the algorithm is demonstrated for parts with large concavities, slender details, internal turrets and housings.

The solutions obtained by this methodology are dimensioned under four objectives: minimizing the difference between the mold cavity surface temperature obtained by means of the optimization problem and the resulting magnitude according to the physical model, maximizing the distance between baffles, minimizing the diameter of the cooling channels and the cycle time. In addition, the geometric solution of the cooling system meets four design conditions: the distance between baffles is greater than the minimum safety distance between mold elements $D_p$ [mm], the location of the baffles is guaranteed for deeper regions of the part (regions difficult to cool), and the resulting system is balanced and uniformly distributed along the geometry of the plastic part.

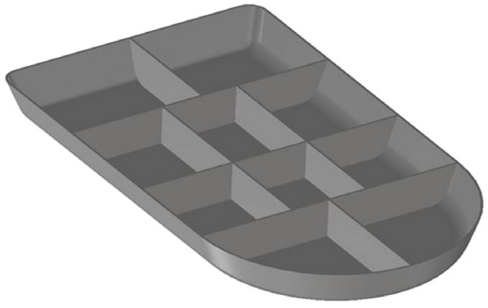

**Fig. 23.** Plastic part, Case B.

*4.1.1. Case A. See Figs. 17–22 and Table 7*
*4.1.2. Case B. See Figs. 23–28 and Table 8*
*4.1.3. Case C. See Figs. 29–34 and Table 9*
*4.1.4. Case D. See Figs. 35–40 and Table 10*

## 5. Conclusions

The work presented in this paper shows a new geometric algorithm for automated design of the layout and dimensioning of the baffles and main cooling channels of the cooling system, based

**Table 7**
Results of the algorithm for Case A: Average mold cavity surface temperature ($\overline{T_m}$) [°C], coolant temperature ($T_c$) [°C], average time required to reach ejection temperature ($t_{cycle}$) [s], coolant quality, distance between baffles ($L_b$) [mm] and diameter of cooling channels ($D_{baffles}$) [mm].

| Nomenclature | Units | Description | Analytical algorithm | Injection molding simulation |
|---|---|---|---|---|
| $\overline{T_m}$ | °C | Average mold cavity surface temperature | 61.5 | 60.3 |
| $T_c$ | °C | Coolant temperature | 51.3 | 51.0 |
| $t_{cycle}$ | s | Average time required to reach ejection temperature | 1.2 | 1.4 |
| $Q$ | – | Cooling quality | – | 100% |
| $L_b$ | mm | Distance between baffles | 30 | 30 |
| $D_{baffles}$ | mm | Diameter of cooling channels | 10 | 10 |

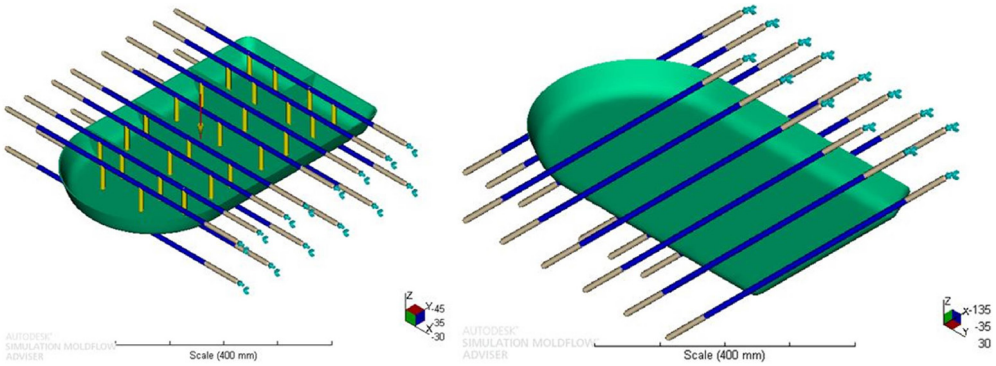


**Fig. 24.** Geometric solution of the hybrid refrigeration system design, Case B.

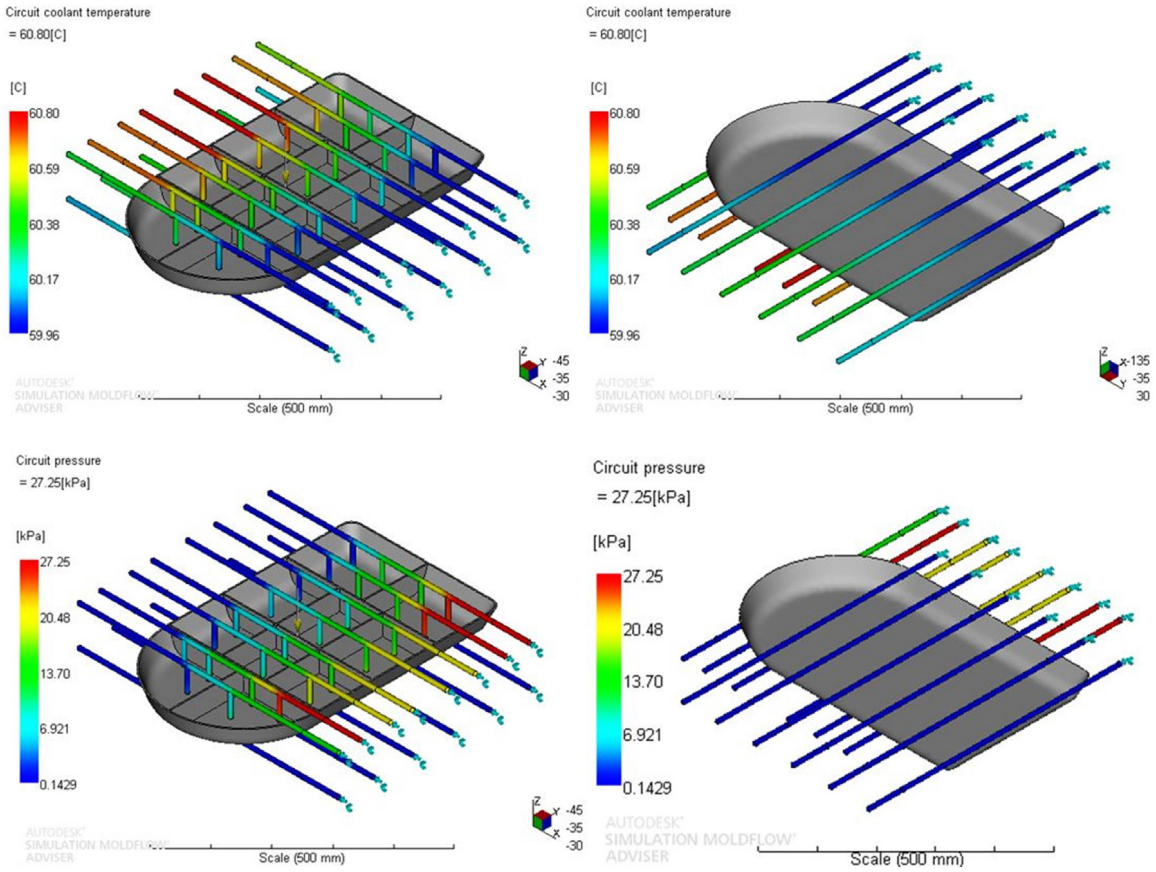


**Fig. 25.** Distribution of the pressure field [kPa] and temperatures [°C] of the cooling fluid throughout the cooling system, Case B.

on the discrete geometry of the plastic part. The methodology has been tested through its application on four plastic parts with different geometries and dimensions, solving and dimensioning the cooling parameters related to the average mold cavity surface temperature, coolant inlet temperature and cycle time. Location and distribution of main cooling channels and baffles for the four case studies were obtained in an automatic way. Results showed the layout with main cooling channels and baffles on the part.

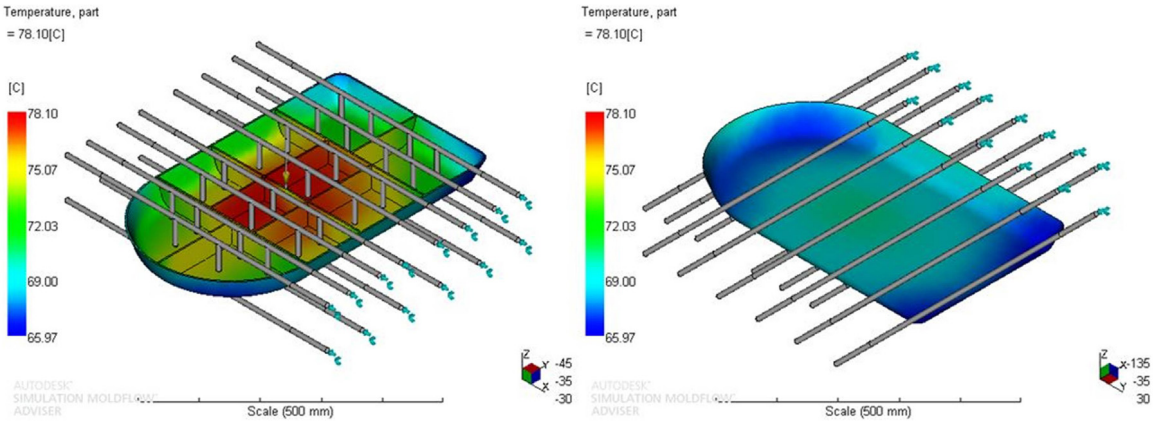


**Fig. 26.** Distribution of the mean temperature field at the surface of the plastic part during the cooling phase, Case B.

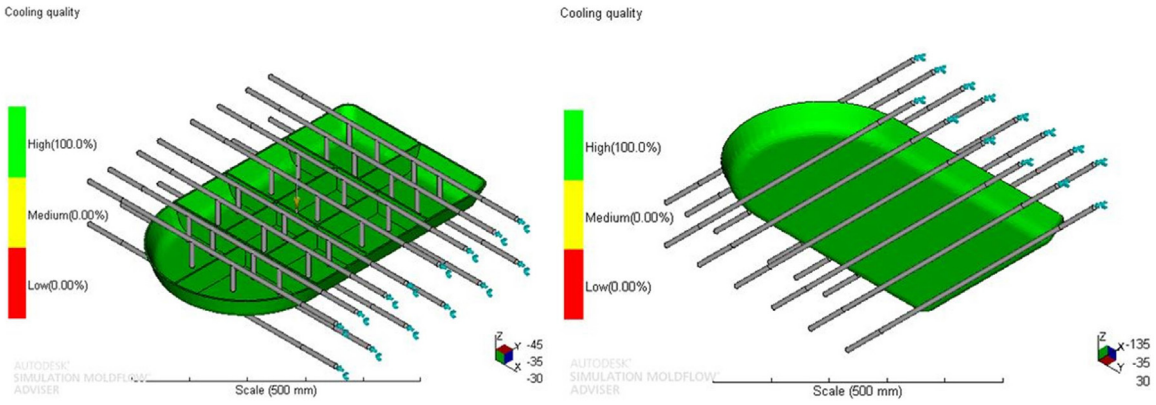


**Fig. 27.** Final quality of cooling along the geometry of the plastic piece, Case B.

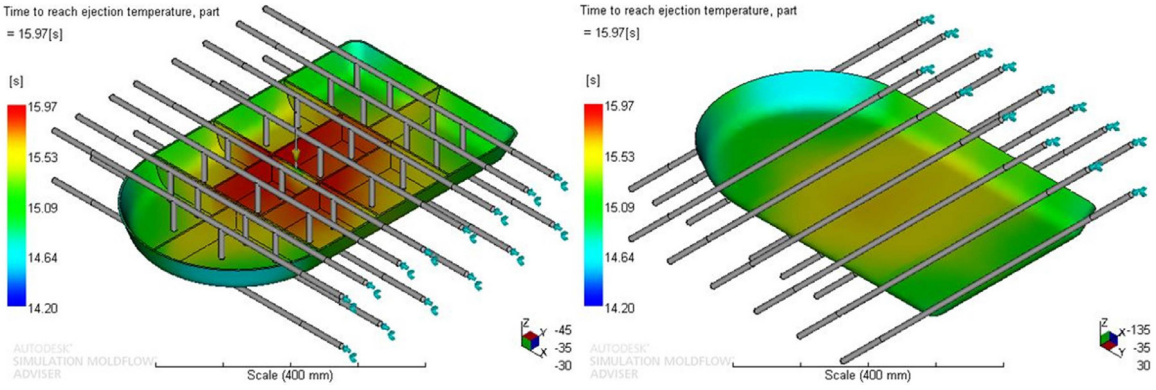


**Fig. 28.** Cycle time distribution [s] or time until the ejection temperature is reached on the surface of the plastic part, Case B.

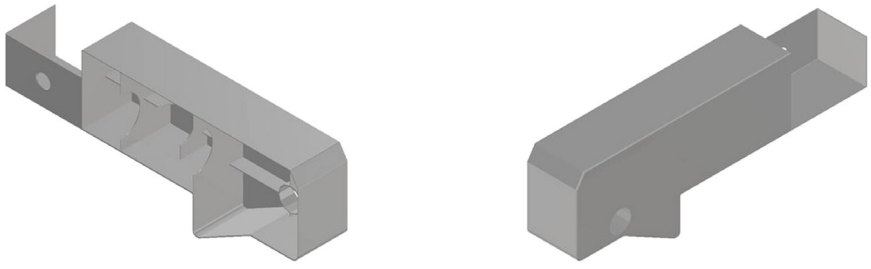

**Fig. 29.** Plastic part, Case C.

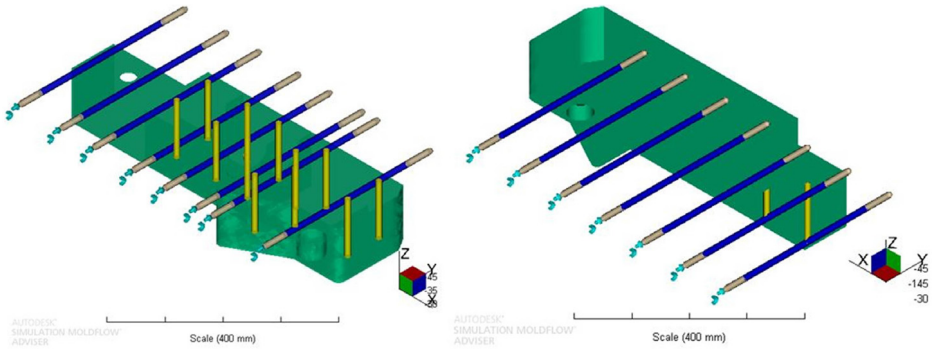


**Fig. 30.** Geometric solution of the hybrid cooling system design, Case C.

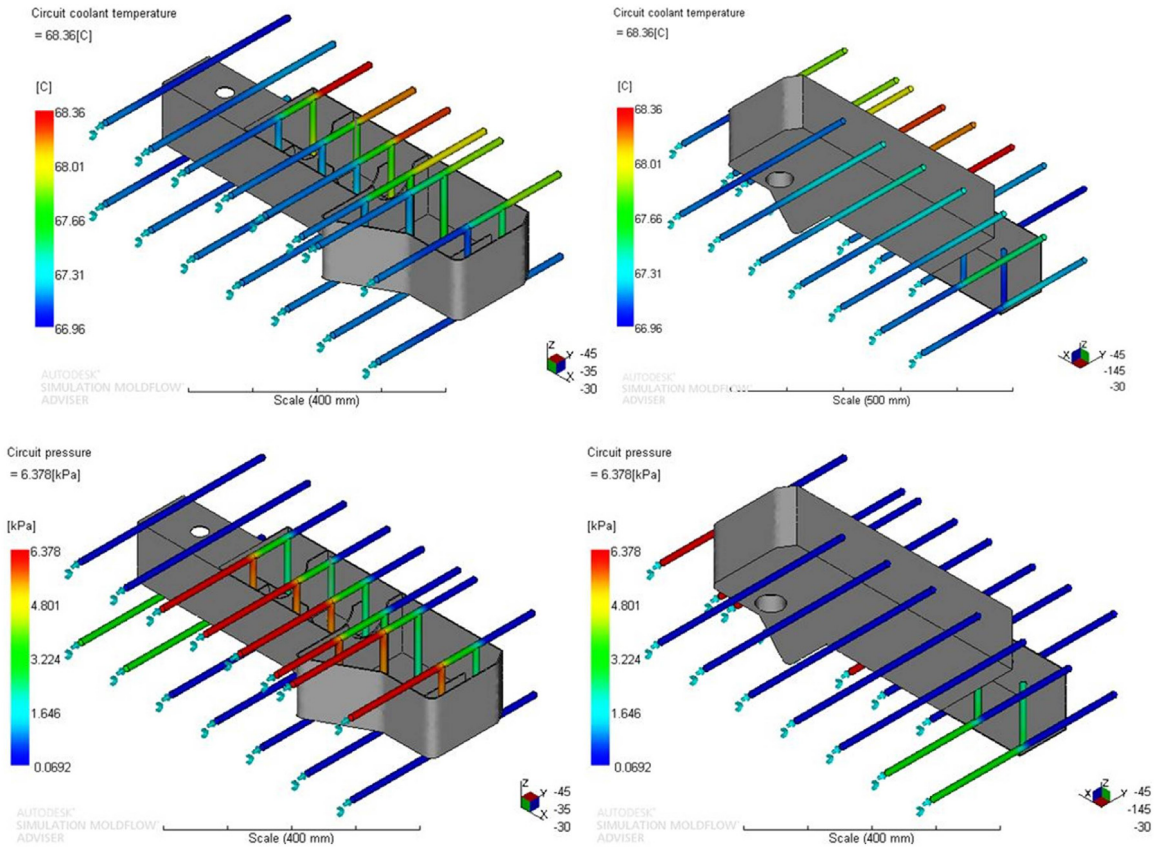


**Fig. 31.** Distribution of the pressure field [kPa] and temperatures [°C] of the cooling fluid throughout the cooling system, Case C.

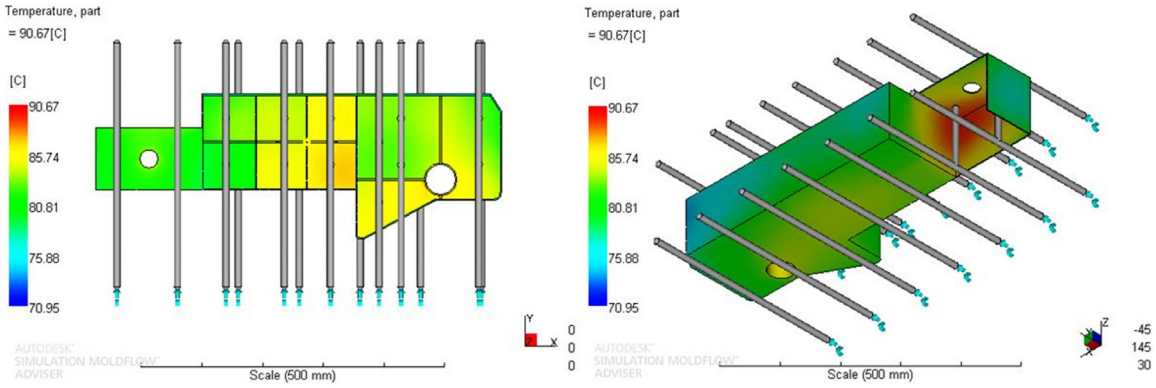


**Fig. 32.** Distribution of the average temperature field on the surface of the plastic part during the cooling phase, Case C.

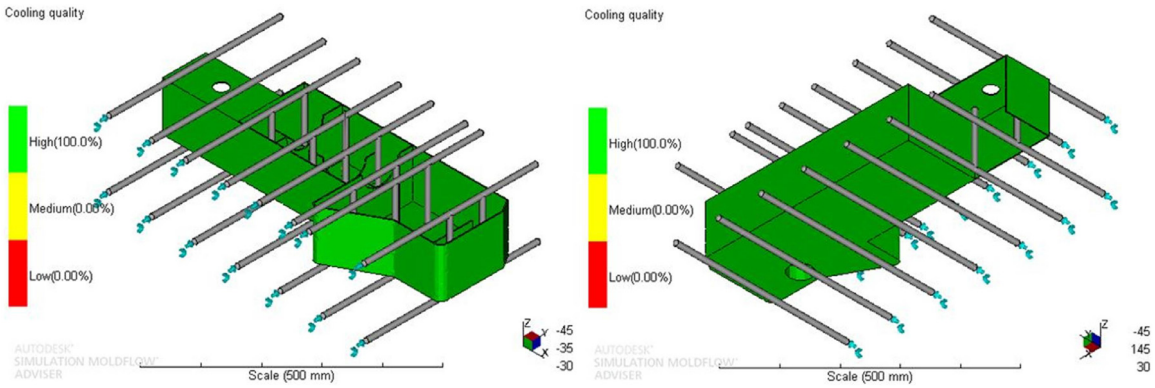


**Fig. 33.** Final quality of cooling along the geometry of the plastic part, Case C.

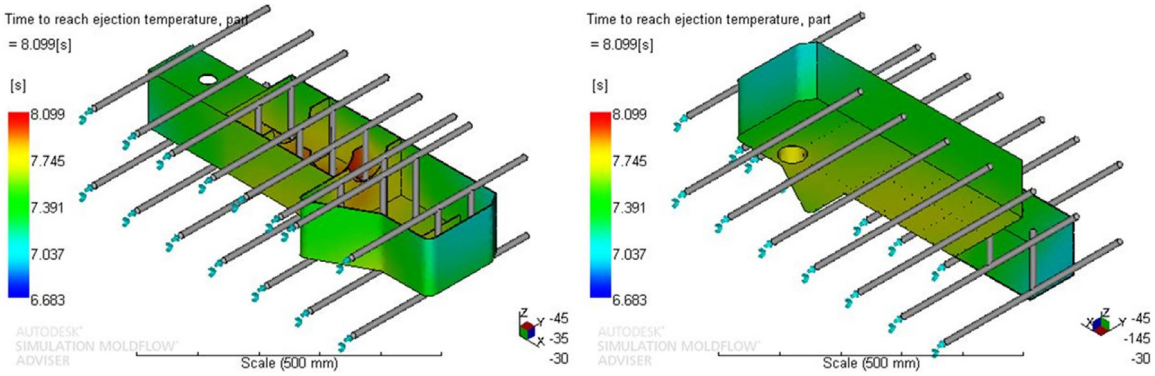


**Fig. 34.** Cycle time distribution [s] or time required to reach the ejection temperature on the surface of the plastic part, Case C.

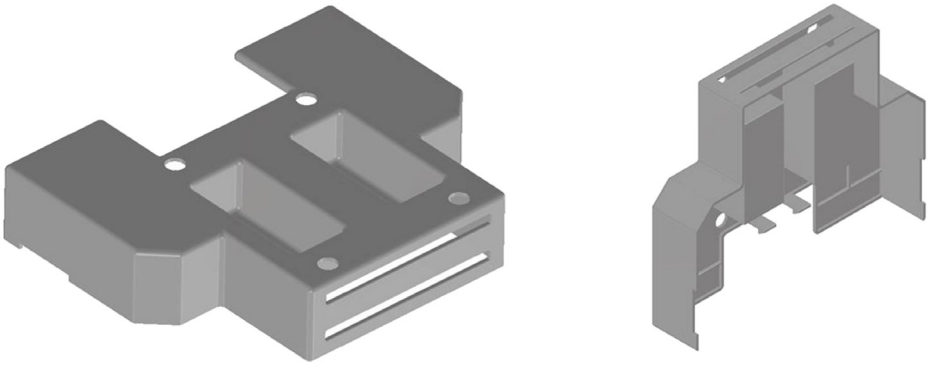

**Fig. 35.** Plastic part, Case D.

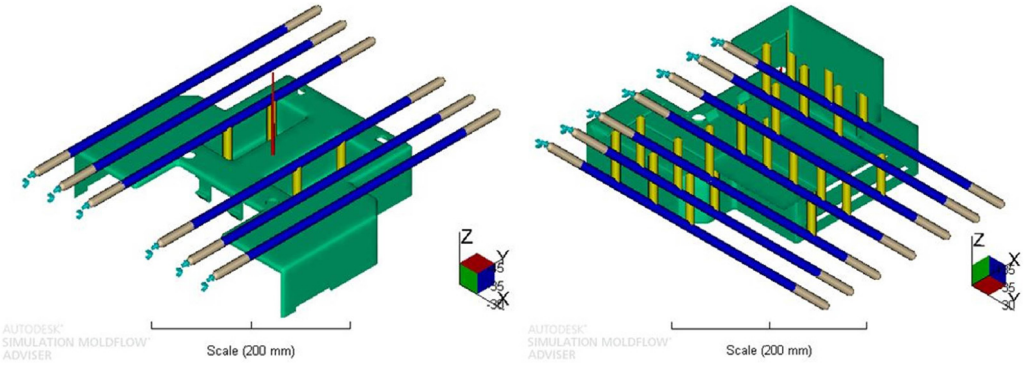


**Fig. 36.** Geometric solution of the hybrid refrigeration system design, Case D.

**Table 8**
Results of the algorithm for Case B: Average mold cavity surface temperature ($\overline{T_m}$) [°C], coolant temperature ($T_c$) [°C], average time required to reach ejection temperature ($t_{cycle}$) [s], coolant quality, distance between baffles ($L_b$) [mm] and diameter of cooling channels ($D_{baffles}$) [mm].

| Nomenclature | Units | Description | Analytical algorithm | Injection molding simulation |
|---|---|---|---|---|
| $\overline{T_m}$ | °C | Average mold cavity surface temperature | 74.4 | 78.7 |
| $T_c$ | °C | Coolant temperature | 60.7 | 60.0 |
| $t_{cycle}$ | s | Average time required to reach ejection temperature | 14.8 | 15.1 |
| $Q$ | – | Cooling quality | – | 100% |
| $L_b$ | mm | Distance between baffles | 65 | 65 |
| $D_{baffles}$ | mm | Diameter of cooling channels | 10 | 10 |

**Table 9**
Results of the algorithm for Case C: Average mold cavity surface temperature ($\overline{T_m}$) [°C], coolant temperature ($T_c$) [°C], average time required to reach ejection temperature ($t_{cycle}$) [s], coolant quality, distance between baffles ($L_b$) [mm] and diameter of cooling channels ($D_{baffles}$) [mm].

| Nomenclature | Units | Description | Analytical algorithm | Injection molding simulation |
|---|---|---|---|---|
| $\overline{T_m}$ | °C | Average mold cavity surface temperature | 77.3 | 81.6 |
| $T_c$ | °C | Coolant temperature | 67.2 | 67.0 |
| $t_{cycle}$ | s | Average time required to reach ejection temperature | 6.7 | 7.4 |
| $Q$ | – | Cooling quality | – | 100% |
| $L_b$ | mm | Distance between baffles | 100 | 100 |
| $D_{baffles}$ | mm | Diameter of cooling channels | 12 | 12 |

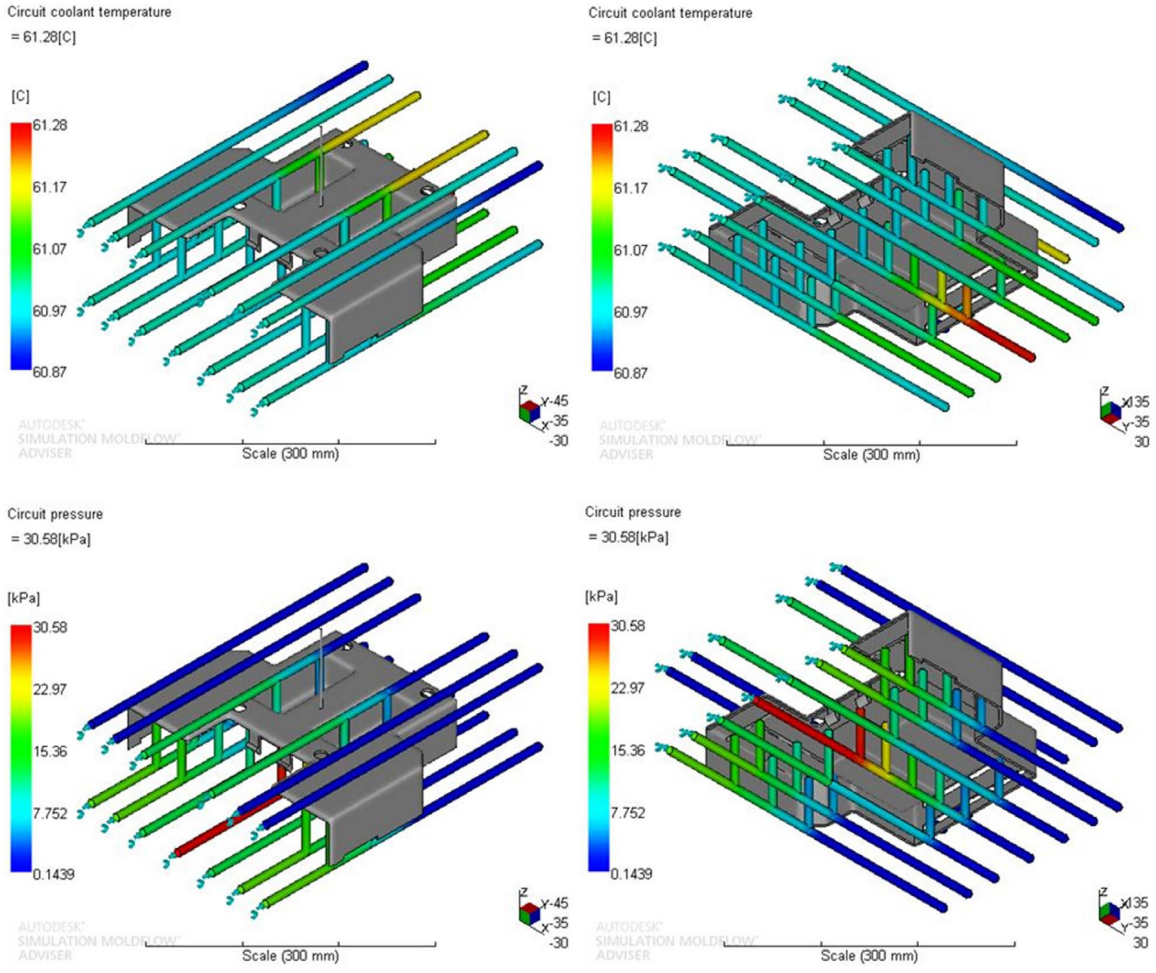


**Fig. 37.** Distribution of the pressure field [kPa] and temperatures [°C] of the refrigerant fluid throughout the refrigeration system, Case D.

Additionally, a detailed data report is obtained as a result of the application. This report includes the diameter $D_{baffles}$ [mm] and coordinates X, Y, Z of each cooling channel and baffle, the average mold cavity surface temperature $\overline{T_m}$ [°C], coolant inlet temperature $T_c$ [°C], cycle time $t_{cycle}$ [s] and distance separation between baffles $L_b$ [mm]. The algorithm of geometric design performs the correct location of the main cooling channels and baffles since the optimization procedure ensures a proper balanced and uniform cooling system, each element of the cooling system is separated from each other at a distance greater than the safety distance $D_p$ [mm] and the location of baffles guarantees the cooling in the regions of the plastic part in which its cooling process is complicated. In addition,

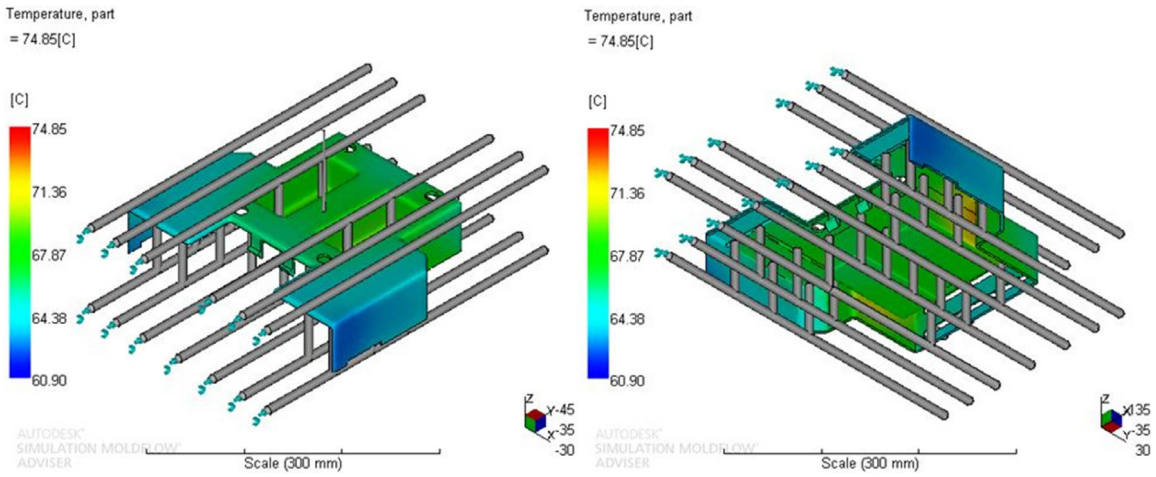


**Fig. 38.** Distribution of the mean temperature field at the surface of the plastic part during the cooling phase, Case D.

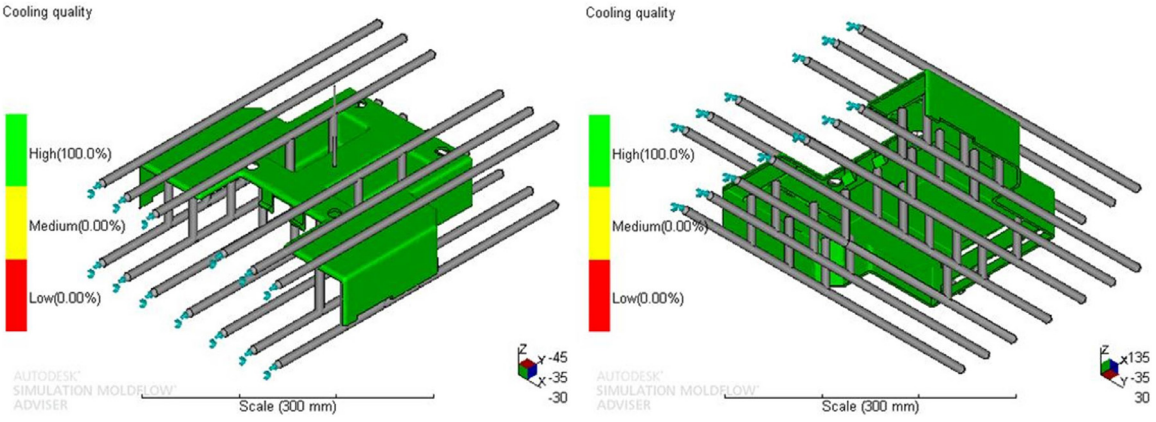


**Fig. 39.** Final quality of cooling along the geometry of the plastic part, Case D.

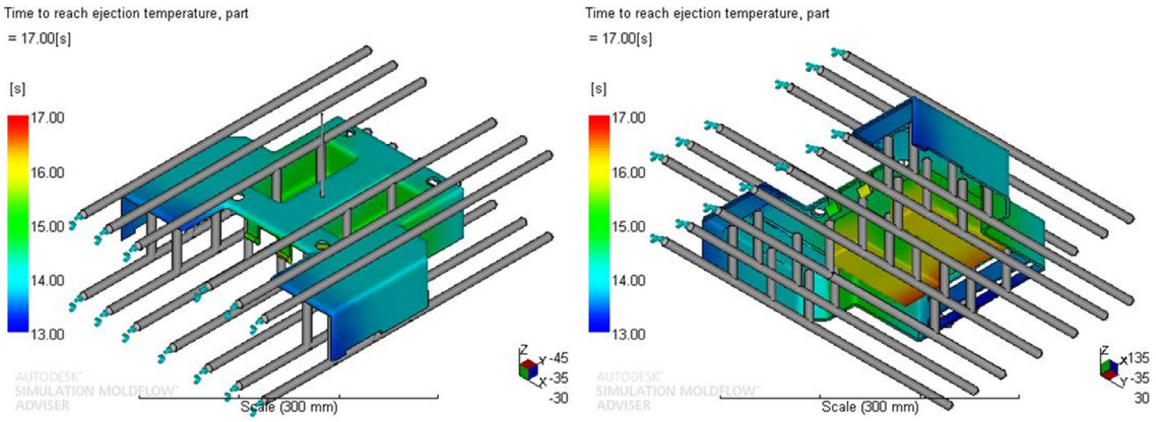


**Fig. 40.** Distribution of the cycle time [s] or time required until the ejection temperature is reached on the surface of the plastic part, Case D.

the resolution by means of genetic algorithm of the physical model proposed for determining the technical parameters of the cooling system has been validated by means of injection molding software, obtaining results that ensure a high quality of plastic parts during the cooling phase and a cycle time reduction. These are the criteria imposed on the fitness functions that the system must meet.

This new method improves the methods used so far as it does not require heuristic methods to achieve the result and does not use the feature recognition method as a tool for recognizing the geometric surface of the plastic, avoiding the problems of dependence on the modeler and the recognition of complex features. The proposed algorithm is applicable to any geometry because it works regardless of the CAD system in which the part has been designed.

## Acknowledgments

This work has been supported by the Consejeria de Economia, Innovación, Ciencia y Empleo (Junta de Andalucia-Spain) through

**Table 10**
Results of the algorithm for Case D: Average mold cavity surface temperature ($\overline{T_m}$) [°C], coolant temperature ($T_c$) [°C], average time required to reach ejection temperature ($t_{cycle}$) [s], coolant quality, distance between baffles ($L_b$) [mm] and diameter of cooling channels ($D_{baffles}$) [mm].

| Nomenclature | Units | Description | Analytical algorithm | Injection molding simulation |
|---|---|---|---|---|
| $\overline{T_m}$ | °C | Average mold cavity surface temperature | 67.3 | 67.9 |
| $T_c$ | °C | Coolant temperature | 61.0 | 61.0 |
| $t_{cycle}$ | s | Average time required to reach ejection temperature | 14.0 | 14.7 |
| $Q$ | – | Cooling quality | – | 100% |
| $L_b$ | mm | Distance between baffles | 40 | 40 |
| $D_{baffles}$ | mm | Cooling channel diameters | 10 | 10 |

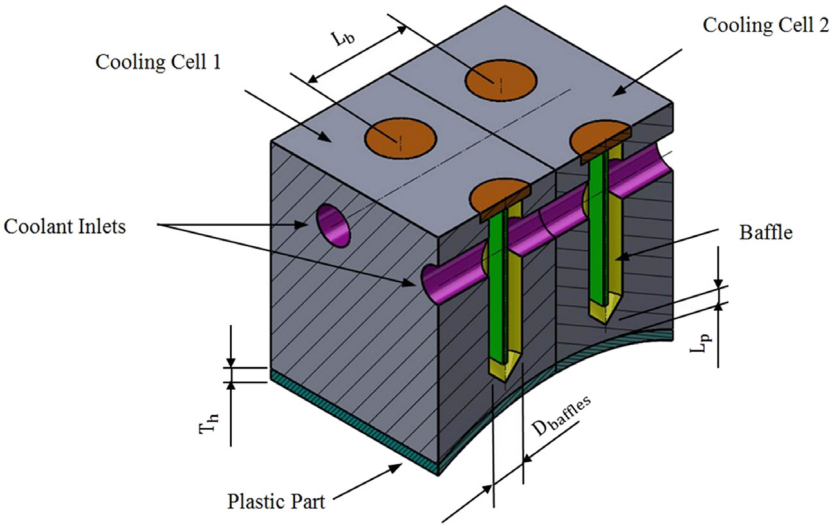


**Fig. 41.** Cooling cell considered for the dimensioning of the complete mold.

the project titled "A vertical design software for integrating operations of automated demoldability, tooling design and cost estimation in injection molded plastic parts. (CELERMOLD)" (Project Code TI-12 TIC 1623). The authors would like to thank the reviewers for comments that improved the exposition.

## Appendix

### A.1. Physical model of the cooling system

The heat transfer model considered in the algorithm focuses on the study of a cooling cell as a way of dimensioning the complete mold cooling system. As shown in Fig. 41, the cooling cell consists of a rectangular prism containing a cylindrical baffle. The cooling cells are parameterized geometrically using the values of the diameter of the baffles $D_{baffles}$ [mm], the separation between baffles $L_b$ [mm] and the separation between the blend of the baffle and the plastic part $L_p$ [mm] (see Fig. 41).

In the physical model of heat transfer between the plastic part and the cooling system, a series of premises have been taken into account with the aim of mathematically simplifying the physical model, Park et al. [31].

- The physical properties of the metal material in the mold are constant.
- The thermal analysis of the melt polymer is considered unidirectional because the thickness of the mold is smaller than the planar dimension.
- Heat exchange between the mold and the outside medium by convection is neglected because it represents less than 5% of overall heat loss.
- The cycle time of the plastic part is assumed equal to packing & cooling time because the filling and the ejection time are substantially shorter than packing & cooling time.
- It is assumed that the flow rate of coolant is large enough to achieve effective turbulent flow.
- The cooling effect of the main cooling channels is included in those regions of the part which do not require baffles.

According to Xu et al. [19], the steady state cycle mold cavity surface temperature, denominated as $\overline{T_m}$ [°C], can be expressed as Eq. (38).

$$\overline{T_m} = T_c + \frac{\rho_p \cdot c_p \cdot T_h \cdot \left(2 \cdot \delta_s \cdot L_b + h \cdot \pi \cdot D_{baffles} \cdot L_p\right) \cdot (T_{melt} - T_{eject})}{h \cdot \pi \cdot D_{baffles} \cdot \delta_s \cdot t_{cycle}} \quad (38)$$

where $T_c$ [°C] represents the temperature of the coolant, $\rho_c$ [kg/mm$^3$] represents the density of the melt plastic, $c_p$ [J/kg °C] represents the specific heat of the melt plastic, $T_h$ [mm] represents the thickness of the plastic part, $\delta_s$ [W/mm °C] represents the thermal conductivity of the mold, $L_b$ [mm] represents the separation between baffles, $h$ [W/mm$^2$ °C] represents the heat transfer coefficient between the mold and the coolant, $D_{baffles}$ [mm] represents the diameter of the baffles, $L_p$ [mm] represents the separation between the plastic part and the baffle for a cooling cell, $T_{melt}$ [°C] represents the melt plastic temperature, $T_{eject}$ [°C] represents the temperature of ejection of the part (characteristic of each polymer) and $t_{cycle}$ [s] represents the cycle time of the plastic part.

This expression allows estimation of the temperature of the surface of the mold cavity; however it is necessary to know the value of the cycle time $t_{cycle}$ [s], since it is an input variable to the model. The cycle time can be defined from the equation that determines one-dimensional heat flow Eq. (39), i.e. the Fourier equation reduced to one dimension. According to Menges et al. [36].

$$\frac{\partial T}{\partial t} = \alpha_s \cdot \frac{\partial^2 T}{\partial^2 z} \quad (39)$$

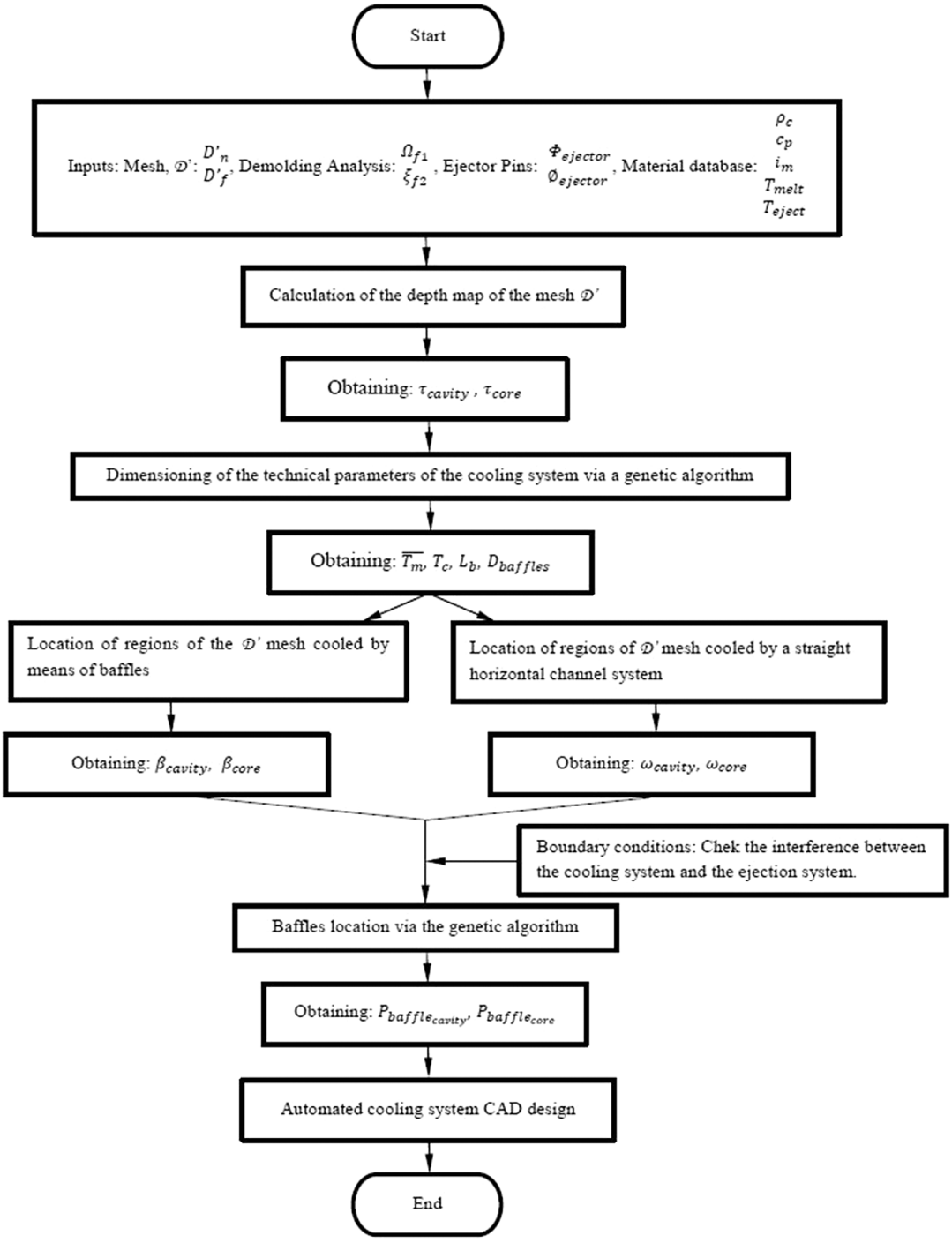


**Fig. 42.** Algorithm for the design and dimensioning of the injection mold cooling system.

where $\alpha_s$ [$m^2/s$] represents the thermal diffusivity coefficient of the mold material. Assuming that, after the filling stage of the mold cavity, the melt plastic temperature has a constant value $T_{melt}$ [°C] and the surface temperature of the mold cavity varies considerably until it remains at a constant value $\overline{T_m}$ [°C], a solution can be established to this second-order and hyperbolic differential equation Eq. (40). The melt plastic temperature at a point on the partition line can be evaluated as a convergence of the Fourier series development of the heat transfer differential equation, such that.

$$\frac{T_{eject} - \overline{T_m}}{T_{melt} - \overline{T_m}} = \frac{4}{\pi} e^{-\frac{\alpha_s \cdot \pi^2}{T_h} \cdot t} \cdot \sin\left(\frac{\pi \cdot x}{S}\right)$$

$$T_{eject} - \overline{T_m} = \frac{4}{\pi} \cdot \left(T_{melt} - \overline{T_m}\right) \cdot \sum_{n=0}^{\infty} \frac{1}{2 \cdot n + 1} \cdot e^{-\frac{\alpha_s \cdot (2 \cdot n+1) \cdot \pi^2}{T_h^2} \cdot t} \cdot \sin\left(\frac{\pi \cdot (2 \cdot n + 1) \cdot x}{S}\right) \quad (40)$$

Resolving the above expression with respect to the cycle time Eq. (41).

$$t_{cycle} = \frac{T_h^2}{\pi^2 \cdot \alpha_s} \cdot \mathrm{Ln}\left(\frac{4}{\pi} \cdot \frac{T_{melt} - \overline{T_m}}{T_{eject} - \overline{T_m}}\right) \quad (41)$$

Thus, in the expression the cycle time is a function of the temperature of the surface of the mold cavity and vice versa. Authors such as Xu et al. [19] proposed the resolution of this model through an iterative process of calculation. Wang et al. [27,28] assigned values of the diameter of the cooling channels and cycle time based on the industrial experience and calculated the other technical and geometric parameters of the physical model. However, models [19,27,28] present problems in their complete resolution, and for this reason the algorithm proposed in this paper employs a genetic optimization algorithm that calculates the optimal technical and geometric parameters of the physical model.

### *A.2. Flowchart of the present methodology*

See Fig. 42.

## References


[1] Martin-Doñate C, Rubio Paramio MA. New methodology for demoldability analysis based on volume discretization algorithms. Comput Aided Des 2013;45(2):229–40.
[2] Mercado-Colmenero Jorge Manuel, Paramio MAR, Perez-Garcia Jesus Maria, Martin-Doñate Cristina. A new hybrid method for demoldability analysis of discrete geometries. Comput- Aided Des 2016;80:43–60.
[3] Martin-Doñate Cristina, Rubio-Paramio Miguel Angel, Mesa-Villar Aurelio. Método de validación automatizada de la fabricabilidad de diseños de objetos tridimensionales en base a su geometría 2015, Patent number: ES2512940B2.
[4] Rubio MA, Pérez JM, Rios J. A procedure for plastic parts demoldability analysis. Robot Comput Integr Manuf 2006;22(1):81–92.
[5] Turng LS, Wang KK. A computer-aided cooling-line design system for injection molds. J Eng Ind-Trans ASME 1990;112(2):161–7.
[6] Opolski SW, Kwon TW. Injection molding cooling system design. In: ANTEC'86. 1987. p. 264–8.
[7] Tang LQ, Pochiraju K, Chassapis C, Manoochehri S. A computer- aided optimization approach for the design of injection mold cooling systems. Trans ASME J Mech Des 1998;120:165–74.
[8] Sanfilippo Emilio M, Borgo Stefano. What are features? An ontology-based review of the literature. Comput Aided Des 2016;80:9–18.
[9] Li CL. A feature-based approach to injection mould cooling system design. Comput Aided Des 2001;33(14):1073–90.
[10] Li CL, Li CG, Mok ACK. Automatic layout design of plastic injection mould cooling system. Comput Aided Des 2005;37(7):645–62.
[11] Li CG, Li CL. Plastic injection mould cooling system design by the configuration space method. Comput Aided Des 2008;40(3):334–49.
[12] Li CG, Li CL, Liu Y, Huang Y. A new C -space method to automate the layout design of injection mould cooling system. Comput Aided Des 2012; 44:811–23.
[13] Sachs E, Wylonis E, Allen S, Cima M, Guo HL. Production of injection molding tooling with conformal cooling channels using the three dimensional printing process. Polym Eng Sci 2000;40(5):1232–47.
[14] Dalgarno KW, Stewart TD. Manufacture of production injection mould tooling incorporating conformal cooling channels via indirect selective laser sintering. Proc Inst Mech Eng B 2001;215(10):1323–32.
[15] Ilyas I, Taylor C, Dalgarno K, et al. Design and manufacture of injection mould tool inserts produced using indirect SLS and machining processes. Rapid Prototyp J 2010;16(6):429–40.
[16] Ferreira JC, Mateus A. Studies of rapid soft tooling with conformal cooling channels for plastic injection moulding. J Mater Process Technol 2003;142(2):508–16.
[17] Saifullah ABM, Masood SH, Sbarski I. Thermal-structural analysis of bi-metallic conformal cooling for injection moulds. Int J Adv Manuf Technol 2012;62(1–4):123–33.
[18] Eiamsa-ard K, Wannissorn K. Conformal bubbler cooling for molds by metal deposition process. Comput-Aided Des 2015;69:126–33.
[19] Xu XR, Sachs E, Allen S. The design of conformal cooling channels in injection molding tooling. Polym Eng Sci 2001;41(7):1265–79.
[20] Dimla DE, Camilotto M, Miani F. Design and optimisation of conformal cooling channels in injection moulding tools. J Mater Process Technol 2005;164:1294–300.
[21] Qiao H. A systematic computer-aided approach to cooling system optimal design in plastic injection molding. Int J Mech Sci 2006;48(4):430–9.
[22] Au KM, Yu KM. A scaffolding architecture for conformal cooling design in rapid plastic injection moulding. Int J Adv Manuf Technol 2007;34(5–6):496–515.
[23] Park HS, Pham NH. Design of conformal cooling channels for an automotive part. Int J Automot Technol 2009;10(1):87–93.
[24] Au KM, Yu KM. Modeling of multi-connected porous passageway for mould cooling. Comput Aided Des 2011;43(8):989–1000.
[25] Au KM, Yu KM, Chiu WK. Visibility-based conformal cooling channel generation for rapid tooling. Comput Aided Des 2011;43(4):356–73.
[26] Au KM, Yu KM. Variable distance adjustment for conformal cooling channel design in rapid tool. J Manuf Sci Eng-Trans ASME 2014;136(4).
[27] Wang Yu, Yu Kai-Min, Wang Charlie CL, et al. Automatic design of conformal cooling circuits for rapid tooling. Comput Aided Des 2011;43(8):1001–10.
[28] Wang Yu, Yu Kai-Min, Wang Charlie CL. Spiral and conformal cooling in plastic injection molding. Comput Aided Des 2015;63:1–11.
[29] Sun YF, Lee KS, Nee AYC. The application of U-shape milled grooves for cooling of injection moulds. Proc Inst Mech Eng B 2002;216(12):1561–73.
[30] Dang Xuan-Phuong, Park Hong-Seok. Design of U-shape milled groove conformal cooling channels for plastic injection mold. Int J Precision Eng Manuf 2011;12(1):73–84.
[31] Park HS, Dang XP. Optimization of conformal cooling channels with array of baffles for plastic injection mold. Int J Precision Eng Manuf 2010;11(6):879–90.
[32] David Kazmer. Injection Mold Design Engineering. 1st ed. Munich: Hanser; 2007.
[33] Mercado-Colmenero Jorge Manuel, Rubio-Paramio MA, Vizan-Idoipe Antonio, Martin-Doñate Cristina. A new procedure for the automated design of ejection system in injection molds. Robot Comput Integr Manuf 2017;46:68–85.
[34] Matlab, R2013a. https://mathworks.com.
[35] Autodesk, MoldFlow Advisor, 2014. http://www.autodesk.com.
[36] Menges G, Mohren P. How to Make Injection Moulds. 3rd ed. Munich, Vienna and New York: Hanser; 2001.



**Jorge Manuel Mercado Colmenero** received his B.Eng. and M.Eng. in Mechanical Engineering in 2012 and 2014 respectively from the University of Jaén in Spain. In 2014 he joined the Design, Engineering Graphics and Project department at Jaen university as a Ph.D. student. He is currently developing his thesis on automatic analyses and design of injection plastic molds, including demoldability, ejection systems, cooling system design and CAD–CAE design and manufacturing.

**Prof. Dr. Miguel Angel Rubio Paramio** received his M.Eng. and Ph.D in Mechanical Engineering in 1992 and 2000 respectively from the Polytechnic University of Madrid in Spain. In 1994 he joined the University of Jaen and currently he teaches courses on Computer-aided Design, Manufacturing and Engineering in the Engineering Graphics, Design and Projects Department. His thesis was focused on the automatic analysis of plastic parts injection. His research interests include CAD–CAM–CAE, Design for Manufacturing, computational geometry, constraint-based parametric modeling, and their applications in plastic injection mold design and manufacturing.

**Prof. Dr. Marquez** received his M.Sc. and Ph.D. degrees in Mechanical Engineering from Universidad Politecnica of Madrid (UPM, Spain) in 1994 and 1998, respectively. He is currently a full time Professor in the Dep. of Mechanical Engineering at ETSII-UPM. His research work focuses on the design and development of high precision manufacturing systems and polymer microfabrication technologies. He has led two research projects in the area of MEMS micromanufacturing, and he has participated as associate researcher in many others. He has been visiting professor at the George W. Woodruff School of Mechanical Engineering at Georgia Institute of Technology (USA) in 1996, 2005 and 2009, collaborating in research groups at the Manufacturing Research Center. He has been on the position as Vice-Dean for Students Affairs and International Relations since 2011 at ETSII-UPM.

**Prof. Dr. Cristina Martín-Doñate** received her B.Eng. and M.Eng. in Electrical–Electronics Engineering and Industrial Engineering (Polytechnic University of Valencia — Spain) and Ph.D in Industrial Engineering (University of Jaen — Spain) in 1997 and 2010 respectively. She performed research at the Technical University of Graz in Austria, in the field of manufacturing systems. She worked for several years as a project manager developing new products in the automotive manufacturing industries. She is currently Full Professor at Jaen University where she develops research and conducts research projects into manufacturing systems, plastic injection mold design and technology, CAD systems and new products development.

Referencia / Reference: **Mercado-Colmenero, Jorge Manuel,** Rubio-Paramio, Miguel Angel, Karlinger, Peter, Martín-Doñate, Cristina. *A new procedure for calculating cycle time in injection molding based on plastic part geometry recognition. The International Journal of Advanced Manufacturing Technology 98 (2018) 441-477. DOI: https://doi.org/10.1007/s00170-018-2080-0*.

Estado / Status: Publicado / Published

Índice de impacto / Impact Factor: 2,601 (JCR Year 2017)

Categoría / Catogory: Engineering, Manufacturing

Ranking: 15/46 (JCR Year 2017)

Quartile: Q2 (JCR Year 2017)

JIF Percentile: 68.478 (JCR Year 2017)

The International Journal of Advanced Manufacturing Technology
https://doi.org/10.1007/s00170-018-2080-0

ORIGINAL ARTICLE

# A new procedure for calculating cycle time in injection molding based on plastic part geometry recognition

Jorge Manuel Mercado-Colmenero[1] · Miguel Angel Rubio-Paramio[1] · Peter Karlinger[2] · Cristina Martin-Doñate[1]

Received: 30 January 2018 / Accepted: 24 April 2018


**Abstract**
The paper presents a new procedure for the automated calculation of cycle time in the injection molding process based on the recognition of the geometry of the plastic part to be manufactured, taking as input data only the geometry of the plastic part in discrete format and the material in which it will be manufactured. In a first phase, the procedure uses a new geometric algorithm of topology recognition of the plastic part based on the projection of a nodal quadrature on the discrete model of the part. The algorithm is able to obtain the set of geometric parameters necessary for the calculation of the cycle time by providing a map of the thicknesses of the part, indicating its average and maximum thickness as well as the maximum distance that the melt plastic flow runs during the injection stage. Afterwards, a second analytical-empirical algorithm performs an automated analysis of the numerical simulations of the injection stage using a rectangular plate shape test part whose geometry is parameterized according to its volume, its thickness, and the path of the melt plastic flow, generating a set of polynomial functions which determine the radius of the feeding system gate. Finally, taking as data, the geometric and technological parameters resulting from the application of the developed sub-algorithms, the cycle time is calculated. The new procedure presented in the paper does not require the use of additional simulation software or the empirical evaluation of experts. It is not linked to the modeler of the given part since it analyzes its surface externally from its discrete format. In this way, it allows designers to give a response to the client quickly and accurately, obtaining the value of the cycle time in a minimum time.

**Keywords** Injection molding · Cycle time · Discrete geometry · Surfaces geometric recognition · Computer-aided manufacturing

## 1 Introduction

Injection molding is a production method widely used in the manufacture of plastic parts of complex geometry and with high production volumes. The molding technology follows a cyclic process that begins with the injection of the melt polymer at high temperature and pressure into the mold cavities, its subsequent packing to compensate for the shrinkage of the material, and its cooling by means a fluid at a lower temperature that allows the plastic part out of the mold to be ejected quickly, starting the cycle again. Each of the phases of the molding cycle (filling, packing, cooling, and ejection), involves a time of manufacture. The profitability of the complete molding process depends on the time used in each of its phases. It is very important to predict the time required to produce the plastic part from the initial stages of the design.

Obtaining the cycle time accurately is a complex task since the calculation depends on multiple factors including the geometric characteristics of the part, plastic material, injection machine, geometry of feeding channels, and the typology of the mold cooling system.

✉ Cristina Martin-Doñate
cdonate@ujaen.es

Jorge Manuel Mercado-Colmenero
jmercado@ujaen.es

Miguel Angel Rubio-Paramio
marubio@ujaen.es

Peter Karlinger
peter.karlinger@fh-rosenheim.de

[1] Department of Engineering Graphics, Design and Projects, University of Jaen, Campus Las Lagunillas, s/n. Building A3-210, 23071 Jaen, Spain

[2] Department of Plastics Engineering, University of Applied Sciences Rosenheim, Rosenheim, Germany

Published online: 12 June 2018

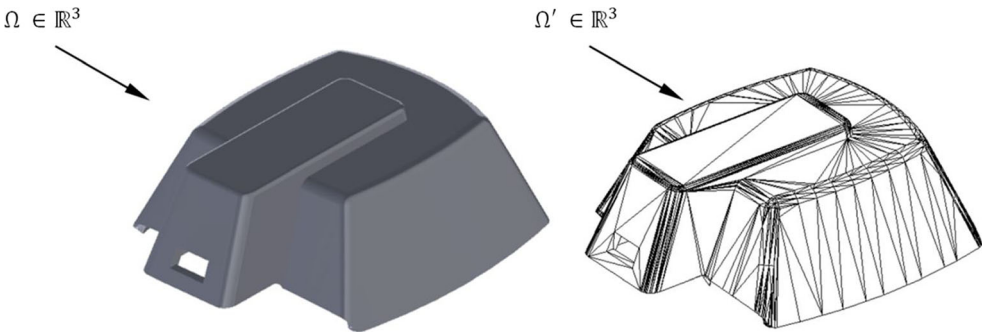


**Fig. 1** Geometry of the plastic part $\Omega$ and discrete model $\Omega'$

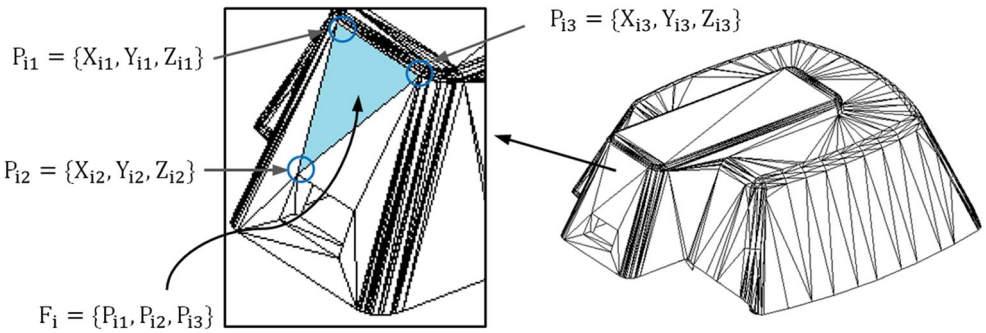


**Fig. 2** Detail of the triangular facet $F_i$ and the nodes $P_{i1}$, $P_{i2}$, $P_{i3}$ of the mesh $\Omega'$

Calculating the value of cycle time quickly and correctly can be decisive when obtaining a contract. Traditionally, the cycle time has been obtained empirically by experienced mold designers, comparing the part to be manufactured with other parts of similar geometric characteristics. This method allows designers to prepare a budget quickly, but it is far from providing the optimal solution. Miscalculations can have serious economic consequences for the company, causing losses throughout the life cycle of the product.

Although there are currently different CAE software applications that uses CFD techniques applied to non-Newtonian fluids to calculate the cycle time, its use requires specific training and experience. On the other hand, the availability of company rheology experts may be limited by their work on other projects, causing delays in the valuations or even the definitive loss of the contracts. For these reasons, this paper presents a new methodology for the automated obtaining of the cycle time value, taking as sole input data the geometry of the plastic part in discrete format and its manufacturing

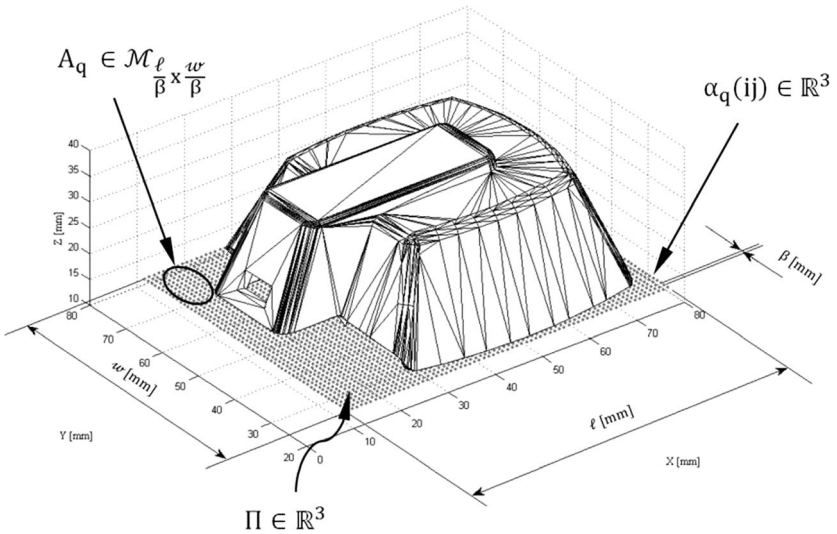


**Fig. 3** Nodal quadrature $A_q$ from the Bounding Box of the plastic part. ($l$ x $w$)

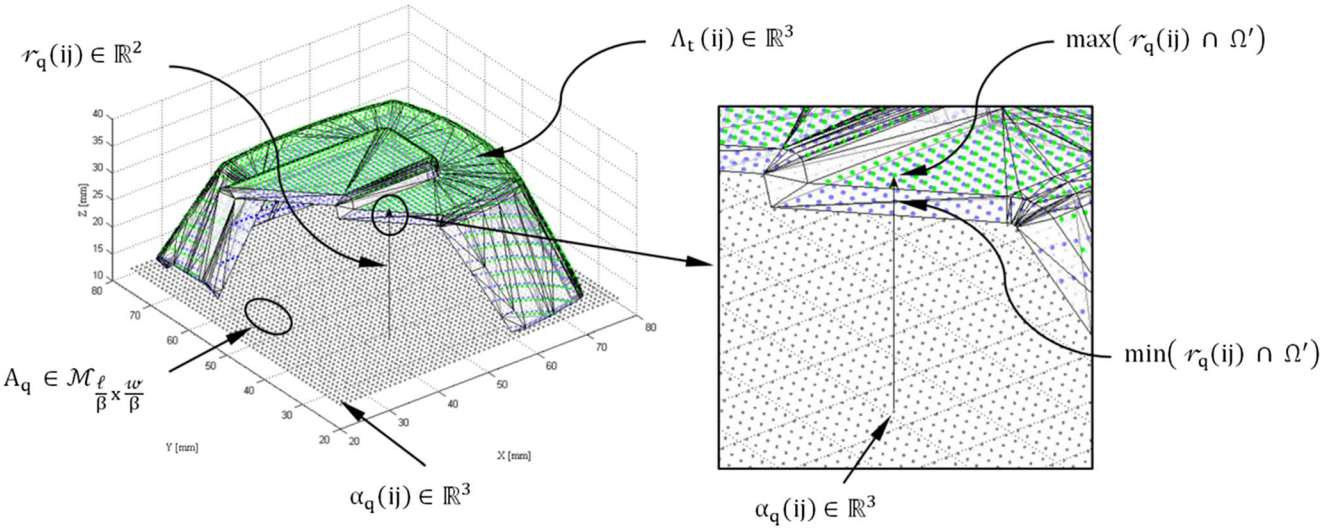


**Fig. 4** Obtaining the intersection points $\Lambda_t(ij)$ between the beam of lines $\mathcal{R}_q$ and the discrete mesh. $\Omega' \in \mathbb{R}^3$

thermoplastic material. The new procedure uses an algorithm for the automated recognition of the discrete surface of the plastic part, capable of extracting the set of geometric parameters necessary for the calculation of the cycle time. A second analytical-empirical algorithm performs an analysis of the numerical simulations of the injection phase, obtaining the technological parameters necessary for the calculation of the cycle time. The new procedure presented in the paper does not require the use of additional simulation software or the empirical evaluation of experts. It is not linked to the modeler of the part since it analyzes its surface externally from its discrete format, and allows designers to give a quick and accurate response to the client by means of obtaining the value of the cycle time in a minimum time.

## 2 Background and related work

Cycle time is one of the most influential parameters in the productivity and efficiency of the plastic injection mold. However, despite its importance research aimed at calculating the value of cycle time, it does not cover all aspects related to the complete molding cycle, focusing only on one of its phases, without evaluating the process at the global level.

The process of filling the mold is a complex process difficult to simulate and analyze. An accurate estimation of the injection time requires a study of the flow of the polymer in its displacement along the runners, gates, and passages of the cavities. However, although this type of detailed study would involve the complete design of the mold cavity and the feeding system, the use of solid modeling and the nonlinear finite element analysis is not justified in the conceptual design stage, when injection time is initially evaluated. Some authors have focused their research on calculating and improving the filling time, among them Zhang et al. [1] uses the Lagrange simulation curve based on the Moldflow analysis to obtain the best filling time. Galantuzzi et al. [2] proposes an integrated approach to evaluating the configurations of the gates system with the aim of optimizing the filling conditions of injection-molded thermoplastic parts through the integration of data between FE analysis and the experimental design approach, analyzing the influence on the filling time. Lam et al. [3]

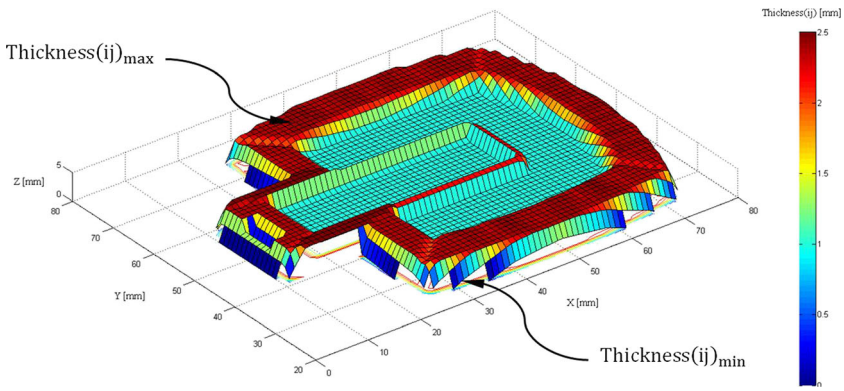


**Fig. 5** Thicknesses Map Thickness(ij) of the plastic part

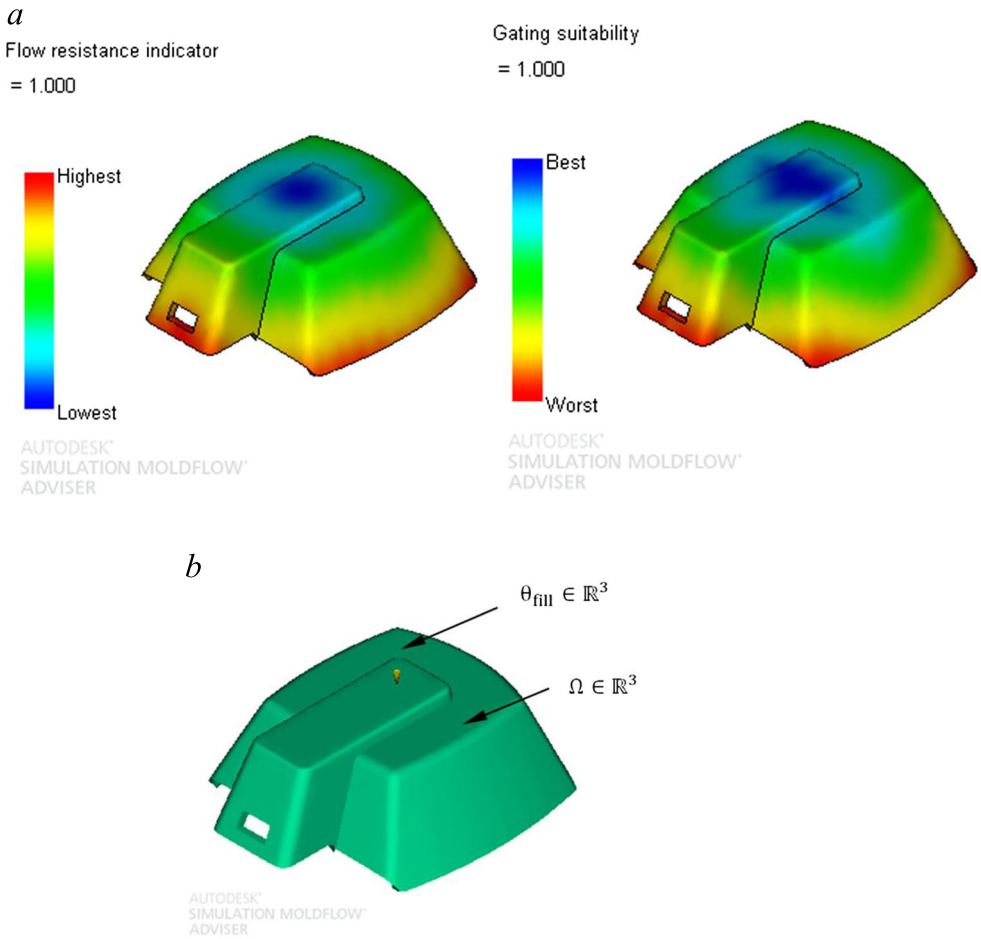


**Fig. 6** **a** Flow resistance indicator and gating suitability for the plastic part Ω. **b** Location of the injection point $\theta_{fill}$ on the geometry of the plastic part Ω

present a flexible computer-aided system designed to assist the designers in determining injection time by using simulation-based technology.

The main function of the packing step is to introduce a quantity of additional melt into the cavity after the initial filling, in order to compensate for the shrinkage of the part and avoid the back reflux of the polymer. The packing time ends when the gate solidifies. The cooling phase takes place concurrently with the filling and packing phases, the cooling time being considered necessary for the part to solidify at

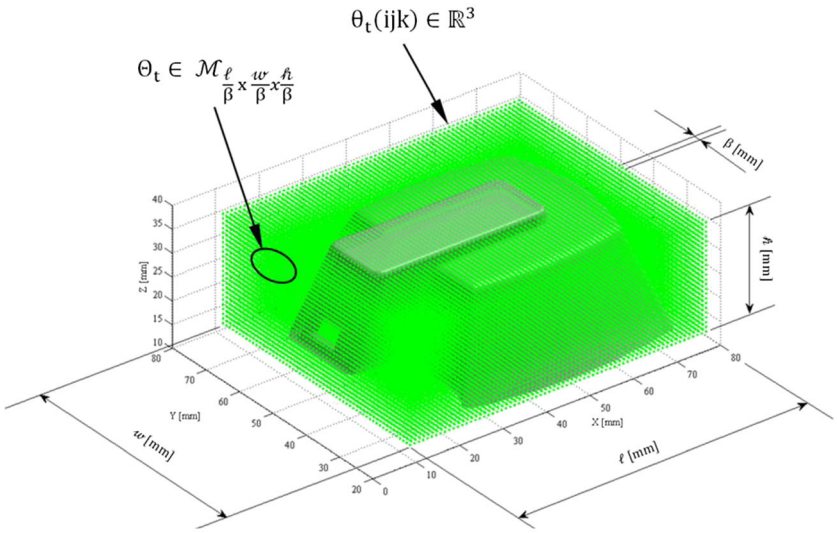


**Fig. 7** Nodal grid $\Theta_t$ obtained from the Bounding Box of the plastic part ($l$ x $w$ x $h$)

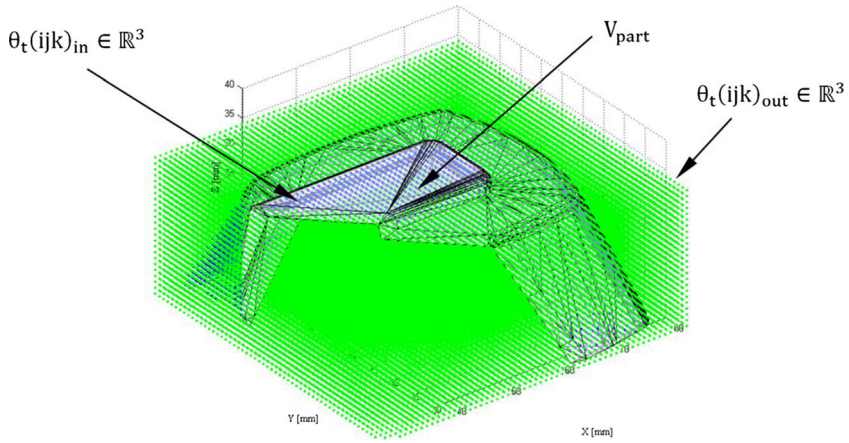


**Fig. 8** Outer points $\theta_t(ijk)_{out}$ and inner points $\theta_t(ijk)_{in}$ of the volume $V_{part}$ of the discrete mesh $\Omega'$ in the 3D nodal grid

80%. The cooling stage is the one with the greatest influence on the molding process since it directly affects the productivity and quality of the molded part, covering more than 70% of the total process cycle time. At this stage, the coolant, which flows through the cooling channels, is responsible for cooling the part by lowering its temperature so that it can be extracted as quickly as possible from the mold. A good design of the cooling channel system reduces the cycle time by providing a greater uniformity in cooling. Despite this advantage, the design of the cooling channels has traditionally been limited to a simple design, based on straight holes drilled in the mold due to the limitations of existing technology. Baffles, bubblers, and thermal pins are alternative devices used to cool small regions or areas away from the main channels. However, these solutions are sometimes not effective, especially for large and medium-sized parts with free-form surfaces. To avoid this problem, several researchers have designed new conformal-type cooling circuits with the objective of adapting to the surface of the part. In this design, the distance between the cooling channels and the surface of the cavities is kept constant, making the heat distribution more uniform. In a pioneering study, Sachs et al. [4] obtained a conformal design

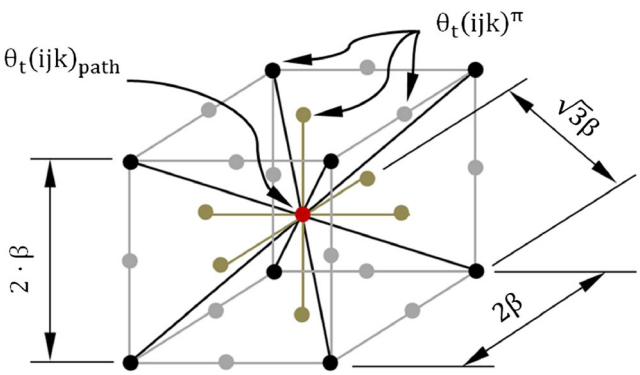


**Fig. 9** Representation of the filling path $\theta_t(ijk)_{path}$ and the set of neighboring nodes $\theta_t(ijk)^{\pi}$

that maintained the most uniform temperature within the mold during an individual molding cycle versus a conventional steel cooling design developed by means of CNC. Saifullah et al. [5] used bent copper tubes for the realization of the conformal cooling channels, but in a mold manufactured by means of CNC, thus fullfilling the surface finishing requirement. In this research, simulation and experimental results show that bimetallic conformal cooling channel design gives better cycle time, which ultimately increases production rate as well as the fatigue life of the mold. Eiamsa et al. [6] used a new MIG/MAG melding torch manufacturing technique attached to a CNC machine as a hybrid system. In his study, he built a layered mold, designing the cooling by means of bubbler channels and then machining the surface. This technology has made it possible to reduce the cycle time and the energy consumption. Xu et al. [7] presented an analytical model for the sizing of the main technological parameters of the cooling system based on the decomposition of the mold surface into small sections called cooling zones, for which it creates an individual channel system. In an extensive comparison of tools made by 3D printing with conformal cooling against conventional tools, the conformally cooled tools were found to provide reductions of 20% in cooling time and 15% less part distortion. Dimla et al. [8] propose a method for the design and optimization of conformal cooling channels in cooling and heating processes using virtual prototypes. Analysis of virtual models showed that those with conformal cooling channels predicted a significantly reduced cycle time as well as marked improvement in the general quality of the surface finish when compared to a conventionally cooled mold. Park et al. [9] used different types of layout (zigzag, parallel, and spiral) for the conformal channels, applying analytical formulas and using CAE flow simulation to verify the results of the optimization process. Due to the shorter time to freeze and lower volume shrinkage, the proposed cooling channels gave a shorter cycle time and a better quality product. More recently, Park et al. [10] presented the development

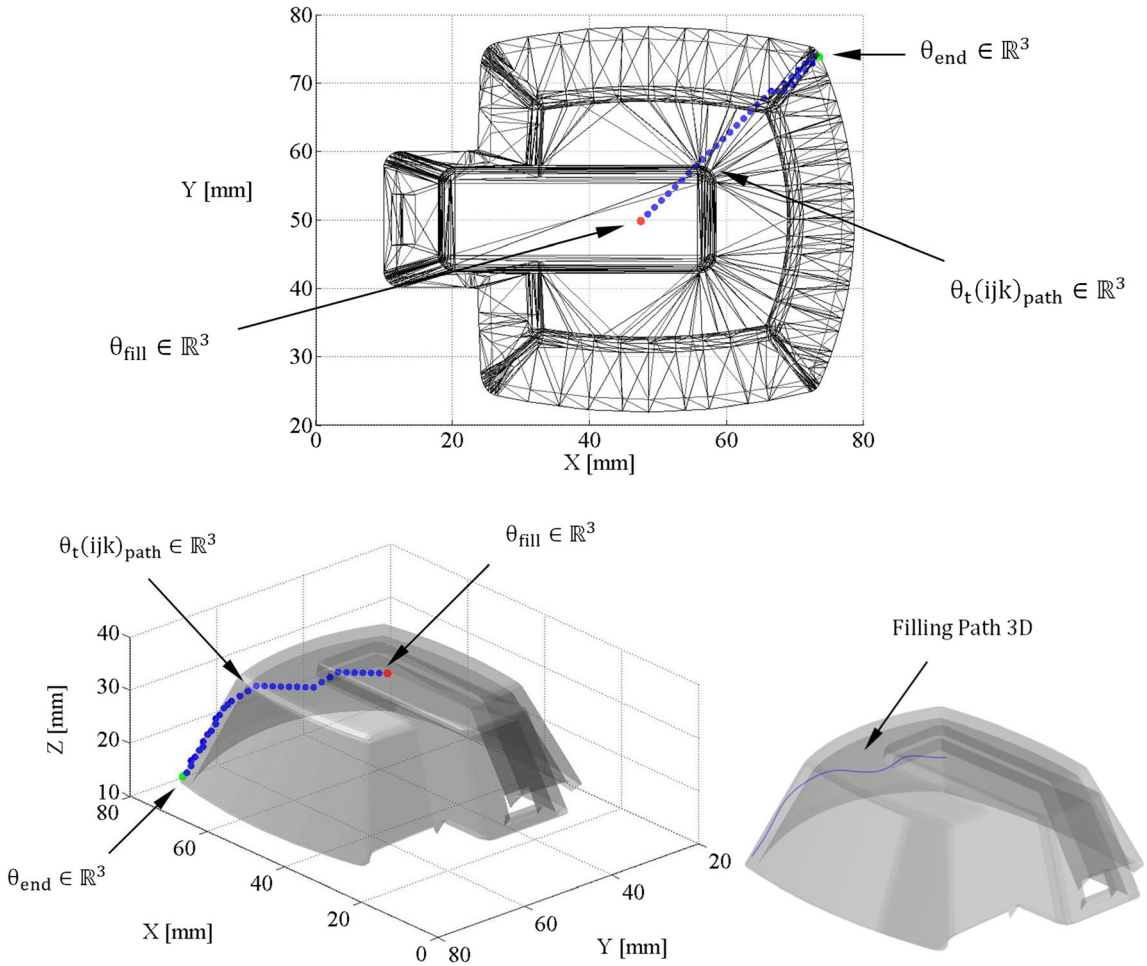


**Fig. 10** Representation of the filling path 3D obtained with the injection start point and the end point

of a smart plastic injection mold with conformal cooling channels for making a complex automotive part with variable thickness at some positions. The mold was designed with special inserts. Selective laser melting (SLM) 3D printing has been used to make the inserts with conformal cooling channels inside. In the first phase of the development process, the research results showed that conformal cooling channels reduce the cycle time by approximately 30% compared to conventional cooling channels. Au et al. [11] proposed a methodology based on the use of geometric visibility algorithms to generate the automated design of the cooling channels and their application to complex surfaces in injection molds. In Au et al. [12], he continued his research by presenting an alternative design method consisting of a conformal cooling passageway with porous multi-connected characteristics, based on the principle of duality. The results of their work provided a more uniform mold cooling profile compared with existing conformal designs. The cumulative effect of the heat energy increases the temperature of the outflow in the conformal cooling channels, so that the amount of heat energy absorbed by the outflow is minimal. In order to compensate the gradual increase in the temperature of the coolant from the input to the output pipes, Au et al. [13] proposed a method of adjusting the distance between the conformal cooling channels and the surface of the cavities. With this new variable distance design, the heat is extracted more efficiently than by means of the existing conformal cooling channel designs.

The time used for mold clamping, mold opening, and part ejection depends on the part geometry and the distance required for ejecting the part from the cavity or the core. Ramos et al. [14] presented a global optimization strategy for the injection molding cycle time, covering all time steps related to the injection molding process including a novel mathematical model designed to predict the ejection time.

Recently, Mercado et al. [15] presented the results of an analytical study aimed to determine the most representative variables which are part of the cycle time and how they influence the magnitude of the cycle time. Ferreira et al. [16] developed a framework that tackles the design of an injection molding system in a global way, through structural, thermal,

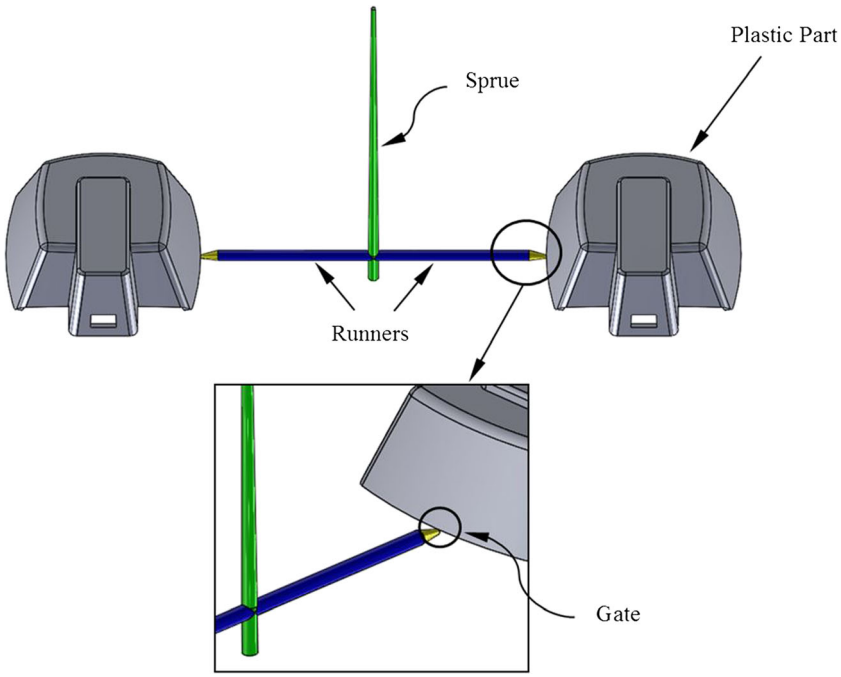


**Fig. 11** Feeding system of an injection mold for two cavities

rheological, and mechanical domain integration. To validate it, single objective optimization is presented, leading to a 42% reduction in cycle time. Dwivedi et al. [17] developed an intelligent knowledge-based tool to aid the plastic injection molding process, collecting the rules and selection of the appropriate expert system shell to organize the rules in a logical fashion. This approach determines cycle time on the basis of a coding system developed by conducting statistical studies on the cycle time as a function of part geometries.

Unfortunately, none of the methods described so far obtains the cycle time in a fully automated way only taking as input data the geometry of the plastic part and the material. The automated recognition of the surface of the plastic part for manufacturing applications presents great advantages [18–21], and]; however, it has not been used so far to obtain the geometric parameters necessary for the calculation of cycle time.

The purpose of the new procedure proposed in this paper is the automated determination of the cycle time for a plastic part, i.e., the time required to produce one or several plastic parts distributed among several cavities. The methodology developed has the advantage of calculating the cycle time in a global way, including an analysis of the main phases of injection molding (filling and cooling) taking as a starting point the geometry of the plastic part in discrete format and the thermoplastic material in which it will be manufactured. A new algorithm recognizes in a first phase the geometry of the part in an automated way, obtaining the set of geometric parameters necessary for the calculation of the cycle time. With the information obtained, a second analytical-empirical algorithm obtains the other technological parameters required for the automated calculation of the injection time, packing time, and cooling time of the plastic part, as well as the radius of the gate. The result is that we obtain one of the most important parameters of the mold in a minimum time, allowing the elaboration of budgets by personnel without experience in injection molding. The developed method has as an advantage its independence from the CAD model and the modeler where the part has been designed, since it works with the

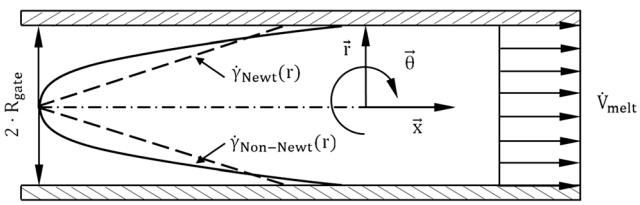


**Fig. 12** Shear velocity profile for a Newtonian and non-Newtonian fluid

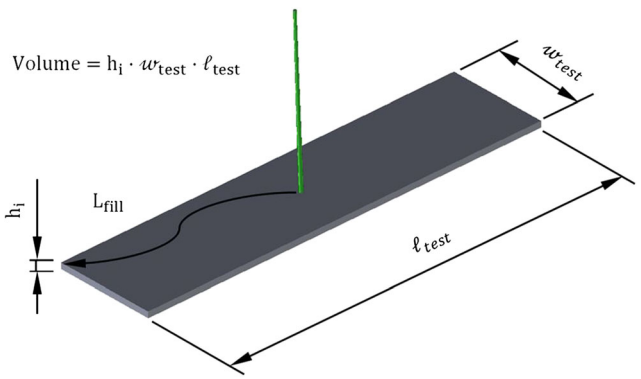


**Fig. 13** Definition of the rectangular plate shape test part used in the empirical model together with the most influential geometric parameters in the injection phase

**Table 1** Geometric characteristics of the rectangular plate shape test part used in the empirical model

| Volume [mm$^3$] | Melt plastic flow path, $L_{fill}$ [mm] | $\exists_{test}$ [mm] | $\ell_{test}$ [mm] | Volume [mm$^3$] | Melt plastic flow path, $L_{fill}$ [mm] | $\exists_{test}$ [mm] | $\ell_{test}$ [mm] |
|---|---|---|---|---|---|---|---|
| $h_i$·200 | 20.616 | 5 | 40 | $h_i$·7200 | 84.853 | 60 | 120 |
| $h_i$·300 | 30.414 | 5 | 60 | $h_i$·8400 | 92.195 | 60 | 140 |
| $h_i$·400 | 22.361 | 10 | 40 | $h_i$·9600 | 100.000 | 60 | 160 |
| $h_i$·600 | 31.623 | 10 | 60 | $h_i$·10,800 | 108.167 | 60 | 180 |
| $h_i$·800 | 41.231 | 10 | 80 | $h_i$·12,000 | 116.619 | 60 | 200 |
| $h_i$·1000 | 50.990 | 10 | 100 | $h_i$·2800 | 72.801 | 70 | 40 |
| $h_i$·800 | 28.284 | 20 | 40 | $h_i$·4200 | 76.158 | 70 | 60 |
| $h_i$·1200 | 36.056 | 20 | 60 | $h_i$·5600 | 80.623 | 70 | 80 |
| $h_i$·1600 | 44.721 | 20 | 80 | $h_i$·7000 | 86.023 | 70 | 100 |
| $h_i$·2000 | 53.852 | 20 | 100 | $h_i$·8400 | 92.195 | 70 | 120 |
| $h_i$·2400 | 63.246 | 20 | 120 | $h_i$·9800 | 98.995 | 70 | 140 |
| $h_i$·2800 | 72.801 | 20 | 140 | $h_i$·11,200 | 106.301 | 70 | 160 |
| $h_i$·3200 | 82.462 | 20 | 160 | $h_i$·12,600 | 114.018 | 70 | 180 |
| $h_i$·3600 | 92.195 | 20 | 180 | $h_i$·14,000 | 122.066 | 70 | 200 |
| $h_i$·4000 | 101.980 | 20 | 200 | $h_i$·3200 | 82.462 | 80 | 40 |
| $h_i$·1200 | 36.056 | 30 | 40 | $h_i$·4800 | 85.440 | 80 | 60 |
| $h_i$·1800 | 42.426 | 30 | 60 | $h_i$·6400 | 89.443 | 80 | 80 |
| $h_i$·2400 | 50.000 | 30 | 80 | $h_i$·8000 | 94.340 | 80 | 100 |
| $h_i$·3000 | 58.310 | 30 | 100 | $h_i$·9600 | 100.000 | 80 | 120 |
| $h_i$·1600 | 44.721 | 40 | 40 | $h_i$·11,200 | 106.301 | 80 | 140 |
| $h_i$·2400 | 50.000 | 40 | 60 | $h_i$·12,800 | 113.137 | 80 | 160 |
| $h_i$·3200 | 56.569 | 40 | 80 | $h_i$·14,400 | 120.416 | 80 | 180 |
| $h_i$·4000 | 64.031 | 40 | 100 | $h_i$·16,000 | 128.062 | 80 | 200 |
| $h_i$·4800 | 72.111 | 40 | 120 | $h_i$·3600 | 92.195 | 90 | 40 |
| $h_i$·5600 | 80.623 | 40 | 140 | $h_i$·5400 | 94.868 | 90 | 60 |
| $h_i$·6400 | 89.443 | 40 | 160 | $h_i$·7200 | 98.489 | 90 | 80 |
| $h_i$·7200 | 98.489 | 40 | 180 | $h_i$·9000 | 102.956 | 90 | 100 |
| $h_i$·8000 | 107.703 | 40 | 200 | $h_i$·10,800 | 108.167 | 90 | 120 |
| $h_i$·2000 | 53.852 | 50 | 40 | $h_i$·12,600 | 114.018 | 90 | 140 |
| $h_i$·3000 | 58.310 | 50 | 60 | $h_i$·14,400 | 120.416 | 90 | 160 |
| $h_i$·4000 | 64.031 | 50 | 80 | $h_i$·16,200 | 127.279 | 90 | 180 |
| $h_i$·5000 | 70.711 | 50 | 100 | $h_i$·18,000 | 134.536 | 90 | 200 |
| $h_i$·6000 | 78.102 | 50 | 120 | $h_i$·4000 | 101.980 | 100 | 40 |
| $h_i$·7000 | 86.023 | 50 | 140 | $h_i$·6000 | 104.403 | 100 | 60 |
| $h_i$·8000 | 94.340 | 50 | 160 | $h_i$·8000 | 107.703 | 100 | 80 |
| $h_i$·9000 | 102.956 | 50 | 180 | $h_i$·10,000 | 111.803 | 100 | 100 |
| $h_i$·10,000 | 111.803 | 50 | 200 | $h_i$·12,000 | 116.619 | 100 | 120 |
| $h_i$·2400 | 63.246 | 60 | 40 | $h_i$·14,000 | 122.066 | 100 | 140 |
| $h_i$·3600 | 67.082 | 60 | 60 | $h_i$·16,000 | 128.062 | 100 | 160 |
| $h_i$·4800 | 72.111 | 60 | 80 | $h_i$·18,000 | 134.536 | 100 | 180 |
| $h_i$·6000 | 78.102 | 60 | 100 | $h_i$·20,000 | 141.421 | 100 | 200 |

mathematical model of the plastic part, analyzing the surfaces externally and can be implemented under any CAD software. In addition, the new algorithm presented in the paper does not require the use of special simulation software or the empirical evaluation of the experts to obtain the value of the cycle time

**Table 2** Thickness of the rectangular plate shape test part used in the empirical model

| | |
|---|---|
| $h_1$ [mm] | 1 |
| $h_2$ [mm] | 2 |
| $h_3$ [mm] | 3 |

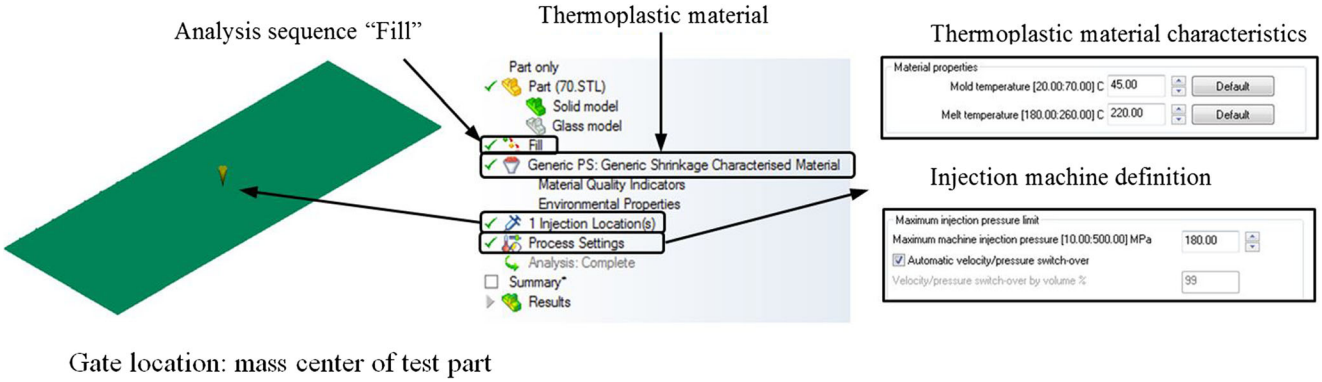


**Fig. 14** "Fill" analysis sequence in the Moldflow Advisor numerical calculation software.

in a minimum time. No existing method obtains the cycle time based on the automated recognition of the plastic part and the automated analysis of the numerical simulations of the injection phase, allowing the non-expert designer to obtain an adequate estimate of the cycle time for its presentation in manufacturing budgets.

## 3 Methodology

The cycle time required for the manufacture of a plastic part can be subdivided into four main times: injection time of the melt plastic, packing time, cooling time, and mold opening-closing time. From these subsets of times, the new procedure presented in the paper focuses on the calculation of the injection time of the melt plastic, packing time, and cooling time. Since the analytical-empirical results obtained are to be compared with the numerical results obtained by means of the CAE MoldFlow Advisor software [22], the mold opening-closing time has not been taken into account because this parameter is entered manually in the numerical calculation software, according to the characteristics of the injection machine available. Therefore, the main time analyzed runs from the beginning of the injection phase of melt plastic until the plastic material of the part reaches the mold ejection temperature or opening temperature (see Eq. 1). The sum of this time together with the opening-closing time of the mold is the total cycle time.

$$T_{\text{cycle}} = T_{\text{fill}} + T_{\text{packing}} + T_{\text{cooling}} + T_{\text{open-close}} \tag{1}$$

Where $T_{\text{fill}}$ [s] represents the analytical time of injection, $T_{\text{packing}}$ [s] represents the analytical time of packing of the plastic part, $T_{\text{cooling}}$ [s] represents the analytical cooling time of the plastic part, and $T_{\text{open-close}}$ [s] represents the mold opening-closing time. The cycle time depends on a set of geometric parameters linked to the topology of the plastic part, as well as parameters dependent on the thermoplastic material of manufacture. In relation to the parameters dependent on geometry, the geometric-analytical procedure proposed in the paper establishes other factors as more influential parameters in the calculation of cycle time: the average and maximum thickness of the plastic part, the volume of the part, and the distance traveled by the melt plastic flow into the cavity of the injection mold. Therefore, prior to the analysis of the different phases of the cycle time, the new procedure automatically obtains the value of these parameters through a new automated recognition algorithm for the geometry of the plastic part in a discrete format. It should be noted that the definition of the volume of the plastic part is obtained using conventional geometric algorithms.

$$T_{\text{cycle}} := T_{\text{cycle}}\left(H_{\text{part}}, H_{\text{part}_{\text{max}}}, V_{\text{part}}, L_{\text{fill}}\right)$$

where $H_{\text{part}}$ [m] represents the average thickness of the plastic part, $H_{\text{part}_{\text{max}}}$ [m] represents the maximum thickness of the plastic part, $V_{\text{part}}$ [$m^3$] represents the total volume of the plastic part, and $L_{\text{fill}}$ [m] represents the distance traveled by the melt plastic flow.

### 3.1 Determination of the thickness map of the plastic part

The present methodology proposes an algorithm for obtaining the geometric variable average thickness $H_{\text{part}}$ and maximum thickness $H_{\text{part}_{\text{max}}}$ (see Eq. 17) of the plastic part. Starting from the 3D geometry of the plastic part $\Omega \in \mathbb{R}^3$, the developed algorithm generates a discrete three-dimensional mesh formed by a set of nodes $\Omega'_{\text{n}} \in \mathbb{R}^3$ and triangular facets $\Omega'_{\text{f}} \in \mathbb{R}^3$. An n×3 range array of triangular facets $\Omega'_{\text{f}}$ is defined from the nodes $\text{F}_{\text{ij}} = \{P_{\text{i1}}, P_{\text{i2}}, P_{\text{i3}}\} \in \Omega'_{\text{f}}$ that compose it. While a 3·n×3 range array of nodes $\Omega'_{\text{n}}$ is defined from the coordinates $X$, $Y$, $Z$ of each node $P_{\text{ij}} = \{X_{\text{ij}}, Y_{\text{ij}}, Z_{\text{ij}}\} \in \Omega'_{\text{n}}$. The value of $n$ coincides with the total number of triangular facets $F_{\text{i}}$ forming the mesh $\Omega' \in \mathbb{R}^3$.

$$\forall \Omega \in \mathbb{R}^3 \rightarrow \Omega' \in M_{1\times 2}(\mathbb{R}) \rightarrow \Omega' = \{\Omega'_{\text{f}}\, \Omega'_{\text{n}}\}$$
$$\Omega'_{\text{f}} \in M_{\text{n}\times\text{m}}\left(\mathbb{R}^3\right) \;;\; \Omega'_{\text{n}} \in M_{3\cdot\text{n}\times\text{m}}\left(\mathbb{R}^3\right)$$

**Table 3** 3D surfaces interpolated by 4th degree polynomials which relate, for a given thickness, the volume of the cavity, the path of the melt plastic, and the optimum gate radius for all the thermoplastic materials used

| Acrylonitrile butadiene styrene (ABS) – $R_{gate_{hat}}$ (Axis Z)vs $L_{fill}$(Axis X) vs Volume (Axis Y) | |
|---|---|
| Plastic Part thickness – 1 mm | Plastic Part thickness – 2 mm |
| 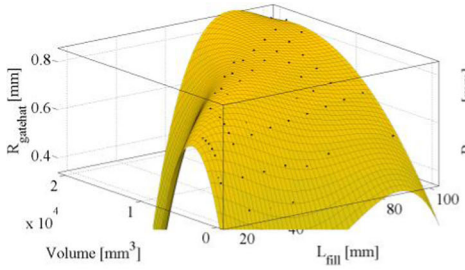 | 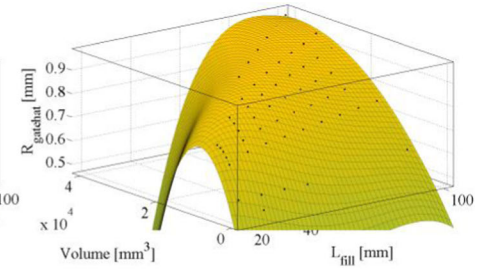 |
| Plastic Part thickness – 3 mm | |
| 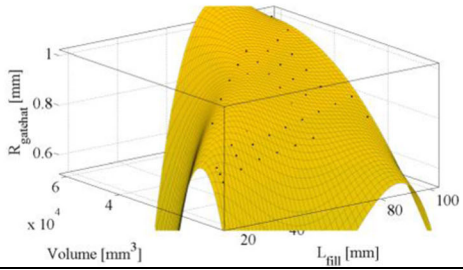 | |
| Polyoxymethylene (POM) – $R_{gate_{hat}}$ (Axis Z)vs $L_{fill}$(Axis X) vs Volume (Axis Y) | |
| Plastic Part thickness – 1 mm | Plastic Part thickness – 2 mm |
| 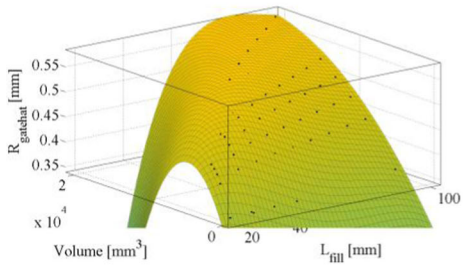 | 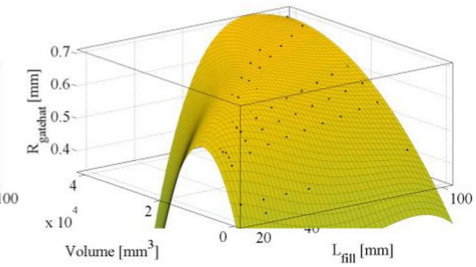 |
| Plastic Part thickness – 3 mm | |
| 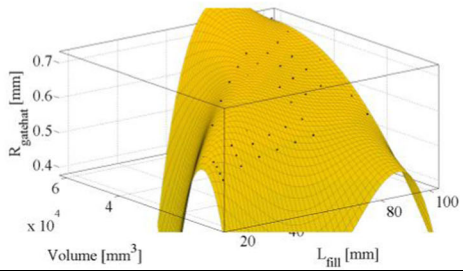 | |
| Polypropylene (PP) – $R_{gate_{hat}}$ (Axis Z)vs $L_{fill}$(Axis X) vs Volume (Axis Y) | |

Figure 1 shows the geometry $\Omega \in \mathbb{R}^3$ next to the discrete mesh $\Omega' \in \mathbb{R}^3$ obtained after the preprocessing phase of the geometry of the plastic part $\Omega \in \mathbb{R}^3$. Figure 2 shows the representation of a facet $F_{ij} = \{P_{i1}, P_{i2}, P_{i3}\} \in \Omega'_f$, and the nodes $P_{ij} = \{X_{ij}, Y_{ij}, Z_{ij}\} \in \Omega'_n$ that compose it.

**Table 3** (continued)

| |
|---|
| Plastic Part thickness – 1 mm<br> 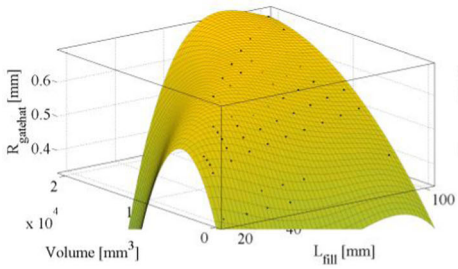 <br> |
| Plastic Part thickness – 2 mm<br> 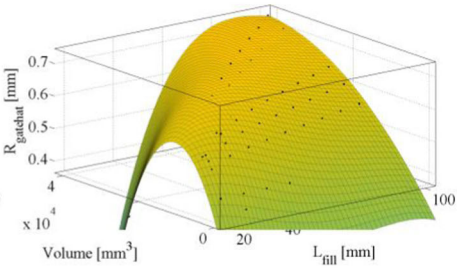 <br> |
| Plastic Part thickness – 3 mm<br> 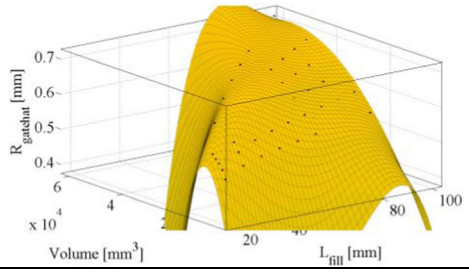 <br> |
| Polystyrene (PS) – $R_{gate_{hat}}$ (Axis Z)vs $L_{fill}$(Axis X) vs Volume (Axis Y) |
| Plastic Part thickness – 1 mm<br> 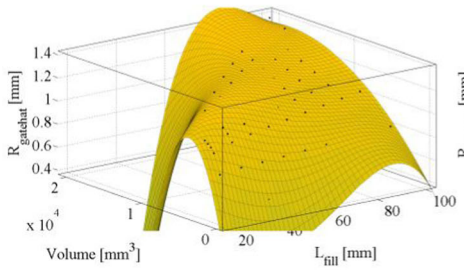 <br> |
| Plastic Part thickness – 2 mm<br> 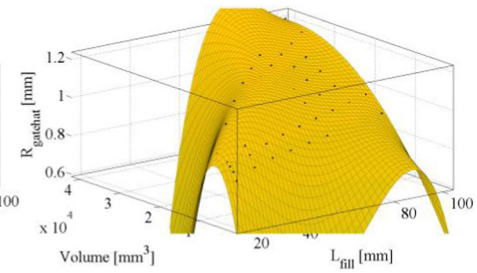 <br> |
| Plastic Part thickness – 3 mm<br> 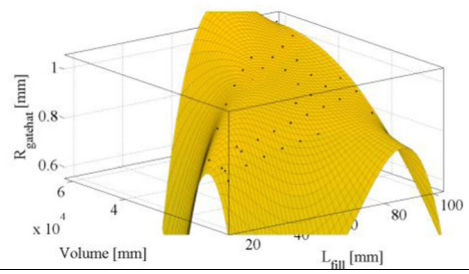 <br> |

After the preprocessing operation of the Ω geometry and obtaining the corresponding discrete mesh $\Omega'$, a nodal mesh or 2D nodal quadrature $A_q \in \mathbb{R}^2$ is defined along a plane Π parallel to the coordinate plane *XY*. This nodal quadrature $A_q \in \mathbb{R}^2$ is generated from the dimensions $\ell \times w$ of the mesh $\Omega'$ coincident with the length $\ell$ and width $w$ of Ω. The quadrature $A_q$ is formed by a set of points $\alpha_q(ij) \in \mathbb{R}^3$ with coordinates *X*, *Y*, *Z* $\left[\alpha_q(ij)_x \quad \alpha_q(ij)_y \quad \alpha_q(ij)_z\right]$, with the value of $\alpha_q(ij)_z$ constant for all points $\alpha_q(ij) \in \mathbb{R}^3$. In turn, $\alpha_q(ij)_z$ has a value equal to the lowest coordinate $Z_{ij}$ of the set of nodes $P_{ij} \in \Omega'_n$ (see Fig. 3).

**Table 4** R-Square obtained in the interpolation by means of 4th degree polynomial functions for the thermoplastic materials used

| Thermoplastic material | Part thickness 1 mm $R_{gate_{hat}}$ vs $L_{fill}$ vs Volume | Part thickness 2 mm $R_{gate_{hat}}$ vs $L_{fill}$ vs Volume | Part thickness 3 mm $R_{gate_{hat}}$ vs $L_{fill}$ vs Volume |
|---|---|---|---|
| Acrylonitrile butadiene styrene (ABS) | 0.9904 | 0.9888 | 0.9692 |
| Polyoxymethylene (POM) | 0.9865 | 0.9862 | 0.9588 |
| Polypropylene (PP) | 0.9884 | 0.9652 | 0.9600 |
| Polystyrene (PS) | 0.9394 | 0.9737 | 0.9416 |

**Table 5** R-Square obtained for the 1st, 2nd, 3rd, 4th, and 5th multi-variable polynomial regressions, for the thermoplastic materials used

| Thermoplastic material | $g_j = 1$ | $g_j = 2$ | $g_j = 3$ | $g_j = 4$ | $g_j = 5$ |
|---|---|---|---|---|---|
| Acrylonitrile butadiene styrene (ABS) | 0.6468 | 0.8829 | 0.9148 | − 0.8358 | − 6.4148 |
| Polyoxymethylene (POM) | 0.7298 | 0.9381 | 0.9514 | − 0.8560 | − 6.3999 |
| Polypropylene (PP) | 0.6002 | 0.8840 | 0.9121 | − 1.5505 | − 8.8087 |
| Polystyrene (PS) | 0.4535 | 0.7652 | 0.8325 | − 1.1562 | − 6.8338 |

$$A_q := \alpha_q(ij)_{\frac{\ell}{\beta}\ x\ \frac{w}{\beta}}$$

$$A_q \in \mathcal{M}_{\frac{\ell}{\beta}\ x\ \frac{w}{\beta}}\ (\mathbb{R}) \rightarrow \alpha_q(ij) = \left[\alpha_q(ij)_x \quad \alpha_q(ij)_y \quad \alpha_q(ij)_z\right] \in \mathbb{R}^3$$

$$\alpha_q(ij)_z = \text{cte}$$

$$1 \le i \le \frac{\ell}{\beta}\ ;\ 1 \le j \le \frac{w}{\beta}$$

Each point of the nodal quadrature $\alpha_q(ij)$ is separated by a distance $\beta$. The value of this geometric parameter corresponds to the minimum detail of the geometry $\Omega$, and represents the precision of the thickness analysis of the plastic part. This

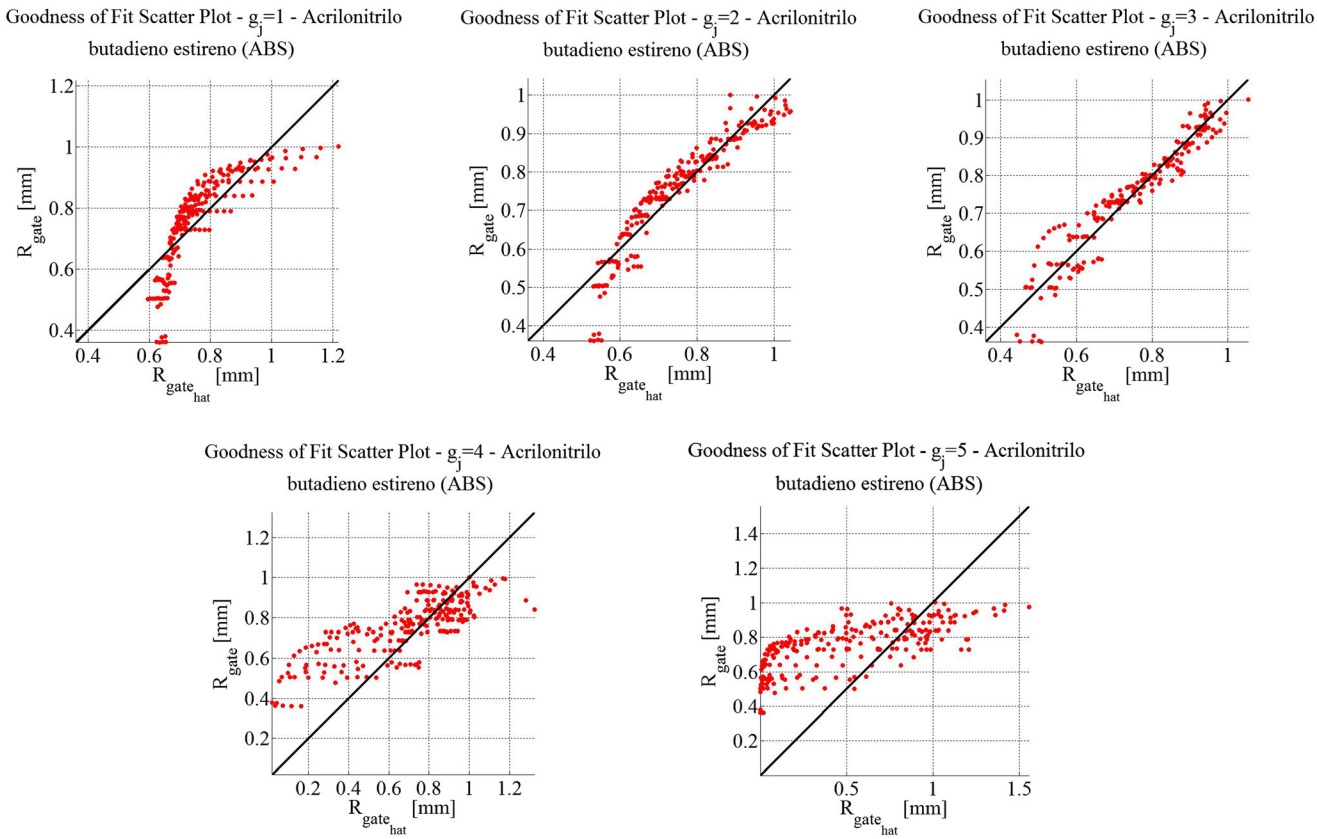


**Fig. 15** Representation of goodness of fit scatter for 1st, 2nd, 3rd, 4th, and 5th polynomials of ABS thermoplastic material

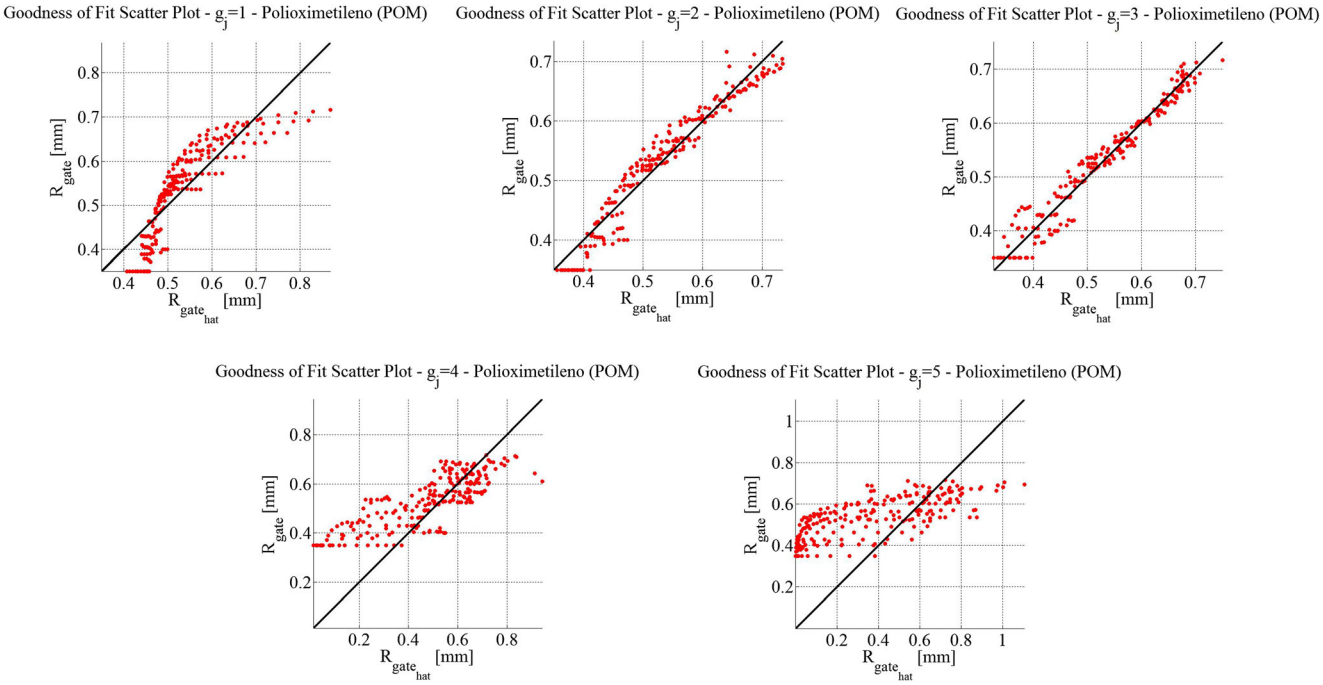


**Fig. 16** Representation of goodness of fit scatter for 1st, 2nd, 3rd, 4th, and 5th polynomials of POM thermoplastic material

parameter can be selected by the user. Then, from the set of points $\alpha_q(ij) \in \mathbb{R}^3$, a beam of lines $\mathcal{R}_q$ with direction $\overrightarrow{D_z}$ (coordinate axis $Z$ along the parting direction) is drawn, obtaining the points of intersection $\Lambda_t$ between the beam of lines $\mathcal{R}_q$ and the discrete mesh $\Omega'$ (see Fig. 4). Those points $\alpha_q(ij)$ that do not intersect with the discrete mesh $\Omega'$ are removed from the analysis.

$$\mathcal{R}_q \in \mathcal{M}_{\frac{\ell}{\beta} x \frac{w}{\beta}} (\mathbb{R}) \rightarrow \mathcal{R}_q := r_q(ij)_{\frac{\ell}{\beta} x \frac{w}{\beta}}$$

$$\forall\, \alpha_q(ij)\ \exists\, r_t(ij) = \left\{ \begin{matrix} \text{Origin: } [\alpha_q(ij)_x \quad \alpha_q(ij)_y \quad \alpha_q(ij)_z] \\ \text{Direction: } [0\ 0\ 1] \end{matrix} \right\} \in \mathbb{R}^3$$

$$\forall r_q(ij)\ \exists\, \Lambda_t(ij) \mid \{ r_q(ij) \cap \Omega' \} \neq \emptyset \rightarrow \alpha_q(ij) = \Lambda_t(ij) \in \mathbb{R}^3$$

Evaluating the height difference along the direction $\overrightarrow{D_z}$, between each pair of intersection points $\Lambda_t(ij)$ for each line $\nabla_q(ij)$ of the beam of lines $\mathcal{R}_q$, the thickness $\mathcal{T}(ij)$ of the plastic part corresponding to each point $\alpha_q(ij)$ is obtained directly. From the value of $\mathcal{T}(ij)$ at each point $\alpha_q(ij)$ of the nodal quadrature $A_q$, the Thicknesses Map, Thickness(ij) of the discrete mesh $\Omega'$ is generated (see Fig. 5). Then, from Thickness(ij), the mean thickness value $H_{part}$ is defined as the arithmetic mean of the set of thicknesses in Thickness(ij) and the maximum thickness $H_{part_{max}}$ as the maximum value of the set of thicknesses in Thickness(ij). All these values are obtained from the discrete geometry of the plastic part $\Omega'$.

$$\forall\, r_q(ij)\ \exists\, \mathcal{T}(ij) = \text{Thickness}(ij) = \max\left( r_q(ij) \cap \Omega' \right)_z - \min\left( r_t(ij) \cap \Omega' \right)_z$$

$$H_{part} = \overline{\text{Thickness}} \quad ; \quad H_{part_{max}} = \text{Max(Thickness)}$$

## 3.2 Distance traveled by the melt plastic flow

In order to calculate the distance traveled by the melt plastic flow, the discrete mesh $\Omega'$ and the coordinates $X$, $Y$, $Z$ of the location of the injection point $\theta_{fill} \in \mathbb{R}^3$ on the plastic part $\Omega$ are taken into account. In the case where the location of the injection point $\theta_{fill} \in \mathbb{R}^3$ is not entered by the user, the geometric algorithm locates the injection point in the region of $\Omega$ closest to its center of mass in order to obtain a filling process of the cavity with the least resistance to the melt plastic flow and a uniform and balanced flow.

$$\theta_{fill} = [\, \theta_{fillX} \quad \theta_{fillY} \quad \theta_{fillZ} \,]$$

Figure 6a shows the flow resistance indicator and gating suitability for the plastic part $\Omega$ obtained by means of MoldFlow Advisor CAE software. Figure 6b shows the location of the injection point $\theta_{fill}$ close to the mass center of the plastic part. Then a 3D nodal grid $\Theta_t \in \mathbb{R}^3$ is generated according to the dimensions $l \times w \times h$ of the Bounding Box of the geometry $\Omega$. Figure 7 shows the 3D nodal grid $\Theta_t \in \mathbb{R}^3$, and each point $\theta_t(ijk) \in \mathbb{R}^3$ that composes it. Similarly, parameter $\beta$ represents the precision of the nodal grid, which can be defined by the user.

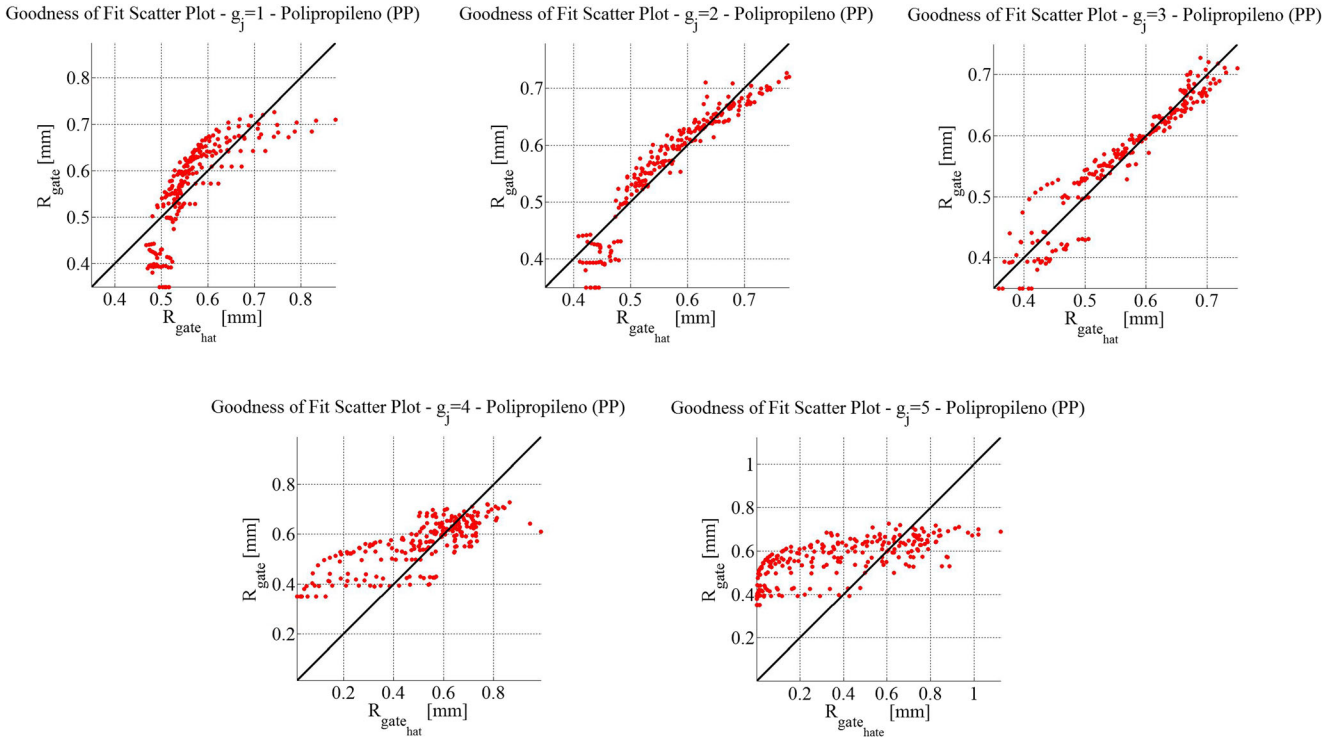


**Fig. 17** Representation of goodness of fit scatter for 1st, 2nd, 3rd, 4th, and 5th polynomials of PP thermoplastic material

$$\Theta_t \coloneqq \theta_t(ijk)_{\frac{\ell}{\beta} x \frac{w}{\beta} x \frac{\hbar}{\beta}}$$

$$\Theta_t \in \mathcal{M}_{\frac{\ell}{\beta} x \frac{w}{\beta} x \frac{\hbar}{\beta}}(\mathbb{R}) \rightarrow \theta_t(ijk) = [\theta_t(ijk)_x \quad \theta_t(ijk)_y \quad \theta_t(ijk)_z] \in \mathbb{R}^3$$

$$1 \le i \le \frac{\ell}{\beta} \; ; \; 1 \le j \le \frac{w}{\beta} \; ; \; 1 \le k \le \frac{\hbar}{\beta}$$

Next, a logical-geometric operation is performed in order to evaluate which points $\theta_t(ijk) \in \mathbb{R}^3$ of the 3D nodal grid $\Theta_t \in \mathbb{R}^3$ lie inside the volume $V_{part}$ of the discrete mesh $\Omega$. Thus, the array of points $\theta_t(ijk) \in \mathbb{R}^3$ belonging to the nodal grid $\Theta_t \in \mathbb{R}^3$ is divided into two subarrays. The first one, $\theta_t(ijk)_{in} \in \mathbb{R}^3$, contains those points $\theta_t(ijk) \in \mathbb{R}^3$ that lie inside the volume $V_{part}$ and the second one, $\theta_t(ijk)_{out} \in \mathbb{R}^3$, contains those points $\theta_t(ijk) \in \mathbb{R}^3$ that lie outside the volume $V_{part}$ (see Fig. 8).

$$\Theta_t(ijk) = \{\theta_t(ijk)_{in} \quad \theta_t(ijk)_{out}\}$$
$$\forall \theta_t(ijk) \left| \begin{pmatrix} \theta_t(ijk) \in V_{part} \rightarrow \theta_t(ijk) \in \theta_t(ijk)_{in} \\ \theta_t(ijk) \in V_{part} \rightarrow \theta_t(ijk) \in \theta_t(ijk)_{out} \end{pmatrix} \right.$$

The path distance of the melt plastic flow is established by means of a filling path 3D. That is, a set of points $\theta_t(ijk)_{path} \in \mathbb{R}^3$ that form the path that runs through the melt plastic flow from the injection point $\theta_{fill}$ to the end point $\theta_{end}$ where the melt plastic flow culminates to complete the volume of the cavity of the injection mold. The end point $\theta_{end}$ is set to that point $\theta_t(ijk)_{in}$ furthest from the injection point $\theta_{fill}$.

$$\forall \theta_t(ijk) \exists \theta_{end} | d(\theta_t(ijk), \theta_{fill}) = \text{Max}(d(\theta_t(ijk), \theta_{fill}))$$
$$\forall \theta_t(ijk) \exists \theta_{fill} | d(\theta_t(ijk), \theta_{fill}) = \text{Min}(d(\theta_t(ijk), \theta_{fill}))$$

The generation of the points $\theta_t(ijk)_{path}$ that make up the filling path 3D is achieved through an iterative process. This process aims to define the points $\theta_t(ijk)_{path}$ from the set of points $\theta_t(ijk)_{in}$ that lie inside the volume $V_{part}$. The first iteration is performed with the first point of the filling path 3D, i.e., the injection point $\theta_{fill}$. According to the nodal grid $\Theta_t$, a point $\theta_t(ijk)$ is distanced from its neighbor points $\theta_t(ijk)^{\pi}$ a distance $\sqrt{3}\beta$, $\sqrt{2}\beta$, or $\beta$, as shown in Fig. 9.

$$\forall \theta_t(ijk) \exists \theta_t(ijk)^{\pi} | d(\theta_t(ijk), \theta_t(ijk)^{\pi}) \le \sqrt{3\beta}$$
$$\pi = \{1, \ldots, 26\}$$

where $\pi$ represents the number of points adjacent to the point of analysis $\theta_t(ijk)$. The first iteration begins by looking for those neighboring points $\theta_t(ijk)^{\pi}$ at the injection point $\theta_{fill}$, since the first point of the filling path 3D is the injection point $\theta_{fill}$. Once those points are obtained $\theta_t(ijk)$ located less than $\sqrt{3}\beta$ from the injection point $\theta_{fill}$, i.e., the neighboring points $\theta_t(ijk)^{\pi}$ to the injection point $\theta_{fill}$, it is determined which one

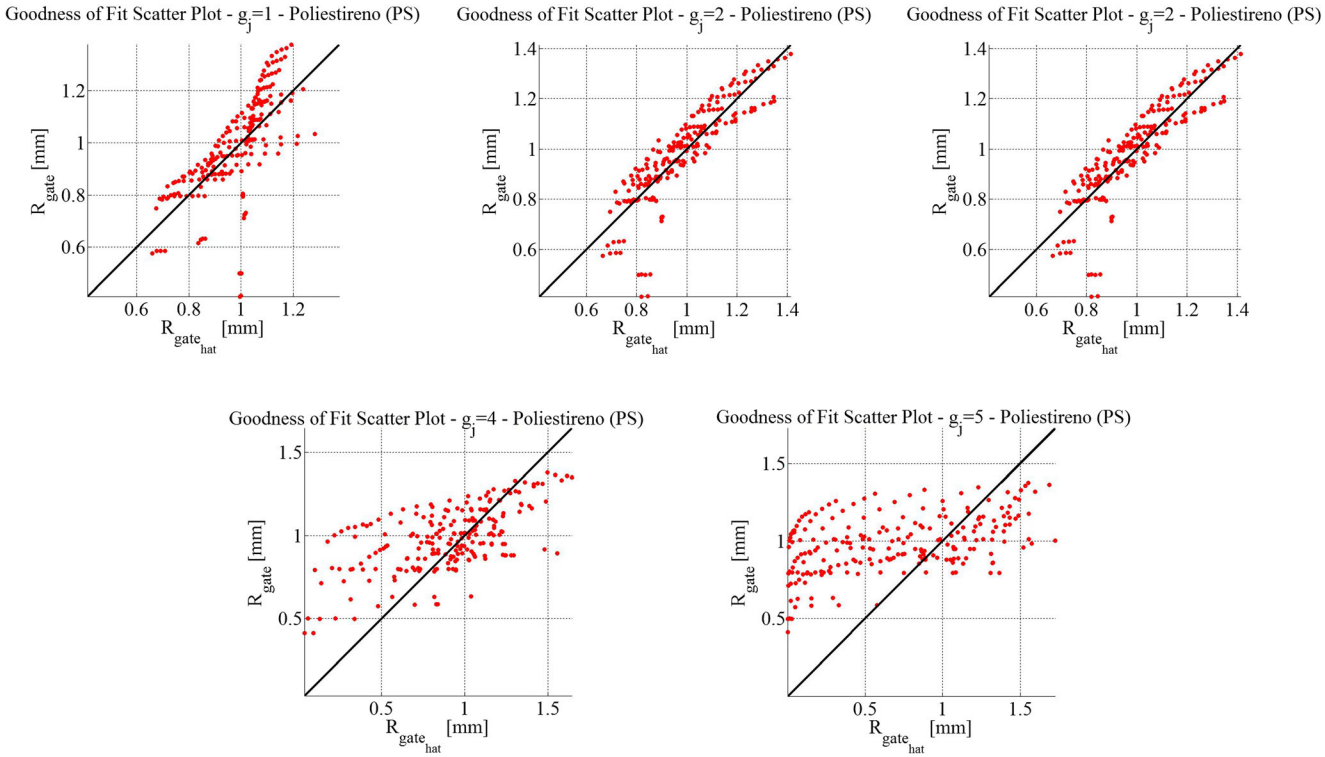


**Fig. 18** Representation of goodness of fit scatter for 1st, 2nd, 3rd, 4th, and 5th polynomials of PS thermoplastic material

of the neighboring points $\theta_t(ijk)^{\pi}$ is closest to the end point of the filling path 3D $\theta_{end}$.

$$\forall\theta_{fill}\exists\left\{\theta_t(ijk)^{\pi},\theta_t(ijk)_{path}\right\}\mid\left(\begin{array}{c}d(\theta_{fill},\theta_t(ijk)^{\pi})\le\sqrt{3}\beta\\ \mathrm{Max}\left(d\left(\theta_t(ijk)_{path},\theta_{end}\right)\right)\end{array}\right)$$

Thus, from the neighbor point $\theta_t(ijk)^{\pi}$ closest to the end point $\theta_{end}$, the following point $\theta_t(ijk)_{path}$ that conforms the filling path 3D is defined. This process searches for the shortest path of the existing $\pi$ paths for each point $\theta_t(ijk)_{path}$. For the other iterations, the analysis point $\theta_t(ijk)$ in each iteration will be the point $\theta_t(ijk)_{path}$ of the filling path 3D obtained in the immediately preceding iteration. This iterative process ends when the distance between the point of analysis of the current iteration $\theta_t(ijk)_{path}$ and the end point $\theta_{end}$ is equal to or less than $\sqrt{3}\beta$, because it means that the point $\theta_t(ijk)_{path}$ of analysis is neighbor to the end point $\theta_{end}$ of the filling path 3D.

Finally, in order to calculate the distance traveled by the melt plastic flow, the sum of the separation distances obtained between all the points $\theta_t(ijk)_{path}$ belonging to the filling path 3D is performed. The total length of the filling path 3D coincides with the length of the 3D spline curve relative to the set of points $\theta_t(ijk)_{path}$ as shown in Fig. 10.

### 3.3 Injection time

This section establishes the calculation of the injection time of a plastic part, applying a new analytic-empirical model. This model analyzes the evolution of the melt plastic flow along the feeding system of the injection mold. According to Fig. 11, the melt plastic flow runs through the different elements of the feeding system: sprue, runner, and gate; until it reaches the cavity of the mold. Referring to Fig. 11, it is verified that the element with the smallest section of the feeding system is the gate. Therefore, in the proposed analytic-empirical model, the hypothesis is formulated that at the gate the shear rate of the melt plastic flow is maximum [24].

The shear rate of a fluid moving in a circular section duct is defined by the variation of the velocity profile along the radius of the section (see Eq. 2).

$$\dot{\gamma}=\frac{\partial v(r)}{\partial r} \tag{2}$$

where $\dot{\gamma}$ [1/s] represents the shear rate, $v(r)$ [m/s] the velocity profile for a circular section duct, and $r$ [m] the radial coordinate of the cylindrical coordinate system in the duct (see Fig. 12). Developing Eq. 2 for a non-Newtonian fluid whose viscosity meets the Power-Law model [23], Eq. 3 is obtained.

**Table 6** Polynomial functions of 4th degree obtained in the multi-variable regression for the thermoplastic materials used

| Thermoplastic material | Multi-variable polynomial regression, $g_j = 3$<br>$X_1 = V_{part}$ ; $X_2 = L_{fill}$; $X_3 = H_{part}$ |
|---|---|
| Acrylonitrile butadiene styrene (ABS) | $C_{1,1} \cdot X_3^2 + C_{1,2} \cdot X_2 + C_{1,3} \cdot X_2 \cdot X_3 + C_{1,4} \cdot X_2 \cdot X_3^2 + C_{1,5} \cdot X_2^2 + C_{1,6} \cdot X_2^2 \cdot X_3 + C_{1,7} \cdot X_1 + C_{1,8} \cdot X_1 \cdot X_3 + C_{1,9} \cdot X_1 \cdot X_3^2 + C_{1,10} \cdot X_1 \cdot X_2 + C_{1,11} \cdot X_1 \cdot X_2 \cdot X_3 + C_{1,12} \cdot X_1 \cdot X_2^2 + C_{1,13} \cdot X_1^2 + C_{1,14} \cdot X_1^2 \cdot X_3 + C_{1,15} \cdot X_1^2 \cdot X_2 + C_{1,16} \cdot X_1^3 + C_{1,17} \cdot X_2^3 + C_{1,18} \cdot X_3^3$ |
| Polyoxymethylene (POM) | $C_{2,1} \cdot X_3^2 + C_{2,2} \cdot X_2 + C_{2,3} \cdot X_2 \cdot X_3 + C_{2,4} \cdot X_2 \cdot X_3^2 + C_{2,5} \cdot X_2^2 + C_{2,6} \cdot X_2^2 \cdot X_3 + C_{2,7} \cdot X_1 + C_{2,8} \cdot X_1 \cdot X_3 + C_{2,9} \cdot X_1 \cdot X_3^2 + C_{2,10} \cdot X_1 \cdot X_2 + C_{2,11} \cdot X_1 \cdot X_2 \cdot X_3 + C_{2,12} \cdot X_1 \cdot X_2^2 + C_{2,13} \cdot X_1^2 + C_{2,14} \cdot X_1^2 \cdot X_3 + C_{2,15} \cdot X_1^2 \cdot X_2 + C_{2,16} \cdot X_1^3 + C_{2,17} \cdot X_2^3 + C_{2,18} \cdot X_3^3$ |
| Polypropylene (PP) | $C_{3,1} \cdot X_3^2 + C_{3,2} \cdot X_2 + C_{3,3} \cdot X_2 \cdot X_3 + C_{3,4} \cdot X_2 \cdot X_3^2 + C_{3,5} \cdot X_2^2 + C_{3,6} \cdot X_2^2 \cdot X_3 + C_{3,7} \cdot X_1 + C_{3,8} \cdot X_1 \cdot X_3 + C_{3,9} \cdot X_1 \cdot X_3^2 + C_{3,10} \cdot X_1 \cdot X_2 + C_{3,11} \cdot X_1 \cdot X_2 \cdot X_3 + C_{3,12} \cdot X_1 \cdot X_2^2 + C_{3,13} \cdot X_1^2 + C_{3,14} \cdot X_1^2 \cdot X_3 + C_{3,15} \cdot X_1^2 \cdot X_2 + C_{3,16} \cdot X_1^3 + C_{3,17} \cdot X_2^3 + C_{3,18} \cdot X_3^3$ |
| Polystyrene (PS) | $C_{4,1} \cdot X_3^2 + C_{4,2} \cdot X_2 + C_{4,3} \cdot X_2 \cdot X_3 + C_{4,4} \cdot X_2 \cdot X_3^2 + C_{4,5} \cdot X_2^2 + C_{4,6} \cdot X_2^2 \cdot X_3 + C_{4,7} \cdot X_1 + C_{4,8} \cdot X_1 \cdot X_3 + C_{4,9} \cdot X_1 \cdot X_3^2 + C_{4,10} \cdot X_1 \cdot X_2 + C_{4,11} \cdot X_1 \cdot X_2 \cdot X_3 + C_{4,12} \cdot X_1 \cdot X_2^2 + C_{4,13} \cdot X_1^2 + C_{4,14} \cdot X_1^2 \cdot X_3 + C_{4,15} \cdot X_1^2 \cdot X_2 + C_{4,16} \cdot X_1^3 + C_{4,17} \cdot X_2^3 + C_{4,18} \cdot X_3^3$ |

| Thermoplastic material | Coefficients | | | |
|---|---|---|---|---|
| Acrylonitrile butadiene styrene (ABS) | $C_{1,1} = 0.1961$ | $C_{1,6} = 7.3657\text{e-}11$ | $C_{1,11} = -7.5012\text{e-}08$ | $C_{1,16} = 2.8546\text{e-}06$ |
| | $C_{1,2} = 3.1016\text{e-}05$ | $C_{1,7} = 0.032915$ | $C_{1,12} = 1.2336\text{e-}11$ | $C_{1,17} = 3.7743\text{e-}15$ |
| | $C_{1,3} = -8.6415\text{e-}06$ | $C_{1,8} = -0.010193$ | $C_{1,13} = -0.00056408$ | $C_{1,18} = -0.047127$ |
| | $C_{1,4} = 3.0993\text{e-}06$ | $C_{1,9} = 0.00012722$ | $C_{1,14} = 7.7161\text{e-}05$ | |
| | $C_{1,5} = -1.9172\text{e-}09$ | $C_{1,10} = 1.1426\text{e-}06$ | $C_{1,15} = -9.9175\text{e-}09$ | |
| Polyoxymethylene (POM) | $C_{2,1} = 0.15822$ | $C_{2,6} = 1.4108\text{e-}10$ | $C_{2,11} = -1.7346\text{e-}07$ | $C_{2,16} = 2.1084\text{e-}06$ |
| | $C_{2,2} = -1.0172\text{e-}05$ | $C_{2,7} = 0.027369$ | $C_{2,12} = 1.1765\text{e-}11$ | $C_{2,17} = 1.0142\text{e-}15$ |
| | $C_{2,3} = 1.6157\text{e-}05$ | $C_{2,8} = -0.011412$ | $C_{2,13} = -0.00043317$ | $C_{2,18} = -0.039619$ |
| | $C_{2,4} = -1.5679\text{e-}06$ | $C_{2,9} = 0.00099613$ | $C_{2,14} = 7.0535\text{e-}05$ | |
| | $C_{2,5} = -1.6757\text{e-}09$ | $C_{2,10} = 1.177\text{e-}06$ | $C_{2,15} = -8.4041\text{e-}09$ | |
| Polypropylene (PP) | $C_{3,1} = 0.14709$ | $C_{3,6} = -9.4582\text{e-}11$ | $C_{3,11} = -2.2491\text{e-}08$ | $C_{3,16} = 2.3725\text{e-}06$ |
| | $C_{3,2} = 2.7784\text{e-}05$ | $C_{3,7} = 0.026629$ | $C_{3,12} = 8.5028\text{e-}12$ | $C_{3,17} = 4.5108\text{e-}15$ |
| | $C_{3,3} = -1.7787\text{e-}05$ | $C_{3,8} = -0.0071481$ | $C_{3,13} = -0.00046786$ | $C_{3,18} = -0.036088$ |
| | $C_{3,4} = 5.3253\text{e-}06$ | $C_{3,9} = -0.00020091$ | $C_{3,14} = 6.0882\text{e-}05$ | |
| | $C_{3,5} = -1.112\text{e-}09$ | $C_{3,10} = 9.051\text{e-}07$ | $C_{3,15} = -8.0587\text{e-}09$ | |
| Polystyrene (PS) | $C_{4,1} = 0.17544$ | $C_{4,6} = 1.5728\text{e-}10$ | $C_{4,11} = -1.6364\text{e-}07$ | $C_{4,16} = 5.3103\text{e-}06$ |
| | $C_{4,2} = 8.4813\text{e-}05$ | $C_{4,7} = 0.058605$ | $C_{4,12} = 2.7602\text{e-}11$ | $C_{4,17} = -2.0513\text{e-}15$ |
| | $C_{4,3} = -4.4919\text{e-}05$ | $C_{4,8} = -0.020103$ | $C_{4,13} = -0.0010224$ | $C_{4,18} = -0.039722$ |
| | $C_{4,4} = 9.0061\text{e-}06$ | $C_{4,9} = 0.0010012$ | $C_{4,14} = 0.0001628$ | |
| | $C_{4,5} = -2.7857\text{e-}09$ | $C_{4,10} = 1.9758\text{e-}06$ | $C_{4,15} = -2.0066\text{e-}08$ | |

$$\dot{\gamma} = \frac{\left(3 + \frac{1}{n}\right) \cdot \dot{V}_{melt}}{\pi \cdot R^3} \tag{3}$$

where $\dot{V}_{melt}$ [$m^3$/s] represents the flow rate of the melt plastic flow running through the feeding system (see Fig. 12) and $R$ [m] represents the radius of the section of the circular duct. Power-Law relates the viscosity and

**Table 7** Main properties of the thermoplastic materials used in the analytic-empirical model

| Thermoplastic material | Acrylonitrile butadiene styrene (ABS) | Polyoxymethylene (POM) | Polypropylene (PP) | Polystyrene (PS) |
|---|---|---|---|---|
| Ejection temperature, $T_{eject}$ [°C] | 115 | 135 | 101 | 75 |
| Thermal diffusivity, $\alpha_s$ [$m^2$/s] | $1.1064 \cdot 10^{-07}$ | $7.6880 \cdot 10^{-08}$ | $8.2185 \cdot 10^{-08}$ | $1.1103 \cdot 10^{-07}$ |
| Temperature of the melt plastic flow, $T_{melt}$ [°C] | 275 | 210 | 240 | 220 |
| Mean temperature of the mold walls, $\overline{T_m}$ [°C] | 70 | 90 | 40 | 45 |
| Viscosity index, $n$ | 0.4000 | 0.6681 | 0.2751 | 0.2200 |
| Maximum shear rate, $\dot{\gamma}_{max}$ [1/s] | 40,000 | 40,000 | 100,000 | 40,000 |

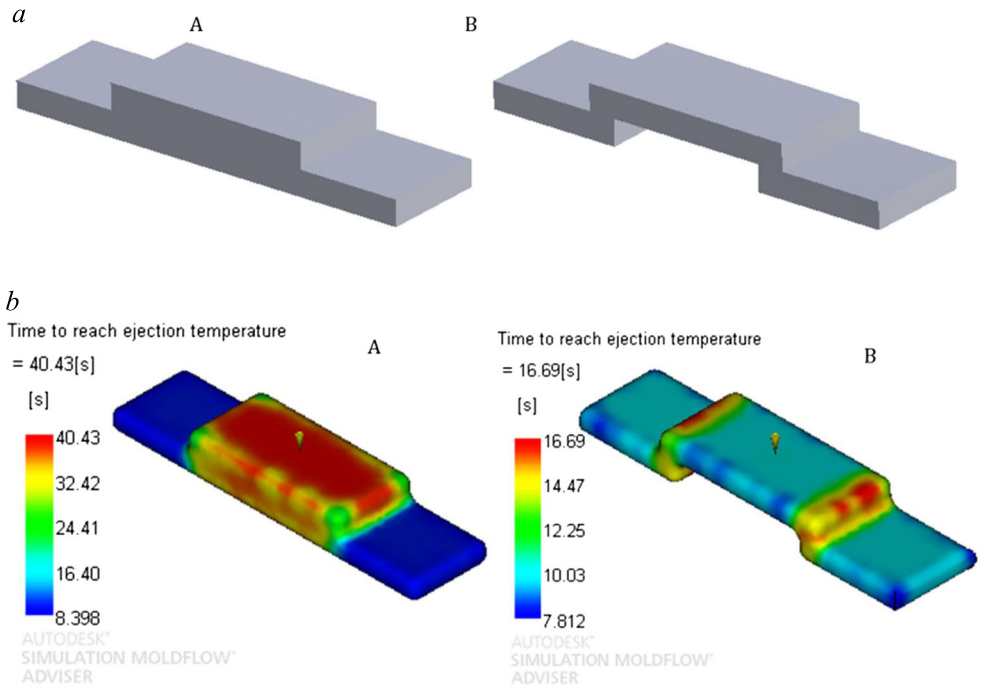


**Fig. 19** **a** A: Plastic part of ABS material with non-uniform thickness and B: Plastic part of ABS material with uniform thickness. **b** Time to reach the ejection temperature for plastic parts A and B

the shear velocity of a non-Newtonian fluid by means of an exponential type function. Equation 4 shows that this model is defined by two non-Newtonian fluid constants: flow consistency index $K$ [Pa·s$^n$] and the viscosity index $n$. The performance of the non-Newtonian fluid viscosity using the Power-Law model is accurate for high shear rates. Therefore, since one of the premises established in the present analytical-empirical model is that the shear rate of the non-Newtonian fluid is maximum, the use of the Power-Law model is correct and accurate.

$$\mu_{\text{melt}} = K \cdot \dot{\gamma}^{\,n-1} \tag{4}$$

where $\mu_{\text{melt}}$ [Pa·s] represents the melt plastic viscosity. Applying Eq. 3, expression of the shear rate, to the gate of the feeding system, and introducing the premise that the shear rate at the gate is maximum, Eq. 5 is obtained.

$$\dot{\gamma}_{\max} = \frac{\left(3 + \frac{1}{n}\right) \cdot \dot{V}_{\text{melt}}}{\pi \cdot R_{\text{gate}}^3} \tag{5}$$

**Table 8** Material properties of the injection mold

| Material: structural steel P-20 | Nomenclature | Value | Units |
|---|---|---|---|
| Thermal conductivity | $\delta_{\text{steel}}$ | $45.00 \cdot 10^{-3}$ | W/mm·°C |
| Thermal diffusivity | $\alpha_{\text{steel}}$ | $8.73 \cdot 10^{-2}$ | mm$^2$/s |

where $\dot{\gamma}_{\max}$ [1/s] represents the maximum shear rate for the melt thermoplastic material and $R_{\text{gate}}$ [m] represents the radius of the gate (see Fig. 11). The maximum shear rate of a thermoplastic material is a parameter established by the manufacturers thereof to advise the molding technicians when exceeding this value during the injection process may involve obtaining defects in the final plastic part. The flow rate of the melt plastic flow can be defined as the ratio between the volume of the plastic part $V_{\text{part}}$ [m$^3$] and the injection time $T_{\text{fill}}$ [s], then replacing in Eq. 5 and clearing the radius of the gate $R_{\text{gate}}$, Eq. 6 is obtained.

$$\dot{\gamma}_{\max} = \frac{\left(3 + \frac{1}{n}\right) \cdot \frac{V_{\text{part}}}{T_{\text{fill}}}}{\pi \cdot R_{\text{gate}}^3} \rightarrow R_{\text{gate}} = \sqrt[3]{\frac{\left(3 + \frac{1}{n}\right) \cdot V_{\text{part}}}{\pi \cdot \dot{\gamma}_{\max} \cdot T_{\text{fill}}}} \tag{6}$$

Equation 6 determines the gate radius of the feeding system in an injection mold, using the material parameters (material viscosity index $n$ and maximum shear rate $\dot{\gamma}_{\max}$ ), the geometric parameters of the part (volume of the plastic part $V_{\text{part}}$), and technological parameters of the manufacturing process (injection time $t_{\text{fill}}$). In the present methodology, an empirical process is proposed according to the analytical study previously proposed. This empirical model consists of the realization of a set of numerical simulations using the MoldFlow Advisor CAE software for the analysis of the injection phase in rectangular plate shape test part. The modeling of the test parts

**Table 9** Geometry properties of plastic parts

| | Units | Case A | Case B | Case C | Case D | Case E | Case F |
|---|---|---|---|---|---|---|---|
| Bounding box, $\ell, w$ | $mm^2$ | [70–56] | [50–50] | [50–58] | [20–54] | [32–35] | [131–71] |
| Average thickness, $H_{part}$ | mm | 1.90 | 0.85 | 3.00 | 1.65 | 0.90 | 2.50 |
| Maximum thickness, $H_{partmax}$ | mm | 2.50 | 1.50 | 3.85 | 2.70 | 1.70 | 5.00 |
| Volume, $V_{part}$ | $mm^3$ | 10,615 | 3520 | 11,806 | 1749 | 1392.6 | 31,668 |
| Melt plastic flow path, $L_{fill}$ | mm | 70 | 40 | 66 | 38 | 30 | 100 |

was carried out according to the most influential geometric parameters during the injection phase: cavity volume, average part thickness, and path of the melt plastic flow along the cavity (see Fig. 13). Table 1 shows the set of rectangular plate shape test parts modeled for the present paper, as well as the numerical values of each influencing geometric parameter in the injection phase.

where in Table 1, $h_i$ [m] $\forall$ i $\in \{1, 2, 3\}$ represents the thickness of the rectangular plate shape test part (see Table 2). The objective of numerically analyzing the filling phase of each of the test parts described in Table 1 is to obtain the injection time $t_{fill}$ in each of them. From this parameter, the optimum gate radius can be determined for each of the test parts, according to the analytical model previously described (see Eq. 6). The modeling of the set of numerical simulations has been performed sequentially. Firstly, the geometries were imported into the Moldflow Advisor numerical calculation software. Next, the center of mass of the test specimens (see Fig. 14) was defined as the point of injection of each test part. And finally, as a sequence of analysis, "Fill," i.e., the simulation of the filling phase in the mold cavity, was established.

It should be noted that each of the specimens was analyzed for four types of different generic thermoplastic materials: Polypropylene (PP), Polystyrene (PS), Polyoxymethylene (POM), and Acrylonitrile butadiene styrene (ABS). The properties of each of the thermoplastic materials tested were obtained from the database of the numerical simulation software.

Once the numerical simulations were executed and the injection time was obtained in each of the samples analyzed, the radius of the optimal gate for each configuration is calculated. Next, the results obtained are compiled to make a set of graphs of interpolated 3D surfaces (see figures included in Table 3) relating, for a material and for a given thickness $h_i$, the volume of the cavity and the path of the melt plastic flow in the cavity with the optimal gate radius for a given plastic part.

Thus, from the cavity of a plastic part with an average thickness, volume, and path of the melt plastic flow, the radius of the optimal gate can be determined using the graphs obtained by the empirical model for the thermoplastic materials: Acrylonitrile butadiene styrene (ABS), Polyoxymethylene (POM), Polypropylene (PP), and Polystyrene (PS) (see Table 3). These graphs were adjusted by means of surfaces based on polynomial functions of degree 4 ($X$ axis, corresponding to the path parameter of the melt plastic flow) and degree 2 ($Y$ axis, corresponding to the volume parameter of the cavity) respectively. The $R$-Square adjustment parameters obtained in each of them are indicated in Table 4.

In addition, in order to establish a useful and direct relationship between the most influential geometric parameters during the injection phase and the radius of the optimal gate for the given plastic part, it is proposed to perform a multi-variable polynomial regression. In this way, a polynomial function is obtained for each thermoplastic material tested which relates the average thickness, volume, and path of the melt plastic to the optimum gate radius for the given plastic part. This facilitates the use of the analytical-empirical model proposed in this paper, since it does not require the use of graphs: gate radius vs plastic volume path (see Table 3), to obtain the radius of the optimal gate for the plastic part. Similarly, the formulation of these polynomial expressions expands the selection range of the part thickness parameter since, if only the graphs are used, the scope of the model part thickness parameter is limited to discrete values: 1, 2, and 3 mm. The multivariable polynomial regression is performed by testing different grades $g_j$ for the polynomial functions of each thermoplastic material analyzed. Table 5 shows the R-Square parameter of each of the degrees $g_j \rightarrow j \in \{1, 2, 3, 4, 5\}$ used in the polynomial regression with cross-validation for each thermoplastic material. Figures 15, 16, 17, and 18 show the scatter plots obtained from each of the degrees $g_j \rightarrow j \in \{1, 2, 3, 4, 5\}$ used in the cross-validated polynomial regression for each thermoplastic material.

where $R_{gatehat}$ [m] represents the estimated gate radius values obtained by means of the polynomial approximation with cross-validation. $R_{gateABS}$ [m], $R_{gatePOM}$ [m], $R_{gatePP}$ [m], and $R_{gatePS}$ [m] represent the radio gate values obtained after the numerical simulations of the samples for the materials Acrylonitrile butadiene styrene (ABS), polyoxymethylene (POM), Polypropylene (PP), and Polystyrene (PS) respectively.

Table 5 shows that the optimum degree for carrying out the multi-variable polynomial regression is 3, since the

estimated results $R_{gatehat}$ approximate with greater confidence to the results $R_{gateABS}$, $R_{gatePOM}$, $R_{gatePP}$, and $R_{gatePS}$ obtained in the numerical simulations of the samples for those materials. Regarding validation of the multi-variable polynomial regression, it has been verified by the one-sample Kolmogorov-Smirnov test that the residual vector obtained for each thermoplastic material, according to the optimal degree of fit in the regression, corresponds to a normal distribution standard, showing that the one-sample Kolmogorov-Smirnov test fails to reject the null hypothesis at the default 5% significance level. Table 6 shows the degree 3 polynomials obtained after multi-variable polynomial regression for each thermoplastic material analyzed; as well as the coefficients thereof.

where $H_{part}$ [m] represents the average thickness of the plastic part, $V_{part}$ [$m^3$] represents the volume of the plastic part, and $L_{fill}$ [m] represents the path of the melt plastic flow in the cavity of the injection mold. Finally, with the approximate gate radius $R_{gatehat}$ (see Table 6) being known for a plastic part with average thickness, volume, and path of the given melt plastic flow, calculation of the injection time is obtained by clearing in Eq. 6 the variable $t_{fill}$ and replacing the variable $R_{gate}$ with the approximate gate radius variable $R_{gatehat}$ obtained by the polynomial functions of the previously established regression for each thermoplastic material.

$$T_{fill} = \frac{\left(3 + \frac{1}{n}\right) \cdot V_{part}}{\pi \cdot \dot{\gamma}_{max} \cdot R^3_{gate_{hat}}} \tag{7}$$

where

$$R_{gate_{hat}} := R_{gate_{hat}}\left(H_{part}, V_{part}, L_{fill}\right) \tag{8}$$

It should be noted that the analytical-empirical model used to calculate the injection time of a plastic part has been carried out assuming that the element section of the gate feeding system is circular. In the case where this element is designed with another geometric section, it would suffice to establish the shear rate equation according to the geometric parameters that define its section. The flow rate of the melt plastic flow is known, since it is calculated from the injection time obtained for an equivalent section of the circular gate (see Eq. 7). Since the maximum shear rate of the thermoplastic material is also known, the only variables to be calculated are the geometric variables that define the gate section. For example, for a rectangular section the shear rate is set to Eq. 7 [25].

$$\dot{\gamma}_{max} = \frac{2 \cdot \left(2 + \frac{1}{n}\right) \cdot \dot{V}_{melt}}{W \cdot T^2} \tag{9}$$

where $W$ [m] and $T$ [m] represent the width and the thickness of a rectangular cross-section respectively. Equation 9 shows that geometric cross-sections defined by means of two geometric parameters require the implementation of a new equation that allows the calculation of these. For this, it is proposed to use the expression of the dimensionless Reynolds number. First, the Reynolds number for the equivalent cross-section of the circular gate is calculated (see Eq. 10).

$$\mathrm{Re}_{gate_{hat}} = \frac{2 \cdot \rho_{melt} \cdot \dot{V}_{melt}}{\pi \cdot \mu_{melt} \cdot R_{gate_{hat}}} \tag{10}$$

where $\rho_{melt}$ [$kg/m^3$] represents the density of the melt plastic flow and $\mu_{melt}$ [Pa·s] represents the dynamic viscosity of the melt plastic flow. And then the value of the Reynolds number is obtained again in Eq. 9, with the objective of leaving Eq. 9 depending on the geometric variables of the cross-section. In turn, it must be checked that the Reynolds number is less than or equal to 2300, since the fluid under study must be a non-Newtonian fluid and the flow of melt plastic must be laminar and dominated by viscous stresses.

$$\mathrm{Re}_{gate_{hat}} = \frac{4 \cdot \rho_{melt} \cdot \dot{V}_{melt}}{\pi \cdot \mu_{melt} \cdot D_h} \rightarrow D_h = \frac{4 \cdot \rho_{melt} \cdot \dot{V}_{melt}}{\pi \cdot \mu_{melt} \cdot \mathrm{Re}_{gate_{hat}}} \tag{11}$$

where $D_h$ [m] represents the equivalent or hydraulic diameter. The hydraulic or equivalent diameter allows the behavior of the melt plastic flow to be studied in geometrical cross-sections of a rectangular, elliptical, etc. type, in the same way as in the case of a pipe with circular cross-section (see Eq. 12).

$$D_h = \frac{4 \cdot A_s}{P_s} \tag{12}$$

where $A_s$ [$m^2$] represents the cross-sectional area and $P_s$ [m] represents the wetted perimeter. Thus, the analytical-empirical model proposed in the present paper could be applied to any type of section with regular geometry by using the equations of Reynolds number, shear rate, and hydraulic or equivalent diameter (Eqs. 9, 11, 12).

### 3.4 Packing time

Once the filling phase of the cavity is completed, the packing phase begins. The packing time can be defined from the equation that determines a one-dimensional heat flow, i.e., the Fourier equation (see Eq. 13) reduced to one dimension, according to Menges et al. [24].

$$\frac{\partial \mathrm{T}}{\partial \mathrm{t}} = \alpha_s \cdot \frac{\partial^2 \mathrm{T}}{\partial^2 \mathrm{z}} \tag{13}$$

where $T$ [°C] represents the temperature variable, $t$ [s] represents the time variable, $z$ [m] represents the dimensional variable along the direction of the analysis geometry, and $\alpha_s$ [$m^2$/s] represents the coefficient of thermal diffusivity. Equation 13 shows the importance of the thermal diffusivity coefficient in this phase of the cycle time, since it determines the ability of the material to transmit heat flow relative to its ability to store it. To establish a rapid heat exchange, the material of the mold must have a high thermal diffusion, for example aluminum. However, these materials tend to have worse structural properties compared to other metals such as steel, hence their exclusive use in molds with low structural performance and few cycles (e.g., prototype molds).

Assuming that, after the injection phase, the temperature of the melt plastic flow has a constant value $T_{melt}$ [°C] and the mold cavity surface temperature varies considerably until it remains at a constant value $\overline{T_m}$ [°C], a solution to this second-order and hyperbolic differential equation can be established (see Eq. 13). The temperature of the melt plastic flow at a point on the partition line can be evaluated as a convergence of the Fourier series development of the heat transfer differential equation (see Eq. 13), such that

$$\frac{T_{eject}-\overline{T_m}}{T_{melt}-\overline{T_m}} = \frac{4}{\pi} e^{-\frac{\alpha_s \cdot \pi^2}{T_h} \cdot t} \cdot \sin\left(\frac{\pi \cdot x}{S}\right) \tag{14}$$

$$T_{eject}-\overline{T_m} = \frac{4}{\pi} \cdot \left(T_{melt}-\overline{T_m}\right) \cdot \sum_{n=0}^{\infty} \frac{1}{2 \cdot n + 1} \cdot e^{-\frac{\alpha_s \cdot (2 \cdot n+1) \cdot \pi^2}{T_h^2} \cdot t} \cdot \sin\left(\frac{\pi \cdot (2 \cdot n + 1) \cdot z}{S}\right) \tag{15}$$

Resolving Eqs. (14)–(15) with respect to the time variable, the expression that determines the packing time is obtained for a circular section (see Eq. 16) [26].

$$T_{packing} = \frac{4 \cdot R_{gate_{hat}}^2}{23.140 \cdot \alpha_s} \cdot \mathrm{Ln}\left(1,602 \cdot \frac{T_{melt}-\overline{T_m}}{T_{eject}-\overline{T_m}}\right) \tag{16}$$

where $T_{melt}$ [°C] represents the temperature of the melt plastic flow, $\overline{T_m}$ [°C] represents the average temperature of the walls of the mold cavity, and $T_{eject}$ [°C] the demolding temperature of the thermoplastic material. The values of these parameters are provided by the manufacturer of the material and therefore for the present paper these are obtained from the database of the software of numerical simulation MoldFlow Advisor. Equation 16 states that the packing time has an important dependence on the radius of the gate, since the relationship between these parameters is exponential. That is, doubling the radius of the gate would mean quadrupling the packing time. In addition, a bad dimension of this parameter can cause the filling of the cavity to be incomplete if the gate and therefore the time of packing is reduced. In contrast, there would be an unnecessary increase in time at this stage of the injection cycle if the gate were larger. Using the polynomials presented in Table 6, this paper establishes the optimal calculation of this parameter for the generic materials Acrylonitrile Butadiene Styrene (ABS), Polyoxymethylene (POM), Polypropylene (PP), and Polystyrene (PS), facilitating the task of designers of injection molds and reducing the time and cost in preliminary phases of mold design and estimation of cycle time.

### 3.5 Cooling time

The cooling phase starts once the gate solidifies. The cooling time corresponds to the time interval between the end of the packing phase to the ejection phase of the plastic part from the injection mold. The cooling time represents, in the approximate majority of cases, more than 70% of the total cycle time. Therefore, this is one of the most important phases in the thermoplastic injection molding process.

Similar to the packing phase, the calculation of the cooling time for a plate section is achieved by solving the convergence of the Fourier series of the differential heat transfer equation (see Eq. 13), solving this convergence with respect to the variable time [26].

$$T_{cooling} = \frac{H_{part_{max}}}{\pi^2 \cdot \alpha_s} \cdot \mathrm{Ln}\left(\frac{4}{\pi} \cdot \frac{T_{melt}-\overline{T_m}}{T_{eject}-\overline{T_m}}\right) \tag{17}$$

where $H_{partmax}$[m] represents the maximum thickness of the plastic part. Unlike the packing time, in the cooling time, the most important geometric parameter is the maximum thickness of the plastic part. As this geometric parameter increases, the cooling time increases exponentially. Using the maximum thickness of the plastic part as a geometric parameter in Eq. 17 is justified because in that region of the part the cooling time is longer and thus encompasses the entire cooling phase of the part (see Fig. 19b, plastic part A). The thickness of a plastic part must be as uniform and as small as possible, so that a homogeneous and optimized cooling time can be obtained. Otherwise, if in a plastic part the thickness map is irregular and unbalanced, the cooling time will not be homogeneous and will increase considerably. Figure 19a, b shows the time distribution until the ejection temperature for plastic parts A and B is reached. Thus, by means of a numerical simulation, the time deviation until the ejection temperature is reached is greater in plastic part A (whose thicknesses are not regular and homogeneous) compared to the time to reach the ejection temperature of plastic part B (whose thicknesses are regular and homogeneous).

As in the previously described packing phase, the values of the temperature parameters of the melt plastic

### 4.1.1 Case A

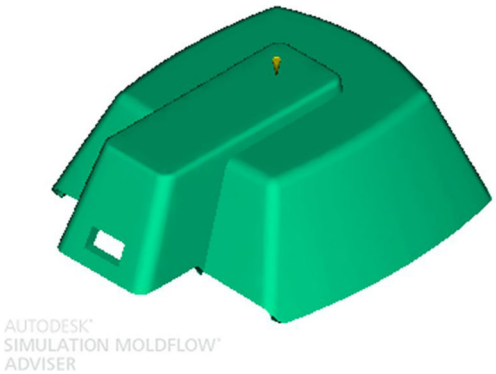


**Fig. 20** Plastic part, Case A

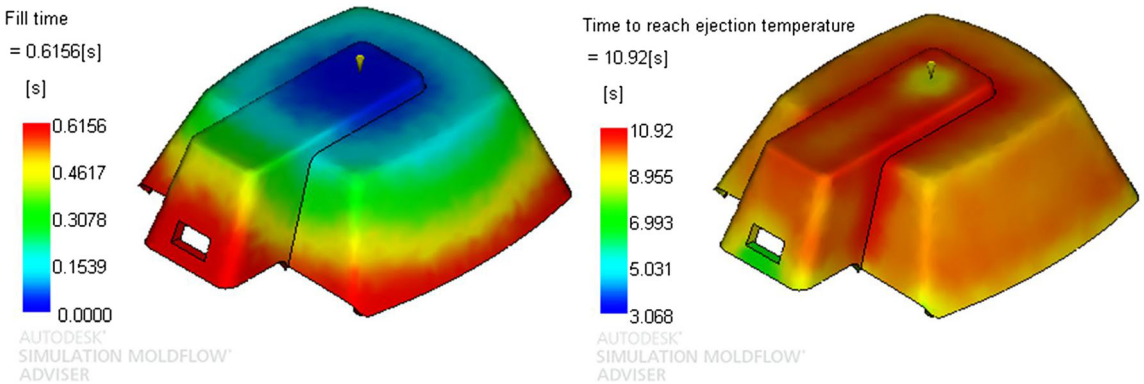


**Fig. 21** Distribution of fill time [s] and time to reach ejection temperature [s] for material Acrylonitrile butadiene styrene (ABS), Case A

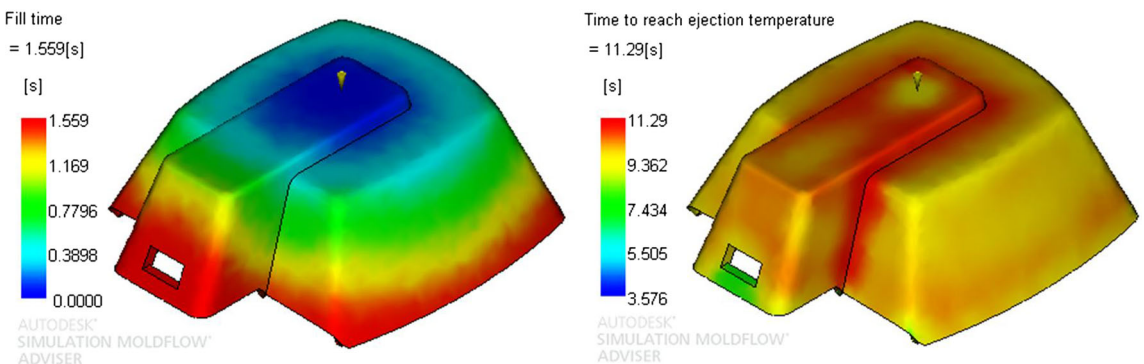


**Fig. 22** Distribution of the fill time [s] and time to reach ejection temperature [s] for the material Polyoxymethylene (POM), Case A

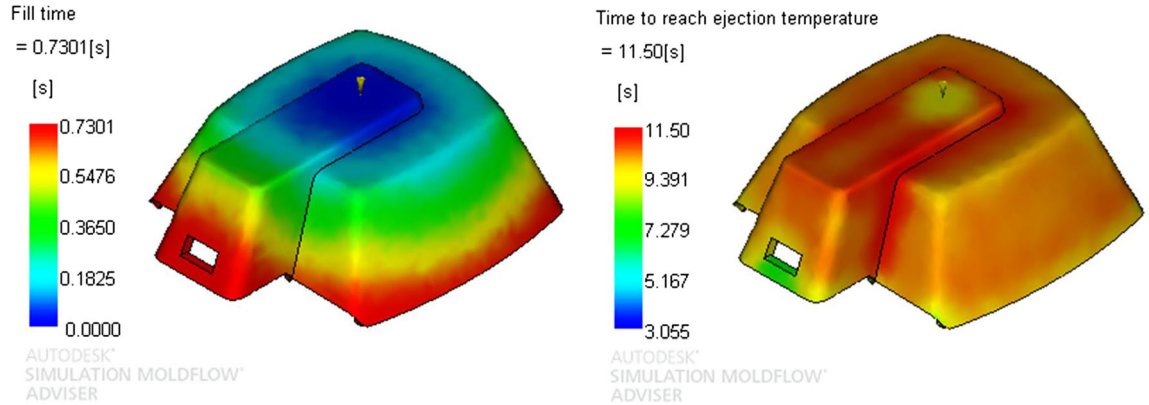


**Fig. 23** Distribution of fill time [s] and time to reach ejection temperature [s] for material Polypropylene (PP), Case A

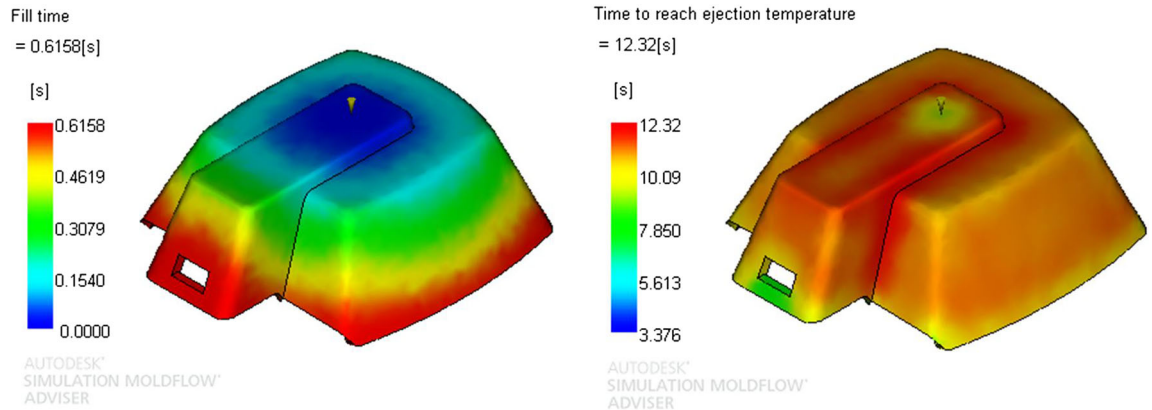


**Fig. 24** Distribution of the fill time [s] and time to reach ejection temperature [s] for the material Polystyrene (PS), Case A

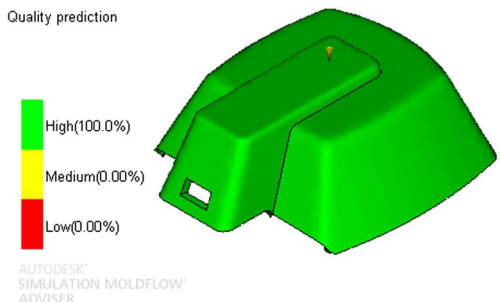


**Fig. 25** Prediction of the final quality of the plastic part, Case A

**Table 10** Results of the analytical model for Case A: Gate radius ($R_{gate_{hat}}$) [mm], Analytical fill time ($T_{fill}$) [s], Numerical fill time ($t_{fill}$) [s], Analytical packing time ($T_{packing}$) [s], Analytical cooling time ($T_{cooling}$) [s], Analytical average of time to reach ejection temperature ($T_{cycle}$) [s], and Numerical average of time to reach ejection temperature ($t_{cycle}$) [s]

| Nomenclature | Units | Description | ABS | POM | PP | PS |
|---|---|---|---|---|---|---|
| $R_{gatehat}$ | mm | Gate radius | 0.7373 | 0.4974 | 0.5293 | 0.8371 |
| $T_{fill}$ | s | Analytical fill time | 0.5773 | 1.5590 | 0.7529 | 0.5121 |
| $t_{fill}$ | s | Numerical fill time | 0.6160 | 1.5372 | 0.7301 | 0.6158 |
| $T_{packing}$ | s | Analytical packing time | 1.6882 | 0.8078 | 0.9774 | 2.4381 |
| $T_{cooling}$ | s | Analytical cooling time | 8.8907 | 9.2794 | 10.1476 | 9.6796 |
| $T_{cycle}$ | s | Analytical average time to reach ejection temperature | 11.1561 | 11.6243 | 11.8779 | 12.6298 |
| $t_{cycle}$ | s | Numerical average time to reach ejection temperature | 10.9200 | 11.2900 | 11.5000 | 12.3200 |
| $\varepsilon_{cycle}$ | – | Average time to reach ejection temperature difference [%] | 2.1621 | 2.9610 | 3.2861 | 2.5146 |

### 4.1.2 Case B

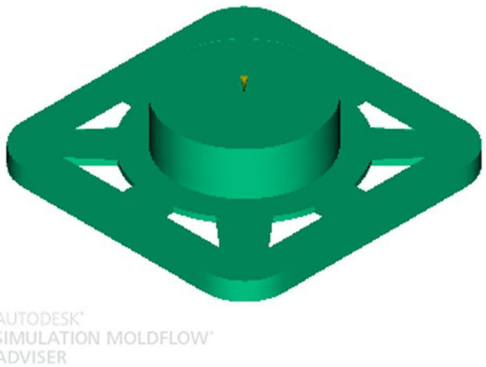


**Fig. 26** Plastic part, Case B

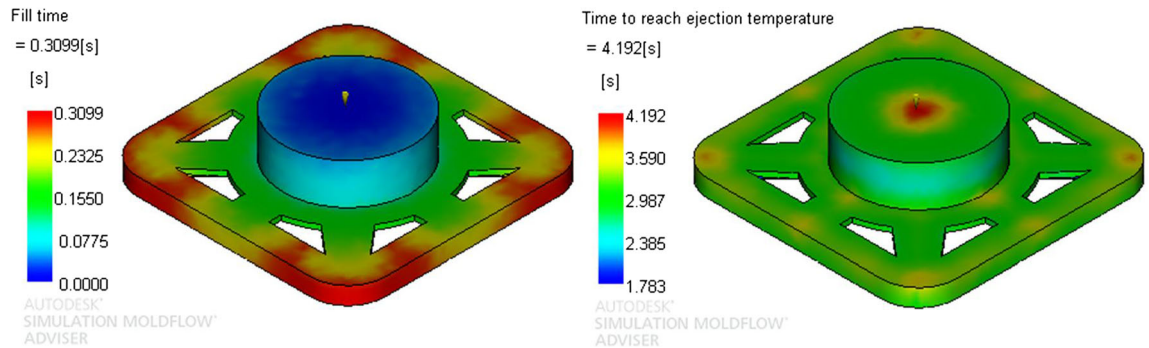


**Fig. 27** Distribution of fill time [s] and time to reach ejection temperature [s] for material Acrylonitrile butadiene styrene (ABS), Case B

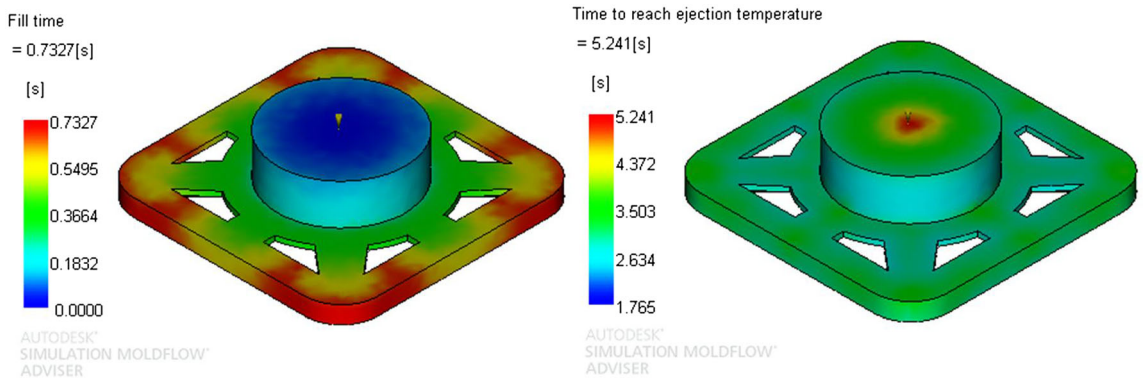


**Fig. 28** Distribution of the fill time [s] and time to reach ejection temperature [s] for the material Polyoxymethylene (POM), Case B

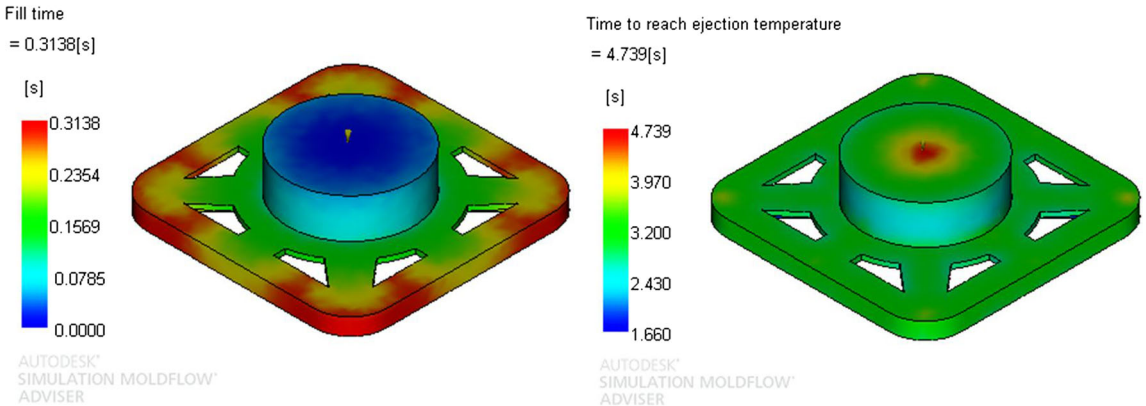


**Fig. 29** Distribution of fill time [s] and time to reach ejection temperature [s] for material Polypropylene (PP), Case B

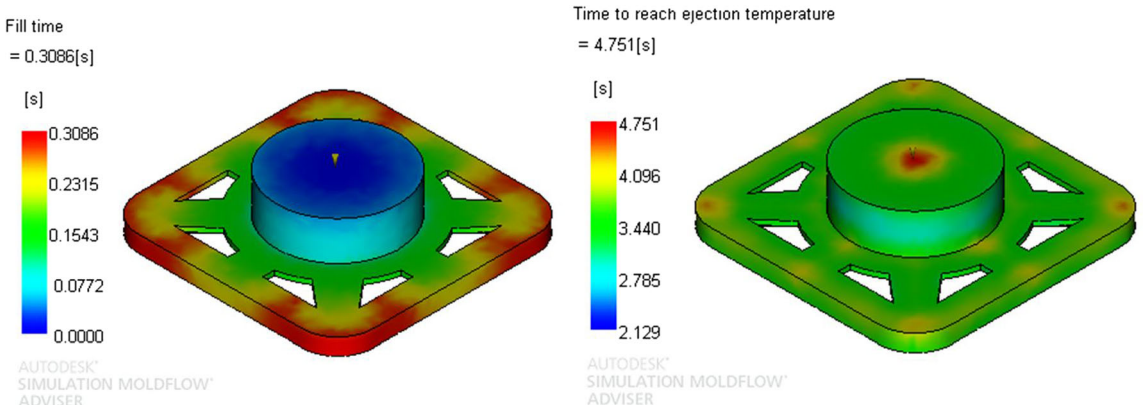


**Fig. 30** Distribution of fill time [s] and time to reach ejection temperature [s] for material Polystyrene (PS), Case B

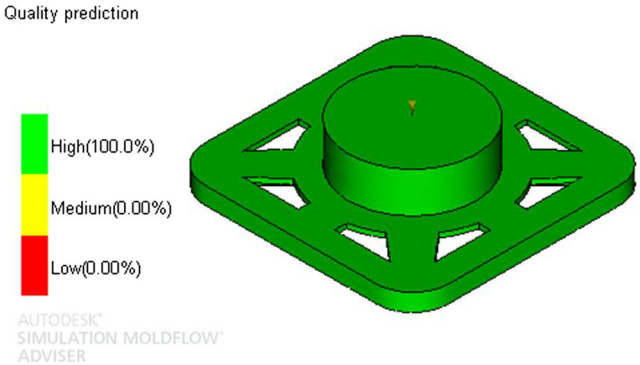


**Fig. 31** Prediction of the final quality of the plastic part, Case B

**Table 11** Results of the analytical model for Case B: Gate radius ($R_{gate_{hat}}$) [mm], Analytical fill time *($T_{fill}$)* [s], Numerical fill time *($t_{fill}$)* [s], Analytical packing time ($T_{packing}$) [s], Analytical cooling time *($T_{cooling}$)* [s], Analytical average of time to reach ejection temperature *($T_{cycle}$)* [s], and Numerical average of time to reach ejection temperature *($t_{cycle}$)* [s]

| Nomenclature | Units | Description | ABS | POM | PP | PS |
|---|---|---|---|---|---|---|
| $R_{gatehat}$ | mm | Gate radius | 0.6034 | 0.4442 | 0.4976 | 0.6876 |
| $T_{fill}$ | s | Analytical fill time | 0.3506 | 0.7184 | 0.3016 | 0.3076 |
| $t_{fill}$ | s | Numerical fill time | 0.3100 | 0.7327 | 0.3138 | 0.3086 |
| $T_{packing}$ | s | Analytical packing time | 1.1307 | 0.6442 | 0.8638 | 1.6450 |
| $T_{cooling}$ | s | Analytical cooling time | 2.7207 | 4.1242 | 3.7040 | 3.0923 |
| $T_{cycle}$ | s | Analytical average time to reach ejection temperature | 4.2020 | 5.4868 | 4.8695 | 5.0449 |
| $t_{cycle}$ | s | Numerical average time to reach ejection temperature | 4.1920 | 5.2910 | 4.7390 | 4.8710 |
| $\varepsilon_{cycle}$ | – | Average time to reach ejection temperature difference [%] | 0.2385 | 3.7006 | 2.7537 | 3.5701 |

### 4.1.3 Case C

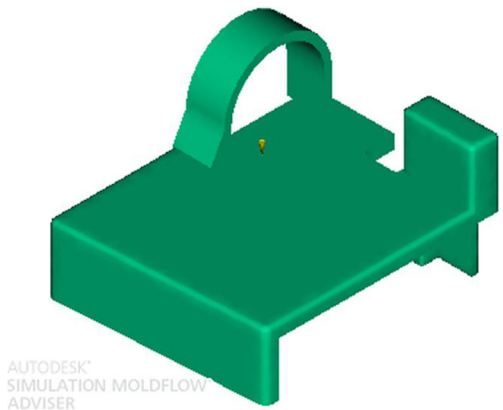


**Fig. 32** Plastic part, Case C

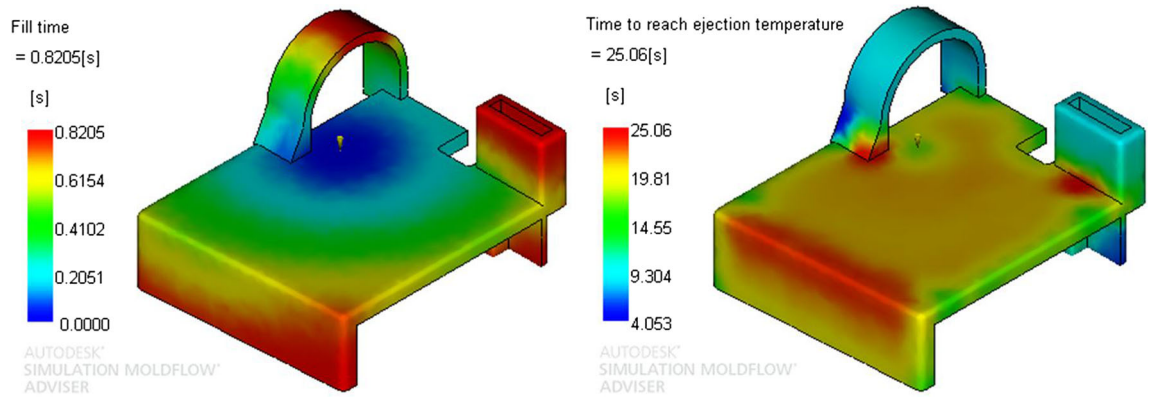


**Fig. 33** Distribution of fill time [s] and time to reach ejection temperature [s] for the material Acrylonitrile butadiene styrene (ABS), Case C

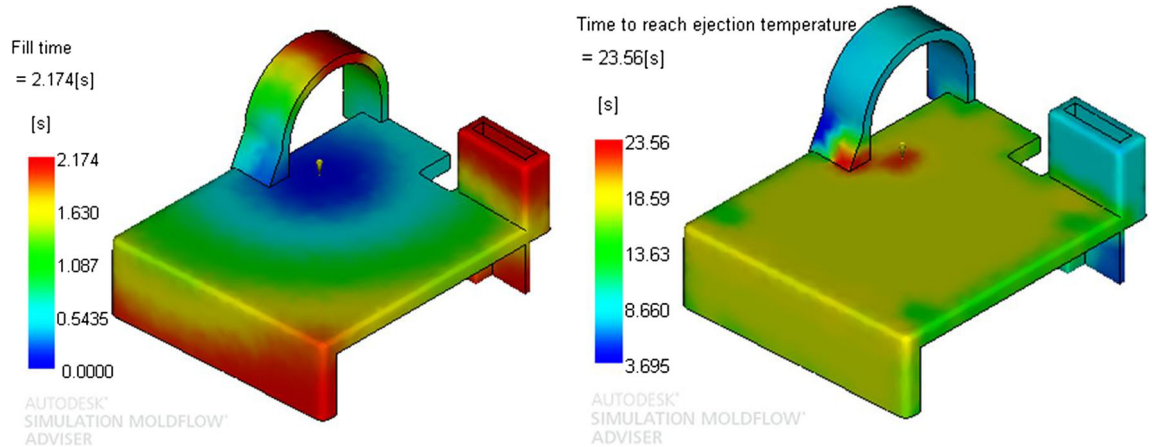


**Fig. 34** Distribution of fill time [s] and time to reach ejection temperature [s] for the material Polyoxymethylene (POM), Case C

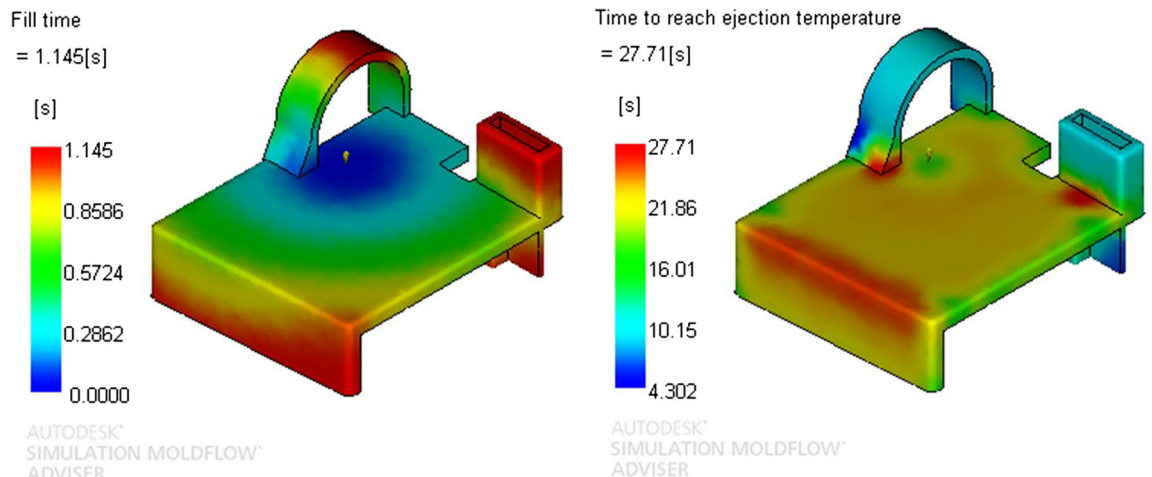


**Fig. 35** Distribution of fill time [s] and time to reach ejection temperature [s] for material Polypropylene (PP), Case C

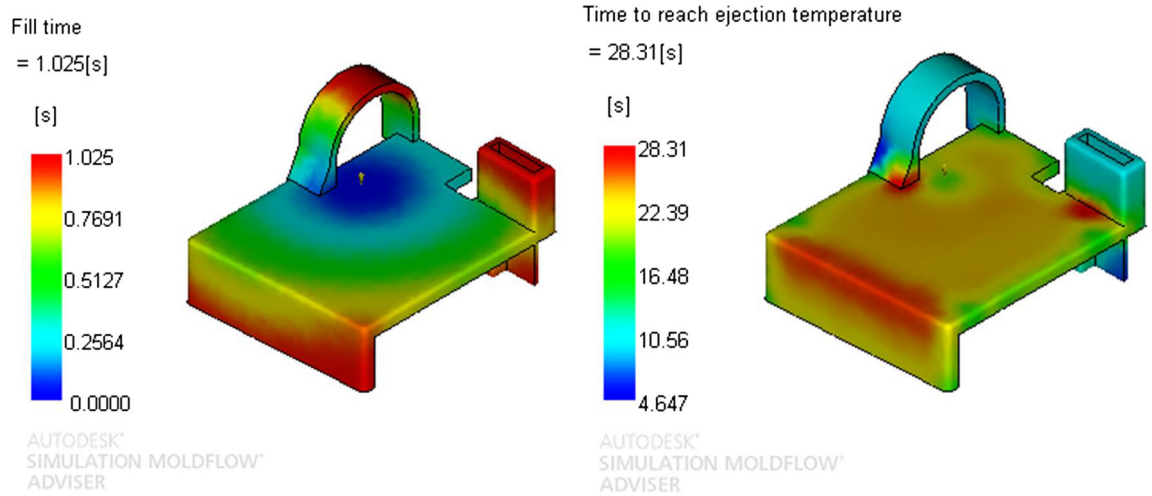


**Fig. 36** Distribution of fill time [s] and time to reach ejection temperature [s] for material Polystyrene (PS), Case C

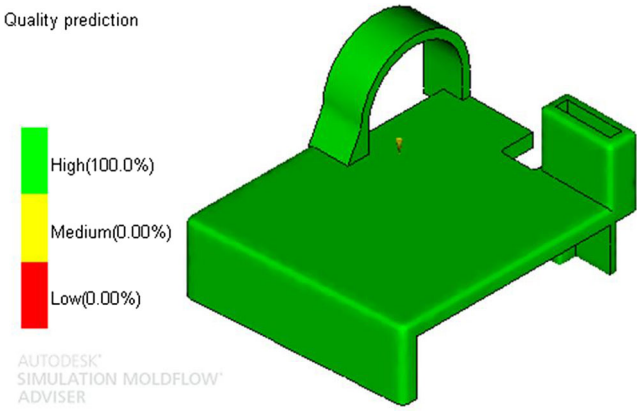


**Fig. 37** Prediction of the final quality of the plastic part, Case C

**Table 12** Results of the analytical model for Case C: Gate radius ($R_{gate_{hat}}$) [mm], Analytical fill time *($T_{fill}$)* [s], Numerical fill time *($t_{fill}$)* [s], Analytical packing time ($T_{packing}$) [s], Analytical cooling time *($T_{cooling}$)* [s], Analytical average of time to reach ejection temperature *($T_{cycle}$)* [s], and Numerical average of time to reach ejection temperature *($t_{cycle}$)* [s]

| Nomenclature | Units | Description | ABS | POM | PP | PS |
|---|---|---|---|---|---|---|
| $R_{gatehat}$ | mm | Gate radius | 0.6647 | 0.4637 | 0.4652 | 0.6903 |
| $T_{fill}$ | s | Analytical fill time | 0.8797 | 2.1187 | 1.2384 | 1.0198 |
| $t_{fill}$ | s | Numerical fill time | 0.8205 | 2.1740 | 1.1450 | 1.0250 |
| $T_{packing}$ | s | Analytical packing time | 1.3721 | 0.7020 | 0.3813 | 1.6580 |
| $T_{cooling}$ | s | Analytical cooling time | 23.2469 | 20.8786 | 26.1133 | 26.4222 |
| $T_{cycle}$ | s | Analytical average time to reach ejection temperature | 25.4987 | 23.6992 | 27.7329 | 29.0999 |
| $t_{cycle}$ | s | Numerical average time to reach ejection temperature | 25.0600 | 23.5600 | 27.7100 | 28.3100 |
| $\varepsilon_{cycle}$ | – | Average time to reach ejection temperature difference [%] | 1.7506 | 0.5908 | 0.0826 | 2.7902 |

### 4.1.4 Case D

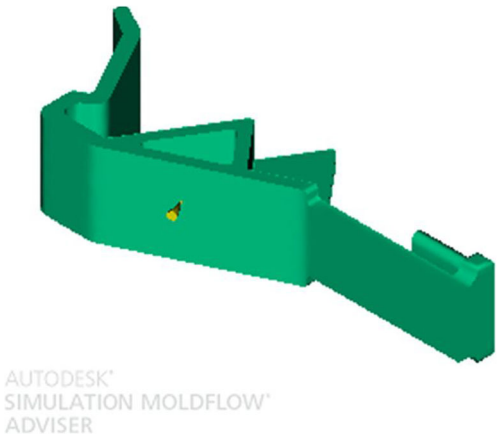


**Fig. 38** Plastic part, Case D

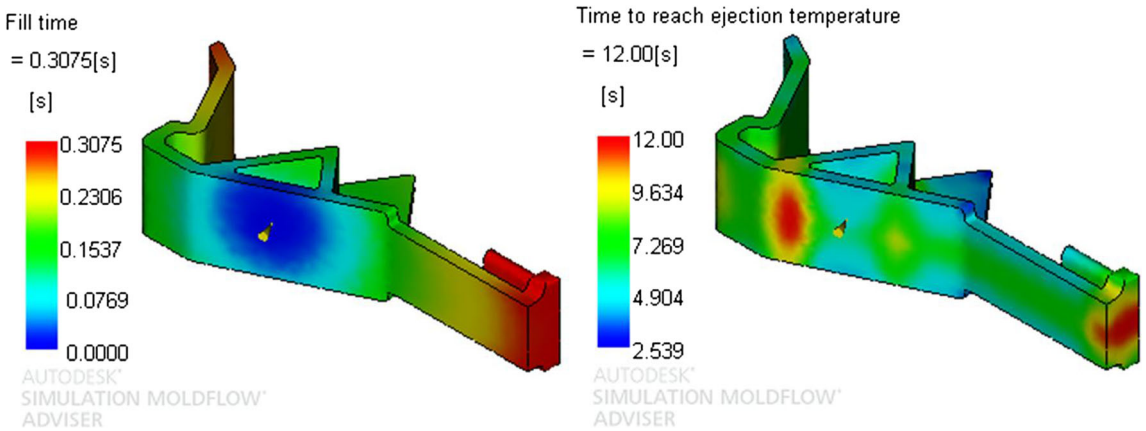


**Fig. 39** Distribution of fill time [s] and time to reach ejection temperature [s] for material Acrylonitrile butadiene styrene (ABS), Case D

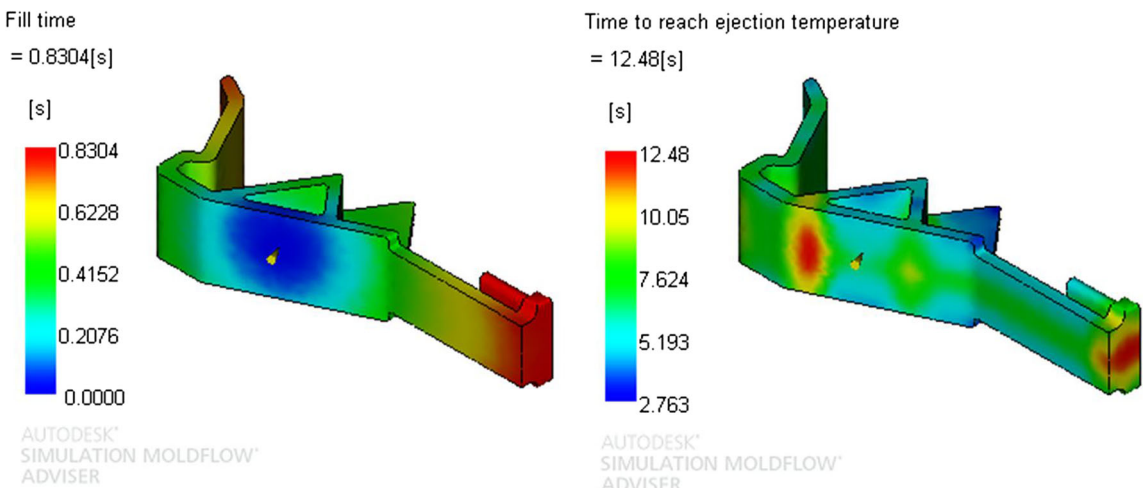


**Fig. 40** Distribution of fill time [s] and time to reach ejection temperature [s] for Polyoxymethylene material (POM), Case D

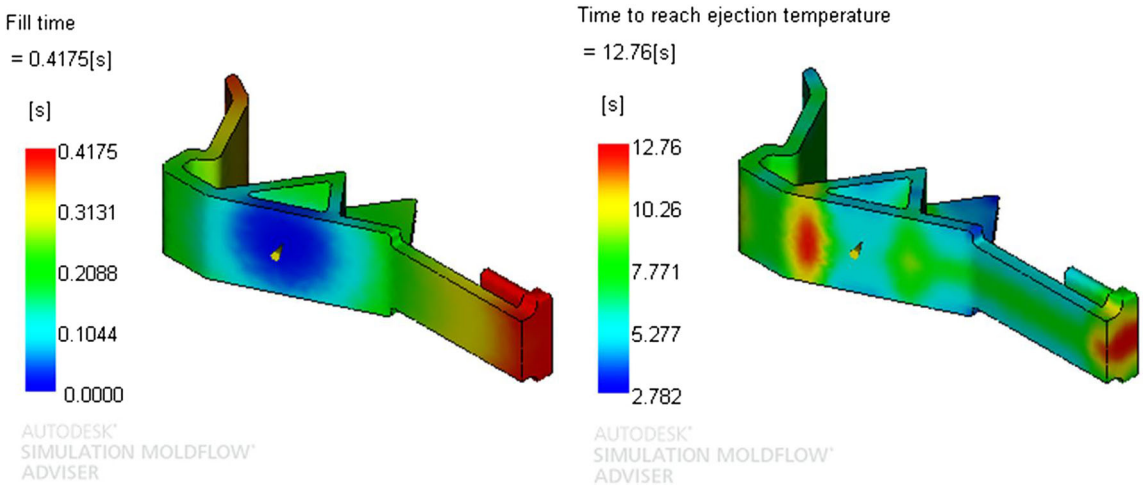


**Fig. 41** Distribution of fill time [s] and time to reach ejection temperature [s] for material Polypropylene (PP), Case D

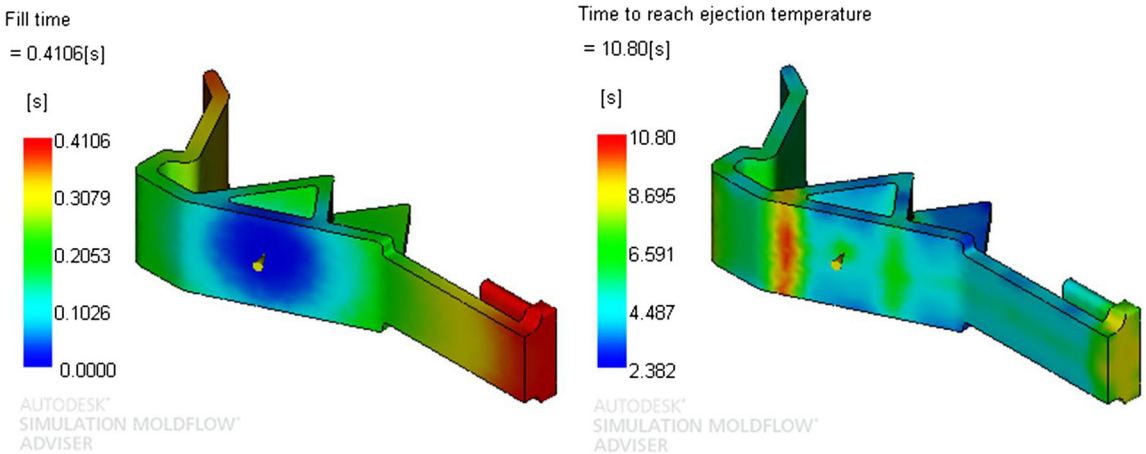


**Fig. 42** Distribution of the fill time [s] and time to reach ejection temperature [s] for the material Polystyrene (PS), Case D

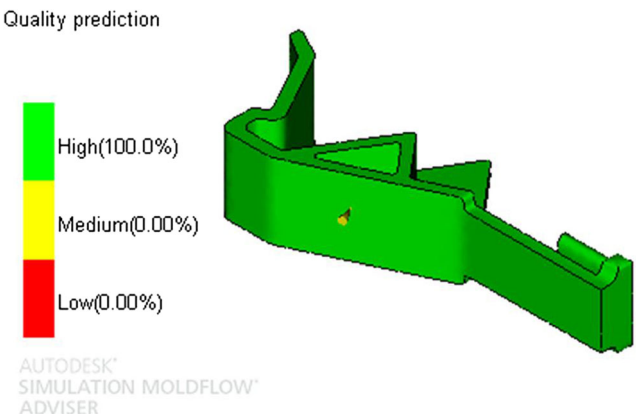


**Fig. 43** Prediction of the final quality of the plastic part, Case D

**Table 13** Results of the analytical model for Case D: Gate radius ($R_{gate_{hat}}$) [mm], Analytical fill time ($T_{fill}$) [s], Numerical fill time ($t_{fill}$) [s], Analytical packing time ($T_{packing}$) [s], Analytical cooling time ($T_{cooling}$) [s], Analytical average of time to reach ejection temperature ($T_{cycle}$) [s], and Numerical average of time to reach ejection temperature ($t_{cycle}$) [s]

| Nomenclature | Units | Description | ABS | POM | PP | PS |
|---|---|---|---|---|---|---|
| $R_{gatehat}$ | mm | Gate radius | 0.4940 | 0.3583 | 0.3583 | 0.6051 |
| $T_{fill}$ | s | Analytical fill time | 0.3175 | 0.6804 | 0.4016 | 0.2243 |
| $t_{fill}$ | s | Numerical fill time | 0.3075 | 0.6229 | 0.4175 | 0.2046 |
| $T_{packing}$ | s | Analytical packing time | 0.7578 | 0.4191 | 0.4479 | 1.2739 |
| $T_{cooling}$ | s | Analytical cooling time | 11.3055 | 11.7442 | 13.3718 | 9.6796 |
| $T_{cycle}$ | s | Analytical average time to reach ejection temperature | 12.3809 | 12.8437 | 13.2215 | 11.1779 |
| $t_{cycle}$ | s | Numerical average time to reach ejection temperature | 12.0000 | 12.4600 | 12.7600 | 10.8000 |
| $\varepsilon_{cycle}$ | – | Average time to reach ejection temperature difference [%] | 3.1742 | 0.1902 | 3.6168 | 3.4991 |

### 4.1.5 Case E

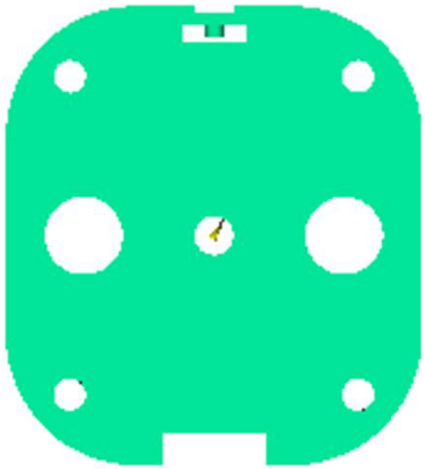


**Fig. 44** Plastic part, Case E

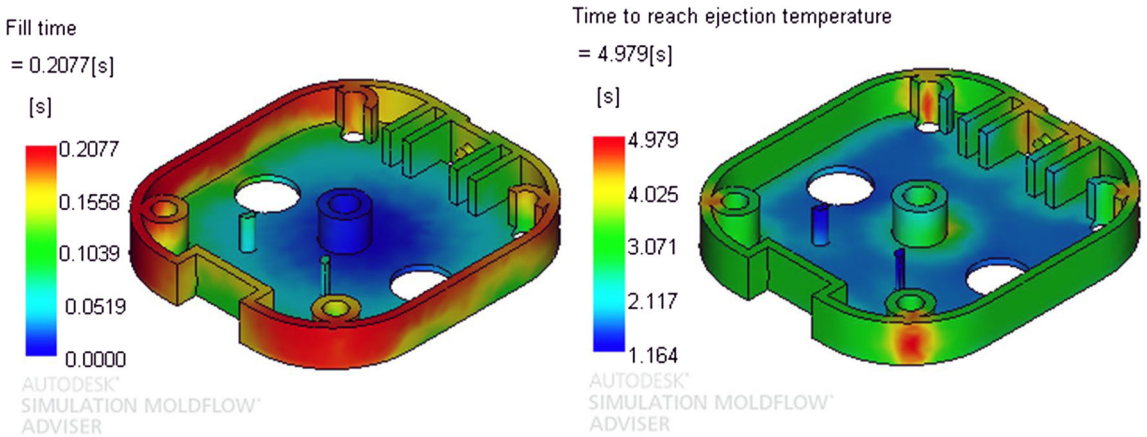


**Fig. 45** Distribution of fill time [s] and time to reach ejection temperature [s] for the material Acrylonitrile butadiene styrene (ABS), Case E

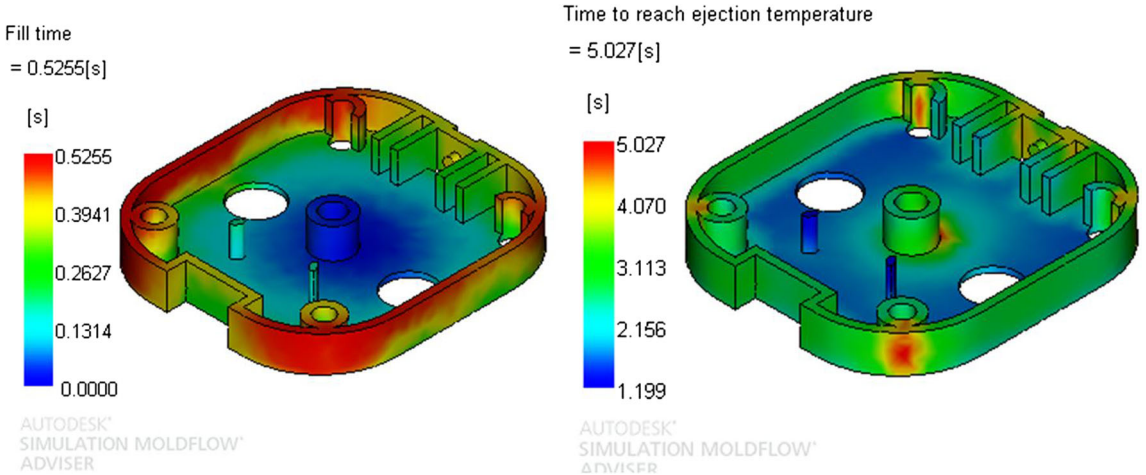


**Fig. 46** Distribution of fill time [s] and time to reach ejection temperature [s] for the material Polyoxymethylene (POM), Case E

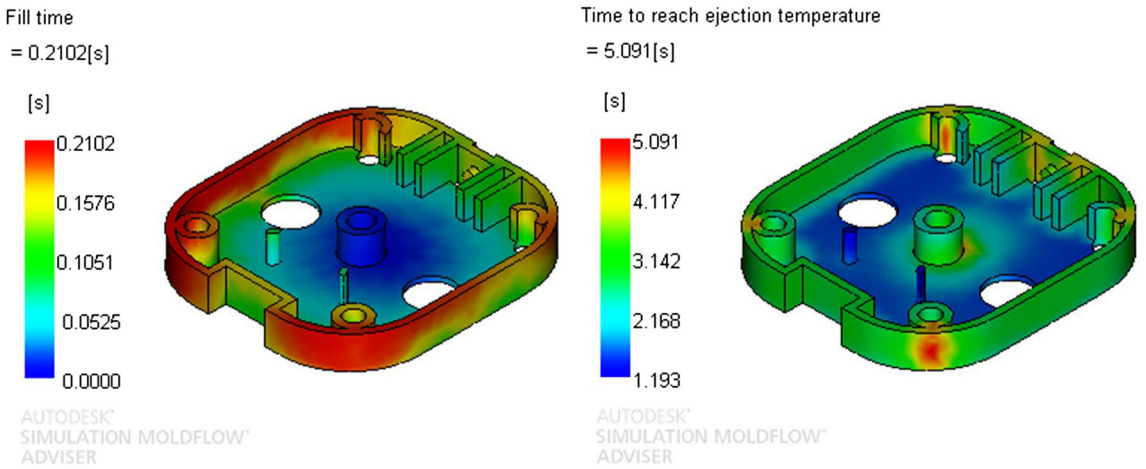


**Fig. 47** Distribution of fill time [s] and time to reach ejection temperature [s] for the material Polypropylene (PP), Case E

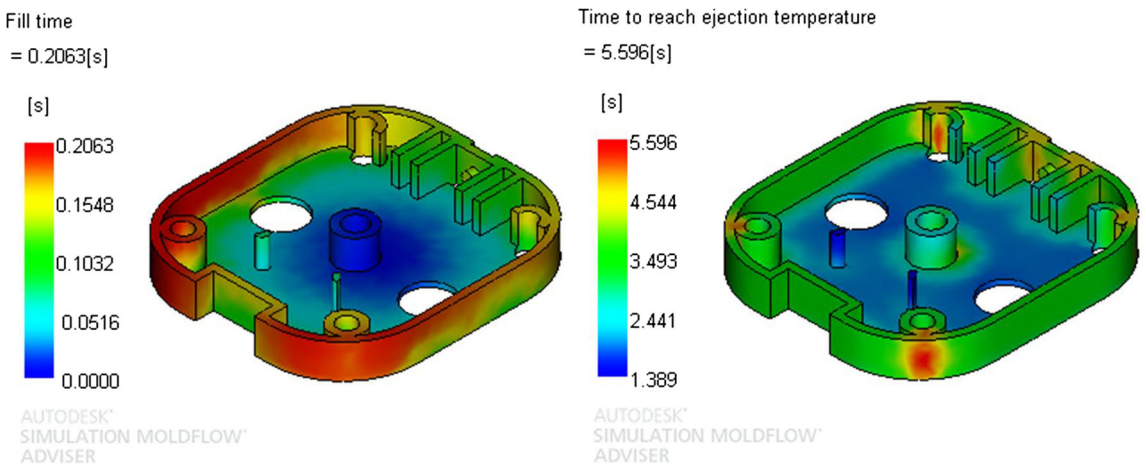


**Fig. 48** Distribution of the fill time [s] and time to reach ejection temperature [s] for the material Polystyrene (PS), Case E

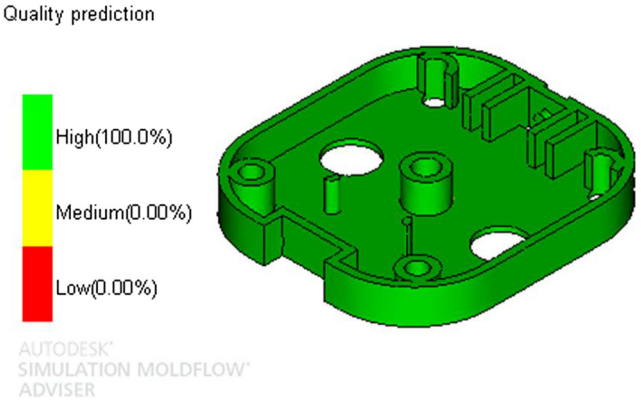


**Fig. 49** Prediction of the final quality of the plastic part, Case E

**Table 14** Results of the analytical model for Case E: Gate radius ($R_{gate_{hat}}$) [mm], Analytical fill time *($T_{fill}$)* [s], Numerical fill time *($t_{fill}$)* [s], Analytical packing time ($T_{packing}$) [s], Analytical cooling time *($T_{cooling}$)* [s], Analytical average of time to reach ejection temperature *($T_{cycle}$)* [s], and Numerical average of time to reach ejection temperature *($t_{cycle}$)* [s]

| Nomenclature | Units | Description | ABS | POM | PP | PS |
|---|---|---|---|---|---|---|
| $R_{gatehat}$ | mm | Gate radius | 0.4843 | 0.3570 | 0.4043 | 05832 |
| $T_{fill}$ | s | Analytical fill time | 0.2683 | 0.5476 | 0.2225 | 0.1995 |
| $t_{fill}$ | s | Numerical fill time | 0.2074 | 0.5255 | 0.2102 | 0.2063 |
| $T_{packing}$ | s | Analytical packing time | 0.7284 | 0.4161 | 0.5703 | 1.1834 |
| $T_{cooling}$ | s | Analytical cooling time | 4.1213 | 4.3860 | 4.5100 | 4.6843 |
| $T_{cycle}$ | s | Analytical average time to reach ejection temperature | 5.1180 | 5.3497 | 5.3028 | 6.0671 |
| $t_{cycle}$ | s | Numerical average time to reach ejection temperature | 4.9790 | 5.2270 | 5.1570 | 5.8560 |
| $\varepsilon_{cycle}$ | – | Average time to reach ejection temperature difference [%] | 2.7917 | 2.9156 | 2.8272 | 3.6048 |

### 4.1.6 Case F

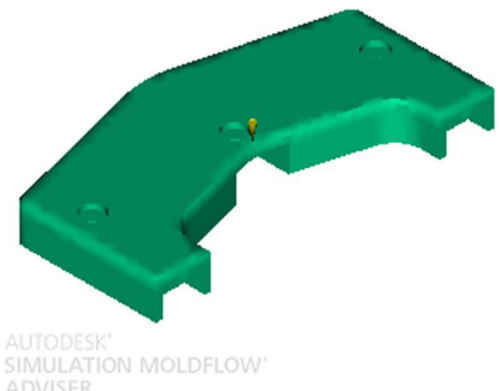


**Fig. 50** Plastic part, Case F

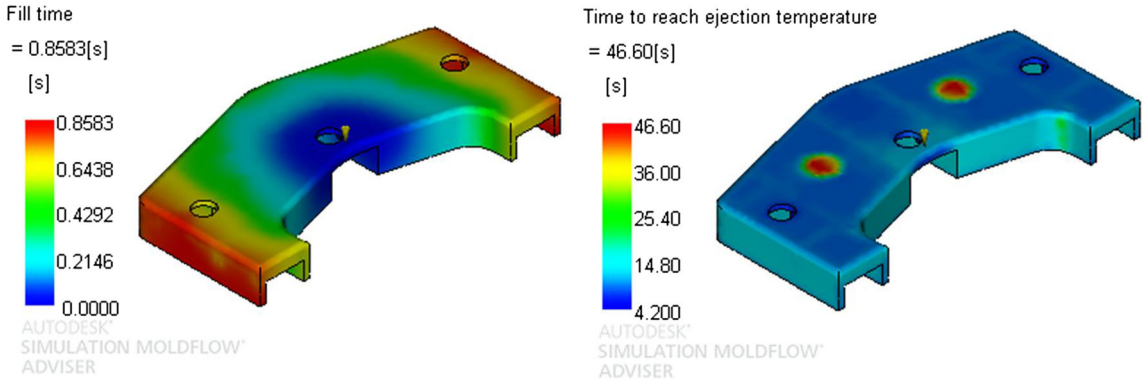


**Fig. 51** Distribution of fill time [s] and time to reach ejection temperature [s] for material Acrylonitrile butadiene styrene (ABS), Case F

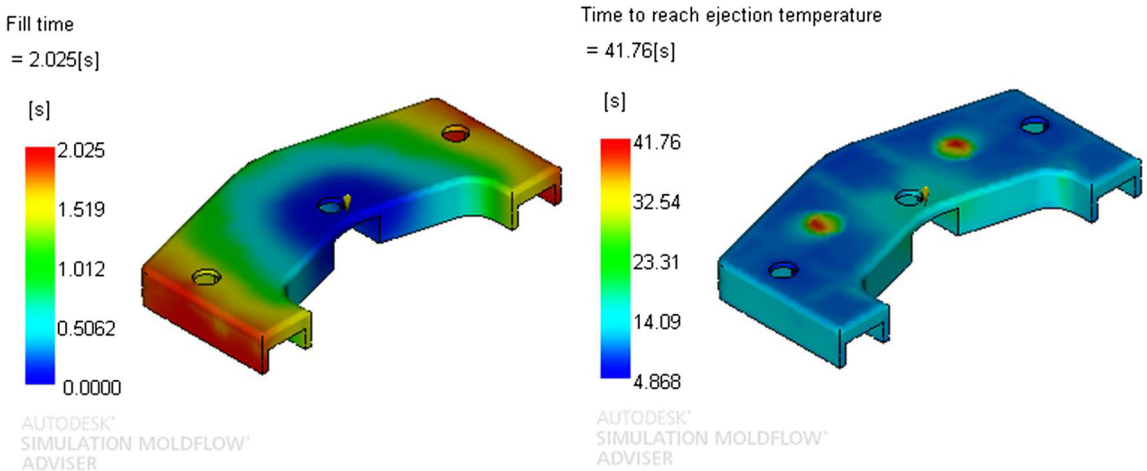


**Fig. 52** Distribution of fill time [s] and time to reach ejection temperature [s] for Polyoxymethylene material (POM), Case F

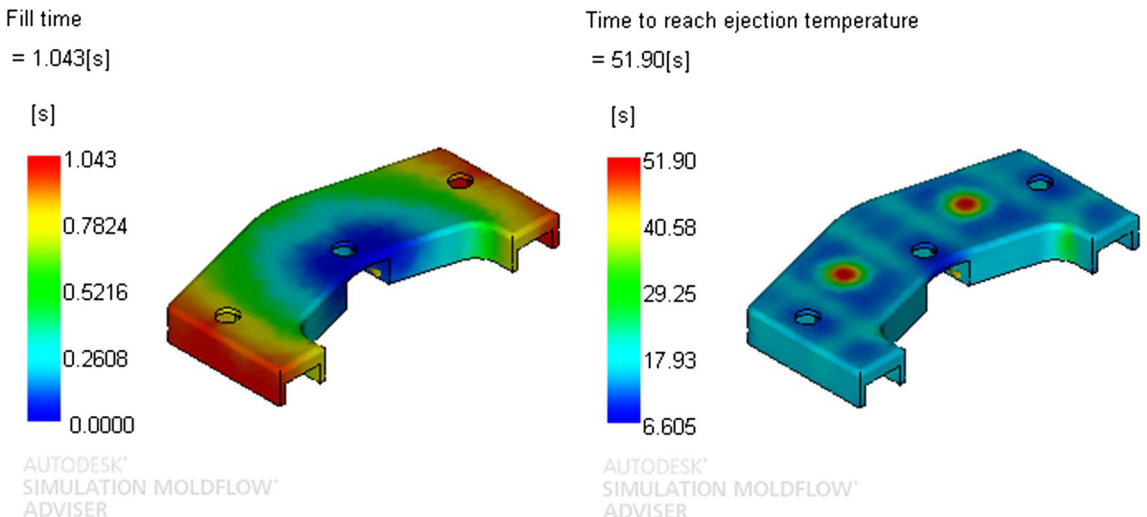


**Fig. 53** Distribution of fill time [s] and time to reach ejection temperature [s] for material Polypropylene (PP), Case F

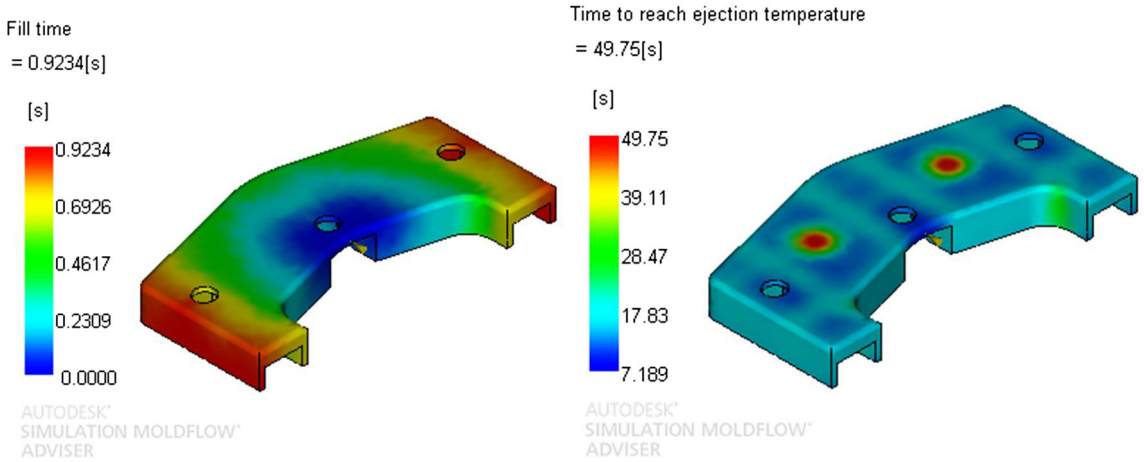


**Fig. 54** Distribution of the fill time [s] and time to reach ejection temperature [s] for the material Polystyrene (PS), Case F

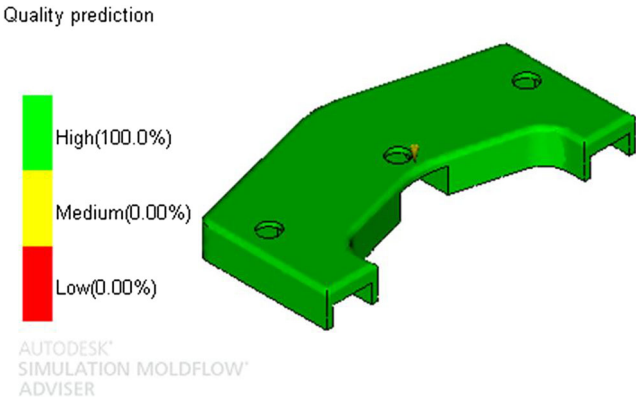


**Fig. 55** Prediction of the final quality of the plastic part, Case F

**Table 15** Results of the analytical model for Case F: Gate radius ($R_{gate_{hat}}$) [mm], Analytical fill time ($T_{fill}$) [s], Numerical fill time ($t_{fill}$) [s], Analytical packing time ($T_{packing}$) [s], Analytical cooling time ($T_{cooling}$) [s], Analytical average of time to reach ejection temperature ($T_{cycle}$) [s], and Numerical average of time to reach ejection temperature ($t_{cycle}$) [s]

| Nomenclature | Units | Description | ABS | POM | PP | PS |
|---|---|---|---|---|---|---|
| $R_{gatehat}$ | mm | Gate radius | 0.9279 | 0.6508 | 0.6712 | 0.9800 |
| $T_{fill}$ | s | Analytical fill time | 0.8674 | 2.0556 | 1.1059 | 0.9560 |
| $t_{fill}$ | s | Numerical fill time | 0.8589 | 2.0260 | 1.0430 | 0.9234 |
| $T_{packing}$ | s | Analytical packing time | 2.6738 | 1.3828 | 1.5717 | 3.3416 |
| $T_{cooling}$ | s | Analytical cooling time | 43.5316 | 38.6801 | 49.4871 | 45.7448 |
| $T_{cycle}$ | s | Analytical average time to reach ejection temperature | 47.0728 | 42.1186 | 52.1647 | 50.0423 |
| $t_{cycle}$ | s | Numerical average time to reach ejection temperature | 46.6000 | 41.7600 | 51.9000 | 49.7500 |
| $\varepsilon_{cycle}$ | – | Average time to reach ejection temperature difference [%] | 1.0146 | 0.8587 | 0.5100 | 0.5875 |

flow $T_{melt}$, the mean temperature of the mold walls $\overline{T_m}$, and the demolding temperature of the thermoplastic material $T_{eject}$ are provided by the manufacturer of the material and therefore these are obtained from the database of the software of numerical simulation MoldFlow Advisor.

## 4 Implementation and results

In order to demonstrate the advantages of the methodology proposed in this paper, it has been applied to six industrial plastic parts, manufactured by means injection molds, with complex geometry. The accuracy of the nodal quadrature $\beta$ for each geometry is set according to the dimension of the smallest detail of the part. The algorithms have been developed in the software Matlab R 2013 [25] with a Toshiba notebook with a Pentium ® Dual-Core CPU T4200@2.20 GHz processor and a RAM memory of 3.00 GB. This can be adapted to any programming language and computer equipment. Similarly, the algorithm can be adapted to any type of polygonal facet for the discrete mesh $\Omega' \in \mathbb{R}^3$ of the plastic part.

The proposed methodology determines the injection time, the packing time, and the cooling time (time until the plastic part reaches the ejection temperature) in an automated way, from the geometry of the plastic part, without the necessity of employing operations and post-processing software. In the same way, the new algorithm developed in the paper dimensions the gate radius of the injection mold feeding system in an automated way. The numerical simulations performed to validate the proposed algorithm have been carried out using the injection molding simulation software MoldFlow Advisor. The proposed methodology generates a resulting array with: the injection time, the packing time, the cooling time, and the radius of the gate. Acrylonitrile butadiene styrene (ABS), Polyoxymethylene (POM), Polypropylene (PP), and Polystyrene (PS) are used as thermoplastic parts materials and structural steel (P20) is employed as the material of the plates and components of the injection mold. The materials (Thermoplastic and steel) and geometry properties used in the validation of the proposed methodology are indicated in Tables 7, 8, and 9.

The set of temperatures, injection of the melt plastic, wall of the injection mold, and ejection of the plastic part, are assumed uniform throughout the analytical study proposed in this paper. The value of each of these parameters is determined by the manufacturer as standard quantities for correct injection, packing, cooling, and expulsion of the thermoplastic material.

### 4.1 Case studies

The validation of the methodology proposed in the paper was carried out using a set of numeric cavity filling simulations for six plastic parts of different topology (Cases A, B, C, D, E, F) Figs. 20, 26, 32, 38, 44, and 50. The distribution of the time used for injection and the time until reaching the ejection temperature of the plastic part were calculated numerically for each case study and for each material used (Figs. 21, 22, 23, 24, 27, 28, 29, 30, 33, 34, 35, 36, 39, 40, 41, 42, 45, 46, 47, 48 and 51, 52, 53, 54). The results of the methodology presented for each plastic part are included in Tables 10, 11, 12, 13, 14, and 15, which contain information about the gate radius $R_{gatehat}$ [m], injection time $T_{fill}$ [s], the packing time $T_{packing}$ [s], the cooling time $T_{cooling}$ [s], and the time to reach the ejection temperature of the plastic part $T_{cycle}$ [s]. The numerical values of the injection time parameter $T_{fill}$ [s] and the time parameter until reaching the ejection temperature $T_{cycle}$ [s] are shown in Tables 10, 11, 12, 13, 14, and 15 for both the analytical solution obtained through the proposed methodology and the solution obtained through the injection molding simulation software. In order to evaluate the quality of the final plastic part, Figs. 25, 31, 37, 43, 49, and 55 show the quality obtained by each plastic part before the ejection phases were included. Since the final part quality has been identical for each material, a single figure is accompanied by the quality prediction of each case study. All this, together with the comparison of results obtained through the proposed analytical model and through the injection molding simulation software, determine that the results obtained by the methodology described in this paper are analogous to the numerical results. In this way, the results validate and demonstrate the efficiency of the analytical-empirical model presented in plastic parts with a variety of thicknesses, volumes, and thermoplastic materials.

## 5 Conclusion

The work presented in this paper shows a new procedure for automated calculation of the injection time, packing time, and cooling time of the plastic part as well as the radius of the gate. In order to obtain these times, two new sub-algorithms have been developed that calculate the time value in each phase of the cycle time of the plastic part. In a first phase a new geometric algorithm allows the automated recognition of the topology of the plastic part using its mathematical model, obtaining the

set of geometric parameters necessary for the calculation of the cycle time. The algorithm developed calculates the path of the melt plastic flow and, by projecting a nodal square on the discrete mesh of the plastic part, determines the thickness map, obtaining the average and maximum thickness of the part. Second, an analytical-empirical algorithm performs an analysis of the numerical simulations of the injection phase in a rectangular plate shape test part (whose geometry is parameterized according to the path of the melt plastic flow, volume and thickness), generating a set of polynomial functions which determine the radius of the feeding system gate. Finally, the cycle time is calculated from the geometric, technological and material parameters of the part, obtained from the sub-algorithms.

The methodology has been tested through its application on six plastic parts with different geometries and thermoplastic material, solving and calculating the fill time, packing time, cooling time, time to reach the ejection temperature and gate radius. Additionally, a detailed data report with information of the values of each of the parameters studied is obtained as a result of the application. This data report can then be used for estimation and rapid injection mold budget generation, improving efficiency and time invested in the early phases of product design.

This new method improves the different methods used so far because it allows designers to generate an automated tool for the calculation of the cycle time without the need to carry out post-processing operations in CAE type software, requiring only the information of the geometry of the part and the data of the thermoplastic material. This allows the designers of the plastic part to evaluate the cycle time of a plastic part in real time, without the need to rely on the experience of industry experts, CAE type commercial software, or advanced knowledge in rheology and analysis of thermoplastic materials. Furthermore, it does not use the feature recognition method as a tool for recognizing the geometric of the plastic, avoiding the problems of dependence on the modeler and the recognition of complex features. The proposed methodology is applicable to any geometry of the plastic part and any programming language because it works regardless of the CAD system in which the part has been designed.

**Acknowledgements** This work has been supported by the Consejeria de Economia, Innovación, Ciencia y Empleo (Junta de Andalucia-Spain) through the project titled "A vertical design software for integrating operations of automated demoldability, tooling design and cost estimation in injection-molded plastic parts. (CELERMOLD)" (Project Code TI-12 TIC 1623). The authors would like to thank the reviewers for comments that improved the exposition.



## Appendix

### Flowchart of the present methodology

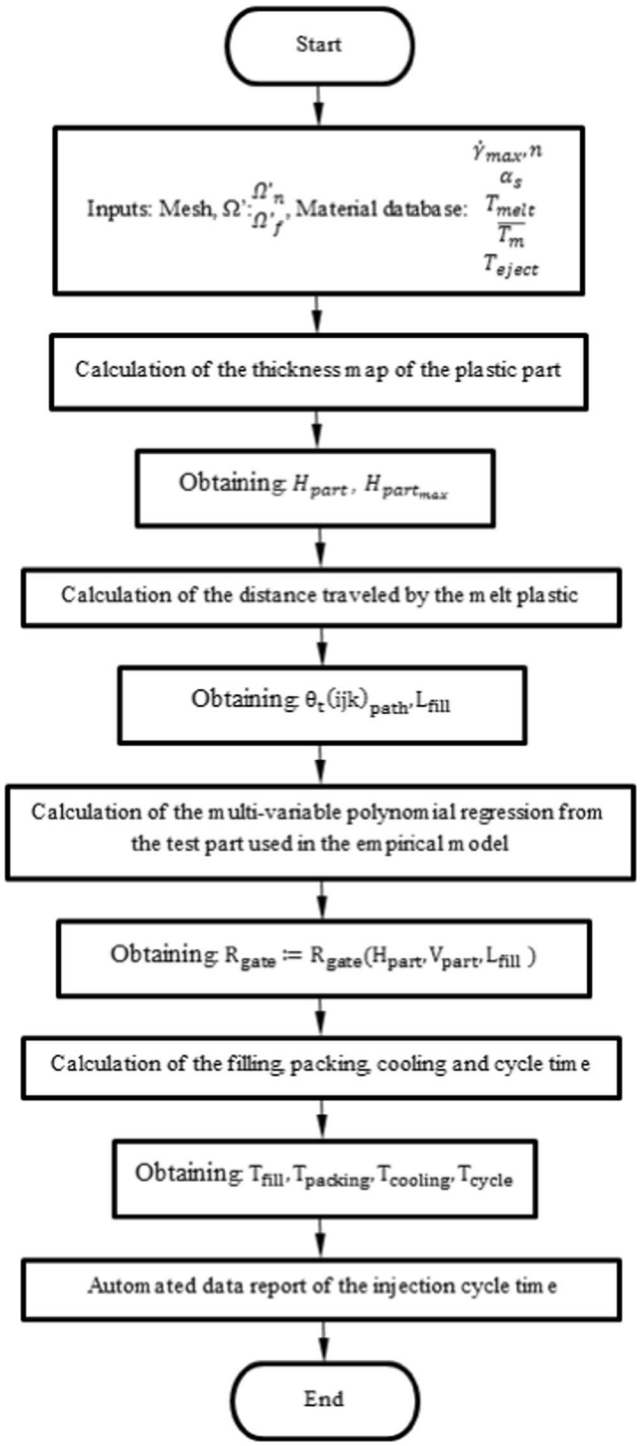


**Fig. 56** Algorithm for the calculation of the cycle time

## References


1. Zhang SQ, Liu HS, Wang HG, Liu XW (2012) New method of optimizing the filling time in injection molding. Adv Mater Res 482–484:470–473. https://doi.org/10.4028/www.scientific.net/AMR.482-484.470
2. Galantucci LM, Spina R (2003) Evaluation of filling conditions of injection moulding by integrating numerical simulations and experimental tests. J Mater Process Technol 141(2):266–275. https://doi.org/10.1016/S0924-0136(03)00276-0
3. Lam YC, Britton GA, Deng Y-M (2003) A computer-aided system for an optimal moulding conditions design using a simulation-based approach. Int J Adv Manuf Technol 22(7–8):574–586. https://doi.org/10.1007/s00170-003-1558-5
4. Sachs E, Wylonis E, Allen S, Cima M, Guo HL (2000) Production of injection molding tooling with conformal cooling channels using the three dimensional printing process. Polym Eng Sci 40(5):1232–1247. https://doi.org/10.1002/pen.11251
5. Saifullah ABM, Masood SH, Sbarski I (2012) Thermal-structural analysis of bi-metallic conformal cooling for injection moulds. Int J Adv Manuf Technol 62(1–4):123–133. https://doi.org/10.1007/s00170-011-3805-5
6. Eiamsa-ard K, Wannissorn K (2015) Conformal bubbler cooling for molds by metal deposition process. Comput Aided Des 69:126–133. https://doi.org/10.1016/j.cad.2015.04.004
7. Xu RX, Sachs E (2009) Rapid thermal cycling with low thermal inertia tools. Polym Eng Sci 49(2):305–316. https://doi.org/10.1002/pen.21261
8. Dimla DE, Camilotto M, Miani F (2005) Design and optimisation of conformal cooling channels in injection moulding tools. J Mater Process Technol 164:1294–1300. https://doi.org/10.1016/j.jmatprotec.2005.02.162
9. Park HS, Pham NH (2009) Design of conformal cooling channels for an automotive part. Int J Automot Technol 10(1):87–93. https://doi.org/10.1007/s12239-009-0011-7
10. Park HS, Dang XP (2017) Development of a smart plastic injection mold with conformal cooling channels. Procedia Manuf 10:48–59. https://doi.org/10.1016/j.promfg.2017.07.020
11. Au KM, Yu KM (2011) Modeling of multi-connected porous passageway for mould cooling. Comput Aided Des 43(8):989–1000. https://doi.org/10.1016/j.cad.2011.02.007
12. Au KM, Yu KM, Chiu WK (2011) Visibility-based conformal cooling channel generation for rapid tooling. Comput Aided Des 43(4):356–373. https://doi.org/10.1016/j.cad.2011.01.001
13. Au KM, Yu KM (2014) Variable distance adjustment for conformal cooling channel design in rapid tool. J Manuf Sci Eng Trans ASME 136(4). https://doi.org/10.1115/1.4026494
14. Ramos, C, et al. (2012) Optimalmould-part II: global optimization of the injection moulding cycle time. AIP Conference Proceedings. Vol. 1479. No. 1. AIP. https://doi.org/10.1063/1.4756465
15. J. M. Colmenero, M. A. Lazaro, C. M. Doñate, M. R. Paramio, A. V. Idoipe, J. M. P. Garcia, J. Marquez Sevillano & Puerto, D. A. (2016). Analytical calculation model for determining the cycle time in injection molding parts applied to design optimization algorithms. High Performance and Optimum Design of Structures and Materials II, 166, 427. https://doi.org/10.2495/HPSM160401
16. Ferreira I, de Weck O, Saraiva P, Cabral J (2010) Multidisciplinary optimization of injection molding systems. Struct Multidiscip Optim 41(4):621–635. https://doi.org/10.1007/s00158-009-0435-8
17. Dwivedi SN, Kumbakonam A, Yammada J (2003) A knowledge-based engineering approach for cycle time estimation for plastic injection moulding process. Int J Mater Prod Technol 19(5):337–350. https://doi.org/10.1504/IJMPT.2003.003227
18. Martin Doñate C, Rubio Paramio MA (2013) New methodology for demoldability analysis based on volume discretization algorithms. Comput Aided Des 45(2):229–240. https://doi.org/10.1016/j.cad.2012.08.005
19. Mercado-Colmenero JM, Paramio MAR, Perez-Garcia JM, Martin-Doñate C (2016) A new hybrid method for demoldability analysis of discrete geometries. Comp-Aided Design 80:43–60. https://doi.org/10.1016/j.cad.2016.06.006
20. Mercado-Colmenero JM, Rubio-Paramio MA, Vizan-Idoipe A, Martin-Doñate C (2017) A new procedure for the automated design of ejection systems in injection molds. Robot Comput Integr Manuf 46:68–85. https://doi.org/10.1016/j.rcim.2016.12.006
21. Martín-Doñate, C; Rubio-Paramio M.A; Vizán-Idoipe A.; Mercado-Colmenero, J ( (2017) Método y sistema de obtención de geometrías virtuales y detección de zonas no moldeables en piezas. Patent number: ES2594772
22. Autodesk, MoldFlow Advisor (2014) http://www.autodesk.com
23. Kazmer D (2007) Injection mold design engineering, 1st edn. Hanser, Munich
24. Menges G, Mohren P (2001) How to make injection moulds, 3rd edn. Hanser, New York
25. Matlab, R (2013) https://mathworks.com

Referencia / Reference: **Mercado-Colmenero, Jorge Manuel,** Rubio-Paramio, Miguel Angel, Guerrero – Villar, Francisca, Martín-Doñate, Cristina. *A numerical and experimental study of a new Savonius wind rotor adaptation based on product design requeriments. Energy Conversion and Management 158 (2018) 210-234. DOI: https://doi.org/10.1016/j.enconman.2017.12.058*.

Estado / Status: Publicado / Published

Índice de impacto / Impact Factor: 6,377 (JCR Year 2017)

Categoría / Catogory: Energy & Fuels

Ranking: 11/97 (JCR Year 2017)

Quartile: Q1 (JCR Year 2017)

JIF Percentile: 89.175 (JCR Year 2017)

Energy Conversion and Management 158 (2018) 210–234

Contents lists available at ScienceDirect

Energy Conversion and Management

journal homepage: www.elsevier.com/locate/enconman

# A numerical and experimental study of a new Savonius wind rotor adaptation based on product design requirements

Jorge Manuel Mercado-Colmenero[a], Miguel Angel Rubio-Paramio[a], Francisca Guerrero-Villar[b], Cristina Martin-Doñate[a,*]

[a] Department of Engineering Graphics Design and Projects, University of Jaen, Spain
[b] Department of Mechanical Engineering, University of Jaen, Spain

ARTICLE INFO

*Keywords:*
Savonius wind rotor
Rotor shape
CFD
Wind tunnel testing
Sustainable product development

ABSTRACT

This paper presents the numerical-experimental study carried out on a new rotor adapted from a Savonius rotor. Aesthetic, ergonomic and functional requirements have been incorporated into it in order to be part of sustainable consumer products. The new rotor consists of a parametric model adaptable to the dimensions and geometry of the products which it will be part of. A set of translation, symmetry, rotation and scaling operations have been applied to the bucket sections of the Savonius rotor by means of transforming the initial cylindrical buckets into topological surfaces with an organic shape. The new modified Savonius rotor and the conventional Savonius with the same Aspect Ratio have been tested in an open jet wind tunnel in order to verify the influence level of product design parameters on rotor performance, in terms of power coefficient, torque coefficient and mechanical power generated. Experimental tests have been carried out for Reynolds values in the range of [$3.430 \cdot 10^4$ and $1.419 \cdot 10^5$]. A numerical analysis using an incompressible unsteady Reynolds average Navier Stockes model has been validated by means of the experimental results. Experimental and numerical results coincide with a 3.5% error. The behavior of the turbine has been analyzed by varying the angle of rotation for the sections of its buckets. Using a rotation angle of 45° the power coefficient values improve by 32% compared to the values obtained using an angle of 0°. The rotor has been dimensioned for its application in a patented consumer product of small dimensions and requirements of lateral accessibility to its interior. Under these limited conditions the rotor meets the small-scale energy requirements of the product. The new rotor is designed as an aid to the energy consumption of the product in which it is incorporated, maintaining the advantages of a conventional Savonius rotor as self-starting, easy manufacture and maintenance, obtaining at the same time a product that sells better, is more able to integrate into its environment and is customizable for the consumer.

## 1. Introduction

Industrial design is a differentiating factor of the product nowadays and a vital strategy tool for the companies, with the function of innovating and creating future markets. Consumers demand products that have little environmental impact, both in their manufacture and during use throughout their life cycle. This fact can become an advantage for a company that designs products that help reduce pollution levels, thus fulfilling the requirements of new generations of consumers. One of the main sources of environmental impact is the energy consumed by the products. Reviewing the design from the functional point of view, looking for opportunities in the reduction of the energy consumption or evaluating the way to generate energy consumption by means of a better geometry can present great advantages.

Wind energy is one of the renewable energy sources capable of generating clean energy economically [1] being a feasible alternative to reduce the dependency on conventional energy sources [2]. Wind energy has been adapted by industries and accommodated by individual users due to its availability, ease of maintenance and low cost operation [3]. In recent years, horizontal-axis turbines have focused research given their high level of aerodynamic efficiency [4], requiring complex design criteria [5]. In contrast, vertical axis turbines have other advantages such as their ability to generate power at relatively low wind speeds [6], simple installation and maintenance [7], ease of manufacture, and a low risk of damage to birds. Savonius rotors fall within the scope of vertical rotors characterized by generating a high starting torque in any wind direction even at low speed [8], being highly silent by operating at a very low tip speed ratio. As a particular advantage,

* Corresponding author at: Campus Las Lagunillas, s/n, Building A3-210, 23071 Jaen, Spain.
*E-mail addresses:* jmercado@ujaen.es (J.M. Mercado-Colmenero), marubio@ujaen.es (M.A. Rubio-Paramio), mgvillar@ujaen.es (F. Guerrero-Villar), cdonate@ujaen.es (C. Martin-Doñate).

https://doi.org/10.1016/j.enconman.2017.12.058
Received 6 September 2017; Received in revised form 12 December 2017; Accepted 16 December 2017
Available online 09 January 2018
0196-8904/ 

**Nomenclature**

| | |
|---|---|
| $\mathscr{S}$ | canonical Savonius rotor |
| $\mathscr{B}_{\mathscr{S}}$ | buckets of the rotor $\mathscr{S}$ |
| $\mathscr{P}_j$ | new rotor adapted from $\mathscr{S}$ |
| $\mathscr{B}_{\mathscr{P}_j}$ | buckets of the $\mathscr{P}_j$ rotor |
| $j$ | number of prototype rotors; in the present paper the value of j = 3 |
| $\pi_i$ | set of cutting-planes of the rotor buckets, parallel to the XY plane |
| $r_{s1i}$, $r_{s2i}$ | buckets sections of the rotor $\mathscr{S}$ |
| $r_{\mathscr{P}j1i}$,$r_{\mathscr{P}j2i}$ | buckets sections of the rotor $\mathscr{P}_j$ |
| $H_s$ | height of the rotor $\mathscr{S}$ [m] |
| $H_p$ | height of the rotor $\mathscr{P}_j$ [m] |
| H | generic height of the rotor [m] |
| δ | torsion angle of the rotors buckets [°] |
| $A_R$ | aspect ratio |
| $e_{p_x}$ | overlap distance on the X axis for $\mathscr{P}_j$ [m] |
| $e_{p_y}$ | overlap distance on the Y axis for $\mathscr{P}_j$ [m] |
| $e_x$ | overlap distance on the axis X for $\mathscr{S}$ [m] |
| $\mathscr{A}$ | internal element to the rotor |
| $a_{shaft}$ | diameter of the internal element to the rotor [m] |
| $\beta_x$ | overlap ratio on the X axis |
| $\beta_y$ | spacing ratio on the Y axis |
| $C_p$ | coefficient of power |
| $C_t$ | coefficient of torque |
| D | rotor diameter [m] |
| $R_s$ | bucket Ratius [m] |
| H | rotor height [m] |
| $\phi$ | golden number |
| $\ell_w$ | distance from downstream rotors |
| $H_{wt}$ | wind tunnel height [m] |
| $W_{wt}$ | wind tunnel width [m] |
| B | blockage ratio |
| l | distance between the rotor axis and the application point of the force [m] |
| T | torque [N·m] |
| $T_s$ | static torque [N·m] |
| $F_{din}$ | force applied by the rotor [N] |
| TSR | tip speed ratio |
| $U_\infty$ | free stream wind velocity [m/s] |
| ω | rotor angular velocity [rad/s] |
| ρ | density of air [kg/m$^3$] |
| μ | viscosity of air [Pa·s] |
| $L_w$ | length of the wind tunnel [m] |
| θ | rotor angle [°] |

they present a simple design of their buckets or buckets, a feature that allows the introduction of criteria of the aesthetic type in its geometry, being suitable for small scale applications.

Improving the performance of the Savonius rotor as well as obtaining the geometric parameters that provide adequate efficiency has focused the attention of a large number of researchers and designers in recent years. The work has focused mainly on evaluating a set of parameters related to the geometric surface of the buckets as well as their relative spacing, the overlap ratio and the number of turbine stages among other variables. The surface of the buckets has a great influence on the performance of the rotor and therefore on the value of Power Coefficient $C_p$. The buckets of the Savonius turbine can have very varied forms depending on the geometry of the curves that make up their topology. In an effort to improve the performance of the Savonius rotor, several researchers have modified the surface of the buckets by evaluating their influence on rotor performance. Saha et al. [9] applied a geometric torsion operation to the three buckets of a Savonius rotor, validating their performance in a wind tunnel at low speed. The experimental results show the potential of the rotor with twisting buckets in terms of increased efficiency, self-starting capability and smoothness compared to those of a conventional Savonius rotor. Roy et al. [10] performed tests on a modified Savonius-style two-buckets turbine, comparing the results of $C_p$ versus the results of other rotors such as a conventional Savonius rotor, a semi-elliptical section rotor, and two other Benesh and Bach type rotors. Their results show a gain of 34% in the maximum power coefficient compared to those obtained with the other designs. Kamoji et al. [11] carried out experimental studies with a modified Savonius rotor (Bach type) of one stage, with end plates, both with and without inner shaft. With an overlap ratio equal to 0, bucket arc angle of 124° and an aspect ratio of 0.7 the modified rotor has a maximum Power Coefficient $C_p$ higher than that of a conventional Savonius rotor. Roy et al. [12] presented a transient analysis of the forces acting on a novel two-bladed Savonius style wind turbine. A significant performance improvement is achieved with the new design as compared to the conventional design due to its increased lift and moment arm contribution. More recently Tian et al. [13] introduced an optimization procedure of a Savonius wind rotor with different convex and concave sides to maximize the power efficiency.

Geometrically transforming the buckets by means of rotating operations allows the obtaining of helical Savonius turbines. Lee et al. [14] studied the variation in power coefficient and flow patterns of a Savonius turbine applying different rotation angles to its buckets and determined that the value of $C_{pmax}$ corresponds to a design with rotation angle of 45°. Damak et al. [15] proposed the use of a Savonius rotor with a rotation angle of 180°. In this design the rotor is obtained from the curve generated by a marker that moves vertically at constant speed over a rotating cylinder. The results obtained by the author indicate that an increase in the Reynolds and in the overlap ratio has a positive effect on the global features of the helical Savonius rotor. Yang et al. [16] carried out an experiment using a helical turbine in a wind tunnel. Their results indicated that an increase in rotation angle improved performance at low speed and reduced the net positive torque.

Another characteristic design parameter of the Savonius rotor geometry is the aspect ratio or ratio between the height $H_S$ of the rotor and the diameter $D_S$ of its buckets. The aspect ratio has an influence on the angular velocity of the rotor and on the torque that it generates, so that when the value of the aspect ratio is reduced the torque generated increases, and by increasing the torque generated the speed of rotation of the rotor also increases [17]. An increase in the aspect ratio may have a considerable influence on the power coefficient. However, it is not desirable to have high values of the aspect ratio due to the decrease in the power-to-weight ratio [18]. Blackwell et al. [19] showed that the efficiency increases slightly when the height/diameter ratio increases. Kamoji et al. [11] found the maximum value of $C_p$ for a rotor with an aspect ratio of 0.7 and with a Savonius rotor design with modified buckets. Saha et al. [20] showed that aspect ratio values of around 4.0 appear to lead to the best power coefficient for the conventional Savonius rotor.

The overlap ratio is defined as the ratio of the overlap distance of the buckets to their $D_S$ diameter. The Savonius rotors that include an overlap between their buckets present better features in their starting [18]. Akwa et al. [21] studied numerically the influence of the overlap ratio on a Savonius rotor. The results showed that the maximum performance appears in an overlap ratio of 0.15. Fujisawa et al. [22] also determined that the torque and the power output of the rotor reaches a maximum for an overlap of 0.15. Ushiyana et al. [23] showed that for buckets with semicircular sections the appropriate overlap ratio is 20 to 30%. Jian et al. [24] indicated in their study that the optimum overlap

ratio is in a value of 0.167 for a single-stage rotor. There are many papers [18] regarding the study of the overlap ratio, establishing the optimal values of this parameter in the range of [0.15–0.25].

The number of buckets in the Savonius rotors is an effective parameter which influences the starting torque but at the same time can decrease the value of $C_p$. The reason is that the increase of the convex area of the buckets in a given position tends to reduce the torque difference of the concave sides, which eventually affects the value of $C_p$. Saha et al. [20] determined that the optimal number of buckets is 2 for a Savonius rotor either of 1, 2 or 3 stages. Ali et al. [25] conducted a comparative experimental study of a 2 and 3 bucket rotor, concluding that the rotor with two buckets is more efficient and has a higher power coefficient than the rotor with three buckets, with the same test conditions. Mahmoud et al. [26] tested rotors of 2, 3 and 4 buckets with different aspect ratios, and without overlap between the buckets. As a conclusion to their research, he determined that the rotor of two buckets for one and two stages and with different aspect ratios provided better performance than rotors with three and four.

The performance of the Savonius rotor can also be improved by introducing several Savonius rotors in different stages. A multi-stage rotor is characterized by having several rotors at different heights which incorporate an angular displacement between them. The most important improvement of introducing rotors in several stages is to generate a more uniform torque throughout the 360°. However, the fact of having rotors in several stages means that the value of $C_p$ decreases. Jian et al. [24] obtained a level of decrease of power when using a rotor of two stages of 20% less than when using a single stage rotor. Hayashi et al. [27] designed a new three-stage rotor with a 120° phase-shift angle in order to decrease torque variation and improve starting features. Although the rotor they developed needs to make improvements in the aspect ratio at each stage, the three-stage rotor without guide has better torque features than the single-stage rotor with guides for a tip speed ratio greater than 0.8. Menet et al. [28] tested Savonius rotors in different stages, obtaining as a result that the coefficient of starting torque of the double-stage rotor is never negative, regardless of the direction of the wind, and never near to the value 0. In this way, the rotor starts after a period without wind. They also found good angular stability of the dynamic torque during rotor operation.

The addition of curtains in front of the rotor significantly improves its performance. The curtains are placed in order to reduce the negative torque caused by the return bucket and increase the power coefficient. Suitable angles for the curtains plates are $\alpha = 45^\circ$ and $\beta = 15^\circ$. Altan et al. [29] designed a curtains to improve the low level of efficiency of Savonius wind turbines. Their design avoids negative torque in the convex bucket of the rotor. In a later study [30] Altan et al. introduced a straight flap which reduces the effects of the compression of the flow within the bucket so that the rotor performance is increased. Based on such optimizations it achieves a power coefficient increase of about 20%. Mohamed et al. [31] positioned an obstacle to protect the return bucket of the Savonius turbine and better drive the orientation of the flow towards the advance bucket. In this way it obtains a considerable improvement of the performance of the Savonius turbines, with a relative increase in the power coefficient of more of 27%. The performance of a Savonius rotor can be improved using multiple quarter blades. Sharma et al. [32] added multiple quarter blades to conventional configuration, observing an improvement in the coefficient of power of 8.89% to 13.69% for different inlet velocities over the conventional configuration. In a later study Sharma et al. [33] quantify the effect of layered multiple miniature blades on the coefficient of power of a Savonius rotor using simulation software, observing an improvement in COP spanning of between 8.1% and 11.34% with the modified configuration. Korprasertsak et al. [34] proposed an optimal design of wind boosters for vertical axis wind turbines at low speed. The wind booster comprises a number of guide vanes, which are mounted around a VAWT. The guide vanes direct wind to impact VAWT blades at effective angles while passages between each guide vane are arranged to accelerate wind. The guiding and throttling effects of the wind booster are able to increase angular speed, leading to an increase in the mechanical power of the VAWT.

The use of end plates in the design of the rotor also improves the performance of the Savonius rotor. Alexander et al. [35] studied the effect of the end plates on the performance of the Savonius rotor, obtaining a high power coefficient. To improve the performance of the rotor, a value of the diameter of the end plates 10% higher than the diameter of the buckets $D_s$, is recommended for a rotor with an aspect ratio of 1.0 [18].

Vertical axis turbines combine functional performance with a strong aesthetic component. The use of this kind of rotor allows the introduction of geometric requirements in its technical specifications which often have an important role in the placement of rotors inside protected areas [36]. Coastal and mountainous areas are optimal for the location of vertical rotors due to wind conditions, however these locations tend to be areas of a high visual impact which can make a poorly harmonic design not suitable for these locations. Vertical rotors have the advantage of operating in a turbulent mode and with low wind speed [37]. They are optimal for use in cities [38], urban areas [39], sub-urban and remote areas [40] since its installation is possible in the top of many buildings [41]. Vertical axis wind turbines have the greatest future prospects among all wind technologies for small-scale power generation in the built environment [42] In addition, the electrical production of the vertical rotors works in a distributed way, managing a large number of small renewable sources as if it were a single larger source, like a virtual power plant. These reasons make vertical rotors suitable for introduction into products for smart cities whose objective is to use resources efficiently, saving energy and improving the environmental footprint [43]. Working on the design of a rotor involves taking into account its appearance, but also incorporating this quality into the achievement of a good technical performance. Wind rotors and specifically vertical rotors are ideal components of consumer products because of their symmetrical topology and small-scale energy requirements. The introduction of technical specifications of the aesthetic and ergonomic type relates the product to the user, allowing it to operate in an intuitive and simple way although the product incorporates a highly complex technology. The current trend in design is to create products which are integrated into the environment. Thus incorporating an aesthetic value in the rotors helps to improve the natural and architectural environment, while humanizing a complex technology [44]. EcoDesign is a growing trend that integrates multifaceted aspects of design and environmental considerations. The objective is to create sustainable solutions that satisfy human needs and desires [45]. Following these lines of work some researchers have designed vertical rotors capable of incorporating aesthetic-ergonomic criteria used in the design of products for the design of the geometry of their buckets, maintaining their technical performance. The vertical rotor described in the patent [46] uses the value of the golden Ratio as the dimensioning parameter of its buckets. The topology of the buckets in the rotor is given by a convex surface generated from logarithmic spirals obtained from the value of the golden ratio. In this regard, the patent [47] describes a vertical rotor whose buckets consist of a spiral-shaped frame whose dimensions are also based on the values of the golden ratio. Unfortunately both rotors do not meet the requirement of lateral accessibility to their inside zone, and are therefore difficult to apply to consumer products.

Introducing aesthetic criteria in vertical rotors at the commercial level is a growing trend nowadays. The Hercules rotor of the Enessere company [48] introduces harmonic requirements into its design, offering great advantages in its setting inside any landscape context, even one of high aesthetic prestige. This rotor has recently been awarded the 2016 Silver Design Award [49]. For the particular use of Savonius rotors adapted to consumer products, the newly constructed artificial tree L'arbre du Vent [50] operates as a small local power generating network in which each bucket (Aeroleaf) is a small wind turbine. The Aeroleaf is

able to take advantage of the slightest wind breeze regardless of the direction of origin, this being optimal for the use of the product in an urban environment. The organic and biomimetic modeling [51] of the surface of the buckets makes them integrate into the environment, differentiating them from the conventional ones. The Wind Tulip turbines from the Leviathan Energy Company [52] are vertical rotors of the Savonius type, which combine aerodynamics and industrial design in the same way, requiring low wind speed to generate energy, being quiet and requiring low maintenance.

The paper presents the numerical-experimental study carried out on a new rotor adapted from a canonical Savonius rotor to which a set of geometric and topological requirements have been introduced. These new requirements cause changes in its geometry which allow the new rotor to be part of sustainable consumer products. The performance of the turbine has been analyzed for different rotation angles of its buckets by means of testing different wind speeds within a range of tip speed ratios. The new power coefficient, torque coefficient, and generated power have been calculated. The new rotor incorporates a parametrized design with geometric variables based on aesthetic specifications. The geometric operations applied to the canonical Savonius rotor have changed the curvature of its buckets by means of transforming the initial cylindrical surfaces into surfaces of an organic type that can be perfectly integrated into the architectural or particular environments which usually present these kinds of shapes. The new rotor features have all the advantages of the Savonius rotor such as self-starting, ease of manufacture and maintenance and operation at low wind speeds, as well as accessibility to its inside zone. The parameterization of variables allows obtaining rotors of different sizes which, when incorporated into sustainable products meet their design requirements while satisfying their functional requirements. While the new rotor partly sacrifices its performance it nevertheless meets the aesthetic and ergonomic requirements of the product, making it easier to sell while still meeting its energy requirements. The new rotor is born as a suitable variant of the Savonius rotor for small scale energy applications and for its application in products where aesthetic requirements need to be combined with a functional performance.

## 2. Description of the new rotor geometry

In order to validate the influence of the aesthetic and ergonomic requirements on the performance of the $\mathscr{S}$ Savonius vertical rotor, three prototype rotors $\mathscr{P}_j$ have been designed and manufactured based on the $\mathscr{S}$ geometry. The new buckets of the rotors $\mathscr{P}_j$ have been obtained by means of geometric operations based on symmetry of translation, rotation and scale on the cross sections $[r_{s1i}, r_{s2i}]$ of the canonical $\mathscr{S}$ rotor. With this procedure it is possible to obtain a set of new profiles $[r_{\mathscr{P}j1i}, r_{\mathscr{P}j2i}]$ for the buckets of $\mathscr{P}_j$ on which a subsequent sweep operation is achieved. The curvature of the buckets of the canonical $\mathscr{S}$ rotor is transformed from cylindrical surfaces to organic ruled surfaces.

The geometry of the Savonius $\mathscr{S}$ rotor (Fig. 1) is encompassed within the scope of the symmetrical bodies. The symmetrical shapes present a set of potentially beneficial qualities for the designers since they allow the creation of harmonious, interesting and memorable designs. Symmetry is associated with beauty and is a geometric property found in almost all forms of nature. This is the reason why they tend to draw attention in the environment in which they are located. There are three types of basic symmetry; reflection symmetry, translational symmetry and rotation symmetry [53]. The three prototype rotors $\mathscr{P}_j$ have been designed to fulfill these three types of symmetry.

### 2.1. Application of the translational symmetry operation to the sections coincident with the mean plane of the rotor Savonius

The sections $[r_{s1i}, r_{s2i}] \in \mathscr{S}$ coinciding with the mean plane of the rotor ($i = \frac{H}{2}$) are separated from each other by a distance $e_x$ along the X axis equal to the distance necessary to be able to locate an element $\mathscr{A}$ with radio $a_{shaft}$ (Fig. 2) in the inside zone of the buckets $\mathscr{B}_{\mathscr{S}}$.

In order to fulfill the ergonomic requirement of lateral accessibility to the inside element $\mathscr{A}$, the sections $[r_{s1i}, r_{s2i}] \in \mathscr{B}_{\mathscr{S}}$ are again displaced on the plane $\pi_{\frac{H}{2}}$ by a length $L_a$ along the direction $\overrightarrow{L_a}$ Eq. (1) and (2). As shown in Fig. 3. $C_S$ represents the center of $[r_{s1i}, r_{s2i}] \in \mathscr{B}_{\mathscr{S}}$, $u_x$ [m] represents the displacement of $[r_{s1i}, r_{s2i}]$ along the X axis, and $u_y$ [m] the displacement of the sections along the Y axis. In this way it has been possible to locate two new sections $[r_{\mathscr{P}j1i}, r_{\mathscr{P}j2i}]$ for $i = \frac{H}{2}$ which act as base profiles of the new prototype rotor geometry $\mathscr{P}_j$ according to the geometric requirement of translation symmetry. The distance $L_a$ Eq. (2) between each pair of sections $[r_{\mathscr{P}j1i}, r_{\mathscr{P}j2i}]$ of the buckets $\mathscr{B}_{\mathscr{P}j}$ is parameterized so that different sized rotors can be obtained by simply replacing the design variables established in the paper. Eqs. (3)–(5).

$$\overrightarrow{L_a} = u_x \cdot \vec{x} + u_y \cdot \vec{y} \tag{1}$$

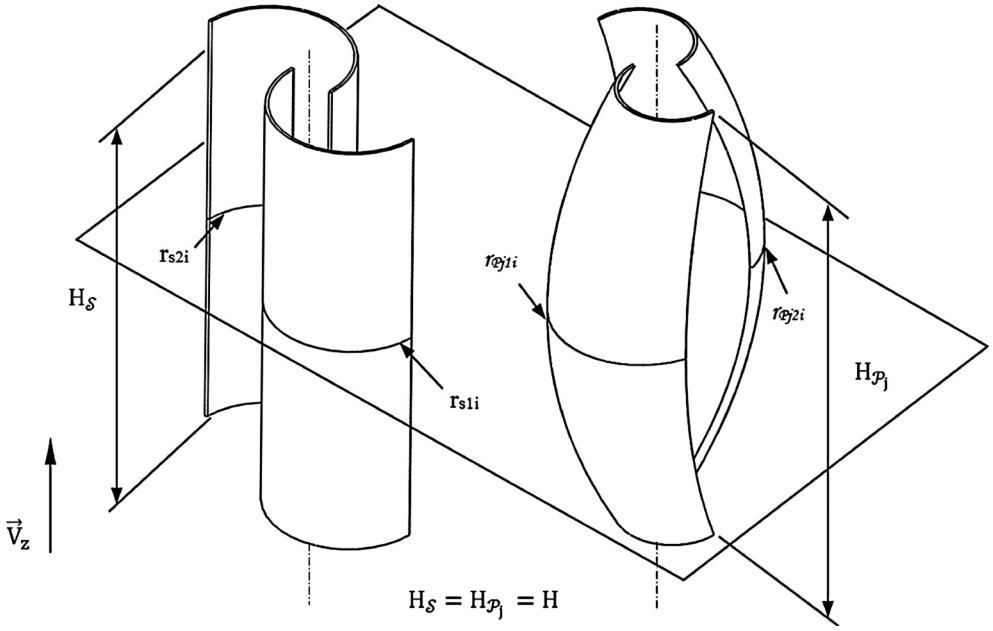


**Fig. 1.** Representation of a generic $\pi_i$ cutting plane and the sections $[r_{s1i}, r_{s2i}] \in \mathscr{S}$ and $[r_{\mathscr{P}j1i}, r_{\mathscr{P}j2i}] \in \mathscr{P}_j$.

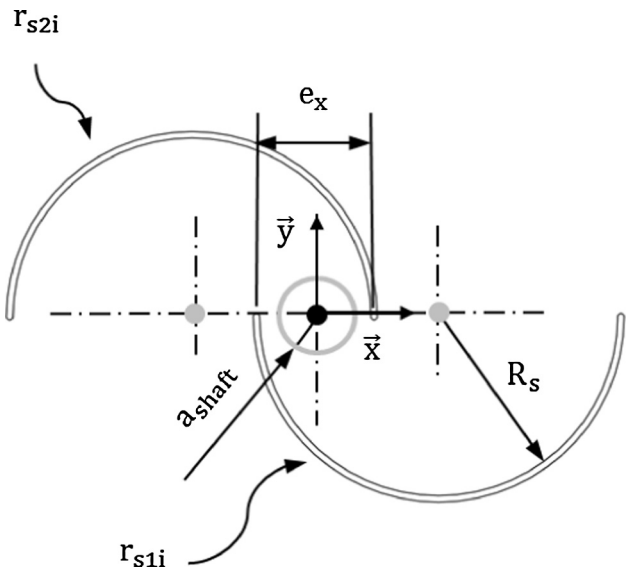


**Fig. 2.** Application of the translation symmetry operation to the sections $[r_{s1i}, r_{s2i}] \in \mathscr{S}$ coincident with the mean plane of the rotor ($i = \frac{H}{2}$).

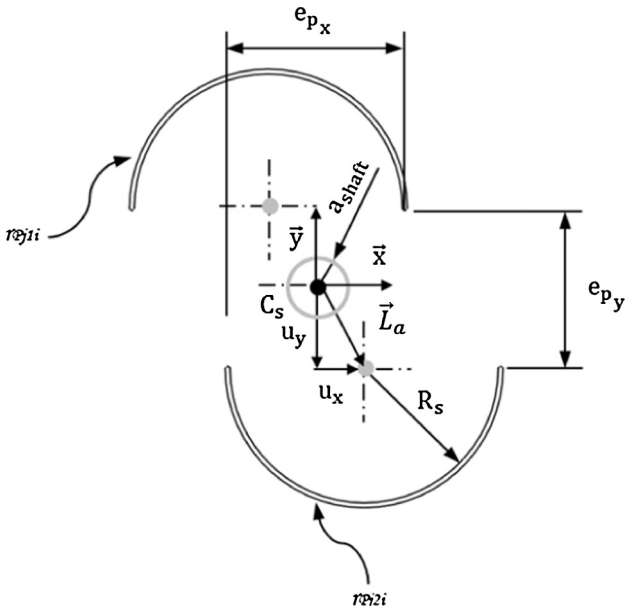


**Fig. 3.** Obtaining the profiles $[r_{\mathscr{P}j1i}, r_{\mathscr{P}j2i}] \in \mathscr{B}_{\mathscr{P}j}$ for a height $i = \frac{H}{2}$.

$$L_a = |\overrightarrow{L_a}| = \sqrt{u_{x+}^2 u_y^2} \tag{2}$$

$$e_{p_x} = e_x + 2\cdot|u_x| \tag{3}$$

$$e_{p_y} = e_y + 2\cdot|u_y| = 2\cdot|u_y| \tag{4}$$

$$e_y = 0 \tag{5}$$

As shown in Fig. 3, the geometric definition of each section $[r_{s1i}, r_{s2i}] \in \mathscr{B}_{\mathscr{S}}$ and $[r_{\mathscr{P}j1i}, r_{\mathscr{P}j2i}] \in \mathscr{B}_{\mathscr{P}j}$ that lies at a height $i = \frac{H}{2}$ can be expressed in parametric form as indicated in Table 1, Eqs. (6)–(9).

The radius $R_P$ of the buckets $\mathscr{B}_{\mathscr{P}j}$ for the sections $[r_{\mathscr{P}1i}, r_{\mathscr{P}2i}]$ at a height $i = \frac{H}{2}$ is analogous to the radius $R_S$ of the sections $[r_{s1i}, r_{s2i}]$ of the canonical Savonius rotor with buckets $\mathscr{B}_{\mathscr{S}}$.

### 2.2. Application of the geometric scaling operation between the sections of the ends of the rotor Savonius. Obtaining sections belonging to the new rotor

In order to obtain the final geometry of the prototype rotors $\mathscr{P}_j$, the sections $[r_{s1i}, r_{s2i}]$ of the ends of the rotor $\mathscr{S}$ are displaced by a distance $L_a$ along the X and Y axis, subsequently applying a reducing scale factor equal to the golden number $\phi$. In this way, the geometric features of the new sections $[r_{\mathscr{P}j1i}, r_{\mathscr{P}j2i}]$ Eqs. (10) and (11) for i = 1, H can be related through the criterion of golden proportionality with the sections $[r_{\mathscr{P}j1i}, r_{\mathscr{P}j2i}]$ for $i = \frac{H}{2}$. Finally the set of sections $[r_{\mathscr{P}j1i}, r_{\mathscr{P}j2i}]$ for heights $i = 1, \frac{H}{2}$, H are joined by means of two 3D spline topology guide curves linking three points $P_i$ contained in each section $[r_{\mathscr{P}j1i}, r_{\mathscr{P}j2i}]$ Fig. 4. The spline curves are used as a spine for the sweep operation of the set of sections $[r_{\mathscr{P}j1i}, r_{\mathscr{P}j2i}]$, obtaining the final surface of the new buckets $\mathscr{B}_{\mathscr{P}j}$. Table 2 shows the parametric equations for the sections $[r_{\mathscr{P}j1i}, r_{\mathscr{P}j2i}]$ for height i = 1, H.

### 2.3. Application of the rotation symmetry operation to the sections del nuevo rotor $\mathscr{P}$. Rotation angle δ for heights coinciding with the middle and extreme planes

Another topological feature of the Savonius rotors is the geometrical transformation of their buckets by applying rotational operations, thus obtaining helical Savonius rotors. This is in order to fulfill the aesthetic requirement of rotation symmetry between its buckets $\mathscr{B}_{\mathscr{P}j}$. This operation has been applied to the sections $[r_{\mathscr{P}j1i}, r_{\mathscr{P}j2i}]$ for values $i = 1, \frac{H}{2}$, H, δ equal to 0°, 22° y 45° respectively, obtaining three prototype rotors $\mathscr{P}_j$ that meet the design requirement.

The new $\mathscr{P}$ rotor has been designed in a parametric way which allows the obtaining of the prototype $\mathscr{P}_j$ rotors by only modifying the value of the parameter δ. In order to validate the performance of the new rotor the values of the design variables have been established according to the dimensions of one of the products that the $\mathscr{P}$ rotor will be part of [54], one application is [55]. For this product dimensions related to lateral accessibility and ergonomics have been obtained from the standard anthropometric measurements of the hand of an adult man [56]. In Table 3 the magnitude of the set of geometric features is shown for both the canonical Savonius rotor $\mathscr{S}$ and the set of prototype $\mathscr{P}_j$ rotors analyzed in the present paper (see Fig. 5).

## 3. Experimental set-up and methodology

In order to analyze the mechanical behavior of each designed rotor, they were tested by means of a low-speed jet-type wind tunnel (see Fig. 6), whose testing trasversal area is 400 mm × 400 mm with a total length of the test channel of 1500 mm. The uniform main flow in the tunnel is produced by a 5 kW rotating fan with a variable speed drive engine, so the flow can reach a maximum speed of 40 m/s. The wind speed has been adjusted for each geometry analyzed according to the given Reynolds number and the maximum allowable speed that the rotors can withstand without load conditions. As is shown in Fig. 6 the wind tunnel was provided with a honeycombe-shaped plates system. Thus, the wind tunnel gave a turbulence level of less than 2%, and a high ratio of flow uniformity. The wind speed is determined by a pitot tube connected to a manometer (Testo 512).

The maximum size of the bounding box of each rotor tested in this study was 200 mm × 200 mm × 320 mm. As shown in Fig. 8, the prototype rotors were located at a distance of 900 mm downstream from

**Table 1**
Parametric equations of the sections $[r_{s1i}, r_{s2i}] \in \mathscr{B}_{\mathscr{S}}$ and $[r_{Pj1i}, r_{Pj2i}] \in \mathscr{B}_{\mathscr{P}j}$ for $i = \frac{H}{2}$.

| | | |
|---|---|---|
| Savonius rotor | $r_{s_{1i}} = \left[R_s - \frac{e_x}{2} \quad 0\right] + R_s\cdot(\mathrm{Cos}(\vartheta),\mathrm{Sin}(\vartheta))\ \forall\ \vartheta \in [0,\pi)$ | (6) |
| | $r_{s_{2i}} = \left[-R_s + \frac{e_x}{2} \quad 0\right] + R_s\cdot(\mathrm{Cos}(\vartheta),\mathrm{Sin}(\vartheta))\ \forall\ \vartheta \in [0,\pi)$ | (7) |
| Prototype rotors | $r_{pj1i} = \left[-R_s + \frac{e_{p_x}}{2} \quad \frac{e_{p_y}}{2}\right] + R_s\cdot(\mathrm{Cos}(\vartheta),\mathrm{Sin}(\vartheta))\ \forall\ \vartheta \in [0,\pi)$ | (8) |
| | $r_{pj2i} = \left[R_s - \frac{e_{p_x}}{2} \quad -\frac{e_{p_y}}{2}\right] + R_s\cdot(\mathrm{Cos}(\vartheta),\mathrm{Sin}(\vartheta))\ \forall\ \vartheta \in [\pi,2\pi)$ | (9) |

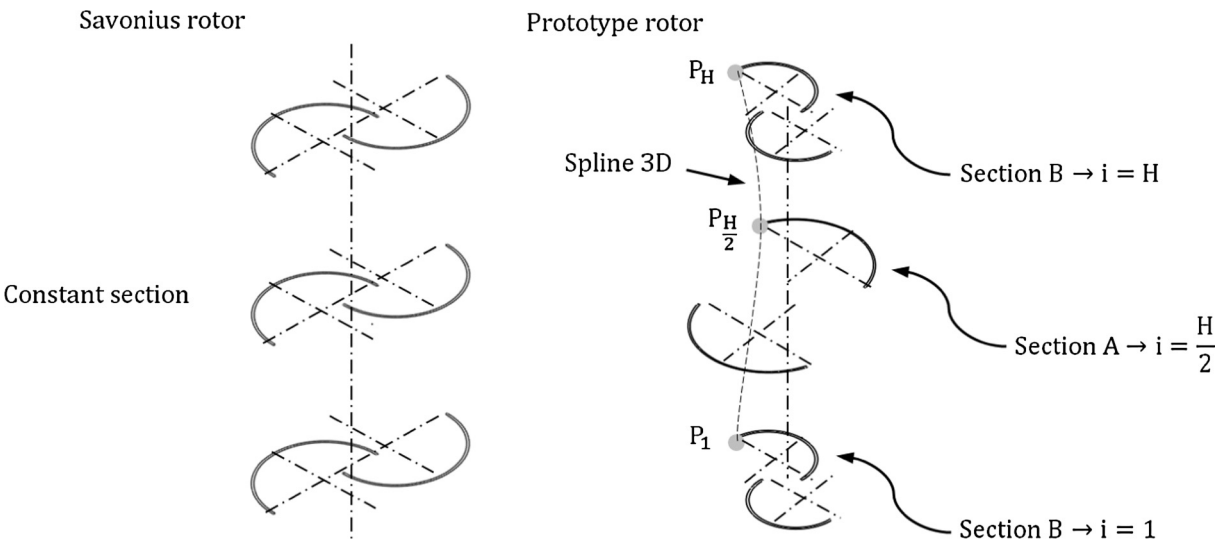


**Fig. 4.** Obtaining of the guide curves in the geometric operation of sweep along the sections in the rotors $\mathscr{P}_j$.

**Table 2**
Parametric equations of the sections $[r_{pj1i}, r_{pj2i}] \in \mathscr{P}_j$ for height values i = 1, H.

| | | |
|---|---|---|
| Prototype rotors | $r_{pj1i} = \frac{1}{\phi}\cdot r_{p1} = \frac{1}{\phi}\cdot\left(\left[-R_s + \frac{e_{px}}{2} \quad \frac{e_{py}}{2}\right] + R_s\cdot(\mathrm{Cos}(\vartheta),\mathrm{Sin}(\vartheta))\ \forall\ \vartheta \in [0,\pi)\right)$ | (10) |
| | $r_{pj2i} = \frac{1}{\phi}\cdot r_{p2} = \frac{1}{\phi}\cdot\left(\left[R_s - \frac{e_{px}}{2} \quad -\frac{e_{py}}{2}\right] + R_s\cdot(\mathrm{Cos}(\vartheta),\mathrm{Sin}(\vartheta))\ \forall\ \vartheta \in [\pi,2\pi)\right)$ | (11) |

**Table 3**
Dimensions of the canonical Savonius rotor $\mathscr{S}$ and the prototype $\mathscr{P}_j$ rotors.

| Savonius rotor $\mathscr{S}$ | | Prototype rotors $\mathscr{P}_j$ for i = $\frac{H}{2}$ | |
|---|---|---|---|
| $R_s$ [mm] | 57.5 | $R_s$ [mm] | 57.5 |
| $e_x$ [mm] | 37.5 | $e_{px}$ [mm] | 68.5 |
| $e_y$ [mm] | 0 | $e_{py}$ [mm] | 99.4 |
| $a_{shaft}$ [mm] | 14.5 | $u_x$ [mm] | 15.5 |
| $H_s$ [mm] | 320.0 | $u_y$ [mm] | 49.7 |
| | | $a_{shaft}$ [mm] | 14.5 |
| | | $H_p$ [mm] | 320.0 |

the entrance of the rectangular test channel. The rotors were fixed to a base composed of two circular plates in the center of which a bearing is located to allow rotation of the axis of the rotors minimizing the friction (see Fig. 7). This base was manufactured in PLA, using the additive manufacturing technique by means of flux deposition. The rotors were fixed to the shaft by means of threaded lugs housed in the rotor supports. The base was attached to the lower surface of the wind tunnel by means of a set of washers and screws. In addition, the center of rotation of the prototype rotors was aligned with the mass center of the main wind area of the tunnel channel, to avoid any kind of eccentricity. The application of this test methodology facilitates the replacement of the rotors for the different analyses performed (see Table 4).

The rotors were placed inside the wind tunnel through a circular window of 200 mm, located at the top of the tunnel. As can be seen in Fig. 6, the length of the rotor shaft is greater than the section height of the tunnel. This allows a direct torque measurement on the rotor shaft with a "Prony brake system" dynamometer and a speed measurement of the rotor through a conventional tachometer, both installed outside the wind tunnel over the ceiling of the testing space. Fig. 8 shows the layout of the arrangement of the main elements and tools used in the rotor tests.

To build the "Prony brake system" a PCE-FB50 dynamometer was used positioned at 30 mm from the turbine axis pointing to a torque arm which is jointed to the rotor shaft with an adjustable brake. The PCE-FB50 dynamometer has a measurement range of between 0 and 50 N, 0.01 N of resolution and an accuracy of ± 0.01 N. To determine the power developed by the turbine it is also necessary to measure turbine speed, therefore a Digital Photo Tachometer model RM-1501 was used as well. The experimental devices were used to predict the static torque of the rotor at a given rotational speed and investigate the conditions experienced by the proposed wind turbines placed in the uniform air flow.

In addition, it is important to note that the results obtained cannot be acquired or compared with results obtained in a non-uniform fully external flow. Therefore, the jet-type wind tunnel (see Fig. 6) has been an important tool for obtaining a non-turbulent uniform flow to characterize the power and moment coefficient curves versus tip speed ratio of the prototype rotors $\mathscr{P}_j$.

## 4. Data reduction

The expression of the Reynolds number Eq. (12) used in the present paper uses as characteristic length the diameter of the prototype rotors and as characteristic speed the speed of the wind tunnel uniform air flow.

$$\mathrm{Re} = \frac{\rho\cdot U_\infty\cdot D}{\mu} \tag{12}$$

where Re is the Reynolds number, $U_\infty$ [m/s] is the wind tunnel uniform air flow velocity, D is the prototype rotor, $\rho$ [kg/m$^3$] is the density of air and $\mu$ [Pa·s] is the absolute viscosity of air.

The expression of the dimensionless speed number, tip speed ratio Eq. (13), is given by.

$$\mathrm{TSR} = \frac{\omega\cdot D}{2\cdot U_\infty} \tag{13}$$

where $\omega$ [rad/s] is the angular velocity of the prototype rotors.

The magnitude of the force obtained by the dynamometer allows us to determine the moment Eq. (14) that the prototype rotor exerts on its

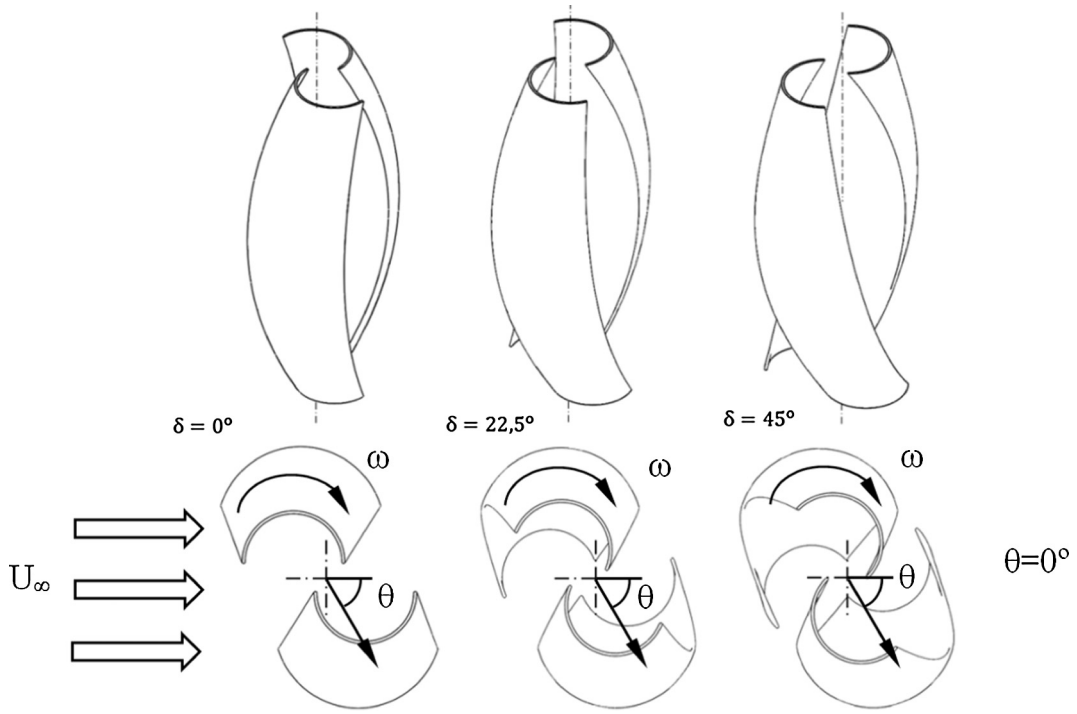


**Fig. 5.** Obtaining the three prototype rotors $\mathscr{P}_j$ for values of δ equal to 0°, 22° y 45°.

**Fig. 6.** Wind tunnel of the Higher Polytechnic School of the University of Jaen, fluid mechanics research group.

**Fig. 7.** Rotors $\mathscr{S}$ and $\mathscr{P}_j$ fixed to the wind tunnel by means of a circular PLA base.

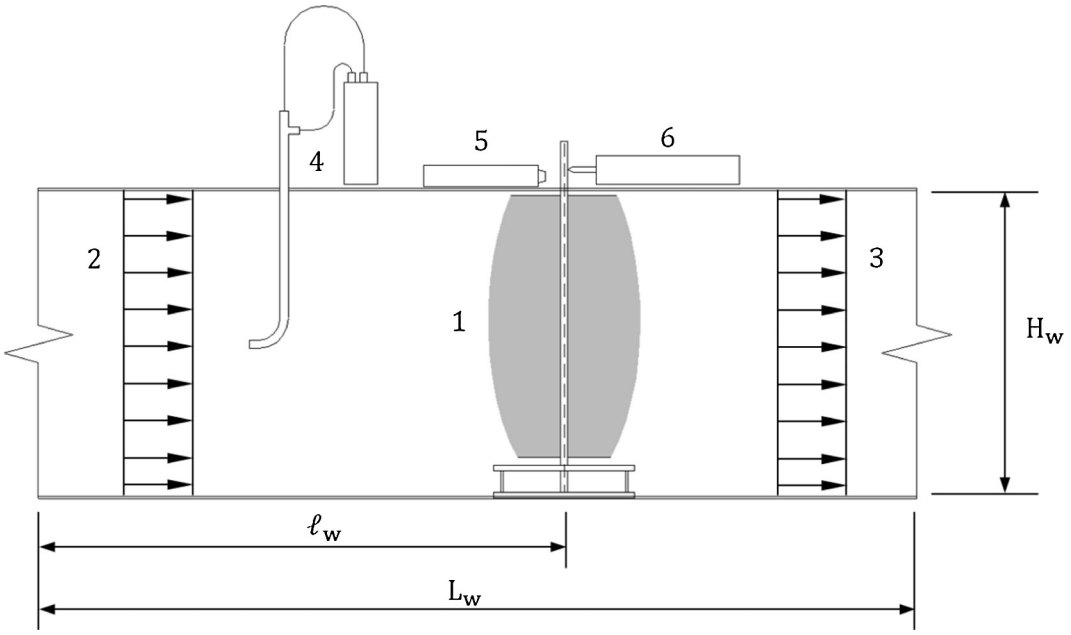


**Fig. 8.** Schematic diagram of the set-up.

**Table 4**
Components of the schematic set-up diagram.

| | | | |
|---|---|---|---|
| 1 | Vertical rotor turbine | 4 | Pitot tuve and manometer |
| 2 | Upstream air flow | 5 | Photo tachometer |
| 3 | Downstream air flow | 6 | Dynamomter |

**Table 5**
Dimensionless geometric parameters of the prototype rotors and the canonical Savonius rotor.

| | $A_R$ | $\beta_x$ | $\beta_y$ |
|---|---|---|---|
| Savonius rotor | 1.618 | 0.343 | 0.000 |
| Prototype rotors | 1.618 | 0.326 | 0.611 |

axis of rotation by means of the following expression.

$$T_s = F_{din} \cdot l \tag{14}$$

where $T_s$ [N·m] is the static torque derived from the prototype rotors, $F_{din}$ [N] is the magnitude of the force obtained by the dynamometer and l [m] the radial distance between the point of measurement or location of the dynamometer and the center of rotation of the prototype rotor.

Statics torque coefficient ($C_{ts}$), torque coefficient ($C_t$) and power coefficient ($C_p$) Eqs. (15)–(17) were given as follows:

$$C_{ts} = \frac{4 \cdot T_s}{\rho \cdot U_\infty^2 \cdot D^2 \cdot H} \tag{15}$$

$$C_t = \frac{4 \cdot T}{\rho \cdot U_\infty^2 \cdot D^2 \cdot H} \tag{16}$$

$$C_p = C_{ts} \cdot TSR = \frac{4 \cdot T_s \cdot \omega \cdot D}{\rho \cdot U_\infty^2 \cdot D^2 \cdot H \cdot 2 \cdot U_\infty} = \frac{2 \cdot T_s \cdot \omega}{\rho \cdot U_\infty^3 \cdot D \cdot H} \tag{17}$$

where T [N·m] is the dynamic toque derived from the prototype rotors.

The aspect ratio ($A_R$) Eq. (18) represents the height of the prototype rotors relative to their diameter. The prototype rotors proposed in this paper are governed by the golden ratio, so the value of this dimensionless parameter is equal to the golden number ($\phi$).

$$A_R = \frac{H}{D} \approx \phi \tag{18}$$

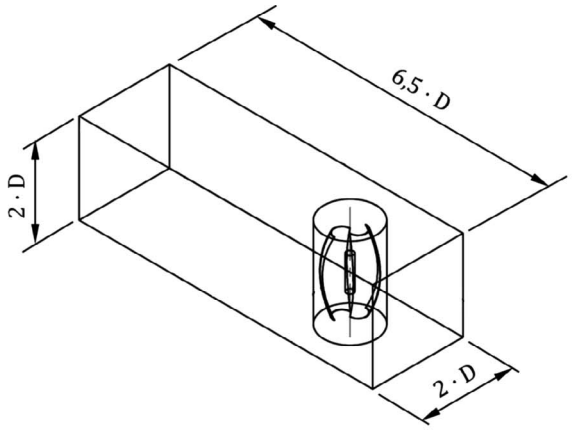


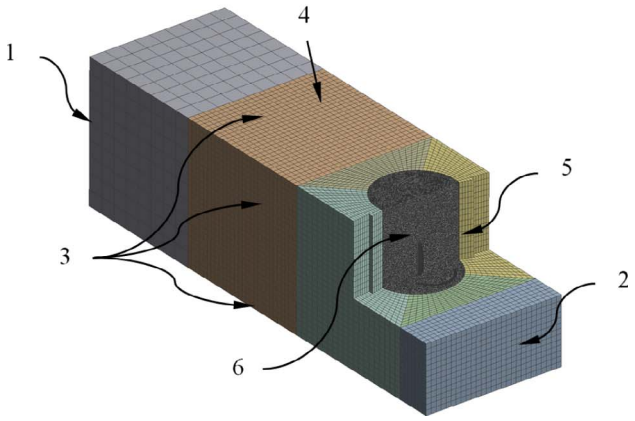


**Fig. 9.** Representation of the computational domain used in the numerical analysis.

**Table 6**
Boundary conditions and computing domain.

| | | | |
|---|---|---|---|
| 1 | Pressure outlet | 4 | Wind tunnel domain |
| 2 | Velocity inlet | 5 | Interface rotor-tunnel domain |
| 3 | Static walls, No-Slip Walls | 6 | Rotor domain |

**Table 7**
Intensity and turbulence length.

| | |
|---|---|
| Intensity | 5% |
| Length scale | 0.1 [m] |

where H [mm] is the height and D [m] is the diameter of the prototype rotors.

The overlap ratio ($\beta_x$,$\beta_y$) Eq. (19) is a dimensionless parameter relative to the separation distance between the buckets of the prototype rotors $\mathscr{B}_{\mathscr{D}_j}$ versus their diameter (see Fig. 3). The expression of this

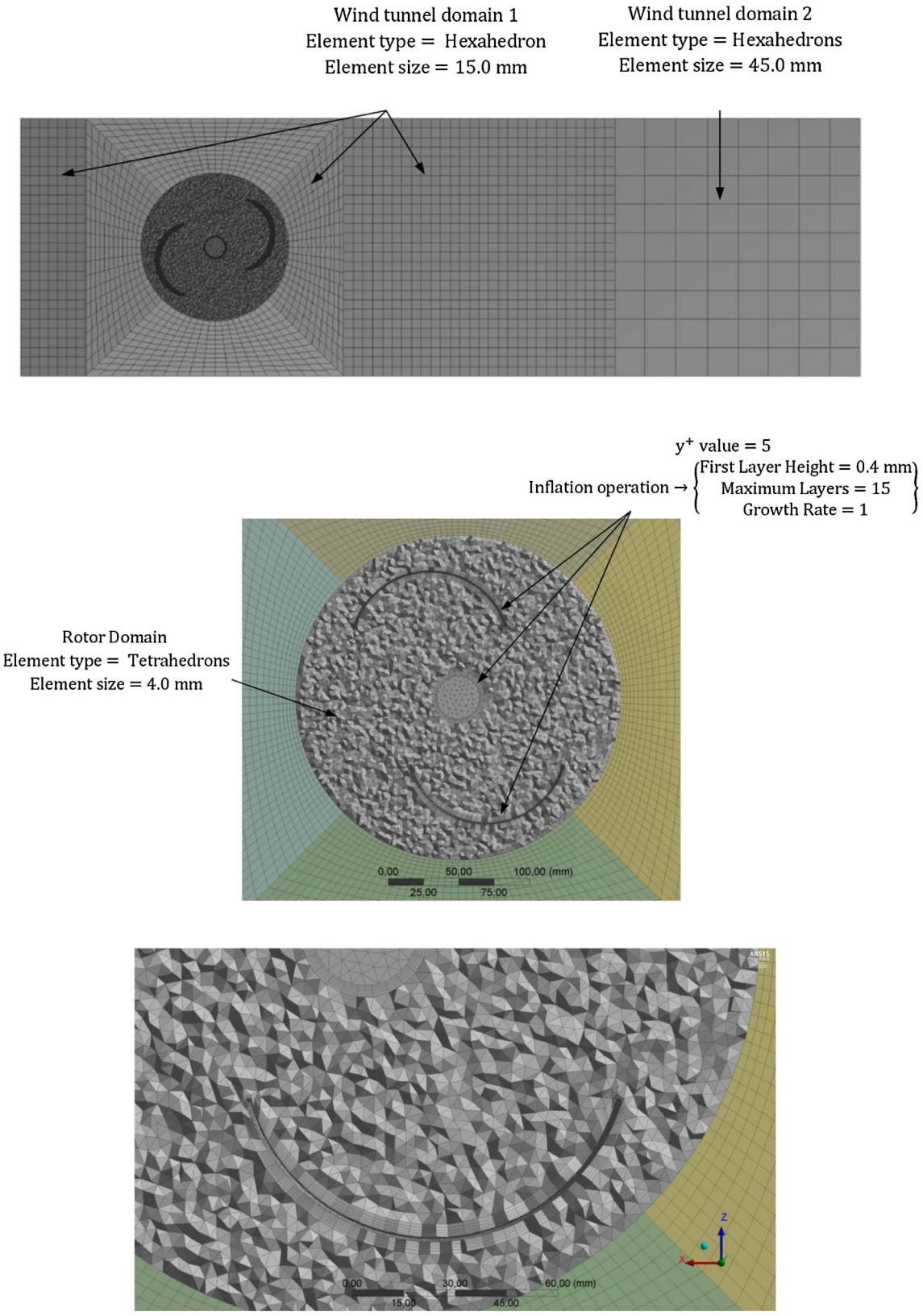


**Fig. 10.** Grid generation for the static domain and the boundary layers.

**Table 8a**
Number of grid points on the Rotor domain along streamwise and spanwise directions.

| | Streamwise | Spanwise |
|---|---|---|
| Savonius rotor $\mathscr{S}$ | 64 | 118 |
| Prototype rotor $\mathscr{P}_j$ for value of δ equal to 0° | 61 | 113 |
| Prototype rotor $\mathscr{P}_j$ for value of δ equal to 22.5° | 60 | 114 |
| Prototype rotor $\mathscr{P}_j$ for value of δ equal to 45° | 62 | 115 |

**Table 8b**
Number of grid points on the buckets along its contour and streamwise and spanwise directions.

| | Streamwise | Spanwise | Buckets contour |
|---|---|---|---|
| Savonius rotor $\mathscr{S}$ | 5 | 81 | 100 |
| Prototype rotor $\mathscr{P}_j$ for value of δ equal to 0° | 5 | 92 | 79 |
| Prototype rotor $\mathscr{P}_j$ for value of δ equal to 22.5° | 5 | 92 | 79 |
| Prototype rotor $\mathscr{P}_j$ for value of δ equal to 45°. | 5 | 92 | 79 |

**Table 9**
Characteristic parameters of the meshes generated for each study geometry.

| | Savonius rotor | Prototype rotors | | |
|---|---|---|---|---|
| | | δ = 0° | δ = 22.5° | δ = 45° |
| Average ortogonal quality | 0.8138 | 0.8169 | 0.8170 | 0.8174 |
| Input tetrahedral element size [mm] | 4.0 | 4.0 | 4.0 | 4.0 |
| Input hexahedral element size [mm] | 15.0/45.0 | 15.0/45.0 | 15.0/45.0 | 15.0/45.0 |
| Number of elements | 2,316,895 | 2,319,440 | 2,323,401 | 2,323,825 |
| Number of nodes | 3,527,442 | 3,492,860 | 3,506,757 | 3,504,981 |

**Table 10**
Values of the main parameters of the governing equations.

| | |
|---|---|
| v,w,k | 1, 2, 3 |
| $C_\mu$ | 0.09 |
| $\sigma_k$ | 1.00 |
| $\sigma_\varepsilon$ | 1.30 |
| $C_{1\varepsilon}$ | 1.44 |
| $C_{2\varepsilon}$ | 1.92 |

**Table 11**
Time step size, Number of time steps and Max iterations employed for each rotor in the numerical analyses.

| | Time step size (s) | Number of time steps | Max iterations |
|---|---|---|---|
| Savonius rotor $\mathscr{S}$ | 0.0049 | 18 | 20 |
| Prototype rotor $\mathscr{P}_j$ for value of δ equal to 0° | 0.0129180 | 18 | 500 |
| | 0.0070319 | 18 | 500 |
| Prototype rotor $\mathscr{P}_j$ for value of δ equal to 22.5° | 0.012256 | 18 | 1000 |
| | 0.005140 | 18 | 500 |
| Prototype rotor $\mathscr{P}$ for value of δ equal to 45° | 0.0101014 | 18 | 1000 |
| | 0.0057100 | 18 | 500 |

dimensionless parameter is given as follows.

$$\beta_x = \frac{e_{p_x} - a_{shaft}}{2 \cdot R_s}; \quad \beta_y = \frac{e_{p_y} - a_{shaft}}{2 \cdot R_s} \tag{19}$$

where $e_{p_x}$ [m] is the separation distance between the buckets of the prototype rotors on the coordinate axis X, $e_{p_y}$ [m] is the separation distance between the buckets of the prototype rotors on the coordinate axis Y, d [m] is the characteristic measure of the prototype buckets and $a_{shaft}$ [m] is the diameter of object $\mathscr{A}$, housed inside the rotor (aligned with the axis of the object).

Table 5 shows the magnitude of the dimensionless geometric parameters for both the canonical Savonius rotor model and the set of prototype rotors.

Finally, the blockage ratio (B) Eq. (20) represents the area of the prototype rotors bounding box relative to the cross area of the wind tunnel.

$$B = \frac{H \cdot D}{H_{wt} \cdot W_{wt}} \tag{20}$$

where $H_{wt}$ [m] is the cross area height of the wind tunnel and $W_{wt}$ is the cross area width of the wind tunnel. Considering Fig. 8, the magnitudes of the geometric parameters of the section of the wind tunnel are the same because it has a square shape. Therefore, substituting the overlap ratio in the expression of the blockage ratio (B) Eq. (21).

$$B = \frac{H \cdot D}{2D \cdot 2D} = \frac{H}{4 \cdot D} = \frac{\phi}{4} \approx 0.405 \tag{21}$$

The maximum blockage ratio is within 40.5% for all the prototype rotor models studied in this paper.

## 5. Numerical method

In order to compare and discuss the experimental results of the present study, a numerical analysis was carried out using a Computational Fluid Dynamics (CFD) commercial software of the different geometries studied for different load scenarios. The commercial software used to perform numerical analysis is Ansys Fluent [57]. Fluent is a Computational Fluid Dynamics software which by means of the mathematical and numerical technique of the finite volumes solves problems of fluid mechanics and transfer of heat around or within geometries with complex surfaces. The modeling of the simulation is performed considering three-dimensional effects given that the geometry of the prototype rotors is not constant along the axial direction, as shown in the CAD modeling Fig. 5. Modeling of the CAD geometry of the rotors and the solid volume of the wind tunnel was performed by using Solidworks [58]. A guided process that offers the interface of the numerical calculation program allows the usual tasks of the process to be performed. These tasks consist of the selection of the physical model of calculation used, the selection and physical characteristics of the fluid and solid materials of the problem, all cell zone conditions, boundary conditions, solution methods and the turbulence model. After that, the values of limit conditions, maximum number of iterations and convergence criteria are defined in order to achieve the numerical analysis.

### 5.1. Computation domains and boundary conditions

The definition of the computational domain of the different numerical analyses was carried out considering the dimensions of the wind tunnel used. As shown in Fig. 9 and Table 6 the dimensions of the computational domain are 2D × 2D × 6.5D, where D [m] is the diameter of the helices. In addition, from the surfaces of this domain, the boundary conditions corresponding to the stationary and moving walls, the uniform inlet airflow and the outlet airflow were defined.

The boundary condition of shear type in the walls of the rotors and in the side walls of the wind tunnel domain has been defined as 'No-Slip Walls'. The definition of this boundary condition contributes to the formation of a boundary layer near the walls of the rotors. The problem presented in this paper does not imply the use of a deformable mesh. Therefore a sliding mesh model was applied to perform the rotational motion of the rotor and analyze its dynamic behavior. Inside the wind

**Table 12**
Maximum values of the curves Ct vs TSR, Cp vs TSR and P vs ω.

| Prototype rotors | $C_{Pmax}$ | Corresponding Re at $C_{Pmax}$ | TSR at $C_{Pmax}$ | $C_{tmax}$ | Corresponding Re at $C_{tmax}$ | TSR at $C_{tmax}$ | $P_{max}$ | Corresponding Re at $P_{max}$ | ω at $P_{max}$ [rad/s] |
|---|---|---|---|---|---|---|---|---|---|
| δ = 0° | 0.031 | $1.36 \cdot 10^5$ | 0.229 | 0.233 | $9.91 \cdot 10^4$ | 0.089 | 0.562 | $1.36 \cdot 10^5$ | 24.81 |
| δ = 22.5° | 0.032 | $1.20 \cdot 10^5$ | 0.217 | 0.186 | $9.91 \cdot 10^4$ | 0.087 | 0.637 | $1.42 \cdot 10^5$ | 33.92 |
| δ = 45° | 0.046 | $1.36 \cdot 10^5$ | 0.335 | 0.227 | $9.91 \cdot 10^4$ | 0.131 | 0.744 | $1.31 \cdot 10^5$ | 30.61 |
| Savonius rotor | 0.252 | $7.75 \cdot 10^4$ | 0.721 | 0.364 | $6.60 \cdot 10^4$ | 0.642 | 1.611 | $7.75 \cdot 10^4$ | 38.22 |

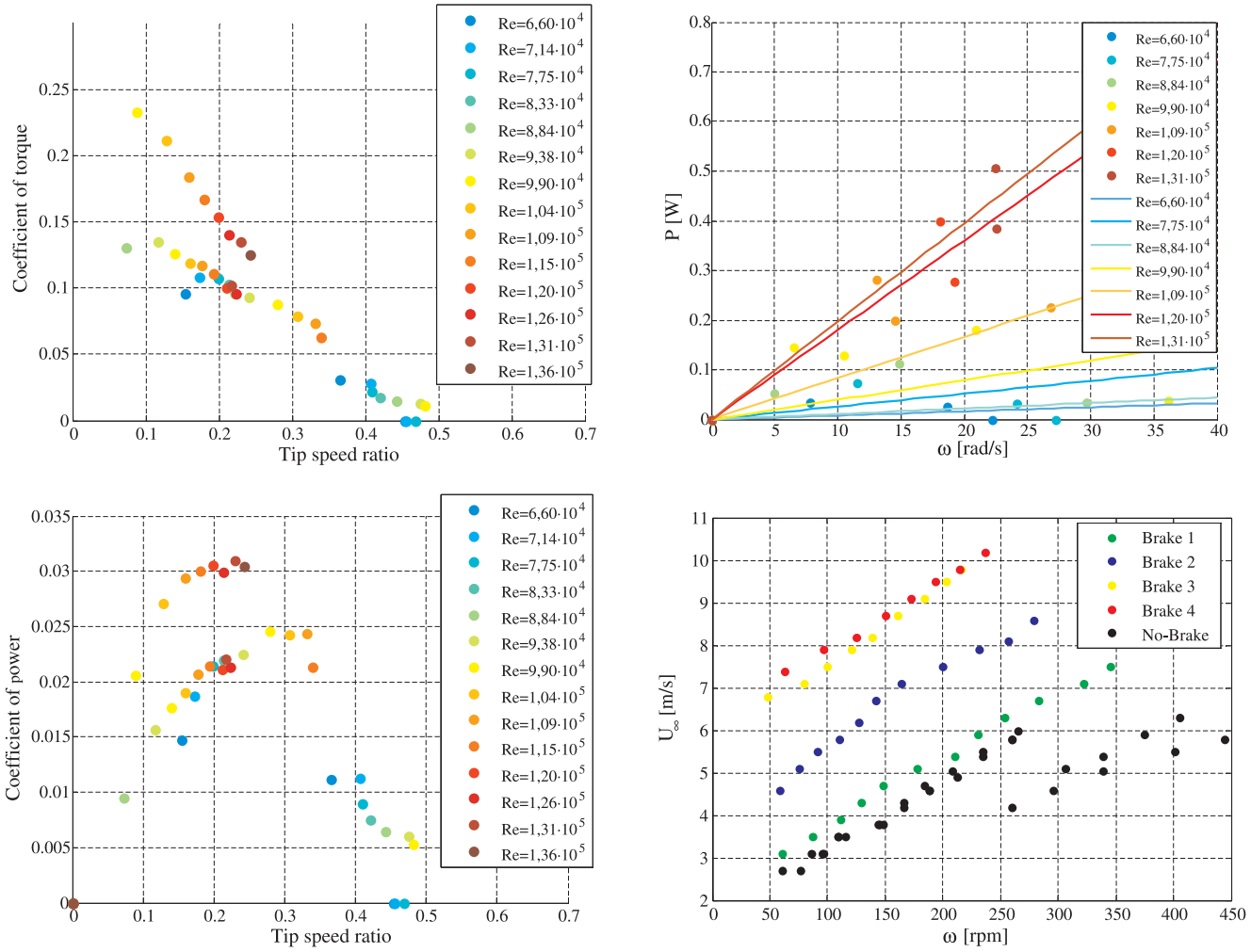


**Fig. 11.** Curves of power coefficient, Torque coefficient, Mechanical power and Wind tunnel velocity vs Angular rotor velocity for the prototype rotor δ = 0°.

tunnel domain a cylindrical domain, where the geometries of the rotors are included, is generated. This domain, called Rotor domain, is independent of the wind tunnel domain. This second domain is located at a distance downstream of 1.5D from the inlet uniform airflow surface and centered on the Wind tunnel domain.

This methodology is simpler and more efficient in comparison with the dynamic mesh model analysis. The technique consists of the realization of a steady model in which the definition of the cell zone condition for the Rotor domain is a moving reference frame, determining the speed (obtained through the experimental tests) and axis of rotation of the prototype rotors. After that, a transient model is generated in which the definition of the cell zone condition for the Rotor domain is obtained by copying the results of the Reference frame model to the section Mesh Motion. One interface surface is performed at the overlap edges between the adjacent domains, the rotor-tunnel domain, allowing the continuity of the solution in the air flow.

A uniform and steady velocity profile is applied at the boundary condition of the velocity inlet. Specification method parameters used in the turbulence definition for the velocity inlet and pressure outlet are intensity and length scale, see Table 7. The walls of the Wind tunnel domain are defined as stationary static walls and the walls of the prototype rotors, with their respective axes and speeds of rotation, are defined as moving walls.

For all numerical analyses performed, the input parameters were supported by experimental data. Therefore, the rotational velocities of the prototype rotors studied for the Rotor domain were defined according to the rotational velocities measured during the experimental test in the wind tunnel. Best parameters were acquired comparing performance values acquired by different prototype rotor geometries.

### 5.2. Mesh definition

In order to compare experimental and numerical results and to improve numerical precision, mesh modeling was performed adaptively

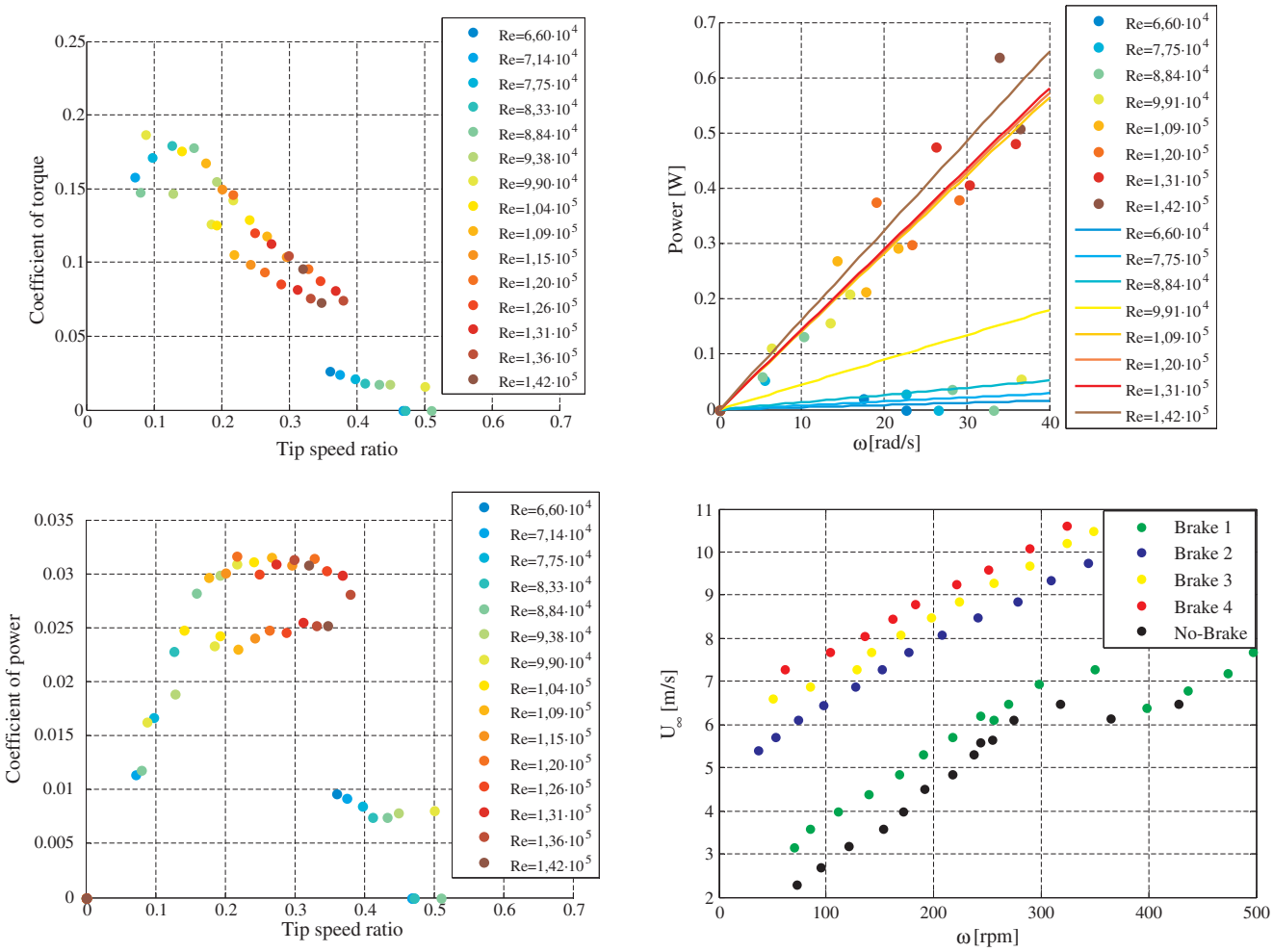


**Fig. 12.** Curves of power coefficient, Torque coefficient, Mechanical power and Wind tunnel velocity vs Angular rotor velocity for the prototype rotor δ = 22.5°.

for each computational domain. The perturbations in the fluids are of the same magnitude order as the objects which cause it, and for this reason aerodynamic studies often use mesh models between 10 and 20 times larger than the size of the airfoils, as Bangga observes [65]; although in the present paper the lateral walls of the tunnel used for the experimental tasks have been included in the mesh, precisely because their proximity can have an effect on the behavior of the turbine. For this reason the sliding mesh is defined within a perimeter of 40 cm × 40 cm in order to compare the numerical study with the experimental test. On the other hand it has been considered that the zones linked through non-conformal interfaces of the sliding meshes remain in contact with each other, and in that way the air will be able to flow from one domain to the other. The mesh node density used in the rotor domain is higher than in the wind tunnel domain, as is shown in Fig. 10. In addition, the geometry of the elements forming the meshes varies for each computational domain. In the case of the Rotor domain, tetrahedral elements with smaller size are used, which allows us to adapt with greater pressure to the geometry of prototype rotor geometries. On the contrary, for the Wind tunnel domain hexahedral elements are used since the size of this domain is greater and these elements improve the time and computational cost of the studies. The selection of tetrahedral elements for the Rotor domain penalizes the computational cost of the simulations; however, it improves the accuracy and adaptability of the mesh to the prototype rotor geometries.

Table 8a shows the grid points on the Rotor domain along streamwise and spanwise directions.

Table 8b shows the grid points along the streamwise and spanwise directions and along the contour of the buckets of the rotors. This grid points number corresponds to the 'inflation' meshing operation performed in order to improve the numerical analysis solution in the geometry regions near the wall of the buckets (the shear layer).

The elements of the mesh are three-dimensional because the geometry of the prototype rotors varies along their rotation axis (axial coordinate). In Table 9, the values of the characteristics parameters used in the modeling of the different meshes are shown.

Where orthogonal quality represents the quality of the elements of the mesh through a range from 0 to 1, with 0 being the low quality indicative.

Finally, in order to enhance the accuracy of the numerical analysis in the boundary layer flow and improve the mesh quality, prismatic mesh elements were extruded from the boundary edges of the prototype buckets (see Fig. 10). The modeling of these elements of the mesh was carried out by means of an inflation operation. The parameters used for the definition of this operation are shown in Fig. 10. These establish a $y^+$ value of the first elements from the wall equal to 5, given the rotational velocity and the position of the elements on the buckets (see Fig. 10). This value $y^+$ is constant for all the geometries analyzed and allows a precise analysis of the boundary layer in the walls of the buckets [60]. In addition, for the numerical analyses carried out, a wall function of the 'Enhanced wall treatment' type was used. This wall treatment combines a two-layer model with enhanced wall functions. It should be noted that the modeling of the surface roughness is not compatible with the wall function established for the turbulence model used.

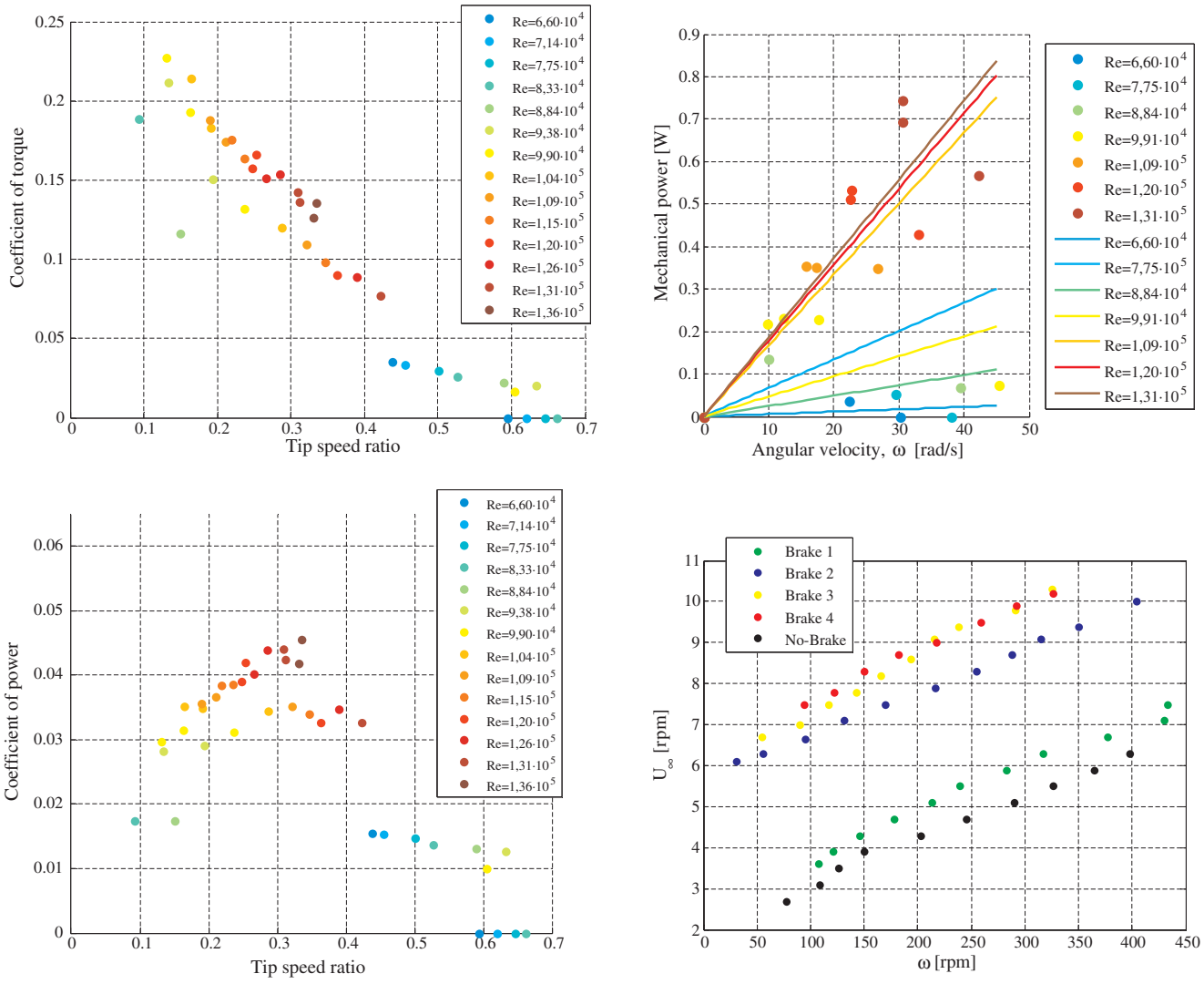


**Fig. 13.** Curves of power coefficient, Torque coefficient, Mechanical power and Wind tunnel velocity vs Angular rotor velocity for the prototype rotor δ = 45°.

**Table 13**
Reynolds number and wind velocity at which the prototype rotors and the canonical Savonius rotor were tested.

| Prototype rotors | | Savonius rotor | |
|---|---|---|---|
| Reynolds number | Wind velocity [m/s] | Reynolds number | Wind velocity [m/s] |
| $6.599 \cdot 10^4$ | 4.929 | $3.436 \cdot 10^4$ | 2.567 |
| $7.137 \cdot 10^4$ | 5.331 | $3.916 \cdot 10^4$ | 2.925 |
| $7.748 \cdot 10^4$ | 5.787 | $4.398 \cdot 10^4$ | 3.285 |
| $8.327 \cdot 10^4$ | 6.220 | $5.026 \cdot 10^4$ | 3.754 |
| $8.848 \cdot 10^4$ | 6.609 | $5.574 \cdot 10^4$ | 4.164 |
| $9.378 \cdot 10^4$ | 7.005 | $6.097 \cdot 10^4$ | 4.554 |
| $9.907 \cdot 10^4$ | 7.400 | | |
| $1.044 \cdot 10^5$ | 7.800 | | |
| $1.094 \cdot 10^5$ | 8.172 | | |
| $1.152 \cdot 10^5$ | 8.606 | | |
| $1.203 \cdot 10^5$ | 8.988 | | |
| $1.258 \cdot 10^5$ | 9.400 | | |
| $1.311 \cdot 10^5$ | 9.794 | | |
| $1.364 \cdot 10^5$ | 10.190 | | |
| $1.419 \cdot 10^5$ | 10.600 | | |

Furthermore, in order to avoid problems of continuity between the different computational domains, a contact surface is established that allows interaction between them.

### 5.3. Turbulence model, governing equations and simulation set up

The viscosity model used in this study is Realizable k–ε with a logarithmic surface function in the analysis of turbulence flow. The Realizable k-ε model includes the effects of mean rotation in the definition of the turbulent viscosity inside the equations, in order to avoid the insensitivity to adverse pressure gradients of the standard k-ε model. This extra rotation effect has been tested on single sliding mesh systems and shown superior behavior over the standard k-ε model [64], or even the SST k-ω model in those cases where the turbulence was established, because the k-ω method has been calibrated to accurately compute flow separation. Nevertheless, due to the nature of the mean rotation modification, its application to multiple sliding meshes systems should be taken with some caution, because several rotating meshes can avoid the rotation turbulent effect added to the equations in some of the meshes. In the present paper, several turbulence models have been used, and finally with the realizable k-ε model the numerical results are closer to the experimental data [62]. Other authors studying VAWT type Savonius use the RNG k-ε model [61] or directly the Standard k-ε model [63], mainly because these turbines work with the drag force effect, instead of lift force as occurs with other airfoil applications.

Momentum equations, x,y,z velocity components, turbulent kinetic energy (k) and the specific dissipation rate of turbulent kinetic energy (ε). Eqs. (22)–(28) are the variables that were resolved by using CFD Fluent software [57]. The equations of mass protection, momentum

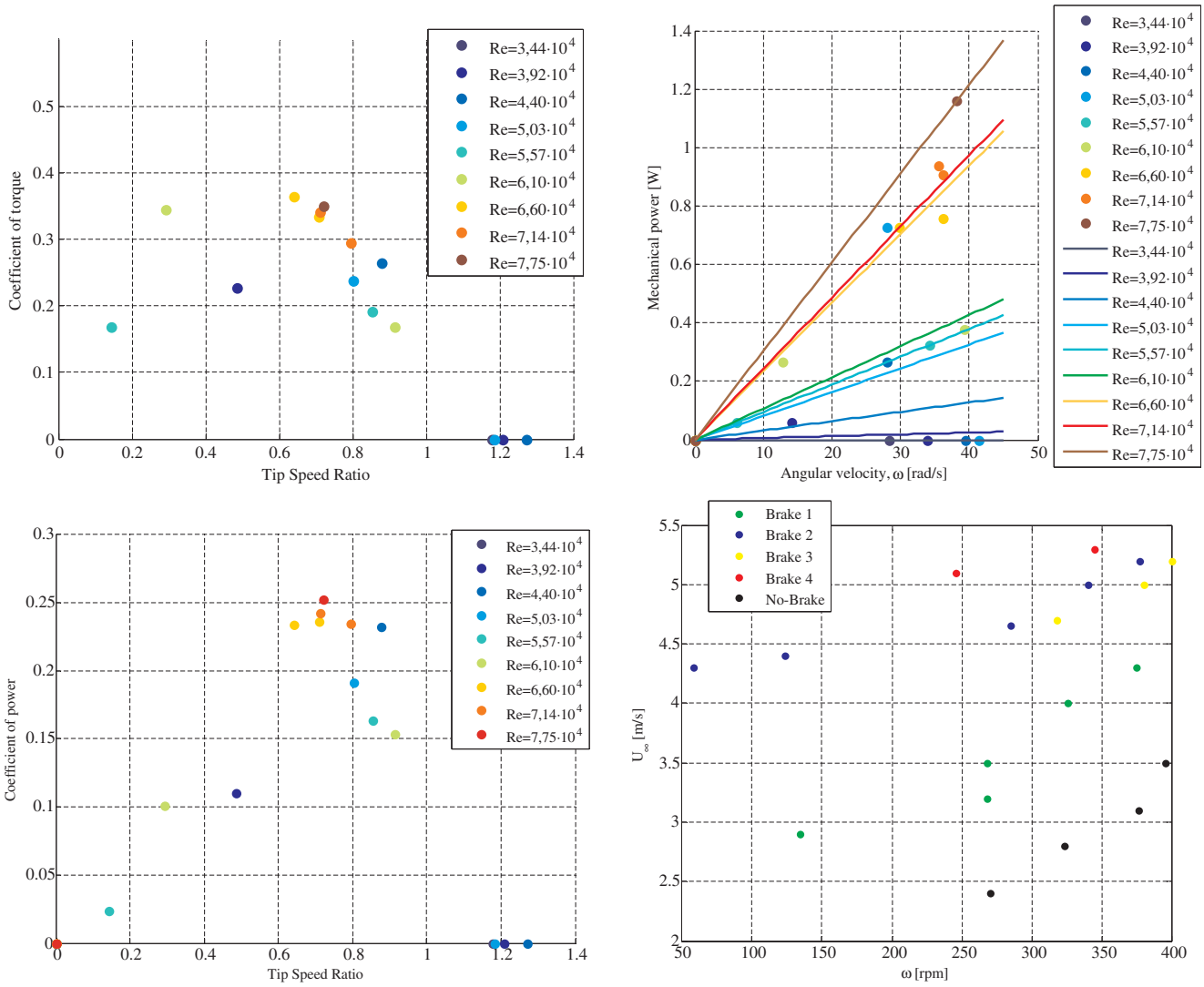


**Fig. 14.** Curves of power coefficient, Torque coefficient, Mechanical power and Wind tunnel velocity vs Angular rotor velocity for the canonical Savonius rotor.

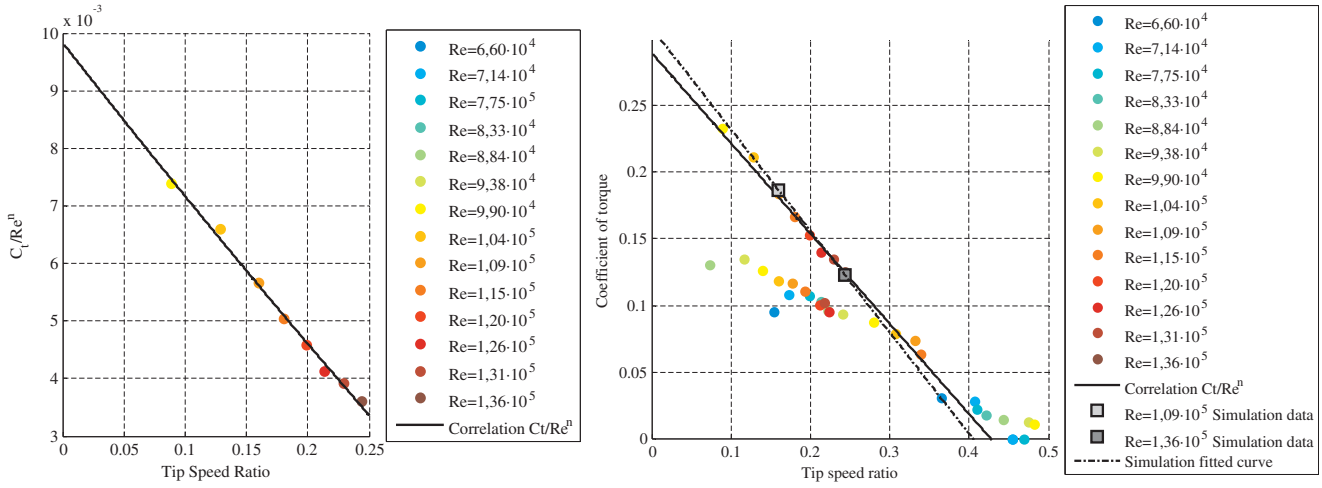


**Fig. 15.** Ct vs TSR and Correlation $Ct/Re^n$, and Simulation fitted curve for the prototype rotor $\delta = 0°$.

protection, stress tensor, turbulence viscosity, turbulence kinetic energy and dissipation rate of turbulence kinetic energy can be expressed for the compressible and incompressible steady flows as follows in the Cartesian tensor rotation [59]:

- Continuity equation:

$$\frac{\partial}{\partial x_w}\cdot(\rho\cdot u_w) = 0 \tag{22}$$

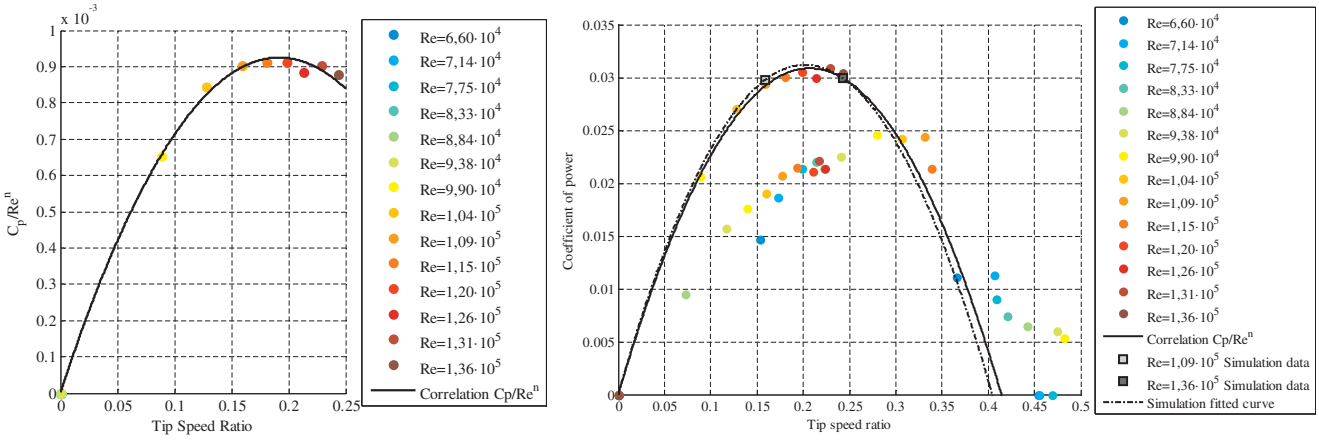


**Fig. 16.** Cp vs TSR and Correlation Cp/Re$^n$, and Simulation fitted curve for the prototype rotor δ = 0°.

**Table 14**
Correlation equations for prototype rotors.

| Prototype rotors | n | Correlation equation | R – Square |
|---|---|---|---|
| δ = 0° | 0.3 | $\frac{C_t}{Re^{0.3}} = -0.025855 \cdot TSR + 0.0097774$ | 99.50% |
| δ = 22.5° | 1.5 | $\frac{C_t}{Re^{1.5}} = -0.012083 \cdot TSR^2 - 0.0082166 \cdot TSR + 0.0067841$ | 94.72% |
| δ = 45° | 0.3 | $\frac{C_t}{Re^{0.3}} = 0.03542 \cdot TSR^2 - 0.03239 \cdot TSR + 0.01069$ | 97.54% |

- Momentum equation:

$$\frac{\partial}{\partial x_w} \cdot (\rho \cdot u_w \cdot u_v - \tau_{vw}) = \frac{\partial P}{\partial x_w} \tag{23}$$

where $x_j$ represents the cartesian coordinate, being j= 1,2,3, $u_j$ represents the absolute velocity components in the $x_w$ direction.$P_l = \partial P/\partial x_w$ represents the reduced pressure loss and $\tau_{vw}$ represents the stress tensor as follows:

- Stress tensor equation:

$$\tau_{vw} = \mu \cdot \left( \frac{\partial u_v}{\partial x_w} + \frac{\partial u_w}{\partial x_v} - \frac{2}{3} \cdot \frac{\partial u_k}{\partial x_k} \cdot \delta_{vw} \right) \tag{24}$$

$$\forall \{v,w\} | \; v \neq w \rightarrow \delta_{vw} = 0 \tag{25}$$

$$\forall \{v,w\} | \; v = w \rightarrow \delta_{vw} = 1 \tag{26}$$

where μ is the viscosity of the air and $\delta_{vw}$ is the Kronecker delta variable. The Kronecker delta variable takes a zero value when the values v and w are different. On the other hand, when the variables v and w are equal the Kronecker delta variable takes value 1.

- Turbulence kinetic energy (k):

$$\frac{\partial}{\partial t}(\rho \cdot k) + \frac{\partial}{\partial x_w} \cdot \left( \rho \cdot u_w \cdot k - \frac{\mu_{eff}}{\sigma_k} \cdot \frac{\partial k}{\partial x_w} \right) = \mu_t \cdot s_{vw} \cdot \frac{\partial u_v}{\partial x_w} - \frac{2}{3} \cdot \left( \mu_t \cdot \frac{\partial u_v}{\partial x_w} + \rho \cdot k \right) \cdot \frac{\partial u_v}{\partial x_w} - \rho \cdot \varepsilon \tag{27}$$

- Dissipation rate of turbulence kinetic energy (ω)

$$\frac{\partial}{\partial t}(\rho \cdot \omega) + \frac{\partial}{\partial x_w} \cdot (\rho \cdot u_w \cdot \omega - \frac{\mu_{eff}}{\sigma_\varepsilon} \cdot \frac{\partial \varepsilon}{\partial x_w}) = C_1 \cdot f_1 \cdot \frac{\varepsilon}{k} \cdot \left[ \mu_t \cdot s_{vw} \cdot \frac{\partial u_v}{\partial x_w} - \frac{2}{3} \cdot (\mu_t \cdot \frac{\partial u_v}{\partial x_w} + \rho \cdot k) \cdot \frac{\partial u_v}{\partial x_w} \cdot \delta_{vw} \right] - c_2 \cdot f_2 \cdot \rho \cdot \frac{\varepsilon^2}{k} - C_3 \cdot \rho \cdot \varepsilon \cdot \frac{\partial u_v}{\partial x_w} \tag{28}$$

where the effective viscosity Eq. (29) is

$$\mu_{eff} = \mu + \mu_t \tag{29}$$

Being.

$$\mu_t = \rho \cdot f_\mu \cdot C_\mu \cdot \frac{k^2}{\varepsilon} \tag{30}$$

Table 10 shows the values defined in the numerical calculation software for the variables v,w,k,$C_\mu$,$\sigma_k$,$\sigma_\varepsilon$,$C_{1\varepsilon}$,$C_{2\varepsilon}$ of the equations shown above [59].

This turbulence model does not require the implementation of transition models since it is valid only for flows developed in complete turbulence [64]. All the above equations were resolved by means of an iterative numerical calculation process, in which the Coupled analysis algorithm is used in order to calculate the field of velocities and pressures in the central point of each mesh elements. In addition, the terms of the second order of pressure, moment, turbulent kinetic energy (k), the specific dissipation rate of turbulent kinetic energy (ω), given in the equations governing the numerical model, are included in the calculation in order to match the numerical result with the experimental results. Furthermore, pressure correction is resolved in order to maintain the availability of the pressure area and mass protection in each iteration.

The number of Courant, CFL used in each numerical analysis is 200. Finally, Table 11 shows the Time step size, Number of time steps and Max iterations used for each numerical analysis. The time step was defined from the rotational speed of the rotors obtained in the experimental tests. For the numerical analysis of the rotors, an experimental value of the wind tunnel velocity and a rotary speed value of the rotors were used, respectively (each rotor has a characteristic speed for a given mechanical load and wind speed). From this rotation speed, the Time step corresponding to the 30° rotation in each rotor was obtained for the different numerical analyses carried out.

## 6. Results and discussion

The set of prototype rotors $\mathscr{P}_j$ presented in this paper together with the Savonius $\mathscr{S}$ canonical rotor were tested in the range of wind speeds

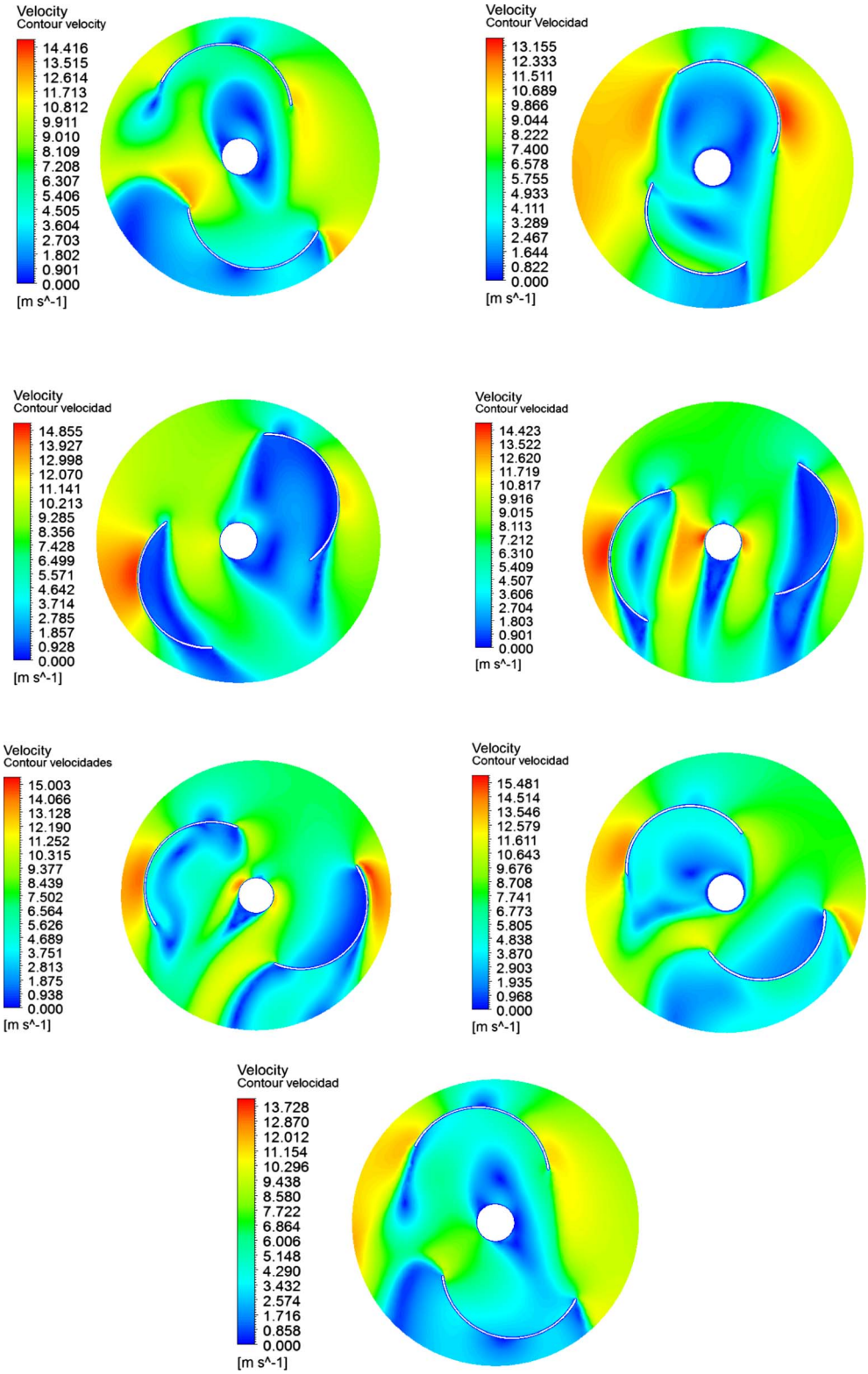


**Fig. 17.** Velocity map with Reynolds number $1.094 \cdot 10^5$ for rotor angle 0°, 30°, 60°, 90°, 120°, 150°, 180°. Prototype Rotor δ = 0°.

between 2.56 m/s and 10.6 m/s. According to the methodology used to perform the experimental tests, each rotor was tested for the different positions of the Prony brake. And for each of these positions of the Prony brake, Reynolds numbers between 3436 · 104 and 1419 · 105 were tested to characterize the behavior of the rotors in all their operating regimes. The objectives of the experimental tests were the determination of the parameters power coefficient, torque coefficient and mechanical power generated. In turn, in order to perform a validation of the methodology used a set of numerical analyses were modeled using the Ansys Fluent software [57], whose results allowed us to determine the evolution of the parameters under study along the circular path of the rotors and contrast those results with those obtained experimentally. The experimental data of the force variables applied by the rotor $F_{din}$ [N] and the rotational speed of the rotors ω [rad/s] were acquired according to the precision and resolution of the measurement instruments used, the PCE-FB50 dynamometer and Digital Photo

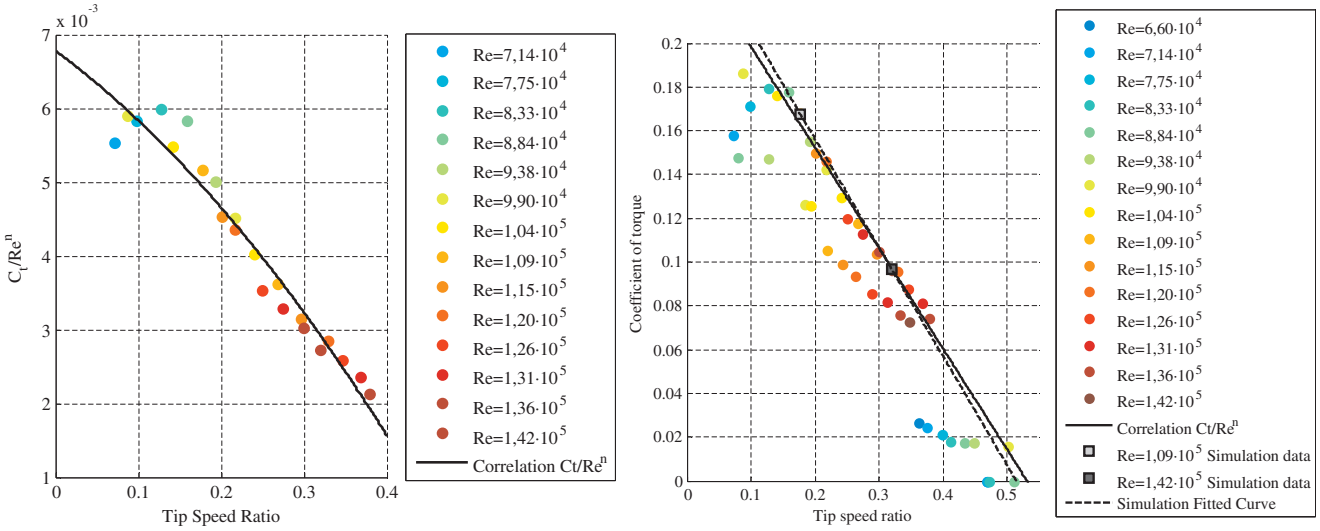


**Fig. 18.** Ct vs TSR and Correlation Ct/Re$^n$, and Simulation fitted curve for the prototype rotor δ = 22.5°.

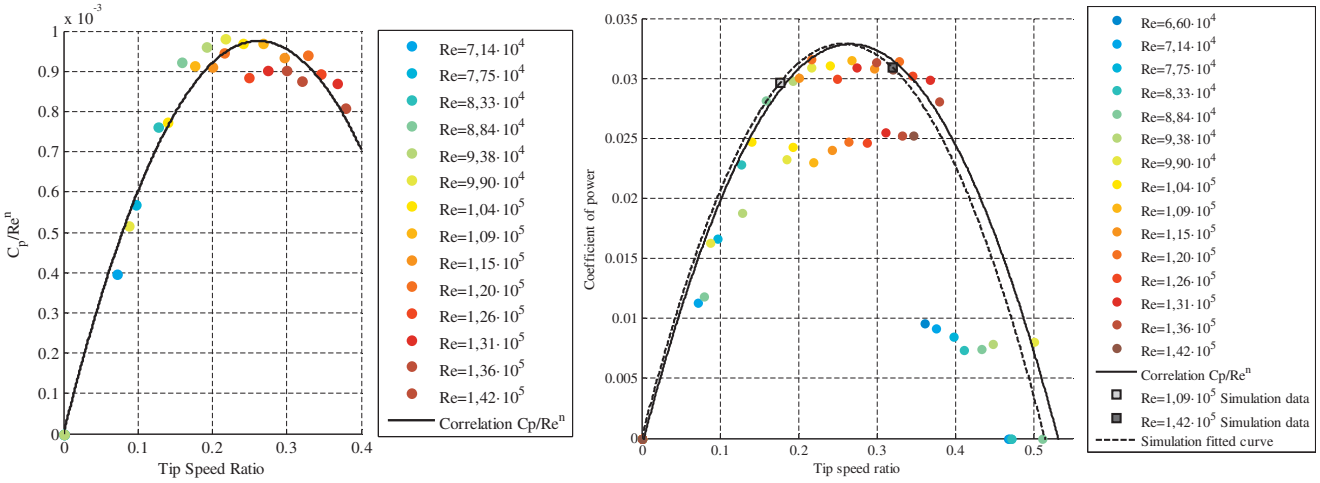


**Fig. 19.** Cp vs TSR and Correlation Cp/Re$^n$, and Simulation fitted curve for the prototype rotor δ = 22.5°.

Tachometer model RM-1501, respectively.

The graphs of power coefficient, torque coefficient and power of the prototype rotors were compared to each other for different magnitudes of the rotation angle parameter, δ = 0°,22.5°,45°. This parameter represents the rotation or torsion angle between the main sections of the prototype rotors (see Fig. 5). The torque coefficient profiles versus the rotational angle of the prototype rotors were compared with the profile obtained by the canonical Savonius rotor, for a wind speed of 5.331 [m/s] and Reynolds number $7.137 \cdot 10^4$ (see Fig. 14). In addition, the maxima in the power coefficient curves versus tip speed ratio of the prototype rotors were evaluated and compared with the values obtained in the power coefficient curve of the canonical Savonius rotor for the same magnitude of tip speed ratio of the maximums obtained (see Table 12). In this way, the influence of the geometric modifications performed in the prototype rotors with respect to the Savonius canonical rotor geometry can be determined for the study parameters: power coefficient, torque coefficient and mechanical power generated.

### 6.1. Effect of rotation or torsion angle δ

Figs. 11–13 show the power coefficient and torque coefficient versus tip speed ratio; the mechanical power generated versus the angular velocity of rotation; and the wind tunnel velocity versus the rotors angular velocity for the prototype rotors with different rotation or torsion angles (δ = 0°,22.5°,45°) and for the canonical Savonius rotor. It may be observed that as the rotation angle δ increases, the maximum value of the curves of both power coefficient and mechanical power generated increase. Similarly, the tip speed ratio associated with these maxima (see Table 12) increases. This fact indicates that as the rotation angle δ increases, the angular velocity of the prototype rotors increases and thus the power coefficient curve is shifted towards values of tip speed ratio and higher power coefficient, improving the performance and behavior of the prototype rotors.

Table 12 shows the maximum values of the power coefficient, torque coefficient and mechanical power generated parameters, as well as the tip speed ratio and the Reynolds number from which these maximum values are calculated. Table 12 shows the difference in the tip speed ratio range for optimal rotor performance between the canonical Savonius $\mathscr{S}$ rotor and the prototype rotors. While in the prototype rotors the tip speed ratio range for optimum operation is 0.229, 0.217 and 0.335 for Reynolds numbers of $1.364 \cdot 10^5$, $1.203 \cdot 10^5$, $1.364 \cdot 10^5$, in the Savonius $\mathscr{S}$ canonical rotor the tip speed ratio for optimum rotor performance is 0.721 for a Reynolds number of $7.748 \cdot 10^5$. That is to say, the tip speed ratio of the optimal operating range of the prototype rotors is lower than that of the Savonius $\mathscr{S}$ canonical rotor, and on the contrary the Reynolds number for the optimal

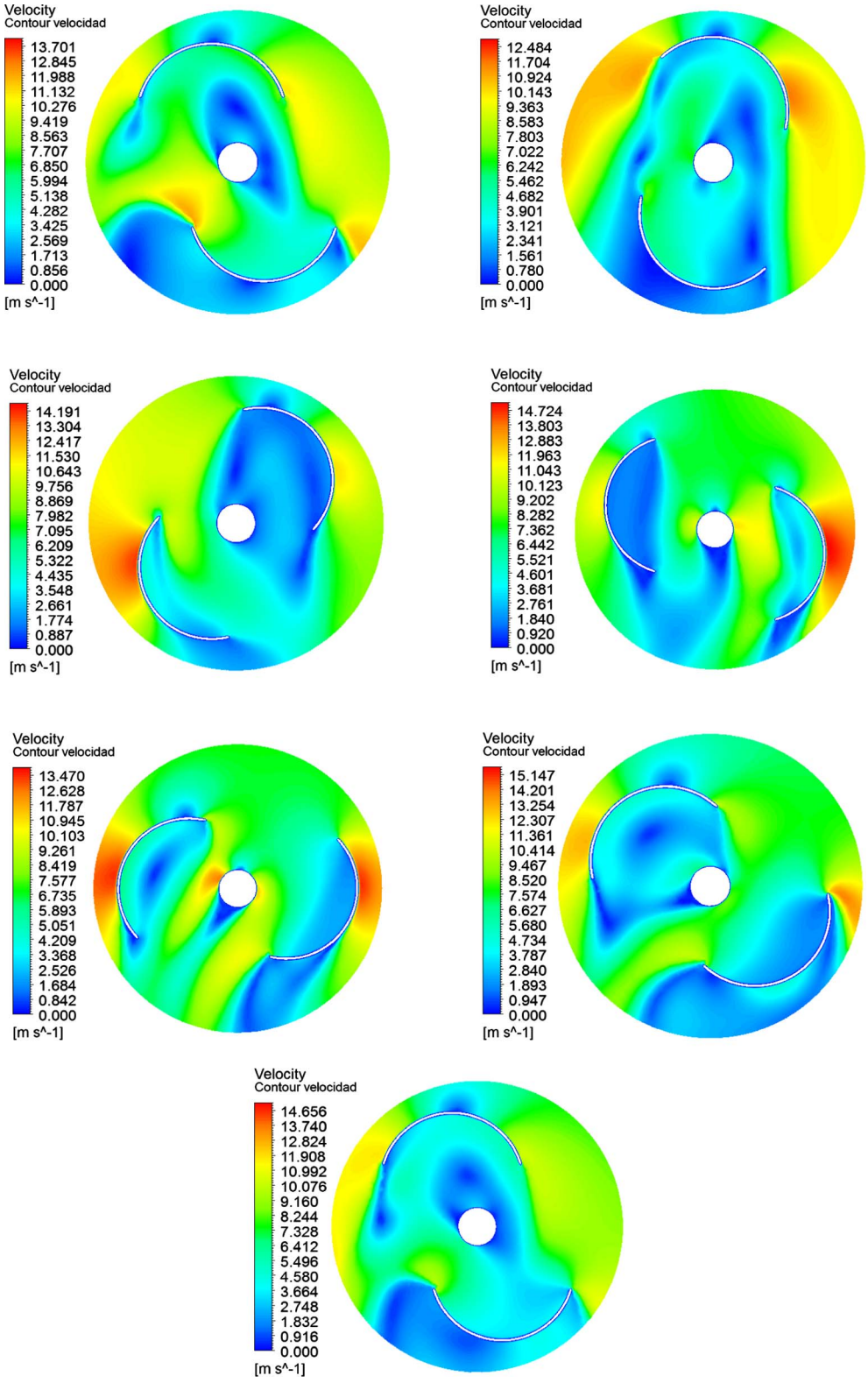


**Fig. 20.** Velocity map with Reynolds number $1.094 \cdot 10^5$ for rotor angle 0°, 30°, 60°, 90°, 120°, 150°, 180°. Prototype Rotor $\delta = 22.5°$.

operating range of the prototype rotors is higher than that of the rotor Savonius $\mathscr{S}$ canonical. Therefore, it can be observed that in order to reach the optimum operating range for prototype rotors the wind speed must be higher compared to the Savonius $\mathscr{S}$ canonical rotor, since these tend to rotate at a lower angular velocity than the canonical Savonius one. This fact can be checked by evaluating the mechanical power generated, because for the prototype rotors the maximum mechanical power generated (0.562 W, 0.637 W, 0.744 W, respectively) reaches a higher number of Reynolds ($1.364 \cdot 10^5$, $1.203 \cdot 10^5$, $1.364 \cdot 10^5$, respectively) and a lower angular speed of rotation (24.81 rad/s, 33.92 rad/s, 30.61 rad/s, respectively) compared to the canonical Savonius rotor (mechanical power generated 1.611 W, Reynolds number $7.748 \cdot 10^5$, angular speed of rotation 38.22 rad/s).

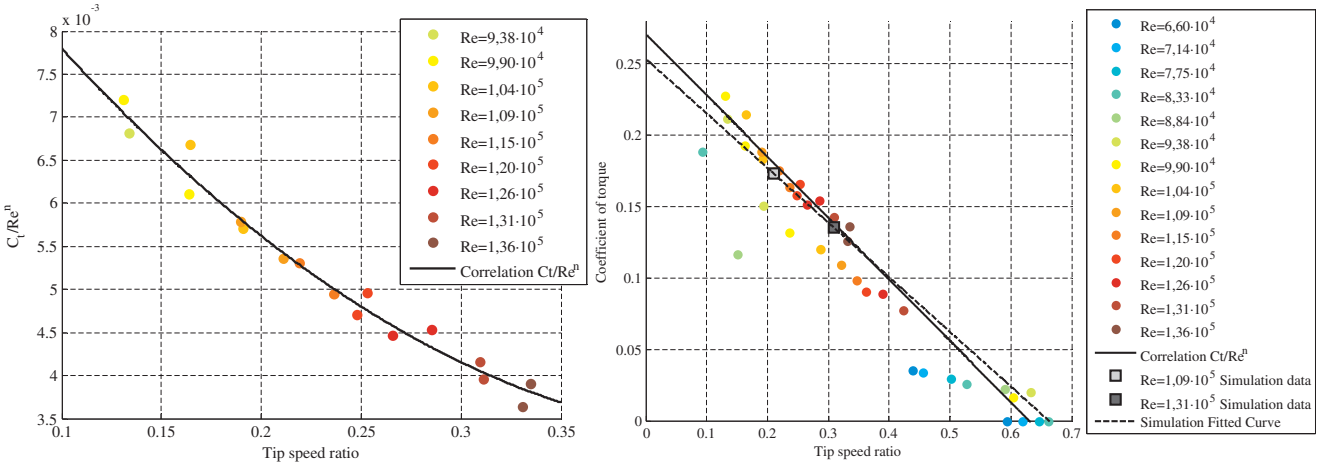


**Fig. 21.** Ct vs TSR and Correlation Ct/Re$^n$, and Simulation fitted curve for the prototype rotor δ = 45°.

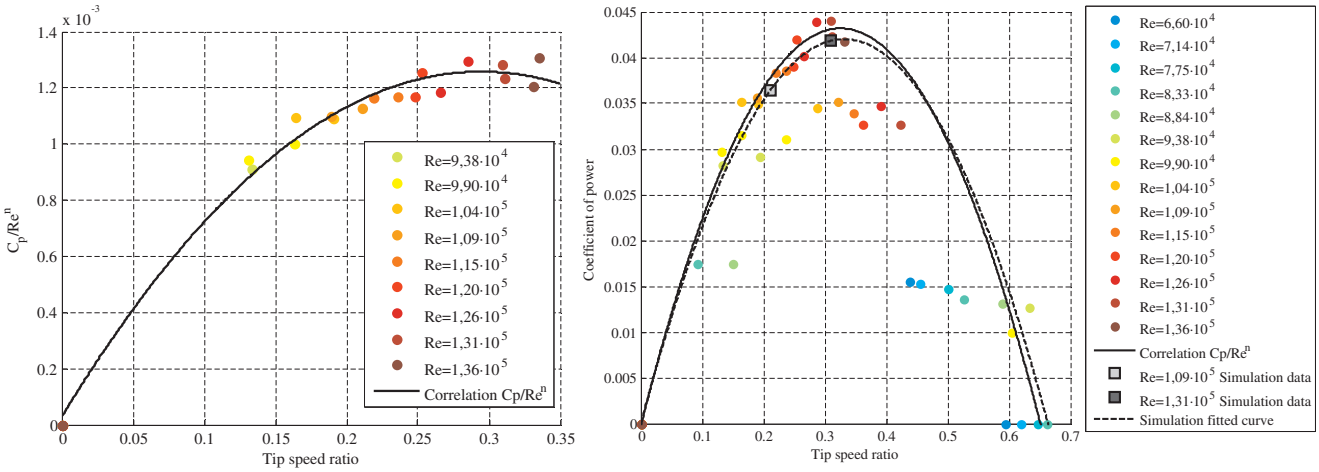


**Fig. 22.** Cp vs TSR and Correlation Cp/Re$^n$, and Simulation fitted curve for the prototype rotor δ = 45°.

### 6.2. Effect of the coefficient of power, coefficient of torque and Reynolds number

Table 13 shows the different Reynolds numbers and their corresponding wind speeds from which the prototype rotors and the Savonius canonical rotor were tested. Figs. 11–14 show the variation of the power coefficient for prototype rotors with a rotation or torsion angle in the bucket section of δ = 0°,22.5°,45° and for the canonical Savonius rotor. According to these results, it is observed that the maximum coefficient of power increases with the increase of the Reynolds number. This fact is also reported by Kamoji et al. [11] and Akwa et al. [21] for conventional Savonius rotors. Furthermore, it is the tip speed ratio at which the maximum coefficient of power, $C_{p_{max}}$ increases with the increase of the Reynolds number from $6.599 \cdot 10^4$ to $0.419 \cdot 10^5$ (prototype rotor) and $3.436 \cdot 10^4$ to $6.097 \cdot 10^4$ (Savonius rotor).

Figs. 11–14 show the torque coefficient variation for prototype rotors with a rotation or torsion angle in the bucket section of δ = 0°,22.5°,45° for the canonical Savonius rotor. The results obtained show that the Reynolds number influences the profiles of the torque coefficient curves. The torque coefficient decreases linearly as the tip speed ratio values increase. However, the trend of the torque coefficient as a function of the Reynolds number is not linear. The torque coefficient increases until the Reynolds number reaches its maximum $C_{t_{max}}$ at a Reynolds number of $9.907 \cdot 10^4$ for the three prototype rotors $\mathscr{P}_j$ and $6.599 \cdot 10^4$ for the Savonius $\mathscr{S}$ (see Table 13). From this value, the maximum torque coefficient for each Reynolds number decreases as the Reynolds number increases.

### 6.3. Correlations for performance of prototype rotors and comparison with the numerical analysis

As shown in Figs. 15 and 16, as the Reynolds number increases the power coefficient and torque coefficient curves have variations. In the case of the power coefficient curves, as the Reynolds number increases the magnitude of the power coefficient increases similarly until the maximum power coefficient $C_{p_{max}}$ (see Table 12) is reached in the parabolic profile. On the other hand, in the case of the torque coefficient curves, as the Reynolds number increases the torque coefficient increases until it reaches its maximum value $C_{t_{max}}$ (see Table 12). From this maximum value, the torque coefficient begins to decrease as the Reynolds number increases. This whole set of curves (torque coefficient versus tip speed ratio curve and power coefficient versus tip speed ratio curve) can be unified in a single curve that approximates the fluid-mechanical behavior of the rotors independently to the evolution of the Reynolds number, as shown in Figs. 15 and 16.

The correlation equation used is a second-order polynomial function $\frac{C_t}{Re^n}$ Eq. (31). To obtain the coefficients that define the correlation equation, the torque coefficients of each prototype rotor were divided by the Reynolds number corresponding to each point, raised to a dimensionless factor n (see Figs. 15 and 16). The curve $\frac{C_t}{Re^n}$ versus the tip speed ratio is interpolated from a second-order polynomial in order to obtain the coefficients that define the correlation equation (see Table 14). It should be noted that for prototype rotors with a rotation angle δ equal to 0° and 45° the correlation equation was applied to points in the torque coefficient curve with a Reynolds number greater

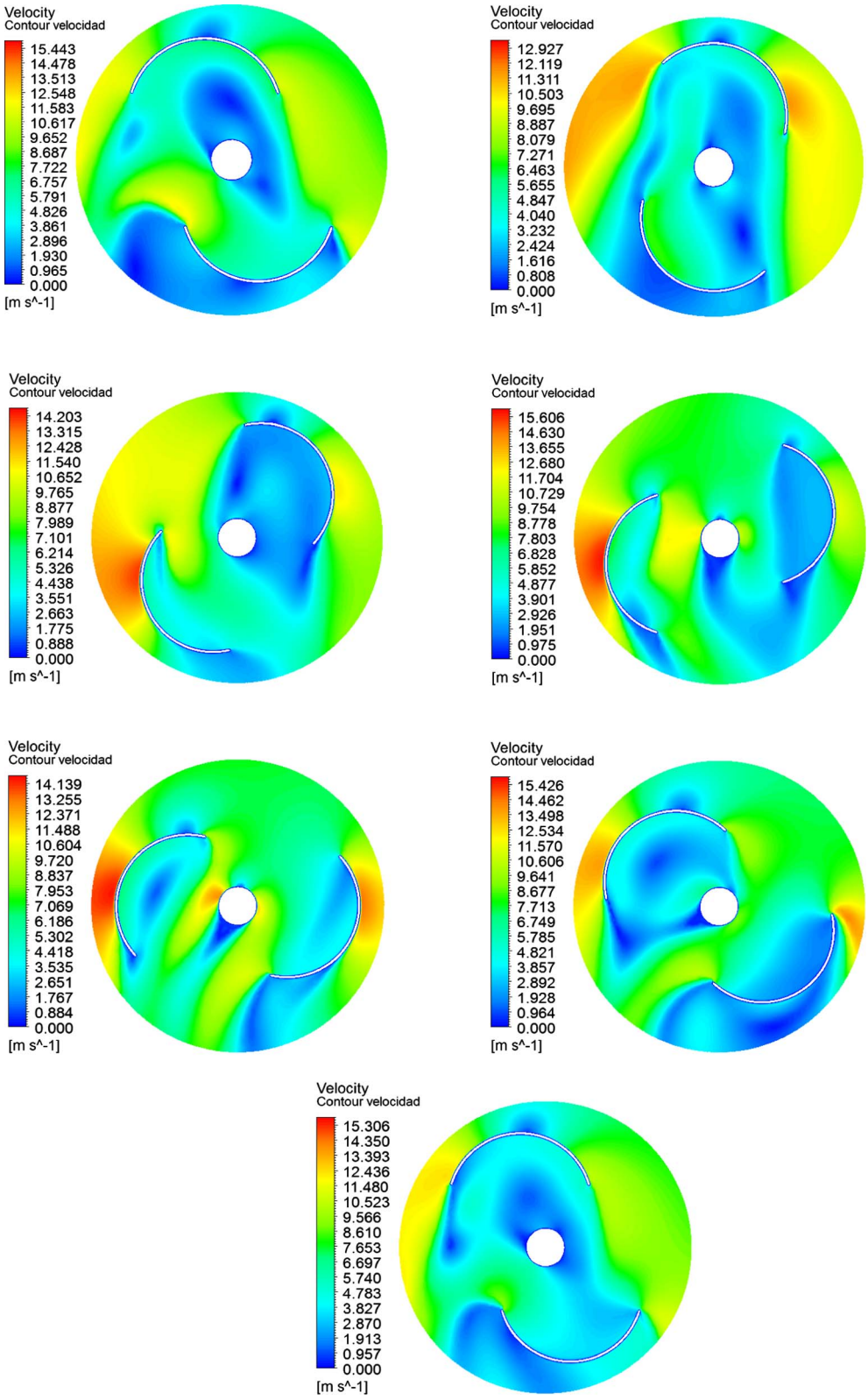


**Fig. 23.** Velocity map with Reynolds number $1.094 \cdot 10^5$ for rotor angle 0°, 30°, 60°, 90°, 120°, 150°, 180°. Prototype Rotor δ = 45°.

**Table 15**
Comparison between the results obtained experimentally by means of the correlation equation and the numerical simulation, for the prototype rotor δ = 0°.

| | TSR | $C_{t_{experimental}}$ | $C_{t_{simulation}}$ | $C_{t_{correlation}}$ | $C_{P_{experimental}}$ | $C_{P_{simulation}}$ | $C_{P_{correlation}}$ |
|---|---|---|---|---|---|---|---|
| $Re = 1.094 \cdot 10^5$ | 0.159 | 0.184 | 0.187 | 0.182 | 0.029 | 0.030 | 0.029 |
| $Re = 1.364 \cdot 10^5$ | 0.243 | 0.125 | 0.123 | 0.126 | 0.030 | 0.030 | 0.030 |

**Table 16**
Error in the approximation of the correlation equation and the numerical simulation for the prototype rotor δ = 0°.

| | Correlation difference [%] | Simulation difference [%] |
|---|---|---|
| $Re = 1.094 \cdot 10^5$ | 1.630 | 1.087 |
| $Re = 1.364 \cdot 10^5$ | 1.600 | 0.800 |

**Table 18**
Error in the approximation of the correlation equation and the numerical simulation for the prototype rotor δ = 22.5°.

| | Correlation difference [%] | Simulation difference [%] |
|---|---|---|
| $Re = 1.094 \cdot 10^5$ | 2.976 | 0.595 |
| $Re = 1.364 \cdot 10^5$ | 1.042 | 1.042 |

than $9.907 \cdot 10^4$, while for the prototype rotor with a rotational angle δ equal to 22.5° the correlation equation was applied for points in the torque coefficient curve with a Reynolds number greater than $7.137 \cdot 10^4$. In this way, lower Reynolds numbers are depreciated where the viscous stresses and the peeling of the boundary layer can cause a distortion in obtaining the correlation equation.

$$\frac{C_t}{Re^n} = p_3 \cdot TSR^2 + p_2 \cdot TSR + p_1 \quad (31)$$

On the other hand, the results obtained from the power coefficient and torque coefficient of the numerical simulations performed for the prototype rotors are shown in Figs. 15, 16, 18, 19, 21, 22. These simulations were performed for Reynolds numbers of $1.094 \cdot 10^5$ and $1.364 \cdot 10^5$ (Prototype rotor with δ = 0°), $1.094 \cdot 10^5$ and $1.419 \cdot 10^5$ (Prototype rotor with δ = 22.5°), $1.094 \cdot 10^5$ and $1.311 \cdot 10^5$ (Prototype rotor with δ = 45°); and for rotational speed equal to 13.51 rad/s and 24.82 rad/s (Prototype rotor with δ = 0°), 14.24 rad/s and 33.93 rad/s (Prototype rotor with δ = 22.5°), 17.28 rad/s and 30.58 rad/s (Prototype rotor with δ = 45°); obtained from the experimental analysis.

In Figs. 17, 20 and 23, the average contour of the velocity field resulting from the numerical simulations for each prototype rotor is shown. Analyzing the average contour of the velocity field, some vortices and backwater points are generated in the concave regions of the buckets of the rotors for their positions of 60°, 90° and 120°. These vortices and backwater points are of greater intensity, cause low pressure on the concave side and their magnitude decreases as the torsion angle of the rotors buckets δ increases. For the rest of the positions of the prototype rotors analyzed, the vortices or backwater points are of lesser intensity and, as in the case of the vortices and backwater points mentioned at 60°, 90° and 120° angles, their intensity decreases as the torsion angle of the rotors buckets δ increases. In order to model a dynamic numerical analysis, the velocity field for each position of the rotor angle between the 0° and 180° range was captured using 30° rotor angle increments.

The selection of the rotor angle range was performed according to the axisymmetric geometry of the prototype rotors. Finally, in Tables 15–20 a comparison is made between the values of the power coefficient and torque coefficient obtained either experimentally by applying the correlation equation $\frac{C_t}{Re^n}$, and those obtained by means of the numerical simulations. As shown in the comparative tables, the relative error between the experimental values and the values obtained by the correlation equation $\frac{C_t}{Re^n}$ and the numerical simulations do not exceed 3.5%. Therefore, experimental data and numerical data are shown to have supported each other.

### *6.4. Comparison between the prototype rotors and the Savonius canonical rotor*

Fig. 24 shows the superposition of the profiles of the torque coefficient versus rotation angle of the rotor, obtained by means of numerical simulations for the Savonius rotors and prototype canonical rotor for a Reynolds number equal to $7.137 \cdot 10^4$. These results show the effect of the geometrical parameters on the coefficient of torque and coefficient of power. As can be seen in Table 21, the maximum and minimum torque coefficient for the prototype rotors is obtained for a different rotor angle than for the canonical Savonius rotor. While for prototype rotors the point of maximum torque coefficient is obtained for an angle of rotor 110–120° ($C_{t_{max}}(\delta = 0°) = 0.371$, $C_{t_{max}}(\delta = 22.5°) = 0.247$, $C_{t_{max}}(\delta = 45°) = 0.251$) for the canonical Savonius rotor the point of maximum coefficient of torque is obtained for a rotor angle of 50° ($C_{t_{max}} = 0.872$). This indicates that in the prototype rotors the influence of the lift component has a greater effect than the drag component for the force generated by the rotors since the point of maximum torque coefficient is obtained for a rotor angle of 110–120°. However, for the canonical Savonius rotor the drag component has greater influence than the lift component for the force generated by the rotor, because the point of maximum torque coefficient is obtained for a rotor angle of 50°.

Fig. 25 shows a comparison of the coefficient of torque and power coefficient between the prototype rotors and the canonical Savonius rotor for a Reynolds number equal to $7.137 \cdot 10^4$. Table 22 collects the magnitude of the maximum values for each coefficient of torque and power curve for the prototype rotors and the Savonius canonical rotor. These results show that the canonical Savonius rotor generates greater torque and power than prototype rotors at a higher tip speed ratio. This is due to the difference in speed of rotation between the prototype rotors and the Savonius canonical rotor. Whereas in the prototype rotors the maximum coefficient of torque and power is obtained for a tip speed ratio of 0.173, 0.072 and 0.455, respectively, For the Savonius canonical rotor the maximum coefficient of torque and power is obtained for a tip speed ratio of 0.712. That is to say, in order to obtain a coefficient of torque and power analogous to that of the canonical Savonius rotor, the prototype rotors must act with a higher Reynolds number (see Fig. 26).

Finally, Table 22 shows the maximum power coefficient values of the prototype rotors, as well as the tip speed ratio and the Reyndols number corresponding to these maximum values. These maximum power coefficients were compared with the power coefficients obtained in the canonical Savonius rotor for the tip speed ratio of the maximum prototypes rotor power coefficient. These results show an approximate reduction of 49–55% of the power coefficient in the prototype rotors versus the canonical Savonius rotor. In addition, it is verified that as the angle of rotation or torsion δ of the prototype rotors improves the behavior of the prototype rotor and increases the coefficient of torque, power coefficient and mechanical power obtained (Table 23).

## 7. Conclusions

This paper presents the numerical-experimental study of a new

**Table 17**
Comparison between the results obtained experimentally by means of the correlation equation and the numerical simulation, for the prototype rotor δ = 22.5°.

| | TSR | $C_{t_{experimental}}$ | $C_{t_{simulation}}$ | $C_{t_{correlation}}$ | $C_{P_{experimental}}$ | $C_{P_{simulation}}$ | $C_{P_{correlation}}$ |
|---|---|---|---|---|---|---|---|
| $Re = 1.094 \cdot 10^5$ | 0.177 | 0.168 | 0.167 | 0.163 | 0.030 | 0.030 | 0. 30 |
| $Re = 1.419 \cdot 10^5$ | 0.320 | 0.096 | 0.097 | 0.097 | 0.030 | 0.031 | 0.031 |

**Table 19**
Comparison between the results obtained experimentally by means of the correlation equation and the numerical simulation, for the prototype rotor δ = 45°.

| | TSR | $C_{t_{experimental}}$ | $C_{t_{simulation}}$ | $C_{t_{correlation}}$ | $C_{P_{experimental}}$ | $C_{P_{simulation}}$ | $C_{P_{correlation}}$ |
|---|---|---|---|---|---|---|---|
| $Re = 1.094 \cdot 10^5$ | 0.211 | 0.174 | 0.173 | 0.180 | 0.037 | 0.037 | 0.038 |
| $Re = 1.311 \cdot 10^5$ | 0.309 | 0.136 | 0.135 | 0.138 | 0.042 | 0.042 | 0.043 |

**Table 20**
Error in the approximation of the correlation equation and the numerical simulation for the prototype rotor δ = 45°.

| | Correlation difference [%] | Simulation difference [%] |
|---|---|---|
| $Re = 1.094 \cdot 10^5$ | 3.448 | 0.575 |
| $Re = 1.311 \cdot 10^5$ | 1.471 | 0.735 |

**Table 21**
Maximum torque coefficient versus rotor angle at a Reynolds number $7137 \cdot 10^4$ for the prototype rotors and the canonical Savonius rotor.

| $Re = 7.137 \cdot 10^4$ | Savonius rotor | Prototype rotors | | |
|---|---|---|---|---|
| | | δ = 0° | δ = 22.5° | δ = 45° |
| $C_{t_{max}}$ | 0.872 | 0.371 | 0.247 | 0.251 |
| $C_{t_{min}}$ | −0.065 | −0.015 | −0.082 | −0.098 |
| Location of $C_{t_{max}}$ [°] | 50° | 110° | 120° | 110° |
| Location of $C_{t_{min}}$ [°] | 160° | 40° | 40° | 40° |

rotor, adapted from a conventional Savonius rotor, to which aesthetic, ergonomic and functional requirements have been incorporated, allowing it to form an integral part of sustainable consumer products. Both studies aim to evaluate the performance of the new rotor. A set of translational, rotational and scale symmetry operations was applied to the bucket sections of a canonical Savonius rotor in order to transform the base cylindrical surfaces into organic type surfaces easily integrated into the product environment. The rotor has been designed in parametric format allowing it to adapt automatically to different products by simply changing its dimensions.

In order to validate the performance of the rotor, this was applied to a patented consumer product integrated into its geometry. The reduced dimensions of the device in which it was integrated and its requirement of lateral accessibility to the inside shaft of the rotor enabled the performance of the rotor to be obtained in design conditions outside the optimum range of the technical parameters of the rotor. The modified Savonius rotor has been compared to a conventional Savonius rotor with the same aspect ratio in terms of power coefficient, torque coefficient and mechanical power generated.

The new rotor was tested in an open jet wind tunnel in order to verify the level of influence of product design parameters on rotor performance. Experiments were carried out for Reynolds values included in the range of [$3.436 \cdot 10^4$ y $1.419 \cdot 10^5$]. The experimental results have been validated with a numerical analysis using an incompressible unsteady Reynolds average Navier-Stokes model, obtaining a deviation of 3.5% between the experimental results and those obtained numerically. For the range of tip speed ratio values between 0.223 and 0.335, the rotor fulfills the functional requirements of the product of small-scale power generation, although in view of the results an increase in the speed of operation analyzed previously in the paper would be favorable.

The set of symmetry and translation operations performed on the canonical Savonius rotor greatly influences the design parameters of the rotor $\beta_x$ and $\beta_y$, increasing its value and affecting its performance. This can be improved in those designs where a large value of lateral accessibility is not required, decreasing the value of the parameters $\beta_x$ and $\beta_y$ and which would favorably influence the performance of the rotor. Introducing the golden ratio in the dimensioning of the rotor greatly improves the harmonic proportions of the product, making it better integrated into the environment. The scaling process of the sections causes the value of $\beta_y$ to be variable along the height of the rotor, decreasing by 61.80% from the central sections to the ends. The aspect

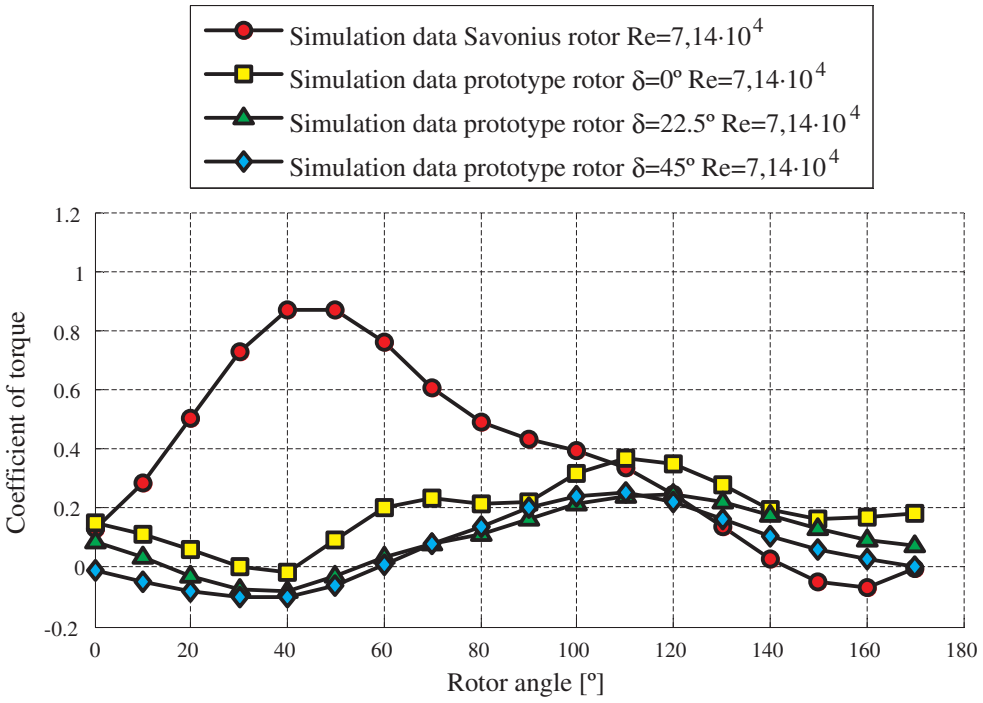


**Fig. 24.** Comparison of Ct vs Rotor angle at a Reynolds number $7.137 \cdot 10^4$ for the prototype rotors and the canonical Savonius rotor.

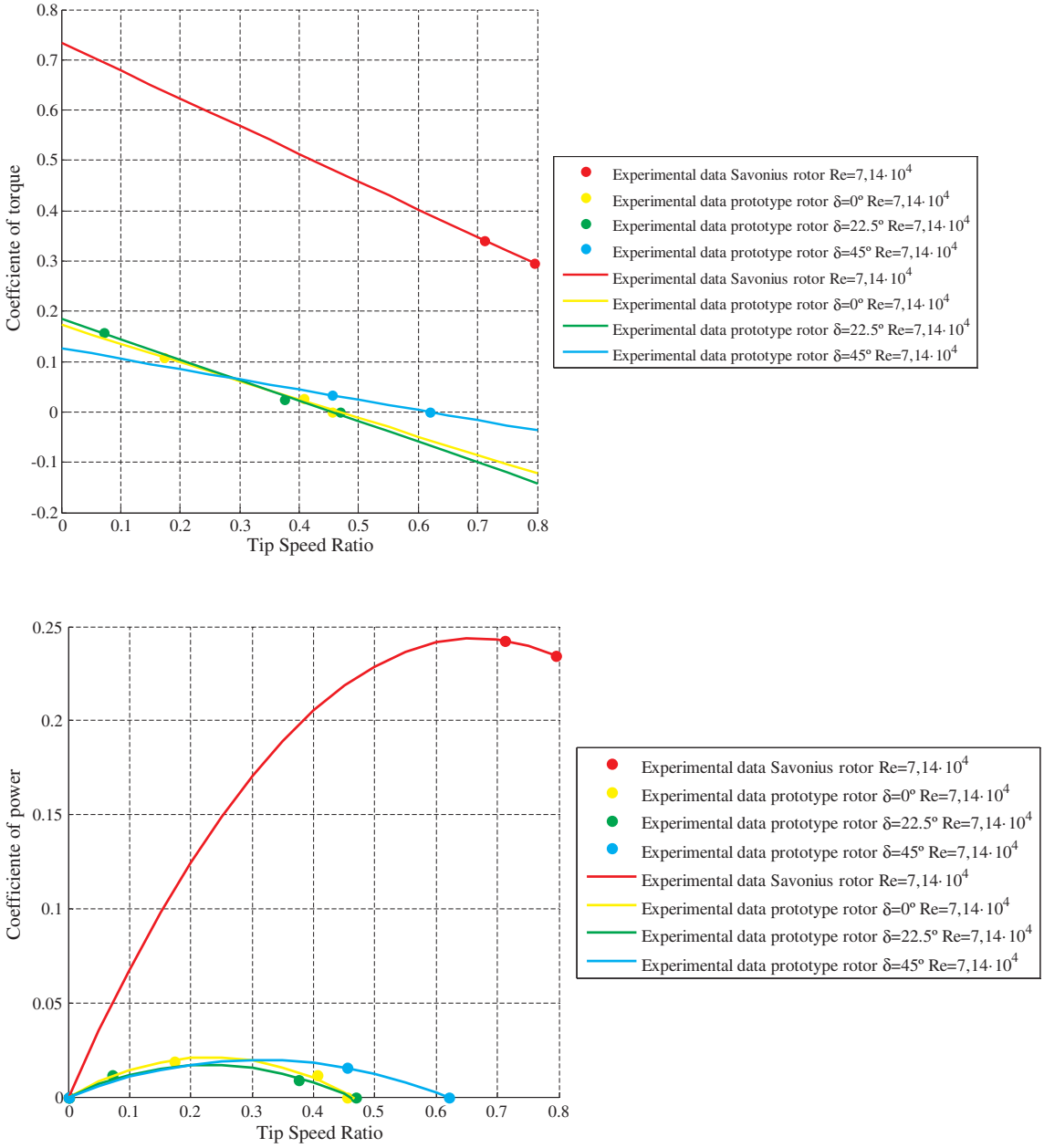


**Fig. 25.** Comparison of Ct vs TSR and Cp vs TSR to a Reynolds number $7.137 \cdot 10^4$ for the prototype rotors and the canonical Savonius rotor.

**Table 22**
Coefficient of torque and coefficient of power with maximum tip speed ratio at a number of Reynolds $7.137 \cdot 10^4$ for prototype rotors and Savonius rotor.

| $Re = 7.137 \cdot 10^4$ | | $C_{t_{max}}$ | $C_{p_{max}}$ | TSR at $C_{p_{max}}$, $C_{t_{max}}$ |
|---|---|---|---|---|
| Prototype rotors | δ = 0° | 0.108 | 0.019 | 0.173 |
| | δ = 22.5° | 0.158 | 0.011 | 0.072 |
| | δ = 45° | 0.034 | 0.015 | 0.455 |
| Savonius rotor | | 0.341 | 0.243 | 0.712 |

ratio AR for the new rotor has a value of 1.608, equal to the golden number, being within the range of recommended values for good technical performance.

The behavior of the rotors with different rotation angles in the sections of their buckets has been analyzed, observing that as the value of the rotation angle δ increases, the speed of the rotor increases, improving the power coefficient and the tip speed ratio, as well as the mechanical power generated. For a rotation angle δ of 45°, the power coefficient values improve by 32% compared to the values obtained for the angle 0°. The experimental and numerical analyses performed on the new rotor show a lower speed ratio compared to that of the conventional Savonius rotor. This indicates that the rotation speed of the new rotor is lower than the Savonius rotor, as it is shown that the Reynolds numbers at which the experimental tests of the new rotor have been performed are higher than in the Savonius rotor. This fact indicates a more favorable operation for the new rotor within a range of wind speeds superior to the range of the Savonius.

The new rotor is born as a suitable variant of the Savonius rotor for small-scale energy applications, or to reduce the energy consumption of products where aesthetic and ergonomic requirements are necessary for sale. The new rotor maintains the advantages of the Savonius rotor at the same time that it integrates perfectly into the geometry of the product, giving it personality and making it desirable for consumers. The new rotor is part of a new line of research consisting of incorporating technical elements capable of contributing to the energy generation of the product, fulfilling its own requirements of aesthetic

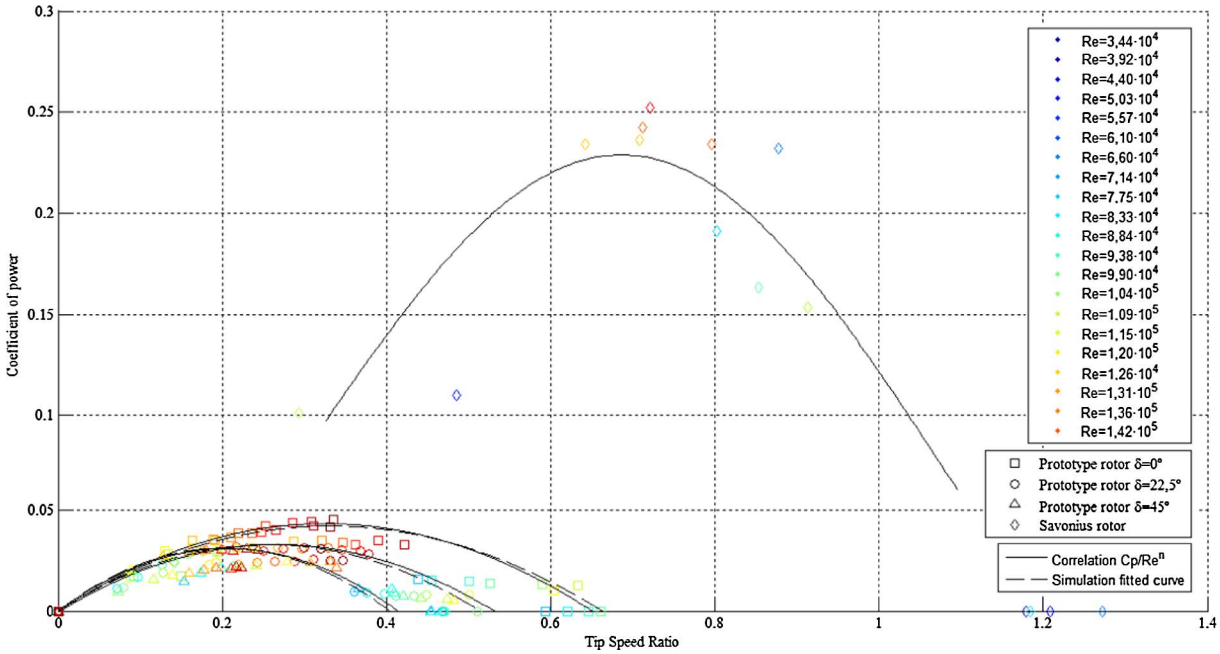


**Fig. 26.** Comparison of Cp vs TSR at a Reynolds number between $3.436 \cdot 10^4$ and $1.419 \cdot 10^5$ for the prototype rotors and the canonical Savonius rotor. Results obtained experimentally and by means of the correlation equation.

**Table 23**
Comparison of maximum power coefficients for prototype rotors and power coefficients for the Savonius rotor a tip speed ratio of the maximum prototypes rotor power coefficient.

| Prototype rotors | $C_{p_{max}}$ | Corresponding Reynolds number | TSR at $C_{p_{max}}$ | Savonius $C_p$ at TSR of the maximum rotor power coefficient | $C_{t,C_p}$ difference [%] |
|---|---|---|---|---|---|
| δ = 0° | 0.031 | $1.36 \cdot 10^5$ | 0.229 | 0.070 | 55.714 |
| δ = 22.5° | 0.032 | $1.20 \cdot 10^5$ | 0.217 | 0.0670 | 52.239 |
| δ = 45° | 0.046 | $1.36 \cdot 10^5$ | 0.335 | 0.091 | 49.451 |

and ergonomic design with the aim of improving the urban sustainability of society.

## Acknowledgments

This work has been supported by the University of Jaen through the project titled " Diseño de un bastón ecológico de senderismo generador eólico hidraulico" Project Code (AC20/2015-12) and (R1 A7/2017). The authors would like to thank the Mechanical Engineering Department at Jaen University for using the wind tunnel to achieve the experimental study. The authors would like to thank the reviewers for comments that improved the exposition.

## References

[1] Marinić-Kragić I, Vučina D, Milas Z. Numerical workflow for 3D shape optimization and synthesis of vertical-axis wind turbines for specified operating regimes. Renewable Energy 2018;115:113–27.
[2] Roy S, Saha UK. An adapted blockage factor correlation approach in wind tunnel experiments of a Savonius-style wind turbine. Energy Convers Manage 2014;86:418–27.
[3] Al-Hadhrami LM. Performance evaluation of small wind turbines for off grid applications in Saudi Arabia. Energy Convers Manage 2014;81:19–29.
[4] Bangga G, Lutz T, Jost E, Krämer E. CFD studies on rotational augmentation at the inboard sections of a 10 MW wind turbine rotor. J Renewable Sustainable Energy 2017;9(2):023304.
[5] Mereu R, Federici D, Ferrari G, Schito P, Inzoli F. Parametric numerical study of Savonius wind turbine interaction in a linear array. Renewable Energy 2017;113:1320–32.
[6] Roy S, Das R, Saha UK. An inverse method for optimization of geometric parameters of a Savonius-style wind turbine. Energy Convers Manage 2018;155:116–27.
[7] Ducoin A, Shadloo MS, Roy S. Direct Numerical Simulation of flow instabilities over Savonius style wind turbine blades. Renewable Energy 2017;105:374–85.
[8] Goodarzi M, Keimanesh R. Numerical analysis on overall performance of Savonius turbines adjacent to a natural draft cooling tower. Energy Convers Manage 2015;99:41–9.
[9] Saha UK, Rajkumar MJ. On the performance analysis of Savonius rotor with twisted buckets. Renewable Energy 2006;31(11):1776–88.
[10] Roy S, Saha UK. Wind tunnel experiments of a newly developed two-bucketd Savonius-style wind turbine. Appl Energy 2015;137:117–25.
[11] Kamoji MA, Kedare SB, Prabhu SV. Experimental investigations on single stage modified Savonius rotor. Appl Energy 2009;86(7):1064–73.
[12] Roy S, Ducoin A. Unsteady analysis on the instantaneous forces and moment arms acting on a novel Savonius-style wind turbine. Energy Convers Manage 2016;121:281–96.
[13] Tian W, Mao Z, Zhang B, Li Y. Shape optimization of a Savonius Wind Rotor with Different Convex and Concave Sides. Renewable Energy 2017.
[14] Lee JH, Lee YT, Lim HC. Effect of twist angle on the performance of Savonius wind turbine. Renewable Energy 2016;89:231–44.
[15] Damak A, Driss Z, Abid MS. Experimental investigation of helical Savonius rotor with a twist of 180. Renewable Energy 2013;52:136–42.
[16] Yang HB. Wind Tunnel study on the performance characteristics of SAvonius Wind Turbine [Master Thesis]. Pusan National University; 2013.
[17] Al-Kayiem HH, Bhayo BA, Assadi M. Comparative critique on the design parameters and their effect on the performance of S-rotors. Renewable Energy 2016;99:1306–17.
[18] Roy S, Saha UK. Review of experimental investigations into the design, performance and optimization of the Savonius rotor. Proc Inst Mech Eng, A: J Power Energy 2013;227(4):528–42.
[19] Blackwell BF, Sheldahl RF, Feltz LV. Wind tunnel performance data for two-and three-bucket Savonius rotors. Albuquerque (NM): Sandia Laboratories; 1977.
[20] Saha UK, Thotla S, Maity D. Optimum design configuration of Savonius rotor through wind tunnel experiments. J Wind Eng Ind Aerodyn 2008;96(8):1359–75.
[21] Akwa JV, da Silva Júnior GA, Petry AP. Discussion on the verification of the overlap ratio influence on performance coefficients of a Savonius wind rotor using computational fluid dynamics. Renewable Energy 2012;38(1):141–9.
[22] Fujisawa N. On the torque mechanism of Savonius rotors. J Wind Eng Ind Aerodyn 1992;40(3):277–92.
[23] Ushiyama I, Nagai H. Optimum design configurations and performance of Savonius rotors. Wind Eng 1988:59–75.
[24] Jian C, Kumbernuss J, Linhua Z, Lin L, Hongxing Y. Influence of phase-shift and overlap ratio on Savonius wind turbine's performance. J Sol Energy Eng 2012;134(1):1–9.
[25] Ali MH. Experimental comparison study for Savonius wind turbine of two & three buckets at low wind speed. Int J Modern Eng Res (IJMER) 2013;3(5):2978–86.
[26] Mahmoud NH, El-Haroun AA, Wahba E, Nasef MH. An experimental study on improvement of Savonius rotor performance. Alexand Eng J 2012;51(1):19–25.
[27] Hayashi T, Yan LI, Yutaka HARA. Wind tunnel tests on a different phase three-stage Savonius rotor. JSME Int J, Ser B 2005;48(1):9–16.

[28] Menet JL. A double-step Savonius rotor for local production of electricity: a design study. Renewable Energy 2004;29(11):1843–62.
[29] Altan BD, Atılgan M. The use of a curtain design to increase the performance level of a Savonius wind rotors. Renewable Energy 2010;35(4):821–9.
[30] Altan BD, Altan G, Kovan V. Investigation of 3D printed Savonius rotor performance. Renewable Energy 2016;99:584–91.
[31] Mohamed MH, Janiga G, Pap E, Thévenin D. Optimization of Savonius turbines using an obstacle shielding the returning bucket. Renewable Energy 2010;35(11):2618–26.
[32] Sharma S, Sharma RK. Performance improvement of Savonius rotor using multiple quarter blades–A CFD investigation. Energy Convers Manage 2016;127:43–54.
[33] Sharma S, Sharma RK. CFD investigation to quantify the effect of layered multiple miniature blades on the performance of Savonius rotor. Energy Convers Manage 2017;144:275–85.
[34] Korprasertsak N, Leephakpreeda T. Analysis and optimal design of wind boosters for Vertical Axis Wind Turbines at low wind speed. J Wind Eng Ind Aerodyn 2016;159:9–18.
[35] Alexander AJ, Holownia BP. Wind tunnel tests on a Savonius rotor. J Wind Eng Ind Aerodyn 1978;3(4):343–51.
[36] Krause CL. Our visual landscape: managing the landscape under special consideration of visual aspects. Landscape Urban Plann 2001;54(1):239–54.
[37] Chong WT, Pan KC, Poh SC, Fazlizan A, Oon CS, Badarudin A, et al. Performance investigation of a power augmented vertical axis wind turbine for urban high-rise application. Renewable Energy 2013;51:388–97.
[38] Müller G, Chavushoglu M, Kerri M, Tsuzaki T. A resistance type vertical axis wind turbine for building integration. Renewable Energy 2017;111:803–14.
[39] Orlandi A, Collu M, Zanforlin S, Shires A. 3D URANS analysis of a vertical axis wind turbine in skewed flows. J Wind Eng Ind Aerodyn 2015;147:77–84.
[40] Bangga G, Lutz T, Dessoky A, Krämer E. Unsteady Navier-Stokes studies on loads, wake, and dynamic stall characteristics of a two-bladed vertical axis wind turbine. J Renewable Sustainable Energy 2017;9(5):053303.
[41] Ferrari G, Federici D, Schito P, Inzoli F, Mereu R. CFD study of Savonius wind turbine: 3D model validation and parametric analysis. Renewable Energy 2017;105:722–34.
[42] Bhuyan S, Biswas A. Investigations on self-starting and performance characteristics of simple H and hybrid H-Savonius vertical axis wind rotors. Energy Convers Manage 2014;87:859–67.
[43] Simões T, Estanqueiro A. A new methodology for urban wind resource assessment. Renewable Energy 2016;89:598–605.
[44] Lockwood T. Design thinking: integrating innovation, customer experience, and brand value. Skyhorse Publishing Inc.; 2010.
[45] Karlsson R, Luttropp C. EcoDesign: what's happening? An overview of the subject area of EcoDesign and of the papers in this special issue. J Cleaner Prod 2006;14(15):1291–8.
[46] Walker James. Golden Ratio axial flow apparatus. Patent Number US9328717; 2016.
[47] Choy Nam Hyun. A rotor for wind power generator. Patent Number KR101590054; 2016.
[48] https://enessere.com/it/hercules/hercules-wind-turbine/.
[49] http://enessere.com/en/enessere-won-the-focus-open-silver-design-award-in-germany/.
[50] http://www.newwind.fr/.
[51] Benyus JM. Biomimicry. New York: William Morrow; 1997. p. 1.
[52] http://leviathanenergy.com/technology/wind-tulips/.
[53] Lidwell W, Holden K, Butler J. Universal principles of design, revised and updated: 125 ways to enhance usability, influence perception, increase appeal, make better design decisions, and teach through design. Rockport Pub; 2010.
[54] Martin-Doñate Cristina, Rubio-Paramio Miguel Angel, Mercado-Colmenero Jorge Manuel, Rus Casas Catalina. Bastón electrónico de senderismo. ES2598296B2; 2017.
[55] http://www.lavanguardia.com/tecnologia/20170717/424184267868/patentan-un-baston-de-senderismo-que-permite-recargar-dispositivos-moviles.html.
[56] Tilley A. The measure of man and woman: human factors in design; 1993.
[57] http://www.ansys.com/es.
[58] http://www.solidworks.es.
[59] Altan Burçin Deda, Atılgan Mehmet. An experimental and numerical study on the improvement of the performance of Savonius wind rotor. Energy Convers Manage 2008;49:3425–32.
[60] Howell Robert, Qin Ning, Edwards Jonathan, Durrani Naveed. Wind tunnel and numerical study of a small vertical axis wind turbine. Renewable Energy 2010;35:412–22.
[61] Tian Wenlong, Song Baowei, VanZwieten James H, Pyakurel Parakram. Computational fluid dynamics prediction of a modified Savonius wind turbine with novel blade shapes. Energies 2015;8:7915–29.
[62] Rogowski Krzysztof, Maronski Ryszard. CFD computation of the Savonius Rotor. J Theoret Appl Mech 2015;53(2015):37–45.
[63] Altan Burcin Deda, Altan Gurkan, Kovan Volkan. Investigation of 3D printed Savonius rotor performance. Renewable Energy 2016;99:584–91.
[64] ANSYS FLUENT Theory Guide. http://ansys.com.
[65] Bangga G, Thorsten L, Kramer E. Root flow characteristics and 3D effects of an isolated wind turbine rotor. J Mech Sci Technol 2017;31(8):3839–44.

**Jorge Manuel Mercado Colmenero** received his B.Eng and M.Eng. in Mechanical Engineering in 2012 and 2014 respectivily from the University of Jaén in Spain. In 2014 he joined the Design, Engineering Graphics and Project departament at Jaen university as a PhD student. He is currently developing his thesis about automatic analyses and design of injection plastic mold, including demoldability, ejection system, cooling system design and CAD-CAE design and manufacturing.

**Dr. Miguel Angel Rubio Paramio** received his MEng and Ph.D in Mechanical Engineering in 1992 and 2000 respectively from Polytechnic University of Madrid in Spain. In 1994 he joined the University of Jaen and currently he teaches courses of Computer-aided Design, Manufacturing and Engineering in the Engineering Graphics, Design and Projects Department. His thesis was focused on automatic analysis of injection plastic part. His research interests include CAD-CAM-CAE, Design for Manufacturing, computational geometry, constraint-based parametric modeling, and their applications on plastic injection mold design and manufacturing.

**Francisca Guerrero-Villar** received his B.Eng and M.Eng. in Mechanical Engineering from the University of Sevilla in Spain She worked for several years (2007–2013) as top head of the Technological Center CETEMET. She has been main researcher in two INNTERCONECTA call grant competitive projects (SEAMAR, ODISEO), and in a INNPACTO call grant competitive project (INNVEXTRAN).Since 2014 until now is a researcher at the Jaen University specialized in renewable energy.

**Dr. Cristina Martín Doñate** received her B.Eng. and M.Eng. in Electrical - Electronics Engineering and Industrial Engineering (Polytechnic University of Valencia - Spain) in 1997 and Ph.D in Industrial Engineering (University of Jaen - Spain) in 2010. She worked for several years as project manager on developing new products in automotive manufacturing industries. She developed research at the Technical University of Graz in Austria, and at the University of Applied sciences of Rosenheim in Germany in the field of manufacturing systems. She is currently Professor at Jaen University where she develops research and conduct research projects in manufacturing systems, plastic injection mold design and technology, CAD systems and new products development.

# 2.2. COMUNICACIONES A CONGRESOS INTERNACIONALES

1. **Mercado-Colmenero, Jorge Manuel,** Almazán-Lazaro, M.A., Martín-Doñate, Cristina, Rubio-Paramio, M.A., Vizán-Idoipe, A., Perez-Garcia, J.M., Marquez-Sevillano, J., Aguilera-Puerto, D. *Analytical calculation model for determining the cycle time in injection molding parts applied to design optimization algorithms (2017). High Performance and Optimum Design of Structures and Materials II (HPSM/OPTI) (2016), 166, 427-438. DOI: http://dx.doi.org/10.2495/HPSM16040.*

2. Martín-Doñate, Cristina, **Mercado-Colmenero, Jorge Manuel**, Rubio-Paramio, Miguel Angel, Vizan-Idoipe, Antonio, Perez-Garcia, Jesus Maria, Marquez-Sevillano, Juan de Juanes, Aguilera-Puerto, Daniel. *Automated system for injection mold design and cost calculation. Objetives and opportunities. XXV International Conference on Graphics Engineering "New Horizons in Graphics Engineering" (2015). Proceedings of the XXV International Conference on Graphics Engineering (2015).132-137.ISBN: 978-84-8081-464-5*

3. Martín-Doñate, Cristina, **Mercado-Colmenero, Jorge Manuel**, Rubio-Paramio, Miguel Angel. *Application of plastic parts discretization for analyzing geometric demoldability. XXV International Conference on Graphics Engineering "New Horizons in Graphics Engineering" (2015). Proceedings of the XXV International Conference on Graphics Engineering (2015).126-131. ISBN: 978-84-8081-464-5*

4. **Mercado-Colmenero, Jorge Manuel**, Rubio-Paramio, Miguel Angel, Martín-Doñate, Cristina. *Method for obtaining an ejection map in ejection molded parts. XXVII International Conference on Graphics Engineering "New research and collaboration models in Graphic Engineering" (2017). Proceedings of the XXVII International Conference on Graphics Engineering (2017).129-133. ISBN: 978-84-16664-64-7*

# 2.3. PATENTES DE INVENCIÓN NACIONALES E INTERNACIONALES

Patentes de Invención Nacionales:

1. Inventores: Martín-Doñate, Cristina, Rubio-Paramio, Miguel Ángel, Vizán-Idoipe, Antonio, **Mercado-Colmenero, Jorge Manuel**. Título: Método y sistema de obtención de geometrías virtuales y detección de zonas no moldeables en piezas. Fecha de concesión: 19.09.2017. ES 2 594 772 B2.

2. Inventores: **Mercado-Colmenero, Jorge Manuel**, Martín-Doñate, Cristina, Rubio-Paramio, Miguel Ángel, Pérez-García, Jesús María. Título: Procedimiento para el diseño del sistema de varillas de expulsión para un molde. Fecha de concesión: 04.05.2017. ES 2 595 099 B2.

3. Inventores: Martín-Doñate, Cristina, Rubio-Paramio, Miguel Ángel, **Mercado-Colmenero, Jorge Manuel**, Rus-Casas, Catalina. Título: Bastón electrónico de senderismo. Fecha de concesión: 18.05.2017. ES 2 598 296 B2.

4. Inventores: Martín-Doñate, Cristina, Rubio-Paramio, Miguel Ángel, Vizán-Idoipe, Antonio, **Mercado-Colmenero, Jorge Manuel**. Título: Método de verificación automatizada de modificaciones en el plegado de piezas de chapa estampadas en frío. Fecha de concesión: 18.04.2018. ES 2 651 196 B2.

Patentes de Invención Internacionales:

1. Inventores: Martín-Doñate, Cristina (ES), Rubio-Paramio, Miguel Ángel (ES), **Mercado-Colmenero, Jorge Manuel** (ES), Rus-Casas, Catalina (ES). Título: Electronic Hiking Pole. Fecha de concesión: 25.01.2018. WO2018015604 (WO/2018/015604).

Esta última patente ha tenido un mayor impacto mediático. Pues la noticia de la invención de este nuevo producto ha tenido difusión en más de 100 medios nacionales e internacionales de prensa escrita, prensa web, radio, televisión y redes sociales. Destacando la intervención de Cristina Martín (Inventora y Directora de la presente tesis) en el programa de internacional de radiotelevisión "Marca España" (dirigido por el Ministerio de Ciencia, Innovación y Universidad, dentro del marco "Estrategia española de Ciencia y Tecnología y de Innovación"), que muestra el impacto de internacional de la presente patente y su contribución a reforzar el concepto de la "Marca España" en el contexto de investigación internacional. Asimismo se adjunta la página web del producto, donde se recoge toda la divulgación mediática de la invención (http://www.ujaen.es/investiga/bastonelectronicosenderismo/).